



Universidade do Minho  
Escola de Engenharia

Farhad Akhoundi | Strategies for Seismic Strengthening of  
Masonry Infilled Reinforced Concrete Frames

Farhad Akhoundi

Strategies for Seismic Strengthening of  
Masonry Infilled Reinforced Concrete Frames



Universidade do Minho  
Escola de Engenharia

Farhad Akhouni

Strategies for Seismic Strengthening of  
Masonry Infilled Reinforced Concrete Frames

Doctoral Thesis  
Civil Engineering

Work performed under the supervision of  
Prof. Graça Vasconcelos  
Prof. Paulo Lourenço

July 2016

## STATEMENT OF INTEGRITY

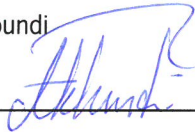
I hereby declare having conducted my thesis with integrity. I confirm that I have not used plagiarism or any form of falsification of results in the process of the thesis elaboration.

I further declare that I have fully acknowledged the Code of Ethical Conduct of the University of Minho.

University of Minho, \_\_\_\_\_

Full name: Farhad Akhondi

Signature: \_\_\_\_\_



## Acknowledgments

The research presented in this dissertation was a unique opportunity to meet and collaborate with a number of great individuals. Of course this endeavor wouldn't have been possible without the financial support of the Portuguese Foundation of Science and Technology for the funding of the project RetroInf– Development of innovative solutions for seismic retrofitting of masonry infill walls (PTDC/ECM/122347/2010).

First, I would like to express my sincere gratitude to my supervisors Prof. Paulo Lourenço and Prof. Graça Vasconcelos for the continuous support of my Ph.D study, for the patience, motivation, and immense knowledge. Not only did they provide me with their exceptional guidance, but they offered me all necessary resources to conduct my research and expand my horizons and interact with other researchers around the world. They always trusted me, encouraged me, supported me and made me feel Portugal as my second home.

I also would like to thank António Matos, Carlos Palha, Marco Jorge, Andreia Martins and Luis Silva for their help and insightful comments during experimental tests in the Civil Engineering Laboratory.

I am also thankful to Prof. Luis Ramos, Dr. Nuno Mendes and Ana Teixeira for their guidance and support during the experimental and numerical program.

I am also hugely appreciative to Prof. Kaynejhad for his kind support.

A special thanks to my family. Words cannot express how grateful I am to my mother-in-law, father-in-law, my mother, my father, my brothers and sister for all of the sacrifices that you've made on my behalf. I would also like to thank to my beloved wife. Thank you for supporting me for everything, and especially I can't thank you enough for encouraging me throughout this experience. To my beloved son, Alp, I would like to express my thanks for being such a good boy always cheering me up.

Finally I thank my God, for letting me through all the difficulties. I have experienced your guidance day by day. You are the one who let me finish my degree.

## Resumo

A vulnerabilidade sísmica de edifícios de betão armado preenchidos com paredes de alvenaria tem vindo a ser constatada durante sismos recentes no sul da Europa, causando um número elevado de mortos e elevados custos de reabilitação ou reconstrução, e justifica a necessidade de estudos detalhados acerca do comportamento sísmico de pórticos de betão armado preenchidos com alvenaria construídos em países do sul da Europa desde 1960. Apesar de existirem vários trabalhos em paredes de enchimento, não existe muita investigação em paredes de enchimento tradicionais do sul da Europa.

Assim, os principais objetivos desta tese consistem em: (1) conseguir uma compreensão do comportamento cíclico no plano e fora do plano de paredes de enchimento tradicionais construídas nas últimas décadas em Portugal; (2) analisar o desempenho de diferentes técnicas de reforço com o objetivo de melhorar o comportamento sísmico das paredes de enchimento; (3) analisar os principais parâmetros que influenciam o comportamento de pórticos de betão armado preenchidos com paredes de enchimento a ações no plano. No sentido de atingir os objetivos propostos, foi definido um plano de trabalhos baseado em análise experimental e numérico. O programa experimental foi composto por três fases, nomeadamente: (1) ensaios estáticos cíclicos no plano; (2) ensaios cíclicos para fora do plano; (3) validação experimental de diferentes técnicas de reforço (argamassa de reboco reforçada e conectores metálicos). Para este efeito foram dimensionados pórticos de betão armados com paredes de enchimento à escala reduzida com base num protótipo seleccionado, considerado representativo da construção tradicional nas últimas décadas.

Foram ensaiados cinco pórticos sujeitos a ações no plano, nomeadamente um pórtico simples, um pórtico com parede de enchimento até à rotura, e três pórticos preenchidos sujeitos a diferentes níveis de deformação lateral (drift de 0.3%, 0.5% e 1%) com o objetivo de impor diferentes níveis de dano e avaliar o seu efeito no comportamento das paredes de alvenaria sujeitas a ações fora do plano. Seis pórticos preenchidos foram ensaiados a ações para fora do plano para caracterizar a influência da qualidade da mão-de-obra, a presença de aberturas e o dano no plano induzido previamente. Os ensaios para fora do plano foram realizados em controlo de deslocamento e a força foi aplicada através de um airbag. O desempenho do reforço através de argamassa reforçada e a ligação dos panos das paredes duplas através de ligadores metálicos também foi avaliado experimentalmente. Para o reboco armado foram seleccionadas duas malhas de reforço à base de fibras de vidro, sendo uma comercial e outra desenvolvida no departamento de Engenharia Têxtil da Universidade do Minho. Com base nos resultados experimentais foi possível concluir que a presença das paredes de enchimento altera significativamente a rigidez e a resistência quando se compara o comportamento do pórtico simples e preenchido. A mão-de-obra tem um papel importante no comportamento das paredes a ações no plano e fora do plano. Verifica-se também que as paredes de enchimento com mais dano prévio apresentam uma resistência e rigidez mais baixa. O reboco armado melhora consideravelmente o comportamento no plano mas a sua eficiência para ações para fora do plano é muito moderada.

O trabalho numérico incluiu a modelação de pórticos preenchidos para ações no plano através de elementos finitos e com base num programa de cálculo comercial. Após a calibração com base em resultados experimentais disponíveis na literatura, foi efetuada uma análise paramétrica com

enfoque na avaliação da influência da distribuição aleatória de aberturas no comportamento no plano. Concluiu-se que as paredes de enchimento com uma distribuição de aberturas aleatória podem ser representadas por bielas equivalentes com uma espessura que tenha em consideração a presença de aberturas. Foi feita ainda a calibração de um modelo numérico para a análise de paredes de enchimento a ações para fora do plano.

## Abstract

Seismic vulnerability of masonry infilled frames observed during past earthquakes in south Europe, caused death of thousands of people and left huge repair or reconstruction costs, justifies the need of deep study of the seismic behavior of masonry infilled frames constructed in South European Countries since 1960s. In spite of several works have been carried out on masonry infills, there is no much investigation on south European traditional infills.

Therefore, the main goals of this thesis are related to (1) better understanding of the cyclic in-plane and out-of-plane behavior of traditional brick infills built in the past decades as enclosures in reinforced concrete (rc) buildings; (2) analysis of different strengthening solutions aiming at enhancing their in-plane and out-of-plane behavior; (3) systematic analysis of the main parameters influencing the in-plane behavior of rc frames with brick infills. To accomplish the defined objectives, extensive experimental and numerical analysis were carried out. The experimental campaign was composed of three phases, namely; (1) static cyclic in-plane testing; (2) out-of plane testing; (3) experimental validation of different strengthening solutions (textile reinforced mortar technique and steel ties). Reduced scale rc frames with brick infills were designed based on a selected prototype representative of construction tradition of rc buildings in the last decades.

Five reduced scale specimens were tested under in-plane loading, namely one bare frame, one rc frame with brick infill tested until failure and more three specimens subjected to different lateral drifts (0.3%, 0.5% and 1%) to impose distinct levels of damage and to investigate the effect of this damage in their out-of-plane response. Six specimens were tested in the out-of-plane direction to characterize the influence of workmanship, presence of central opening and of existence of prior in-plane damage on the out-of-plane response. The out-of-plane testing was performed under displacement control method by using an airbag. The performance of the textile reinforced mortar applied on the surfaces of the brick infills and of the connection of the leaves of the traditional double leaf walls were also evaluated experimentally. For the textile reinforced mortar technique two different types of meshes were used, namely a commercial textile mesh and a textile mesh that was developed at the university in collaboration with the textile department. It was concluded that presence of infill inside the bare frame could significantly enhance the in-plane stiffness and resistance of bare frame. The workmanship played an important role in the in-plane and out-of-plane behaviour of rc frames with brick infills. It is also found that specimens with higher in-plane damage presented lower out-of-plane stiffness and resistance. It was also concluded that TRM technique could enhance the in-plane behaviour of infilled frames but its efficiency on the out-of-plane was very moderate.

Numerical modelling of one-bay and one-storey masonry-infilled reinforced concrete frames was performed using commercial software. After the calibration based on experimental results available in literature, a parametric study was carried out focusing on the evaluation of the influence of random distribution of openings in the in-plane behaviour of the infilled frames. It was also concluded that infill panels with any type of opening can be replaced by an equivalent diagonal strut, whose width can be calculated according to the proposed formula, taking into account different types of openings and relative positioning within the masonry infill. Additionally, the calibration of a numerical model for describing the out-of-plane behaviour was also carried out.

# Table of Contents

<b>Resumo .....</b>	<b>iv</b>
<b>Table of Contents .....</b>	<b>vii</b>
<b>List of Tables .....</b>	<b>x</b>
<b>List of Figures .....</b>	<b>xii</b>
<b>1 Introduction .....</b>	<b>1</b>
1.1 Objectives and methodology .....	3
1.2 Thesis Outline .....	4
<b>2 Literature Review.....</b>	<b>7</b>
2.1 In-Plane behavior of masonry infilled frames.....	8
2.1.1 Insight into experimental investigations .....	9
2.1.2 Empirical formulas to predict stiffness and strength .....	12
2.1.3 Numerical investigation.....	16
2.2 Out-of-plane behavior of masonry infilled frames .....	21
2.2.1 Experimental investigation .....	22
2.2.2 Numerical investigation.....	27
2.3 Retrofitting techniques of masonry infilled frames .....	28
2.3.1 Composite Materials.....	29
2.4 Textile reinforced mortar (TRM) technique.....	31
<b>3 Experimental assessment of the in-plane behavior of masonry infilled reinforced concrete frames.....</b>	<b>36</b>
3.1 Introduction .....	36
3.2 Characterization of Prototype .....	36
3.3 Design of reduced-scale specimens .....	39
3.4 Characterization of reduced-scale specimens.....	41
3.5 Construction of the specimens .....	42
3.6 Experimental setup and instrumentation .....	44
3.7 Loading Protocol .....	46
3.8 Experimental results .....	47
3.8.1 Specimen BF-I.....	47
3.8.2 Specimen SIF-I-2L(NC)-A.....	52
3.8.3 Specimen SIF-IO(0.3%)-2L(NC)-B .....	61
3.8.4 Specimen SIF-IO(0.5%)-2L(NC)-B .....	65
3.8.5 Specimen SIF-IO(1%)-2L(NC)-B .....	73
3.9 Comparison of the results of the specimens.....	81
3.10 Conclusions.....	85



<b>4</b>	<b>Experimental assessment of the out-of-plane behavior of masonry infilled reinforced concrete frames.....</b>	<b>88</b>
4.1	<i>Introduction</i> .....	88
4.2	<i>Characterization of the specimens</i> .....	88
	SIF-O-1L-B .....	89
	PIF-O-1L-B .....	89
	SIF-IO(0.3%)-2L(NC)-B .....	89
4.3	<i>Experimental setup and instrumentation</i> .....	89
4.4	<i>Loading pattern</i> .....	91
4.5	<i>Experimental results</i> .....	92
4.5.1	Specimen SIF-O-1L-A .....	92
4.5.2	Specimen SIF-O-1L-B.....	99
4.5.3	Specimen PIF-O-1L-B.....	106
4.5.4	Specimen SIF-IO(0.3%)-2L(NC)-B .....	112
4.5.5	Specimen SIF-IO(0.5%)-2L(NC)-B .....	119
4.5.6	Specimen SIF-IO(1%)-2L(NC)-B .....	125
4.6	<i>Comparison of the results</i> .....	131
4.6.1	Effect of prior in-plane damage on the out-of-plane response.....	131
4.6.1	Effect of workmanship on the out-of-plane response .....	135
4.6.2	Influence of openings on the out-of-plane response .....	136
4.6.3	Plastic or residual deformations in out-of-plane loading .....	137
4.6.4	Energy dissipation capacity .....	138
4.7	<i>Conclusions</i> .....	139
<b>5</b>	<b>Strengthening of brick masonry infills.....</b>	<b>141</b>
5.1	<i>Introduction</i> .....	142
5.2	<i>Brief overview of the strengthening techniques</i> .....	142
5.2.1	Metal ties connectors .....	142
5.2.2	Textile reinforced mortar (TRM).....	144
5.3	<i>Description of specimens</i> .....	147
	SIF(DTRM)-I-2L(NC)-B.....	147
	SIF(CTRM)-I-2L(NC)-B.....	147
5.4	<i>Behavior of the strengthened masonry infills under in-plane loading</i> .....	147
5.4.1	Experimental details .....	147
5.4.2	Results - specimen SIF(CTRM)-I-2L(NC)-B.....	148
5.4.3	Results - specimen SIF(DTRM)-I-2L(NC)-B.....	155
	Figure 5.19 Force-displacement diagram of specimen SIF(DTRM)-I-2L(NC)-B.....	156
5.5	<i>Behavior of strengthened masonry infills under out-of-plane loading</i> .....	161
5.5.1	Results - specimen SIF-O-2L(C)-B .....	162
5.5.2	Results - specimen SIF(CTRM)-O-1L-B .....	169
5.5.3	Results - specimen SIF(DTRM)-O-1L-B .....	172
5.6	<i>Comparison of the results</i> .....	180
5.6.1	In-plane behavior.....	180
5.6.2	Out-of-plane testing.....	183
5.7	<i>Conclusions</i> .....	186

<b>6</b>	<b>Characterization of the mechanical properties .....</b>	<b>189</b>
6.1	<i>Characterization of masonry components .....</i>	190
6.1.1	Fresh and hardened properties of mortar .....	190
6.1.2	Mechanical properties of bricks.....	193
6.2	<i>Characterization of masonry assemblages .....</i>	198
6.2.1	Compressive strength of masonry .....	198
6.2.2	Tensile and shear strength of masonry .....	201
6.2.3	Flexural behavior of masonry.....	203
6.2.4	Shear properties of the unit-mortar interfaces .....	209
6.3	<i>Conclusions.....</i>	212
<b>7</b>	<b>Numerical Analysis of rc Frames with Brick Infills.....</b>	<b>213</b>
7.1	<i>Introduction .....</i>	214
7.2	<i>In-plane numerical modelling of rc frames with brick infills.....</i>	215
7.2.1	Numerical model .....	215
7.2.2	Validation of the numerical model based on experimental results .....	216
7.2.3	Analysis of the material properties .....	222
7.2.4	Influence of openings in the in-plane response.....	224
7.3	<i>Out-of-plane behavior of masonry infilled reinforced concrete frames.....</i>	237
7.3.1	Numerical model for out-of-plane behavior .....	237
7.3.2	Validation of the numerical model based on experimental results .....	239
7.4	<i>Conclusions.....</i>	240
<b>8</b>	<b>Conclusion.....</b>	<b>244</b>
8.1	<i>Future works.....</i>	246
	<b>Appendix I.....</b>	<b>255</b>
	<b>Compressive and Flexural Tests of Mortar Samples.....</b>	<b>255</b>

## List of Tables

Table 2-1 Statistical summary of corner crushing results .....	14
Table 2-2 Equations proposed for out-of-plane resistance of masonry infills .....	24
Table 2-3 Values of $\lambda_2$ with respect to height to thickness ratio (interpolation shall be used ....	27
Table 3-1 Relation between different parameters of prototype and model based on Cauchy's Similitude Law .....	40
Table 3-2 Designation of the specimens for in-plane static cyclic loading.....	42
Table 3-3 Key parameters characterizing the in-plane behavior of the rc bare frame .....	48
Table 3-4 Key parameters related to the in-plane behavior of SIF-I-2L(NC)-A.....	54
Table 3-5 Key parameters related to the in-plane behavior of SIF(0.3%)-I-2L(NC)-B in positive and negative directions.....	62
Table 3-6 Key parameters related to the in-plane behavior of SIF(0.5%)-I-2L(NC)-B.....	66
Table 3-7 Key parameters related to the in-plane behavior of SIF(1%)-I-2L(NC)-B.....	74
Table 3-8 Comparison of lateral stiffness and strength.....	81
Table 4-1 Designation of the specimens tested under out-of-plane loading .....	89
Table 4-2 Secant stiffness and out-of-plane strength of different specimens built with mason type B .....	132
Table 4-3 Comparison between experimental and analytical results .....	133
Table 4-4 Comparison between experimental and analytical results .....	134
Table 4-5 Comparison between experimental and analytical results .....	135
Table 4-6 Initial stiffness and out-of-plane resistance of the solid infilled frame and infilled frame with central opening.....	137
Table 5-1 Consistency, compressive and flexural test results of the specimens .....	147
Table 5-2 Labelling of the retrofitted specimens .....	147
Table 5-3 Key parameters describing the in-plane behavior of bare frame .....	150
Table 5-4 Key parameters related to the in-plane behavior of bare frame.....	156
Table 5-5 Lateral stiffness and strength of strengthened and unstrengthened specimens.....	181
Table 5-6 Comparison of the secant stiffness and out-of-plane resistance .....	184
Table 6-1 Consistency, compressive and flexural strength of mortar .....	192
Table 6-2 Summary of the mechanical properties of mortar for each leaf of the brick infill....	192
Table 6-3 Measurement of the thick bricks used in exterior leaf.....	194
Table 6-4 Measurement of the thin bricks used in interior leaf .....	194
Table 6-5 Compressive strength and elastic modulus of bricks with thickness of 75mm.....	195
Table 6-6 Compressive strength and elastic modulus of bricks with thickness of 58m.....	196
Table 6-7 Compressive strength and elastic modulus of bricks with thickness of 75m.....	196
Table 6-8 Compressive strength and elastic modulus of bricks with thickness of 58m.....	197
Table 6-9 Compressive test results of all specimens with thickness of 75mm in direction parallel to their thickness .....	197
Table 6-10 Compressive test results of all specimens with thickness of 58mm in direction parallel to their thickness .....	198
Table 6-11 Summary of the results of the specimens under uniaxial compressive loading.....	200
Table 6-12 Statistical information for specimen of thickness 75mm.....	200
Table 6-13 Characteristic compressive strength of masonry infill.....	201
Table 6-14 Shear strength and shear modulus obtained for the wallets tested under diagonal compression.....	203

Table 6-15 Statistical information for specimen of thickness 75mm.....	203
Table 6-16 Flexural strength of each specimen parallel to bed joint .....	206
Table 6-17 Statistical study for the flexural strength in specimen with thickness of 75mm.....	206
Table 6-18 Flexural strength of the specimens perpendicular to the bed joints .....	208
Table 6-19 Statistical study for the flexural strength parallel to bed joint in specimen with thickness of 75mm .....	208
Table 6-20 Shear strength of the specimens due to pre-compression level.....	210
Table 6-21 Characteristic value for initial shear strength of masonry .....	212
Table 7-1 Information about the components of each brick masonry infill masonry wall .....	217
Table 7-2 Secant stiffness and lateral strength of test specimens .....	218
Table 7-3 Mechanical properties of the components for walls specimens [3] .....	218
Table 7-4 Mechanical properties adopted for the interface elements.....	219
Table 7-5 Mechanical Properties of the interface after rendering.....	221
Table 7-6 Results of numerical analysis in terms of initial stiffness, lateral resistance and failure mode.....	222
Table 7-7 Geometrical characterization of the openings.....	225
Table 7-8 Initial stiffness and lateral strength of the different models.....	230
Table 7-9 Results of empirical equation compared with numerical results .....	232
Table 7-10 Comparison of the analysis of results between the finite element modelling and equivalent diagonal strut model .....	236
Table 7-11 Mechanical properties adopted for the interface elements.....	239

## List of Figures

Figure 2.1 Negative effects of infill panel in structure; a)soft story mechanism [37], b)short column mechanism [38].....	9
Figure 2.2 Details on the response of masonry infilled frames under in-plane loading; a)separation of the walls from the structural frame; b)equivalent strut model .....	9
Figure 2.3 Failure mechanisms of masonry infilled frames [2] .....	10
Figure 2.4 Shear connectors inside confining cage [15] .....	11
Figure 2.5 Schematic of the masonry infilled rc frame .....	13
Figure 2.6 Design model for masonry infilled frame subjected for in-plane loading; a)composite frame-panel b)proposed strut-tie model c)equivalent tensile strength for a typical diagonal step crack [68] .....	16
Figure 2.7 Equivalent bi-diagonal strut model.....	17
Figure 2.8 Modification on the equivalent bi-diagonal strut model [82-85].....	17
Figure 2.9 Proposed strut model to take into account horizontal sliding .....	18
Figure 2.10 Proposed hysteretic force-deformation relationship for the strut [45].....	18
Figure 2.11 Proposed hysteretic behavior for non-integral systems [88].....	18
Figure 2.12 Proposed hysteretic behavior for the strut [89].....	19
Figure 2.13 Proposed multi strut model [90] .....	19
Figure 2.14 Nonlinear behavior of the central element [90] .....	19
Figure 2.15 Proposed strut model for taking into account the coupling behavior [91, 92].....	20
Figure 2.16 various strut and tie models proposed by Hashemi et al [93] .....	20
Figure 2.17 Different details that can be adopted micro-modelling approach: a)masonry wall; b)detailed micro-model; c)simplified micro-model; d)finite element macro-model.....	21
Figure 2.18 Damage in non-structural elements [19].....	22
Figure 2.19 Detachment of the leaves in multi leaf walls [19] .....	22
Figure 2.20 Rocking at base due to insufficient confinement of masonry infill wall .....	23
Figure 2.21 a)Vertical and b)horizontal arching mechanism .....	23
Figure 2.22 Formation of two way arching mechanism.....	23
Figure 2.23 Strut and tie model proposed by Hashemi and Mosalam [93].....	28
Figure 2.24 Proposed infill model using beam-column elements with fiber discretization .....	28
Figure 2.25 Constituents of FRP .....	29
Figure 2.26 Different FRP configuration techniques studied in [28].....	30
Figure 2.27 cross section of a braided mesh [35].....	33
Figure 3.1 Statistical information about geometry and mechanical properties of typical South European masonry infilled frames a) year of construction b) number of storey c) type of concrete d) cross-section of columns e) width of beams f) height of beams .....	37
Figure 3.2 Statistical Information about presence of different types of openings within infill...	38
Figure 3.3 Masonry infilled frame as a prototype (dimensions in m) .....	38
Figure 3.4 Cross-section and reinforcement scheme of the beams and columns (dimensions in m) .....	39
Figure 3.5 Cross-section of the infills in the prototype .....	39
Figure 3.6 Geometry and reinforcement scheme of the reduced scale rc frame .....	40
Figure 3.7 Cross-sections of columns and beams in reduced scale rc frames.....	41
Figure 3.8 Brick units and cross section of reduced scale masonry infill: a) bricks of 80mm thickness used in exterior leaf ; b) bricks of 60mm thickness used in interior leaf of the infill; c) cross-section of the infill in reduced scale specimens.....	41

Figure 3.9 Wooden molds and reinforcement inside them .....	42
Figure 3.10 Absence of stirrups in the connection point of column to beam.....	43
Figure 3.11 Construction of the frames a) concrete casting b) compaction of concrete by its vibration .....	43
Figure 3.12 a)Transportation of the frames to the storage area and and b) construction of the infills .....	43
Figure 3.13 Test setup for in-plane cyclic loading.....	44
Figure 3.14 Out-of-plane support of the upper beam in the in-plane testing .....	45
Figure 3.15 Instrumentation for in-plane loading; a) external leaf b) internal leaf.....	45
Figure 3.16 Measurement of average shear distortion of infill with measurements of LVDTs..	46
Figure 3.17 Displacement protocol for in-plane testing.....	46
Figure 3.18 Lateral force-displacement diagram of the bare frame .....	47
Figure 3.19 Strength degradation of the specimen in two successive cycles.....	48
Figure 3.20 Average shear distortion of the bare frame.....	49
Figure 3.21 Stiffness degradation in bare frame .....	49
Figure 3.22 Crack propagation in the specimen at lateral drift of a)0.14% in positive direction b)0.14% in negative direction c)0.2% in positive direction d)0.2% in negative direction e)0.54% in positive direction f)0.54% in negative direction .....	50
Figure 3.23 Crack propagation in the specimen at lateral drift of a)0.75% in positive direction b)0.75% in negative direction c)1.48% in positive direction d)1.48% in negative direction e)3.5% in positive direction f)3.5% in negative direction .....	51
Figure 3.24 Energy dissipated at each cycle for bare frame.....	52
Figure 3.25 Cumulative energy dissipation of bare frame .....	52
Figure 3.26 In-Plane force-displacement diagram of specimen SIF-I-2L(NC)-A .....	53
Figure 3.27 Strength degradation of the specimen in two successive cycles of each step in positive and negative direction .....	53
Figure 3.28 Stiffness degradation curve for specimen SIF-I-2L(NC)-A .....	54
Figure 3.29 Crack propagation in the specimen at lateral drift of a)0.1% in positive direction b)0.1% in negative direction c)0.14% in positive direction d)0.14% in negative direction e)0.27% in positive direction f)0.27% in negative direction g)0.38% in positive direction h)0.38% in negative direction .....	55
Figure 3.30 Crack propagation in the specimen at lateral drift of a)0.54% in positive direction b)0.54% in negative direction c)0.75% in positive direction d)0.75% in negative direction e)2.5% in positive direction f)2.5% in negative direction .....	56
Figure 3.31 Out-of-plane bulging of the interior leaf during in-plane loading at lateral drift of a)1% b)2%.....	56
Figure 3.32 Energy dissipated at each cycle for specimen SIF-I-2L(NC)-A .....	57
Figure 3.33 Cumulative energy dissipation of SIF-I-2L(NC)-A.....	57
Figure 3.34 Relation between lateral force and average shear distortion of the reinforced concrete frame .....	58
Figure 3.35 Relation between lateral force and average shear distortion of the external leaf.....	58
Figure 3.36 Relation between lateral force and average shear distortion of the internal leaf .....	59
Figure 3.37 Relative displacement of masonry infill from its bounding frame with respect to the force and lateral displacement applied to the structure for a)lower right corner b)lower right corner c)upper left corner d)upper left corner e)upper right corner f)upper right corner g)lower left corner h)lower left corner.....	60
Figure 3.38 Lateral force-displacement diagram of SIF-IO(0.3%)-2L(NC)-B .....	61

Figure 3.39 Monotonic force-displacement diagram of two successive cycles .....	62
Figure 3.40 Stiffness degradation curve for specimen SIF(0.3%)-I-2L(NC)-B.....	62
Figure 3.41 Crack propagation in the specimen at lateral drift of a)0.05% in positive direction b)0.05% in negative direction c)0.07% in positive direction d)0.07% in negative direction e)0.11% in positive direction f)0.11% in negative direction.....	63
Figure 3.42 Crack propagation in the specimen at lateral drift of a)0.16% in positive direction b)0.16% in negative direction c)0.3% in positive direction d)0.3% in negative direction.....	64
Figure 3.43 Energy dissipation at each cycle for specimen SIF(0.3%)-I-2L(NC)-B.....	64
Figure 3.44 Cumulative energy dissipation of specimen SIF(0.3%)-I-2L(NC)-B.....	65
Figure 3.45 In-Plane force-displacement diagram of the specimen SIF-IO(0.5%)-2L(NC)-B...	65
Figure 3.46 Monotonic envelop of the force-displacement diagram at two successive cycles...	66
Figure 3.47 Stiffness degradation curve of specimen SIF(0.5%)-I-2L(NC)-B.....	67
Figure 3.48 Crack propagation in the specimen at lateral drift of a)0.05% in positive direction b)0.05% in negative direction c)0.1% in positive direction d)0.1% in negative direction e)0.0.14% in positive direction f)0.14% in negative direction g)0.2% in positive direction h)0.2% in negative direction.....	68
Figure 3.49 Crack propagation in the specimen at lateral drift of a)0.27% in positive direction b)0.27% in negative direction c)0.38% in positive direction d)0.38% in negative direction e)0.5% in positive direction f)0.5% in negative direction .....	69
Figure 3.50 Energy dissipation at each cycle for specimen SIF(0.5%)-I-2L(NC)-B.....	70
Figure 3.51 Cumulative energy dissipation of specimen SIF(0.5%)-I-2L(NC)-B.....	70
Figure 3.52 Average shear distortion of a) external leaf (8cm thickness) and b) internal leaf (6 cm thickness).....	71
Figure 3.53 Average shear distortion of RC frame .....	71
Figure 3.54 Relative displacement of masonry infill in relation to the rc frame at a) lower right corner b) lower right corner c) upper left corner d) upper left corner e) upper right corner f) upper right corner g) lower left corner h) lower left corner .....	72
Figure 3.55 Force-displacement diagram of the specimen SIF-IO(1%)-2L(NC)-B .....	73
Figure 3.56 Monotonic force-displacement diagram of the specimen SIF-IO(1%)-2L(NC)-B at two successive cycles.....	74
Figure 3.57 Stiffness degradation curve of specimen SIF(1%)-I-2L(NC)-B.....	75
Figure 3.58 Crack propagation in the specimen at lateral drift of a)0.05% in negative direction b)0.05% in positive direction c)0.07% in negative direction d)0.07% in positive direction e)0.1% in negative direction f)0.1% in positive direction g)0.14% in negative direction h)0.14% in positive direction i)0.2% in negative direction j)0.2% in positive .....	76
Figure 3.59 Crack propagation in the specimen at lateral drift of a)0.27% in negative direction b) 0.27% in positive direction c)0.54% in negative direction d)0.54% in positive direction e)0.75% in negative direction f)0.75% in positive direction g)1% in negative direction h)1% in positive direction.....	77
Figure 3.60 Energy dissipation at each cycle for specimen SIF(1%)-I-2L(NC)-B.....	78
Figure 3.61 Cumulative energy dissipation of specimen SIF(1%)-I-2L(NC)-B.....	78
Figure 3.62 Average shear distortion of a) external leaf (8cm thickness) and b) internal leaf (6 cm thickness).....	79
Figure 3.63 Average shear distortion of RC frame .....	79
Figure 3.64 Relative displacement of masonry infill from its bounding frame with respect to the force and lateral displacement applied to the structure for a)lower right corner b)lower right corner	

c)upper left corner d)upper left corner e)upper right corner f)upper right corner g)lower left corner h)lower left corner .....	80
Figure 3.65 Monotonic in-plane force-displacement diagram of all specimens .....	81
Figure 3.66 Strength degradation of a)SIF-I-2L(NC)-A b)SIF-IO(0.3%)-2L(NC)-B c)SIF-IO(0.5%)-2L(NC)-B d)SIF-IO(1%)-2L(NC)-B .....	82
Figure 3.67 Strength degradation of bare frame.....	83
Figure 3.68 Stiffness degradation of the specimens constructed with mason B .....	83
Figure 3.69 Trend of variation of the stiffness among the specimens of bare frame, SIF-I-2L(NC)-A and SIF(1%)-I-2L(NC)-B.....	84
Figure 3.70 Cracking pattern of the specimens at lateral drift of 1% a) Bare frame b) SIF-I-2L(NC)-A c) SIF(1%)-I-2L(NC)-B .....	84
Figure 3.71 Cumulative energy dissipated during in-plane cyclic loading .....	85
Figure 3.72 Average shear distortion of the exterior and interior leaf of specimen a)SIF-I-2L(NC)-A b) SIF-IO(0.5%)-2L(NC)-B c) SIF-IO(1%)-2L(NC)-B .....	85
Figure 4.1 Test setup for out-of-plane testing .....	89
Figure 4.2 Instrumentation for out-of-plane testing; a) infill wall with a central opening; b) solid infill walls.....	90
Figure 4.3 Loading pattern applied for SIF-O-1L-A.....	91
Figure 4.4 Loading protocol applied for specimens built by mason B .....	91
Figure 4.5 Force-displacement response of SIF-O-1L-A.....	92
Figure 4.6 Monotonic curves of force-displacement diagram for 1st and 2nd cycles.....	93
Figure 4.7 Stiffness degradation curve of specimen SIF-O-1L-A .....	93
Figure 4.8 Cracking pattern mapping in the specimen SIF-O-1L-A at different out-of-plane displacements .....	94
Figure 4.9 Final cracking pattern of the specimen SIF-O-1L-A .....	95
Figure 4.10 Deformation of the infill during out-of-plane loading .....	95
Figure 4.11 Comparison of the deformation of a) central vertical profile b) central horizontal profile .....	96
Figure 4.12 Sliding of the interfaces during out-of-plane loading .....	96
Figure 4.13 Deformation of the infill at different out-of-plane displacements .....	97
Figure 4.14 Plastic deformations in specimen SIF-O-1L-A at two successive cycles.....	97
Figure 4.15 Plastic deformation of SIF-O-1L-A at two successive cycles; a) first cycle b) second cycle .....	98
Figure 4.16 Dissipation of energy at each cycle during out-of-plane loading for specimen SIF-O-1L-A .....	98
Figure 4.17 Cumulative dissipation of energy for specimen SIF-O-1L-A.....	99
Figure 4.18 Force-displacement response of the SIF-O-1L-B .....	99
Figure 4.19 Monotonic force-displacement envelopes at two successive cycles.....	100
Figure 4.20 Stiffness degradation curve of specimen SIF-O-1L-B.....	100
Figure 4.21 Crack propagation of SIF-O-1L-B.....	101
Figure 4.22 Deformation of the infill during out-of-plane loading.....	102
Figure 4.23 Comparison of the deformation of a) central vertical profile b) central horizontal profile .....	103
Figure 4.24 Deformation of the infill at different out-of-plane displacements. ....	103
Figure 4.25 Sliding of the infill-rc frame interfaces during out-of-plane loading.....	104
Figure 4.26 Plastic deformation in the masonry infill at 1st and 2nd cycles of each step.....	104



Figure 4.27 Plastic deformation of SIF-O-1L-B at two successive cycles; a) first cycle b) second cycle .....	105
Figure 4.28 Dissipation of energy at each cycle for specimen SIF-O-1L-B .....	105
Figure 4.29 Cumulative dissipation of energy until each cycle for specimen SIF-O-1L-B .....	105
Figure 4.30 Force-displacement diagram of PIF-O-1L-B .....	106
Figure 4.31 Monotonic force-displacement diagram for successive cycles .....	106
Figure 4.32 Force-displacement diagram of specimens PIF-O-1L-B versus SIF-O-1L-B at two different point; a) control point b) point with maximum deformation .....	107
Figure 4.33 Stiffness degradation curve of specimen PIF-O-1L-B .....	107
Figure 4.34 Crack propagation observed in specimen PIF-O-1L-B .....	108
Figure 4.35 Out-of-plane failure of the right part of the masonry infill .....	109
Figure 4.36 Deformation of the infill at central horizontal profile .....	109
Figure 4.37 Deformation of the infill at different points with respect to the control point .....	109
Figure 4.38 Deformation of the infill for different out-of-plane displacements .....	110
Figure 4.39 Plastic deformation of PIF-O-1L-B at two successive cycles .....	110
Figure 4.40 Plastic deformation of masonry infill PIF-O-1L-B at two successive cycles; a) first cycle b) second cycle .....	111
Figure 4.41 a) Energy dissipation at each cycle b) cumulative energy dissipation until each cycle .....	111
Figure 4.42 Force-displacement diagram obtained for specimen SIF-IO(0.3%)-2L(NC)-B .....	112
Figure 4.43 Monotonic force-displacement envelop at two successive cycles .....	112
Figure 4.44 Stiffness degradation curve for specimen SIF-IO(0.3%)-2L(NC)-B .....	113
Figure 4.45 Crack propagation of SIF-IO(0.3%)-2L(NC)-B .....	114
Figure 4.46 Final cracking pattern of the specimen .....	115
Figure 4.47 Deformation of different points in the infill with respect to the control point .....	115
Figure 4.48 comparison between the deformation of a) upper and bottom part of infill b) right and left part of infill .....	116
Figure 4.49 Deformation of the interfaces during out-of-plane loading .....	116
Figure 4.50 Deformation of the infill at different out-of-plane displacements .....	117
Figure 4.51 Plastic deformation of the infill at two successive cycles .....	117
Figure 4.52 Plastic deformation of SIF-IO(0.3%)-2L(NC)-B at two successive cycles; a) first cycle b) second cycle .....	118
Figure 4.53 a) Energy dissipation capacity of the specimen at each cycle) b) Total energy dissipation until each cycle .....	118
Figure 4.54 Force-displacement response of SIF-IO(0.5%)-2L(NC)-B .....	119
Figure 4.55 Monotonic force-displacement envelopes for two successive cycles .....	119
Figure 4.56 Stiffness degradation curve for specimen SIF-IO(0.5%)-2L(NC)-B .....	120
Figure 4.57 Crack propagation of SIF-IO(0.5%)-2L(NC)-B .....	121
Figure 4.58 Deformation of infill at different points .....	122
Figure 4.59 Comparison of the deformation of a) central vertical profile b) central horizontal profile .....	122
Figure 4.60 Displacement of each interface between infill and RC frame during out-of-plane loading .....	123
Figure 4.61 Deformation of the infill at different out-of-plane displacements .....	123
Figure 4.62 Plastic deformation of the specimen at each successive cycles .....	124
Figure 4.63 Plastic deformation of SIF-IO(0.5%)-2L(NC)-B at two successive cycles; a) first cycle b) second cycle .....	124

Figure 4.64 a)Energy dissipation capacity of the specimen at each cycle b) cumulative energy dissipation of the specimen until each cycle .....	125
Figure 4.65 Force-displacement diagram of SIF-IO(1%)-2L(NC)-B during out-of-plane loading .....	126
Figure 4.66 Monotonic force-displacement envelop of SIF-IO(1%)-2L(NC)-B at each successive cycle .....	126
Figure 4.67 Stiffness degradation curve for specimen SIF-IO(1%)-2L(NC)-B.....	126
Figure 4.68 Crack propagation of SIF-IO(1%)-2L(NC)-B .....	127
Figure 4.69 Deformation of the infill at different points with respect to the deformation of the control point.....	128
Figure 4.70 Comparison of the deformation of a) central vertical profile b) central horizontal profile.....	128
Figure 4.71 Displacement measured in the interface during out-of-plane loading for specimen SIF-IO(1%)-2L(NC)-B.....	129
Figure 4.72 Deformation of the infill at different out-of-plane displacements .....	130
Figure 4.73 Plastic deformation of the specimen at two successive cycles .....	130
Figure 4.74 Plastic deformation of the specimen at two successive cycles; a)first cycle b)second cycle .....	130
Figure 4.75 a)Energy dissipation in specimen with prior in-plane damage corresponding to 1% lateral drift b)cumulative energy dissipated until each cycle .....	131
Figure 4.76 Out-of-plane force-displacement monotonic envelops of specimens constructed with mason type B.....	132
Figure 4.77 Variation of a)initial stiffness and b)out-of-plane strength with respect to prior in-plane drift .....	132
Figure 4.78 Variation of the initial stiffness of the specimens with respect to prior in-plane damage .....	134
Figure 4.79 Stiffness degradation curve of the specimens constructed by mason B.....	134
Figure 4.80 Experimental monotonic envelops for specimens built with different masons .....	135
Figure 4.81 Stiffness degradation of masonry infill built by different masons .....	136
Figure 4.82 Force-displacement diagram of PIF-O-1L-B and SIF-O-1L-B in their control points .....	136
Figure 4.83 Stiffness degradation curve of solid infill and infill with central opening.....	137
Figure 4.84 Plastic deformations observed in all the specimens.....	138
Figure 4.85 Total dissipated energy of specimens with different prior in-plane damage .....	138
Figure 4.86 Total dissipated energy of specimens constructed by different masons and with central opening.....	139
Figure 5.1 Helical ties used for connecting the leaves of brick infills .....	143
Figure 5.2 Details of the connections of the leaves through metal ties: a)pilot holes in the masonry b)metal tie connecting both leaves together and c)distribution pattern of helical ties .....	143
Figure 5.3 Cross section of a braided mesh [35].....	144
Figure 5.4 Details of the mesh connectors; a)pattern of the connectors b)plastic row plug and glass fiber connector .....	145
Figure 5.5 Application of the reinforced rendering; a)drilling the pilot holes b)cleaning the holes c)applying the first layer of mortar .....	145
Figure 5.6 Application of the reinforced rendering; a)positioning of the textile mesh b)application of the second layer of mortar c)regularized rendering surface.....	146

Figure 5.7 Three steps for installing the connectors; a)placing the textile mesh on the first layer of mortar b)filling the hole with chemical anchor c)inserting the connectors into the hole.....	146
Figure 5.8 Instrumentation of the specimen for in-plane loading a)external leaf b)internal leaf .....	148
Figure 5.9 Force-displacement diagram of specimen SIF(CTRM)-I-2L(NC)-B .....	149
Figure 5.10 Monotonic force-displacement envelops of SIF(CTRM)-I-2L(NC)-B at each successive cycles .....	150
Figure 5.11 Stiffness degradation curve of specimen SIF(CTRM)-I-2L(NC)-B .....	151
Figure 5.12 Crack propagation of SIF(CTRM)-I-2L(NC)-B .....	152
Figure 5.13 Detachment of the reinforced mortar layer applied on external leaf from rc frame at different points .....	152
Figure 5.14 Detachment of the reinforced mortar layer applied on internal leaf from rc frame at different points .....	153
Figure 5.15 Detachment of the reinforced mortar layer at lateral drift of a) 0.27% b) 2.89% c) shear failure of the connectors between retrofitting layer and rc frame .....	153
Figure 5.16 View of the crushing of bricks of the infill after removing some parts of the retrofitting layer in specimen SIF(CTRM)-I-2L(NC)-B .....	154
Figure 5.17 Energy dissipation of the strengthened specimen at each cycle .....	154
Figure 5.18 Total dissipation of energy until each cycle .....	155
Figure 5.19 Force-displacement diagram of specimen SIF(DTRM)-I-2L(NC)-B .....	156
Figure 5.20 Monotonic envelope obtained in specimen SIF(DTRM)-I-2L(NC)-B at each successive cycles .....	156
Figure 5.21 Stiffness degradation curve of specimen SIF(DTRM)-I-2L(NC)-B .....	157
Figure 5.22 Crack propagation of SIF(DTRM)-I-2L(NC)-B .....	157
Figure 5.23 Detachment of the strengthening mortar layer from the specimen SIF(DTRM)-I-2L(NC)-B at its external side .....	158
Figure 5.24 Detachment of the strengthening mortar layer from the specimen SIF(DTRM)-I-2L(NC)-B at its internal side .....	159
Figure 5.25 Detachment of the strengthening mortar layer at lateral drift of a) 0.2% b) 3.5% c) shear failure of the connectors between retrofitting layer and rc frame .....	159
Figure 5.26 External leaf of the brick infill wall crane after the test.....	160
Figure 5.27 Energy dissipation capacity of the strengthened specimens at each cycle.....	160
Figure 5.28 Total energy dissipation capacity of the strengthened specimen until each cycle.	161
Figure 5.29 Instrumentation adopted in the out-of-plane testing a) SIF-O-2L(C)-B b) specimens strengthened with TRM technique .....	161
Figure 5.30 Force-displacement diagram of the specimen SIF-O-2L(C)-B under out-of-plane loading.....	162
Figure 5.31 Monotonic force-displacement envelope of the specimen SIF-O-2L(C)-B at each successive cycles .....	162
Figure 5.32 Stiffness degradation curve of specimen SIF-O-2L(C)-B .....	163
Figure 5.33 Crack propagation of SIF-O-2L(C)-B – external leaf.....	164
Figure 5.34 Cracking of the specimen at the end of the test .....	165
Figure 5.35 Deformation of the infill at measured points .....	165
Figure 5.36 Displacement of the LVDTs along the central horizontal profile of the brick infill .....	166
Figure 5.37 Displacement of the LVDTs along the central vertical profile of the brick infill..	166
Figure 5.38 Displacements measured on the interfaces between brick infill and rc frame .....	166

Figure 5.39 Deformation of the infill at different out-of-plane displacements .....	167
Figure 5.40 Plastic deformation of the specimen at two successive cycles .....	168
Figure 5.41 Plastic deformation of SIF-O-2L(C)-B at two successive cycles; a) first cycle b) second cycle .....	168
Figure 5.42 Energy dissipation capacity of the specimen at each cycle .....	168
Figure 5.43 Total energy dissipated until each cycle compared with SIF-O-1L-B.....	169
Figure 5.44 Final deformation of the infill; a)total deformation, b)detachment of the wall from bottom rc beam c)detachment of the wall from upper rc beam.....	170
Figure 5.45 Force-relative displacement measured in the control point for specimen SIF(CTRM)-O-1L-B .....	171
Figure 5.46 Crack propagation recorded in the reinforced mortar layer in specimen SIF(CTRM)-O-1L-B .....	171
Figure 5.47 Out-of-plane damage in the interior part of the infill.....	172
Figure 5.48 Alternative connection of the LVDTs supports to the rc beams of the frame .....	172
Figure 5.49 Force-displacement diagram of the specimen SIF(DTRM)-O-1L-B.....	173
Figure 5.50 Final state of the specimen SIF(DTRM)-O-1L-B a)front view b)lateral view .....	173
Figure 5.51 Monotonic force-displacement envelope of the specimen SIF(DTRM)-O-1L-B for successive cycles .....	174
Figure 5.52 Stiffness degradation curve of specimen SIF(DTRM)-O-1L-B .....	174
Figure 5.53 Crack propagation in specimen SIF(DTRM)-O-1L-B.....	175
Figure 5.54 Deformation in LVDTs capturing the detachment between reinforced mortar layer and the rc frame with brick infill.....	176
Figure 5.55 Deformation of the infill at different positions .....	176
Figure 5.56 Displacements along the central vertical profile.....	177
Figure 5.57 Displacements along the central horizontal profile.....	177
Figure 5.58 Deformation of the infill at different out-of-plane displacements .....	178
Figure 5.59 Detachment of the connectors from rc frame .....	178
Figure 5.60 Plastic deformations in the strengthened specimen at each successive cycles .....	179
Figure 5.61 Plastic deformation at two successive cycles; a) first cycle b) second cycle.....	179
Figure 5.62 Energy dissipation capacity of the strengthened specimen at each cycle .....	180
Figure 5.63 Total energy dissipation capacity of the strengthened specimen until each cycle compared with reference specimen .....	180
Figure 5.64 Force-displacement envelopes for unstrengthened and strengthened specimens ....	181
Figure 5.65 Stiffness degradation curves of unstrengthened and strengthened specimens.....	182
Figure 5.66 Comparison of the damage of the brick infill after the test a) unstrengthened brick infill b) strengthening with commercial textile mesh c) strengthening with designed textile mesh .....	182
Figure 5.67 Energy dissipation capacity of strengthened and unstrengthened specimens .....	183
Figure 5.68 Monotonic envelop obtained in out-of-plane tests.....	183
Figure 5.69 Force-displacement hysteresis for a) SIF(DTRM)-O-1L-B b)SIF-O-2L(C)-B c) SIF-O-1L-B .....	184
Figure 5.70 Stiffness degradation curves of strengthened versus reference specimen .....	185
Figure 5.71 Energy dissipation capacity of strengthened specimens versus reference specimen .....	185
Figure 5.72 cracking pattern at the end of the test for specimens a)SIF-O-1L-B b)SIF-O-2L(C)-B c)SIF(CTRM)-O-1L-B d)SIF(DTRM)-O-1L-B.....	186

Figure 6.1 Test procedure for evaluation of mortar consistency; a)preparation of the mold b)placing the mortar in the mold and compacting c)removing the mold and jolting the flow table d)measure two vertical diameters of the mortar .....	191
Figure 6.2 Mold used for determining the flexural and compressive strength of mortar .....	191
Figure 6.3 a)Flexural and b)compressive testing of the mortar .....	191
Figure 6.4 Measurement positions taken for the bricks .....	193
Figure 6.5 Measurement of the dimensions of the bricks .....	193
Figure 6.6 Surface preparation of the brick specimens with a) mortar b) polyester .....	194
Figure 6.7 Uniaxial compression tests of brick parallel to perforation a) before test b) after test .....	195
Figure 6.8 Compressive testing of the brick parallel to height a) before test b) after test.....	196
Figure 6.9 Compressive testing of the bricks in direction parallel to thickness a) before test b) after test.....	197
Figure 6.10 Masonry specimen configuration for compression tests.....	198
Figure 6.11 Details of compressive testing a)before test b)after test .....	199
Figure 6.12 Stress-strain diagrams under uniaxial compressive loading .....	200
Figure 6.13 Diagonal shear test of masonry specimens a) scheme b) view of the specimen before testing.....	201
Figure 6.14 Cracking patterns a) specimen S2 b) specimen S1 .....	202
Figure 6.15 Stress-strain diagrams obtained for diagonal testing .....	203
Figure 6.16 Dimension of brick masonry under flexure a) parallel to bed joints b) perpendicular to bed joints.....	204
Figure 6.17 Details of experimental testing a) test setup for flexural testing b) transportation of the specimens .....	204
Figure 6.18 Horizontal cracking of the mortar joints due to flexural testing parallel to the bed joints.....	205
Figure 6.19 Force-displacement diagram of all specimen in flexural test parallel to bed joint	205
Figure 6.20 Flexural testing of the specimen perpendicular to the bed joints.....	207
Figure 6.21 a)Cracking pattern of the specimens and b)its deformation in flexural test perpendicular to the bed joints .....	207
Figure 6.22 Force-displacement diagram of the specimens in flexural test perpendicular to the bed joints.....	208
Figure 6.23 Specimens for initial shear test .....	209
Figure 6.24 Initial shear test; a)general configuration b)typical failure pattern.....	210
Figure 6.25 Force-displacement diagram of the specimens due to shear forces .....	211
Figure 6.26 Correlation between shear strength and normal stress.....	211
Figure 7.1 Different details that can be adopted micro-modelling approach: (a) masonry wall; (b) detailed micro-model; (c) simplified micro-model; (d) finite element macro-model .....	214
Figure 7.2 Geometry and reinforcement scheme of the rc frame (dimensions in m) [3] .....	215
Figure 7.3 Finite element model of the rc frame with brick infill.....	216
Figure 7.4 Stress-strain relationship adopted for Total Strain Crack model: a) exponential softening curve to describe tension and b) parabolic constitutive laws to describe compression .....	216
Figure 7.5 Two-dimensional interface yield function [134] .....	216
Figure 7.6 Pushover diagrams of the test specimens.....	217
Figure 7.7 Crack patterns of test specimens a) Wall-Ref-01 b) Wall-Ref-02 c) Wall-JAR.....	218
Figure 7.8 Crushing of loaded corner in the test specimen .....	218

Figure 7.9 Lateral force-displacement obtained in numerical analysis and experimental test (Wall-Ref-01) .....	219
Figure 7.10 a)Schematic distribution of minimum principal stresses in numerical model (Wall-Ref-01) b)Deformed mesh of the infill panel at failure.....	220
Figure 7.11 Thickness of the brick infill masonry walls after rendering in contact with the concrete enclosure .....	221
Figure 7.12 Comparison of the force-displacement diagrams obtained in experimental program with numerical analysis: a) Wall-Ref-02 b) Wall-JAR.....	221
Figure 7.13 Pushover diagrams of the numerical models .....	222
Figure 7.14 Pushover force-displacement diagrams obtained in the numerical model.....	223
Figure 7.15 Comparison of the force-displacement diagrams for models with varying tensile strength of masonry.....	223
Figure 7.16 Force-displacement diagrams for RC frame models with distinct stiffness of the brick masonry infill .....	224
Figure 7.17 Geometry of the central openings .....	225
Figure 7.18 Schematic representation of crack propagation in the numerical models by increasing the lateral load.....	225
Figure 7.19 Schematic distribution of minimum principal stresses .....	226
Figure 7.20 Pushover diagrams of the numerical models with increasing opening ratio.....	226
Figure 7.21 Influence of the opening area A on the mechanical properties of the rc masonry infill: a) variation of initial stiffness; b) variation of lateral strength.....	227
Figure 7.22 Trend of variation of initial stiffness in relation to opening area for different authors .....	227
Figure 7.23 Simplified and detailed approaches for: a) initial stiffness; b) lateral strength.....	228
Figure 7.24 Typical openings in masonry infill walls in southern European countries .....	228
Figure 7.25 Schematic distribution of minimum principle stresses; a)in wall O(2W)1; b)wall O(2D)1 (left); c)wall O(DW)1 (right).....	229
Figure 7.26 Crack propagation in wall O(2W)1.....	229
Figure 7.27 Possible positions of window openings: a)O(2W)1, b)O(2W)2, c)O(2W)3, d)O(2W)4, e)O(2W)5.....	230
Figure 7.28 Possible positions of door openings: a)O(2D)1, b)O(2D)2, c)O(2D)3, d)O(2D)4, e)O(2D)5 .....	230
Figure 7.29 Possible positions of door and window openings: a)O(DW)1, b)O(DW)2, c)O(DW)3, d)O(DW)4, e)O(DW)5, f)O(DW)6 .....	230
Figure 7.30 Prediction of key parameters of the in-plane behavior of the walls; a) initial stiffness and b) lateral strength of the walls with different opening types .....	231
Figure 7.31 Width and height of the piers to be used for calculation of Eq.7-7 .....	232
Figure 7.32 Replacement of masonry infill with a diagonal strut.....	233
Figure 7.33 Variation of initial stiffness with the width of diagonal strut .....	233
Figure 7.34 Equivalent width of strut for different proposed equations .....	234
Figure 7.35 Numerical modelling of three multi-story structures in DIANA .....	236
Figure 7.36 Geometry and reinforcement scheme of the reduced scale specimens .....	237
Figure 7.37 Cross-sections of columns and beams in reduced scale specimens .....	237
Figure 7.38 Finite element modelling of the rc frame with brick infill in DIANA software ....	238
Figure 7.39 Stress-strain relationship adopted for Total Strain Crack model: a)exponential softening curve to describe tension and b)parabolic constitutive laws to describe compression .....	238

Figure 7.40 Three dimensional interface material law .....	238
Figure 7.41 Force-displacement diagrams of the numerical and experimental model.....	239
Figure 7.42 Propagation of cracks in the numerical model.....	240

# **CHAPTER 1**

## **INTRODUCTION**



## 1 Introduction

Masonry infills have been widely used in the building construction as enclosure walls in the reinforced concrete (rc) or steel structures for many decades due to their good thermal and acoustic insulation properties and also reasonable fire resistance. Even nowadays masonry infills are typically employed in most modern buildings in the form of partition walls and enclosures in reinforced concrete frames. Generally they are assumed as non-structural elements and are not considered in the design process of the buildings. Although the infill panels are assumed as non-structural elements, their damage or collapse is not desirable, given the consequences in terms of human life losses and repair or reconstruction costs.

The research conducted on the infill walls highlighted the development of strong interaction between the infills and their bounding frame during cyclic actions [1-3]. This interaction could be positive or negative. When it is positive, the presence of infill improves the global behavior of the rc infilled frames. The negative interaction is related mainly to the formation of soft-storey mechanism or short column effect which can lead to the global or local collapse of the structure. The soft-storey mechanism is generally associated to the irregular distribution of the masonry infills in the height of the structure, whereas the short column mechanism can be the result of the geometric irregularity along the height of the masonry infill. The formation of the short column phenomenon happens when masonry infills leave a short portion of the column clear, leading to the shear collapse of the columns.

Additionally, different researchers found that some parameters such as mechanical properties of the materials, aspect ratio, boundary conditions, presence of reinforcement and presence of openings affect the behavior of masonry infill walls under the in-plane and out-of-plane loading [4-15]. These studies helped to understand the mechanical behavior of the masonry infilled frames to better act in the mitigation of seismic effects.

There are huge number of field evidences on the vulnerability of infills during seismic actions, namely based on what has been observed after the occurrence of important earthquakes; Mexico City earthquake in 1985 [16], Kocaeli (Turkey) earthquake in 1999 [17] Bhuj earthquake in 2001 [18], L'Aquila earthquake in 2009 [19]. These earthquakes caused the death of hundreds of people, affected the lives of millions and left enormous repair or reconstruction costs. With this respect it is important to underline that appropriate retrofitting techniques should be provided to enhance the behavior of these composite structures.

Different methods, conventional techniques (ferrocement, shotcrete and etc.) or innovative materials (using FRP) have been proposed for in-plane and out-of-plane strengthening of infilled frames. Some disadvantages of conventional techniques such as space reduction, addition of heavy mass and consequently changing the dynamic properties of the building as well as corrosion of the steel are some common problems that have resulted in the use of composite materials for strengthening [20, 21]. With this respect, composite materials such as fiber reinforced polymers (FRPs) have been receiving large attention from the research community to be used as a strengthening technique on strengthening of infilled frames [22-31]. Some drawbacks of FRPs such as poor behavior of epoxy resins at high temperatures, relatively high cost of epoxy, non-applicability of FRPs on wet surfaces or at low temperatures and incompatibility of epoxy resins with some substrate materials such as clay [32] resulted in replacing the organic binders with

inorganic ones such as cement based mortars. The smeared fibers can also be replaced by reinforcing meshes such as textile meshes with different continuous fibers. This new technique (since 1980s) is called as textile reinforced mortar technique (TRM) and has been studied by few researchers [33-36].

Therefore, the main factors that justify the present work consist of: (1) the wide use of brick masonry infills in rc buildings as an enclosure and partition walls in Portugal (cavity or double leaf walls), being this scenario very common in different Mediterranean countries; (2) the seismic hazard in some zones and consequently the seismic vulnerability of the masonry infills lead to moderate to high seismic risk of the rc building with masonry infills; (3) the poor construction quality used in the construction of masonry infills taking into account that they are considered as non-structural elements and are not considered in the design process of the buildings. Besides the poor material and poor workmanship, absence of fasteners connecting the brick leaves of the infills to the rc columns is an important issue in the vulnerability of the masonry infills to out-of-plane loading induced by earthquakes.

## 1.1 Objectives and methodology

As mentioned before, recent earthquakes highlighted the vulnerability of brick masonry infills and revealed remarkable deficiencies in these kind of structures during earthquakes. Therefore, as a primary step it is important to better understand the seismic behavior of brick infills under in-plane and out-of-plane loading and in particular the brick infills that are typical of the construction typology of South European Countries since 1960s. The objectives of this research program are: (1) experimental characterization of the in-plane and out-of-plane behavior of rc frames with typical brick infills; (2) experimental investigation of the influence of different parameters such as construction quality and presence of openings on the in-plane and out-of-plane response of masonry infills; (3) analysis of the influence of previous in-plane damage on the out-of-plane behavior of brick masonry infill walls; (4) assessment of different strengthening techniques in the enhancement of the in-plane and out-of-plane response of the infilled frames, namely textile reinforced mortar (TRM) technique applied as a rendering layer and steel ties connecting the leaves of the cavity wall; (5) numerical analysis of infilled frames and analysis of different parameters focusing on the influence of the presence and distribution of openings in the in-plane behavior of the rc frames with brick infills.

To accomplish the objectives of the thesis, the work carried out is concentrated on extensive experimental characterization of materials and composite structure composed of one-bay one-story brick masonry infilled rc frames under in-plane and out of plane loading. For this, reduced scale specimens were designed based on a database composed of rc buildings constructed in the past decades that are representative of the construction in Portugal. Besides, the experimental work included the specimens strengthened with textile reinforced mortar to be tested under in-plane and out-of-plane loading. For this, a commercial mesh and a mesh developed in the textile department of Civil Engineering department were adopted. Additionally, it was also decided to connect the leaves of the typical double leaf infills through steel ties to assess their out-of-plane behavior.

Finally, a numerical analysis based on finite element modeling was carried out to assess the influence of different parameters like the properties of materials and height to length ratio on the in-plane response of the brick infills. Additionally, a proposal was provided to calculate the stiffness and strength of brick infill with a random distribution of openings.

## **1.2 Thesis Outline**

Besides the introductory chapter, in which the framework and the definition of objectives and methodology are presented, this PhD thesis is composed of more 7 chapters, where the presentation and discussion of the work on the experimental and numerical research are provided.

Chapter 2 provides an overview about the experimental and numerical studies carried out on the in-plane and out-of-plane behavior of infilled frames. An overview of different strengthening techniques investigated by different researchers is also presented. Chapter 2 concludes with a review of various numerical modelling approaches of masonry infilled frames.

Chapter 3 describes the prototype of the masonry infilled frame along with designing the half-scale models to be tested in the in-plane and out-of-plane directions. Additionally, the description of the details of the experimental setup and procedures of the in-plane static cyclic tests is carried out. The in-plane testing is focused on double leaf brick infills, which are characteristic of masonry infills of rc buildings constructed in the past decades in Portugal and other Mediterranean countries. The in-plane tests are carried out until the collapse of the brick infills and until different lateral drifts in some specimens aiming at imposing distinct levels of in-plane damage. All the results are presented and discussed in this chapter.

Chapter 4 deals with the out-of-plane testing of masonry infilled frames. For this, a novel experimental setup based on airbags to apply a uniform out-of-plane loading is developed. Besides the test setup, the procedure, instrumentation and loading protocol are described. In the out-of-plane testing campaign different parameters are considered aiming at evaluation of their influence on the out-of-plane response, namely: (1) workmanship used in the construction of the masonry infills. For this, two different masons are used in the construction of the brick infills; (2) presence of opening in the out-of-plane response of brick infills; (3) prior in-plane damage corresponding to distinct levels of lateral drift imposed in the in-plane cyclic tests. All results are presented and discussed and a comparative analysis among the specimens is carried out to better understand the influence of different parameters under analysis.

Chapter 5 assesses the performance of the textile reinforced mortar as a strengthening technique of the masonry infills under in-plane and out-of-plane loading. One textile mesh is designed and manufactured in the textile department of Minho University, being compared with an equivalent commercial textile mesh. The details of the application of the strengthened rendering, as well as all experimental results are presented and discussed. A comparison between strengthened and unstrengthened brick infills are presented. The effect of connecting the leaves of the brick infills through commercial ties on the out-of-plane response of infilled frames is also investigated in this chapter. The connection of brick leaves is viewed as a strengthening technique as it is known that this procedure could enhance the out-of-plane response of double leaf infilled frames and consequently reduce its seismic vulnerability.

Chapter 6 is focused on mechanical characterization of the materials and assemblages of masonry that are representative of the brick infills tested in this thesis. Besides compressive tests of bricks

and mortars, results of experimental tests like uniaxial and diagonal compression, flexural in the direction parallel and perpendicular to bed joints carried out in brick assemblages are presented and discussed. Additionally, initial shear test is carried out to obtain the main shear resisting parameters of the unit-mortar interfaces. Based on these tests it is possible to obtain the main mechanical properties of materials and brick masonry assemblages (compressive strength, elastic modulus, shear resistance, shear modulus and flexural strength of brick infills).

Chapter 7 deals with the numerical analysis of the masonry infilled frames under in-plane loading. A finite element model is built and calibrated based on experimental results available in literature. The masonry and concrete are modeled as isotropic and homogeneous materials, being connected together with interface elements. The concrete and masonry are modeled with four-noded elements and their nonlinear behavior are modeled through a Total Strain Crack Model by considering stress-strain curves with exponential and parabolic constitutive laws for tension and compression regimes respectively. For the interface between rc frame and brick infill, a tension-shear-compression cap model is considered to describe different resisting mechanisms that can be mobilized at the levels of the interface. After this, a numerical parametric analysis is carried out to investigate the influence of the material properties and geometry of the infills in the in-plane response of brick infill. Additionally, a particular study is carried out to assess the influence of the presence of openings and their random distribution in the stiffness and strength of brick infills. This Chapter is concluded with the calibration of a finite element model of a brick infill tested in this thesis under out-of-plane loading.

Finally, Chapter 8 presents the main conclusions on the research carried out towards investigation of in-plane and out-of-plane response of infilled frames and also development of strengthening technique based on TRM method. Additionally, some future works are also recommended.



# **CHAPTER 2**

# **LITERATURE REVIEW**

## 2 Literature Review

Based on past earthquakes, it has been observed that reinforced concrete rc buildings with brick masonry infills presented structural deficiencies, which should be associated to the negative interaction between reinforced concrete frames and masonry infill walls. The negative interaction can be associated to the irregularity of masonry infill in the plane and also in the elevation which results in asymmetric distribution of stiffness, promoting collapse mechanisms associated to soft story. The negative effect of the masonry infill on the rc columns associated to localized shear effects results from the geometric discontinuity of masonry infills (for instance the presence of openings very close to the columns) or from the shear damage of masonry infills. Besides, it is also important to focus on the non-structural masonry infills, which have been exhibited a clear vulnerability under seismic actions, both in the in-plane and out-of-plane directions. The in-plane damage includes diagonal cracking and crushing of the top and bottom corners, sliding of the bricks within the infill. The out-of-plane damage of masonry infill develops through its horizontal, vertical or diagonal cracking and often through its vertical rotation as a cantilever due to the inefficient connection of the infill to the RC frame.

These observations have motivated past research on masonry infilled frames to understand the mechanical behavior of the composite structures (masonry infills within RC frames) under seismic action to better act in the mitigation of the seismic effects. With this respect it is important to underline the retrofitting techniques that have been applied in order to improve the seismic performance of masonry infill walls.

This section presents an overview of the main scientific investigations on the in-plane and out-of-plane behavior of masonry infilled RC frames, namely at the level of in-plane and out-of-plane resisting mechanisms, failure modes, empirical formulation to predict the stiffness and resistance. Besides, an overview of the materials and techniques used to strengthen masonry infill walls is also provided.

### 2.1 In-Plane behavior of masonry infilled frames

Past earthquakes such as Mexico City earthquake in 1985 [16], Kocaeli (Turkey) earthquake in 1999 [17] Bhuj earthquake in 2001 [18], L'Aquila earthquake in 2009 [19] have confirmed that masonry infills can affect the global and local behavior of the reinforced concrete (rc) or steel frames. This influence can be positive or negative. When it is positive it means that the presence of masonry infills increases the strength and stiffness of the structure to resist the lateral loads due to earthquakes. As mentioned before, the negative influence mainly relates to the formation of soft story and short column phenomena, which can result in the global or local failure of the structure. As it is shown in the Figure 2.1, the formation of the short column phenomenon happens when masonry infills leave a short portion of the column clear, leading to the shear collapse of the columns. The soft story phenomenon can be observed when the distribution of the infill walls along the height of the structure is irregular.

Aiming at understanding the mechanical behavior of masonry infilled frames different researchers have focused on the in-plane behavior by performing experimental investigations and numerical analysis. An overview of the main issues related to experimental and numerical investigations are provided in the following sections.

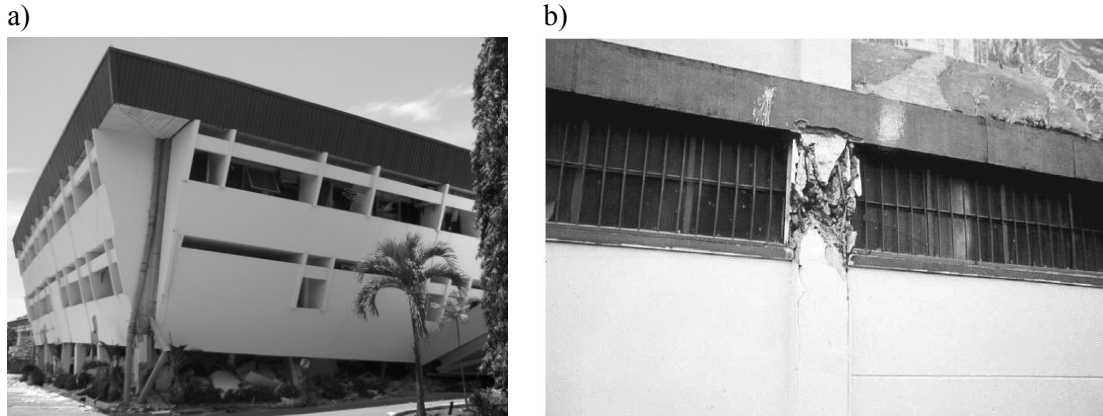


Figure 2.1 Negative effects of infill panel in structure; a)soft story mechanism [37], b)short column mechanism [38]

### 2.1.1 Insight into experimental investigations

In-plane interaction of infill panel with its surrounding frame was studied by different researchers, either considering reinforced concrete (RC) [1-3, 39-42] or steel [10, 13, 43, 44] as structural frames. As common output of the different experimental researches, it is concluded that in the low levels of in-plane loading, the infilled frame acts as a monolithic load resisting system and when the lateral load increases, the infill tends to partially separate from its bounding frame and a compression strut mechanism develops. This assumption for the infill walls behaving as a compression strut seems to be reasonable and has been supported in several experimental researches [45, 46]. Figure 2.2 shows the separation of the masonry infill from its surrounding frame and also the representation of the compression strut model. The dashed line is a compressive strut that develops when the direction of lateral load is in the opposite direction.

The lateral resistance of the infilled frame is not just equal to the sum of the lateral resistances of the infill and the surrounding frame, because the interaction between them alters their independent load resisting mechanisms [2]. A common conclusion among the studies is that the added infills significantly improve the lateral strength and initial stiffness of the bare frame and also change its dynamic properties [39] [47], which results in a relevant change in the seismic demand of the structure. Another contribution of the masonry infill within the frame is the enhancement of the energy dissipation capacity during earthquake due to the cracking of the masonry infill, being possible to increase the damping ratio from 4-6% to 12%, according to what is pointed out in [47].

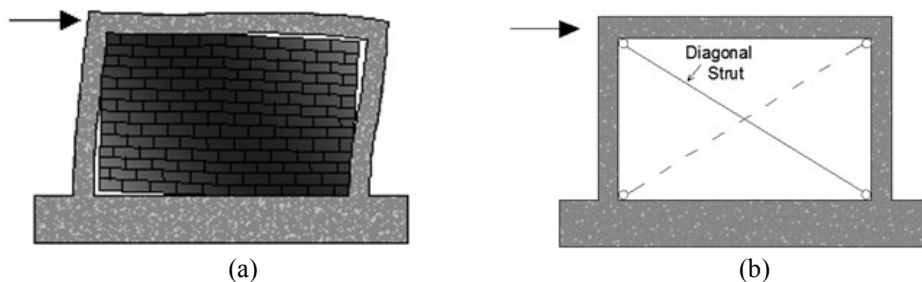


Figure 2.2 Details on the response of masonry infilled frames under in-plane loading; a)separation of the walls from the structural frame; b)equivalent strut model



On the basis of experimental observations, five main failure mechanisms could be investigated as probable failure modes in the infilled frames as it is shown in the Figure 2.3 [2]. Those failure modes depend on the relative strength and stiffness of the bounding frame with respect to those of the infill, the geometric configuration of the frame, as well as the loading condition. In the flexural failure mode the infilled frame is rocking on one of its toes and horizontal cracking form at the base of the structure. Diagonal cracking of the specimen could be observed by formation of stair-step cracks passing through the mortar joints across the compressed part of the infill which is due to the shear failure of the infill. Horizontal slip and mid-height crack failure patterns usually take place in the infill having weak mortar joints and are described as shear failure of infill bed joints. Finally the corner crushing is related to the crushing of masonry in at least one of its corners. This failure mode is related to the formation of high compressive stress at the corners.

Different studies have been carried out to find out the parameters influencing the in-plane behavior of masonry infilled frames [6, 7]. These parameters can be classified into three different categories: a) geometry and mechanical properties of the infill; b) geometry and mechanical properties of the surrounding frame; c) characteristics of the infill-frame interface.

The specimens with strong infills seem to exhibit a better performance than those with weak infills in terms of lateral strength, initial stiffness and energy dissipation capacity [7]. Additionally, it is observed that the mechanical properties of the RC frame, such as compressive strength of the concrete, ratio of longitudinal and transversal reinforcement along with its cross section and element's moment of inertia have significant effect in the behavior of the masonry infilled frame. According to [6], the lateral strength of the system increased nearly 100% when the reinforcement ratio increased from 1.1% to 2.2%. On the other hand, the increase of lateral strength by increasing the reinforcement ratio from 2.2% to 3.4% was moderate [6].

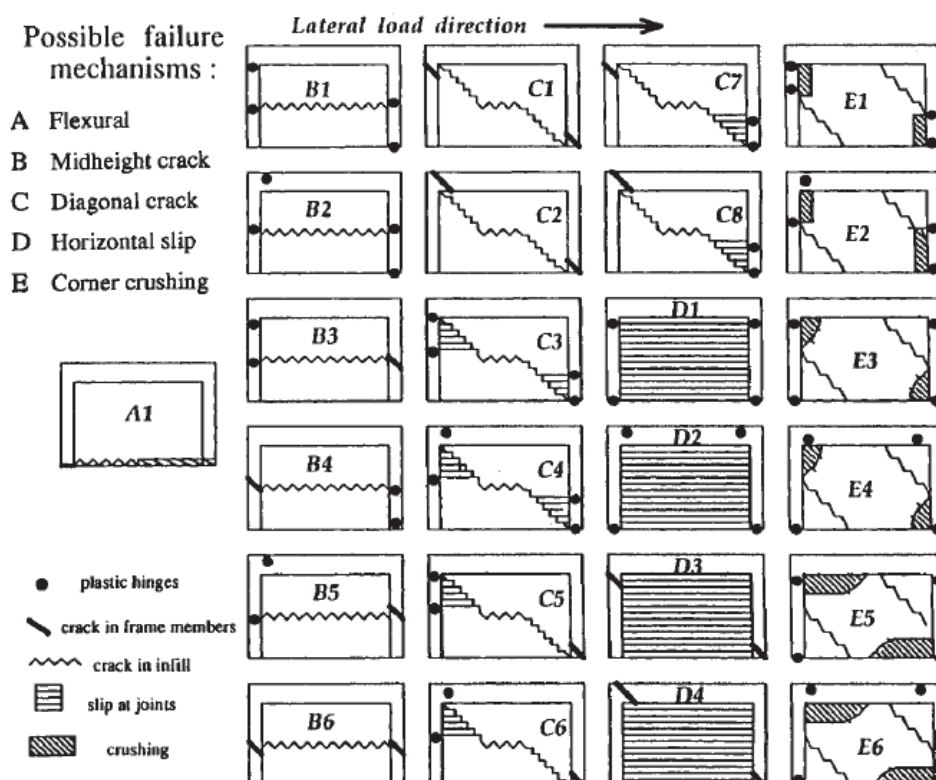


Figure 2.3 Failure mechanisms of masonry infilled frames [2]

The characteristics of the interface between masonry infill and its surrounding frame can also affect the behavior of the masonry infilled frames. With this respect, the unintentional gap between the infill and surrounding frame, which is generally due to the shrinkage in the masonry, is one of the factors that can affect the behavior and the levels of this influence depend on the thickness of the gap. When the width of the gap is very small, the behavior of the infilled frame is slightly affected in the initial stage being reflected by an initial slackness in the force-displacement diagram [48]. By increasing the lateral load, the gap closes and the interface can transfer the shear and normal stresses. On the contrary, when there is a large gap between infill and the frame, the compressive strut develops only partially and the behavior of the structure changes considerably [13, 14]. Another important aspect of the interface between masonry and rc frames is the presence of shear connectors along the interface of the infill and its surrounding frame. It was observed from the experimental results that shear connectors along the whole perimeter of the interface enhance the behavior of the structure by increasing the strength and stiffness [49]. If the shear connectors are only used in the corners they contribute only for the enhancement of the stiffness [50]. On the other hand, the presence of the shear connectors can have a negative effect on the behavior of the structure by providing premature collapse of the infill in areas near the shear studs, where stress concentration develops. The effective way to prevent this brittle fracture mode is to place the shear studs inside a reinforced confining cage [15], see Figure 2.4.

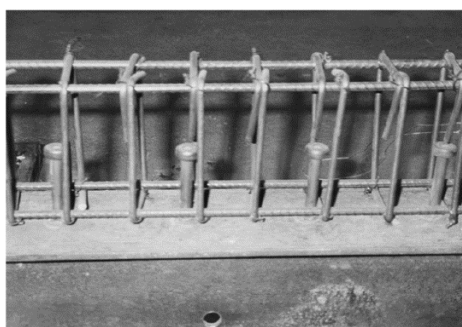


Figure 2.4 Shear connectors inside confining cage [15]

A parameter that has been deserving interest from the scientific community is the influence of openings and of their position in the in-plane behavior of infilled frames [7, 9, 10, 12, 13, 51]. A detailed review of research studies on masonry infilled frames with openings was provided by Surendran et al. [52]. Generally, the presence of openings in the wall decreases the lateral strength and stiffness of the solid infilled frame and changes its cracking pattern [11]. However, the reduction of the lateral resistance of the infill frame is not proportional to the reduction of the area of the infill. According to [53], 50% reduction in the infill area leads to a decrease of lateral strength of the infilled frame in a range between 20-28%. The effect of different positions of the openings on the in-plane behavior of infilled frames was studied by Mallick and Garg [9], where recommendations for the position of the openings were provided. It is recommended that the door opening can best be located in the center of the lower half of the panel and the window opening in the mid-height region of the left or right half of the panel as near to the vertical edge of the panel as possible. Based on the experimental results found by Dawe et al [13], it was concluded that moving the position of the opening towards the loading side results in the decrease on the ultimate load. Kakaletsis [51] also concluded that the movement of the opening towards the center of the span results in further decrease of the lateral strength, stiffness and ductility. Asteris [54] and Giannakes et al [55] proposed stiffness reduction factors of infilled frames for percentage of

openings less than 49%. This reduction factor depends on the percentage of opening area. In the research of Mosalam et al. [10] carried out on four two-bay, one-storey specimens it was concluded that the presence of openings in the infills reduces the stiffness by about 40%, for a lateral load below the cracking load level. Tasnimi et al. [12] tested six large-scale, single-storey and single-bay infilled frames, with central openings of different dimensions and concluded that the presence of openings causes a reduction in stiffness and lateral strength in relation to the solid infilled frame.

### 2.1.2 Empirical formulas to predict stiffness and strength

In this section an overview of different empirical formulations for the estimation of the initial stiffness and lateral strength of one bay and one storey masonry infilled rc frames is presented. These formulations are based on different experimental and numerical studies. The quantitative prediction of the strength and stiffness, gives a preliminary idea about the mechanical properties of the composite structures in the in-plane loading.

The first proposal for prediction of main mechanical properties of masonry infilled frames in the in-plane direction was provided by Holmes [56] by predicting the lateral strength by taking into account the crushing of the infill as failure mechanism, and thus determining the lateral resistance:

$$K = \frac{24E_f I_c \varepsilon_i d \cos \theta}{h^3 \left[ 1 + \left( \frac{I_c}{I_b} \right) \cot \theta \right]} + \frac{t d f'_i \cos \theta}{3} \quad \text{Eq. 2-1}$$

In which  $E_f$  is the modulus of elasticity of the frame,  $I_c$  and  $I_b$  are the inertia moment of columns and beams respectively,  $\varepsilon_i$  is the maximum strain of masonry,  $d$  is the diagonal length of the frame,  $h$  is the height of the frame,  $t$  is the thickness of the infill,  $\theta$  is the angle of diagonal to horizontal and  $f'_i$  is the diagonal compressive strength of masonry infill.

According to this author [56, 57], the lateral stiffness of the infilled frame can be estimated based on the following equation:

$$K = \frac{24E_f I_c}{h^3 \left[ 1 + \left( \frac{I_c}{I_b} \right) \cot \theta \right]} + \frac{t f'_i}{3 \varepsilon_i} \quad \text{Eq. 2-2}$$

Stafford Smith [58] has proposed an equation that predicts the lateral stiffness of the infilled frame by taking into account the strain energies of the windward column, the compressive strut and of the rc frame as:

$$K = \frac{A + B + C}{C(A + B)} \quad \text{Eq. 2-3}$$

$$A = \frac{h \tan(2\theta)}{A_c E_f}, \quad B = \frac{d}{w t E_i (\cos 2\theta)}, \quad C = \frac{h^3 (3I_b h + 2I_c L)}{12E_f I_c (6I_b h + I_c L)} \quad \text{Eq. 2-4}$$

Here, A is the strain energy from tension in the windward column, B is the strain energy from compression in the equivalent strut and C is the strain energy from bending of the rc frame. In the equations 2-4,  $h$  is the height of the column (inches),  $\theta$  is the angle that diagonal of the masonry infill makes with horizontal direction (degrees),  $A_c$  is the cross-sectional area of the column

( $inch^2$ ),  $E_f$  is the elastic modulus of frame (ksi),  $d$  is the diagonal length of the infill panel (inches),  $w$  is the width of the equivalent strut (inches),  $t$  is the thickness of the infill panel (inches),  $E_i$  is the elastic modulus of the infill panel (ksi),  $I_b$  is the moment of inertia of the beam ( $inch^4$ ),  $I_c$  is the moment of inertia of the column ( $inch^4$ ) and  $L$  is the length of the beam (inches).

This author also proposed a dimensionless parameter,  $\lambda_h$ , that expresses the relative stiffness of the infill panel in relation to the frame [59, 60], according to eq. 2-5 (the schematic of the dimensions is shown in the Figure 2.5):

$$\lambda_h = h^4 \sqrt{\frac{E_i t \sin(2\theta)}{4E_c I_c h_i}} \quad \text{Eq. 2-5}$$

In which  $E_i$  is the elastic modulus of the infill panel.

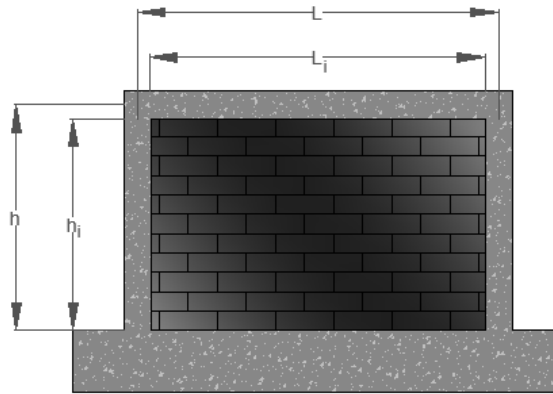


Figure 2.5 Schematic of the masonry infilled rc frame

Mainstone [61] has provided an equation to calculate the initial stiffness of the infilled frames based on the width of the equivalent diagonal strut ( $w_{ef}$ ):

$$w_{ef} = 0.175(\lambda_h h)^{-0.4} \sqrt{h^2 + L^2}, \quad \lambda_h = h^4 \sqrt{\frac{E_i t \sin(2\theta)}{4E_c I_c h_i}} \quad \text{Eq. 2-6}$$

$$K = \frac{E_i w_{ef} t}{\sqrt{L^2 + h^2}} \cos^2(\theta) \quad \text{Eq. 2-7}$$

In the equation presented by Bazan and Meli [62], a dimensionless parameter,  $\beta$ , was introduced, which contrary to the Stafford's second equation evaluates the relative stiffness of the rc frame in relation to the infill panel:

$$\beta = \frac{E_c A_c}{G_i A_i} \quad \text{Eq. 2-8}$$

Where,  $E_c$  is the modulus of elasticity of the rc column,  $A_c$  is the gross area of the rc column,  $G_i$  is the shear modulus of the infill and  $A_i$  is area of the masonry panel in the horizontal plane.

For predicting the lateral strength of the infilled frame, Bashandy [63] has modified the equation represented by Holmes [56] as:

$$H = \frac{24E_f I_c \varepsilon_i d \cos\theta}{h^3 \left[ 1 + \left( \frac{I_c}{I_b} \right) \cot\theta \right]} + A f'_i \cos\theta \quad \text{Eq. 2-9}$$

$$\frac{24EI_c \varepsilon_i d \cos\theta}{h^3 \left[ 1 + \left( \frac{I_c}{I_b} \right) \cot\theta \right]} \leq \frac{4M_{pc}}{h}, \frac{4M_{pb}}{h} \quad \text{Eq. 2-10}$$

Here,  $M_{pb}$  and  $M_{pc}$  are the plastic moments of the beams and the columns respectively.  $A$  is the area of the diagonal strut obtained by using the graphs pointed out by Stafford Smith [59]. The first term on the right-hand side of the Eq. 2-9 represents the load carried by the frame and the second term represents the load that carried by the infill.

A decade after the pioneering work of the Holmes [56] for predicting the in-plane strength of the infilled frames, Mainstone and Weeks [64] proposed equation Eq. 2-11 for taking into account the end crushing of the infill in the corners:

$$H = 0.56(\lambda h)^{-0.875} f'_m h t \cot(\theta) \quad \text{Eq. 2-11}$$

In which  $\lambda$  is the area of the diagonal strut. It is stressed that in this case the lateral strength is only related to the resistance of the masonry infill and the resistance of the rc frame is not considered. On the other hand, Stafford Smith and Coull [65] proposed an equation for predicting the in-plane strength of the infilled frames by taking into account not only the behavior of infill but also its surrounding frame:

$$H = f'_m t \frac{\pi}{2} \sqrt[4]{\frac{4E_c I_c h_i}{E_i t}} \quad \text{Eq. 2-12}$$

Based on the series of large-scale tests on the infilled frames, a simplified method for determining the corner crushing strength of the infilled frames was proposed by Flanagan et al [66] as follows:

$$H = K_{ult} t f'_i \quad \text{Eq. 2-13}$$

In which  $K_{ult}$  is an empirical constant. If the gross area is used for calculating compressive strength ( $f'_i$ ), then the gross area will be used in Eq. 2-13 and if the net area is used for  $f'_i$  then the net thickness will be used for calculating the maximum lateral strength. Table 2-1 provides values for the empirical constant  $K_{ult}$  for each type of infill and surrounding frame.

Table 2-1 Statistical summary of corner crushing results

Specimen Characteristics		Statistical Results of $K_{ult}$		
Infill masonry type	Frame	Number of tests	Mean (mm)	Coefficient of variation (%)
Clay tile	Steel	18	246	23.5
Brick (with outlier removed)	Steel	12(11)	191(201)	17.1(4.6)
Concrete	Steel	19	259	17.3
Concrete	Concrete	10	257	23.3
Clay tile and concrete combined	Steel and Concrete	47	253	20.7
All	All	58	243	21.2

The determination of the maximum strength of the masonry infilled rc frame was made also by Zarnic et al [67] as follows:

$$H = 0.818 \frac{L_i t f_{ci}}{C_1} \left( 1 + \sqrt{C_1^2 + 1} \right), \quad C_1 = 1.925 \frac{L_i}{h_i} \quad \text{Eq. 2-14}$$

Where  $f_{ci}$  is the cracking strength of the infill obtained from diagonal compressive tests.

Lourenco et al [68] have proposed a model that takes into account multiple failure mechanisms by replacing the infill by means of strut-tie model, see Figure 2.6.

The capacity of the tie is associated to the horizontal shear crack collapse mechanism of the masonry infill, and is computed using Eq. 2-15 and Eq. 2-17. The capacity of the strut represents the crushing of the masonry, and can be computed using Eq. 2-18, Eq. 2-19 and Eq. 2-20.

$$f_{crack} = \frac{f_t l t}{2 \tan \gamma} \quad \text{Eq. 2-15}$$

$$\tan \gamma = \alpha \frac{\sqrt{2} \cos \theta}{2 l} \quad \text{Eq. 2-16}$$

$$f_t^* = \frac{f_v a}{2b} \cos^2 \theta \quad \text{Eq. 2-17}$$

$$H_1 = \frac{f_c^{biax,*} \alpha t}{2}, \quad H_2 = \frac{f_c^{biax,*} \alpha t}{2 \tan \theta}, \quad H = \text{Min}[H_1, H_2] \quad \text{Eq. 2-18}$$

$$f_c^{biax} = \frac{1 + 3.65 \tan \theta}{(1 + \tan \theta)^2} f_c \quad \text{Eq. 2-19}$$

$$f_c^* = \left( 0.7 - \frac{f_c}{200} \right) f_c \quad \text{Eq. 2-20}$$

Here,  $f_t$  is the masonry tensile strength,  $l$  is the length of the infill wall,  $t$  is the thickness of the infill wall,  $f_t^*$  is the equivalent tensile strength along the direction of the tie,  $f_v$  is the shear strength of the units,  $b$  is the height of the masonry unit,  $a$  is the length of the masonry unit,  $\theta$  is the angle of the strut from horizontal line,  $\alpha$  is the contact length between the frame and the panel,  $H$  is the maximum horizontal force,  $f_c^*$  is the effective stress and  $f_c$  is the uniaxial compressive strength of masonry. The contact length between frame and infill panel can be calculated using Eq. 2-21 proposed by Stafford Smith et al [60]:

$$\lambda L = L^4 \sqrt{\frac{E_t t}{4 E_c I_c h_i} \sin 2\theta}, \quad \frac{\alpha}{L} = \frac{\pi}{2 \lambda L} \quad \text{Eq. 2-21}$$

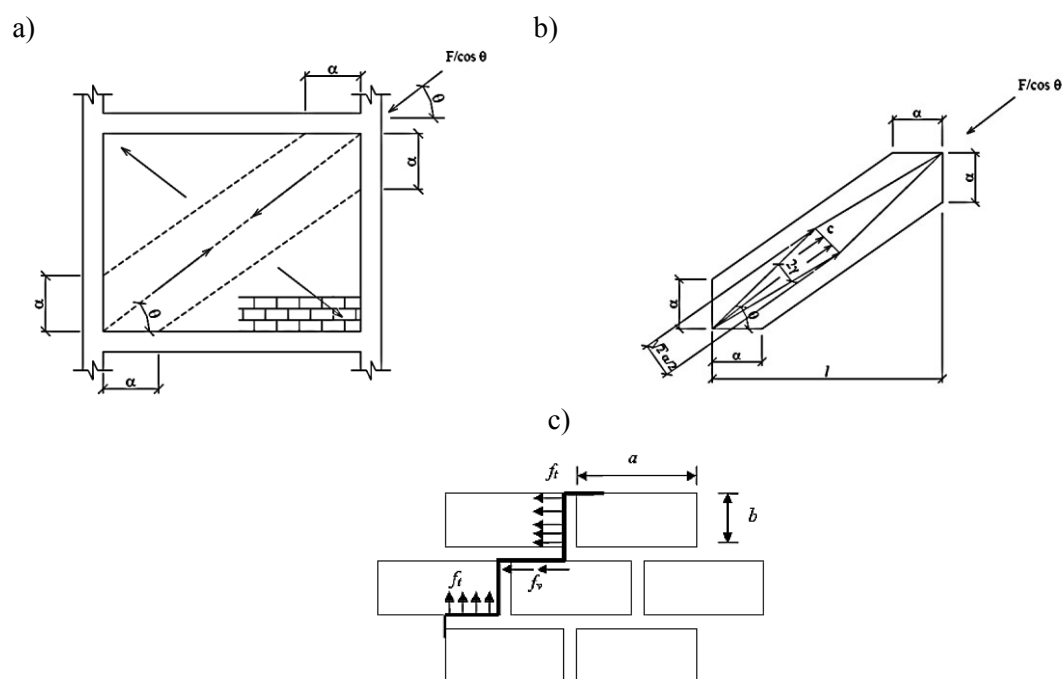


Figure 2.6 Design model for masonry infilled frame subjected for in-plane loading; a) composite frame-panel b) proposed strut-tie model c) equivalent tensile strength for a typical diagonal step crack [68]

### 2.1.3 Numerical investigation

From the numerical point of view two approaches are proposed for analyzing the infilled frames, namely micro modelling and macro modelling. In the micro modelling approach more accurate representation of infill walls' behavior can be obtained, being often used to take into account local effects in detail. This method is useful for local analysis and also for understanding the interaction between rc frame and masonry infills but it is impractical for global analysis due to need for calibrating a large number of parameters and also making enormous calculations. Macro modelling approach is a simplified method intending to describe the role of the masonry infills in the global seismic behavior of rc buildings with masonry infills. In this approach the masonry infill walls are represented by diagonal struts.

#### 2.1.3.1 Macro modelling approach

As a consequence of the experimental results observed in masonry infills under lateral in-plane loading, the masonry infills have been represented numerically through diagonal struts. In this respect, bi-diagonal equivalent-strut model is a widely used method for analyzing the infill behavior within rc or steel frame structures. Polyakov as reported in [46, 53] carried out experimental tests on masonry infills and proposed that the effect of infill panels due to lateral loads is equivalent to a diagonal strut, as it is shown in Figure 2.7. The diagonal strut should be represented by an adequate width so that its linear elastic, mainly related to the stiffness, and nonlinear behavior are adequately reproduced. First, the width of one-third of the diagonal length of the panel was proposed for the diagonal strut [56]. However, other equations along with special charts have been proposed for calculating the width of the equivalent diagonal strut [69-80]. In

the mentioned models, it is assumed that the diagonal strut is active when it is in compression. Another strut model was proposed in [81] by using tension-compression truss elements with half of the equivalent strut's width for diagonal strut in each direction.

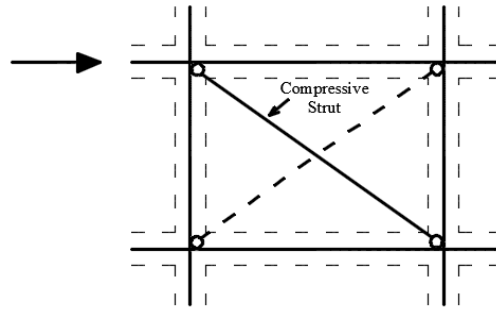


Figure 2.7 Equivalent bi-diagonal strut model

The single diagonal strut model is simple and capable of representing the global behavior of the masonry infill. It cannot predict local effects in the rc frame resulting from interaction between infill and frame. This means that the bending moment and shear forces in the rc frame are not realistic and the location of potential plastic hinges cannot be adequately predicted. For these reasons, modifications on the strut models were done by different researchers [82-85] to overcome the limitations associated to single diagonal strut. The modifications are associated to the increase on the number of diagonal struts representing the masonry infill walls, according to what can be observed from Figure 2.8.

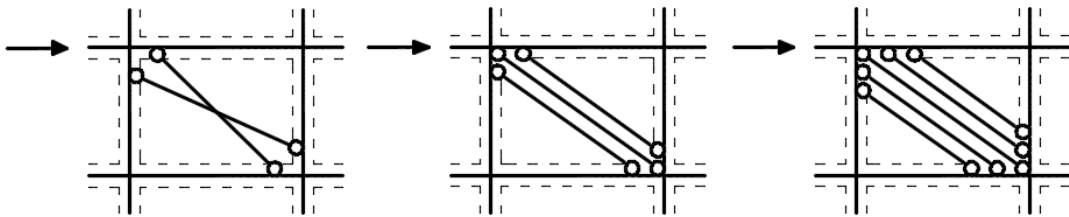


Figure 2.8 Modification on the equivalent bi-diagonal strut model [82-85]

As reported in [6], other complex strut models are proposed for dynamic analysis of the masonry infilled rc frames, in which shear and axial stiffness of the masonry infill is taken into account through diagonal and vertical struts that are connected to the frame as pin-jointed connections [86]. Those struts are uniformly distributed in the panel which represent the shear and axial stiffness of masonry infill. In order to take into account the partial separation of the infill from its bounding frame, the contact length is calculated and those ineffective struts are removed. The effect of openings and also the partial separation between infill and frame are also taken into account in this model. The same procedure was used in this study by removing the struts crossing the opening areas [86].

The models presented before in this section for macro modelling are not capable of describing the horizontal shear slide in the infill walls. To overcome this issue “Knee Braced Frame” model was proposed by Fiorato et al [53]. The struts could capture the bending moments and also shear forces induced in the central zones of the columns. It is also possible to consider the friction mechanism developing along the cracks, which controls the strength of the system. Furthermore, another



model was proposed to represent the horizontal shear sliding in the infill walls as shown in Figure 2.9 [87].

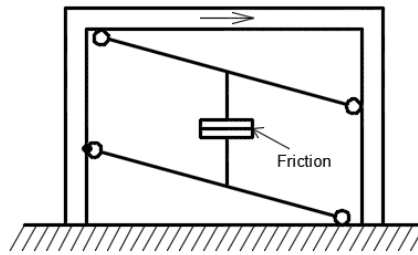


Figure 2.9 Proposed strut model to take into account horizontal sliding

In order to implement nonlinear dynamic or cyclic analysis, the material model of the masonry infill should be described through the force-displacement relationship assigned to the diagonal strut representing its hysteretic behavior. Different models have been proposed to numerically describe the masonry infills with an equivalent diagonal strut model. According to the force-displacement hysteresis diagrams shown in Figure 2.10, the unloading stiffness is always equal to the initial stiffness and the stiffness degradation is taken into account in the reloading branch. The comparison between analytical and experimental results carried out in [45] shows poor agreement between them by using the mentioned material model.

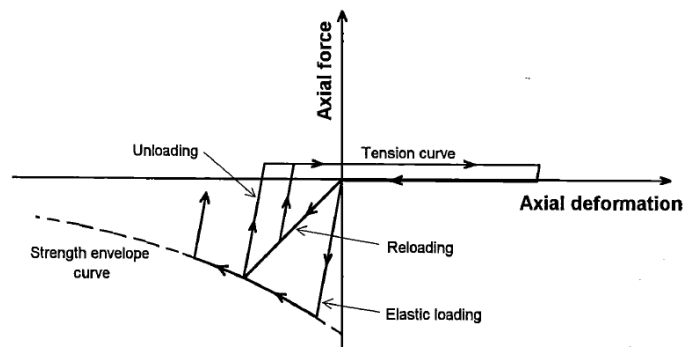


Figure 2.10 Proposed hysteretic force-deformation relationship for the strut [45]

To take into account the gap between the masonry infill and its surrounding frame, the hysteretic model shown in Figure 2.11 was proposed. This material model also takes into account the strength degradation [88].

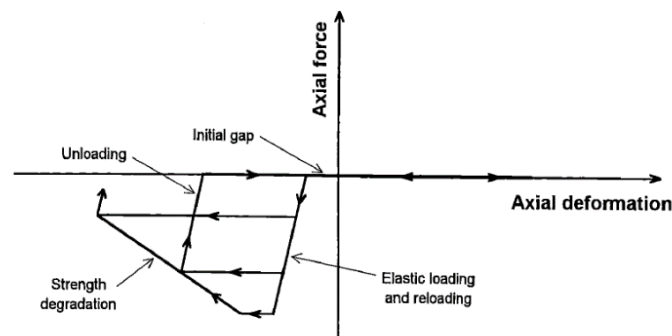


Figure 2.11 Proposed hysteretic behavior for non-integral systems [88]

Another hysteresis law proposed in the literature is shown in Figure 2.12. In this model the strength degradation starts after the strength of the strut has been reached [89].

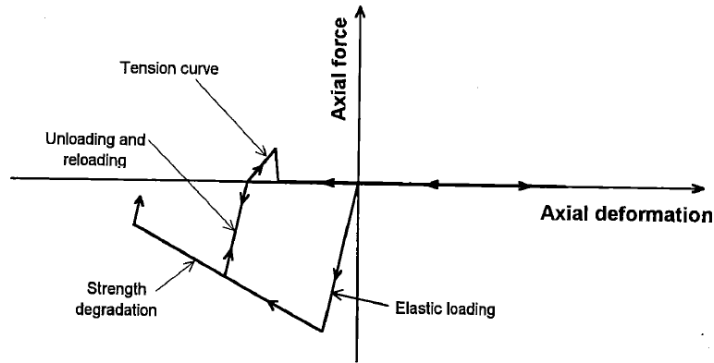


Figure 2.12 Proposed hysteretic behavior for the strut [89]

All of three methods mentioned here, take into account the strength degradation and are similar to each other but the energy dissipation obtained from methods differ from each other. In the conventional bi-diagonal equivalent-strut model, the diagonal struts are assumed to be uncoupled while in reality the infill is composed of only one element, which can lead to the inaccurate results. The proposed models which take into account the coupling of the diagonal struts are discussed in [90-92]. As it is shown in the Figure 2.13, in this case, the masonry infill is assumed as four support strut elements with rigid linear behavior and a central element in which the nonlinear hysteretic behavior is concentrated on it. [90]. The non-linear behavior of the central element is characterized by a multi-linear envelop curve, see Figure 2.14.

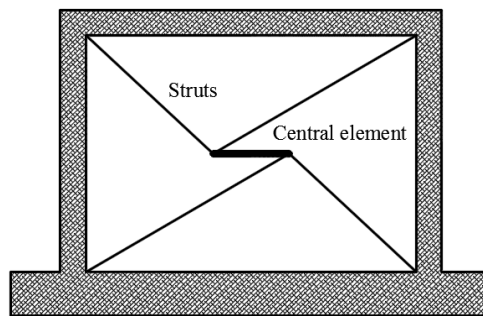


Figure 2.13 Proposed multi strut model [90]

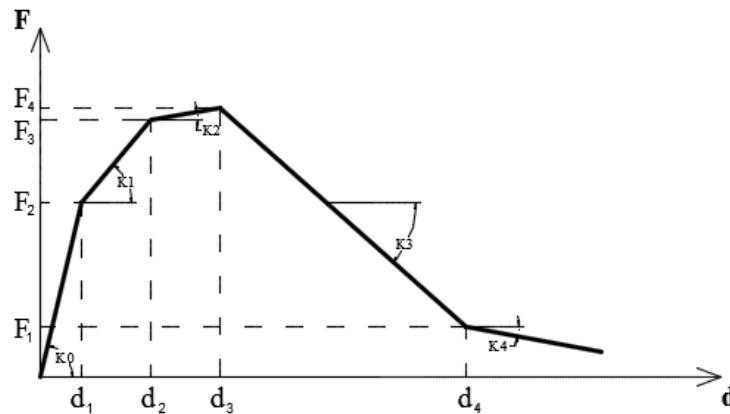


Figure 2.14 Nonlinear behavior of the central element [90]

To take into account the coupling between the struts, Puglisi et al [91, 92] introduced the concept of plastic concentrator that links the two struts and allows for a transfer of effects between them, see Figure 2.15. The experimental results demonstrated that the results of this technique do not match the results of the experiments.

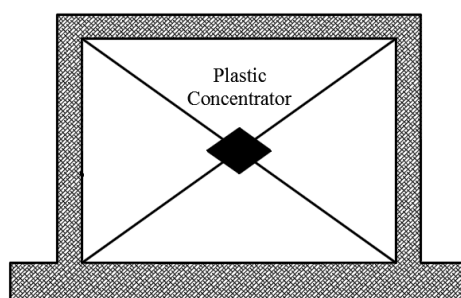


Figure 2.15 Proposed strut model for taking into account the coupling behavior [91, 92]

Various strut and tie models (SAT) were proposed for simple numerical modelling of the infilled frames [93], see Figure 2.16. The choice of the geometric details of the SAT model for infilled rc frames is somewhat arbitrary and can be adjusted based on the experience of the designer and on the balance between the practicality and the accuracy of the model. In general, the material properties of each horizontal strut or tie are obtained from the shear capacity of the interface between the mortar joint and the masonry units. Likewise, the material properties of the vertical struts and ties are obtained from the behavior of the masonry prisms in compression and tension. Similarly, the material properties of the diagonal struts and ties can be estimated from the diagonal compression and tension behavior of masonry assemblies. The area of each strut and tie can be chosen by a trial and error procedure such that the assembly has the same strength and stiffness as predicted by experiments or by FE analyses. The benefits and limitations of each model is discussed in [93] and it is concluded that when carefully calibrated, such simple models lead to acceptable results in the in-plane direction.

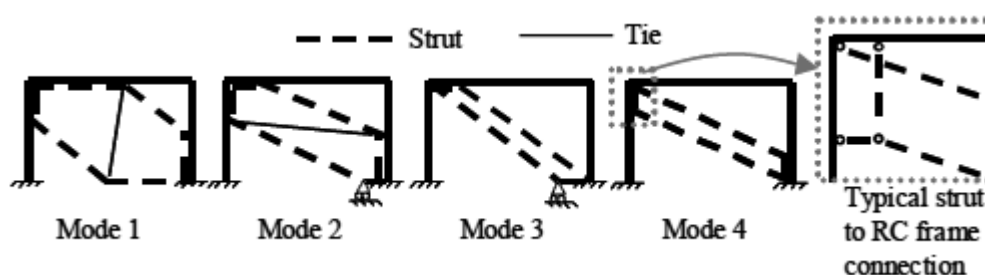


Figure 2.16 various strut and tie models proposed by Hashemi et al [93]

### 2.1.3.2 *Micro modelling approach*

As mentioned before, the micro-modelling approach is followed when detailed analysis of the masonry infilled rc frames is required. Each component of masonry infilled frame has to be modeled with different elements in the finite element method and with different material models. The surrounding frame can be modeled with beam or continuum elements, masonry infill can be modeled as continuum elements and infill/frame interface can be modeled with interface elements. For modelling the masonry infills it is recommended to take into account the masonry nonlinearity to have accurate response. Although using finite element method needs more time

and more computational efforts to prepare the input data, the exact and local response of the structure can be achieved like cracking, crushing and contact interaction [46].

The masonry panel can be modeled following three distinct alternatives [94]: (a) in the first approach, which is called “detailed micro modelling approach”, the masonry is modeled as a set of three different elements, namely masonry units, mortar and interface between unit and mortar with different material properties assigned to them [94, 95], see Figure 2.17b. In this approach, the mechanical behavior of the masonry unit and mortar is needed. Debonding, slip and separation can be observed by using interface elements between masonry and units; (b) with simplified micro-modelling approach, the masonry is modeled as a set of two different elements, namely masonry units and interface elements [96, 97]. Masonry units are considered as continuum elements, whereas the mortar joints are considered as interface elements. These interface elements not only represent the behavior of masonry unit/mortar interface but also the elastic and plastic deformations of mortar itself. Bricks are expanded in two directions with the thickness of a joint to keep the dimensions of the model intact. This is therefore called as “expanded brick model”, see Figure 2.17c; (c) as it is shown in Figure 2.17d, in the third approach, the masonry itself is considered as an homogeneous material [98]. The proper failure criterion should be taken into account by considering the exact material properties to have accurate responses.

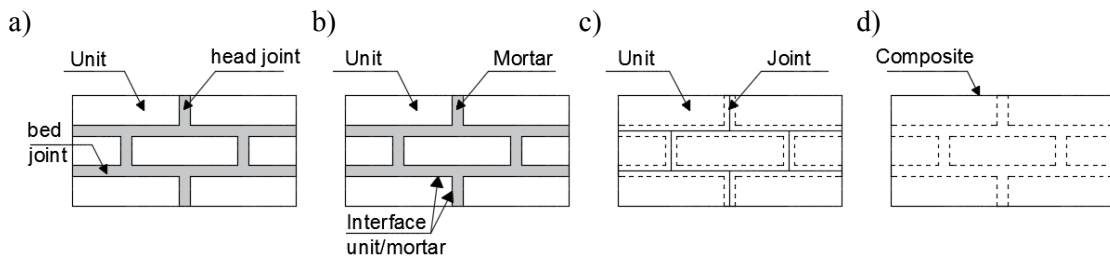


Figure 2.17 Different details that can be adopted in micro modelling approach: a)masonry wall; b)detailed micro-model; c)simplified micro-model; d)finite element macro-model

The modelling of the surrounding frame in the micro-modelling approach can be done using beam elements [99] or continuum elements [2, 84, 100]. In the case of using continuum elements for rc frames, the reinforcing bars must be modeled as additional elements and this needs more effort, whereas in the case of using beam elements, the effect of reinforcing bar is considered implicitly in the element. Interface elements represent the interaction between panel and its surrounding frame and also the discontinuity between them. The behavior of the interface can be modelled by using tie-link [101, 102] or interface elements [84, 100]. More accurate description of the panel and frame is achieved by using interface elements.

## 2.2 Out-of-plane behavior of masonry infilled frames

The vulnerability of masonry infills within concrete frames under out-of-plane loading induced by earthquakes has been observed in several past earthquakes through severe damage and often total collapse [19]. Although the infill panels are assumed as non-structural elements, their damage or collapse is not desirable, given the consequences in terms of human life losses and repair or reconstruction costs. In addition, this type of damage can limit the immediate occupancy after the earthquake event. Aforementioned earthquakes such as L'Aquila earthquake [19], highlight the damages developed in the infill walls in relation to the minor cracks observed in the

structure. In these cases, it was observed that no immediate occupancy was possible due to the generalized damage developed in the masonry infills. As it is observed in Figure 2.18, the ground motion was not strong enough to cause structural damage but due to improper anchorage and interaction of the infill walls with surrounding frame, the exterior walls tore away and the concrete beam and columns were exposed. Out-of-plane failure of the infills such as rocking failure can be observed in partition walls and also in cavity walls when there is no proper transversal connection between the leaves as it is shown in Figure 2.19.



Figure 2.18 Damage in non-structural elements [19]



Figure 2.19 Detachment of the leaves in multi leaf walls [19]

The literature review about out-of-plane behavior of infilled frames is carried out in two levels: (a) experimental investigations which briefly describe the main experimental results available in literature; (b) numerical investigations which focuses on the results of the numerical analysis performed on these kind of structures.

### 2.2.1 Experimental investigation

In spite of out-of-plane behavior of masonry infilled frames have been less studied than masonry infill under in-plane loading, some studies on the out-of-plane behavior of masonry infilled rc frames can be found in literature [30, 103-106]. From experimental analysis, it has been observed that the masonry infill panel surrounded by rc or steel frame can resist significant out-of-plane loads due to formation of arching mechanism [106]. The development of the arching mechanism in the masonry infill is dependent on its confinement by the surrounding frame. When there is no confinement, the out-of-plane resistance is controlled by the rocking resistance along its base as is shown in Figure 2.20.

According to FEMA 356 [107] the formation of arching mechanism is ensured when all the following conditions are satisfied simultaneously: (a) the panel is in full contact with the surrounding frame components; (b) the product of the elastic modulus,  $E_f$ , of the surrounding frame times its moment of inertia,  $I_f$ , of the most flexible frame component exceeds a value of  $24.82 \times 10^6 \text{ N.mm}^2$ ; (c) the frame components have sufficient strength to resist thrusts from

arching of an infill panel; (d) the height ( $h_{inf}$ ) to thickness ( $t_{inf}$ ) ratio of the masonry infill wall is less than or equal to 25. Arching mechanism within the infill may form in horizontal, vertical or in both horizontal and vertical directions. When only horizontal or vertical arching mechanism develops, it means that the masonry infill has no proper confinement in its upper or bottom interfaces or in the vertical interfaces respectively, see Figure 2.21. When all the interfaces between infill and frame provide confinement to the infill, both horizontal and vertical arching mechanism develops leading to the typical cracking pattern shown in Figure 2.22.

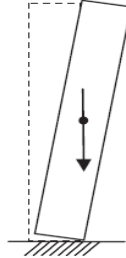


Figure 2.20 Rocking at base due to insufficient confinement of masonry infill wall

An experimental campaign on 21 full scale concrete block walls under out-of-plane loading was carried out by [105] to investigate the influence of different boundary conditions and vertical pre-compression load on their out-of-plane behavior. The out-of-plane load was applied monotonically by increasing the pressure inside an airbag. Tests were performed with simple support conditions on all four boundaries, on the bottom and two sides, on only two sides and on only top and bottom of the wall. It was concluded that the failure mode of each masonry panel was totally compatible with the concept of the yield line theory that is usually used in the slabs.

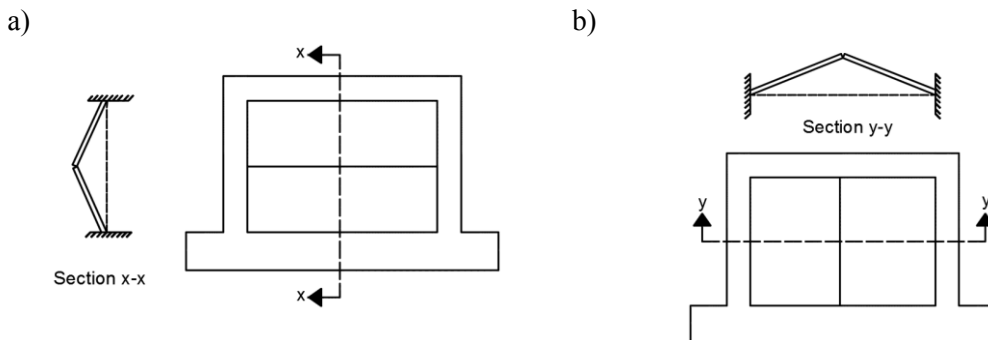


Figure 2.21 a)Vertical and b)horizontal arching mechanism

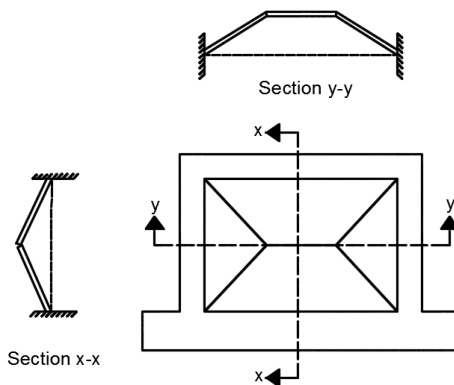


Figure 2.22 Formation of two way arching mechanism

The effect of different boundary conditions on the out-of-plane behavior of the infilled frames was also investigated by other researchers [30, 103, 108]. Different connecting conditions at the top interface between the infill and the frame were considered: (1) joint completely filled with mortar; (2) joint partially filled with mortar; (3) joint with a horizontal gap of 3 mm due to shrinkage of the fresh mortar and (4) masonry infill with unsupported top. No significant differences in the behavior of the infills with complete and partially filled top joint have been found. In case of the gap with 3 mm thickness in the upper mortar joint a clearly modified behavior of the specimen was recorded. The presence of an initial gap in the top joints increases the relative displacement in the gap causing tilting of the infill panel. Infill panel with unsupported top behaved as cantilever beam. It was also concluded that the presence of opening does not alter the specimen's dynamic behavior.

The experimental program carried out by Dawe and Seah [104] included 9 full scale masonry infilled steel frames subjected to uniformly distributed lateral pressure applied in small increments. The influence of boundary conditions, joint reinforcement, panel thickness and presence of openings was investigated. From the experimental results, it was concluded that infill compressive strength, panel dimension, boundary conditions and rigidity of the surrounding frame have a significant effect on the ultimate load. For instance it was concluded that the infill having four supports at its boundaries without any slippage at them, represents higher out-of-plane resistance. It was also concluded that the ultimate load increases parabolically with increasing panel thickness, but decrease with increasing panel length and height. On the other hand, the presence of a central opening with about 20% of the infill area did not affect the ultimate strength but reduced postcracking deformation ability. An extensive parametric study was conducted and empirical equations for the prediction of the out-of-plane resistance, corresponding to different boundary conditions, were represented in Table 2-2.

Table 2-2 Equations proposed for out-of-plane resistance of masonry infills

Proposed equation	Boundaries	Conditions
$q_{ult} = 800(f'_m)^{0.75} t^2 \alpha / L^{2.5}$	panel supported on three sides and free at the top	$\alpha = \frac{1}{H} (EI_c H^2 + GJ_c tH)^{0.25} \leq 75$
$q_{ult} = 800(f'_m)^{0.75} t^2 (\alpha / L^{2.5} + \beta / H^{2.5})$	panel supported on four sides	$\alpha = \frac{1}{H} (EI_c H^2 + GJ_c tH)^{0.25} \leq 50$ $\beta = \frac{1}{L} (EI_b L^2 + GJ_b tL)^{0.25} \leq 50$

In which  $q_{ult}$  is the ultimate load in (kPa),  $f'_m$  is the compressive strength of the infill (MPa),  $t$  is the thickness of the panel (mm),  $L$  is the length of panel (mm),  $H$  is the panel height (mm),  $E$  and  $G$  are Young's and shear modulus of the frame members respectively (MPa),  $I_c$  and  $I_b$  are the moment of inertia of the columns and beams respectively ( $\text{mm}^4$ ) and  $J_c$  and  $J_b$  are torsional stiffness of the columns and beams, respectively ( $\text{mm}^4$ ).

A series of experiments were performed by Angel et al [109] focusing on the out-of-plane resistance of masonry infill walls. The panels varied from uncracked specimens, cracked specimens and repaired specimens, to specimens tested with loads applied in both the in-plane and the out-of-plane directions. The tests were performed monotonically by means of airbag in pressure control until the maximum allowable capacity of the system was reached. It was

concluded that the in-plane cracking reduces the out-of-plane capacity of the slender panels by a factor as high as 2 and the out-of-plane capacity of the panels are totally dependent on its slenderness ratio and compressive strength. It was also concluded that the repairing techniques increased the out-of-plane capacity of damaged infills by a factor as high as 5. Analytical equations were proposed for out-of-plane strength of the infill taking into account the effect of prior in-plane damage. It seems that the proposed equation is based on the formation of two-way arching mechanism.

$$q = \frac{2f'_i}{\left(\frac{h_i}{t}\right)} R_1 R_2 \lambda \quad \text{Eq. 2-22}$$

In which  $f'_i$  is the compressive strength of the infill,  $h_i$  is the height of the infill,  $t$  is the thickness of the panel,  $R_1$  is the reduction factor for prior in-plane loading and  $R_2$  is the reduction factor for accounting non rigid bounding frame.

$$R_1 = \left( 1.08 + \left(\frac{h_i}{t}\right) \left\{ -0.015 + \left(\frac{h_i}{t}\right) \left[ -0.00049 + 0.000013 \left(\frac{h_i}{t}\right) \right] \right\} \right)^{1/2 \Delta_{cr}} \quad \text{Eq. 2-23}$$

In which  $\Delta$  is the maximum in-plane drift and  $\Delta_{cr}$  is the in-plane drift at cracking.

$$R_2 = 0.357 + (2.49 \times 10^{-14} EI) \leq 1.0 \quad \text{Eq. 2-24}$$

In the above equation,  $EI$  is the flexural stiffness of the smallest member of the confining frame at the panel edge with no continuity ( $N.mm^2$ ). The authors suggest that a value of  $R_2$  be calculated for both vertical and horizontal arching, and the largest value be adopted. This is because the panel will arch as long as there is confinement in one direction, even if there is no confinement in the other direction.

For the typical value of the height to thickness ratio, ranging from 10 to 40, the equation for the parameter of  $\lambda$  is:

$$\lambda = 0.154e^{-0.0985 \frac{h_i}{t}} \quad \text{Eq. 2-25}$$

Dynamic tests on 8 half-scale bare and infilled frames with increasing levels of ground motion were carried out by Bashandy et al [63]. From the results, it was concluded that both out-of-plane resistance and stiffness of the panel are affected by the compressive strength of the masonry. For the prediction of the out-of-plane resistance, the authors proposed the following equation

$$q = \frac{8}{h_i^2 L_i} \left\{ M_{yv} [(1 - h_i) + h_i \ln(2)] + M_{yh} \left( \frac{x_{yv}}{x_{yh}} \right) \ln \left( \frac{L_i}{L_i - h_i/2} \right) L_i \right\} \quad \text{Eq. 2-26}$$

The terms  $x_{yv}$  and  $x_{yh}$  are the maximum out-of-plane deflection for vertical and horizontal strips (mm),  $E_i$  is the modulus of elasticity of the infill (MPa) and  $f_i$  is its compressive strength of masonry (MPa).

The moment  $M_{yv}$  ( $N.mm/mm$ ) is given by:



$$M_{yv} = \frac{0.85f'_i}{4} (t - x_{yv})^2, \quad x_{yv} = \frac{tf'_i}{E_i \left[ 1 - \frac{h_i}{2\sqrt{(h_i/2)^2 + t^2}} \right]} \quad \text{Eq. 2-27}$$

The moment  $M_{yh}$  (N.mm/mm) is given by:

$$M_{yh} = \frac{0.85f'_i}{4} (t - x_{yh})^2, \quad x_{yh} = \frac{tf'_i}{E_i \left[ 1 - \frac{L_i}{2\sqrt{(L_i/2)^2 + t^2}} \right]} \quad \text{Eq. 2-28}$$

A summary of large and reduced scale unreinforced masonry infill testing program is presented in [110]. Some of the tests were performed statically and some of them were performed dynamically by using a shaking table. In the large-scale panels tested with an airbag it was concluded that out-of-plane strength of the infill is many times greater than the predicted values that do not take into account the influence of arching mechanism.

In the sequential tests performed by Calvi et al. [111], the out-of-plane strength of the infill was obtained as a function of prior in-plane damage. Out-of-plane forces were applied monotonically in a four point loading configuration. The effect of putting light reinforcement in the mortar joints or internal plaster were investigated to improve the response of the infilled frame in terms of out-of-plane strength.

An extensive experimental test was performed by Pereira et al [3], which also compared their results related to the out-of-plane resistance with analytical methods available in the literature and also recommendation of standards. It was concluded that that the analytical equation of Angel et al [109] is the most suitable equation, being modified to:

$$q = \frac{f_{cmw}}{\left( \frac{h}{t_w} \right)} R_1 R_2 \lambda \left[ 0.77 C_f \left( \frac{h}{l} \right) + 0.34 C_f \right] \quad \text{Eq. 2-29}$$

$$C_f = \frac{f_{x1}^i}{f_{x1(Ref-01)}} \quad \text{Eq. 2-30}$$

Here,  $f_{cmw}$  is the compressive strength of masonry,  $h$ ,  $l$  and  $t_w$  are the height, length and thickness of the infill wall,  $R_1$ ,  $R_2$  and  $\lambda$  are defined in [109] as mentioned before,  $f_{x1}^i$  the flexural strength in the direction parallel to the bed joints and  $f_{x1(Ref-01)}$  is the flexural strength in the direction parallel to the bed joints of the wall to be taken as a reference, i.e. the unreinforced solution.

The out-of-plane strength of an infill panel in pounds per square foot ( $q_{in}$ ) calculated according to standard FEMA 356 [107] is determined using the following equation;

$$q_{in} = \frac{0.7 f'_m \lambda_2}{\left( \frac{h_{inf}}{t_{inf}} \right)} \times 144 \quad \text{Eq. 2-31}$$

In which  $f'_m$  is the lower bound of masonry compressive strength and  $\lambda_2$  is a slenderness parameter provided in FEMA 356. It is worthy to note that the lower bound material properties

shall be based on mean values from test data minus one standard deviation. The values of the parameter  $\lambda_2$  depend on the masonry infill wall slenderness, see Table 2-3.

It is also mentioned that in the case of formation of arching mechanism, the mid-height deflection of the infill panel,  $\Delta_{inf}$ , divided by the infill height,  $h_{inf}$ , shall be determined in accordance with:

$$\frac{\Delta_{inf}}{h_{inf}} = \frac{0.002 \left( \frac{h_{inf}}{t_{inf}} \right)}{1 + \sqrt{1 - 0.002 \left( \frac{h_{inf}}{t_{inf}} \right)^2}} \quad \text{Eq. 2-32}$$

Table 2-3 Values of  $\lambda_2$  with respect to height to thickness ratio (interpolation shall be used)

$h_{inf}/t_{inf}$	5	10	15	25
$\lambda_2$	0.129	0.060	0.034	0.013

### 2.2.2 Numerical investigation

As mentioned before, the numerical analysis of infilled frames is commonly carried out through two different modelling approaches, namely macro and micro modelling approach. It should be stressed that the out-of-plane numerical modelling of masonry infilled rc frames in terms of macro modelling approach is not so advanced, when compared with in-plane numerical analysis.

With respect to macro modelling approach, a 3D strut and tie model (3D SAT), see Figure 2.23, was proposed by Hashemi and Mosalam [93] to directly couple the in-plane and the out-of-plane internal forces by introducing a normal-to-the-wall degree-of-freedom at the center of the infill wall, which can be assigned mass and out-of-plane forces.

The model consists of eight compression-only struts, arranged as shown, connected with a tension-only tie at the center point of the infill panel. The nature of the compressive stress-strain relationship is indicated in Figure 2.23. From zero to peak stress the relationship is parabolic, whereas the post-peak relationship is linear, down to a constant residual resistance. As discussed in [112], the proposed 3D SAT model may be problematic under certain conditions. For instance the model could become unstable under combinations of high in-plane displacements and high out-of-plane loads.

To deal with these kind of problems, a new model with fiber discretization was developed by Kadysiewsky et al [112]. As it is shown in Figure 2.24, for each infill panel, representing a single bay in a single story, the model consists of one diagonal member. That member is composed of two beam-column elements, joined at the midpoint node. This node is given a lumped mass in the out-of-plane direction.

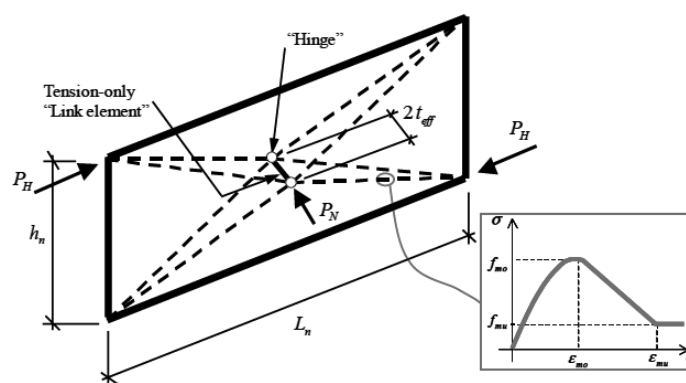


Figure 2.23 Strut and tie model proposed by Hashemi and Mosalam [93]

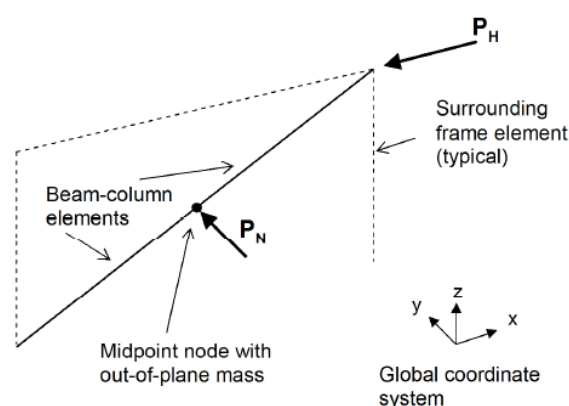


Figure 2.24 Proposed infill model using beam-column elements with fiber discretization

Besides the problems related to the proposed model discussed in [112], it was concluded that for pure out-of-plane deflections, the model provides acceptable results in terms of natural frequency and support reactions where it is originally attached to the surrounding structure.

For numerical analysis of infilled frames in out-of-plane direction using micro modelling approach, few studies are available in literature [93, 113]. In this case each component of the masonry infilled rc frames is modelled separately. Masonry infill could be modelled similar to micro modelling approach in the in-plane direction. To do this, three different modelling approaches of detailed, expanded and homogeneous types could be used. The modelling of the surrounding frame in the micro-modelling approach can be done using beam elements or continuum elements. The behavior of the interface can be modelled by using tie-link or interface elements.

### 2.3 Retrofitting techniques of masonry infilled frames

The high seismic vulnerability of the masonry infilled frame structures observed during the last decades has promoted research on the techniques and materials to strengthen the masonry infill walls and thus to improve their seismic performance. With this respect, conventional techniques or innovative materials for in-plane and out-of-plane strengthening has been presented. The conventional techniques such as jacketing, ferrocement, shotcrete and repointing needs evacuation of the buildings and also have some disadvantages like space reduction, addition of heavy mass and corrosion. The strengthening can also change the behavior of the structure by changing its fundamental period of the structure as well as the center of mass and stiffness. The

advantages and disadvantages of the conventional technique are deeply discussed in [20, 21]. For instance, using shotcrete and ferrocement techniques enhances the out-of-plane stability of the infilled frame. In the in-plane direction, the advantages of ferrocement technique could be summarized as low cost, low technology and limited added mass while its disadvantages are space reduction, limited efficiency in terms of enhancing stiffness and strength and energy dissipation capacity. Although by using shotcrete technique, very significant enhancement in the strength and energy dissipation capacity of the specimen could be obtained, it is a space reduction technique which adds heavy mass to the structure that totally changes its dynamic behavior.

In terms of advanced strengthening techniques, composite materials have been receiving large attention from the research community and they have been already applied in real context. In this section, a brief overview of past research carried out in the scope of strengthening of masonry infills with composite materials and the presentation of an alternative material that has been under development at University of Minho are provided.

### 2.3.1 Composite Materials

As it is shown in the Figure 2.25, fiber reinforced polymers (FRP's) consist of three different components, namely reinforcement, matrix and reinforcement-matrix interface. Reinforcement is a discontinuous part that is responsible for the strength and stiffness characteristics of the FRP. Matrix is the continuous component which protects the reinforcement and finally the interface is attributed to the chemical interaction between reinforcement and matrix. The reinforced polymer materials based on carbon fibers (CFRP), glass fibers (GFRP) and aramid fibers (AFRP) are many times stronger than the steel and their stress-strain behavior is linear elastic until the failure and typically exhibit brittle failure.

The fiber reinforced polymers (FRP's) are a class of advanced composite polymers that have been widely used in space industries and due to its exclusive characteristics like lightweight, corrosion resistance, good mechanical properties and easiness of installation is one of the most common materials in the field of civil engineering [114]. With this regard, different researchers investigated the effect of using FRPs on the in-plane [22-25, 28] and out-of-plane [29, 31] behavior of masonry infilled frames.

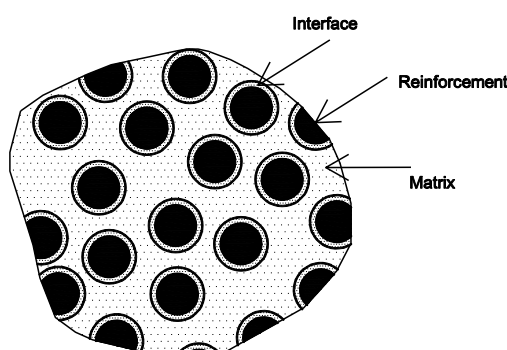


Figure 2.25 Constituents of FRP

The effect of different FRP configuration on the in-plane behavior of infilled frames were investigated by Yuksel et al and Ozkaynak et al [26, 28], see Figure 2.26. It is observed that all the FRP retrofitting configurations increase the strength of the system by a factor of 14-69%,

stiffness by a factor of 2.86–4.03 times and energy dissipation capacity by a factor of 0.5 to 1.5 times when compared with un-retrofitted system. By comparing the different configurations it is also observed that cross diamond-braced frame exhibited considerable increase in strength and energy dissipation capacity and lower amount of damage among other configurations [28].

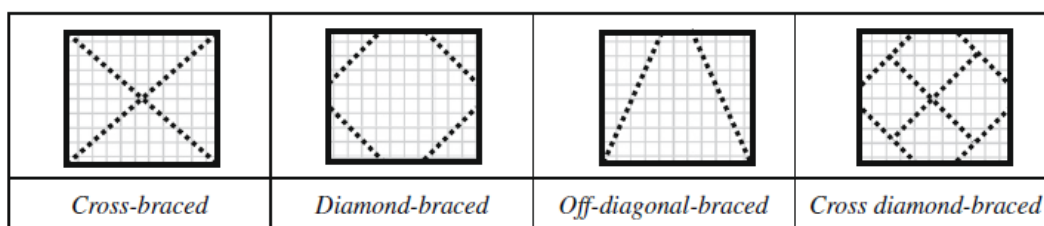


Figure 2.26 Different FRP configuration techniques studied in [28]

In the experimental study carried out by Ozkaynak et al [26], twelve 1/3-scaled rc frames were built and tested under in-plane loading configuration: (a) bare frame; (b) masonry infilled control specimens without reinforcement; (c) masonry infilled frames with cross-braced strengthening; (d) masonry infilled frames with cross diamond braced strengthening. Two testing techniques, namely quasi-static (QS) and pseudo-dynamic (PsD) tests were considered. A significant enhancement of the seismic performance was achieved with the cross-braced and cross diamond-braced strengthening configurations in terms of inter-storey drift, lateral load capacity, energy dissipation capacity, stiffness and the observed damages. It was also observed that the force-displacement diagrams obtained in pseudo-dynamic and quasi-static loading fits together with negligible differences. On the other hand, the cumulative energy dissipation in quasi-static tests was found to be lesser than the one obtained from pseudo-dynamic test due to the great number of reverse cycles used in this loading type. Besides, it was observed that pseudo dynamic tests caused more damage than quasi-static tests.

Valluzi et al [27] conducted an in-plane experimental study on brick masonry panels retrofitted with different configurations of FRP laminates. The specimens were subjected to diagonal compression tests and it was concluded that one-side retrofitting of the panels provide limited effectiveness and the diagonal configuration is more efficient in terms of shear capacity than the grid set up. It was also seen that less stiff FRP's system seem to be more effective in terms of strength and stiffness.

In the study carried out by Altin et al [22], ten specimens of masonry infilled non-ductile rc frames retrofitted by CFRP laminates in diagonal configuration were tested under in-plane cyclic loading. It was observed that the specimens receiving CFRP strips in diagonal configuration showed higher lateral strength and stiffness. It was also found that the lateral strengths of specimens with CFRP strips on both sides of the infill wall increased by 2.18 and 2.61 times when compared to the values obtained in specimens with CFRP strips on one side only. The increase in lateral stiffness for the same specimens was 4 and 6 times in relation to the reference specimen. The specimens with CFRP strips installed on the interior side have the same strength and stiffness as the specimens with CFRP on exterior side. Therefore, if it is desired to use FRP sheets in only one side, there is no difference to install the FRP sheet on interior or exterior side. Another contribution of this study is that when the width of the CFRP increases, the increase in strength and stiffness can be limited.

Few researchers investigated the out-of-plane behavior of infilled frames even if this type of failure has been often observed during past earthquakes. In the research conducted by Yi-Hsuan Tu et al [30], four full scale single-storey infilled frame were tested dynamically on a shaking table. The test results revealed that the masonry panel could sustain considerable out-of-plane loads. It was also concluded that the out-of-plane capacity of the structure can be improved if their boundaries could properly strengthened. Another important factor is the thickness of the panel or its slenderness. The panels with double leaf exhibited much higher strength and stiffness than the specimen with one leaf panel.

In the research carried out by Wei Wen Chen et al [29] four infilled frames were tested by applying the out-of-plane load to the top beam. The effect of pre-laid (laying brick wall first and then constructing rc frame) and post-laid technique were investigated to study how the shrinkage affect the behavior of infilled frames. The shrinkage leads to small gap between the masonry wall and its surrounding frame. This shrinkage gap is often observed when the surrounding frame is constructed first and to prevent this the masonry wall is sometimes constructed first. The experiments state that the out-of-plane behavior of the pre-laid (laying brick walls first and then constructing rc frames) and post-laid specimens is similar in terms of force-displacement diagram. The CFRP retrofitted specimens exhibited higher out-of-plane strength (on average, 1.8 times) than un-retrofitted specimens.

Besides the strengthening of masonry walls inside the rc frames, some other research works focused on the experimental assessment of the flexural strength of masonry after strengthening. An example is the work carried out on masonry panels retrofitted through Near Surface Mounted technique (NSM) based on bending tests [31]. With this technique, mortar bed joints were cut, FRP strips were laid horizontally and finally the grooves were filled with mortar. It was concluded that the NSM technique enhances the load carrying and displacement capacity of the masonry. The effective parameter in the use of this technique is the presence of vertical loading which increases the FRP confinement efficiency. The test revealed that the introducing compressive load increases the maximum strength of the specimens by improving the FRP confinement efficiency.

FRC (Fiber Reinforced Composite) is a type of composite that seems to improve some drawbacks of concrete such as brittleness and low tensile strength. This product is obtained by randomly adding a small quantity of short fibers into a cementitious matrix and improves many of its properties such as compressive strength, split tensile strength, flexural strength, shear strength, impact, fatigue, deformation capacity, load bearing capacity after cracking, and toughness properties. The degree of improvement depends upon many factors such as size, type, aspect ratio, and volume fraction of fibers [115].

The in-plane strength and initial stiffness of hollow-brick masonry infill panels that are strengthened with this type of mortars is about 2 and 3 times of un-strengthened structure respectively. Because this strengthening technique is recently developed, it needs further study to investigate its effect on in-plane and out-of-plane behavior of the masonry infill frames [115].

#### **2.4 Textile reinforced mortar (TRM) technique**

In spite of many advantages associated with use of FRPs, this retrofitting technique is not problem-free. Some of its drawbacks are related to the poor behavior of epoxy resins at high temperatures, relatively high cost of epoxy, non-applicability of FRPs on wet surfaces or at low temperatures and incompatibility of epoxy resins with some substrate materials such as clay. Specific properties of clay such as porosity and roughness, which affects the epoxy-brick bond behavior could inhibit the use of FRP [32].

One possible solution to the above mentioned problems can be the replacement of organic binders with inorganic ones such as cement based mortars. The smeared fibers can be replaced by reinforcing meshes such as textile meshes with different continuous fibers. This results in the textile reinforced mortar technique (TRM).

This technique is relatively new (it was started to be used in early 1980s) and has been studied by few researchers [32, 116-118].

From the experimental work carried out by [32] on twelve brick masonry wallets subjected to cyclic out-of-plane loading aiming at investigating the effectiveness of TRM versus FRP and NSM technique it was concluded that the TRM technique leads to higher strength and displacement at failure than FRP. It was also pointed out that NSM technique is less effective in strength but more effective in deformability than FRP and TRM techniques. The authors believe that TRM technique could be a promising solution in seismic retrofitting of structures. The experimental work carried out by Papanicolaou et al [118] on different masonry wallets subjected to in-plane and out-of-plane cyclic loading also revealed that TRM enhances the in-plane and out-of-plane behavior of masonry. For out-of-plane loading, the TRM is more effective than FRP in terms of lateral strength and displacement at failure. For the case of in-plane loading, TRM (compared with FRP) results in reduced effectiveness for strength (but not more than 30%). Nevertheless, in terms of deformation capacity (being of crucial importance in seismic retrofitting of unreinforced masonry walls) TRM is more effective than FRP.

The effect of a new application method in TRM technique was studied in [116] by testing nineteen samples of masonry strengthened with TRM. In the new technique (TRSM) the mortar is projected to the masonry surface to save the application time. Three point bending tests have been performed on the specimens to compare the flexural strength between cases with manually applied mortar (TRM) and sprayed application (TRSM) of the mortar layer. It was concluded that the strengthening mortar has considerable influence on the failure mode. The results show that the productivity of the TRM technique in terms of load bearing capacity and ductility could be increased by spraying the mortar (using TRSM).

The effectiveness of Textile Reinforced Mortar (TRM) as a mean of increasing the flexural capacity of reinforced concrete beams was investigated by performing four point bending tests [117]. A total number of six rc beams were tested and it was concluded that TRM-based strengthening system is slightly less effective in terms of enhancing the flexural strength of rc beams but more effective in terms of deflection ductility. It is also indicated that using polymer-modified cementitious mortar provides better bond between textile sheets and concrete substrate than cementitious mortar.

Martins et al [35] proposed and innovative strengthening technique of TRM on infills by making some bending tests on masonry wallets. The strengthening material is designated as braided composite rod (BCR) and it results from a braiding process. In Figure 2.27 the representative scheme of the original transversal section of a BCR can be observed, having 16 multifilaments of polyester and a core filled with multifilaments of reinforcing fibers. In order to fill the voids between the materials and to give stability and homogeneity to the composite, a resin matrix is applied.

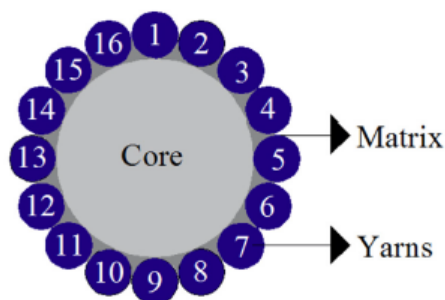


Figure 2.27 cross section of a braided mesh [35]

Different typologies of braided structures were investigated by pull-out tests and finally it was concluded that braided structure with 15 multifilaments of polyester with 11 Tex and one braided element with a simple structure consisted of 8 braided polyester yarns produce at the maximum speed of the production equipment (1.07m/min) could be assumed as optimum material which provides enhanced bond adherence between polyester rods and the rendering mortar.

Then, fifteen wallets of masonry were tested under four-point bending tests; namely three wallets as reference specimen, three specimens retrofitted by commercial glass fibers, three specimen retrofitted by commercial carbon fibers, three specimens retrofitted by optimum developed BCR meshes of carbon and three specimens retrofitted by optimum developed BCR meshes of glass fiber. It was concluded that retrofitted specimens provide enhanced behavior in terms of increasing the flexural cracking load and maximum resistance to bending. It was also concluded that the specimens strengthened with manufactured reinforcing meshes of glass fibers with BCRs exhibits higher resistance to bending than other retrofitted specimens. It should be also mentioned that the specimen retrofitted with manufactured meshes of braided composite materials with a core of glass fibers present remarkably better post-peak behavior than the other retrofitted specimen.

Finally the authors recommended that the meshes produced with glass fibers are advantageous in terms of their mechanical behavior and can be custom-designed.

In a recent study carried out by Da Porto et al [33] the effectiveness of different strengthening solutions for light masonry infills were investigated by testing eight full-scale one-bay one-storey clay masonry infilled frames. In this context the solutions were considered as: 1) special lime-based plaster with geo-polymer binder, 2) bidirectional composite meshes applied with inorganic materials (TRM), 3) TRM improved by anchorage of the mesh to the rc frame. The specimens were subjected to the combined in-plane/out-of-plane loading. Cyclic in-plane loading until lateral drift of 1.2% was applied to the specimens and then they were subjected to the out-of-plane loading to be collapsed. It was concluded that application of special plasters or TRM strengthening systems does not significantly change the initial stiffness or maximum in-plane resistance of the reference frame. The main contribution could be related to reducing the damage in the infill. It was also concluded that using TRM strengthening systems further improve the out-of-plane behavior of infill walls. The specimens strengthened with TRM had out-of-plane capacity on average 3.5 times higher than that of the reference specimen and 30% higher than that of specimens made with the same plasters but without any mesh.





# **CHAPTER 3**

## **EXPERIMENTAL ASSESSMENT OF THE IN-PLANE BEHAVIOR OF MASONRY INFILLED REINFORCED CONCRETE FRAMES**

### **3 Experimental assessment of the in-plane behavior of masonry infilled reinforced concrete frames**

#### **3.1 Introduction**

Following the objectives defined for this thesis related to the characterization of the in-plane and out-of-plane behavior of brick masonry infills in reinforced concrete rc frame buildings, which are typical of Portuguese residential construction until the 20th century, an extensive experimental program was designed based on in-plane and out-of-plane static tests. The experimental characterization is intended to assess the main seismic vulnerability issues of masonry infill walls in rc frames. Both the brick masonry and rc frame used in the experimental campaign were defined based on an extensive research carried out on typical residential rc buildings built from 1960 until 1990s.

The experimental program on the in-plane static cyclic tests is composed of five brick masonry infilled rc frames built at reduced scale, taking into account the facilities available at the laboratory of University of Minho. The design of the reduced scale specimens was based on Cauchy's similitude law and the loading pattern complies with FEMA-461 guidelines [119]. Details about the prototype walls, the design of the reduced scale specimens, tests setups and loading pattern are represented in this Chapter. Furthermore, the experimental response of the specimens in terms of force-displacement diagram, stiffness degradation curve, energy dissipation capacity, crack pattern and deformation characteristics are also represented here.

#### **3.2 Characterization of Prototype**

Aiming at characterizing the typical rc buildings of South European countries since 1960s, an extensive research was carried out in [120]. About 80 buildings were analyzed to identify the cross section of beams and columns, the reinforcing schemes of those elements, the geometry of the brick masonry walls and finally the number and typology of the openings within the walls and also their position. Some statistical information regarding the year of construction, number of stories, concrete and reinforcement type and cross-section of beams and columns are shown in Figure 3.1. It can be observed that the investigated buildings were constructed in different periods of time in the last decades, and the higher number of infilled frames was constructed during 1980 to 1984. The majority of the buildings have between 6 and 8 floors. In medium rise buildings, the columns and beams frequently have the cross-sections of  $30 \times 30 \text{ cm}^2$  and  $30 \times 50 \text{ cm}^2$ , respectively. In general, masonry infills were built as double leaf walls with external and internal leaf of 15 cm and 11 cm respectively and with 4 cm gap between the leaves to increase its thermal and acoustic efficiency. The exterior leaf of the masonry infill was constructed with horizontal perforated ceramic bricks of  $30 \times 20 \times 15 \text{ cm}^3$  (length x height x thickness) and the internal leaf was built with horizontal perforated bricks with  $30 \times 20 \times 11 \text{ cm}^3$  (length x height x thickness). The typology of the openings and their distribution within the masonry infill walls are shown in Figure 3.2. It is observed that the majority of the masonry infills have central openings (window and doors) but it is possible to find several arrangements of openings, even if they are less representative.

This study was important to define the geometry of the reinforced concrete rc frame and also the typology of the masonry infill to be considered in the experimental models, given that the aim of the experimental campaign is to characterize the behavior of rc frames with typical masonry infill that can be found in existing buildings.

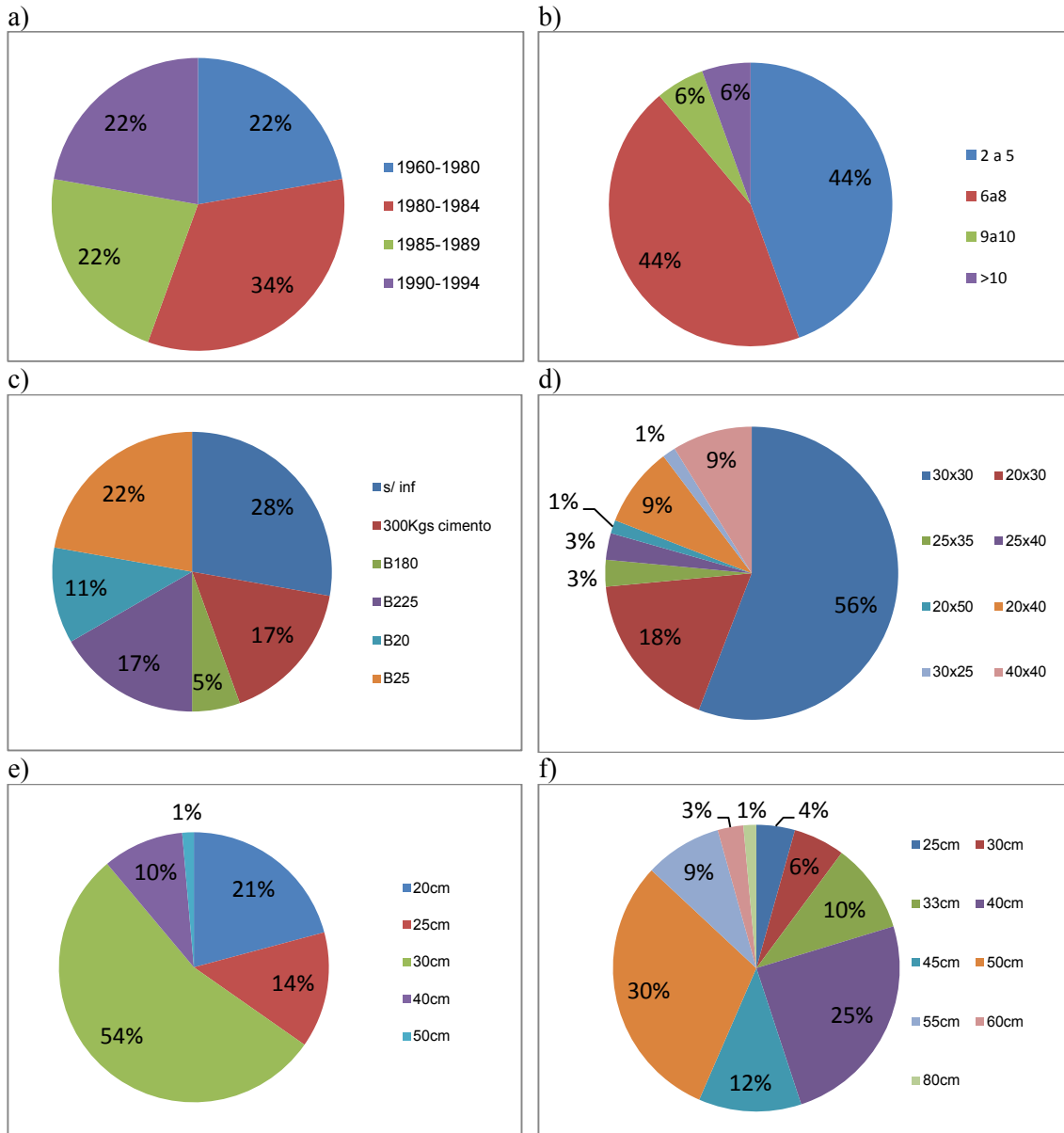


Figure 3.1 Statistical information about geometry and mechanical properties of typical South European masonry infilled frames a)year of construction b)number of storey c)type of concrete d)cross-section of columns e)width of beams f)height of beams [120]

A view of the prototype of the masonry infilled rc frame and also the construction details of the columns and beams can be observed in Figure 3.3 to Figure 3.5. This prototype was used to define the experimental model used in the experimental campaign carried out at laboratory.

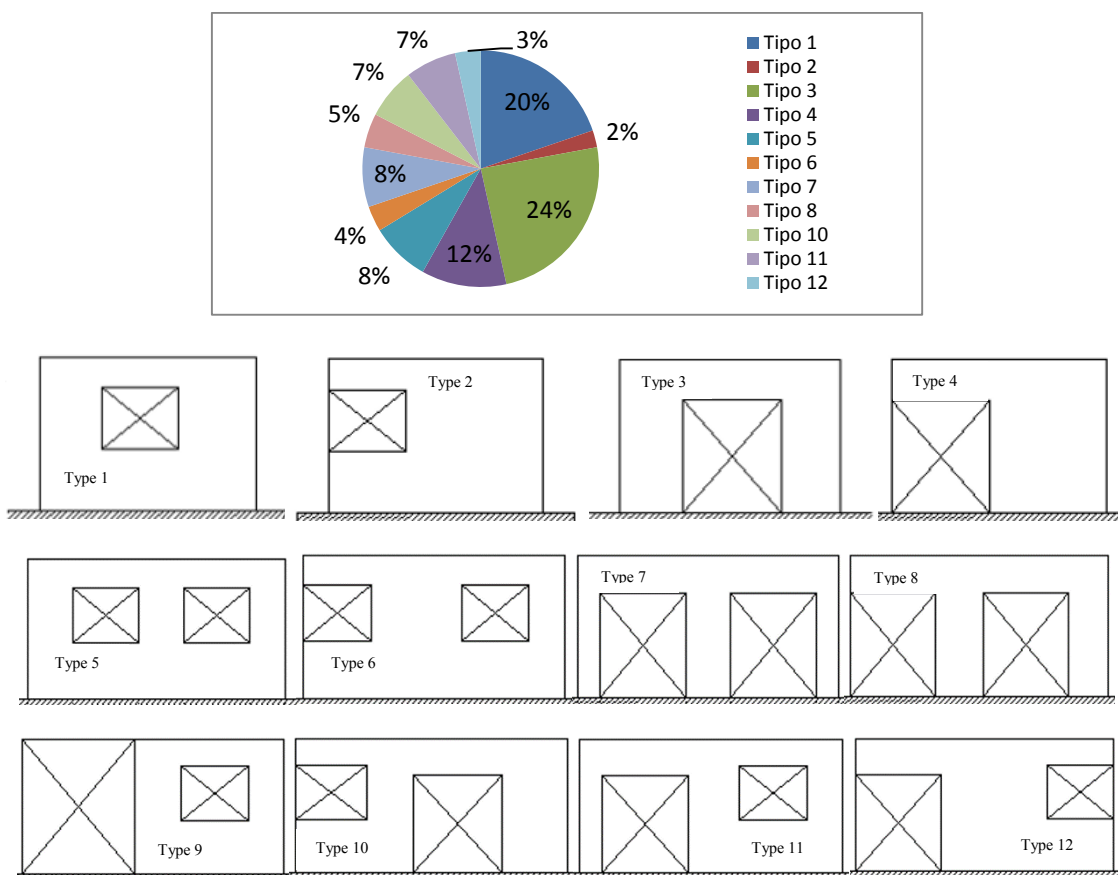


Figure 3.2 Statistical Information about presence of different types of openings within infill [120]

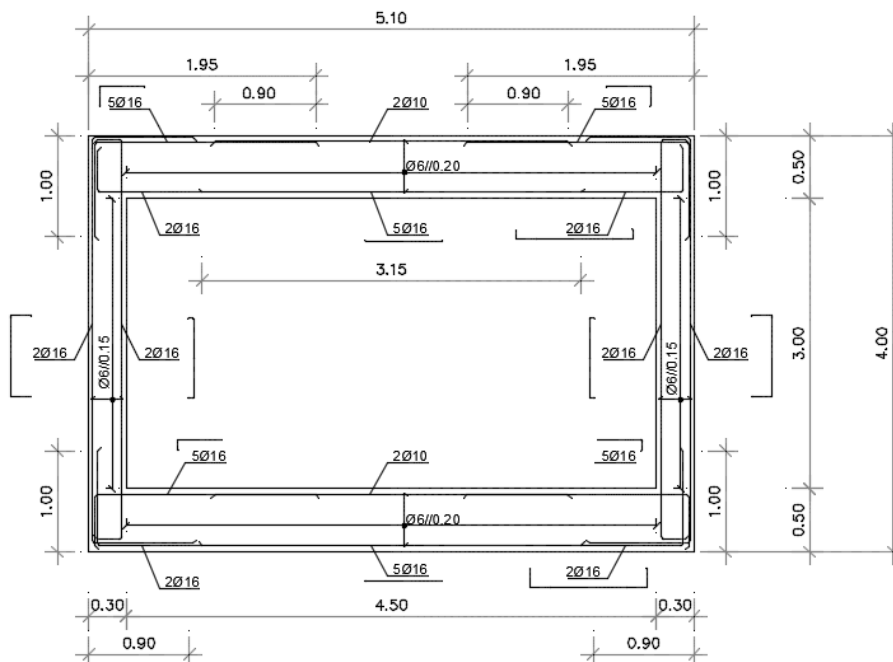


Figure 3.3 Masonry infilled frame as a prototype (dimensions in m)

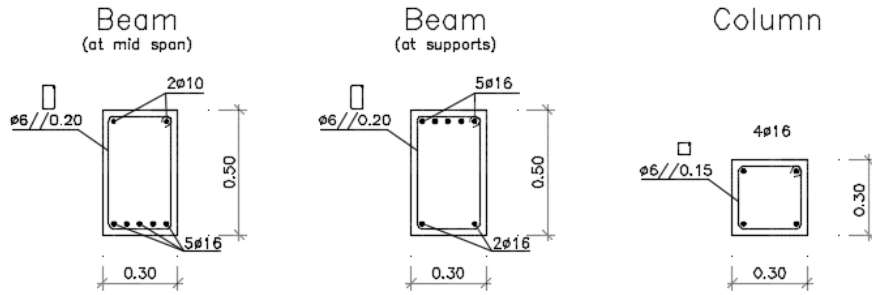


Figure 3.4 Cross-section and reinforcement scheme of the beams and columns (dimensions in m)

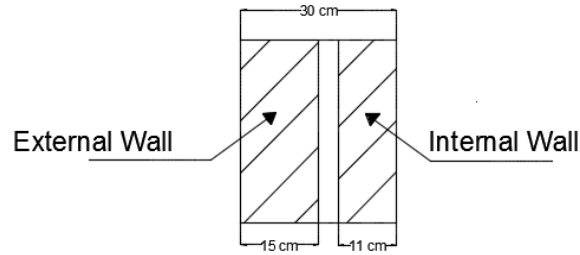


Figure 3.5 Cross-section of the infills in the prototype

### 3.3 Design of reduced-scale specimens

As mentioned before, due to some limitations in the laboratory of Structures at University of Minho, it was decided to test reduced scale specimens of masonry infilled rc frames. The base of design was the prototype shown in Figure 3.3 with the characteristics of rc buildings from last decades of past century. For the design of reduced scale specimens, an allowable stress design approach was followed. A scale factor of 0.54 was selected to overcome the limitation in the laboratory facilities and also to perform the scaling of all elements, including the dimensions of the bricks. In the first step, the sections of the rc columns and beams of the rc frame prototype were analyzed based on ACI 318-08 [121] guidelines in order to obtain the maximum resisting forces and flexural moments in the columns and beams. Then Cauchy's similitude law (Table 3-1) was applied to the maximum allowable forces and flexural moments of real scale sections obtained in the first step to calculate the maximum allowable forces and bending moments of reduced scale cross sections. Finally, cross-sections and reinforcement of the reduced scale structural elements were designed based on the same allowable stress design approach. An overview of the reinforcement schemes of the rc frame and of the cross section of the columns and beams can be seen in Figure 3.6 and Figure 3.7. For the masonry infills, horizontally perforated bricks of 240 mm x 115 mm x 60 mm and of 240mm x 115 mm x 80mm were used. The selection of these commercial units was carried out by taking into account that the double leaf masonry walls in the prototype is composed of the brick units of 300mmx200mmx110mm for the internal leaf and brick units of 300mmx200mmx150mm for the external leaf. To keep the same brick's height to length ratio of 0.67 in the reduced scale specimens, the length of the reduced scale units was reduced to 175 mm. Additionally, based on the information of the manufacturer, it was ensured that the compressive strength of the reduced scale masonry units was close to the compressive strength of the full scale brick units. Figure 3.8 shows the dimensions of the bricks used in the reduced scale specimens, as well as the cross section of the reduced scale double leaf brick masonry infill walls.

Table 3-1 Relation between different parameters of prototype and model based on Cauchy's Similitude Law

Parameter	Scale Factor	Parameter	Scale Factor
Length (L)	$\frac{L_P}{L_m} = \lambda$	Mass (m)	$\frac{m_P}{m_m} = \lambda^3$
Elasticity Modulus (E)	$\frac{E_P}{E_m} = 1$	Weight (W)	$\frac{W_P}{W_m} = \lambda^3$
Specific Mass ( $\rho$ )	$\frac{\rho_P}{\rho_m} = 1$	Force (F)	$\frac{F_P}{F_m} = \lambda^2$
Area (A)	$\frac{A_P}{A_m} = \lambda^2$	Flexural Moment (M)	$\frac{M_P}{M_m} = \lambda^3$
Volume (V)	$\frac{V_P}{V_m} = \lambda^3$	Stress ( $\sigma$ )	$\frac{\sigma_P}{\sigma_m} = 1$
Displacement (d)	$\frac{d_P}{d_m} = \lambda$	Strain ( $\epsilon$ )	$\frac{\epsilon_P}{\epsilon_m} = 1$
Velocity (v)	$\frac{v_P}{v_m} = 1$	Time (t)	$\frac{t_P}{t_m} = \lambda$
Acceleration (a)	$\frac{a_P}{a_m} = \lambda^{-1}$	Frequency (f)	$\frac{f_P}{f_m} = \lambda^{-1}$

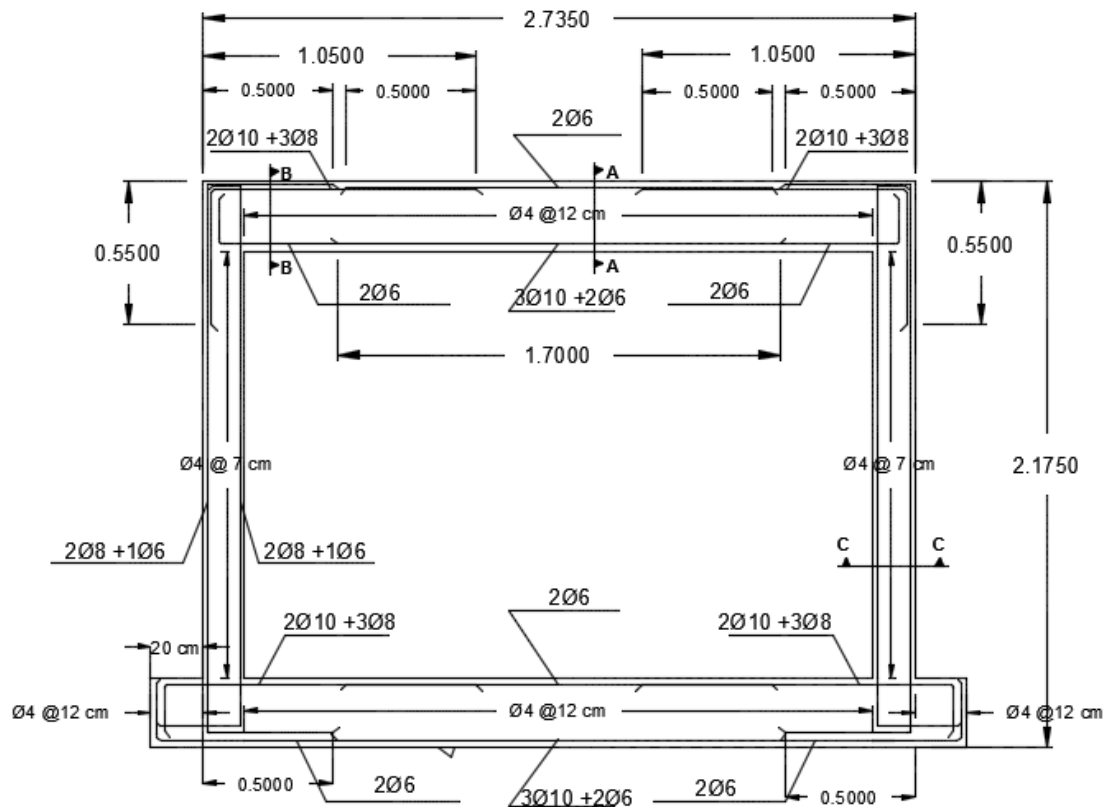


Figure 3.6 Geometry and reinforcement scheme of the reduced scale rc frame

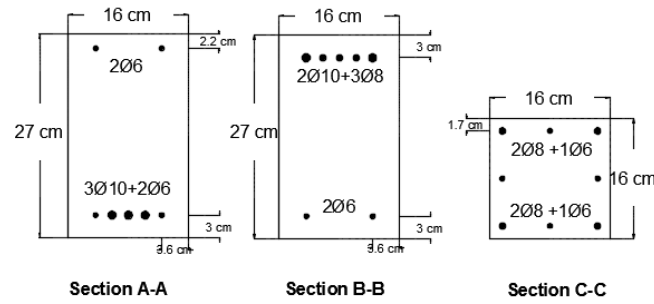


Figure 3.7 Cross-sections of columns and beams in reduced scale rc frames

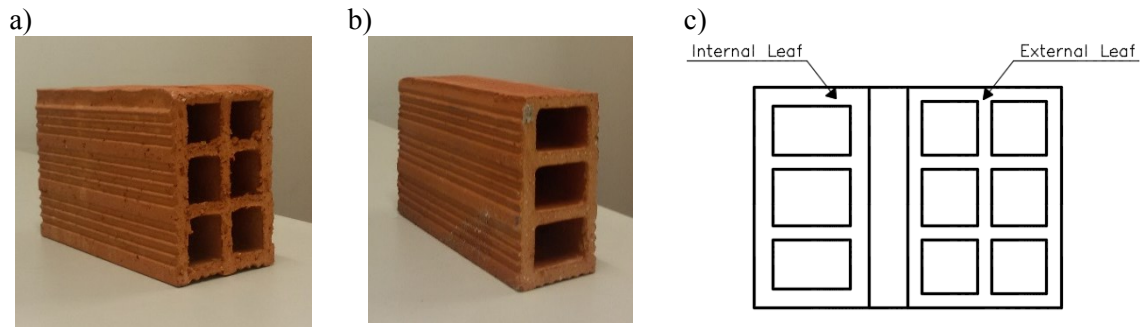


Figure 3.8 Brick units and cross section of reduced scale masonry infill: a) bricks of 80mm thickness used in exterior leaf ; b) bricks of 60mm thickness used in interior leaf of the infill; c) cross-section of the infill in reduced scale specimens

### 3.4 Characterization of reduced-scale specimens

The experimental characterization of the in-plane behavior of masonry infill walls in rc frames was carried out based on static in-plane tests performed on five reduced scale specimens. Three specimens were subjected to different lateral drifts to impose a certain level of damage and then they were tested again under out-of-plane loading. The latter tests aimed at assessing the influence of prior in-plane damage on the out-of-plane behavior of masonry infill walls. A summary of the specimens tested under in-plane cyclic loading is presented in Table 3-2. In the labeling process of the specimens, the first section refers to the type of the infilled frame, e.g. “BF” for bare frame, and “SIF” for solid infilled frame. The second section refers to the type of the loading. For example, “I” refers to in-plane loading, “O” to out-of-plane loading and “IO” to sequential in-plane and out-of-plane loading. The parenthesis after this section refers to the level of the in-plane drift that was applied to the specimens. For instance, IO(0.3%) means that a prior in-plane drift of 0.3% was applied to the specimen before out-of-plane loading. The third section refers to the number of the leaves in the infill, namely 2L refers to double leaf infill and 1L refers to one leaf infill. The parentheses indicate the presence of connection between the leaves. If there is not any connection between them it is written as “NC”. Given that two different groups of masons built the masonry infills to investigate the effect of workmanship on the behavior of the specimens, the last section refers to the group of the mason: “A” refers to group A and “B” refers to group B.



Table 3-2 Designation of the specimens for in-plane static cyclic loading

Name	Type of specimen	Type of loading	Number of leaves during construction	Group of Mason
<b>BF-I</b>	Bare frame	In-plane	-	
<b>SIF-I-2L(NC)-A</b>	Solid infilled frame	In-plane	Double leaf with no connection	A
<b>SIF-IO(0.3%)-2L(NC)-B</b>	Solid infilled frame	Prior In-plane drift of 0.3% then out-of-plane	Double leaf with no connection	B
<b>SIF-IO(0.5%)-2L(NC)-B</b>	Solid infilled frame	Prior In-plane drift of 0.5% then out-of-plane	Double leaf with no connection	B
<b>SIF-IO(1%)-2L(NC)-B</b>	Solid infilled frame	Prior In-plane drift of 1% then out-of-plane	Double leaf with no connection	B

### 3.5 Construction of the specimens

The construction of the specimens for experimental characterization was divided in two phases, namely the casting of the rc frames and the construction of the brick masonry infill walls. In order to make the casting of the rc frames easier, it was decided to put the wooden molds in the horizontal position, see Figure 3.9. The reinforcement was mounted separately and then placed inside the wooden mold, see Figure 3.9. One of the major problems related to the design of rc frames in South Europe and specially in Portugal during the last century is the lack of rules for seismic design until 1980s, which resulted in the absence of stirrups in the extremities of columns intersecting with beams. This feature could be observed in the construction of the reduced scale specimens, which is representative of rc frame that comply with 1970s common construction, see Figure 3.10. As there is little space between the longitudinal reinforcement of the beams in the reduced scale specimens, a concrete of class B20 (according to the previous Portuguese code for reinforced concrete structures) with a maximum aggregate of 9mm was ordered from a company that provides fresh concrete. This decision was taken to ensure uniform concrete in the specimen, even in the places where little space exists between the reinforcements. The casting of concrete for all the specimens was made at the same time to have similar concrete. Compaction of the concrete was performed by vibrators to expel the entrapped air inside it, see Figure 3.11



Figure 3.9 Wooden molds and reinforcement inside them

When the casting of concrete and vibration process of each specimen was completed, the surface was rectified to have smooth surfaces in all elements of the rc frame. The specimens were cured and demolded in the construction place. About 45 days after the construction of the specimens, they were carefully transported to the storage area at the University of Minho. The specimens were placed on top of each other by putting wooden spacers between them and transported horizontally to avoid their cracking during the transportation. At the storage area, the rc frames were mounted in the vertical direction, adequately supported to avoid any out-of-plane instability, see Figure 3.12 a.



Figure 3.10 Absence of stirrups in the connection point of column to beam

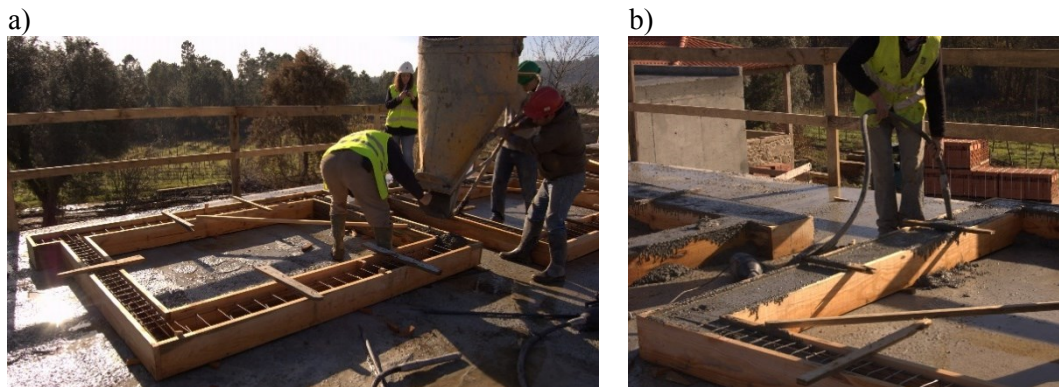


Figure 3.11 Construction of the frames a) concrete casting b) compaction of concrete by its vibration



Figure 3.12 a) Transportation of the frames to the storage area and b) construction of the infills

The construction of the masonry infills was carried out in the storage area and after finishing the construction process they were covered to be protected from the rain, see Figure 3.12b. After 28 days of curing time for masonry infills, the rc frames with brick masonry infills were carefully transported to the testing place by means of a crane to avoid any cracking.

### 3.6 Experimental setup and instrumentation

The test setup designed for the static cyclic in-plane testing of the rc frames with masonry infills is shown in Figure 3.13. The rc frame with masonry infill was placed on two steel beams (HEA300) that were firmly attached to the strong floor to avoid their sliding and uplifting. Additionally, the sliding of the rc frame was prevented by bolting an L-shape steel profile of L200\*200\*20 to each side of the steel beam. In turn, the uplifting was additionally prevented by bolting two tubular steel profiles to the steel beams. The tubular steel profile was made by welding two UNP140 steel profiles. The out-of-plane movement of the enclosure frame was restrained by putting an L-shaped steel profile of L100\*100\*10 at each side of the upper concrete beam that was bolted to the top steel frame, as shown in Figure 3.14. Three rollers were placed on upper L-shaped profiles to completely minimize or even eliminate the friction between them and the upper reinforced concrete beam during in-plane loading.

Two vertical jacks were placed on the top of the columns to apply the vertical load of 160 kN, corresponding to 40% of the column's axial force capacity. Each jack was pinned to the lower steel beam by means of four vertical rods (diameter of 16 mm), two at each side.

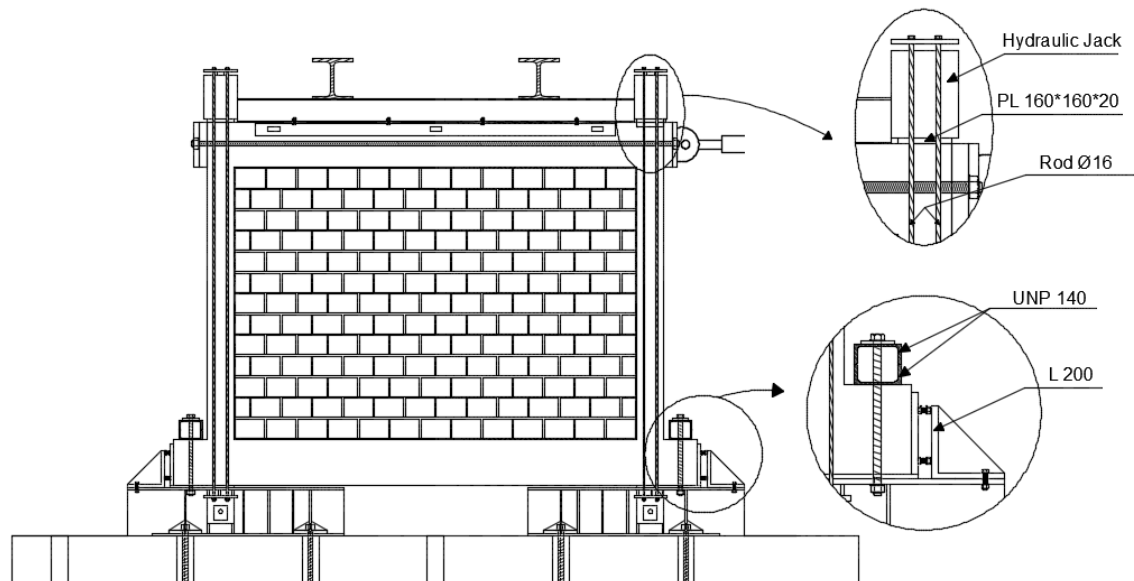


Figure 3.13 Test setup for in-plane cyclic loading

A hydraulic actuator with a capacity of 250kN was attached to the reaction wall and connected at mid height of the top concrete beam of the rc frame. Two steel plates ( $400 \times 300 \times 30 \text{ mm}^3$ ) were mounted on the left and right side of top rc beam in which the right steel plate was connected to the horizontal actuator by means of a hinge. These plates are connected by two  $2\phi 50$  steel rods confining the top rc beam and enabling the application of reversed cyclic loading.

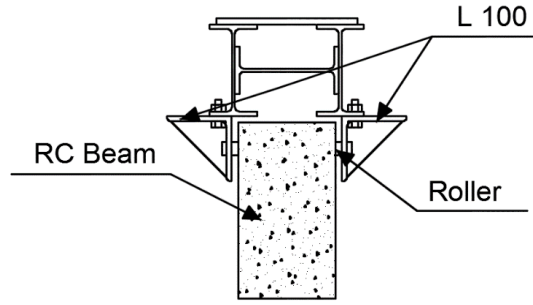


Figure 3.14 Out-of-plane support of the upper beam in the in-plane testing

The instrumentation adopted for the measurement of the most relevant displacements during the static cyclic in-plane testing is shown in Figure 3.15. Twenty two linear variable differential transformers (LVDT) were used to record the key displacements. From these LVDTs, four LVDTs were mounted on the masonry infill to measure the diagonal deformation of both leaves (L1, L2, L21 and L22). Two LVDTs were placed on the reinforced concrete frame to measure the diagonal deformation of the surrounding frame (L19 and L20). Eight LVDTs were used to measure the relative displacement of the infill with respect to the surrounding frame in the corners (L3, L4, L5, L6, L7, L8, L9 and L10). LVDTs L11 and L12 measured the sliding and uplifting of the infilled frame with respect to the steel profile. Four LVDTs of L13, L14, L15 and L16 measured the sliding and uplifting of the steel profiles with respect to the strong floor. These measurements were taken to control the reliability of the test setup. The LVDTs L17 and L18 measured the horizontal displacement of the upper beam of the reinforced concrete frame.

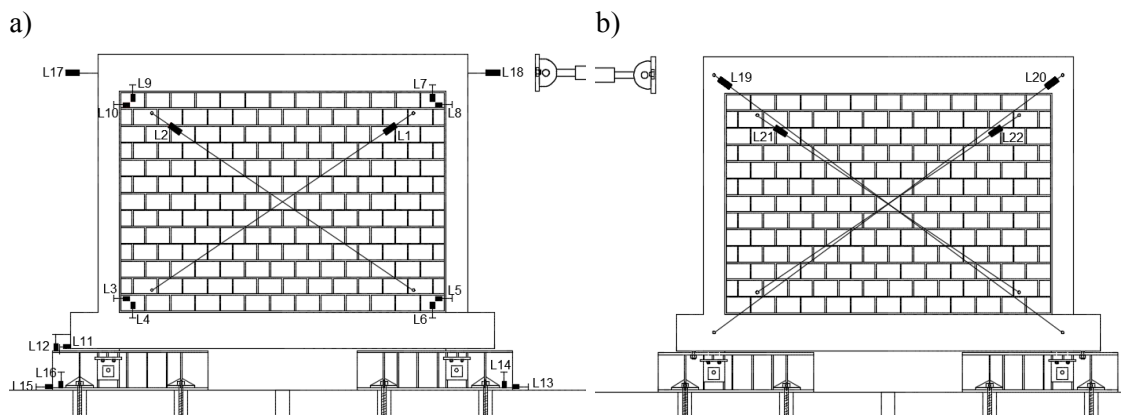


Figure 3.15 Instrumentation for in-plane loading; a) external leaf b) internal leaf

The shear deformation of the masonry infill can be calculated based on the diagonal displacements measured by the diagonal LVDTs placed along the corners of masonry infill, see Figure 3.16. The average shear distortion can be calculated using Eq. 3-1:

$$\gamma = \frac{(\Delta d_1 - \Delta d_2)L_d}{2L_h L_v} \quad \text{Eq. 3-1}$$

Where  $\Delta d_1$  and  $\Delta d_2$  are the length change of diagonals AD (measured through L1 for external leaf, L21 for internal leaf and L19 for rc frame) and BC (measured through L2 for external leaf, L22 for internal leaf and L20 for rc frame) respectively. The length  $L_d$  is the initial length of the diagonals (AD and BC),  $L_h$  is the initial horizontal length between points A and B and  $L_v$  is the initial vertical length between A and C, see Figure 3.16.

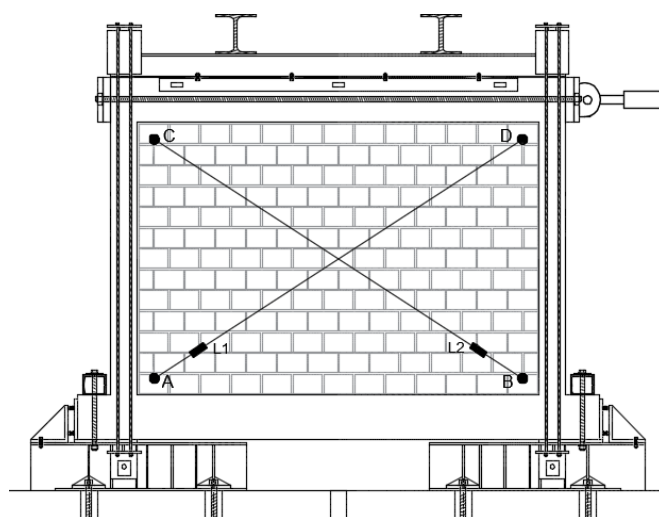


Figure 3.16 Measurement of average shear distortion of infill with measurements of LVDTs

### 3.7 Loading Protocol

The in-plane static cyclic tests were performed in displacement control method by imposing different pre-defined levels of displacements through an LVDT connected to the horizontal hydraulic actuator. The loading protocol adopted for in-plane quasi static cyclic testing, which is in accordance with the guidelines provided by FEMA 461[119], is shown in Figure 3.17.

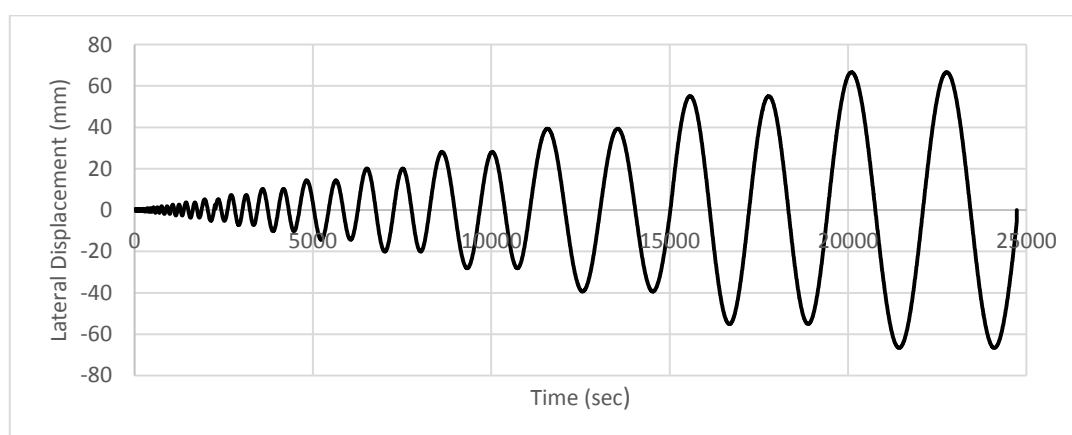


Figure 3.17 Displacement protocol for in-plane testing

The loading protocol includes sixteen different sinusoidal steps, starting from a displacement of 0.5mm, representing 0.03% drift, calculated as the ratio between the top lateral displacement and the height at which the horizontal load is applied from the base of the frame. The maximum lateral displacement in the protocol is 66.68mm, corresponding to a lateral drift of 3.5% drift. Each step was repeated two times, except the first step that was repeated six times. The displacement amplitude  $a_{i+1}$  of step  $i+1$  is 1.4 times the amplitude  $a_i$  of step  $i$ :

$$a_{i+1} = 1.4a_i \quad \text{Eq. 3-2}$$

### 3.8 Experimental results

The analysis of results of the in-plane static cyclic tests carried out on the rc frames with masonry infills is carried out individually for each specimen considering different response indicators, namely the lateral load-displacement diagrams, stiffness degradation curve, cracking patterns, energy dissipation capacity and deformation characteristics. In the next sections, the presentation and discussion of results is provided.

#### 3.8.1 Specimen BF-I

##### 3.8.1.1 *Lateral load-displacement response*

The lateral force-displacement diagram of the bare frame is shown in Figure 3.18. The positive direction is considered to be the direction in which the hydraulic actuator pushes the specimen whereas the negative direction is the direction in which the actuator pulls the specimen through two plates that were connected with two thick steel rods (see also Figure 3.13). It is clear that the specimen shows symmetric behavior in the positive and negative direction.

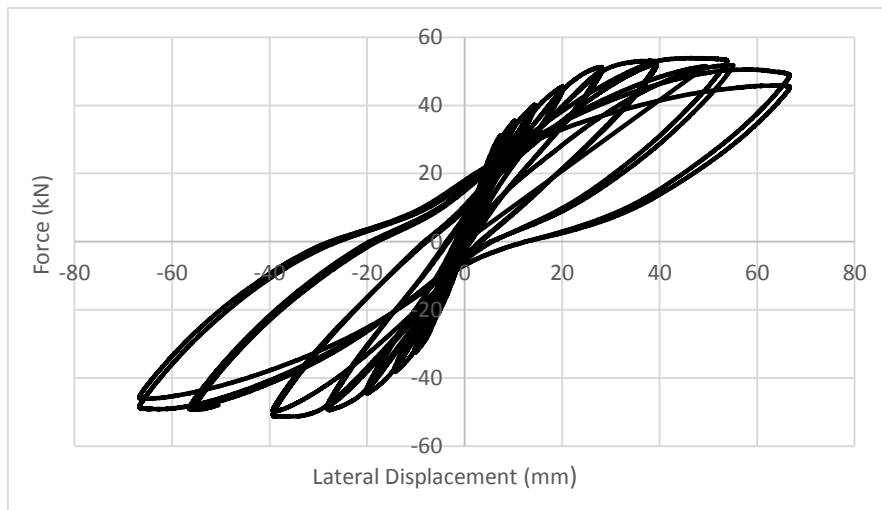


Figure 3.18 Lateral force-displacement diagram of the bare frame

The first small cracking developed in the bare frame was observed at the lateral displacement of 2.67mm, corresponding to the lateral drift of 0.14% in the negative direction leading to a decrease of the initial stiffness. In the positive direction, the first cracking leading to a decrease in the initial stiffness was recorded to a lateral displacement of 3.74mm corresponding to the lateral drift of 0.2%.

After the lateral force of 51.24kN recorded for a lateral displacement of 28.13mm (corresponding to lateral drift of 1.48%) in positive direction, the force-displacement diagram exhibited a plateau, meaning that increasing the lateral displacement results in a very small increase in the lateral resisting force. The specimen reached the peak load of 53.91kN at the lateral displacement of 53.82mm, corresponding to lateral drift of 2.82%. After the peak resistance is attained, the increase in the lateral displacement led to a decrease of the lateral force in which at lateral displacement of 66.68mm the lateral force reached 49.50kN. In the negative direction, the same plateau was observed in the force-lateral diagram after the lateral displacement of 28.13 mm, corresponding to the lateral drift of 1.48% and to the lateral force of 49.38kN. By imposing further

displacement to the rc frame, the specimen reached the peak load of 51.38kN at the lateral displacement of 39.32mm corresponding to the lateral drift of 2.06%. Similar to the positive direction, after the peak point, the increase in the displacement does not lead to significant change in the lateral force until a lateral displacement of 66.68mm, corresponding to lateral drift of 3.5%.

The monotonic force-displacement curve of the specimen at two successive cycles is shown in Figure 3.19. Until the lateral drift of 0.5%, both curves are completely overlapped, but after this displacement a very slight strength degradation occurred, being considered as negligible. Only after a lateral drift of 2.5% a visible strength degradation developed between the first and second cycles, which should be associated to a more important damage accumulation.

Based on the monotonic force-displacement diagram of the specimen, it is possible to derive the key parameters characterizing the in-plane behavior, namely the initial stiffness, lateral strength and the displacement corresponding to the lateral strength, see Table 3-3. The initial stiffness is defined as the secant stiffness of the specimen at the cracking initiation, see Eq. 3-3.

$$K_e = \frac{H_{cr}}{d_{cr}} \quad \text{Eq. 3-3}$$

In which  $H_{cr}$  and  $d_{cr}$  are the lateral force and deformation of the specimen at first cracking respectively. The lateral strength of the specimen ( $H_{max}$ ) is defined as the maximum force obtained in the force-displacement diagram and  $d_{Hmax}$  represents the displacement corresponding to the maximum force attained during the cyclic test.

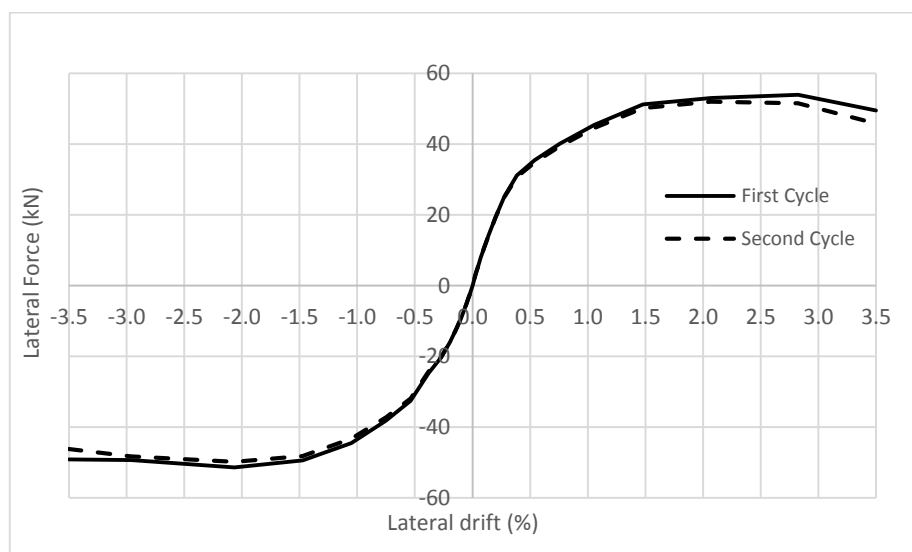


Figure 3.19 Strength degradation of the specimen in two successive cycles

As shown in Table 3-3, although cracking of the specimen in the negative direction initiated earlier than positive direction, the secant stiffness calculated for both directions are similar.

Table 3-3 Key parameters characterizing the in-plane behavior of the rc bare frame

Positive direction					Negative direction				
$H_{cr}$ (kN)	$d_{cr}$ (mm)	$K_e$ (kN/mm)	$H_{max}$ (kN)	$d_{Hmax}$ (mm)	$H_{cr}$ (kN)	$d_{cr}$ (mm)	$K_e$ (kN/mm)	$H_{max}$ (kN)	$d_{Hmax}$ (mm)
19.2	3.7	5.1	53.9	53.8	-12.2	-2.7	4.6	-51.4	-39.3

The average shear distortion of the bare frame is shown in Figure 3.20. For low levels of imposed lateral displacement, the shear distortion of the frame increased linearly until the first cracking of the frame in positive and negative directions. The average shear distortion of the frame at initiation of cracking in positive direction was 0.0021 and in negative direction reached -0.0016. As it is shown in Figure 3.20, after the cracking of the bare frame, the average shear distortion increased rapidly and at failure point of the specimen reached the value of 0.037 in positive direction and of -0.037 in negative direction.

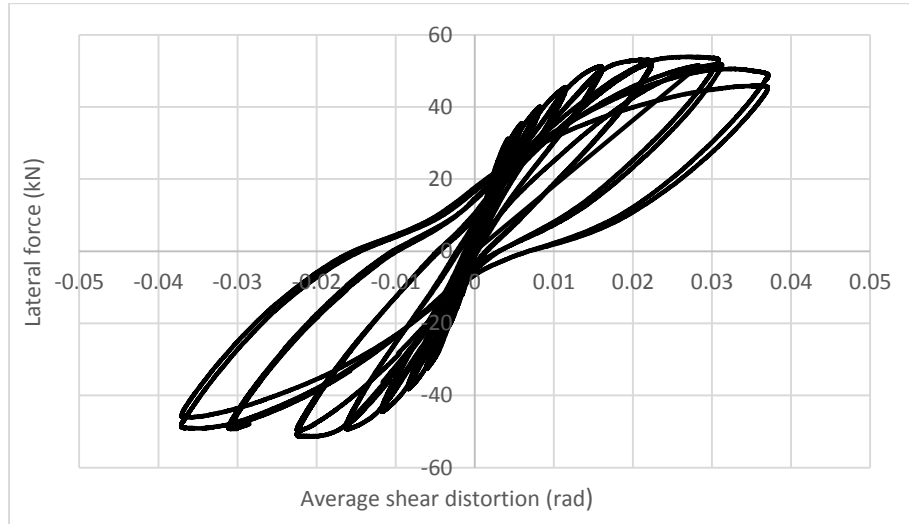


Figure 3.20 Average shear distortion of the bare frame

### 3.8.1.2 *Stiffness Degradation*

The stiffness degradation curve representing the stiffness of the rc frame at each lateral drift is shown in Figure 3.21. The stiffness at each lateral drift is defined as the secant stiffness representing the slope of the line connecting the origin to the point corresponding to the maximum force obtained in the first cycle of monotonic force-displacement diagram. It is observed that stiffness degradation curve presents a similar trend in the positive and negative directions. It is also clear that the stiffness degradation level for low drifts is higher. The stiffness degradation until lateral drift of 1% in the positive and negative directions is about 57% and 51% respectively in relation to the initial stiffness.

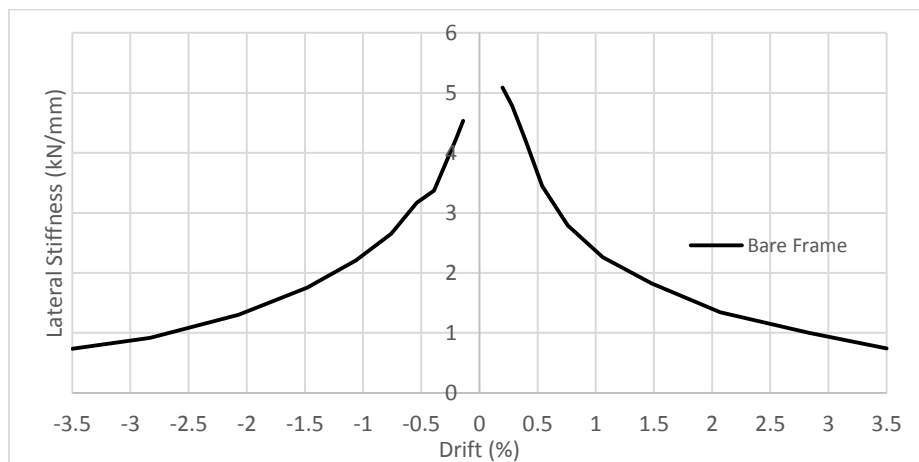


Figure 3.21 Stiffness degradation in bare frame



### 3.8.1.3 Crack pattern

The cracking pattern developed in the bare frame corresponding to distinct lateral drifts is shown in Figure 3.22 and Figure 3.23. As already mentioned, the first cracking of the specimen develops at the lateral drift of 0.14% in the negative direction at the top left connection between the column and the beam. Similar crack opens in the opposite corner at the lateral drift of 0.2% in the positive direction. By imposing further displacements, the existing cracks extend and some new cracks develop in the bottom connection between the beam and column. In the negative direction, the new cracks in the bottom connection develop at lateral drift of 0.54%, whereas in the positive direction the cracking starts at the lateral drift of 0.75%. By applying more lateral displacements, new cracks propagate in a considerable length of the columns at the top and bottom edges. By further increasing the lateral displacements, plastic hinges form in the top and bottom part of the columns where the concentration of the cracks is higher, see Figure 3.23. The final cracking patterns of the bare frame shows that all the cracks are only concentrated in the columns. This behavior should be associated to the design criteria used before the 1980s, when no specific seismic design was used for the rc building. It can be concluded that based on the experimental results, the concept of weak column-strong beam characterized this prototype of rc frame built before 1980s.

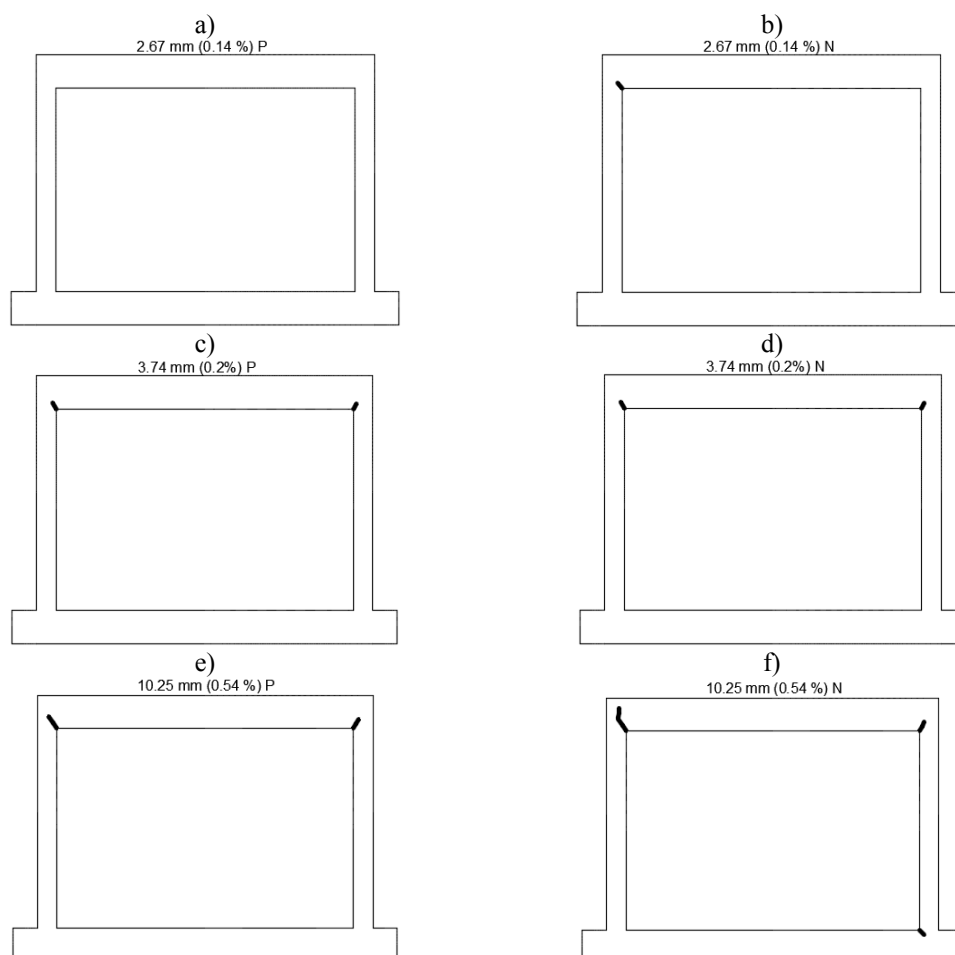


Figure 3.22 Crack propagation in the specimen at lateral drift of a) 0.14% in positive direction b) 0.14% in negative direction c) 0.2% in positive direction d) 0.2% in negative direction e) 0.54% in positive direction f) 0.54% in negative direction

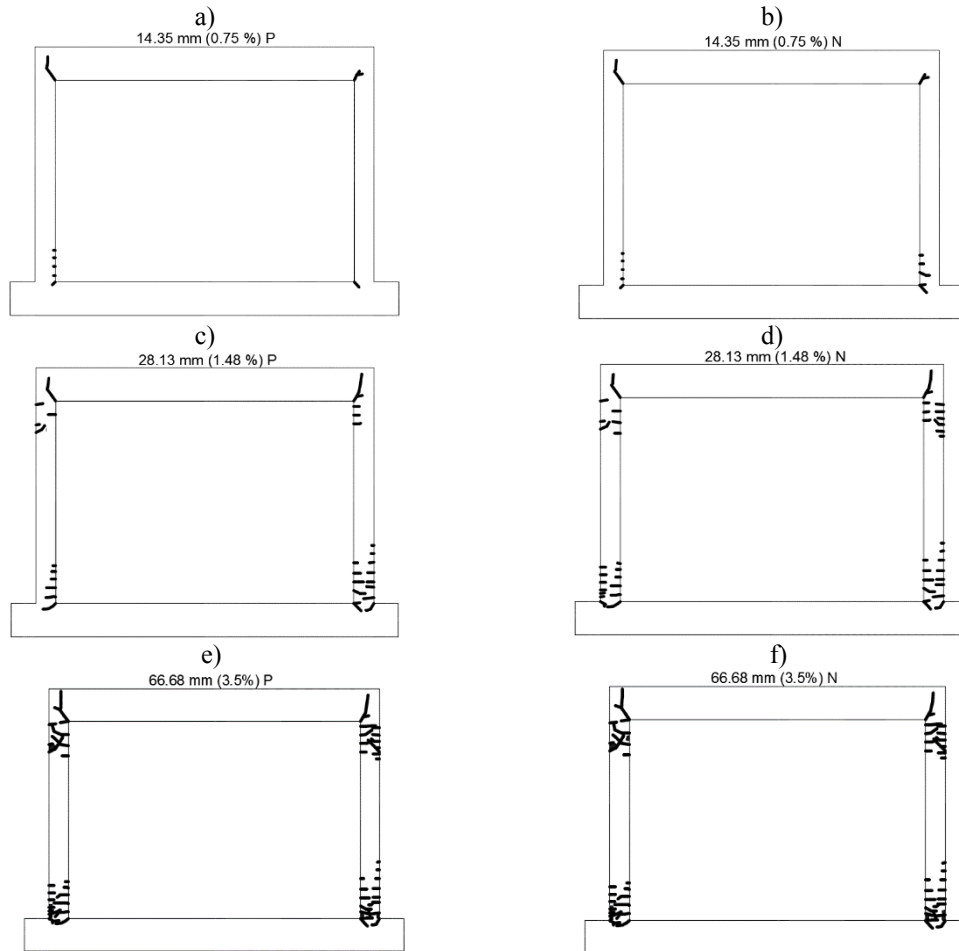


Figure 3.23 Crack propagation in the specimen at lateral drift of a)0.75% in positive direction b)0.75% in negative direction c)1.48% in positive direction d)1.48% in negative direction e)3.5% in positive direction f)3.5% in negative direction

#### 3.8.1.4 Energy dissipation

The energy dissipation at each cycle is usually determined by calculating the area inside the hysteretic force-displacement loop corresponding to that cycle. The evolution of energy dissipation of the bare frame at each cycle is shown in Figure 3.24. It is clear that the energy dissipated at small lateral drifts is negligible. It is also observed that the energy dissipation at larger lateral drifts is higher than the one recorded for smaller drifts. This is related to the accumulation of damage at larger lateral drifts which is the main cause for energy dissipation. The energy dissipated at lateral drift of 2.07% is more than the double of the energy dissipated at lateral drift of 1.5%.

Based on the energy dissipated at each cycle, it is possible to calculate the total energy dissipated until each lateral drift. The cumulative energy dissipation of the bare frame increases exponentially, as shown in Figure 3.25. It is observed that the total energy dissipated during cyclic loading until lateral drifts of 2.8% and 3.5% is 9084 kN.mm and 15635 kN.mm respectively.

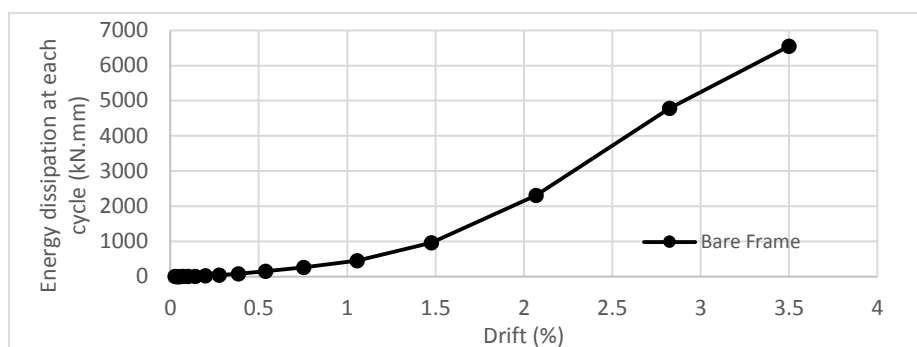


Figure 3.24 Energy dissipated at each cycle for bare frame

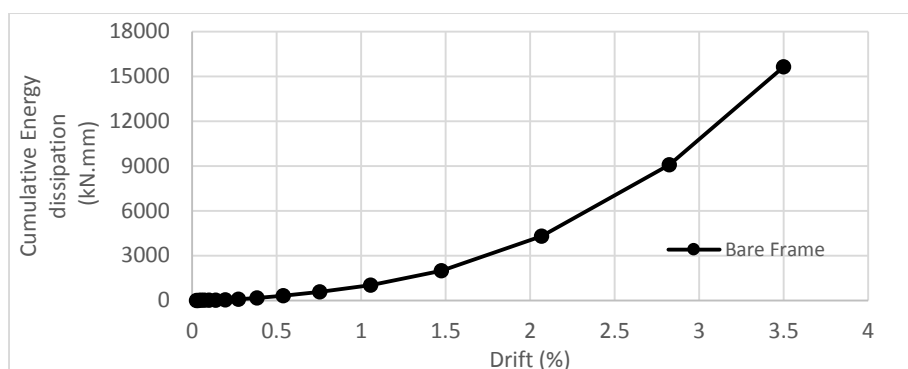


Figure 3.25 Cumulative energy dissipation of bare frame

### 3.8.2 Specimen SIF-I-2L(NC)-A

#### 3.8.2.1 Lateral load-displacement response

The lateral force-displacement diagram of the specimen SIF-I-2L(NC)-A recorded during in-plane cyclic loading is shown in Figure 3.26. As mentioned before, the positive direction is considered to be the direction in which the hydraulic actuator pushes the specimen, whereas the negative direction is the direction in which the actuator pulls the specimen. It is evident that the specimen exhibits slightly different behavior in positive and negative directions. In the positive direction, the stiffness of the specimen started to decrease at the lateral displacement of 2.67mm (0.14% lateral drift) corresponding to the lateral force of 89.04kN due to cracking of the infill in the central region. The specimen reached the peak load of 133.94kN at the displacement of 10.3mm corresponding to the lateral drift of 0.54%. After the peak load, the lateral force decreased gradually to reach the residual strength of 94.84kN at displacement of 47.63mm (2.5% drift).

In the negative direction, the rc frame with masonry infill exhibits a linear elastic behavior until the first cracking in the central region of the wall. The cracking resulted in the decrease of the initial stiffness of the specimen at displacement of 1.84mm (lateral drift of 0.1%), corresponding to the lateral force of 52.27kN. The specimen reached peak load of 103.56kN at displacement of 10.3mm (lateral drift of 0.54 %). By applying increasing lateral displacements, large number of cracks formed in the specimen at the lateral drift of 2.5% and the test was stopped due to the severe damage in the specimen. It is evident that after the maximum force, the successive increments in the lateral displacement resulted in the gradual reduction of the lateral strength until it reached the value of 86.69kN at the displacement of 47.63 (2.5% drift).

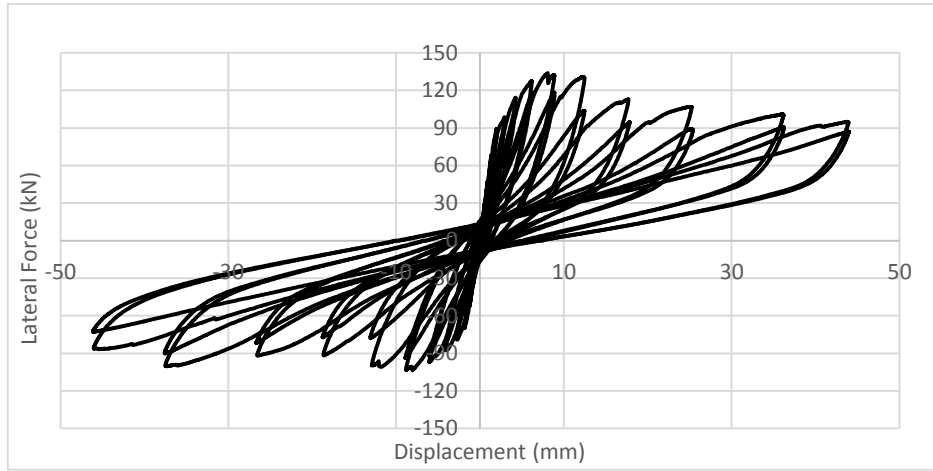


Figure 3.26 In-Plane force-displacement diagram of specimen SIF-I-2L(NC)-A

The strength degradation of the specimen during two successive cycles in each step is shown in Figure 3.27. It is observed that at the first levels of loading in both directions (until 0.4% lateral drift) it is negligible. It is increased when considerable cracks developed in the specimen (at lateral drift of 0.54%). Maximum strength degradation of 26% in positive direction is achieved at the lateral drift of 0.75%. In the negative direction the maximum strength degradation of 29% occurred at lateral drift of 0.75%. It seems that the presence of the masonry infill in the frame is the main cause of the strength degradation as strength degradation in the bare frame is negligible, being related to the higher damage that is developed in the masonry infill.

Looking at the monotonic force-displacement diagram of the specimen SIF-I-2L(NC)-A, it is feasible to obtain the key parameters related to its in-plane behavior. The initial stiffness related to the secant stiffness at the first cracking point, the maximum force attained during the in-plane loading and the displacement corresponding to the maximum force were calculated and presented in Table 3-4. It is observed that the presence of the brick infill inside the bare frame could significantly change the in-plane response of the bare frame by increasing its initial stiffness by 5.5 and 5 times in the positive and negative directions respectively. The enhancement in the lateral strength is calculated as 1.5 and 1 times in the positive and negative directions respectively.

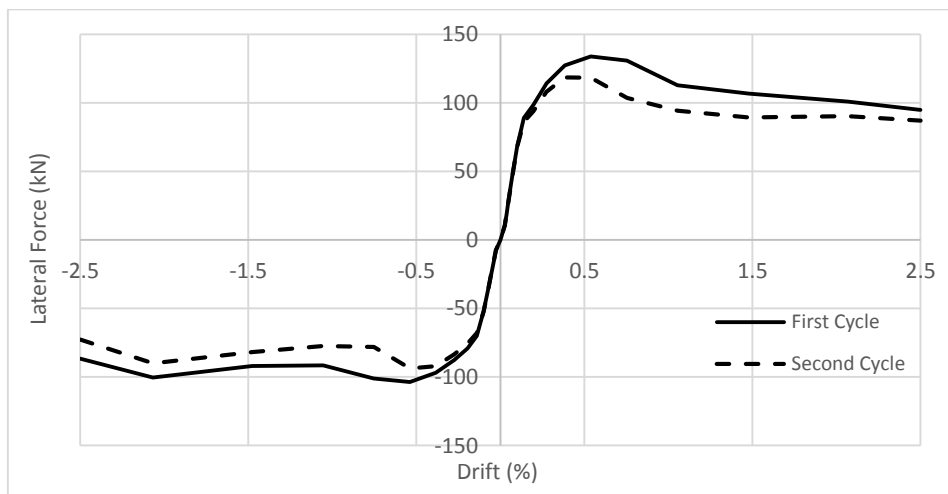


Figure 3.27 Strength degradation of the specimen in two successive cycles of each step in positive and negative direction

Table 3-4 Key parameters related to the in-plane behavior of SIF-I-2L(NC)-A

Positive direction					Negative direction				
$H_{cr}$ (kN)	$d_{cr}$ (mm)	$K_e$ (kN/mm)	$H_{max}$ (kN)	$d_{Hmax}$ (mm)	$H_{cr}$ (kN)	$d_{cr}$ (mm)	$K_e$ (kN/mm)	$H_{max}$ (kN)	$d_{Hmax}$ (mm)
89.0	2.7	33.4	133.9	10.3	-52.3	-1.9	27.4	-103.6	-10.3

### 3.8.2.2 Stiffness Degradation

The secant stiffness of the specimen calculated in the first cycle of the force-displacement diagram at each level of lateral drift is shown in Figure 3.28. This curve represents the stiffness degradation during the in-plane loading. It is observed that the stiffness degradation curves exhibit similar path in the positive and negative directions. It is also observed that the stiffness of the specimen is reduced considerably at first levels of loading, which is related to the propagation of cracks in the infill. The amount of degradation until lateral drift of 1% in the positive and negative directions was about 83%.

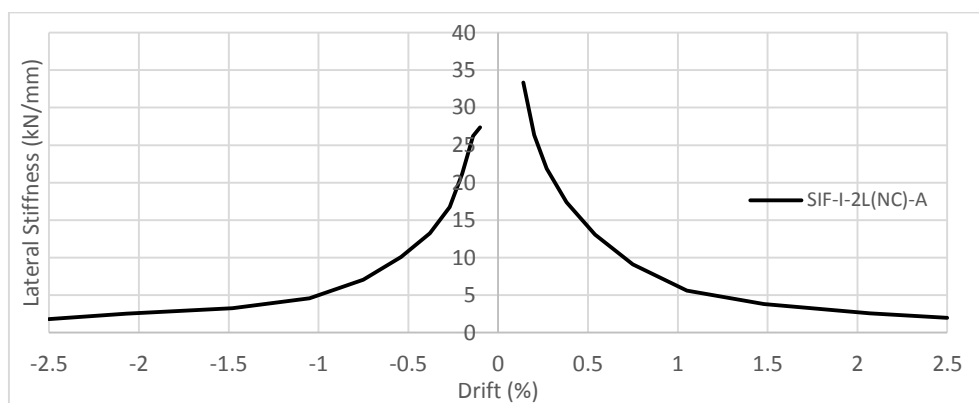


Figure 3.28 Stiffness degradation curve for specimen SIF-I-2L(NC)-A

### 3.8.2.3 Crack patterns

As the specimen under analysis has a double leaf brick masonry infill, the cracking patterns of the external leaf with thickness of 8cm are shown in Figure 3.29 and Figure 3.30. The first crack, occurring at the mortar bed joints, started when the lateral load was applied in the negative direction at the lateral drift of 0.1%. In the positive direction, the cracking initiated at a displacement of 2.67mm corresponding to lateral drift of 0.14%. At this stage, the upper left corner of the infill started to separate from its bounding frame. The separation of the right top corner of the infill from the rc frame also occurred at the same lateral drift in the negative direction. By increasing the lateral displacement, the cracks propagate in the diagonal direction as stair step cracks passing through mortar joints, see Figure 3.29c and d. The first flexural cracks in the reinforced concrete frame formed at the lateral drift of 0.27% in the left column when the force was applied in the negative direction. At lateral drift of 0.38% the cracks in the infill continued to propagate in diagonal direction and masonry infill totally separated from its bounding frame, see Figure 3.29g and h. Crack pattern recorded at the maximum lateral force is shown in Figure 3.30a and b. The first crushing of the bricks was observed at the lateral drift of 0.75%, progressing by increasing the lateral displacement. At the lateral drift of 2.5%, the crushing of the bricks, mainly at the top row of the masonry infill was observed due to the severe compressive stress concentration, see in Figure 3.30c to in Figure 3.30f.

It was not possible to monitor the crack propagation in the internal leaf of the specimen (with a thickness of 6cm) during in-plane cyclic test but it was observed that at lateral drift of 1%, it started to bulge in out-of-plane direction and at lateral drift of 2.5% it was totally collapsed due to excessive bulging as it is shown in Figure 3.31.

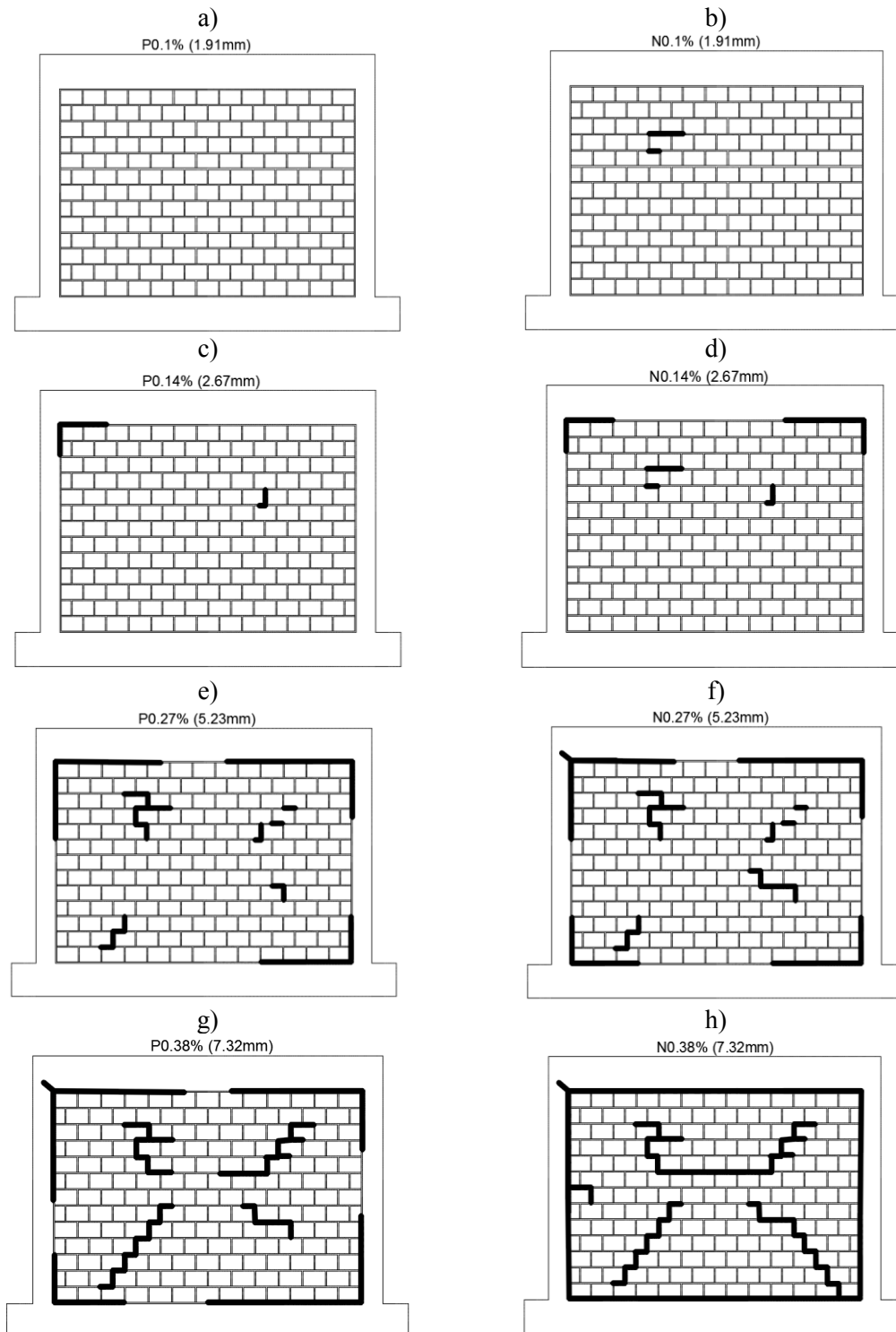


Figure 3.29 Crack propagation in the specimen at lateral drift of a)0.1% in positive direction b)0.1% in negative direction c)0.14% in positive direction d)0.14% in negative direction e)0.27% in positive direction f)0.27% in negative direction g)0.38% in positive direction h)0.38% in negative direction

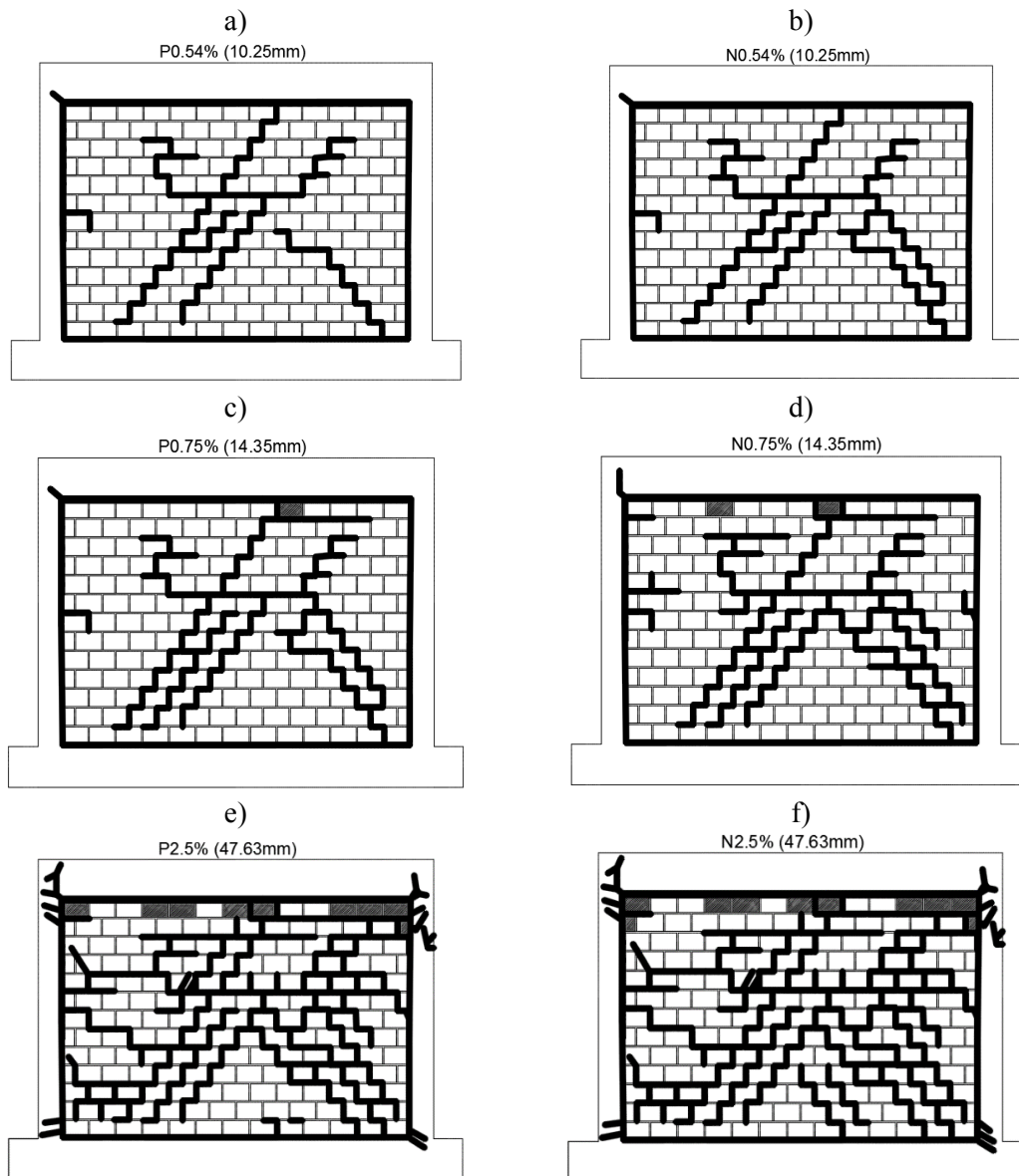


Figure 3.30 Crack propagation in the specimen at lateral drift of a)0.54% in positive direction b)0.54% in negative direction c)0.75% in positive direction d)0.75% in negative direction e)2.5% in positive direction f)2.5% in negative direction



Figure 3.31 Out-of-plane bulging of the interior leaf during in-plane loading at lateral drift of a)1% b)2%

### 3.8.2.4 Energy dissipation

The energy dissipation of the specimen during in-plane loading at each cycle is shown in Figure 3.32. It is observed that at early stages of loading, the dissipation of energy is negligible. For higher displacements, the dissipation of energy is increased due to the propagation of cracks in the masonry infill. It is also observed that the dissipation of energy at lateral drift of 0.5% is 1150kN.mm which is 7.6 times of energy dissipation obtained in the bare frame at the same lateral drift.

The total dissipation of energy for this specimen until each cycle is shown in Figure 3.33. It is observed that the total energy dissipated until lateral drifts of 0.54%, 1.05% and 2.07% is 1793 kN.mm, 3269 kN.mm and 6341 kN.mm respectively which is 5.7, 3.2 and 1.5 times of total energy dissipation recorded in the bare frame for the same lateral drifts. It is clear that energy dissipation rate of the bare frame is more than infilled frame at higher lateral drifts.

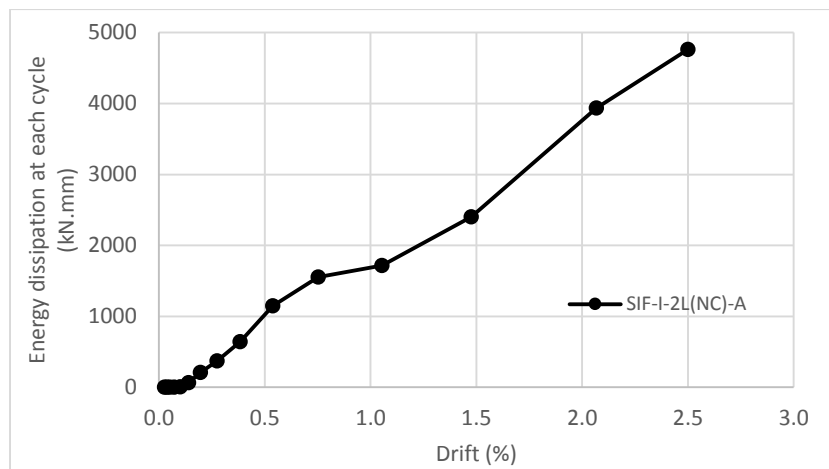


Figure 3.32 Energy dissipated at each cycle for specimen SIF-I-2L(NC)-A

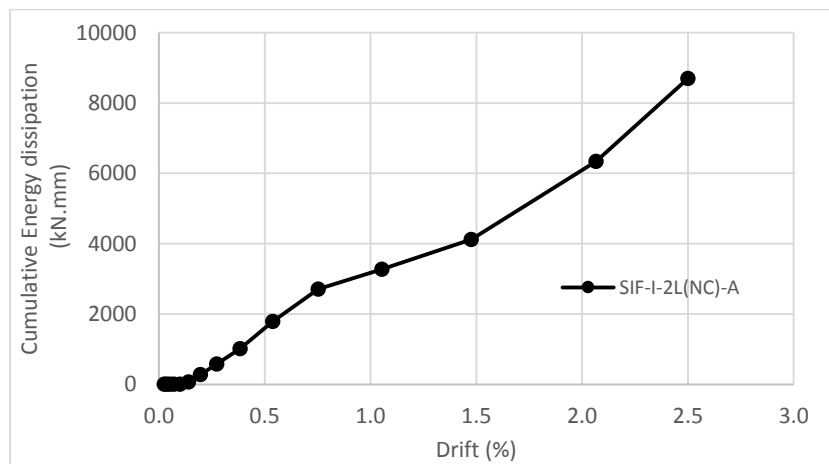


Figure 3.33 Cumulative energy dissipation of SIF-I-2L(NC)-A

### 3.8.2.5 Deformation Characteristics

The in-plane testing of the infilled frame was performed until the lateral drift of 2.5% both in the positive and negative directions but due to crushing of the masonry infill and falling of the LVDTs, it was not possible to measure the diagonal length changes of the infill and frame after



1.5% lateral drift. The lateral force versus average shear distortion of the rc frame is shown in Figure 3.34, whereas the relation between the lateral force and average shear distortion of the external and internal leaf of the masonry infill are shown in Figure 3.35 and Figure 3.36 respectively. The nonlinearity in the shear distortion of the reinforced concrete frame in the positive direction started at lateral force of 89kN corresponding to the lateral drift of 0.14% due to the formation of the first cracks in the infill. In the negative direction, the shear distortion increased rapidly at lateral drift of 0.14%. At peak lateral force in the positive direction, the average shear distortion of the frame reached 0.004 (rad), whereas in the peak lateral force of the negative direction it reached the value of 0.00594 (rad). Finally, at maximum lateral drift of 1.5%, the average shear distortion reached 0.0125 (rad) in the positive direction and 0.013 (rad) in the negative direction.

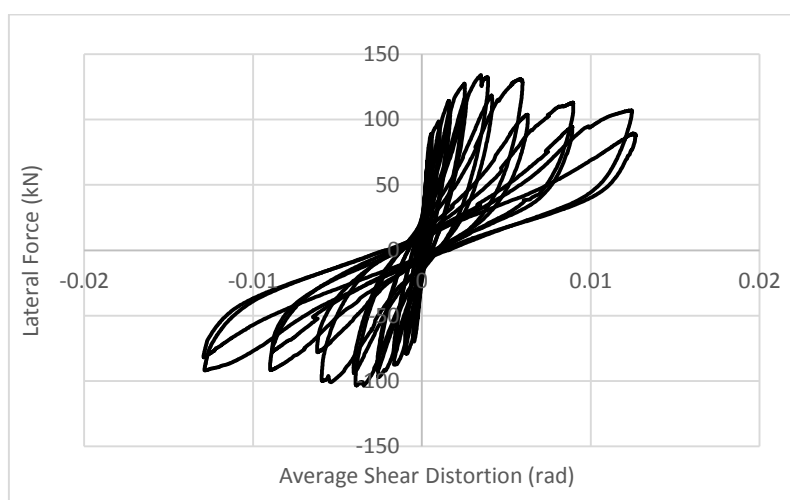


Figure 3.34 Relation between lateral force and average shear distortion of the reinforced concrete frame

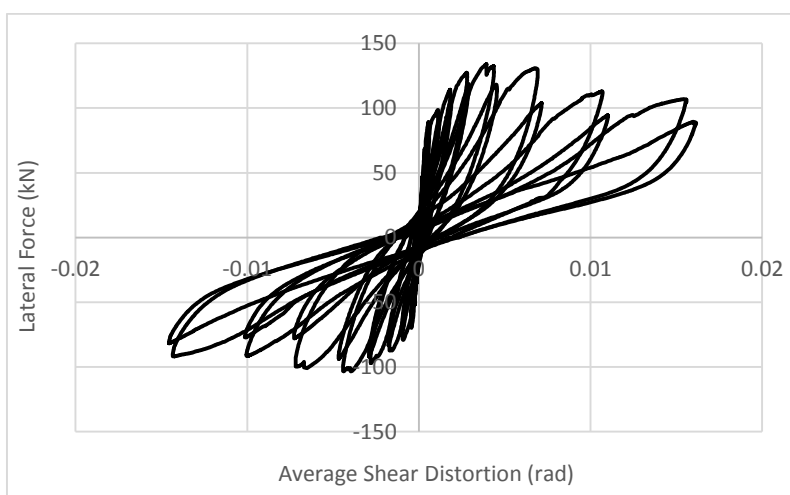


Figure 3.35 Relation between lateral force and average shear distortion of the external leaf

The shear distortion of the external leaf of the infill wall started at lateral drift of 0.14% resulting from minor cracking in the masonry infill and its separation from the RC frame. The shear distortion reached the value of 0.0044 (rad) at lateral drift of 0.54% recorded for the maximum lateral force in the positive direction. The value of the shear distortion corresponding to the peak load in the negative direction was 0.0072 (rad), being associated to the lateral drift of 0.54%. At

the lateral drift of 1.5% the average shear distortion of the infill in the positive direction was 0.0156 (rad) and in the negative direction was 0.0146 (rad). For the internal leaf of the masonry infill the trend is similar to the external leaf.

In average, the shear distortion in the internal leaf started at lateral drift of 0.14% in the positive and negative directions. At the peak lateral force, the average shear distortion in the positive direction was 0.0043 (rad), corresponding to lateral drift of 0.54%, and was 0.0062 (rad) in the negative direction. Finally, at the lateral drift of 1.5%, the average shear distortion reached the value of 0.016 (rad) and 0.012 (rad) in the positive and negative directions, respectively.

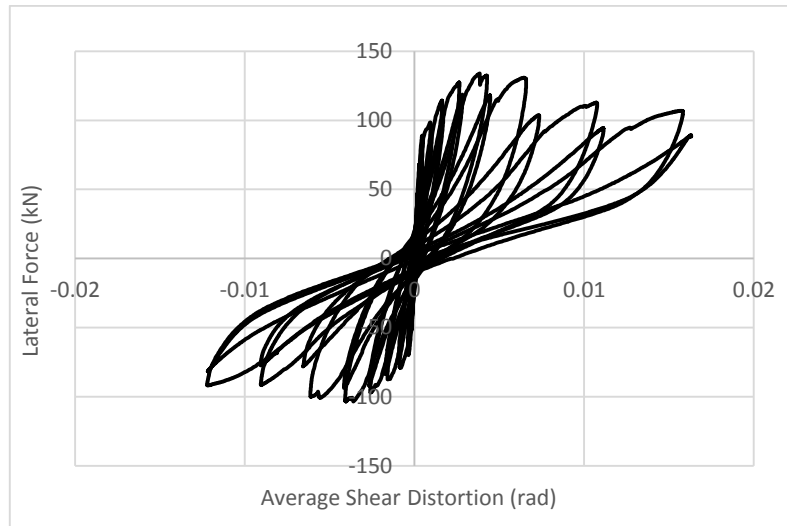


Figure 3.36 Relation between lateral force and average shear distortion of the internal leaf

The relative displacement (separation) of the masonry infill from its bounding frame with respect to the lateral displacement and lateral force applied to the specimen is shown in Figure 3.37. The results obtained in LVDTs L9 and L10 indicate that the first separation of the infill from rc frame occurs at upper left corner at lateral displacement of 2.67 mm, corresponding to lateral drift of 0.14% when lateral load is applied in the positive direction. Based on the displacements measured in LVDTs L7 and L8, it is possible to conclude that the separation of the brick infill from the rc frame at the upper right corner occurs at displacement of 2.67mm, corresponding to a lateral drift of 0.14%, see Figure 3.37e and f. By applying further displacement to the specimen, the infill separates in its lower part at lateral displacement of 5.23mm corresponding to lateral drift of 0.27% in the positive and negative directions. In the present test the separation of the lower part of the infill happens after the separation of the upper part. The weight of the infill can be an important issue on the later separation of the bottom part of the infill.

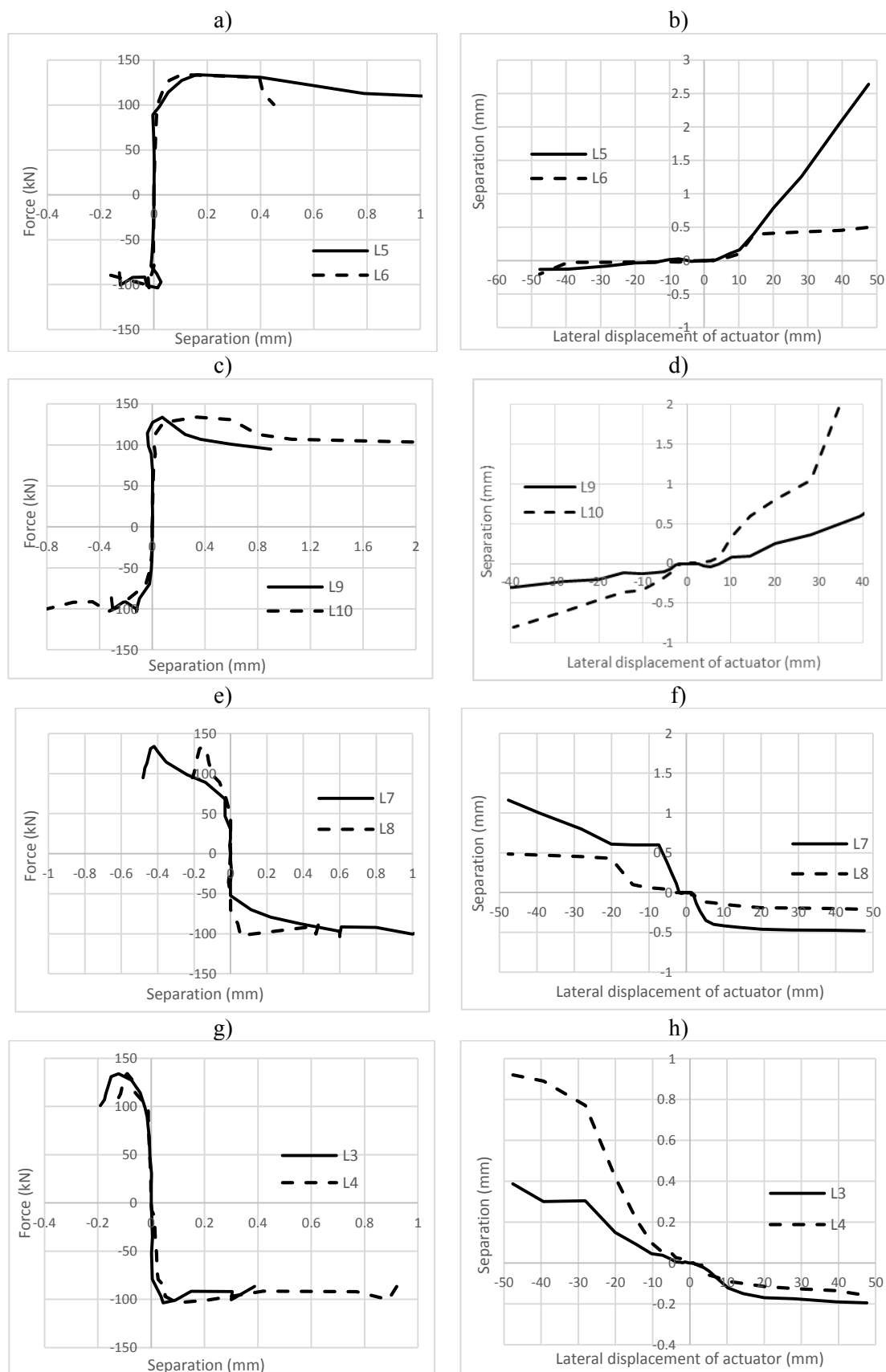


Figure 3.37 Relative displacement of masonry infill from its bounding frame with respect to the force and lateral displacement applied to the structure for a)lower right corner b)lower right corner c)upper left corner d)upper left corner e)upper right corner f)upper right corner g)lower left corner h)lower left corner

### 3.8.3 Specimen SIF-IO(0.3%)-2L(NC)-B

#### 3.8.3.1 Lateral load-displacement response

In addition to the in-plane static test carried out until failure, three additional in-plane cyclic tests were carried out on the same typologies by imposing lateral displacement until specific lateral drifts to simulate the effect of different previous in-plane damages on their out-of-plane behavior. In this section the results of the in plane testing of rc frame with masonry infill tested until a lateral drift of 0.3% are presented and discussed.

The force-displacement diagram describing the in-plane response of the specimen is shown in Figure 3.38. At the first levels of loading the infilled frame behaved monolithically to resist the lateral load. This behavior continued until the opening of the first crack at mid span of the wall, with its separation in the upper right and bottom left corners from the rc frame at lateral drift of 0.05%, corresponding to the lateral force of -64kN in the negative direction. Towards positive direction, reduction of the stiffness initiated at lateral drift of 0.07% corresponding to lateral force of 105.29kN. After this point, the lateral displacement was increased until lateral drift of 0.3% was achieved. The maximum force in the positive and negative directions at lateral drift of 0.3% reached 165.42kN and -133.79kN respectively.

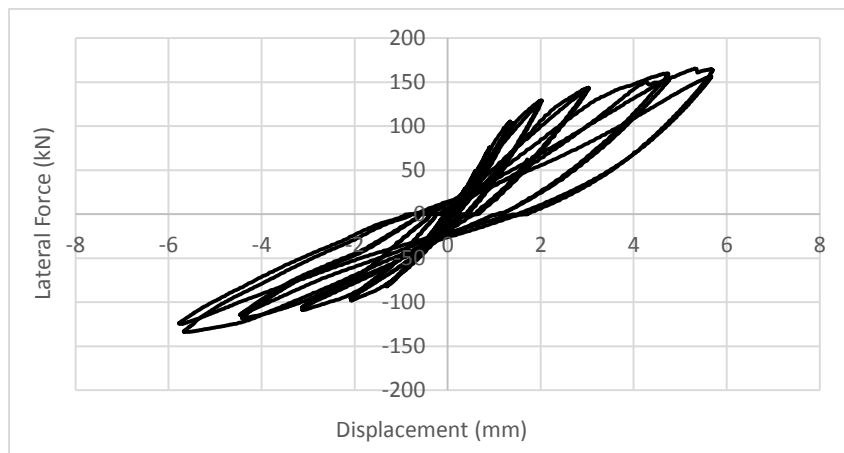


Figure 3.38 Lateral force-displacement diagram of SIF-IO(0.3%)-2L(NC)-B

The force-displacement diagram representing the monotonic envelop of the cyclic hysteresis loops defined at two successive cycles is shown in Figure 3.39. It is observed that a very slight strength degradation occurred after the initiation of cracking, achieving very moderate values at the lateral drift of 0.3% (7.3% and 5.6% at the maximum force in the negative and positive directions respectively). This is in line with the previous results of the in-plane testing of the rc frame with brick infill, taking into consideration that a very low lateral drift is experienced by this specimen. Given that the maximum lateral drift considered for this specimen was only 0.3%, it was not possible to obtain the complete behavior and the corresponding key parameters of the brick masonry infill enclosed in the rc frame. Only the secant stiffness was calculated at the crack initiation point and compared with that of the infill tested until failure (Table 3-5). Therefore, the crack initiation occurred at lateral displacements,  $d_{cr}$ , of 1.35mm (drift of 0.07%) in the positive direction and of 0.9 mm (drift of 0.05%) in the negative direction. The cracking initiation load,  $H_{cr}$ , was 105.3kN and 63.6kN in the positive and negative directions respectively. In terms of secant stiffness, values of 78.0 kN/mm and 70.7 kN/mm were found in the positive and negative

directions respectively. By comparing these values with the secant stiffness obtained in SIF-I-2L(NC)-A (33.4kN/mm in the positive direction and 27.4 kN/mm in the negative direction) it can be easily concluded that the workmanship could significantly affect the in-plane behavior of the infilled frames.

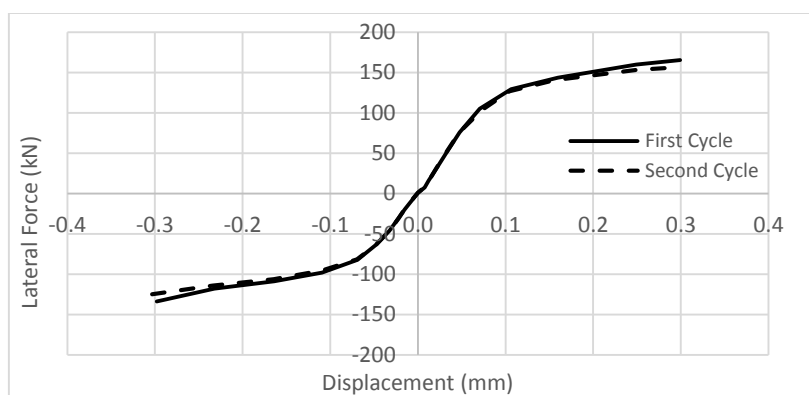


Figure 3.39 Monotonic force-displacement diagram of two successive cycles

As small amount of displacement was applied on this specimen in the in-plane direction, small deformations formed within the structure. For this reason, it was decided not to present the diagrams of local deformation of the interface between the brick infill and the rc frame.

Table 3-5 Key parameters related to the in-plane behavior of SIF(0.3%)-I-2L(NC)-B in positive and negative directions

Positive direction					Negative direction				
$H_{cr}$ (kN)	$d_{cr}$ (mm)	$K_e$ (kN/mm)	$H_{max}$ (kN)	$dH_{max}$ (mm)	$H_{cr}$ (kN)	$d_{cr}$ (mm)	$K_e$ (kN/mm)	$H_{max}$ (kN)	$dH_{max}$ (mm)
105.3	1.35	78.0	-	-	-63.6	-0.9	70.7	-	-

### 3.8.3.2 Stiffness degradation

This specimen was tested until small lateral drift of 0.3% in the in-plane direction. The stiffness degradation curve representing the stiffness of the specimen at each lateral drift is shown in Figure 3.40. Similar to what was observed in the specimens tested before, considerable decrease in the stiffness of the specimen was happened in the first levels of loading. For instance 63% and 67% decrease in the stiffness of the specimen until lateral drift of 0.3% was observed in the positive and negative directions respectively.

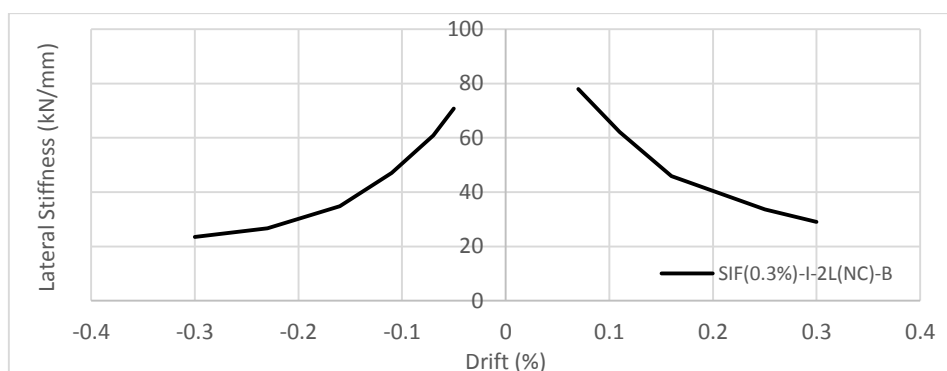


Figure 3.40 Stiffness degradation curve for specimen SIF(0.3%)-I-2L(NC)-B

### 3.8.3.3 Crack patterns

The crack patterns observed in the specimen at different levels of loading are shown in Figure 3.41 and Figure 3.42. The first cracking of the infill occurred at its central region by formation of some cracks along the unit-mortar interfaces at lateral drift of 0.05% corresponding to lateral force of 64kN, when the loading was applied in the negative direction. At this lateral drift, the infill separated from its bounding frame at upper right and bottom left corners. When the load was applied in the positive direction the crack initiation took place at lateral drift of 0.07%, combining the cracking of infill at the center part and its separation from the rc frame (Figure 3.41c). By increasing the lateral displacement, cracks propagated along the compressed diagonal alternatively when the lateral load was applied in the positive and negative directions. For instance at the lateral drift of 0.11%, the diagonal cracks propagated towards the corners, as can be seen in Figure 3.41e and f. The diagonal cracks were almost completely formed, connecting the top and bottom corners, at the lateral drift of 0.3% in both positive and negative directions, see Figure 3.42c and d.

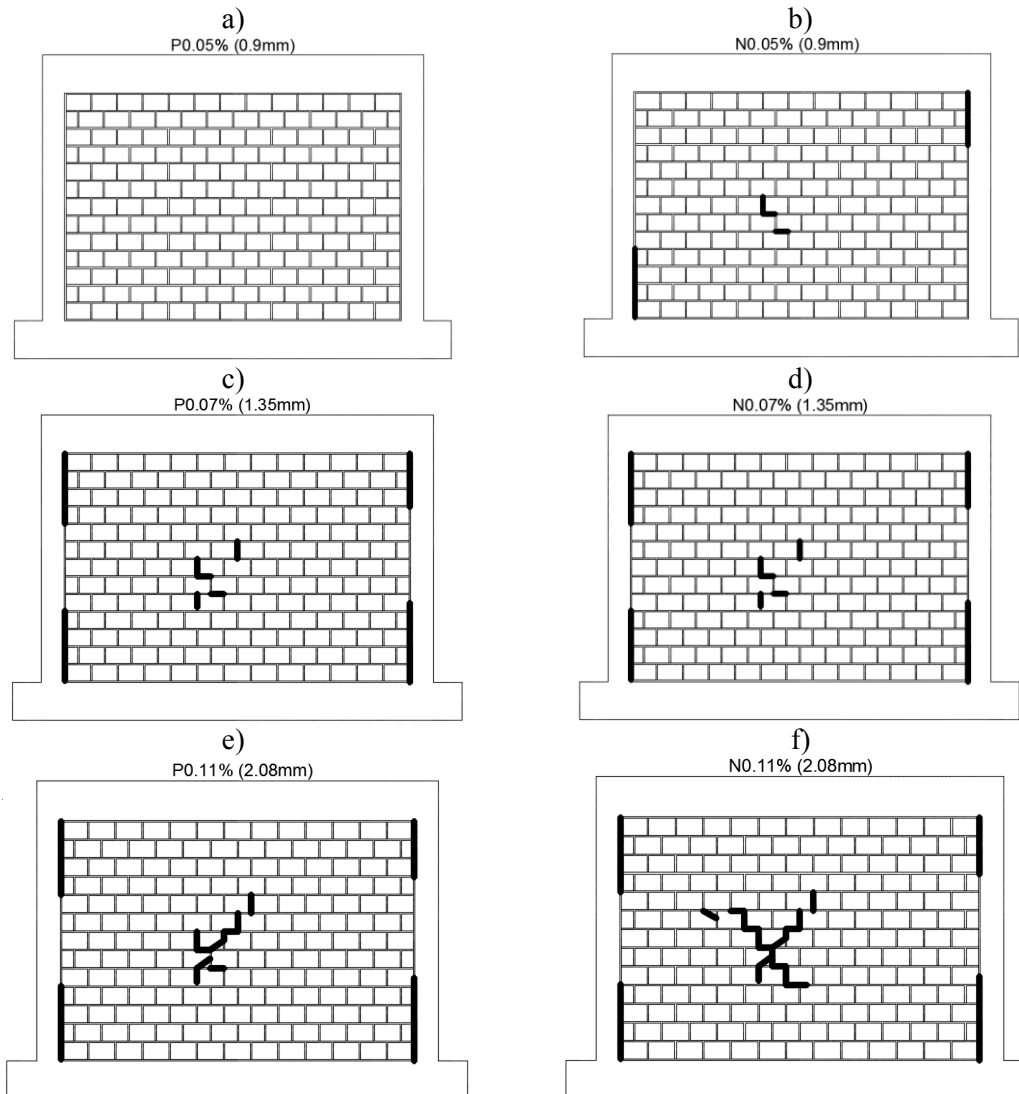


Figure 3.41 Crack propagation in the specimen at lateral drift of a)0.05% in positive direction b)0.05% in negative direction c)0.07% in positive direction d)0.07% in negative direction e)0.11% in positive direction f)0.11% in negative direction

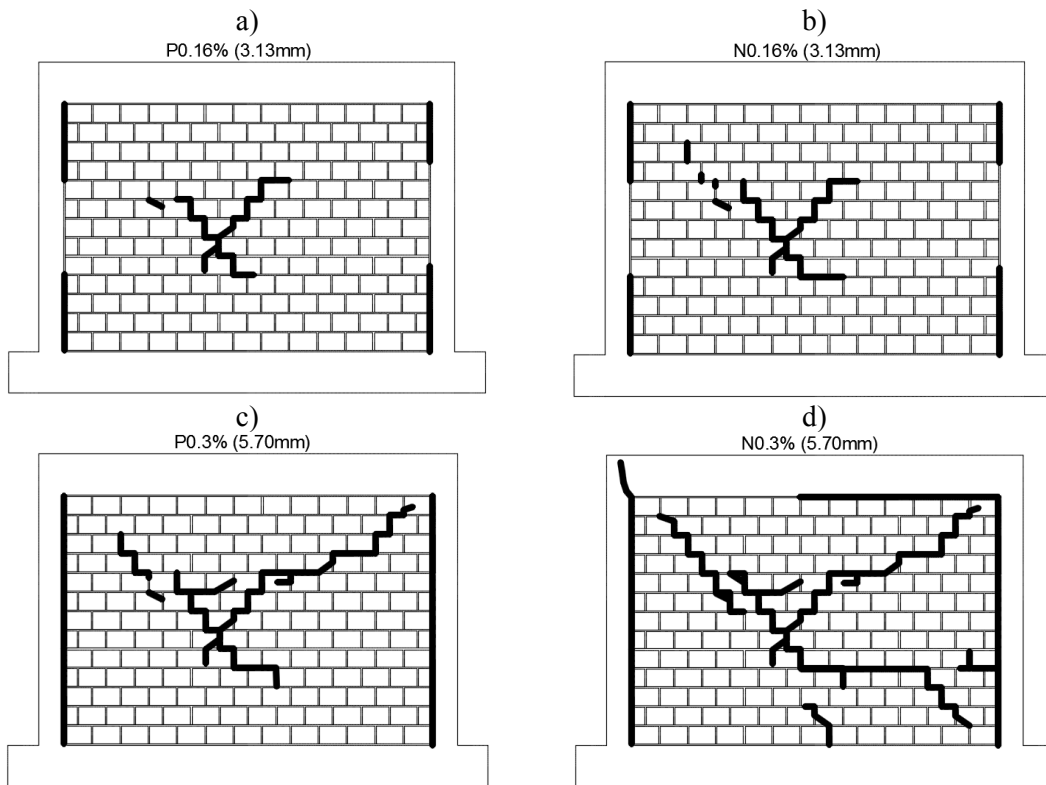


Figure 3.42 Crack propagation in the specimen at lateral drift of a)0.16% in positive direction b)0.16% in negative direction c)0.3% in positive direction d)0.3% in negative direction

### 3.8.3.4 Energy dissipation

Dissipation of energy due to in-plane testing of the specimen at each cycle was calculated based on the area of each hysteretic loop of that cycle and shown in Figure 3.43. It is clear that the energy dissipated by formation of cracks and in this specimen, it is observed that the amount of the energy dissipation increased after lateral drift of 0.1% when significant cracking was formed. The total energy dissipation of the specimen is also shown in Figure 3.44. It is observed that the total energy dissipated at the end of the test (at lateral drift of 0.3%) is 1888kN.mm.

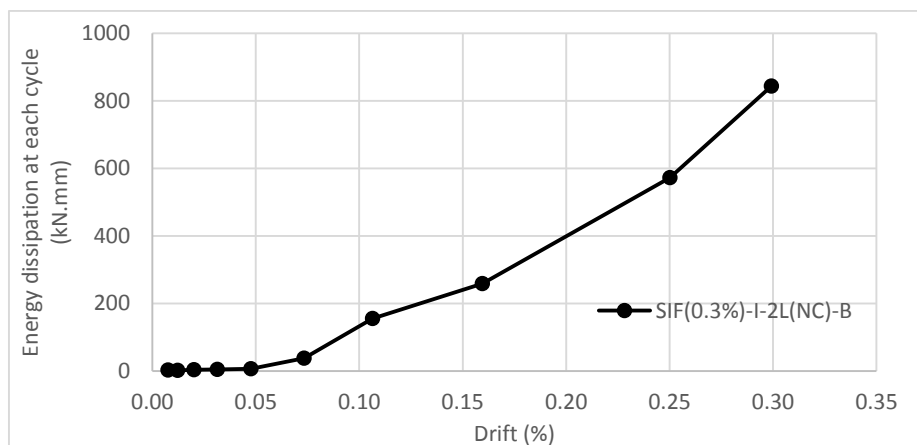


Figure 3.43 Energy dissipation at each cycle for specimen SIF(0.3%)-I-2L(NC)-B

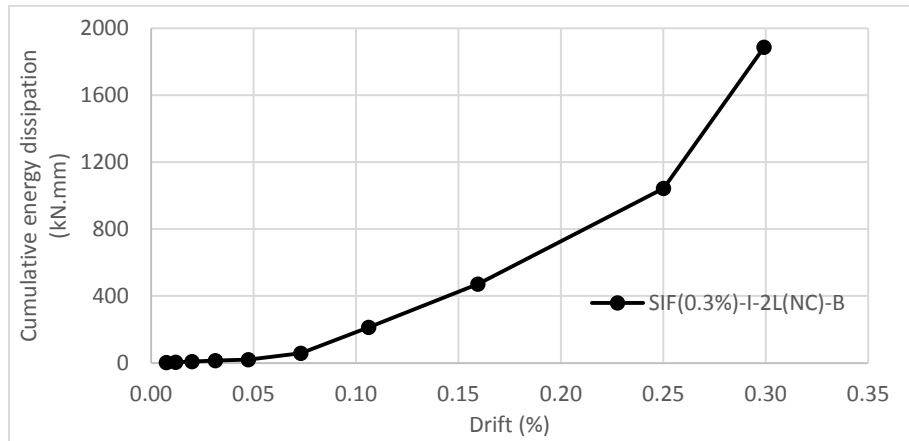


Figure 3.44 Cumulative energy dissipation of specimen SIF(0.3%)-I-2L(NC)-B

### 3.8.4 Specimen SIF-IO(0.5%)-2L(NC)-B

#### 3.8.4.1 Lateral load-displacement response

The lateral Load-displacement diagram obtained for the specimen subjected to a maximum lateral drift of 0.5% is shown in Figure 3.45. The linear elastic behavior was observed until a lateral displacement of 1.35mm corresponding to lateral drift of 0.07% both in the positive and negative directions. The lateral load corresponding to crack initiation was 113.51kN in positive direction and -104.37kN in the negative direction. Applying increasing displacements resulted in pre-peak nonlinear behavior until the peak lateral load was achieved. In the positive direction, the maximum force was 175.17kN, obtained at lateral drift of 0.38% (7.3mm), whereas in the negative direction, the maximum force of -168.43kN was recorded at lateral drift of 0.27% (5.2mm). After the peak lateral load was attained, noticeable reduction in the lateral force was observed in the negative direction, being calculated as 20%. In the positive direction, the decrease was only about 4.3%.



Figure 3.45 In-Plane force-displacement diagram of the specimen SIF-IO(0.5%)-2L(NC)-B

The monotonic envelop of the hysteretic force-displacement diagram at two successive cycles is shown in Figure 3.46. No strength degradation is observed until the first cracking of the specimen



at lateral drift of 0.07% in the positive and negative directions. It seems that crack propagation in the infill is the main cause of the strength degradation. In the positive direction, a maximum strength degradation of 12% was observed at the lateral drift of 0.38%, corresponding to the maximum lateral force of 175.17kN. The maximum strength degradation of 30% was observed at lateral drift of 0.27% in the negative direction.

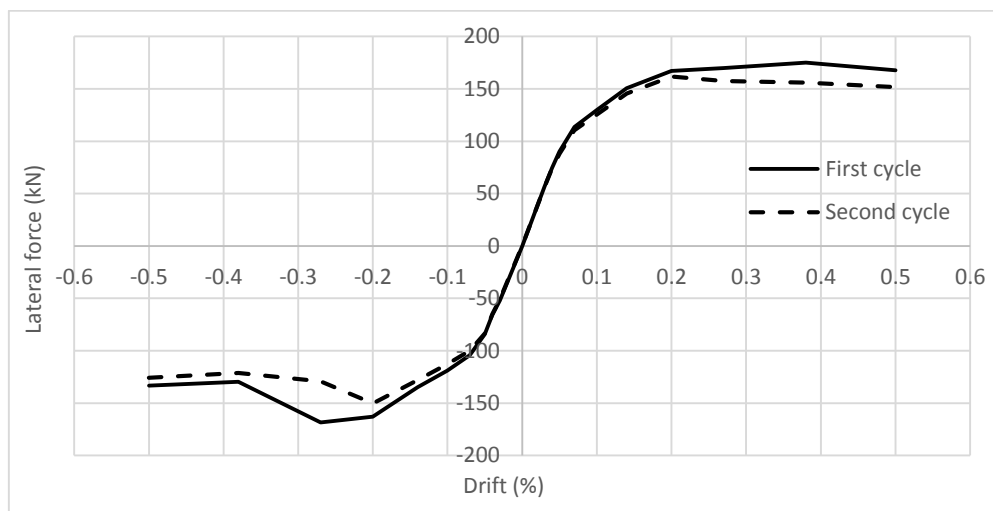


Figure 3.46 Monotonic envelop of the force-displacement diagram at two successive cycles

The key parameters characterizing the in-plane response of the specimen were derived and shown in Table 3-6. The initial stiffness of the specimen was calculated based on the secant stiffness at crack initiation point. From Figure 3.45, it is clear that the specimen could achieve the maximum lateral resistance both in the positive and negative directions. At positive direction the specimen reached the maximum force of 175.17kN at lateral drift of 0.38% and in negative direction it reached the maximum force of 168.43kN at lateral drift of 0.27%.

Table 3-6 Key parameters related to the in-plane behavior of SIF(0.5%)-I-2L(NC)-B

Positive direction					Negative direction				
$H_{cr}$ (kN)	$d_{cr}$ (mm)	$K_e$ (kN/mm)	$H_{max}$ (kN)	$d_{Hmax}$ (mm)	$H_{cr}$ (kN)	$d_{cr}$ (mm)	$K_e$ (kN/mm)	$H_{max}$ (kN)	$d_{Hmax}$ (mm)
113.5	1.35	84.1	175.2	7.32	-104.4	-1.35	77.3	-168.4	-5.23

By comparing the secant stiffness obtained in this specimen with the stiffness of the specimen tested until failure and with the specimen tested until a lateral drift of 0.3%, it is clear that the secant stiffness is reasonably close to the secant stiffness observed in the specimen tested until failure. It is observed that the initial stiffness of the specimen constructed with mason B increased about 1.5 and 1.8 times in positive and negative directions respectively with respect to the specimen that was constructed with mason A. The increase in the lateral strength is also calculated and it is found that increase of about 31% and 62% in positive and negative directions were recorded respectively. Based on these results, it can be concluded that the construction quality can take a major role on the in-plane response of masonry infills.

### 3.8.4.2 *Stiffness degradation*

The stiffness degradation curve obtained for this specimen is shown in Figure 3.47. It is clear that the trend of variation of the stiffness is very similar to the one recorded in the previous specimens. In addition, the amount of stiffness degradation at the first levels of loading in both positive and negative directions is very considerable, which is in accordance with what was observed in specimens tested until failure and tested until the lateral drift of 0.3%. The stiffness degradation recorded until lateral drift of 0.5% was about 79% and 82% for positive and negative directions respectively.

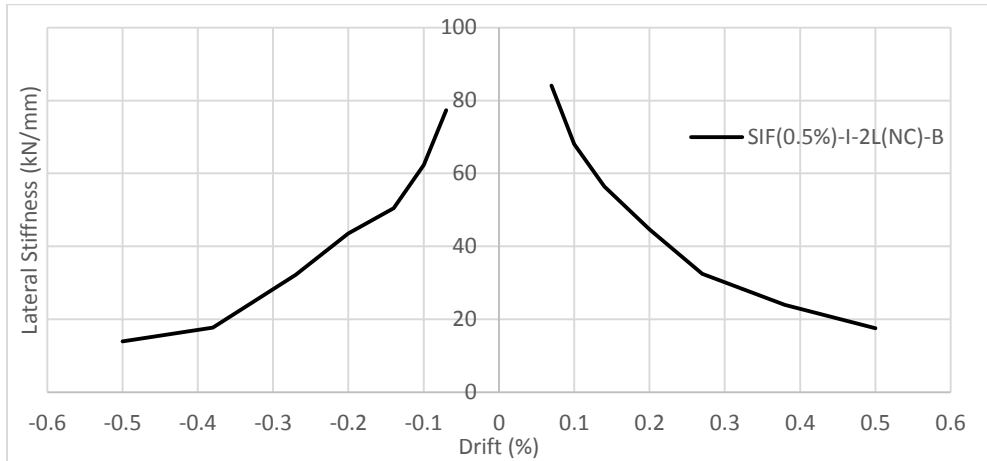


Figure 3.47 Stiffness degradation curve of specimen SIF(0.5%)-I-2L(NC)-B

### 3.8.4.3 *Crack patterns*

The crack propagation in the specimen under study is shown in Figure 3.48 and Figure 3.49. The cracking of the specimen leading to the decrease in the initial stiffness was observed at lateral drift of 0.07% corresponding to the lateral force of 113.51kN in positive direction. At this lateral drift some diagonal cracks were formed in the center part of the infill along with its separation from rc frame in upper left corner, see Figure 3.48a. In the negative direction, the crack initiated at the central part of the specimen at the same lateral drift of 0.07%, corresponding to lateral force of -104.37kN. Additionally, the separation of the upper right corner of the wall from the rc frame was also recorded. The crack propagation follows the same trend described previously for the other specimens. By increasing lateral displacements, the length of the diagonal crack increased and developed towards the top and right corners, see Figure 3.48c to f. The first cracking in the rc frame was observed at lateral drift of 0.2% corresponding to lateral force of 162.90kN in negative direction. The crack developed at an angle of 45° located in the upper left connection of the column and the top beam, see Figure 3.48h. In the positive direction, the same type of cracking developed at lateral drift of 0.27% corresponding to lateral force of 169.75kN, see Figure 3.49a. At the same lateral drift of 0.27% in the negative direction, shear cracks along unit-mortar interfaces were observed, see Figure 3.49b. In this case, the bricks of the fifth row from top slid over the bricks of the sixth row, leading to the development of horizontal crack along the mortar joints. Shear sliding of the infill was also observed at lateral drift of 0.38% in the positive direction, see Figure 3.49c. The increase of the lateral displacement resulted in the development of a considerable diagonal cracks with the trend to reach the corners, see Figure 3.49e and f.

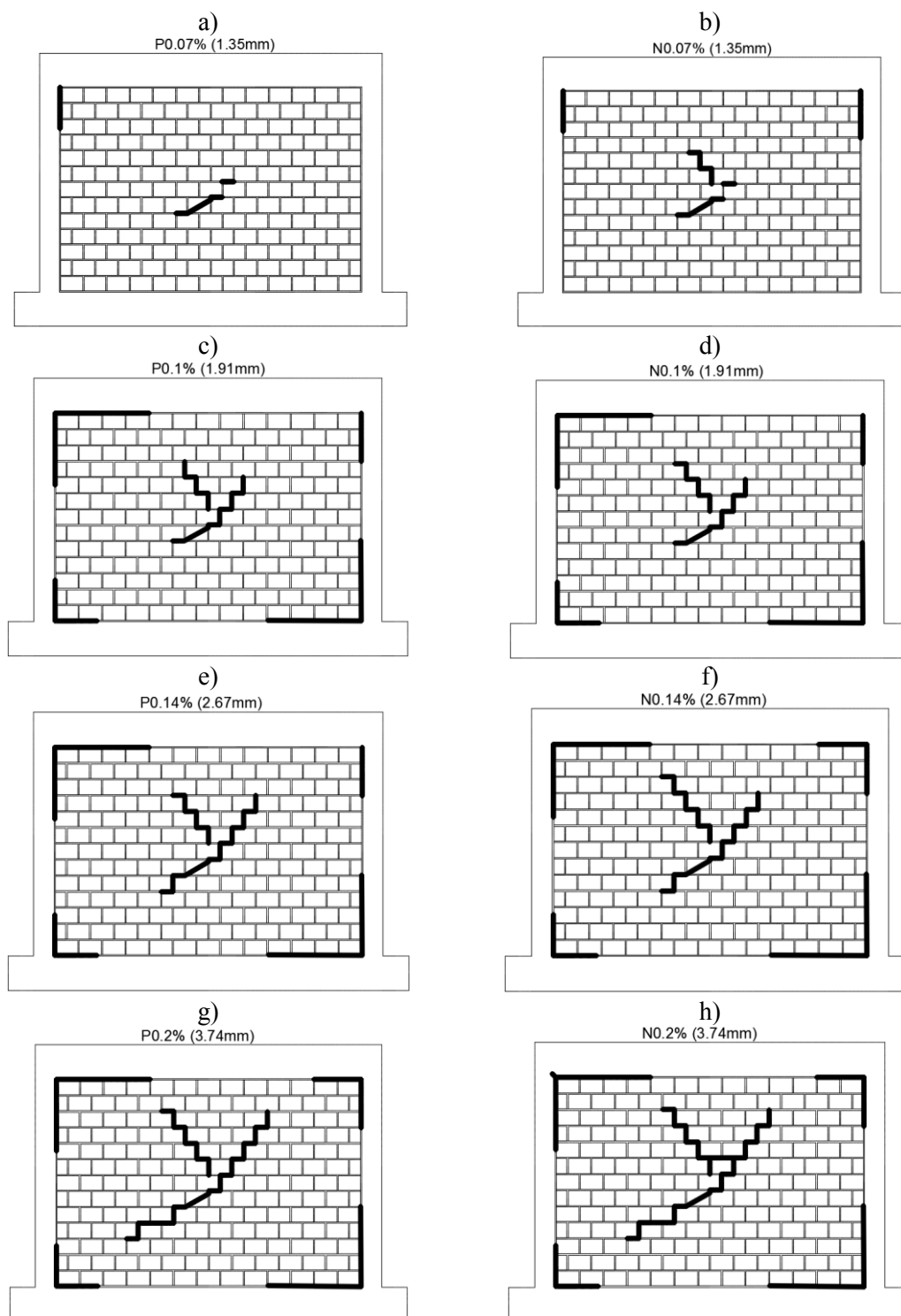


Figure 3.48 Crack propagation in the specimen at lateral drift of a)0.05% in positive direction b)0.05% in negative direction c)0.1% in positive direction d)0.1% in negative direction e)0.0.14% in positive direction f)0.14% in negative direction g)0.2% in positive direction h)0.2% in negative direction

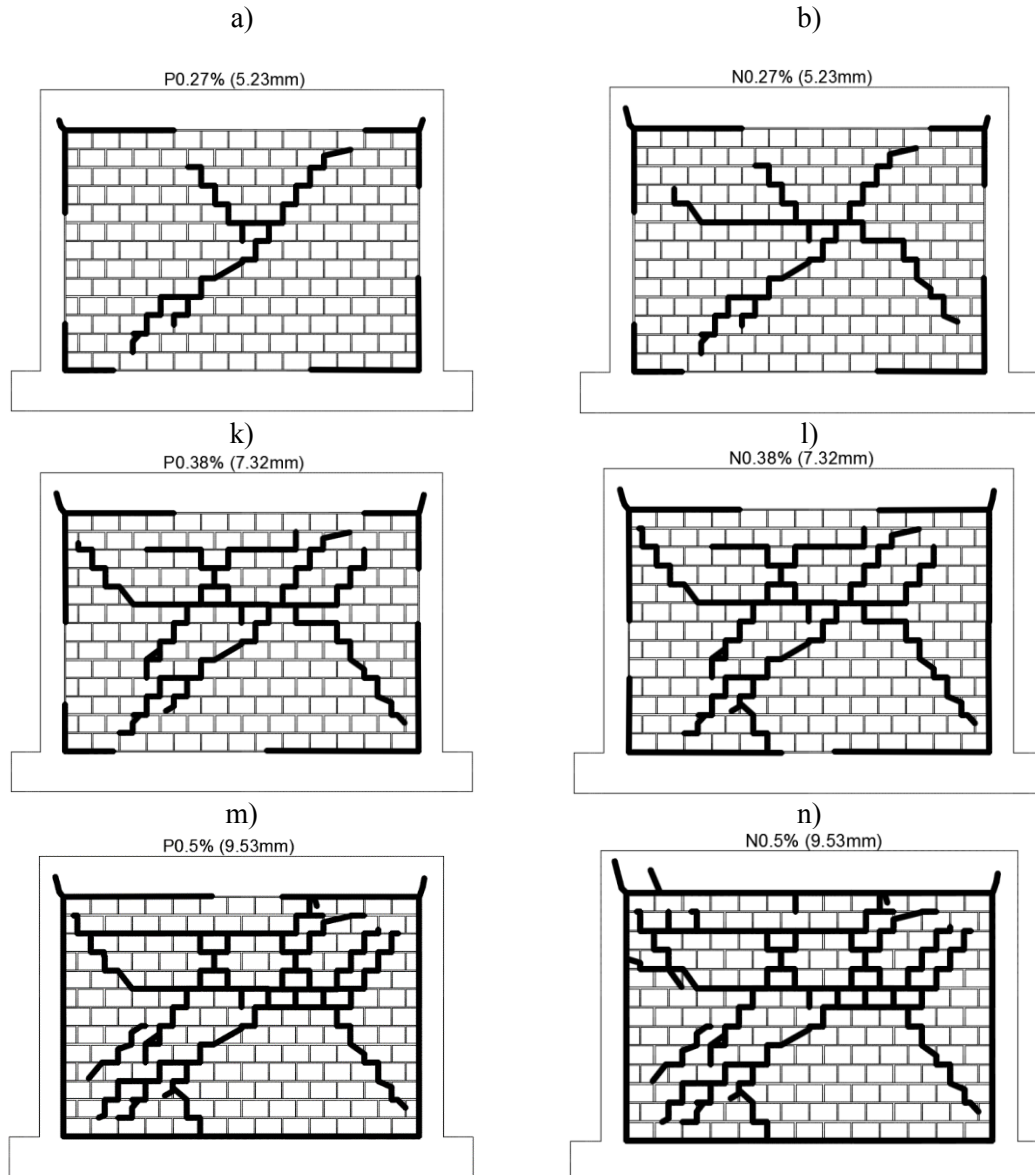


Figure 3.49 Crack propagation in the specimen at lateral drift of a)0.27% in positive direction b)0.27% in negative direction c)0.38% in positive direction d)0.38% in negative direction e)0.5% in positive direction f)0.5% in negative direction

#### 3.8.4.4 *Energy dissipation*

The energy dissipation calculated for this specimen under in-plane cyclic testing at each cycle is shown in Figure 3.50. It is observed that the amount of energy dissipation increased considerably at lateral drift of 0.07%, which is due to the formation of diagonal cracks in the specimen.

By comparing the total energy dissipation of this specimen with the one obtained in specimen SIF(0.3%)-I-2L(NC)-B, it is clear that the total amount of dissipated energy is higher in this specimen, as more damage was induced by increasing the lateral drift, see Figure 3.51. However, it is seen that the total energy dissipated at the cycle corresponding to lateral drift of 0.3% in the specimen SIF(0.3%)-I-2L(NC)-B is 1888kN.mm, whereas in the present specimen the amount of dissipation of energy is calculated as 3010kN.mm at the cycle corresponding to lateral drift of

0.27%. This could be related to the high amount of damage that is observed in the specimen SIF(0.5%)-I-2L(NC)-B at lateral drift of 0.27%.

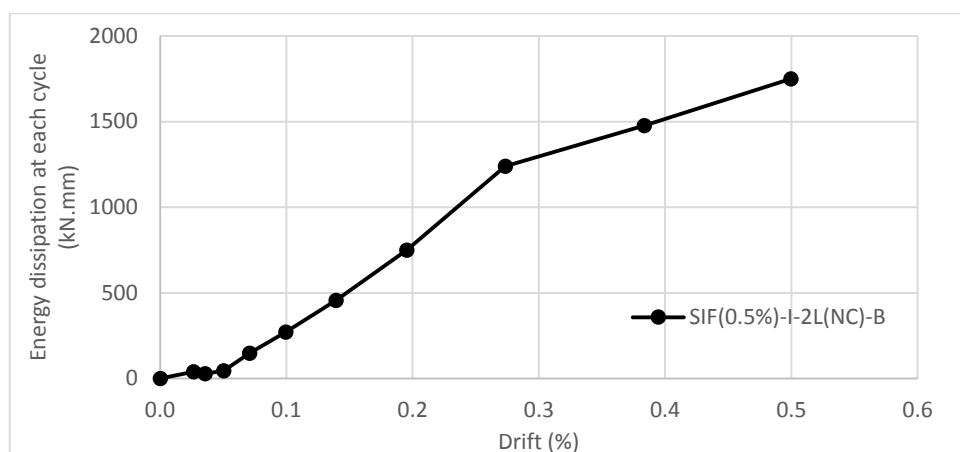


Figure 3.50 Energy dissipation at each cycle for specimen SIF(0.5%)-I-2L(NC)-B

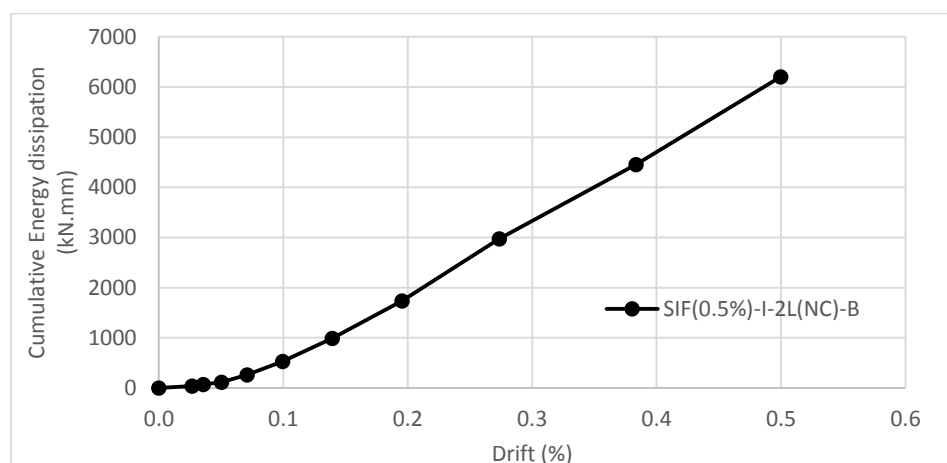


Figure 3.51 Cumulative energy dissipation of specimen SIF(0.5%)-I-2L(NC)-B

#### 3.8.4.5 Deformation Characteristics

The average shear distortions of the infill and frame are shown in Figure 3.52 and Figure 3.53. It is observed that the average shear distortion of the infill presents larger values at lateral drift of 0.2% corresponding to lateral load of 166.96kN and 162.90kN in positive and negative directions respectively due to heavy cracking of the external and internal leaf. The plateau branch is also initiated at lateral drift of 0.2%, where large diagonal cracks developed in the infill. The average shear distortion of the external and internal leaves are the same in the negative direction but in positive direction the external leaf exhibits higher shear distortion than the internal leaf, which can be related to the higher damage observed in the external leaf.

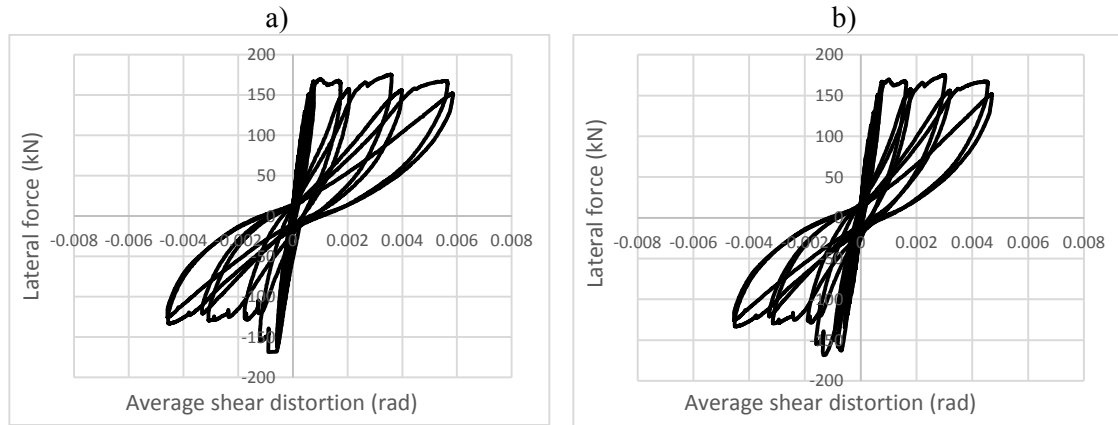


Figure 3.52 Average shear distortion of a) external leaf (8cm thickness) and b) internal leaf (6 cm thickness)

As it is shown in Figure 3.53, the average shear distortion of the rc frame starts to increase rapidly at lateral drift of 0.07% corresponding to the lateral load of 113.51kN and -104.35kN in the positive and negative directions respectively. At this lateral drift, the cracking of the infill and also its separation from rc frame is initiated. The rc frame exhibits higher shear distortion in the positive direction than in the negative direction. The higher shear distortion of the rc frame in comparison with the masonry infill is directly associated to the separation of the infill from the rc frame and to consequent development of the shear strut connecting the upper and bottom corners.

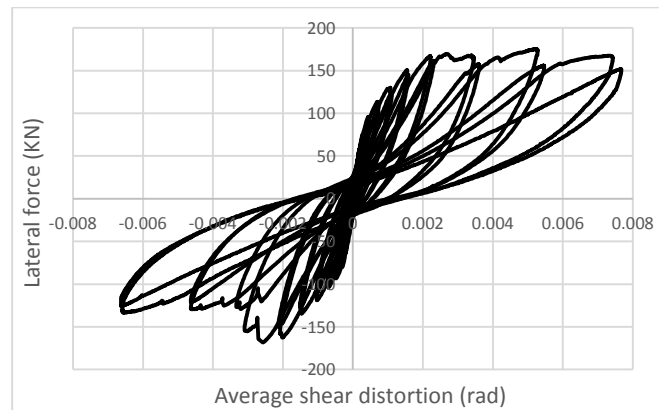


Figure 3.53 Average shear distortion of RC frame

The separation of the infill from its enclosing frame at each corner is investigated by displacements recorded in each LVDTs located on the infill. As it is shown in Figure 3.54, the separation of the infill starts at lateral drift of 0.05% by the formation of two vertical cracks at each upper corner of the infill. The increase in the lateral displacement resulted in the separation of the infill at each corner (except at upper right corner) through the formation of horizontal and vertical cracks along the brick infill-rc frame interfaces. The horizontal crack in the upper right corner of the infill (L7), which is related to the separation of infill from rc frame in horizontal joint, developed at lateral drift of 0.14%.

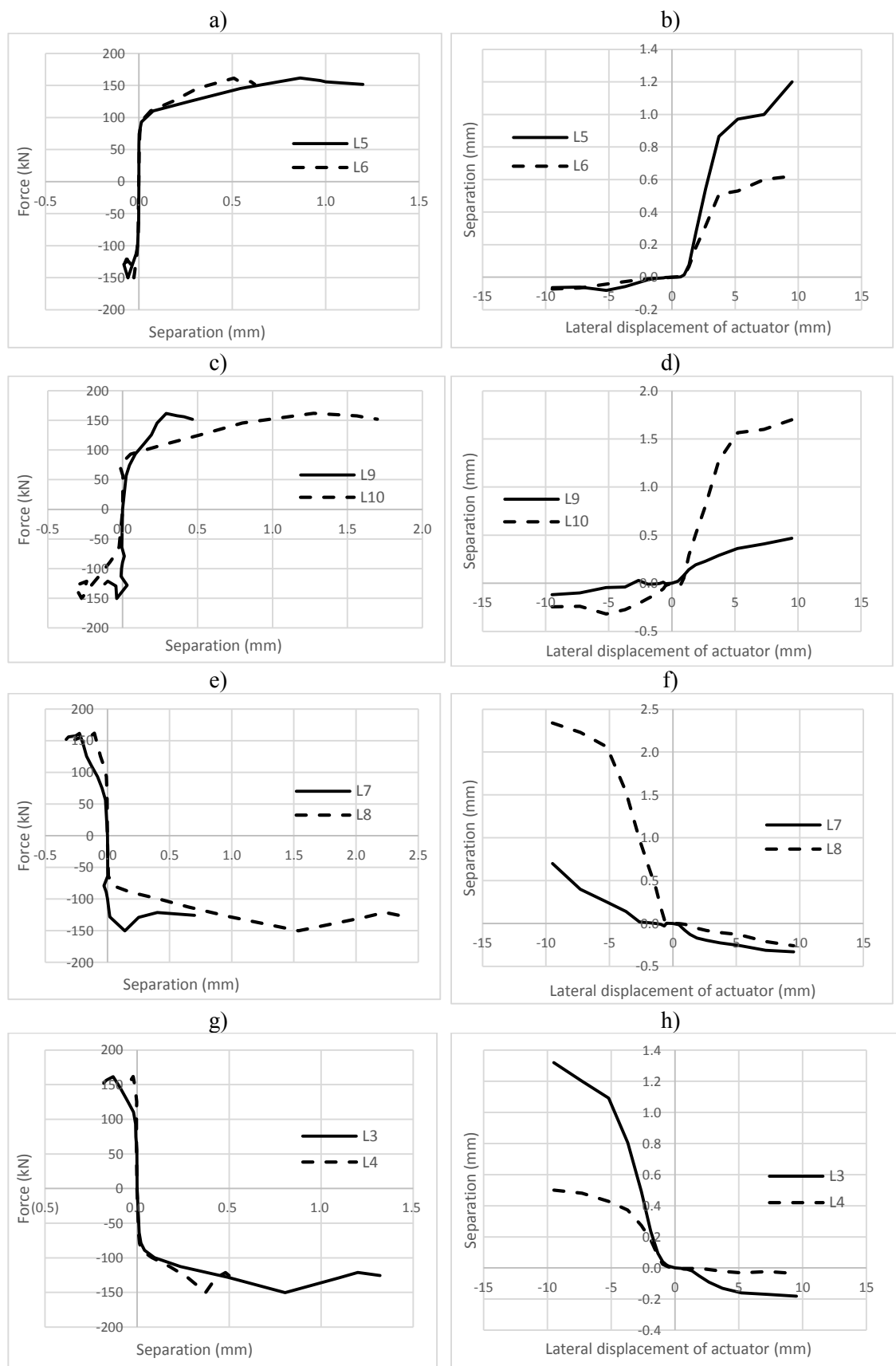


Figure 3.54 Relative displacement of masonry infill in relation to the rc frame at a) lower right corner b) lower right corner c) upper left corner d) upper left corner e) upper right corner f) upper right corner g) lower left corner h) lower left corner

### 3.8.5 Specimen SIF-IO(1%)-2L(NC)-B

#### 3.8.5.1 Lateral load-displacement response

The force-displacement diagram of the rc frame with masonry infill until the lateral drift of 1% is shown in Figure 3.55. The loading of this specimen was initiated in the negative direction. The first cracking observed in the specimen was located at the bottom left corner of the infill through the formation of vertical crack, in the mortar joint, which is related to the separation of the infill from its enclosing frame. This occurred at lateral drift of 0.05%, corresponding to the lateral force of -80.21kN. Then, the lateral force was increased until -87.32kN corresponding to the lateral drift of 0.07%, after which the cracking of the specimen was initiated by the formation of some stair stepped cracks at the central region of the wall. Applying further displacements led to a gradual increase of the lateral strength, achieving the value of -130.61kN at the drift of 1%. By comparing the value of the lateral force at 1% lateral drift (-130.61kN) with the lateral force of -129.08kN, which was reached in the previous cycle at lateral drift of -0.75%, it is observed that further displacements resulted in very little increase of the lateral force. This means that the specimen reached the peak resistance. Therefore, it is feasible to assume that the maximum lateral resistance of about -130.61kN was achieved at the lateral drift of 1%.

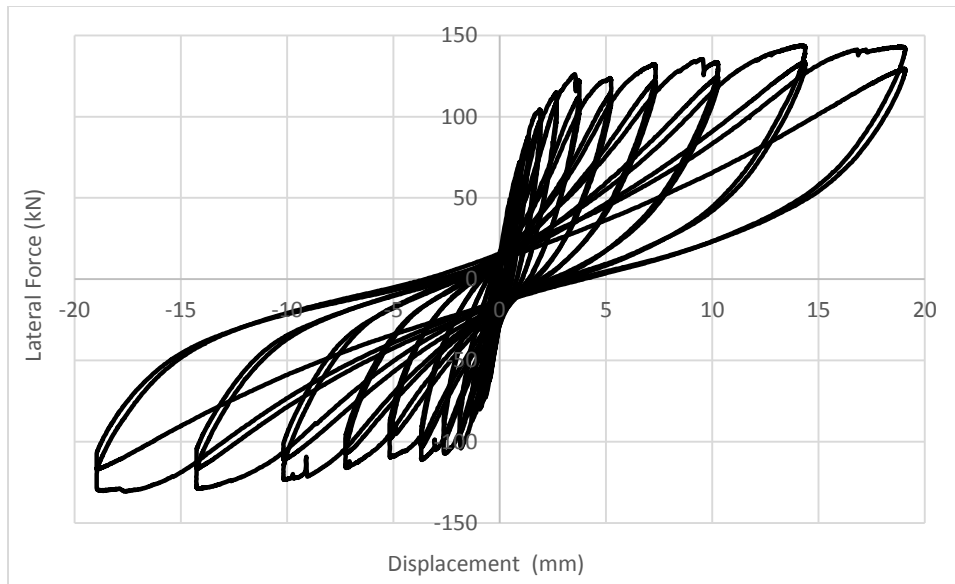


Figure 3.55 Force-displacement diagram of the specimen SIF-IO(1%)-2L(NC)-B

In the positive direction, similar to the negative direction, at lateral drift of 0.05% corresponding to the lateral force of 72.45kN the vertical crack was observed in the mortar joint at upper left corner which is related to the separation of the infill from rc frame. At lateral drift of 0.07% corresponding to the lateral force of 87.88kN, cracking of the infill was initiated by formation of some stair step cracks in its mid part. It seems that the specimen reached the maximum strength of 143.93kN at lateral drift of 0.75%, as by increasing the lateral displacement corresponding to the lateral drift of 1%, a slight reduction in the lateral force was observed (143.18kN).

By analyzing the force-displacement diagram obtained in the specimen SIF-IO(0.5%)-2L(NC)-B, it is observed that the maximum lateral force was recorded at lateral drifts of 0.38% and 0.27% in the positive and negative direction, respectively. This means that the lateral resistance was attained at much lower lateral drifts when compared with the specimen to which the maximum



lateral drift of 1% was imposed. In this case the lateral resistance was mobilized to 0.75% and 1% in the positive and negative direction respectively.

The monotonic force-displacement diagram of the specimen at two successive cycles is shown in Figure 3.56. It is observed that the degradation in the lateral force was initiated after cracking of the specimen and increases with the propagation of cracks. Maximum strength degradations of 13% and 12% are observed in the specimen in the positive and negative directions respectively.

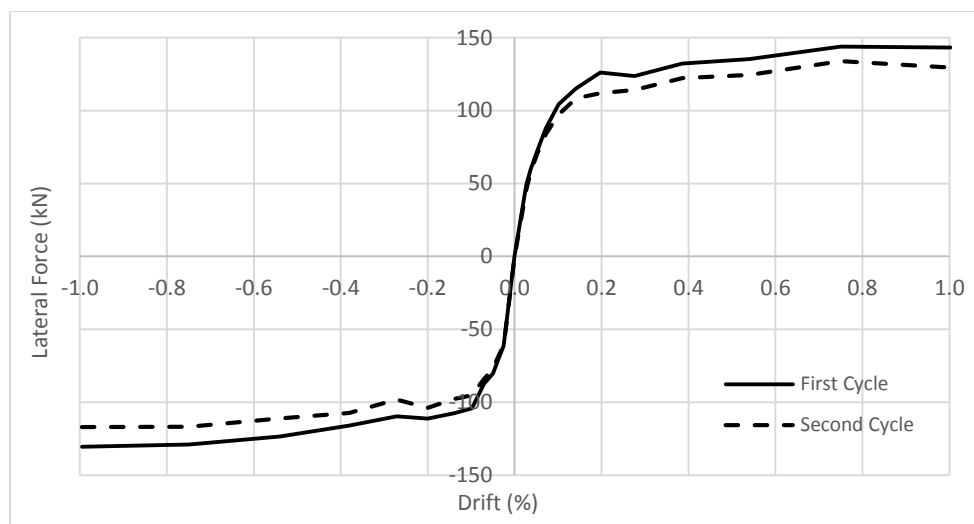


Figure 3.56 Monotonic force-displacement diagram of the specimen SIF-IO(1%)-2L(NC)-B at two successive cycles

The key parameters characterizing the monotonic envelope of the hysteresis loops recorded in the cyclic in-plane tests are presented in Table 3-7.

Table 3-7 Key parameters related to the in-plane behavior of SIF(1%)-I-2L(NC)-B

Positive direction					Negative direction				
$H_{cr}$ (kN)	$d_{cr}$ (mm)	$K_e$ (kN/mm)	$H_{max}$ (kN)	$d_{Hmax}$ (mm)	$H_{cr}$ (kN)	$d_{cr}$ (mm)	$K_e$ (kN/mm)	$H_{max}$ (kN)	$d_{Hmax}$ (mm)
72.5	0.98	74.0	143.9	14.35	-80.2	-0.95	84.4	-130.6	-19.05

Similar to what was recorded for the rc frames with brick infills subjected to lateral drifts of 0.3% and 0.5%, these specimens presented values of initial stiffness substantially higher than the values recorded for the specimen built by the first mason (mason A). In detail, it is observed that the initial stiffness of this specimen in positive and negative directions is 2.2 and 2.8 times higher than the stiffness of specimen built with mason A. The increase in the lateral strength with respect to the specimen built with mason A in the positive and negative directions is 7% and 26% respectively. This result highlights again the importance of the workmanship used in the construction of brick infills in their in-plane behavior.

### 3.8.5.2 Stiffness degradation

The curve representing the stiffness of this specimen at each lateral drift is shown in Figure 3.57. It is observed that due to cracking of the specimen at early stages of loading in the positive and negative directions, considerable decrease in the stiffness of the specimen was obtained. The

amount of degradation in the first levels of loading is higher which is similar to the specimens tested before. The total stiffness degradation of this specimen achieves very high levels at the end of the test (lateral drift of 1%, being calculated as 90% and 92% in the positive and negative directions respectively).

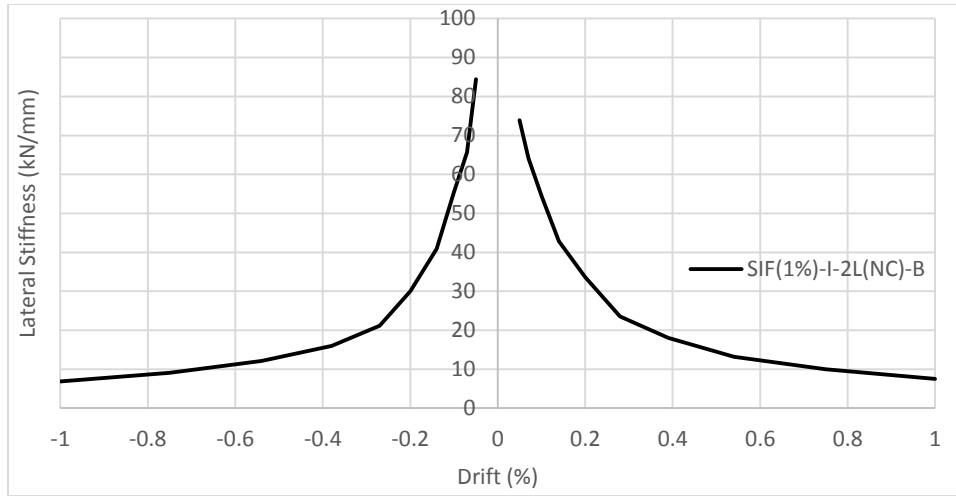


Figure 3.57 Stiffness degradation curve of specimen SIF(1%)-I-2L(NC)-B

### 3.8.5.3 Crack patterns

The crack pattern of the specimen recorded at different lateral drifts is shown in Figure 3.60 and Figure 3.59. The masonry infill was separated from its surrounding frame at lateral drift of 0.05% in the negative direction, which was visible through the vertical crack developed in the mortar joints at the interface between rc frame and infill at bottom left corner. The same vertical cracking pattern was observed in the upper left corner at lateral drift of 0.05% in the positive direction, see Figure 3.60a and b. The increase in the lateral displacements resulted in the development of stair stepped cracks passing through the mortar joints according to the patterns shown in Figure 3.60c to h. At the lateral drift of 0.2% some horizontal shear cracks were formed in the upper part of the infill in the positive and negative directions, see Figure 3.60i and j.

The first cracking of the concrete frame was observed at lateral drift of 0.27% in the negative direction by development of a diagonal crack in the connection point of left column and the upper beam, see Figure 3.59a. Similar cracking was also developed in the right column-beam connection when the load was applied in the positive direction, see Figure 3.59b.

The masonry infill was totally separated from its surrounding frame at lateral drift of 0.75%, meaning that the total separation occurred at considerably higher drift when compared to the specimen SIF-IO(0.5%)-2L(NC)-B, which was totally separated at lateral drift of 0.5%, see Figure 3.59f. At lateral drift of 1%, the masonry was totally cracked and further cracking of the concrete frame was observed in the lower part of the right and left columns, see Figure 3.59g and h.

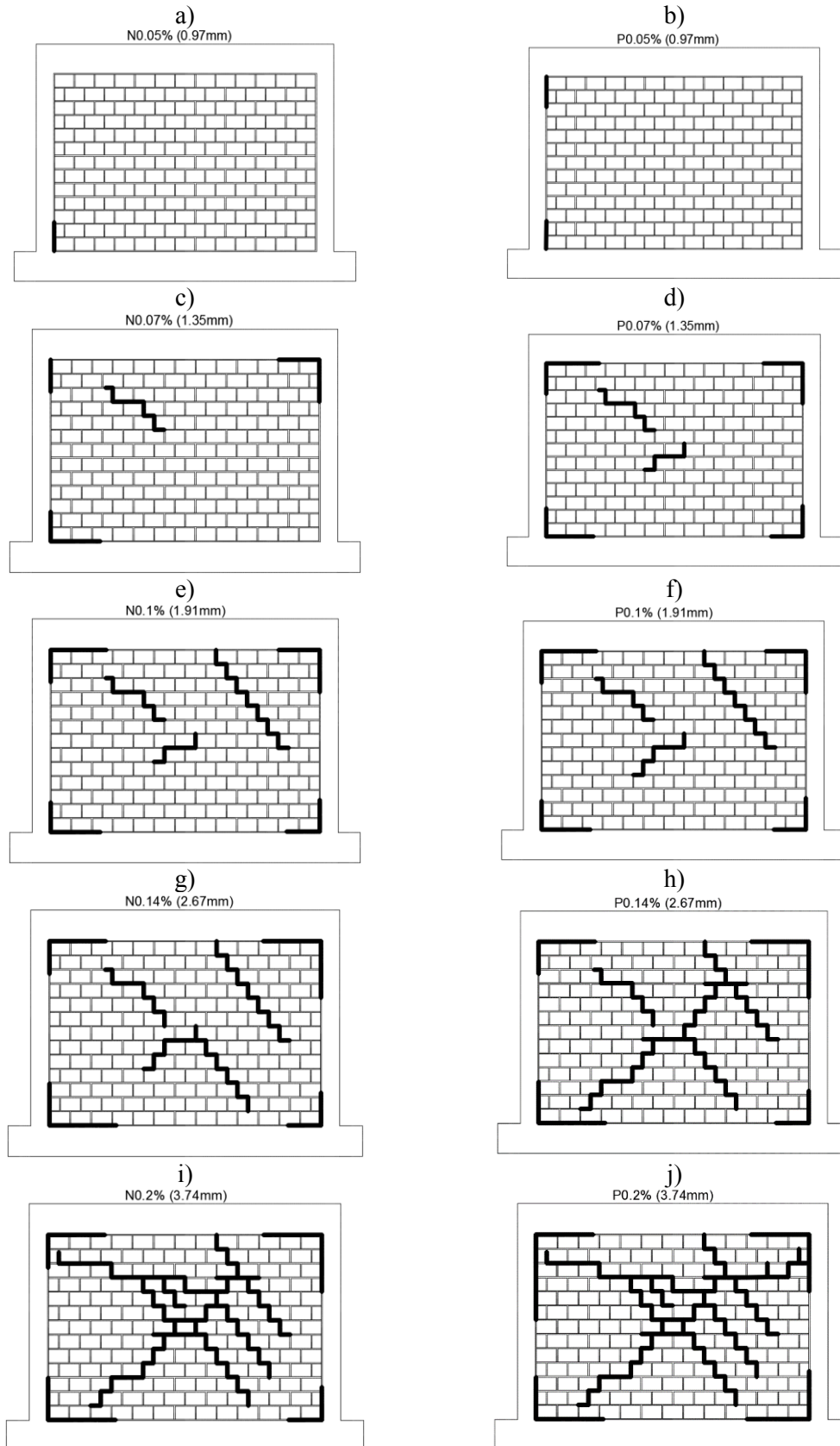


Figure 3.58 Crack propagation in the specimen at lateral drift of a)0.05% in negative direction b)0.05% in positive direction c)0.07% in negative direction d)0.07% in positive direction e)0.1% in negative direction f)0.1% in positive direction g)0.14% in negative direction h)0.14% in positive direction i)0.2% in negative direction j)0.2% in positive

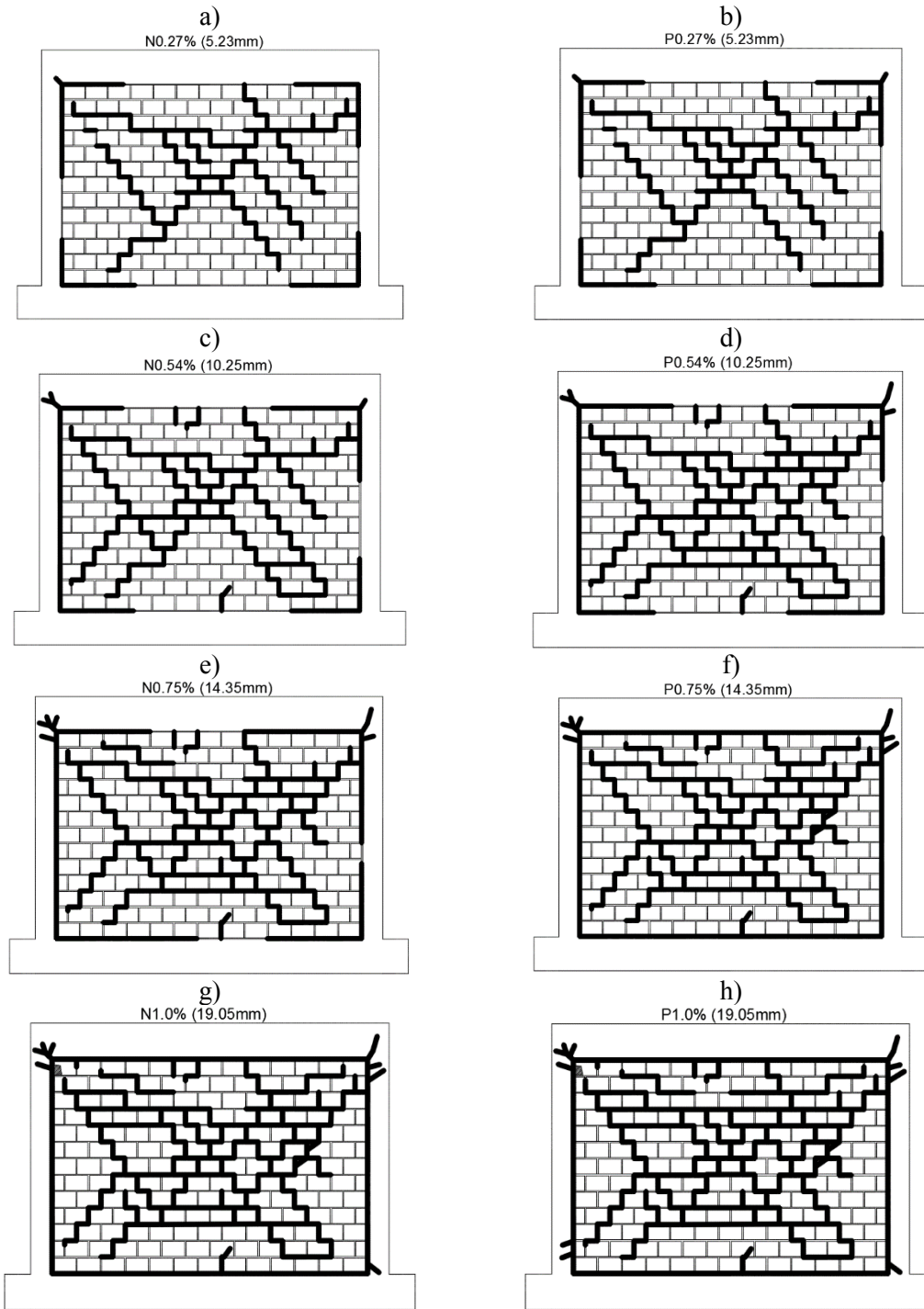


Figure 3.59 Crack propagation in the specimen at lateral drift of a)0.27% in negative direction b) 0.27% in positive direction c)0.54% in negative direction d)0.54% in positive direction e)0.75% in negative direction f)0.75% in positive direction g)1% in negative direction h)1% in positive direction

#### 3.8.5.4 Energy dissipation

The energy dissipated at each cycle during the in-plane cyclic test is shown in Figure 3.60. It is clear that at the first levels of loading the amount of energy dissipation is almost negligible. It is clear that the amount of energy dissipation increases after lateral drift of 0.05%, which is related to the initiation of crack.

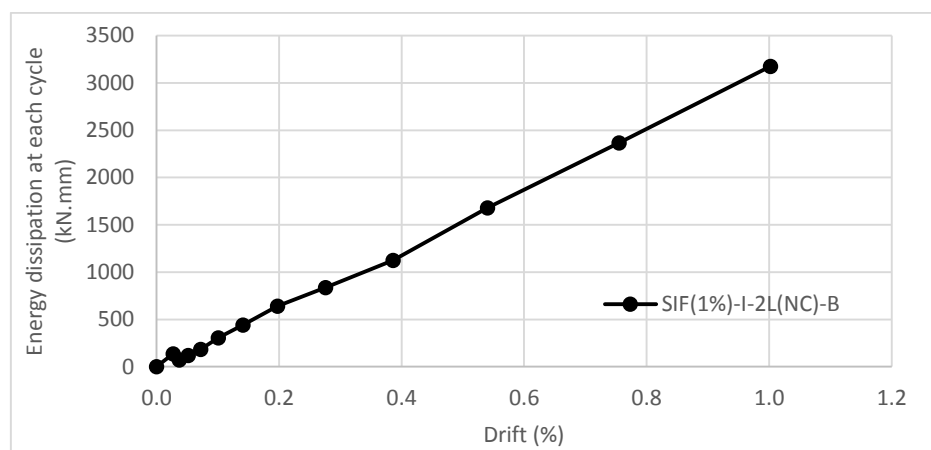


Figure 3.60 Energy dissipation at each cycle for specimen SIF(1%)-I-2L(NC)-B

The total energy dissipated until each cycle is also shown in Figure 3.61. By comparing the total energy dissipated in this specimen with the energy dissipation of specimen SIF(0.5%)-I-2L(NC)-B at lateral drift of 0.28% it is evident that both specimens represented similar energy dissipation capacities. But for increasing the lateral drifts, it is observed that the total energy dissipated in the specimen SIF(0.5%)-I-2L(NC)-B at lateral drift of 0.5% (6205kN.mm) is higher than that of the specimen SIF(1%)-I-2L(NC)-B at the same lateral drift (5105kN.mm). This means that higher energy is dissipated in the specimen SIF(0.5%)-I-2L(NC)-B between lateral drifts of 0.28% and 0.5%, which can be related to the formation of more cracks in the specimen between this range of lateral drifts.

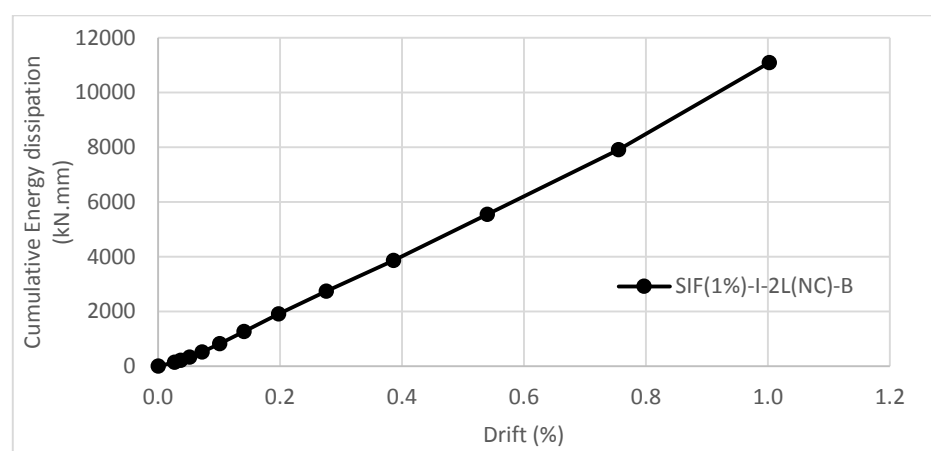


Figure 3.61 Cumulative energy dissipation of specimen SIF(1%)-I-2L(NC)-B

### 3.8.5.5 Deformation Characteristics

The average shear distortion of the internal leaf, external leaf and reinforced concrete frame are shown in Figure 3.62 and Figure 3.63. The shear distortion of the external and internal leaf increased significantly after the lateral drift of 0.1% in both positive and negative directions. This is related to the development of diagonal cracks in the masonry infill. The different level of cracking between internal and external leaf justifies the slightly higher shear distortion of the internal leaf in relation to the external leaf recorded at the lateral drift of 1%.

The shear distortion of the rc frame at the lateral drift of 0.1% is calculated and it is found that it is higher than the sum of the shear distortion of the external and internal leaves. This is generally justified by the onset of separation of the brick infill from the rc frame.



Figure 3.62 Average shear distortion of a) external leaf (8cm thickness) and b) internal leaf (6 cm thickness)

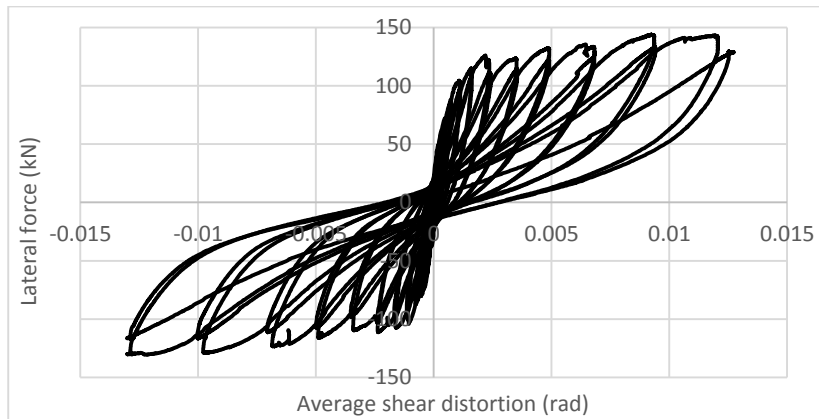


Figure 3.63 Average shear distortion of RC frame

The separation of the infill from its surrounding frame at different levels of loading is represented in Figure 3.64. It is clear that the first separation occurs at the bottom left corner of the infill at lateral in-plane drift of 0.05%. This finding is similar to the cracking pattern that is drawn in Figure 3.59. By applying further lateral displacements, the width of the vertical crack corresponding to the separation of the infill from the rc frame increases, see Figure 3.64. It is also clear that at lateral drift of 0.07% the infill was completely separated from the bounding frame at all corners. These separations of the infill could be observed by formation of vertical or horizontal cracks in the mortar joints adjacent to the rc frame recorded by different LVDTs.

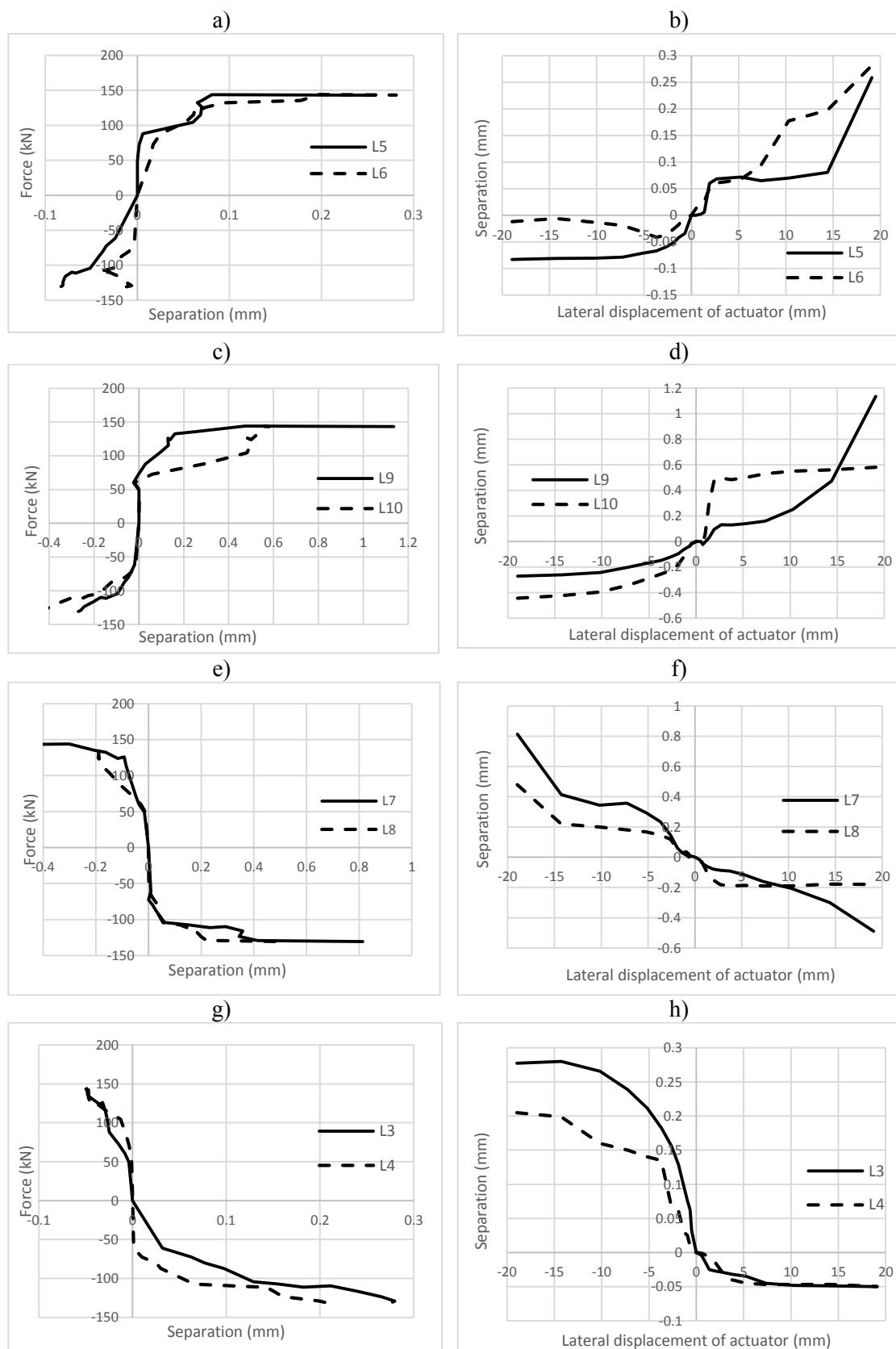


Figure 3.64 Relative displacement of masonry infill from its bounding frame with respect to the force and lateral displacement applied to the structure for a) lower right corner b) lower right corner c) upper left corner d) upper left corner e) upper right corner f) upper right corner g) lower left corner h) lower left corner

### 3.9 Comparison of the results of the specimens

Aiming at better understanding the in-plane behavior of the rc frames with double leaf brick infills subjected to different levels of lateral drift, a comparison of the main results was carried out, namely at the level of monotonic envelopes and comparison of the main key parameters. The specimens subjected to 0.3%, 0.5% and 1% lateral drifts were built with mason B, whereas the brick infilled frame tested until failure was built with mason A. The contribution of the infills in the in-plane behavior was also evaluated by comparing the key parameters such as lateral strength, initial stiffness and energy dissipation capacity.

The monotonic force-displacement diagrams of all specimens are shown in Figure 3.65. The results in terms of initial stiffness and lateral strength in the positive and negative directions are represented in Table 3-8.

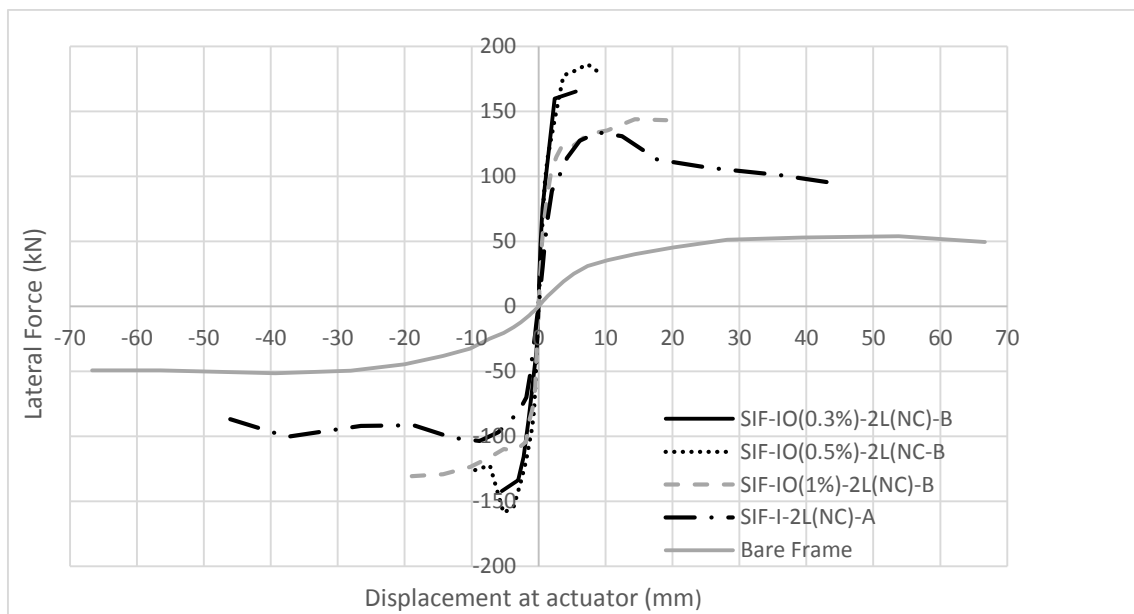


Figure 3.65 Monotonic in-plane force-displacement diagram of all specimens

It is clear that the presence of infill significantly increases the initial stiffness and lateral strength of the rc frame. This increase in the initial stiffness and lateral strength is about 5.2 and 1.3 times in case of brick infill built with mason A. In case of brick infill built with mason B, the improvement on the initial stiffness and lateral strength is even higher, being approximately 14.9 and 1.9 times respectively. This result points out the importance of the quality of masonry construction.

Table 3-8 Comparison of lateral stiffness and strength

Model	Positive Direction		Negative Direction		Average	
	Stiffness (kN/mm)	Strength (kN)	Stiffness (kN/mm)	Strength (kN)	Stiffness (kN/mm)	Strength (kN)
Bare Frame	5.1	53.9	4.6	51.4	4.9	52.7
SIF-I-2L(NC)-A	33.4	133.9	27.4	103.6	30.4	118.8
SIF-IO(0.3%)-2L(NC)-B	78.0	165.4	70.7	133.8	78.1	152.9
SIF-IO(0.5%)-2L(NC)-B	84.1	175.2	77.3	168.4		
SIF-IO(1%)-2L(NC)-B	74.0	143.9	84.4	130.6		



The specimens constructed with mason B subjected to lateral drifts of 0.3%, 0.5% and 1% (specimens SIF-IO(0.3%)-2L(NC)-B, SIF-IO(0.5%)-2L(NC)-B and SIF-IO(1%)-2L(NC)-B) presented similar responses in terms of initial stiffness, but the specimen loaded until the lateral drift of 0.5% presented higher lateral strength. On the other hand, it is seen that the lateral drift at which the maximum lateral strength is achieved appears to be higher in the specimen tested until lateral drift of 1%. It is concluded that the specimens that demonstrated higher lateral in-plane resistance and initial stiffness presented lower lateral drifts corresponding to their lateral strength, which should be associated to the higher brittleness of the masonry.

The strength degradation recorded in all infilled frames is shown in Figure 3.66 and Figure 3.67. It is clear that at the first levels of loading, in which there is no cracking, the amount of the strength degradation is very low (close to zero). By imposing increasing lateral displacements, crack density increases, leading to the strength degradation between two successive cycles. It is also seen that no significant differences on the strength degradation occurs among the different brick masonry infills. However, the strength degradation is higher in the rc frames with double leaf brick infills than in the bare frame, meaning that the damage progress in the brick infills influences the rate of strength degradation.

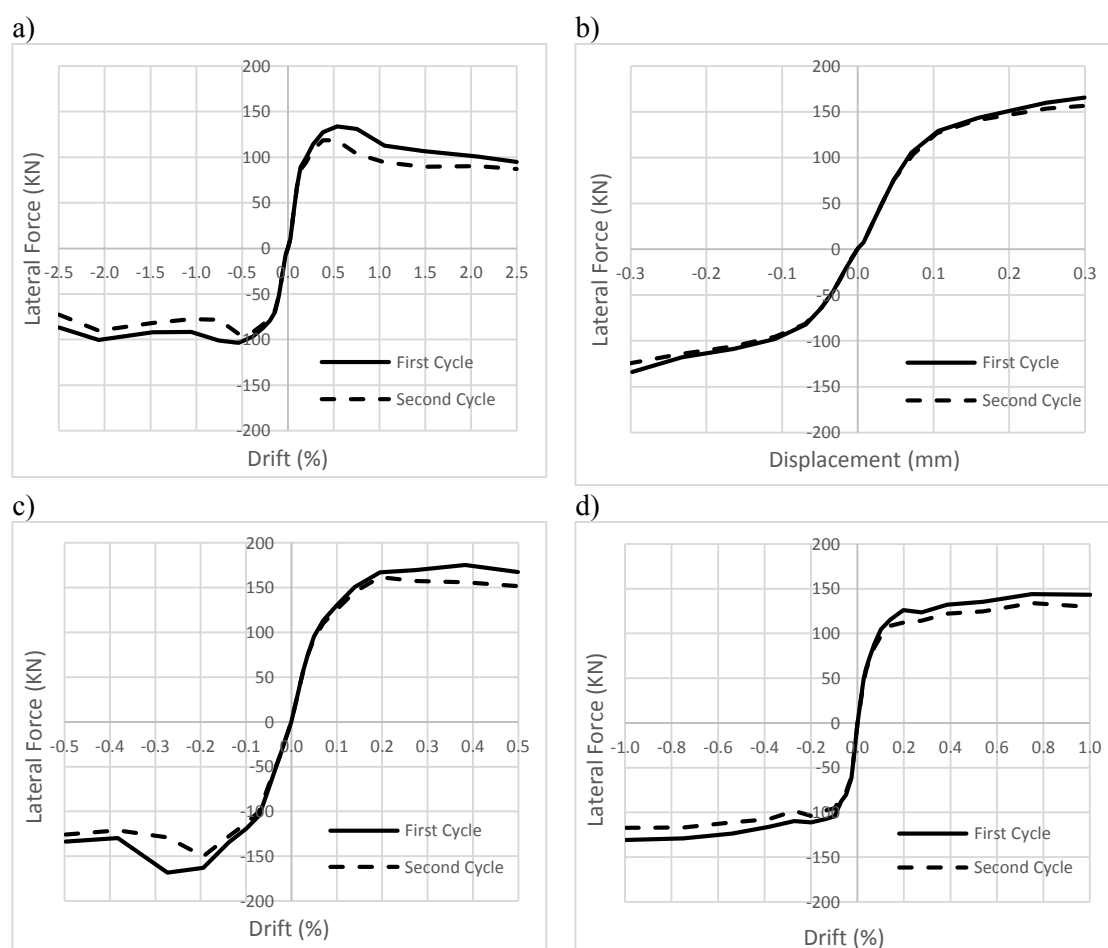


Figure 3.66 Strength degradation of a)SIF-I-2L(NC)-A b)SIF-IO(0.3%)-2L(NC)-B c)SIF-IO(0.5%)-2L(NC)-B d)SIF-IO(1%)-2L(NC)-B

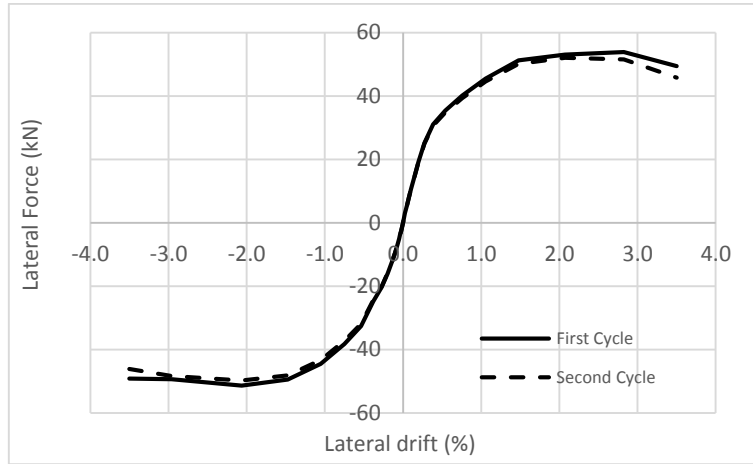


Figure 3.67 Strength degradation of bare frame

The stiffness degradation curve of the specimens tested in the in-plane direction at each lateral drift is shown in Figure 3.68 and Figure 3.69. It is observed that stiffness degradation in the rc frames with brick infills is initiated due to cracking of the masonry infills. It is also clear that all specimens present a similar trend of variation in their stiffness degradation curves: (a) high stiffness degradation at very low lateral drifts; (b) stabilization of stiffness degradation at increasing lateral drifts, particularly after peak lateral strength. However, it is observed that the specimens with higher initial stiffness exhibit higher degradation rate, particularly at low levels of lateral drift, see Figure 3.69. For higher lateral drifts (0.5%), the stiffness degradation is practically the same in specimens built with different masons. The stiffness degradation of the bare frame occurs at different rate when compared to the rc frames with brick infills, because the stiffness degradation is mostly related to the stiffness degradation of the brick infills in case of rc frames filled with brick infills. As expected, for high levels of damage of the brick infills, the lateral stiffness tends to approach the lateral stiffness of the bare rc frame, as expected.

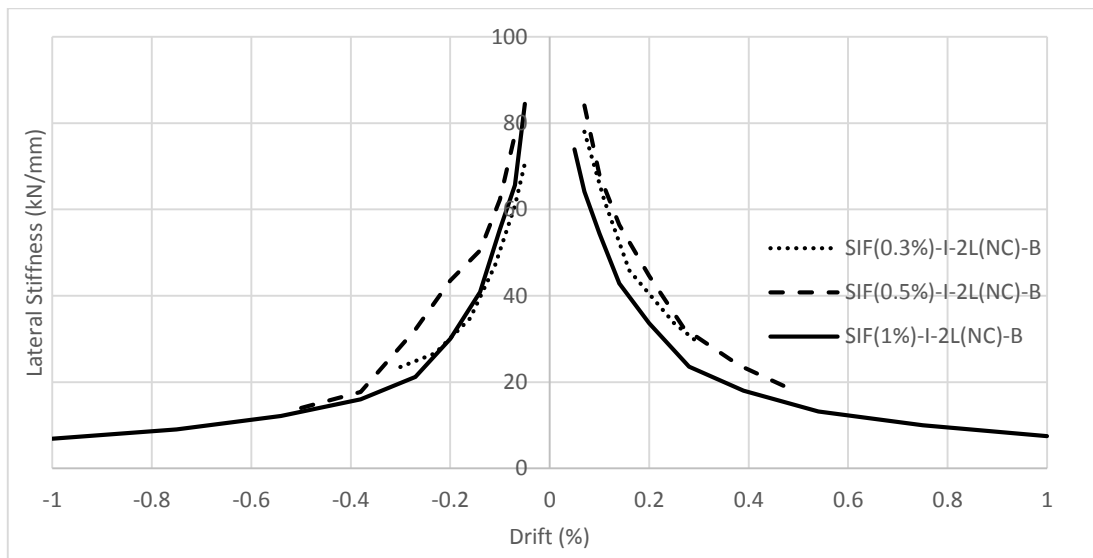


Figure 3.68 Stiffness degradation of the specimens constructed with mason B

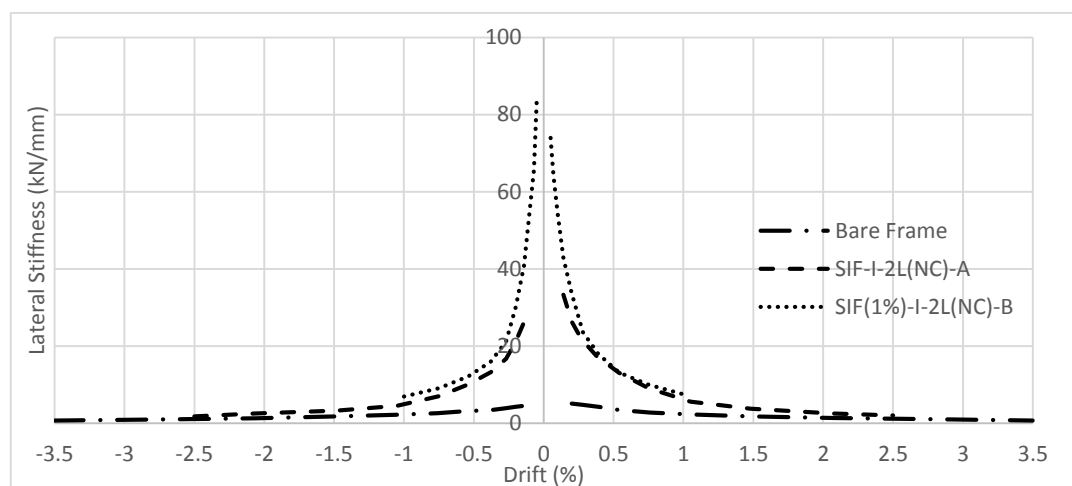


Figure 3.69 Trend of variation of the stiffness among the specimens of bare frame, SIF-I-2L(NC)-A and SIF(1%)-I-2L(NC)-B

The cracking patterns of the bare rc frame, specimen SIF-I-2L(NC)-A and specimen SIF(1%)-I-2L(NC)-B at lateral drift of 1% are shown in Figure 3.70. It is clear that the damage of the bare rc frame is higher than the one observed when it is filled with the double leaf brick infill. This appears to indicate the positive contribution of the masonry infill in the composite behavior of masonry infilled frames. This is particularly remarkable when the stiffness of the brick infills is lower. This means that presence of infill avoids the development of hinges in the rc columns, which in turn reduce their seismic vulnerability. In the experimental campaign carried out here, any local negative influence of the brick infills was detected.

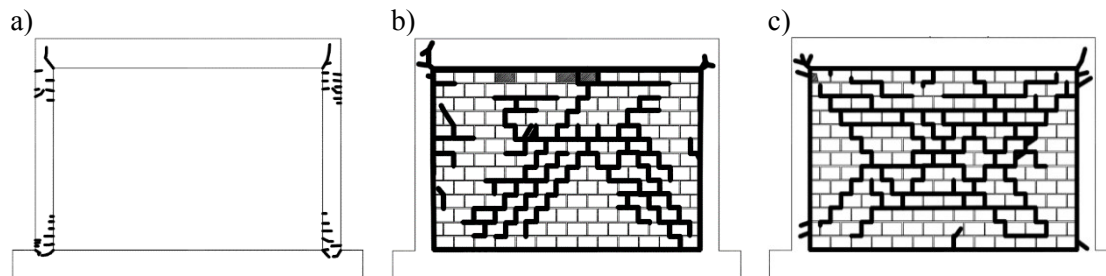


Figure 3.70 Cracking pattern of the specimens at lateral drift of 1% a) Bare frame b) SIF-I-2L(NC)-A c) SIF(1%)-I-2L(NC)-B

The total energy dissipated during the in-plane loading until each cycle is shown in Figure 3.71. By comparing the results, it is clear that the presence of infill leads to the significant increase in the energy dissipation, when compared to the bare frame. This is naturally due to the dissipative nature of the brick infills, associated to the smeared cracking developed during in-plane loading. It is also observed that the infilled frames constructed with mason B exhibit higher energy dissipation capacity than the specimen constructed with mason A.

The analysis of the average distortion of the internal and external leaves of the double leaf infilled frames during in-plane loading is shown in Figure 3.72. It is observed that the external and internal leaves of the infill behave in a similar way. The difference found for the average distortion between external and internal leaves in the specimen SIF-I-2L(NC)-A can be related to the out-of-plane bulging of the internal leaf when the lateral load is applied in the negative direction.

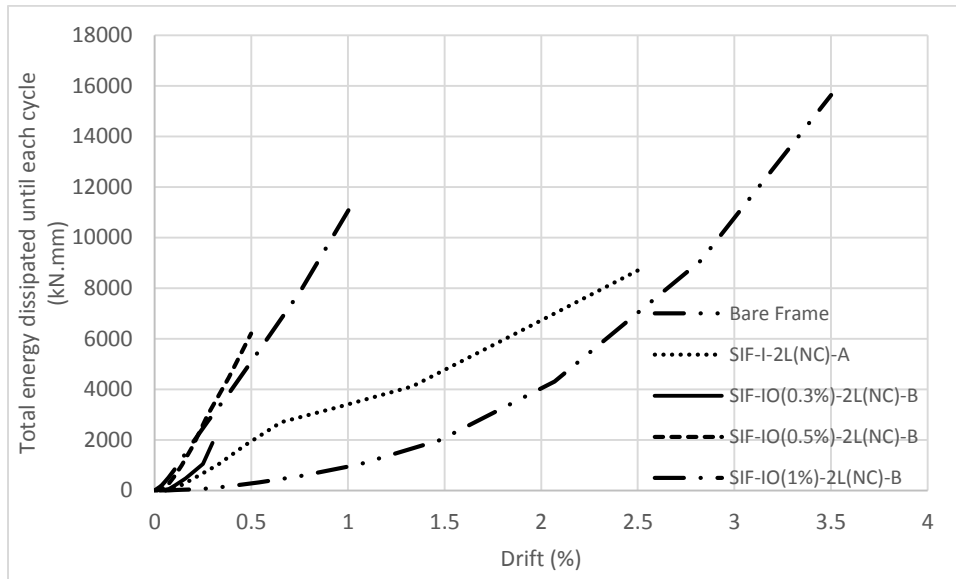


Figure 3.71 Cumulative energy dissipated during in-plane cyclic loading

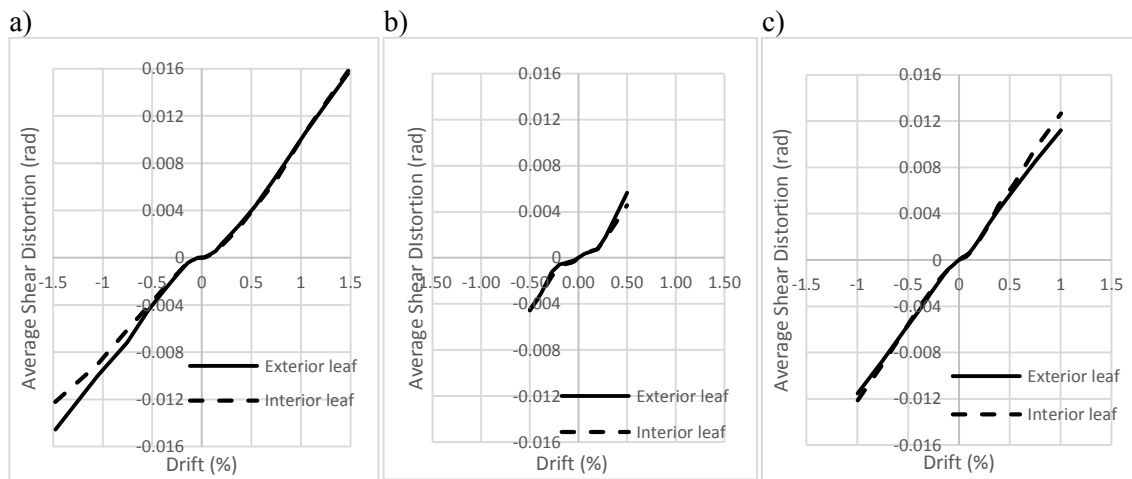


Figure 3.72 Average shear distortion of the exterior and interior leaf of specimen a) SIF-I-2L(NC)-A b) SIF-IO(0.5%)-2L(NC)-B c) SIF-IO(1%)-2L(NC)-B

### 3.10 Conclusions

Based on the test results of this chapter the following conclusions can be drawn for the in-plane behavior of infilled frames:

- 1) The presence of low strength infills within the bare frame increases the initial stiffness and lateral strength of the bare frame significantly. The increase in the initial stiffness ranges from 5.2 to 14 times and in the lateral strength ranges from 1.3 to 1.9 times, depending on the quality of workmanship.
- 2) The specimens constructed by experienced mason demonstrated higher initial stiffness and lateral strength.

- 4) The strength degradation of the specimens initiates due to the formation of the cracks and increases after the lateral strength of the specimen is achieved.
- 5) It is observed that stiffness degradation rate of the infilled frames is considerably higher than the rate observed in the bare frame at the first levels of loading.
- 6) It is evident that the presence of infill within the bare frame could enhance energy dissipation capacity of the specimens. The enhancement amount is higher for the specimens constructed with experience mason.
- 7) It is also concluded that presence of infill within the bare frame limits the amount of damage in the bare frame caused by in-plane loading.

# **CHAPTER 4**

## **EXPERIMENTAL ASSESSMENT OF THE OUT-OF-PLANE BEHAVIOR OF MASONRY INFILLED REINFORCED CONCRETE FRAMES**

## **4 Experimental assessment of the out-of-plane behavior of masonry infilled reinforced concrete frames**

### **4.1 Introduction**

In order to investigate the out-of-plane response of the masonry infills within reinforced concrete rc buildings built in the past decades in Portugal and other South European countries (in the 1980s), an experimental campaign was designed based on static out-of-plane tests. The characteristics of the prototype and the design of the reduced scale masonry infilled rc frames were described in the previous chapter. For the out-of-plane loading of the masonry infill, quasi static test was intended to be performed by using an airbag to apply the out-of-plane load in a uniform manner, contrarily to point load configuration.

As the cavity walls usually are built without any ties between their internal and external leaves, there will be no interconnection between the leaves. This led to consider only the exterior leaf in the experimental program which the studies also show that it collapses very often during the earthquakes [19].

In the experimental campaign, different variables were considered, namely: (a) workmanship; (b) presence of openings and (c) previous in-plane damage. According to what was presented in Chapter 3 in relation to the in-plane characterization of masonry infill walls, double leaf masonry infills were tested in the in-plane direction. Therefore, after the imposition of in-plane damage, corresponding to a selected lateral drift, it was decided to remove the internal leaf and apply the out-of-plane load on the external leaf.

### **4.2 Characterization of the specimens**

The description of the specimens of masonry infilled rc frames tested in the out-of-plane direction is given in Table 4-1. Three specimens were tested to investigate the out-of-plane response of the brick masonry infills without any initial damage, and also to characterize the influence of the workmanship (SIF-O-1L-A, built by mason A, and specimens SIF-O-1L-B, built by mason B). Additionally, the presence of a central opening was also studied in order to evaluate its influence in the out-of-plane response (PIF-O-1L-B). The central opening has a size corresponding to 12.8% of the area of the masonry infill.

Three specimens were also tested in the out-of-plane direction, after imposing prior in-plane damage corresponding to different drift levels of 0.3%, 0.5% and 1%. All these specimens were built by mason B. In order to have a logical basis for comparison of the out-of-plane response of these damaged specimens with specimens without any prior damage, after performing prior in-plane test that was carried out on double leaf infill, the interior leaf was removed and out-of-plane test was performed on only exterior leaf.

The construction of the specimens for out-of-plane testing was done according to the procedure described in Chapter 3. The rc frames were constructed first and after 45 days they were transported to the area where the brick infills were constructed and then transported to the laboratory testing area.

Table 4-1 Designation of the specimens tested under out-of-plane loading

Specimen	Masonry infill	Prior damage	Number of leaves during construction	Mason
SIF-O-1L-A	Solid	None	One leaf	A
SIF-O-1L-B	Solid	None	One leaf	B
PIF-O-1L-B	With central opening (12.8%)	None	One leaf	B
SIF-IO(0.3%)-2L(NC)-B	Solid	Prior in-plane damage - drift of 0.3%	Double leaf with no connection	B
SIF-IO(0.5%)-2L(NC)-B	Solid	Prior in-plane damage - drift of 0.5%	Double leaf with no connection	B
SIF-IO(1%)-2L(NC)-B	Solid	Prior in-plane damage - drift of 1%	Double leaf with no connection	B

### 4.3 Experimental setup and instrumentation

The test setup for the out-of-plane testing is shown in Figure 4.1. It should be mentioned that the test setup was already described in Chapter 3. Aiming at strengthening the top boundary condition in order to have the top beam adequately restrained to out-of-plane movements, a distinct solution was designed. The top beam was restrained to the out-of-plane movements by using four steel rods M40 attached to a steel triangular structure, connected to two HEB 240 steel profiles that were fixed to the lateral reaction wall.

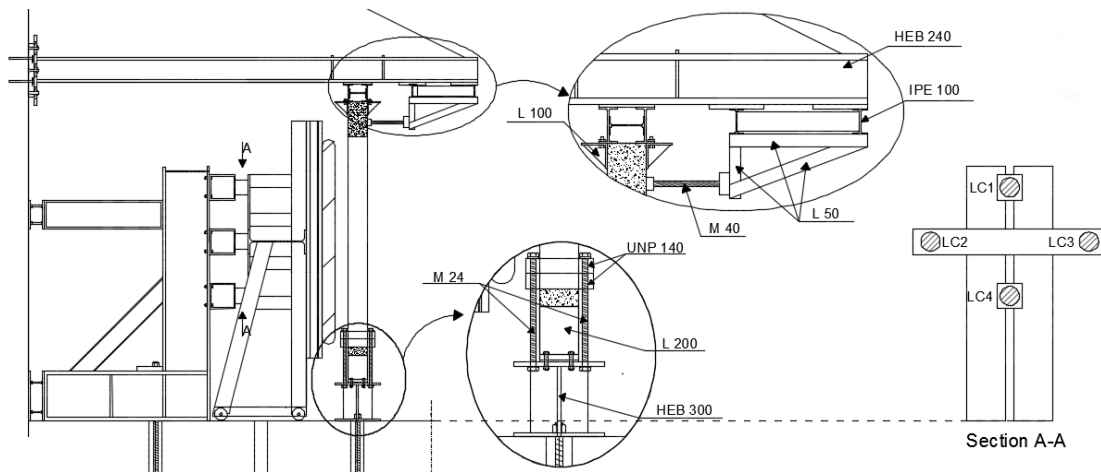


Figure 4.1 Test setup for out-of-plane testing

The out-of-plane loading was applied by means of an airbag installed between the masonry infill and the steel frame. The airbag was attached to the steel frame by using a stiff wooden sandwich panel. The steel frame was also connected to the lateral reaction wall and strong floor by rigid L-shaped steel profile of HEB360 to completely prevent its uplifting and sliding during the test. The L shape profile is stiffened at the top with a horizontal steel profile of HEB220 and with an inclined steel profile of HEB160. The steel frame is connected to the L shape steel structure by means of four loadcells so that the total force applied by the airbag to the structure could be



recorded. The configuration of the load cells is also presented in Figure 4.1. Four rollers were added on the bottom part of the steel frame to enable its mobility along the horizontal direction without development of friction and erroneous record of the force applied by the airbag. In case of the specimen with a central opening, the airbag that was used to apply the out-of-plane load had a central opening to ensure an adequate adjustment to the infill wall.

The instrumentation plan defined to record the most important displacements in the brick masonry infill subjected to out-of-plane loading is shown in Figure 4.2 both for the solid infill wall and for the infill wall with a central opening. In specimens with solid infill walls the displacement transducer selected as control point was LVDT L5, while in the specimen with central opening the control LVDT was L9 that was placed in the center point of the lintel.

The deformation of the brick infill, as well as the cracking propagation, was monitored in the opposite face of the surface where the airbag was in contact with. The crack propagation was also recorded at that surface. For this, in case of solid infills, fifteen LVDTs were placed on the specimen to monitor its out-of-plane deformation: (1) LVDTs 1 to 9 recorded the displacement of the infill panel during loading (L1 to L9); (2) LVDTs 10 to 13 measured the possible relative displacement of the masonry infill from the surrounding rc frame; (3) two additional LVDTs were placed to control the out-of-plane movement of the boundaries, namely the bottom and top rc beams (L14 and L15). In case of infill with central opening 16 LVDTs were used to measure the deformation of the infill during the test: 1) LVDTs 1 to 10 recorded the displacement of the infill panel during loading (L1 to L10); (2) LVDTs 11 to 14 measured the possible relative displacement of the masonry infill from the surrounding rc frame; (3) two additional LVDTs were placed to control the out-of-plane movement of the boundaries, namely the bottom and top rc beams (L15 and L16).

The out-of-plane test was performed under displacement control method by applying the out-of-plane load uniformly with airbag. In order to implement the test under displacement control, the input and output air in the airbag were controlled by using a LabVIEW software to apply a specific pre-defined displacement in the control point of the infill wall. Those pre-defined displacement values match the loading protocol of each specimens.

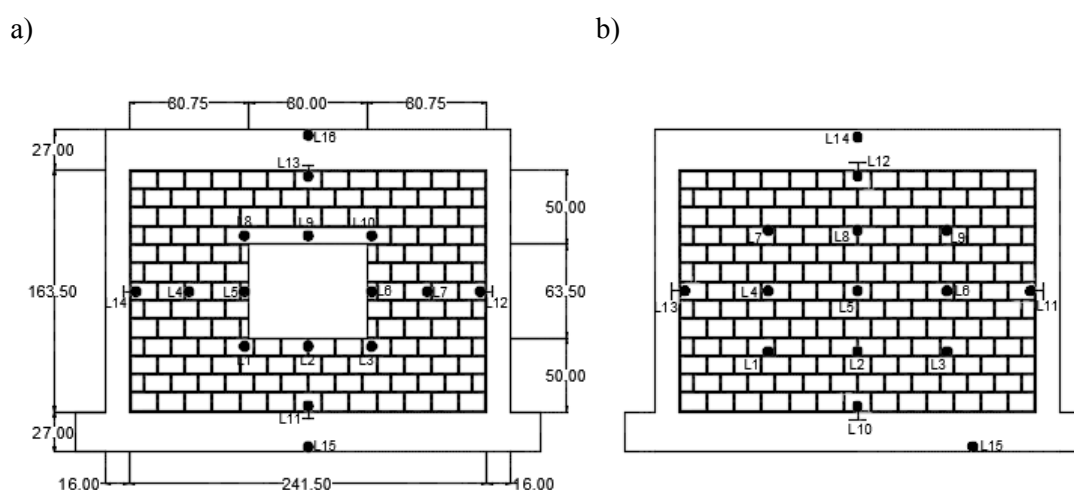


Figure 4.2 Instrumentation for out-of-plane testing; a) infill wall with a central opening; b) solid infill walls

#### 4.4 Loading pattern

The displacement-time history defined for the control point to be used in the quasi-static cyclic testing of specimen SIF-O-1L-A is displayed in Figure 4.3. It is composed of twenty five different displacement amplitudes, the first displacement increment being repeated for six times and the others repeated two times so that it is possible to evaluate the stiffness and strength degradation of the masonry infill at each imposed displacements. The displacement increment at each stage  $i$  was defined as 1.4 times of the displacement at stage  $i-1$ , following the recommendations given in FEMA461[119] for in-plane quasi-static cyclic loading.

Due to the development of plastic deformation in the specimens, the recovery of the total displacement in the unloading branch at the control point was not possible. Therefore, the real minimum displacement in the unloading process was not zero. The control software was able to invert the cycles once the residual displacement is attained. Based on the force-displacement diagram obtained for the first specimen, it was decided to define another displacement-time history by considering lower number of small displacement amplitudes, which in principle are associated to linear regime of the brick infill, see Figure 4.4

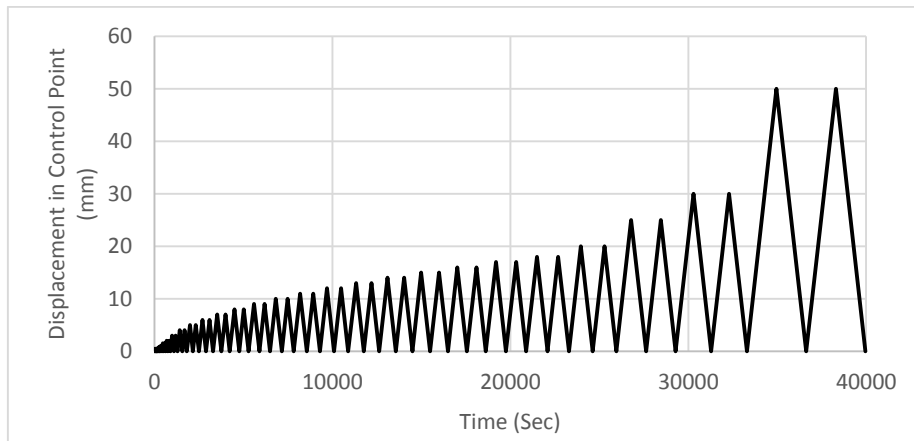


Figure 4.3 Loading pattern applied for SIF-O-1L-A

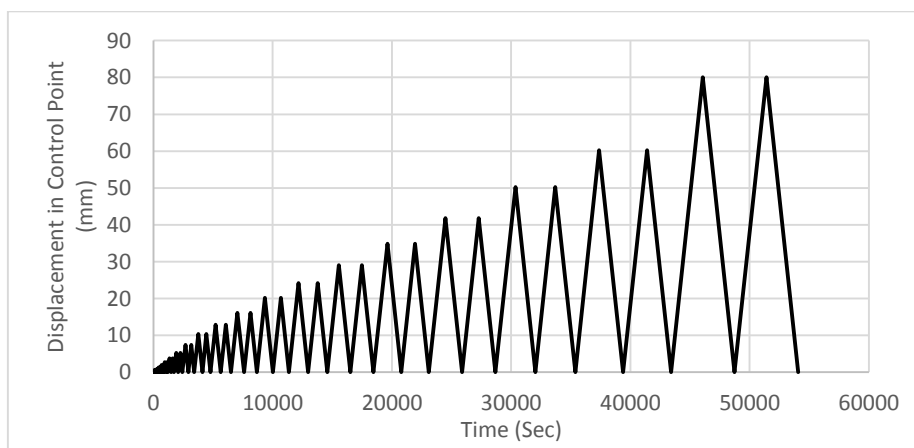


Figure 4.4 Loading protocol applied for specimens built by mason B

## 4.5 Experimental results

The analysis of results obtained in the out-of-plane tests of masonry infill walls is carried out based on: (1) load-displacement diagrams; (2) cracking pattern; (3) stiffness degradation curve; (4) deformation characteristics; and (5) energy dissipation capacity.

### 4.5.1 Specimen SIF-O-1L-A

#### 4.5.1.1 Load-displacement response

The force-displacement diagram obtained in the out-of-plane test of the brick infill built with mason A (specimen SIF-O-1L-A) is shown in Figure 4.5. The displacement used in the graph is measured in the control point (LVDT 5). It is clear that increasing the displacement in the control point resulted in the increase of the out-of-plane force measured by the loadcells until the first significant cracking in the infill at displacement of 5mm corresponding to out-of-plane force of 28.6kN. This crack was formed horizontally in the mid part of the infill. After this point, further displacement imposed to the masonry infill resulted in slight increase of the out-of-plane force. In fact, the increase of 20mm at the central point of the wall after cracking results in the increase in the out-of-plane force of about 6.3kN. In this case the specimen reached the peak force of 34.9kN at displacement of 25mm.

After the peak force is attained, the increase in the displacements is followed by a sudden drop in the out-of-plane force. A decrease of about 33% in the peak force was observed at displacement of 30mm. The specimen reached the out-of-plane force of 23.52kN at the second cycle of imposed displacement of 30mm. Further increasing displacements led to the progressive reduction of the out-of-plane resistance. Finally, the specimen was extremely damaged at displacement of 50mm corresponding to the force of 19.4kN and the test was stopped to keep the instrumentation intact.

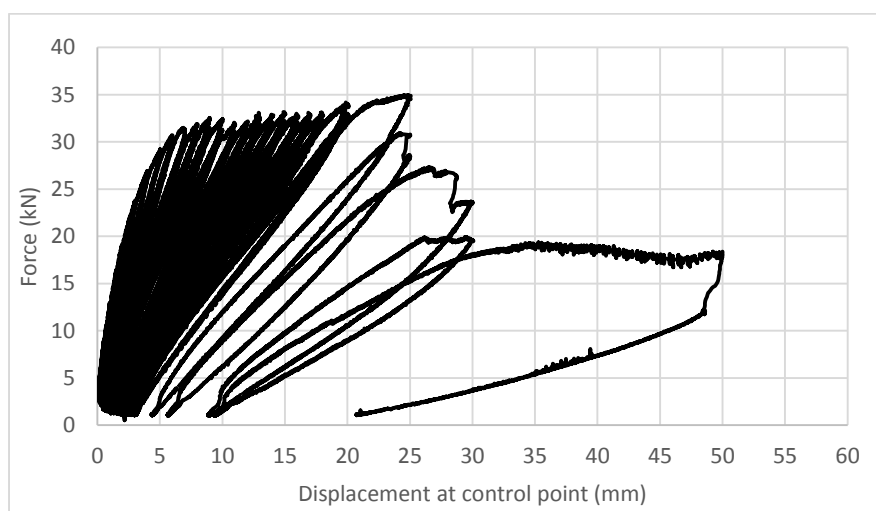


Figure 4.5 Force-displacement response of SIF-O-1L-A

The monotonic envelope curve of the force-displacement diagram at the first and second cycles of each step is shown in Figure 4.6.

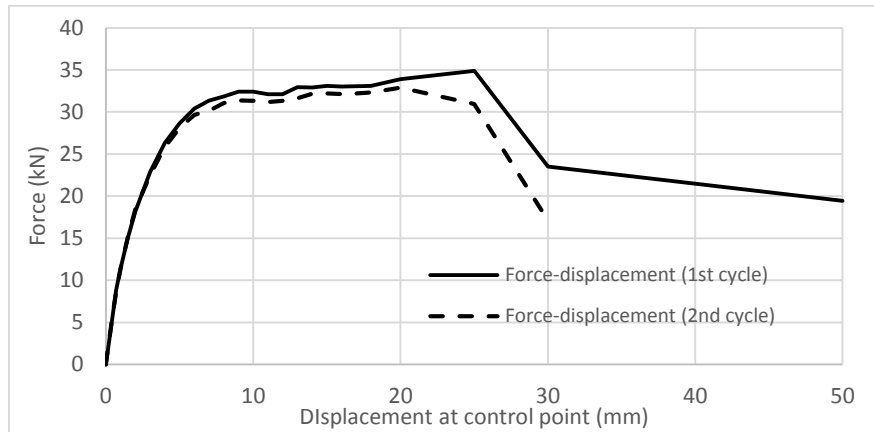


Figure 4.6 Monotonic curves of force-displacement diagram for 1st and 2nd cycles

It is observed that strength degradation of the specimen at two successive cycles is very low until out-of-plane displacement of 25 mm at which the sliding of the top interface is recorded. After this point, the strength degradation at the second cycle is significant and can be considered as a result of the crack propagation, both in terms of number of cracks and their size. Strength degradation of about 13% was observed at the peak out-of-plane resistance. At the displacement of 30mm in which the infill was totally cracked, the strength degradation was about 27%.

#### 4.5.1.2 *Stiffness degradation curve*

The stiffness degradation curve of the specimen is shown in Figure 4.7. The stiffness at each displacement cycle is calculated as the secant stiffness by considering the inclination of the line connecting the origin and the maximum lateral resistance measured in the first cycle of the monotonic force-displacement diagram. It is clear that the reduction of the stiffness at early stages of loading is very significant. The stiffness reduction was calculated as 69% when the out-of-plane displacement in the control point was 10mm.

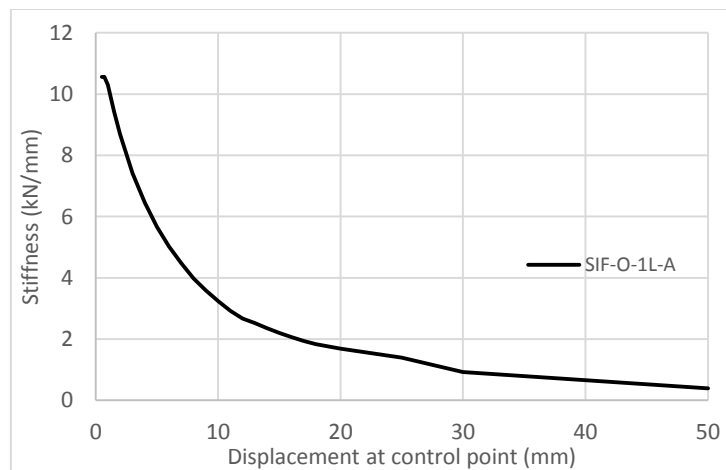


Figure 4.7 Stiffness degradation curve of specimen SIF-O-1L-A

#### 4.5.1.3 *Cracking Pattern*

As mentioned before, the cracking of the specimen initiated at the displacement of 5mm corresponding to the out-of-plane load of 28.6kN through the formation of a horizontal crack in the center part of the infill, as it is shown in Figure 4.8a. The increase of the out-of-plane

displacement at the control point resulted in the extension of the horizontal crack and in the development of diagonal cracks towards the top and bottom corners, see Figure 4.8b to f. The first cracking in the surrounding frame was observed at lateral displacement of 14mm corresponding to the lateral force of 32.9kN through the development of diagonal cracks in the top right beam-column connection. The cracking pattern in which the diagonal cracks were extended to all corners is shown in Figure 4.8f that is compatible with the cracking pattern of two-way slabs drawn via yield line theory. This confirms the formation of two-way arching mechanism and consequently states that the interfaces between the brick infill and the rc frame remain intact. The resisting mechanism is valid until the collapse or sliding of the infill-rc frame interfaces due to high compressive or shear stresses.

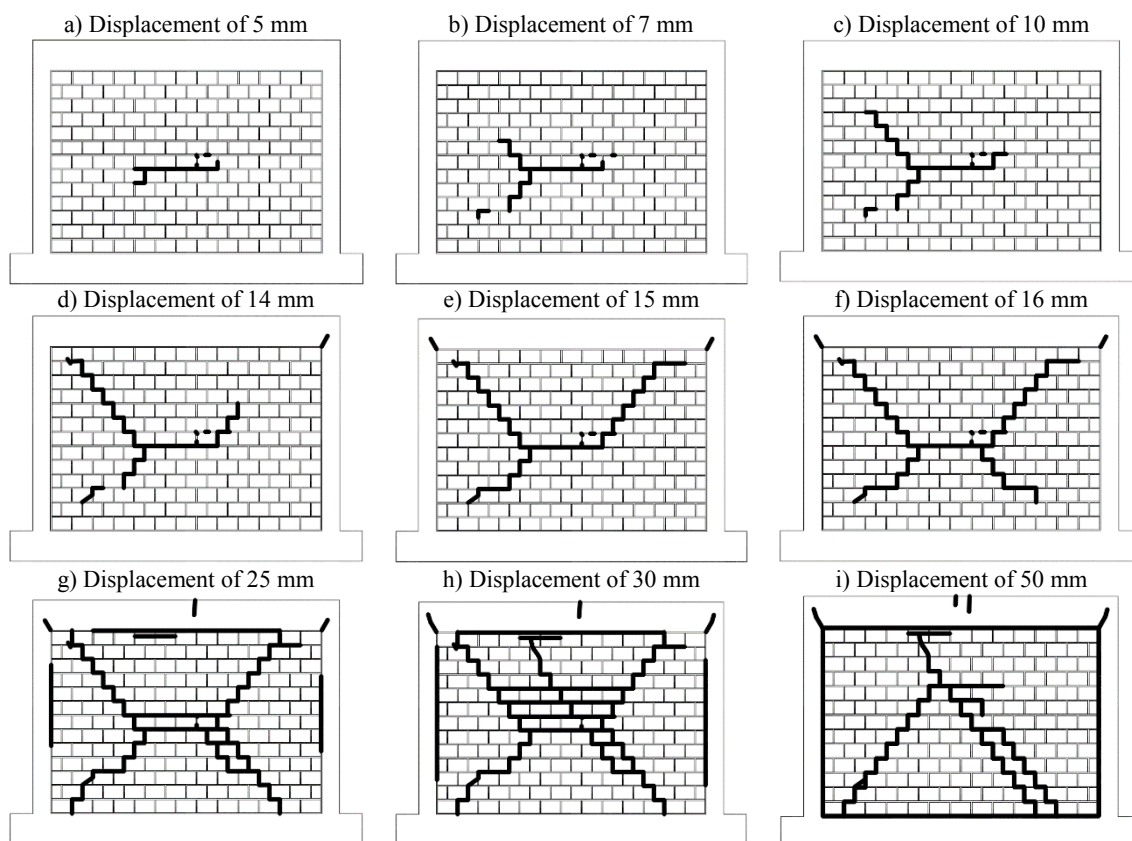


Figure 4.8 Cracking pattern mapping in the specimen SIF-O-1L-A at different out-of-plane displacements

At the second cycle corresponding to the out-of-plane displacement of 25mm, the upper infill-frame interface slid in the out-of-plane direction and a horizontal cracking almost extended at complete length of the interface, see Figure 4.8g. At this stage, vertical cracking was also observed at mid span of the upper rc beam.

By sliding the upper infill-frame interface the resisting two-way arching mechanism with supports on all sides changed to a predominant two-way arching mechanism with three supports, leading to significant change in the crack pattern of the specimen, see Figure 4.8i. The cracking pattern represented in Figure 4.8i is compatible with the cracking pattern of two-way slabs with three supports and one free edge at top. Based on the deformation of the infill during the out-of-plane loading, the upper interface between infill and frame could not be assumed as totally fixed or totally free. Also, it should be mentioned that some of the cracks developed at the displacement

of 30mm closed at displacement of 50mm and, thus, they were not represented in the cracking pattern shown in Figure 4.8i. The final cracking of the specimen is also shown in Figure 4.9.

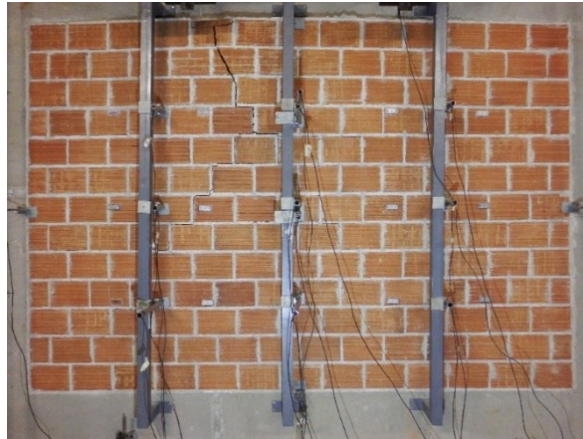


Figure 4.9 Final cracking pattern of the specimen SIF-O-1L-A

4.5.1.4 *Deformation characteristic of the brick infill wall*

The deformation of the brick infill recorded by all LVDTs placed on the specimen during the out-of-plane loading is shown in Figure 4.10. It is clear that the displacement at the control point located at the center point of the infill remains almost as the point with maximum deformation during the loading procedure. The exception is observed in the last cycle corresponding to the imposed displacement of 50mm, in which the total collapse of the upper infill-frame interface occurred. In fact, the displacement recorded in LVDT L8, placed in the top region of the infill, increased considerably once the cracking of the top interface initiated at imposed out-of-plane displacement of 25mm.

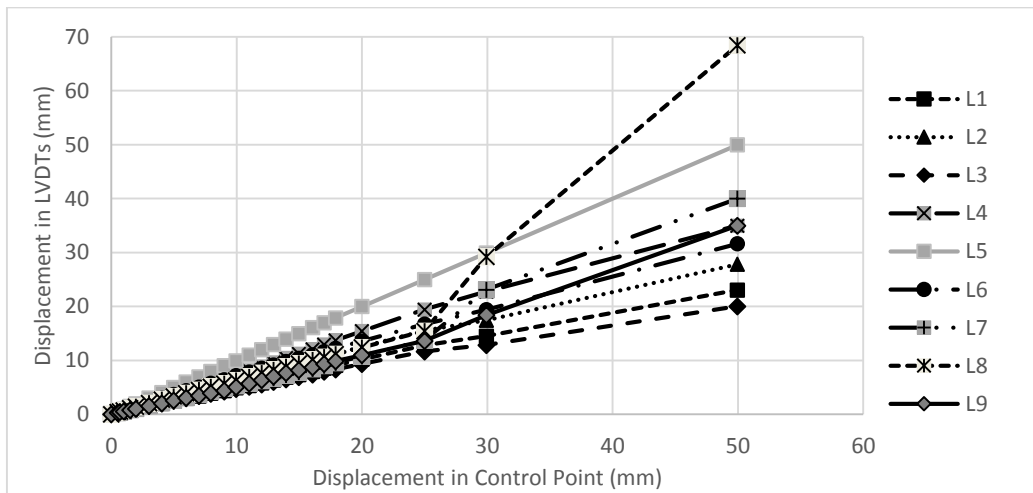


Figure 4.10 Deformation of the infill during out-of-plane loading

From the analysis of the central vertical profile of displacement along the height of the infill by comparing the results of LVDTs L2, L5 and L8, it is observed that the upper and bottom parts of the infill wall have the same deformations until the cracking of the upper interface at imposed displacement of 25mm in the control point. This is also valid for central horizontal profile, where the displacements recorded in the LVDTs L4 and L6 are very close until the displacement of 25mm, see Figure 4.11. This deformation pattern confirms the symmetric deformation of the brick

infill during the development of the two-way arching mechanism. However, after cracking of the upper interface, the two-way arching mechanism supported on all sides was replaced by the predominant two-way arching mechanism with three supports and one free edge. At this stage, the upper part of the infill wall bulged outside but the displacements at the left and right part of the infill remained similar, confirming that no significant cracking at the vertical interfaces developed.

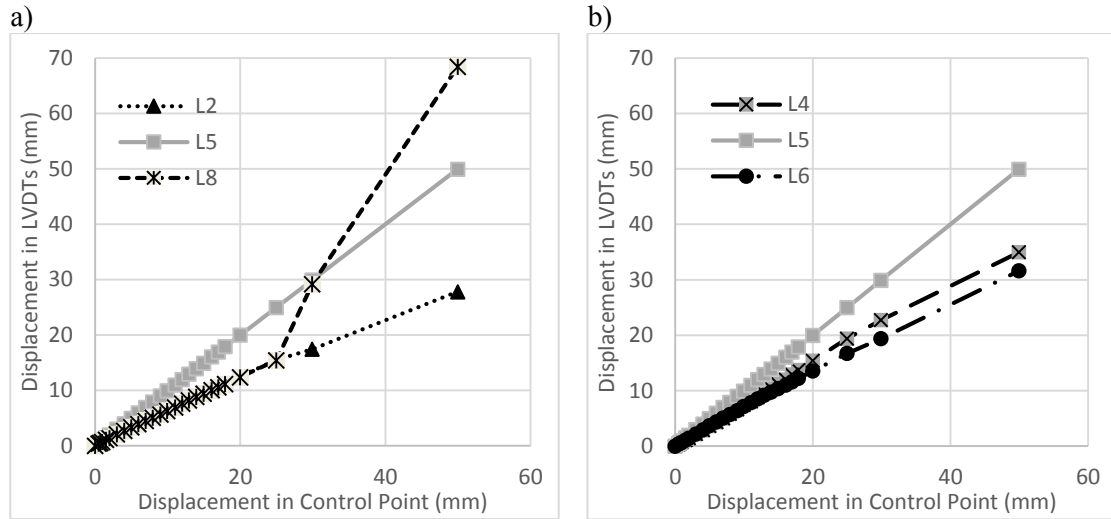


Figure 4.11 Comparison of the deformation of a) central vertical profile b) central horizontal profile

This conclusion is also supported by the evolution of the displacements measured at the infill-frame interfaces (LVDTs L10, L11, L12 and L13), measuring possible sliding of interfaces, see Figure 4.12. It is observed that the displacement recorded in LVDT L12 presents a sharp increase at lateral displacement of 25 cm, corresponding to the onset of top interface sliding, according to what was already observed in Figure 4.8g. In relation to the sliding of the vertical interfaces (displacements measured by LVDTs L13 in the left and by LVDT L 11 in the right) and to the sliding of the bottom interface (LVDT 10), it is seen that very low values were recorded.

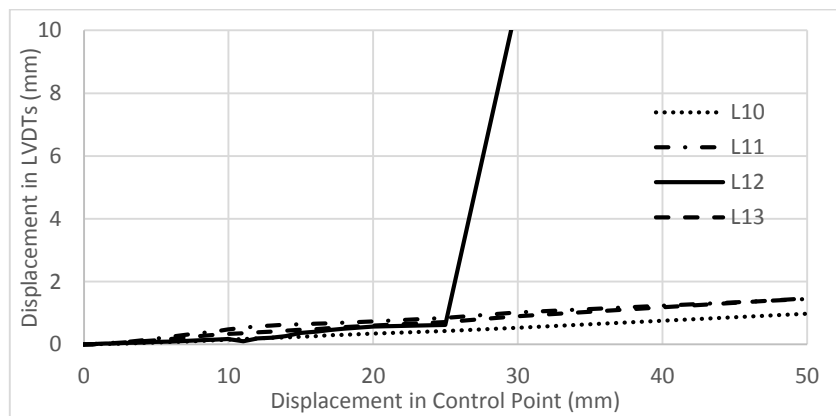


Figure 4.12 Sliding of the interfaces during out-of-plane loading

Figure 4.13 shows the graphic deformation of the infill wall subjected to out-of-plane loading as contour lines. As mentioned before, the infill exhibited symmetric behavior before bulging of the upper infill-frame interface. Up to the out-of-plane displacement of 25mm, practically no sliding

of all interfaces was recorded. After cracking of the upper interface between infill and the rc frame, the interface bulged outside and the upper part of the infill exhibited more deformation than the lower part, see Figure 4.13c and d. It is also clear that up to cracking of the upper interface, the area with maximum deformation was located at the center part of the infill but after cracking of the interface it moved slightly upward towards upper interface.

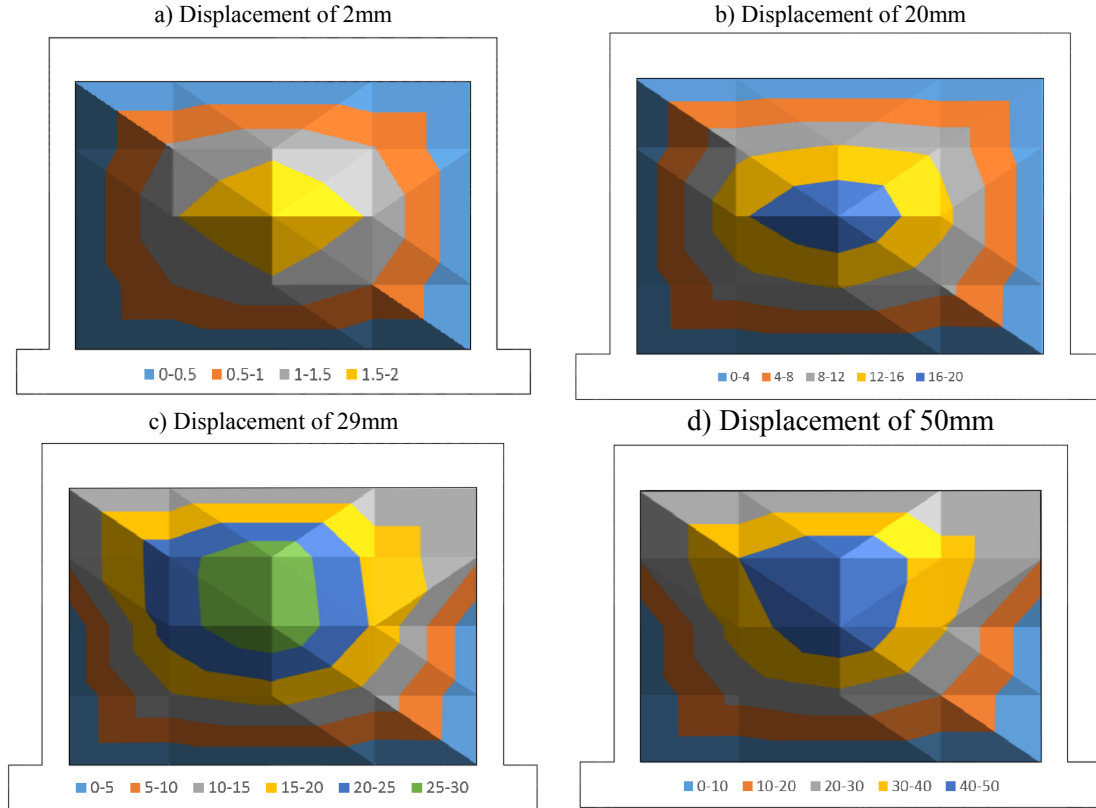


Figure 4.13 Deformation of the infill at different out-of-plane displacements

The residual plastic deformation of the infill in the unloading process is shown in Figure 4.14. Its trend of variation may be approximated by a polynomial function of second order, see Figure 4.15. It is seen that until displacement of 25mm, low values of plastic deformation were observed, which is associated to the successive opening-closing of the initial cracks in the loading and unloading procedure and to the slow propagation of additional cracks.

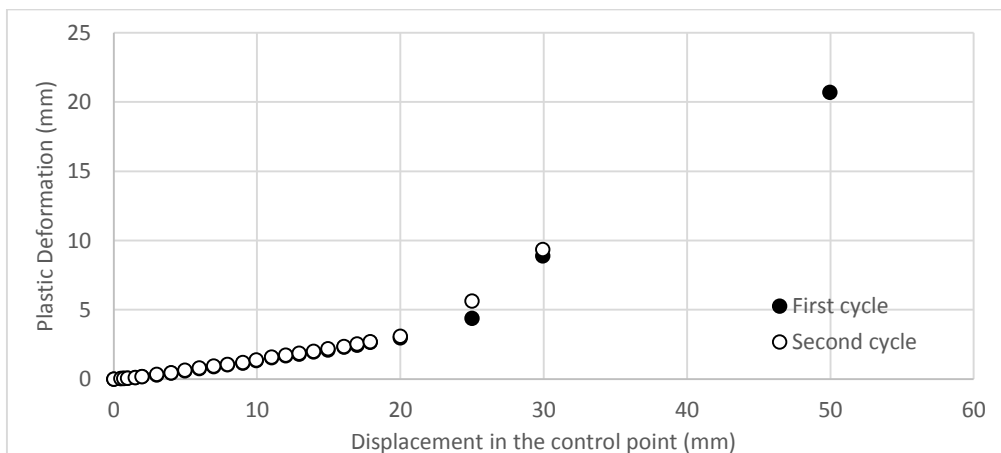


Figure 4.14 Plastic deformations in specimen SIF-O-1L-A at two successive cycles



This means that a great percentage of the out-of-plane deformation was recovered before cracking of the upper interface. After the lateral displacement of 25mm and cracking of the upper interface, the upper interface started to move outwards, resulted in significant increasing of plastic deformations.

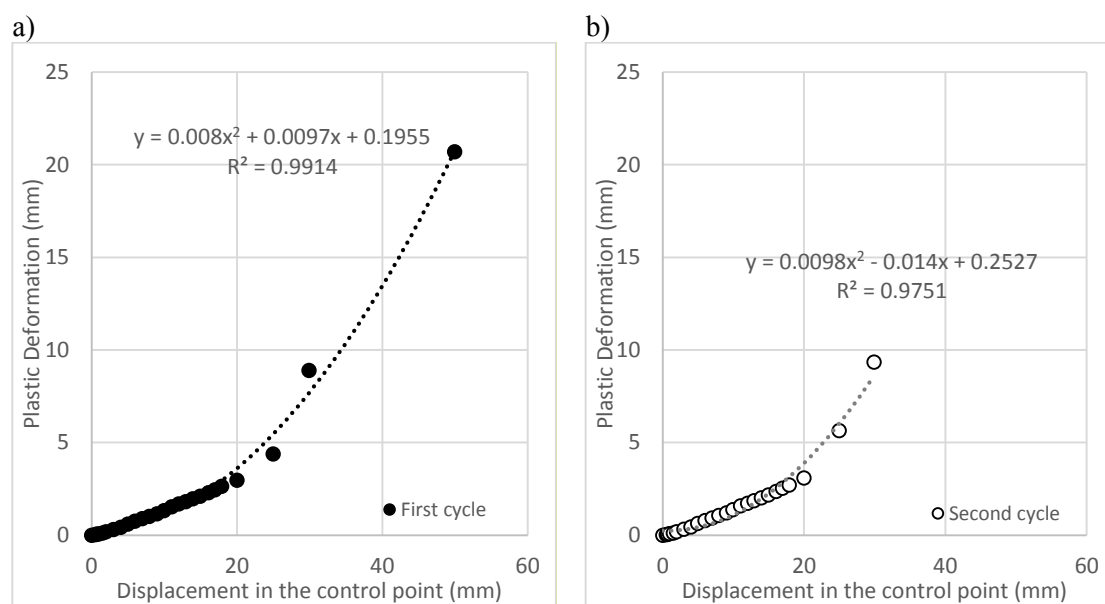


Figure 4.15 Plastic deformation of SIF-O-1L-A at two successive cycles; a) first cycle b) second cycle

#### 4.5.1.5 Energy dissipation capacity

The energy dissipation of the specimen during out-of-plane loading at each cycle is shown in Figure 4.16. It is calculated as the area of the hysteretic loop between the loading and unloading path in the force-displacement diagram. It is clear that applying larger displacements increases the energy dissipation of the specimen. This is related to the progressive cracking of the infill during out-of-plane loading. Significant increase in the energy dissipation of the infill was observed at out-of-plane displacement of 25mm which is related to the cracking of upper interface. Dissipation of energy at displacement of 25mm was calculated to be 3.5 times of dissipation of energy at displacement of 20mm.

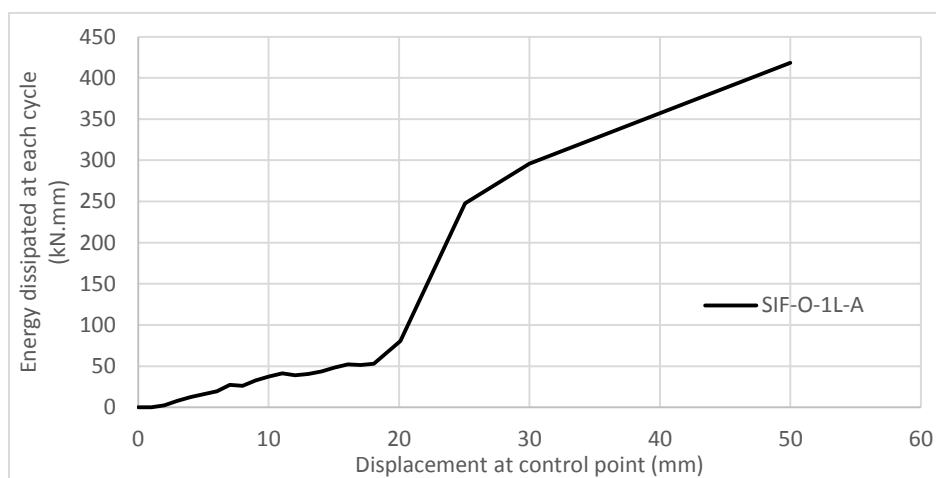


Figure 4.16 Dissipation of energy at each cycle during out-of-plane loading for specimen SIF-O-1L-A

The cumulative energy dissipation of the specimen at each displacement level is calculated as the sum of the dissipated energies enclosed in all hysteresis loops until that displacement level, see Figure 4.17. As expected, the cumulative energy dissipation was increased by applying larger displacements to the control point. The total amount of the energy dissipated was about 1600kN.mm at displacement of 50mm in the control point.

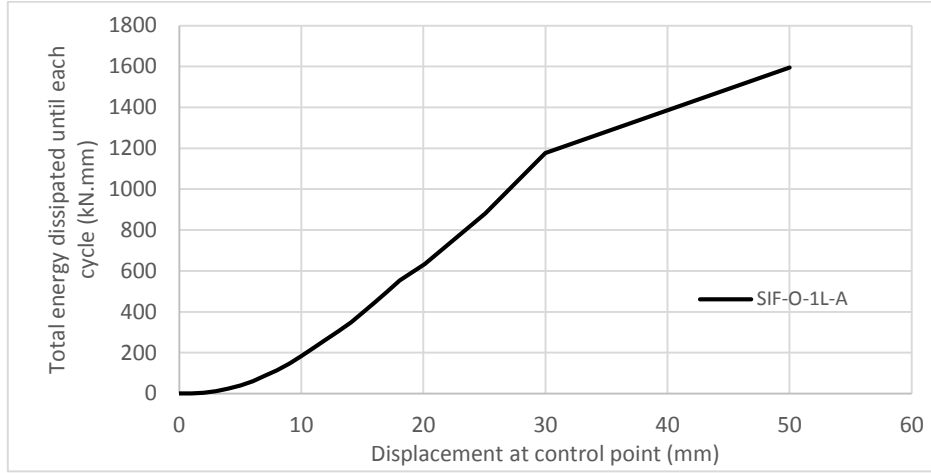


Figure 4.17 Cumulative dissipation of energy for specimen SIF-O-1L-A

## 4.5.2 Specimen SIF-O-1L-B

### 4.5.2.1 Load-displacement response

The force-displacement diagram obtained for the out-of-plane response of the specimen SIF-O-1L-B is shown in Figure 4.18. It is observed that the crack initiation occurred at displacement of 3.76 mm by development of a horizontal crack at mortar joints in the central region of the wall. A significant decrease of the initial slope of the force-displacement diagram could be observed after displacement of 5.27mm, corresponding to the out-of-plane force of 30.9kN. This is more related to the initiation of the diagonal cracking at this stage.

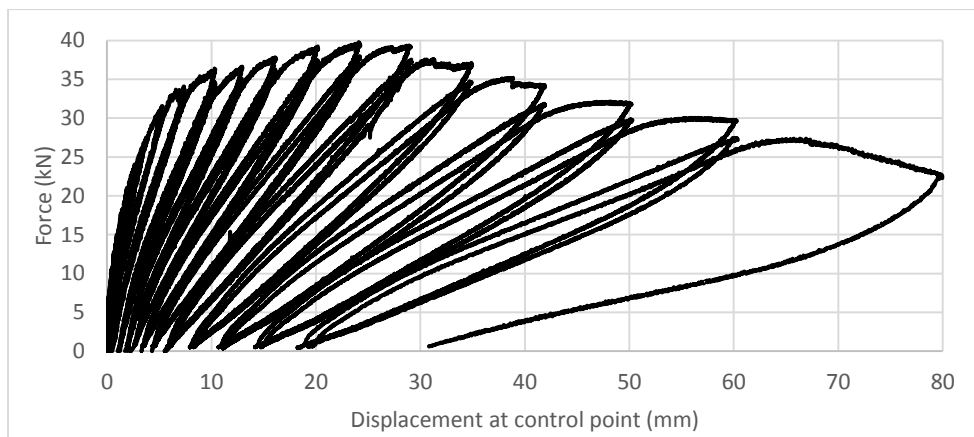


Figure 4.18 Force-displacement response of the SIF-O-1L-B

By imposing higher displacements, the out-of-plane force increased slowly until it reached the value of 39.7kN at displacement of 24.21mm. After the peak load, by increasing the displacement at control point, slow reduction of the lateral resistance was observed, resulting in a much extended softening branch until lateral displacement of 80 mm, corresponding to the residual strength of 22.4kN, calculated as 56% of the peak load. Because the specimen was collapsed at the first cycle of the displacement of 80mm, the second cycle was not performed.

The monotonic envelopes of the force-displacement diagrams for the first and second cycles are shown in Figure 4.19. It is observed that the strength degradation is not significant and initiates after diagonal cracking. The maximum strength degradation was calculated as 10% at the lateral displacement of 60.5mm.

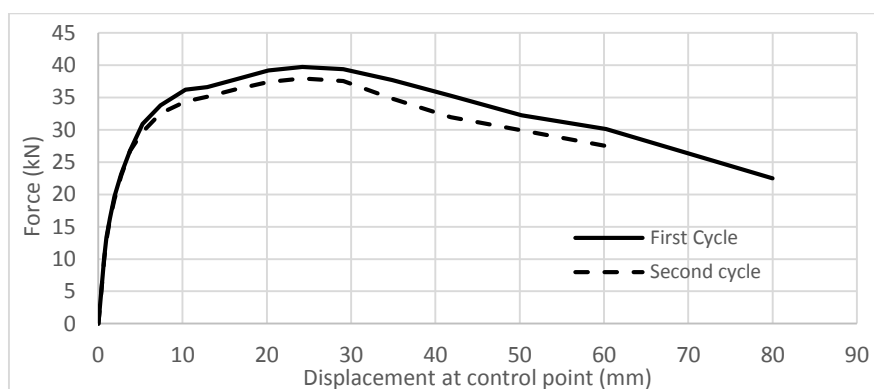


Figure 4.19 Monotonic force-displacement envelopes at two successive cycles

#### 4.5.2.2 *Stiffness degradation curve*

The secant stiffness of the specimen during the out-of-plane loading is calculated according to what was mentioned before and shown in Figure 4.20. It is clear that the stiffness degradation curve presents a logarithmic decreasing trend. This means that the stiffness of the specimen degraded rapidly at early stages of loading. The secant stiffness degraded about 55% until out-of-plane displacement of 5.3mm.

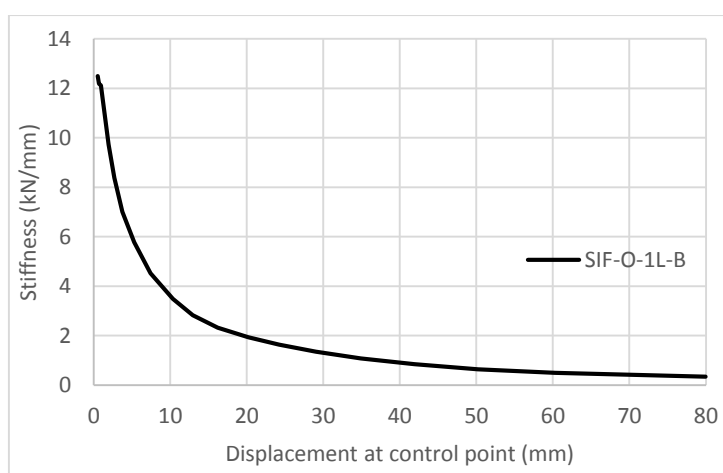


Figure 4.20 Stiffness degradation curve of specimen SIF-O-1L-B

#### 4.5.2.3 Cracking Pattern

The cracking patterns of the specimen for different levels of imposed out-of-plane displacements are shown in Figure 4.21. As already mentioned, the first significant cracking of the specimen was observed at displacement of 3.76 mm, corresponding to the out-of-plane force of 26.8kN by formation of some horizontal cracks in the mid part of the infill, see Figure 4.21a. By increasing the out-of-plane displacement, diagonal cracks developed at the mid part of the infill extending towards the corners, according to the patterns shown in Figure 4.21b-d. At the imposed displacement of 16.14 mm, corresponding to out-of-plane force of 37.7kN, some diagonal cracks developed in the rc frame at the upper beam-column connections. By applying higher out-of-plane displacements, the cracking propagated in the infill and new vertical cracks appeared at mid span of the top beam at the displacement of 20.18mm corresponding to the force of 39.2kN, see Figure 4.21e-f. The out-of-plane visible movement of the upper infill-frame interface was seen at lateral displacement of 16.14 mm resulting in a horizontal crack along the interface. Imposing further displacement resulted in a sharp increase of the out-of-plane movement of the upper interface and consequently in the formation of vertical cracks connecting the horizontal crack in the center part of the infill to the horizontal interface cracks, see Figure 4.21h.

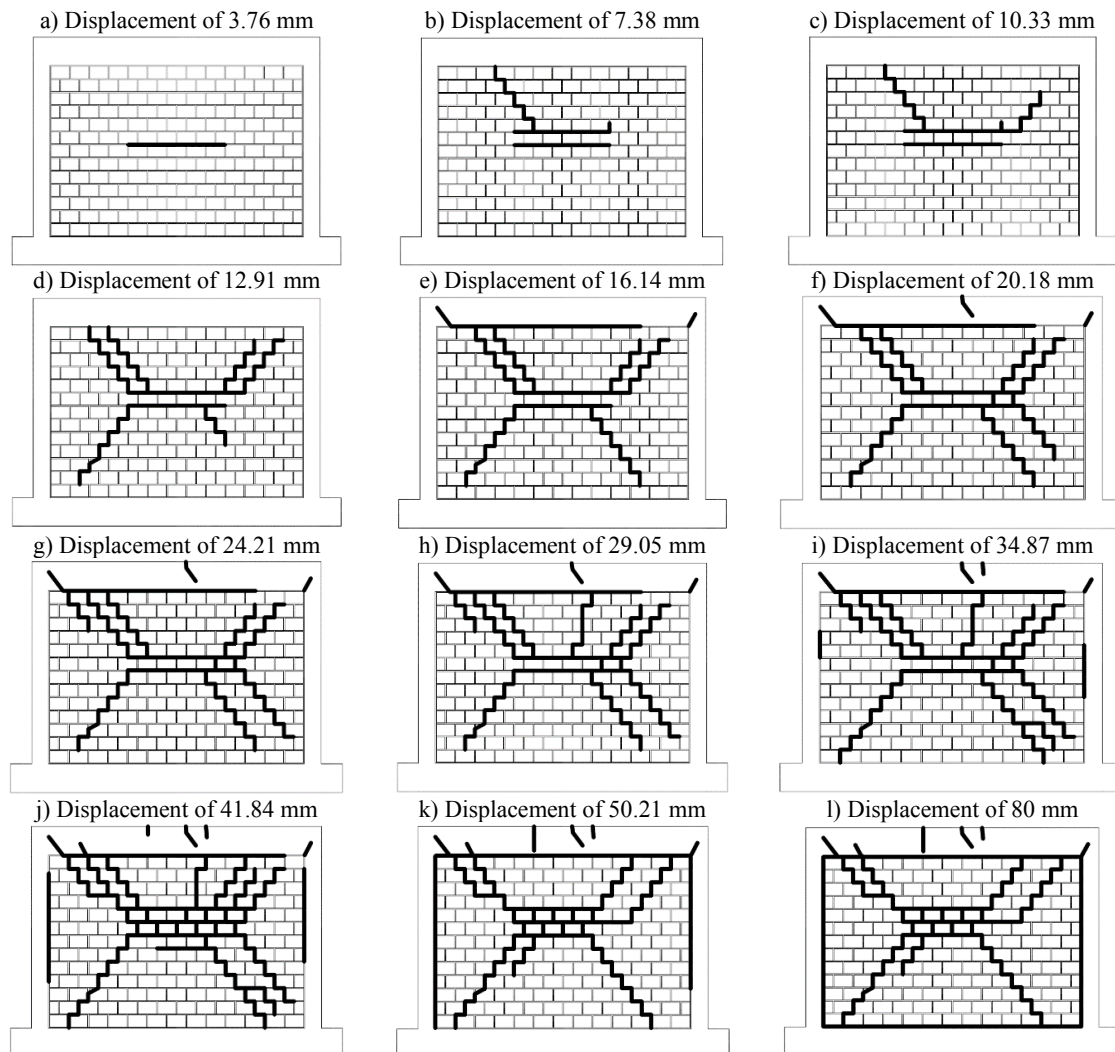


Figure 4.21 Crack propagation of SIF-O-1L-B

It is observed that by applying higher displacements some of the cracks got closed, which is related to the cyclic nature of the loading. This behavior was visible at lateral displacement of 50.21 mm, in which some of the old cracks got closed and some new cracks were formed, see Figure 4.21k. The final cracking pattern of the specimen is shown in Figure 4.21l, where it is seen that all interfaces between infill and the rc frame were cracked.

By analyzing the crack pattern it appears that two way arching mechanism formed in the specimen controls the resisting mechanism of the masonry infill under out-of-plane loading. In spite of sliding of the upper interface and crack formation at the top of the infill-beam interface, it appears that the out-of-plane resisting mechanism is governed predominantly by two-way arching mechanism supported on all sides, which is also compatible with the cracking patterns developed.

#### 4.5.2.4 Deformation of the Infill

The evolution of the displacements measured in the different LVDTs placed on the masonry infill during the out-of-plane loading is shown in Figure 4.22. By comparing the displacements it is clear that the displacement at central part of the infill (L5) has the highest value, even after cracking the upper interface and its bulging in the out-of-plane direction. Analyzing the deformations of the upper and bottom part of the infill by comparing the results of LVDT L8 and LVDT L2 in Figure 4.23a reveals that until the horizontal cracking of the upper interface at displacement of 16.14mm, the upper and bottom part of the infill have similar deformations with negligible differences. However, after cracking of the upper interface, the upper part of the infill deforms more than the bottom part. It is also clear that the right side of the infill has similar deformation as the left side during all steps of the out-of-plane loading, meaning that the cracking at the vertical interfaces is not significant, see Figure 4.23b.

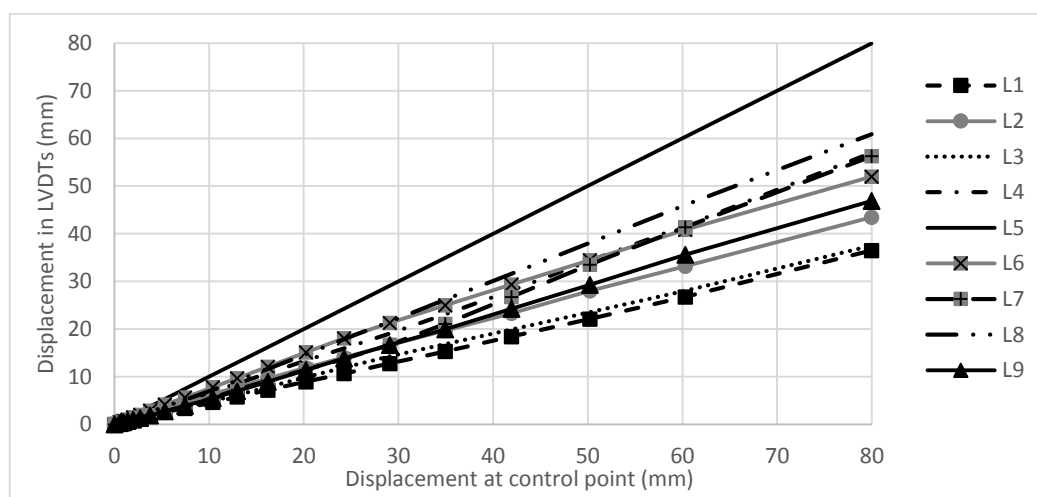


Figure 4.22 Deformation of the infill during out-of-plane loading

Figure 4.24 shows the deformation of the infill as contour levels at different levels of imposed out-of-plane displacements. As explained before, it is evident that the infill behaves symmetrically during the out-of-plane loading until its failure at displacement of 80mm. At the first levels of loading, a two-way resisting arching mechanism develops and keeps working even after the upper interface cracks and bulges outside. It should be stressed that, in spite of cracking of the upper infill-frame interface, its out-of-plane movement recorded by LVDT L12 is

considerably lower than that LVDT in specimen built by mason A, where the total collapse of the interface occurred.

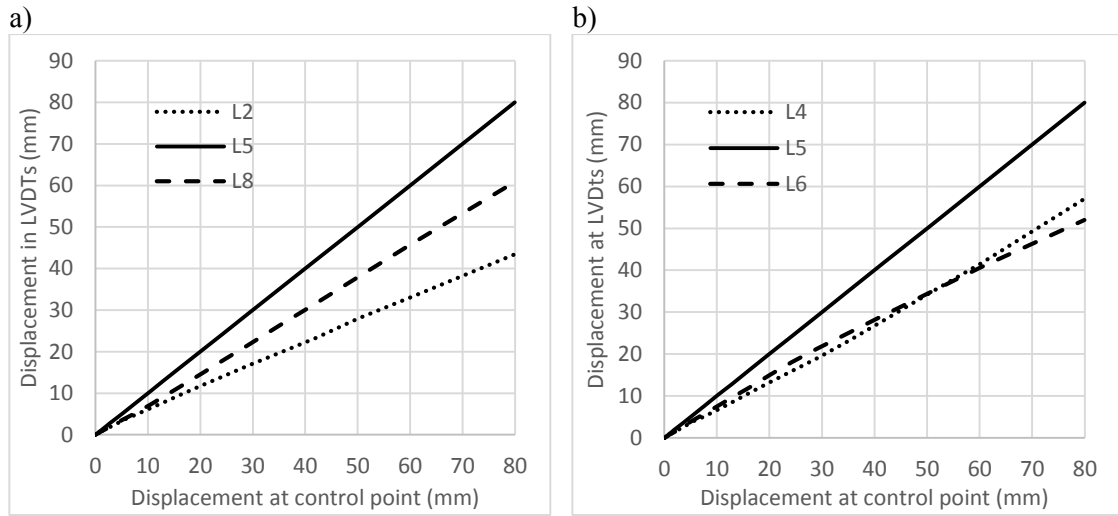


Figure 4.23 Comparison of the deformation of a) central vertical profile b) central horizontal profile

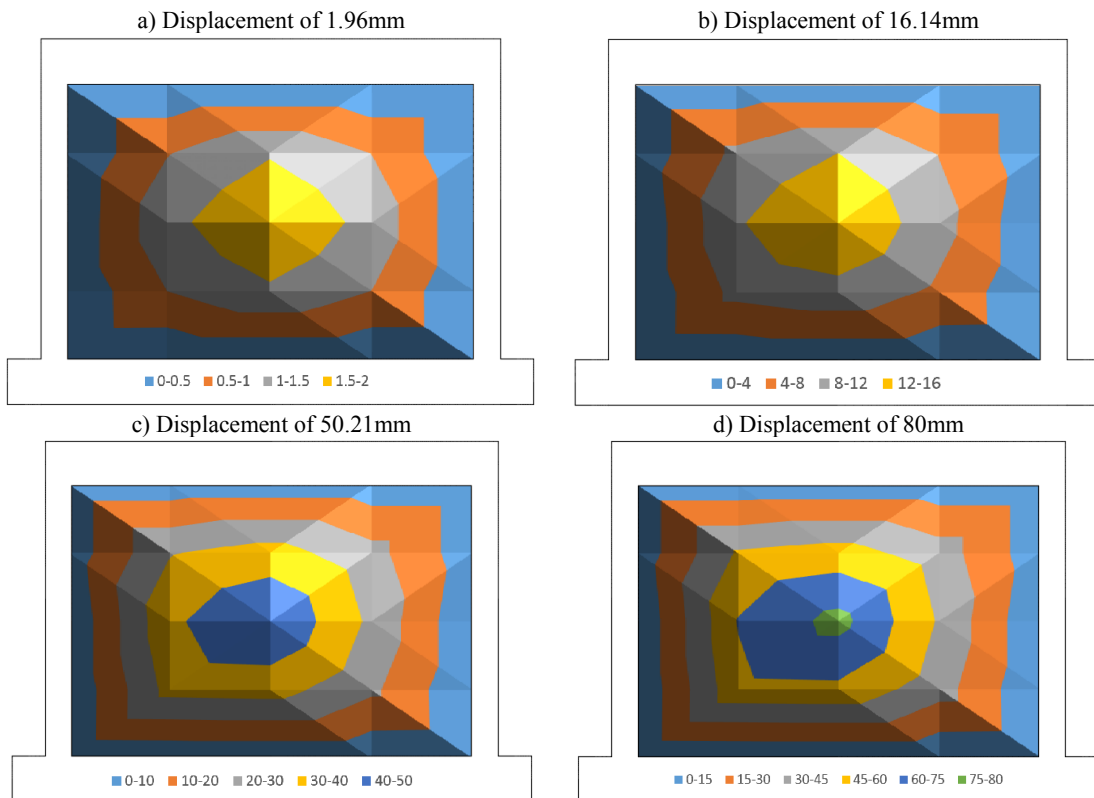


Figure 4.24 Deformation of the infill at different out-of-plane displacements.

In effect, according to the values of the displacements measured at the interfaces shown in Figure 4.25, it is seen that very low values were recorded, even if the upper interface moved in the out-of-plane direction. This resulted in a considerable symmetry of the infill deformation and in the predominant two-way resisting mechanism until the imposed lateral displacement of 80mm. This result reveals the influence of the construction quality on the out-of-plane behavior of infills,

particularly with regard to the filling of the upper interface with mortar, which can change the resisting mechanism to out-of-plane loading.

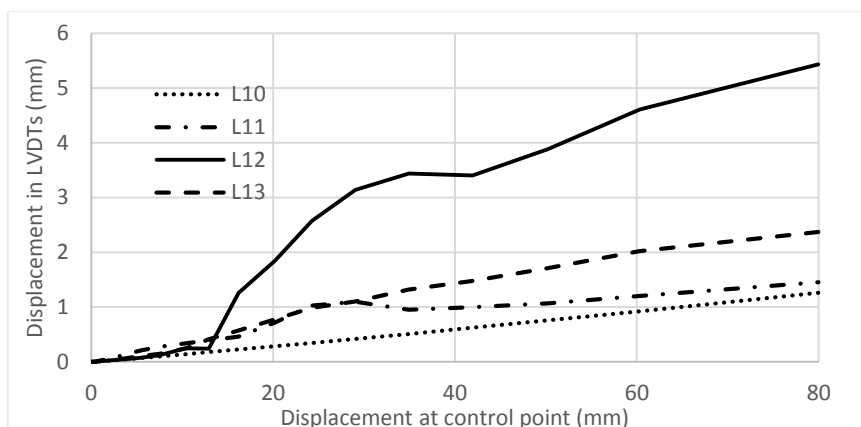


Figure 4.25 Sliding of the infill-rc frame interfaces during out-of-plane loading

The plastic deformations of the masonry infill in the first and second cycles of each step are shown in Figure 4.26. It is observed that at early stages of deformation, the plastic deformations are practically zero, corresponding to the initial elastic behavior of the masonry infill. The plastic deformation increases by increasing imposed displacement, particularly after the displacement of 7.38mm, corresponding to the out-of-plane force of 34.1kN. This behavior results naturally from the progress of damage associated to the cracking of the masonry infill. It is also seen that the plastic deformations follow similar trend of the plastic deformations observed in the masonry infill built by mason A. Thus, according to Figure 4.27, the plastic deformations can be described through a polynomial function of second order, having a statistical correlation coefficient of  $r^2=0.999$ .

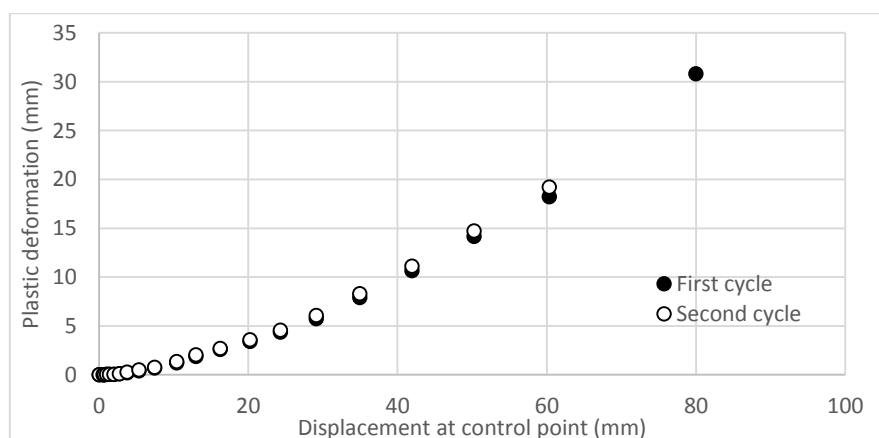


Figure 4.26 Plastic deformation in the masonry infill at 1st and 2nd cycles of each step

#### 4.5.2.5 Energy dissipation capacity

The dissipation of energy at each out-of-plane displacement involved in the cracking of the masonry specimen is presented in Figure 4.28. The cumulative energy dissipation during the out-of-plane test, calculated as the sum of the energy dissipated at each cycle is shown in Figure 4.29. It is clear that higher imposed displacements lead to higher dissipation of energy. By comparing this result with the result of specimen SIF-O-1L-A it is observed that total dissipation of energy

of specimen SIF-O-1L-B is more than two times of the total dissipation of energy of specimen SIF-O-1L-A at the end of the test when the infill was totally damaged.

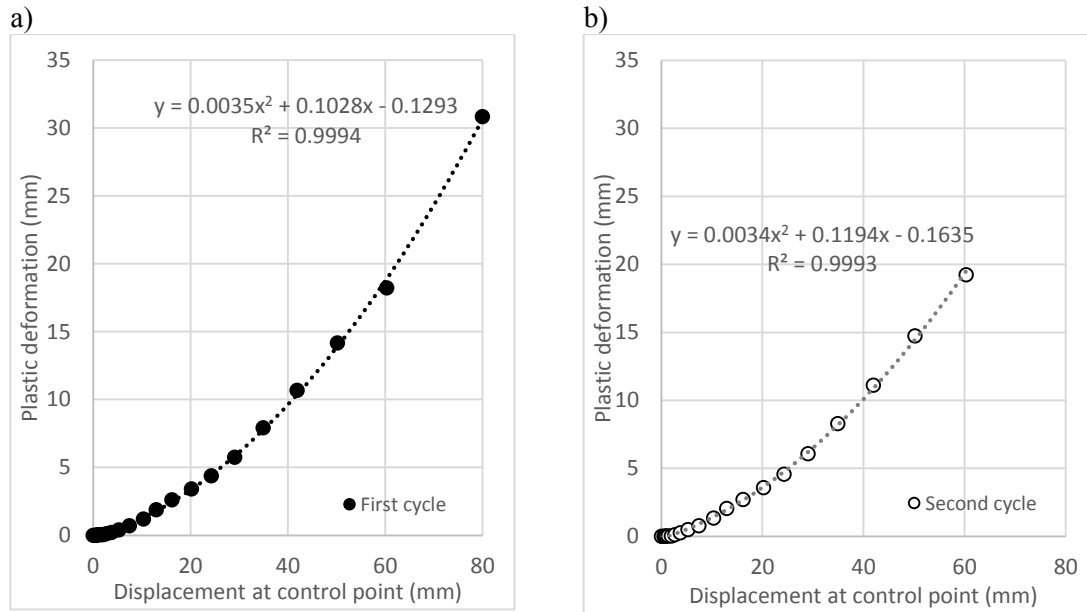


Figure 4.27 Plastic deformation of SIF-O-1L-B at two successive cycles; a) first cycle b) second cycle

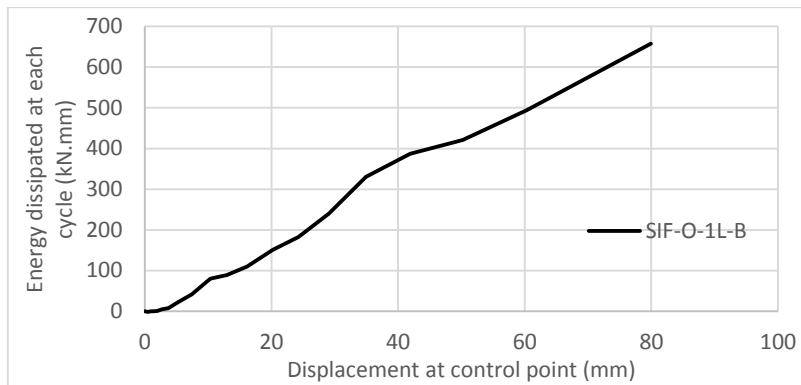


Figure 4.28 Dissipation of energy at each cycle for specimen SIF-O-1L-B

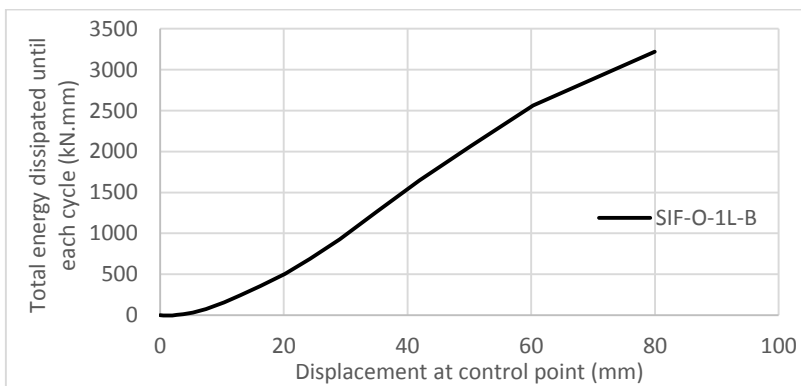


Figure 4.29 Cumulative dissipation of energy until each cycle for specimen SIF-O-1L-B



### 4.5.3 Specimen PIF-O-1L-B

#### 4.5.3.1 Load-displacement response

The force-displacement diagram of the specimen with a central opening, recorded in the control point is shown in Figure 4.30. It is observed that the first cracking initiated at displacement of 3.76mm corresponding to the out-of-plane force of 26.6kN. It is stressed that the masonry infill exhibited a nonlinear behavior since very early stages of loading, even before crack initiation was recorded. The peak load of 39kN was achieved at displacement of 12.91mm recorded in the control point. After this stage, the increase of the displacement in control point resulted in small and progressive decreasing of the out-of-plane resistance. The specimen was collapsed at displacement of 24.46mm, corresponding to the out-of-plane force of 31.1kN. The collapse occurred due to the out-of-plane failure of the masonry pier in the right side of the central opening. The right part of the infill experienced more severe damage when compared to other parts in the infill. In spite of the adequate initial adjustment of the airbag, it is possible that the progress of damage led to the uneven distribution of airbag loading and thus to the unsymmetrical deformation of the infill.

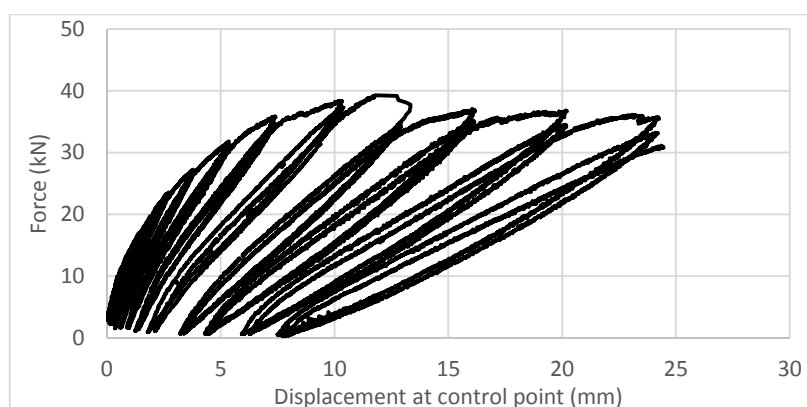


Figure 4.30 Force-displacement diagram of PIF-O-1L-B

The monotonic force-displacement envelopes for each successive cycles are shown in Figure 4.31. It is observed that the strength degradation in the specimen starts with the development of higher density of cracks, similar to what was recorded in the previous specimens. The maximum strength degradation of 12% was recorded at lateral displacement of 12.91mm corresponding to the peak load of 39kN.

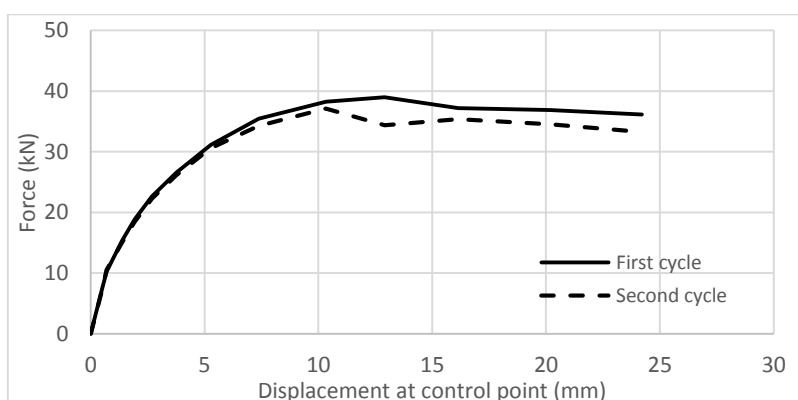


Figure 4.31 Monotonic force-displacement diagram for successive cycles

The force-displacement diagram of this specimen is compared with reference specimen (SIF-O-1L-B) in two different points: the control point of PIF-O-1L-B (L9) and the point where the specimen PIF-O-1L-B exhibited maximum deformation (L6), see Figure 4.32. It seems that presence of the central opening with small size resulted in significant decrease of the deformation capacity when compared with the reference specimen. Nevertheless, no significant change of the lateral strength was recorded.

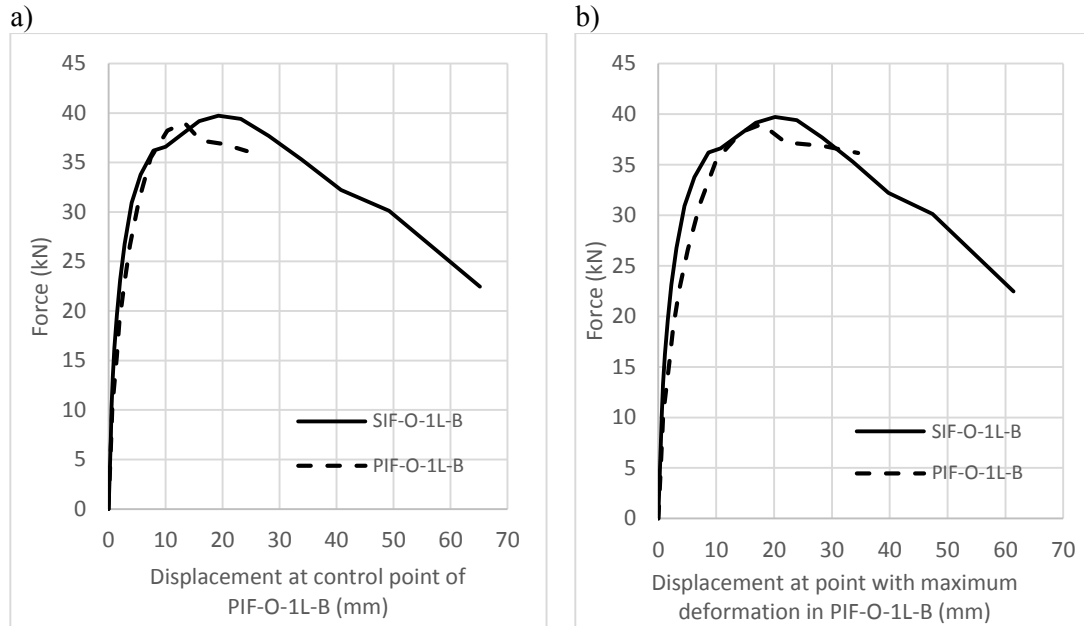


Figure 4.32 Force-displacement diagram of specimens PIF-O-1L-B versus SIF-O-1L-B at two different point; a) control point b) point with maximum deformation

#### 4.5.3.2 Stiffness degradation curve

The variation of the stiffness during the out-of-plane loading is shown in Figure 4.33. It is clear that the secant stiffness of the masonry infill with central opening exhibits the same decreasing trend (logarithmic decrease). This means that the stiffness degradation rate at lower displacement is higher. The stiffness of the specimen at the lateral displacement of 10mm reached 23% of the initial value meaning that high amount (77%) of the initial stiffness degraded until displacement of 10mm.

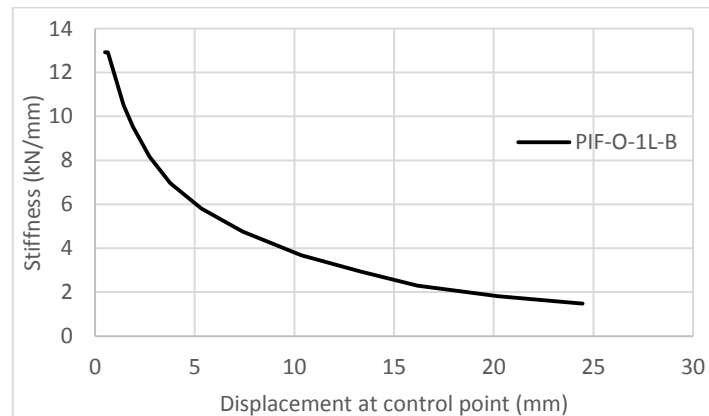


Figure 4.33 Stiffness degradation curve of specimen PIF-O-1L-B

### 4.5.3.3 Cracking pattern

The cracking pattern recorded in the masonry infill with a central window opening is shown in Figure 4.34. The first cracking initiated at a displacement of 3.76mm corresponding to out-of-plane force of 26.6kN by developing diagonal cracks at upper corners of the opening, see Figure 4.34a-b. By increasing the imposed out-of-plane displacement, the cracks extended towards the top corners of the infill as diagonal cracks along the mortar joints of the masonry, see Figure 4.34c-d, and reached the corners of the masonry infill at the out-of-plane displacement of 10.33mm. Additionally, at this stage the upper interface started to crack at its mid length and the first cracking in the rc frame was developed in the connection point of the upper beam and columns. The lintel at the top of the opening was totally separated from the brick layer due to the development of a horizontal crack at the lateral displacement of 12.91mm corresponding to maximum out-of-plane force of 39kN, see Figure 4.34e. Applying further displacements resulted in the development of new diagonal cracks at the bottom corners of the window opening towards the bottom corners of the masonry infill, according to what was observed in Figure 4.34f-i. Finally, the collapse of the masonry infill occurred due to the failure of the right part of the infill as shown in Figure 4.35. This is possible due to the high cracking density observed in the pier at the right part of the window opening which leads to non-uniform distribution of pressure inside airbag, resulting in premature collapse of the infill.

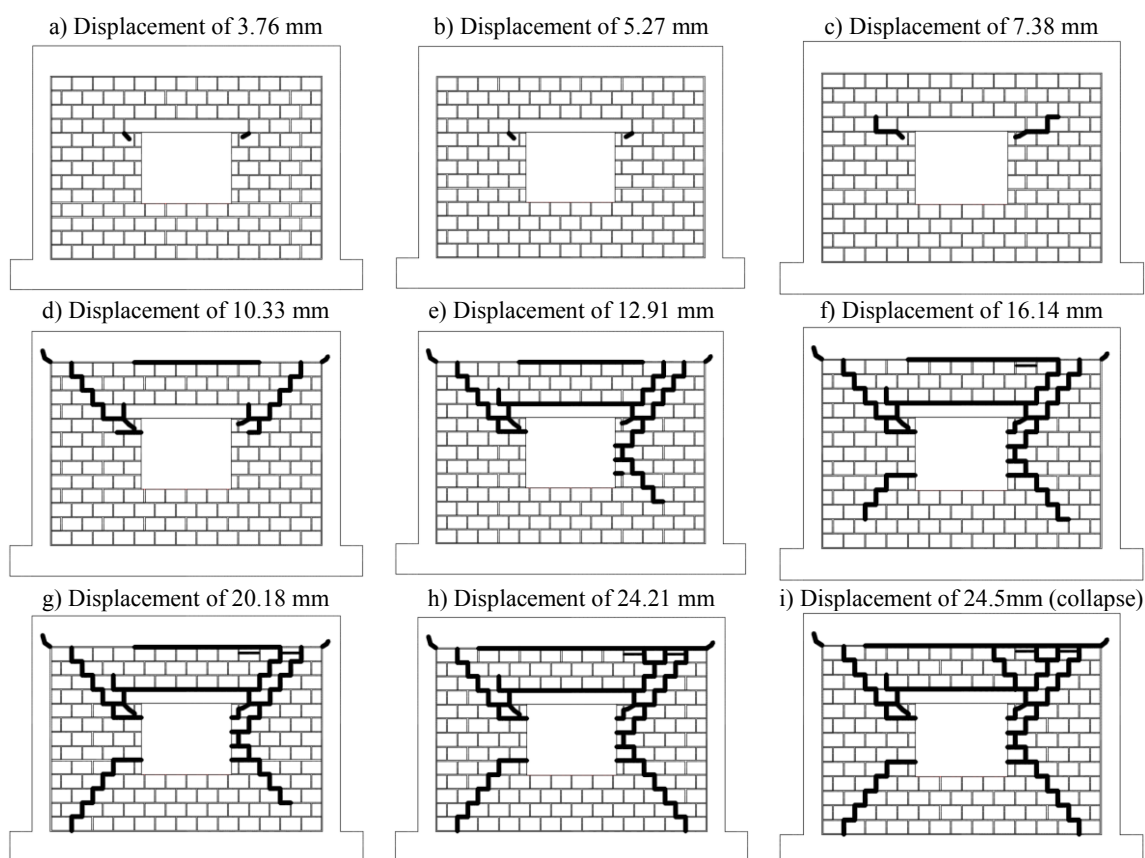


Figure 4.34 Crack propagation observed in specimen PIF-O-1L-B



Figure 4.35 Out-of-plane failure of the right part of the masonry infill

#### 4.5.3.4 Deformation of the Infill

The deformation of the masonry infill at different points during the out-of-plane loading is shown in Figure 4.36 and Figure 4.37. It seems that until the onset of the main diagonal cracks in the infill and sliding of its top interface at displacement of 10.33mm, the deformation pattern was practically symmetric; meaning that the right part of opening deforms similarly to the left part and its upper part deforms similarly to the lower part. After this point, the right part of the infill deforms more than the left part and collapses at out-of-plane displacement of 24.5mm.

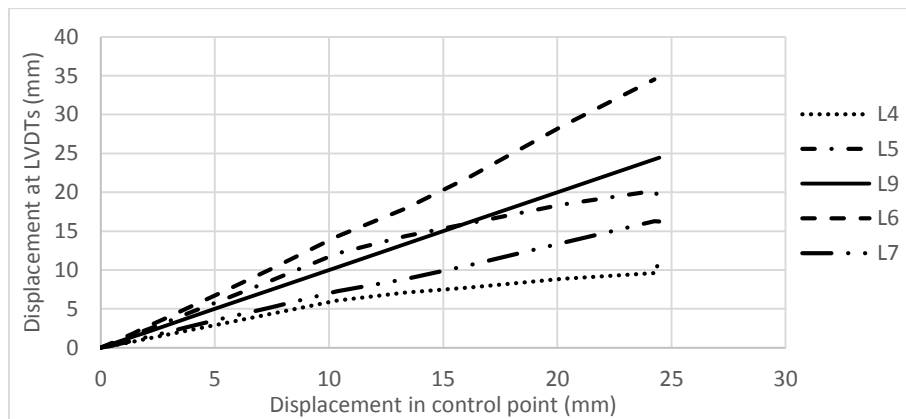


Figure 4.36 Deformation of the infill at central horizontal profile

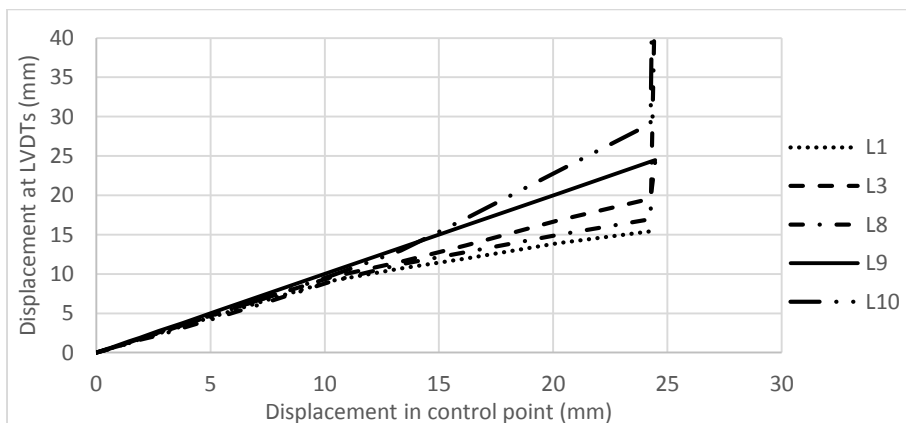


Figure 4.37 Deformation of the infill at different points with respect to the control point

The deformation of the infill is also shown as contour levels in Figure 4.38. This deformation pattern confirms that symmetric deformation of the infill is achieved until out-of-plane displacement of 12.91mm. After this point, the right part of the opening deformed more than the left part, which is also reflected in Figure 4.38d. This should be attributed to the concentration of more damage in the right part and consequently to the uneven pressure distribution in the airbag.

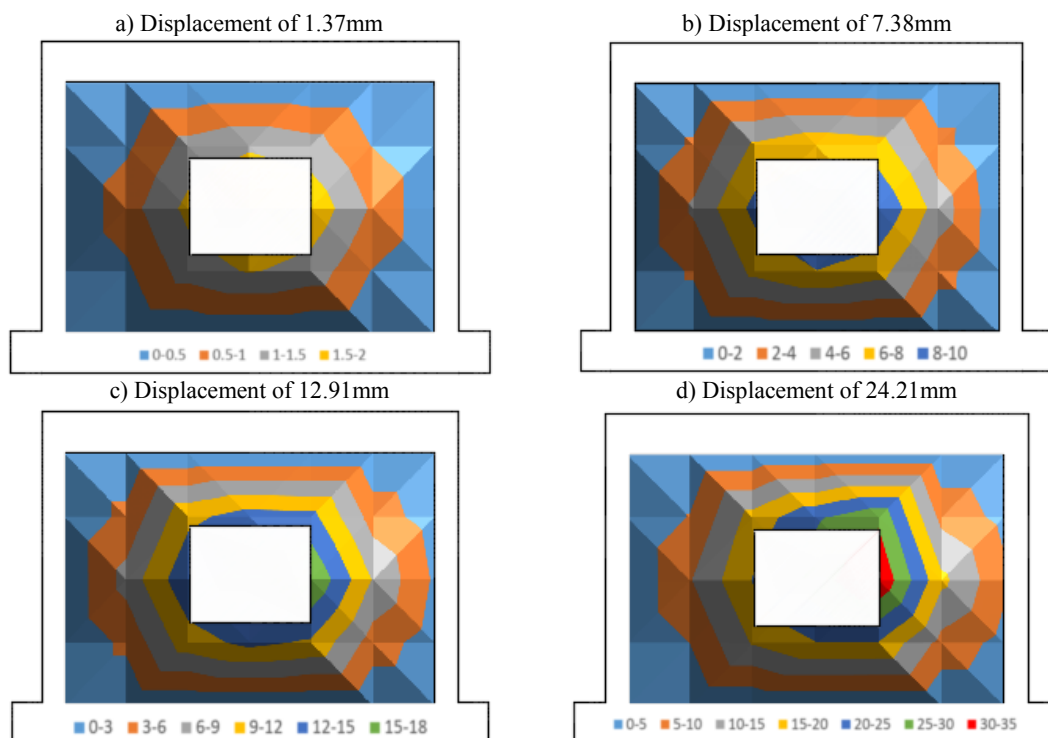


Figure 4.38 Deformation of the infill for different out-of-plane displacements

The plastic deformation of the masonry infill with the central opening at two successive cycles is shown in Figure 4.39 and Figure 4.40. It is observed that significant increase in the out-of-plane plastic deformation can be seen after the lateral displacement of 10.33mm in which significant diagonal cracking and upper interface cracking were observed. Before this displacement, the plastic deformation was negligible. It can be also concluded that the plastic deformation of the specimen at each cycle could be approximated with a polynomial function of second order, similarly to the previous specimens related to solid masonry infills.

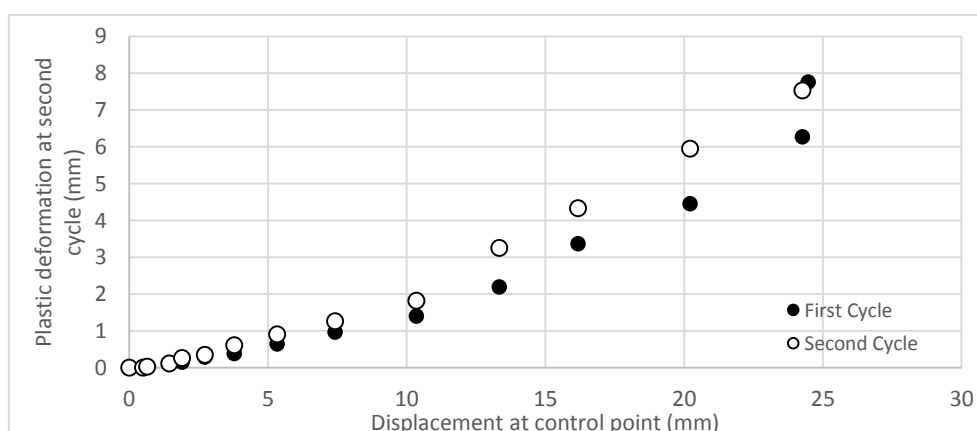


Figure 4.39 Plastic deformation of PIF-O-1L-B at two successive cycles

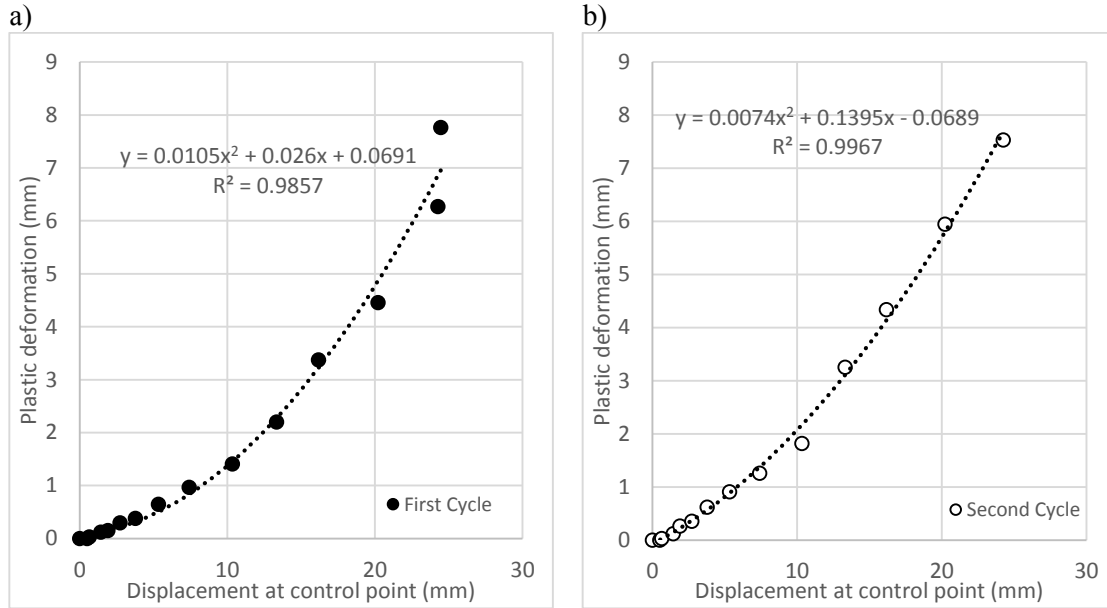


Figure 4.40 Plastic deformation of masonry infill PIF-O-1L-B at two successive cycles; a) first cycle b) second cycle

4.5.3.5 *Energy dissipation capacity*

The energy dissipation at each cycle and the cumulative energy dissipation in the specimen are shown in Figure 4.41. It is clear that the amount of energy dissipated increases as the lateral imposed displacement increases. This is related to the increasing and progressive damage observed in the specimen. It is also observed that the total amount of energy dissipated in this specimen until displacement of 24.21mm is 1.28 times of the energy dissipated in the specimen SIF-O-1L-B until displacement of 24.21mm.

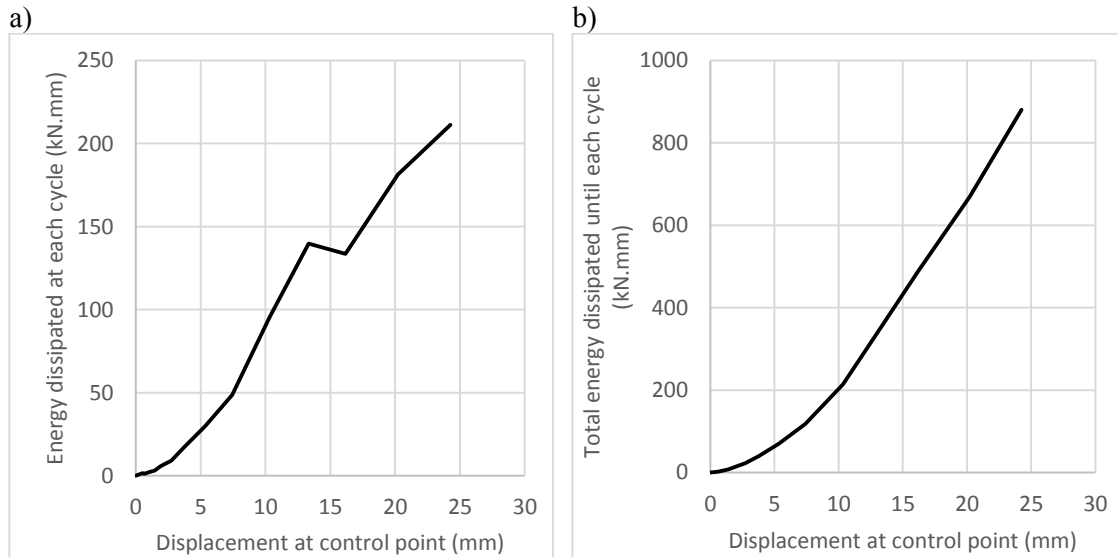


Figure 4.41 a) Energy dissipation at each cycle b) cumulative energy dissipation until each cycle

#### 4.5.4 Specimen SIF-IO(0.3%)-2L(NC)-B

##### 4.5.4.1 Load-displacement response

As mentioned before, three specimens were damaged previously in the in-plane direction to evaluate the influence of prior in-plane damage on the out-of-plane response of the masonry infills. The specimen SIF-IO(0.3%)-2L(NC)-B was subjected to an in-plane lateral drift of 0.3%. The out-of-plane tests were carried out in the same conditions considered for undamaged masonry infills. The force-displacement diagram obtained for the out-of-plane test of the masonry infill subjected to a prior in-plane lateral drift of 0.3% is shown in Figure 4.42. The crack initiation, resulting from the application of the out-of-plane loading of the masonry infill, was visually detected at displacement of 1.37mm, corresponding to the out-of-plane force of 8kN. This crack is considered to be a crack that was formed previously in the in-plane direction and re-opened due to the out-of-plane loading. The out-of-plane resistance of the masonry infill of 34kN was attained at displacement of 29.05mm. After the peak load, increasing the out-of-plane displacements resulted in a very smooth reduction of the lateral resistance until achieving the value of 28.6kN at displacement of 56mm at which the specimen collapsed.

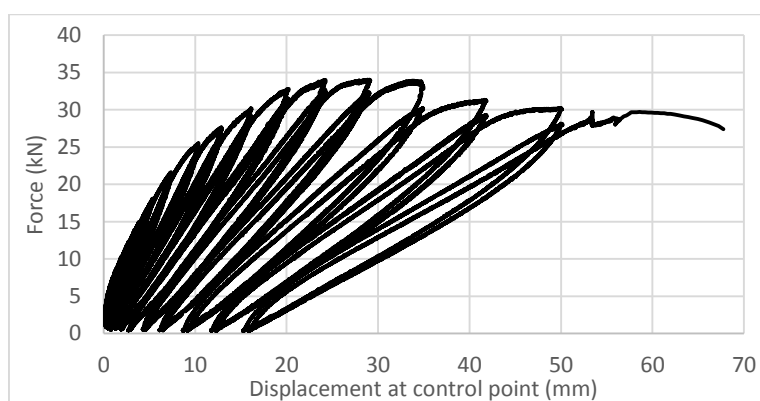


Figure 4.42 Force-displacement diagram obtained for specimen SIF-IO(0.3%)-2L(NC)-B

The monotonic force-displacement envelopes defined at each successive cycles are shown in Figure 4.43. Similarly to the other specimens, the strength degradation at the second cycle for a given displacement is not significant. The maximum strength degradation was observed at the peak load, similar to what was also recorded in the other specimens.

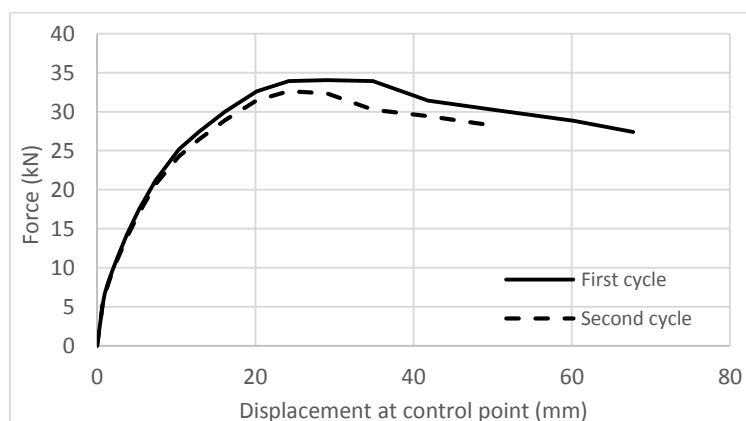


Figure 4.43 Monotonic force-displacement envelop at two successive cycles

#### 4.5.4.2 *Stiffness degradation curve*

The stiffness degradation curve obtained for this specimen is shown in Figure 4.44. It is clear that lower amount of stiffness was attained at the initiation of the test with respect to the undamaged specimen of SIF-O-1L-B. This is related to the presence of prior in-plane damage in the specimen. The trend of variation of the stiffness during the out-of-plane loading is similar to the trend found in the undamaged specimens, following a logarithmic reduction as the out-of-plane displacement increases. This means that the stiffness of the specimen is degraded rapidly in the range of low displacements. For instance, 65% of the initial stiffness was degraded until the displacement of 10.33mm.

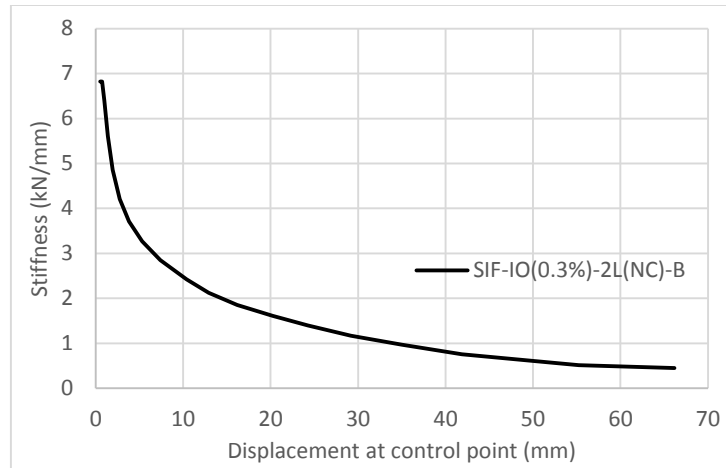


Figure 4.44 Stiffness degradation curve for specimen SIF-IO(0.3%)-2L(NC)-B

#### 4.5.4.3 *Crack patterns*

The crack pattern corresponding to different levels of out-of-plane loading is shown in Figure 4.45. The prior in-plane damage is highlighted by red lines (Figure 4.45a) to distinguish between the previously opened cracks due to the in-plane loading and newly opened cracks during out-of-plane loading. As already mentioned, the first diagonal cracks opened at the displacement of 1.37mm, resulting from re-opening of the cracks that were formed in the previous in-plane loading, see Figure 4.45b. This behavior was also observed at the lateral displacement of 3.76mm, see Figure 4.45c. At displacement of 7.38mm, new diagonal cracks were formed in the specimen, apart from the existing ones developed due to prior in-plane damage.

Although the specimen was previously damaged in the in-plane direction, it seems that two-way arching mechanism was formed to resist the out-of-plane loading. The diagonal cracking initiated from the central part of the wall extending towards the corners of the masonry infill reveals the predominant resisting arching mechanism in both vertical and horizontal directions. The main issue is that at early stages of loading, the cracking pattern followed the previous cracks formed in the in-plane direction but by increasing the out-of-plane displacements new cracks developed, forming an X-shaped cracking patterns, see Figure 4.45d.

The first sliding recorded at the interfaces was observed at the left interface by formation of vertical crack in the mortar joint at displacement of 10.33mm, see Figure 4.45e. Horizontal crack in the upper interface was observed at displacement of 20.18mm, which were due to the sliding of the upper interface between infill and rc frame, see Figure 4.45f.



It is observed that by applying increasing out-of-plane displacements, some of the cracks that were formed in the in-plane direction were closed and new cracks were opened due to the formation of two-way arching mechanism, see Figure 4.45g-i. After displacement of 29.05mm, it is considered that the X-shaped cracking pattern stabilized in the masonry infill and new progressive movement at the top interface was recorded, see Figure 4.45j-k. The final cracking pattern observed at the collapse of the specimen at lateral displacement of 68mm is shown in Figure 4.45l and Figure 4.46. It should be mentioned that the cracking pattern of the specimen at low levels of loading is affected by the prior in-plane damage, but at higher levels of loading its influence is reduced. Inclusively, the cracking observed at the vertical right interface almost did not evolved in the out-of-plane loading.

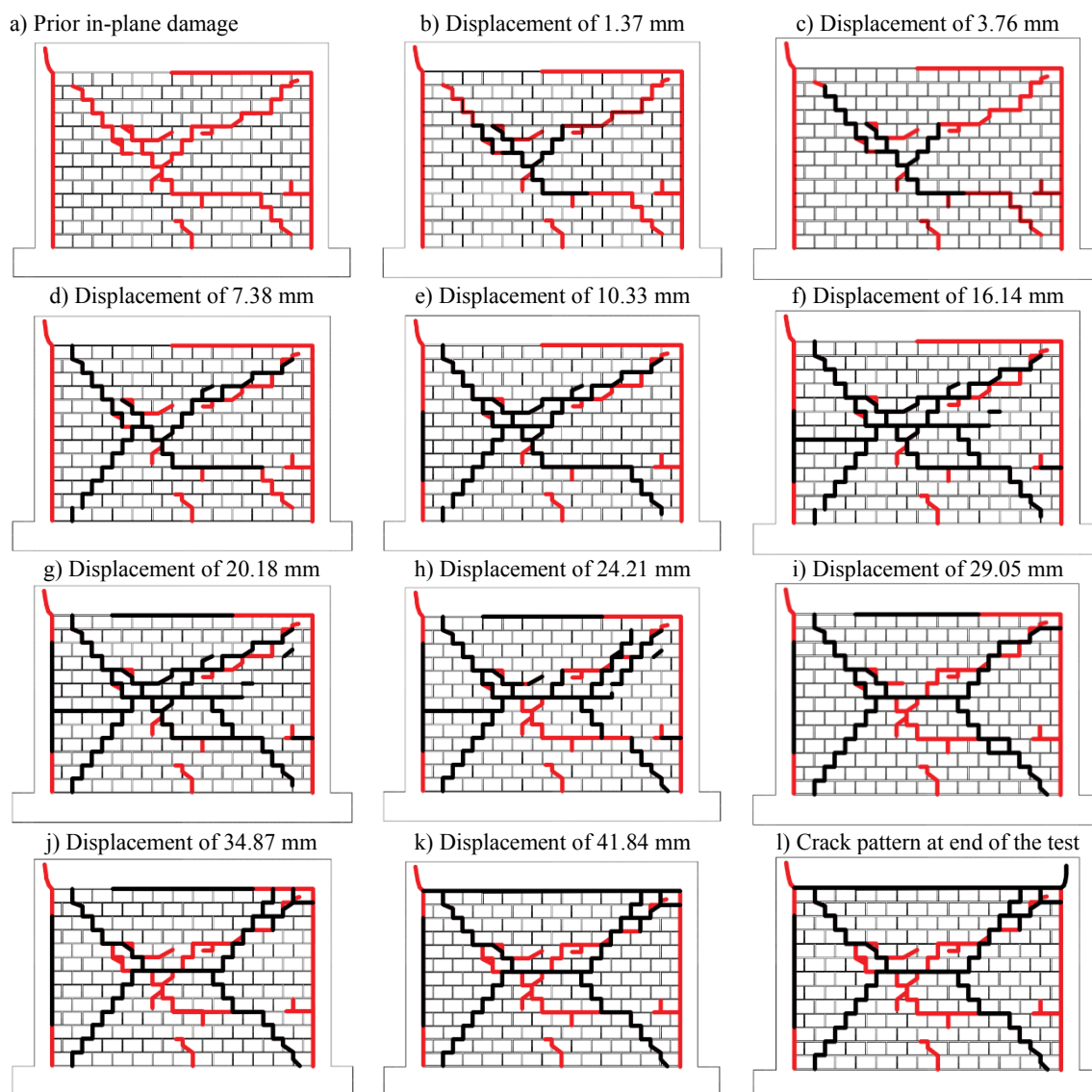


Figure 4.45 Crack propagation of SIF-IO(0.3%)-2L(NC)-B



Figure 4.46 Final cracking pattern of the specimen

#### 4.5.4.4 Deformation of the infill

The deformation of the infill at different points with respect to the control point is shown in Figure 4.47. It is observed that center point of the infill, which is assumed as control point, has the highest deformation during the out-of-plane loading. The exception refers to the displacement of 56mm in which the specimen collapsed and the displacement recorded at the upper part of the infill exceeded the displacement at the control point.

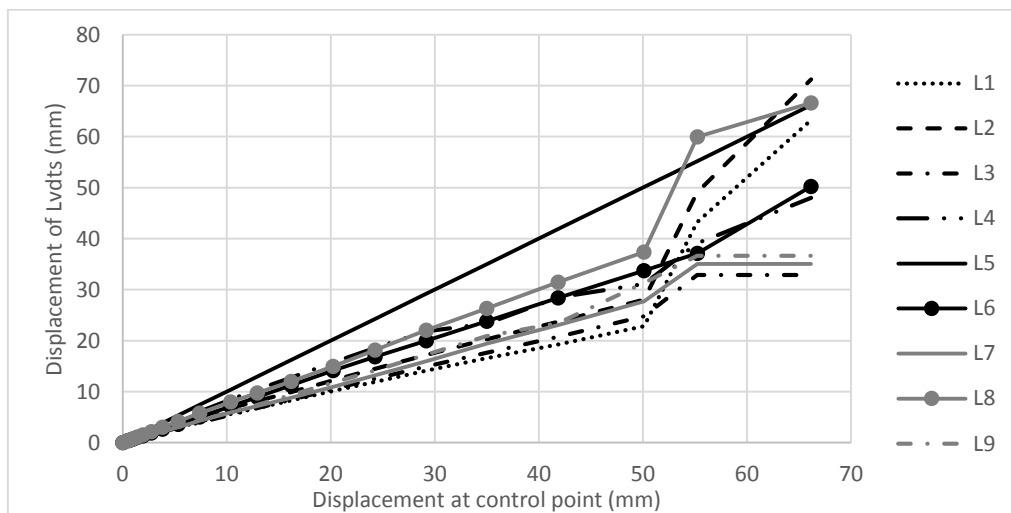


Figure 4.47 Deformation of different points in the infill with respect to the control point

The deformation of the infill along the central vertical (L2, L5 and L8) and central horizontal profiles (L4, L5 and L6) recorded by various LVDTs enables us to compare the deformation of the infill in the central profiles in relation to the control point, see Figure 4.48. It is observed that during the out-of-plane testing the upper part of infill exhibited higher deformation than the bottom part, which should be associated to the some movement observed in the upper interface between the masonry infill and the rc frame. On the other hand, it is seen that the infill presented an almost symmetric deformation in the horizontal direction, given that the deformation recorded by LVDTs L4 and L6 are practically coincident, Figure 4.48b. This result indicates that the displacements at the vertical interfaces are negligible.

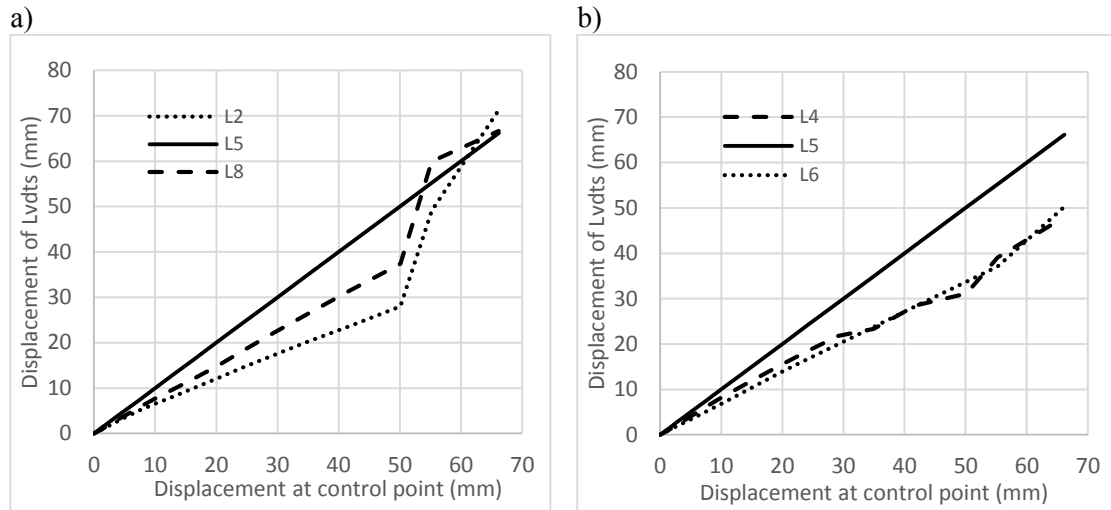


Figure 4.48 comparison between the deformation of a) upper and bottom part of infill b) right and left part of infill

This assumption is confirmed through the evolution of the displacements measured at infill-rc frame interfaces, see Figure 4.49. It is clear that the left interface started to slide earlier than the others, which was also detected visually, according to what was already discussed in the cracking patterns. However, the trend is decreasing at higher displacements, stabilizing at 2mm and increasing for later stages of loading until approximately 4mm in the collapse of specimen. It is stressed that the measured values are very low, which justifies their negligible influence on the cracking pattern of the infill. On the other hand, by increasing the out-of-plane imposed displacements, the upper interface slid towards out-of-plane direction and a horizontal crack appeared in the upper interface. In this case, the cracking developed along the entire upper interface. The results confirm that almost no sliding occurred in the bottom and right interfaces.

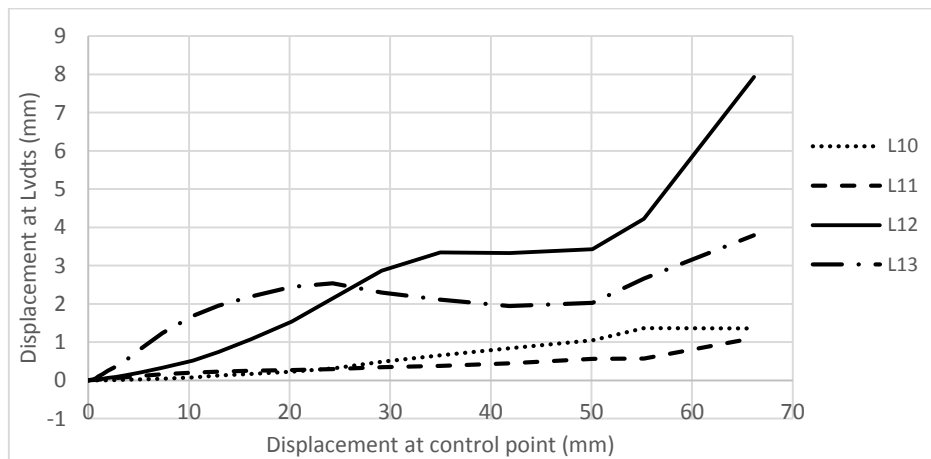


Figure 4.49 Deformation of the interfaces during out-of-plane loading

In a more integrated way, the out-of-plane deformation of the masonry infill during the out-of-plane loading is shown in Figure 4.50 as contour lines. It is observed that the infill deforms almost symmetrically during the out-of-plane loading even if there are some differences in the deformations of the upper and bottom part of the infill. The formation of two-way arching mechanism in this specimen could be confirmed by deformation scheme of the infill during out-of-plane loading as shown in Figure 4.50. Also the crack pattern developed in the specimen

reveals its compatibility with the crack pattern of two-way slabs drawn via yield line theory. This mechanism is important in the resistance to out-of-plane loadings and it seems that it develops even after presence of prior in-plane damage.

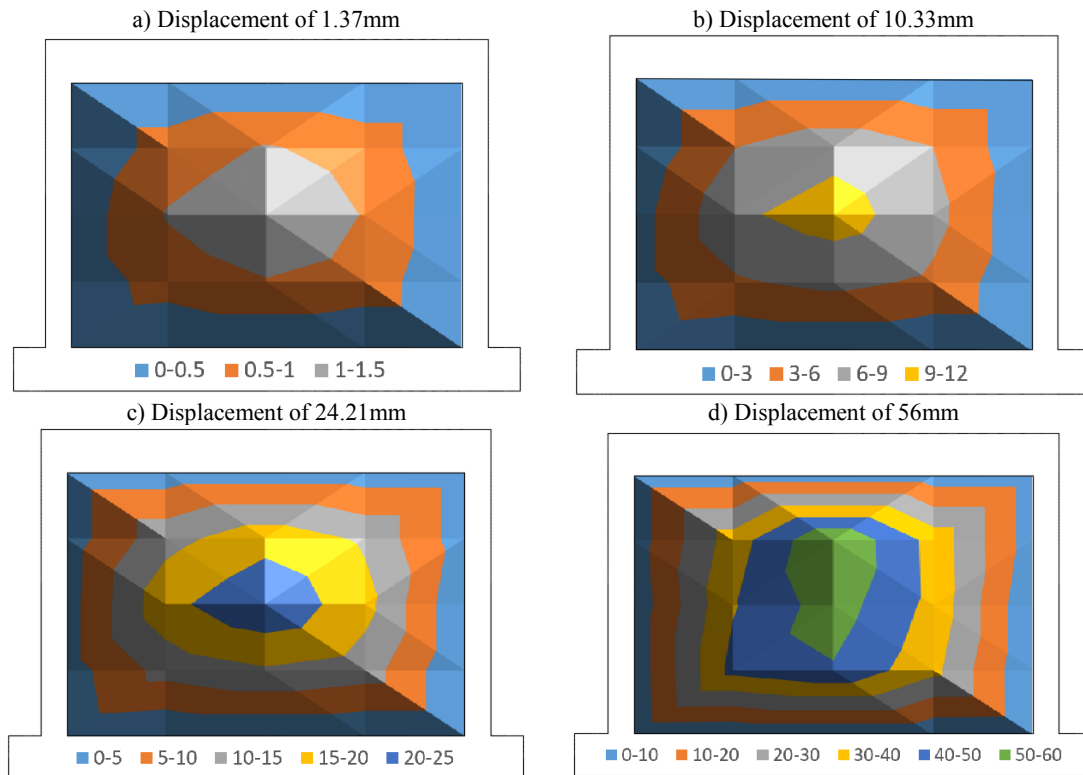


Figure 4.50 Deformation of the infill at different out-of-plane displacements

The plastic deformation of the infill at each cycle for a given out-of-plane induced displacement is shown in Figure 4.51.

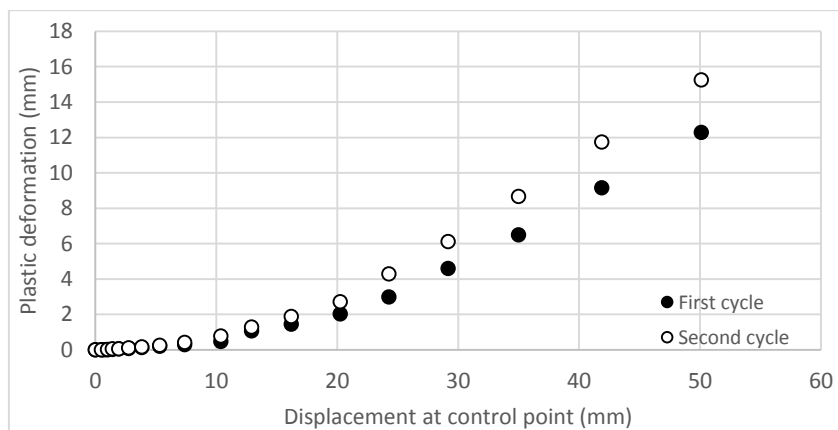


Figure 4.51 Plastic deformation of the infill at two successive cycles

It is observed that the plastic deformation increases by increasing the applied out-of-plane displacement, due to the propagation of cracks. It is also clear that the plastic deformation obtained for the second cycle of each pre-defined out-of-plane displacement is higher than that of the first cycle and the difference between them increases at higher displacements. This is attributed to the stiffness degradation of the masonry infill and to the propagation of damage

between the cycles. Similar to the previous specimens, the plastic deformation at each cycle could be approximated with a polynomial function of second order, see Figure 4.52.

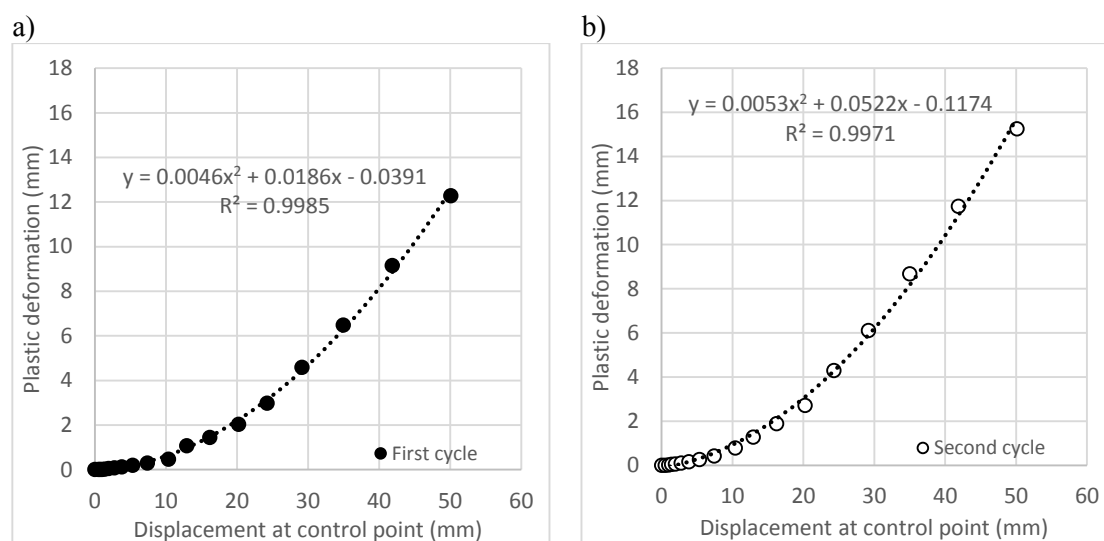


Figure 4.52 Plastic deformation of SIF-IO(0.3%)-2L(NC)-B at two successive cycles; a) first cycle b) second cycle

#### 4.5.4.5 Energy dissipation capacity

The dissipation of energy in the specimen at each cycle and the cumulative energy dissipation until each cycle during the out-of-plane loading is shown in Figure 4.53. It is clear that the trend of variation of the energy dissipation of the specimen is increasing, meaning that higher energy dissipation values are obtained at higher out-of-plane displacements, see Figure 4.53a. This is related to the accumulation of damage as the out-of-plane displacement increases. The total amount of dissipation of energy at displacement of 50mm in this specimen seems to be less than the one obtained in the undamaged infill wall at the same displacement. The total energy dissipated in this specimen until 50mm is about 85% of the energy dissipated in specimen SIF-O-1L-B. This should be related to the cracks developed in the prior in-plane test that served as crack path at early stages of out-of-plane loading.

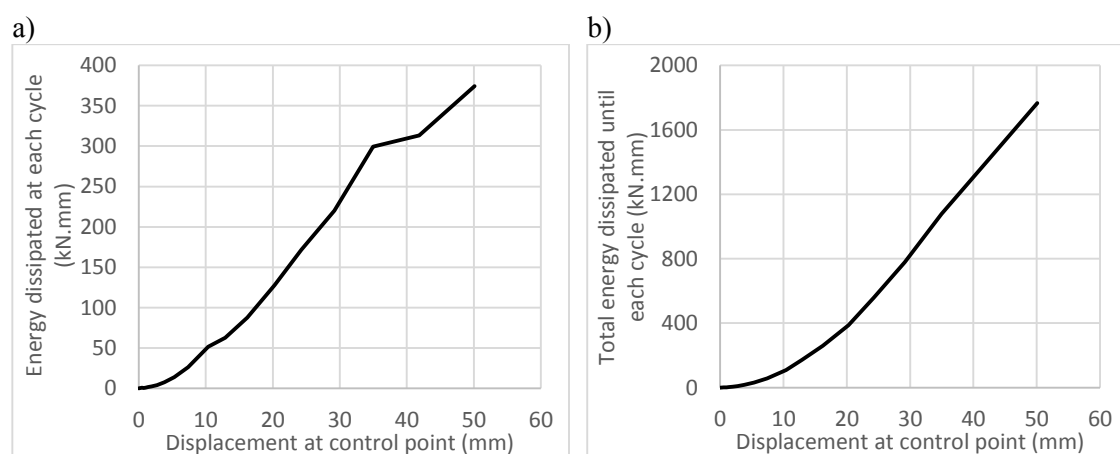


Figure 4.53 a) Energy dissipation capacity of the specimen at each cycle b) Total energy dissipation until each cycle

### 4.5.5 Specimen SIF-IO(0.5%)-2L(NC)-B

#### 4.5.5.1 Load-displacement response

The out-of-plane force-displacement diagram of the specimen subjected to previous in-plane damage, corresponding to 0.5% lateral drift, is shown in Figure 4.54. Due to the presence of prior in-plane damage in the specimen, the damage caused by out-of-plane loading progressed at early stages of loading. During the early out-of-plane deformation, previous in-plane cracks opened again, being the onset of re-opening of existing cracks at the out-of-plane displacement of 1.92mm, corresponding to the force of 5.4kN. This is accompanied by a very early change of stiffness at very low values of out-of-plane displacement. Significant decreasing of the slope of the force-displacement diagram was recorded at the out-of-plane displacement of 12.91mm, corresponding to the force of 18.6kN. The maximum out-of-plane force of 26.4kN was observed at displacement of 50.21mm. At displacement of 56.9mm corresponding to out-of-plane force of 25.1kN the masonry infill collapsed suddenly and the displacement in the control point increased to 76.5mm immediately.

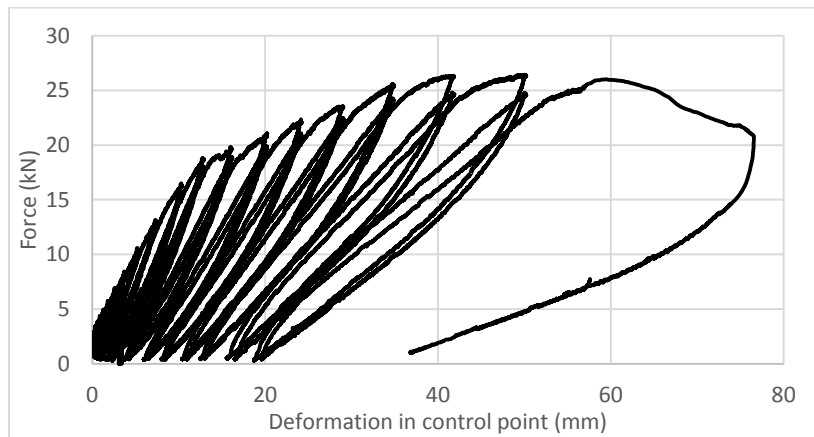


Figure 4.54 Force-displacement response of SIF-IO(0.5%)-2L(NC)-B

The strength degradation obtained for two successive cycles is shown in Figure 4.55. Similar to the previous specimens, strength degradation starts after significant opening of existing cracks and increases due to their propagation in the infill. However, it should be stressed that no significant strength degradation was observed, being the maximum value of 6% recorded for the peak load.

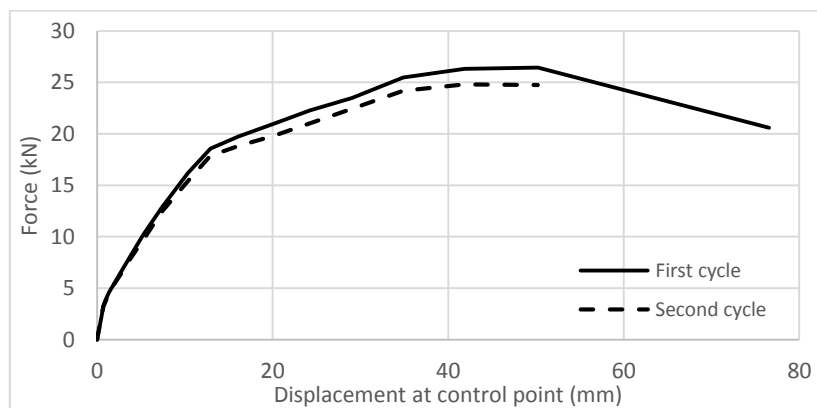


Figure 4.55 Monotonic force-displacement envelopes for two successive cycles

#### 4.5.5.2 *Stiffness degradation curve*

The trend of variation of the secant stiffness of the specimen during the out-of-plane loading is shown in Figure 4.56. Similar to the previous masonry infills, this specimen exhibits a logarithmic trend of reduction on the secant stiffness as the out-of-plane displacement increases. It is evident that the highest amount of the initial stiffness is degraded at lower displacements. For instance, 55% of stiffness degradation occurred until out-of-plane displacement of 10.33mm.

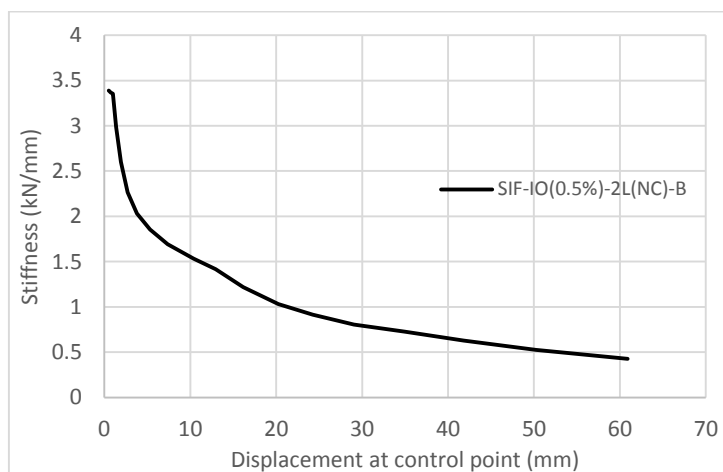


Figure 4.56 Stiffness degradation curve for specimen SIF-IO(0.5%)-2L(NC)-B

#### 4.5.5.3 *Crack patterns*

The propagation of cracks in the specimen during out-of-plane loading is shown in Figure 4.57. The cracks that were formed due to prior in-plane loading are drawn in red lines. It is clear that the cracks that previously opened in the central region of the infill during the prior in-plane loading were re-opened at out-of-plane induced displacement of 1.92mm, corresponding to the force of 5.4kN, see Figure 4.57b. The cracking pattern contains the horizontal crack in the mid part of the infill along with some diagonal cracks connected to it. By applying higher displacements, it was seen that other horizontal and vertical cracks that were formed due to the prior in-plane damage, re-opened in the out-of-plane loading of the specimen, see Figure 4.57c-d. The cracking of the upper interface happened at displacement of 7.38mm corresponding to the out-of-plane force of 12.8kN, see Figure 4.57d. For this displacement level, the upper interface started to crack, and horizontal crack along the interface was appeared. It seems that prior in-plane damage of the specimen accelerated the cracking of the upper interface.

Increasing the out-of-plane displacements in the control point resulted in flexural cracking of the upper rc beam at its mid span at displacement of 20.18mm corresponding to the out-of-plane force of 21kN, see Figure 4.57g. After this displacement, some of the cracks that were formed previously were closed, namely diagonal cracks connecting the central horizontal crack to the upper right corner of the masonry infill. Additionally, some new cracks were formed and the final cracking pattern at the out-of-plane displacement of 56.9mm in which the specimen was collapsed is shown in Figure 4.57l. It should be stressed that the cracking patterns observed in the out-of-plane loading are mostly influenced by the in-plane cracking that previously were developed due to the prior in-plane lateral drift of 0.5%. Only for higher levels of out-of-plane displacement new cracks developed. In addition, it should be mentioned that the higher density of cracks that is found to characterize the out-of-plane cracking of the specimen at the final stage, is directly

related to its prior cracking. It is clear that applying higher amount of prior in-plane drift can influence the final cracking pattern of the specimen in out-of-plane direction. In this case its resisting mechanism (two-way arching mechanism supported on three sides and one free edge) is similar to the specimen that constructed with mason B.

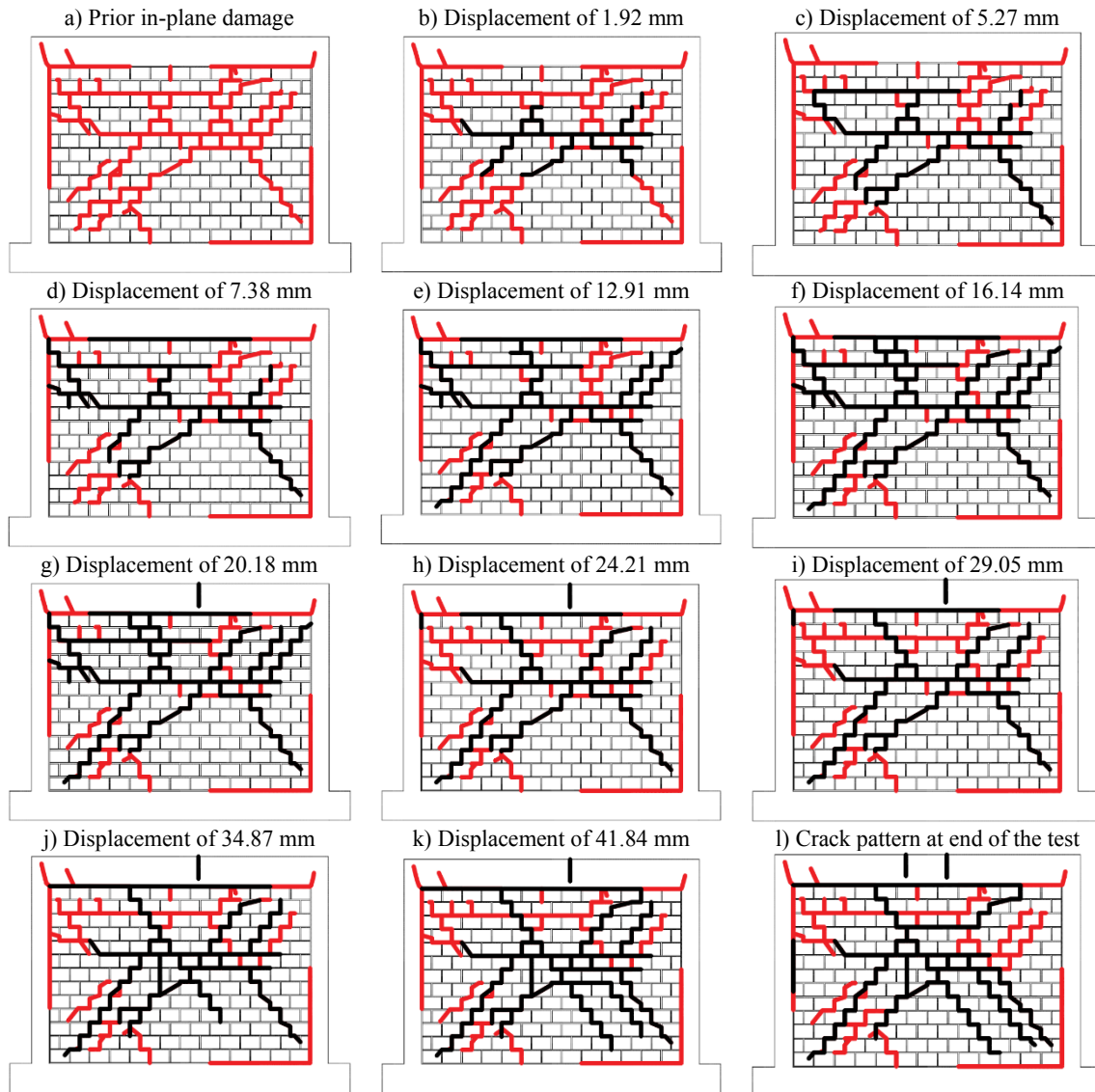


Figure 4.57 Crack propagation of SIF-IO(0.5%)-2L(NC)-B

#### 4.5.5.4 Deformation of the infill

The deformation of the infill at different points is shown in Figure 4.58. It is observed that the center point of the infill, which is assumed as control point, presented the highest deformation during the out-of-plane loading except in the final cycle of the loading in which the LVDT L8 placed at near the top interface presented the maximum displacement.

The displacements measured along the central vertical profile (LVDTs L2, L5 and L8) and along the central horizontal profile (LVDTs L4, L5 and L6) are presented separately in Figure 4.59. It is observed that the LVDT L8 presented almost similar displacements with the central LVDT L5 from early stages of deformations. This indicates that the failure of the upper infill-rc frame interface and consequently its out-of-plane movement occurred since the beginning of the out-of-



plane test. This is certainly related to the prior in-plane damage induced in the infill and mainly to the cracking of the upper interface associated to prior in-plane loading. It is also observed that the LVDTs L4 and L6 presented the same deformations and their values are clearly lower than the values recorded in the central LVDT L5, see Figure 4.59b, which demonstrates the symmetric deformation of the masonry infill along the horizontal profile.

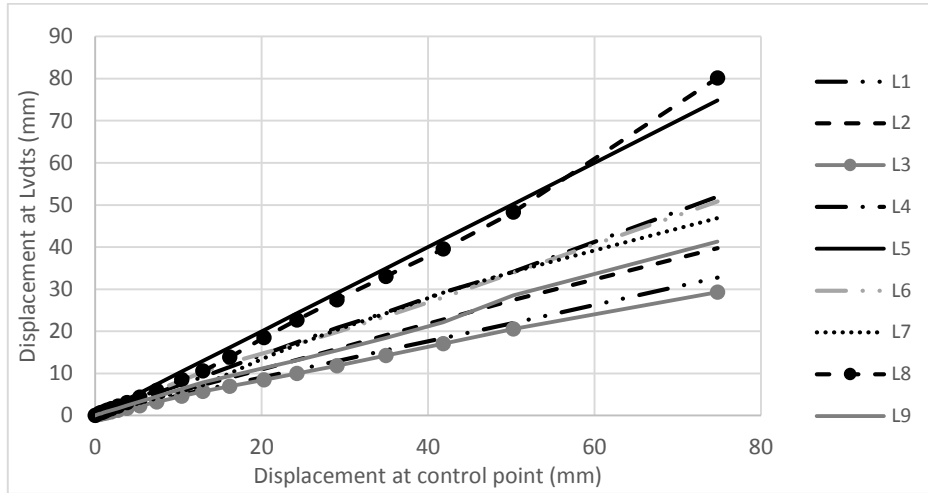


Figure 4.58 Deformation of infill at different points

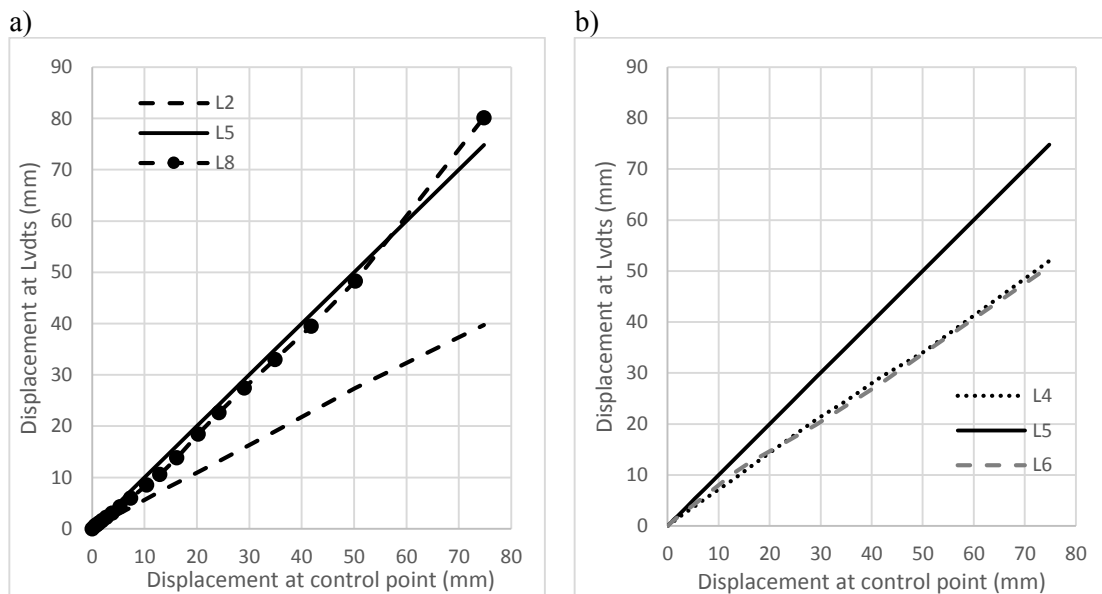


Figure 4.59 Comparison of the deformation of a) central vertical profile b) central horizontal profile

The displacement recorded at each interface between infill and the surrounding frame during out-of-plane loading is shown in Figure 4.60. These records confirm that the sliding of the upper interface occurs from early stages of loading, increases sharply after the out-of-plane displacement of 16.14mm and reaches its maximum value when the peak force is achieved. It is also seen that the other interfaces present very low deformations meaning that no sliding occurs along them.

In an integrated manner, the deformation of the infill during the out-of-plane loading is shown in Figure 4.61 as contour areas corresponding to different ranges of displacements. It is clear that from first levels of loading the upper part of the infill moves similar to the center part, highlighting

the formation of two-way arching mechanism supported by three fixed supports and one semi-rigid support (upper interface). This is particularly clear from the deformation of the infill at higher displacements, see Figure 4.61c and d.

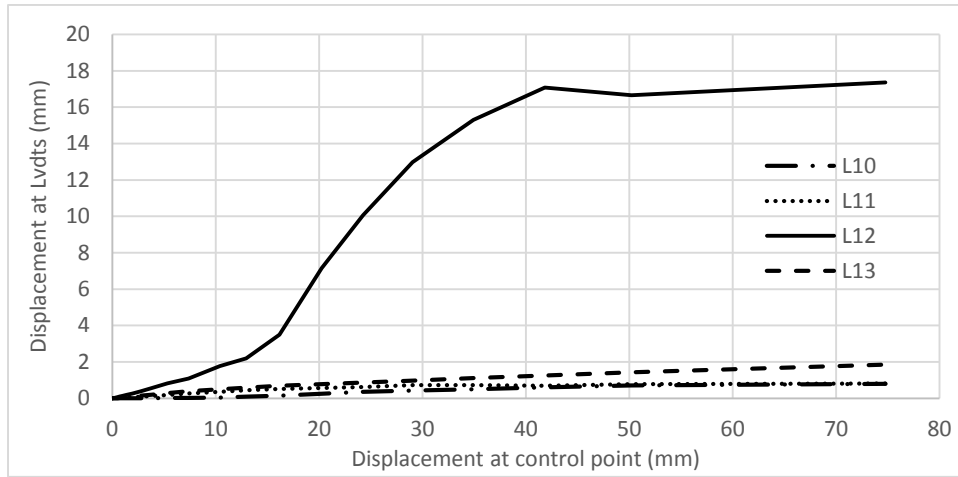


Figure 4.60 Displacement of each interface between infill and RC frame during out-of-plane loading

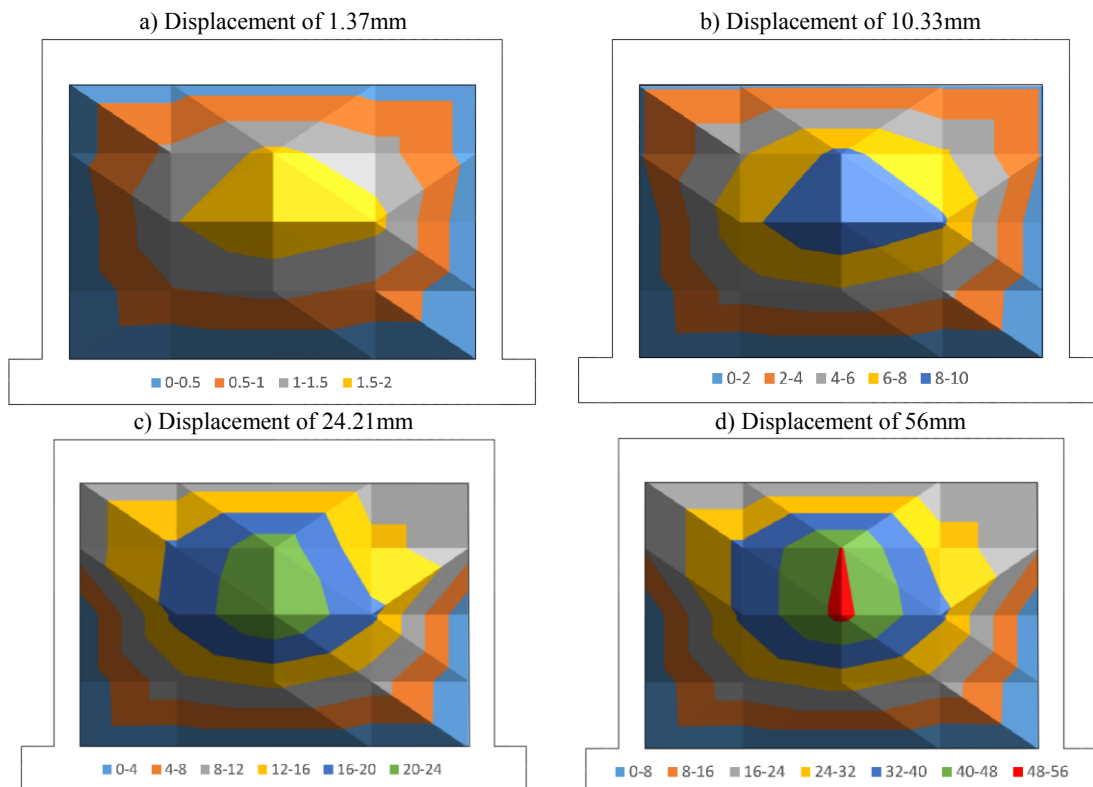


Figure 4.61 Deformation of the infill at different out-of-plane displacements

The plastic or residual deformation of the infill is shown in Figure 4.62. It is concluded that by imposing the same pre-defined level of displacement to the specimen, plastic deformation increases in its second cycle, even if it is not significant. This should be related to the slight propagation of cracks in the second cycles. It is also evident that, similar to the previous specimens, the plastic deformation of this specimen at each cycle can be approximated by a polynomial function of second order, see Figure 4.63.

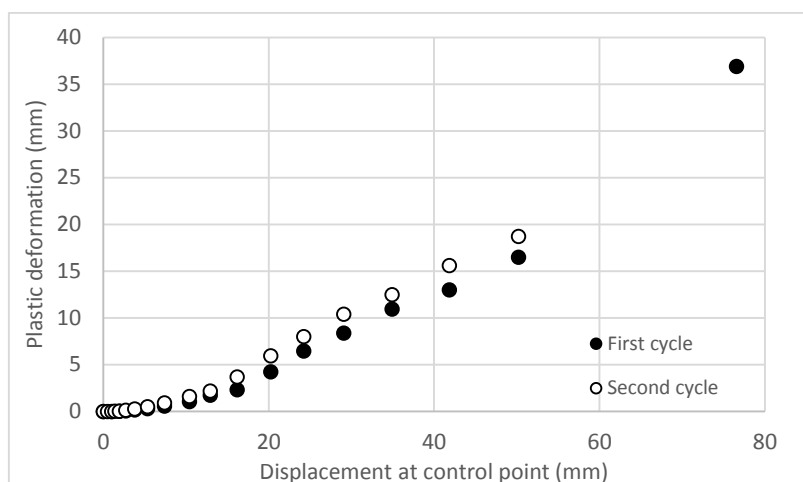


Figure 4.62 Plastic deformation of the specimen at each successive cycles

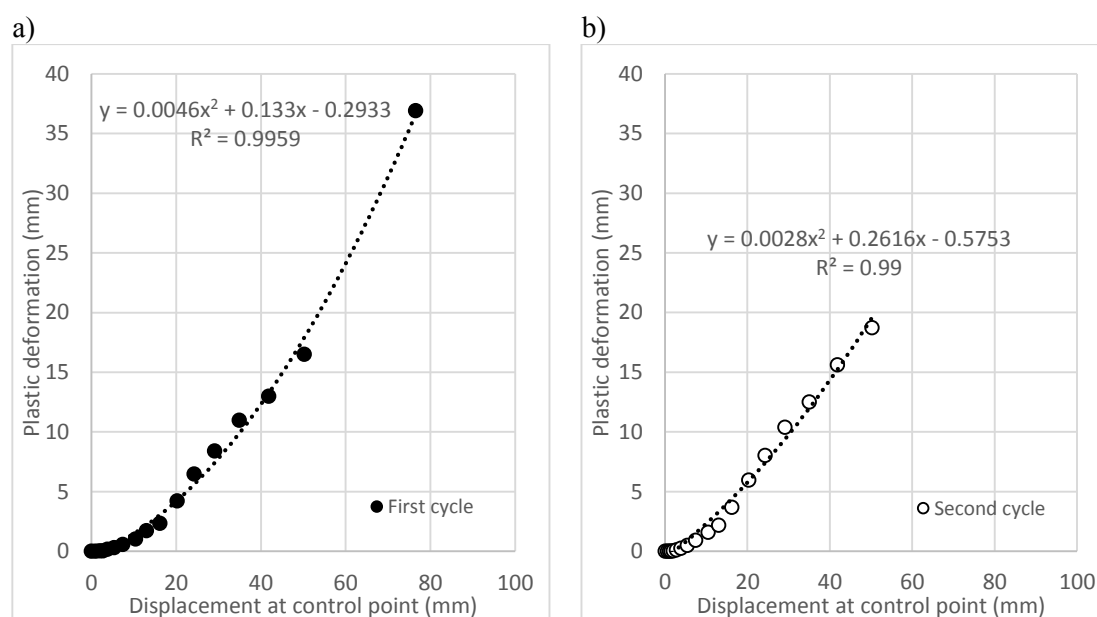


Figure 4.63 Plastic deformation of SIF-IO(0.5%)-2L(NC)-B at two successive cycles; a) first cycle b) second cycle

#### 4.5.5.5 Energy dissipation capacity

The dissipation of energy at each cycle and the cumulative energy dissipated until each cycle during the out-of-plane loading is shown in Figure 4.64. Higher amount of dissipation of energy is obtained at higher displacements, which is related to the higher density of cracks at higher imposed displacements. It is also clear that the total dissipation of energy in this specimen is relatively lower than the one obtained for the specimen with prior in-plane damage corresponding to the lateral drift of 0.3%. Until the displacement of 50mm the total energy dissipated in the specimen is 68% of the specimen with less in-plane damage (SIF-IO(0.3%)-2L(NC)-B). It seems that presence of higher prior in-plane damage reduces the total dissipation of energy in the out-of-plane direction.

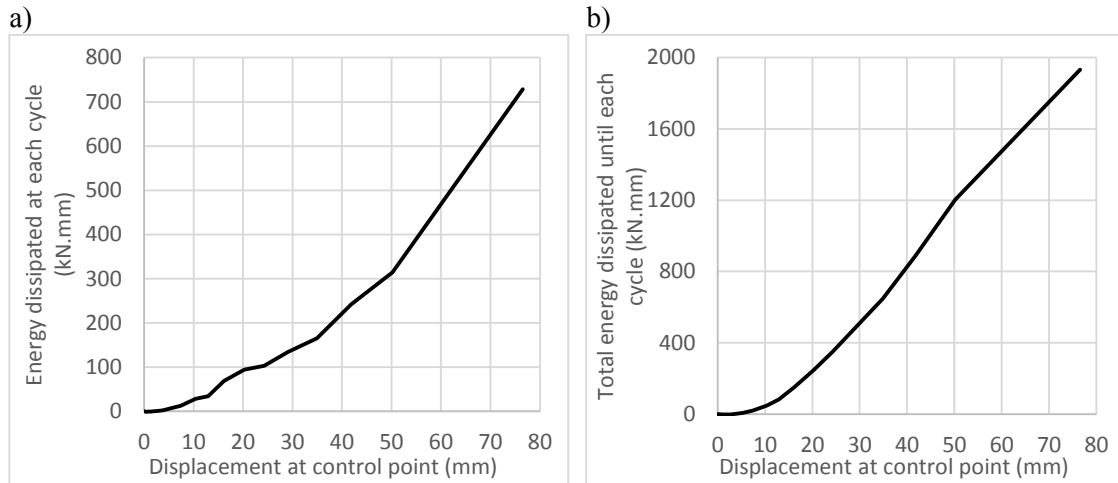


Figure 4.64 a) Energy dissipation capacity of the specimen at each cycle b) cumulative energy dissipation of the specimen until each cycle

#### 4.5.6 Specimen SIF-IO(1%)-2L(NC)-B

This specimen was initially subjected to the in-plane drift of 1%. After the test, the internal leaf was removed and the out-of-plane test was performed on the external leaf. During the removing of the internal leaf, when the vertical forces of the columns were removed, it was observed that the external leaf had totally lost its connection with upper beam and oscillated with a negligible out-of-plane load. It was assumed that the exterior leaf was unstable and would fall down with a low level of out-of-plane load. However, when the axial forces were applied to the column sections, the gap between the upper beam and infill was filled and the external leaf recovered its stability. Notice that between the in-plane and out-of-plane loading the vertical load was released.

##### 4.5.6.1 Load-displacement response

The force-displacement diagram obtained for the out-of-plane loading is shown in Figure 4.65. The cracking in the specimen initiated at displacement of 3.76mm by re-opening the cracks that previously formed in the prior in-plane loading. By imposing higher out-of-plane displacements to the specimen, the out-of-plane load increased until it reached the maximum force of 20.26kN at out-of-plane displacement of 60mm in the control point. At the maximum force, the upper interface was totally separated from the frame, which led to the significant reduction of the force at displacement of 80mm. At this step, the infill lost its stability and the test was stopped to keep the instrumentation intact.

The monotonic force-displacement envelope of the specimen at each successive cycle is shown in Figure 4.66. It is clear that the strength reduction of the specimen is not significant until the maximum force is achieved but it reached 30% at displacement of 80mm.

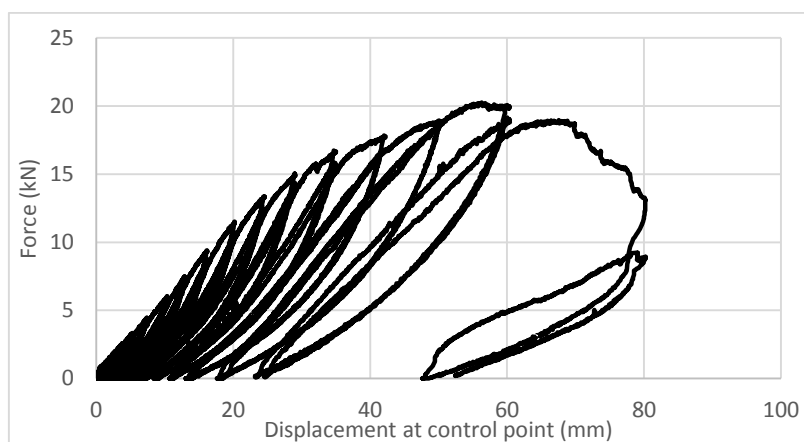


Figure 4.65 Force-displacement diagram of SIF-IO(1%)-2L(NC)-B during out-of-plane loading

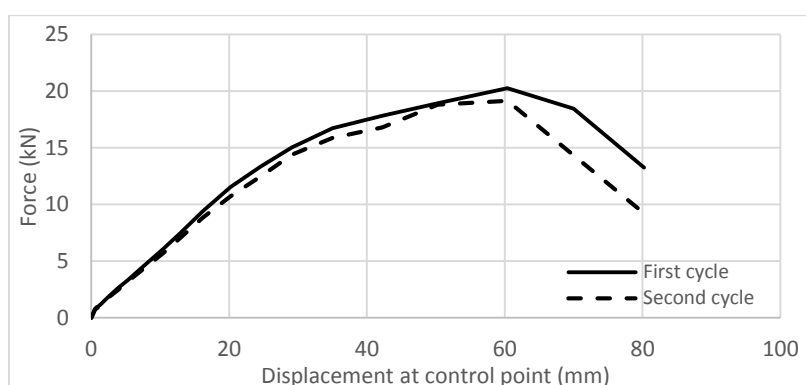


Figure 4.66 Monotonic force-displacement envelop of SIF-IO(1%)-2L(NC)-B at each successive cycle

#### 4.5.6.2 *Stiffness degradation curve*

The secant stiffness of the specimen at each cycle is obtained by calculating the slope of the line connecting the origin and the maximum force attained in the first cycle of loading, see Figure 4.67. It is concluded that the presence of prior in-plane damage has decreased the amount of the initial stiffness in the out-of-plane direction. It is clear that more degradation of the stiffness occurred at lower displacements. For instance, 51% of the initial stiffness was degraded until the out-of-plane displacement of 5.33mm.

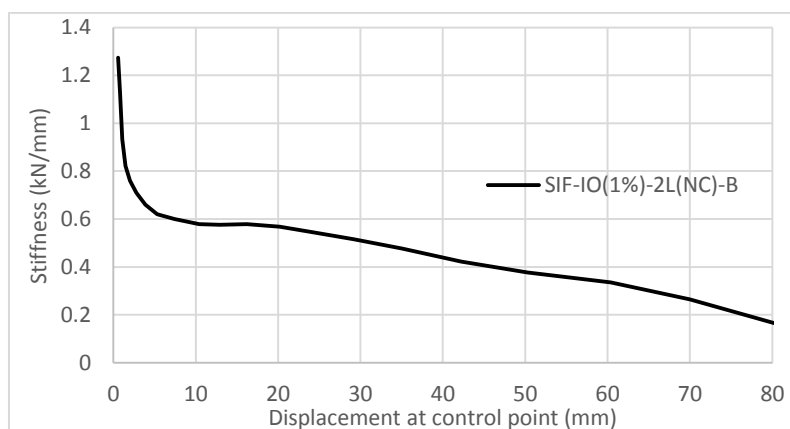


Figure 4.67 Stiffness degradation curve for specimen SIF-IO(1%)-2L(NC)-B

#### 4.5.6.3 Crack patterns

The crack propagation observed during out-of-plane loading is shown in Figure 4.68. Also in these cracking schemes, the crack patterns developed during previous in-plane test are highlighted with red lines. The onset of crack opening due to out-of-plane induced displacements was observed at displacement of 3.76mm corresponding to the out-of-plane force of 2.59kN. At this stage, previously opened cracks re-opened at the central region of the masonry infill in stair stepped pattern, see Figure 4.68b. Also at this stage, the infill panel was totally separated from the upper rc beam. The crack density increased by increasing the imposed displacements which was generally overlapping the existing cracks through mortar joints. It is clear that the out-of-plane cracking scheme is totally related to the cracking pattern of the prior in-plane loading. It means that by applying the out-of-plane displacements the cracks that were formed in the prior in-plane loading are getting visible again. At the out-of-plane displacement of 7.38mm, some horizontal cracks were observed in the upper part of the infill, connecting the existing diagonal cracks to the vertical crack at the left infill-frame interface.

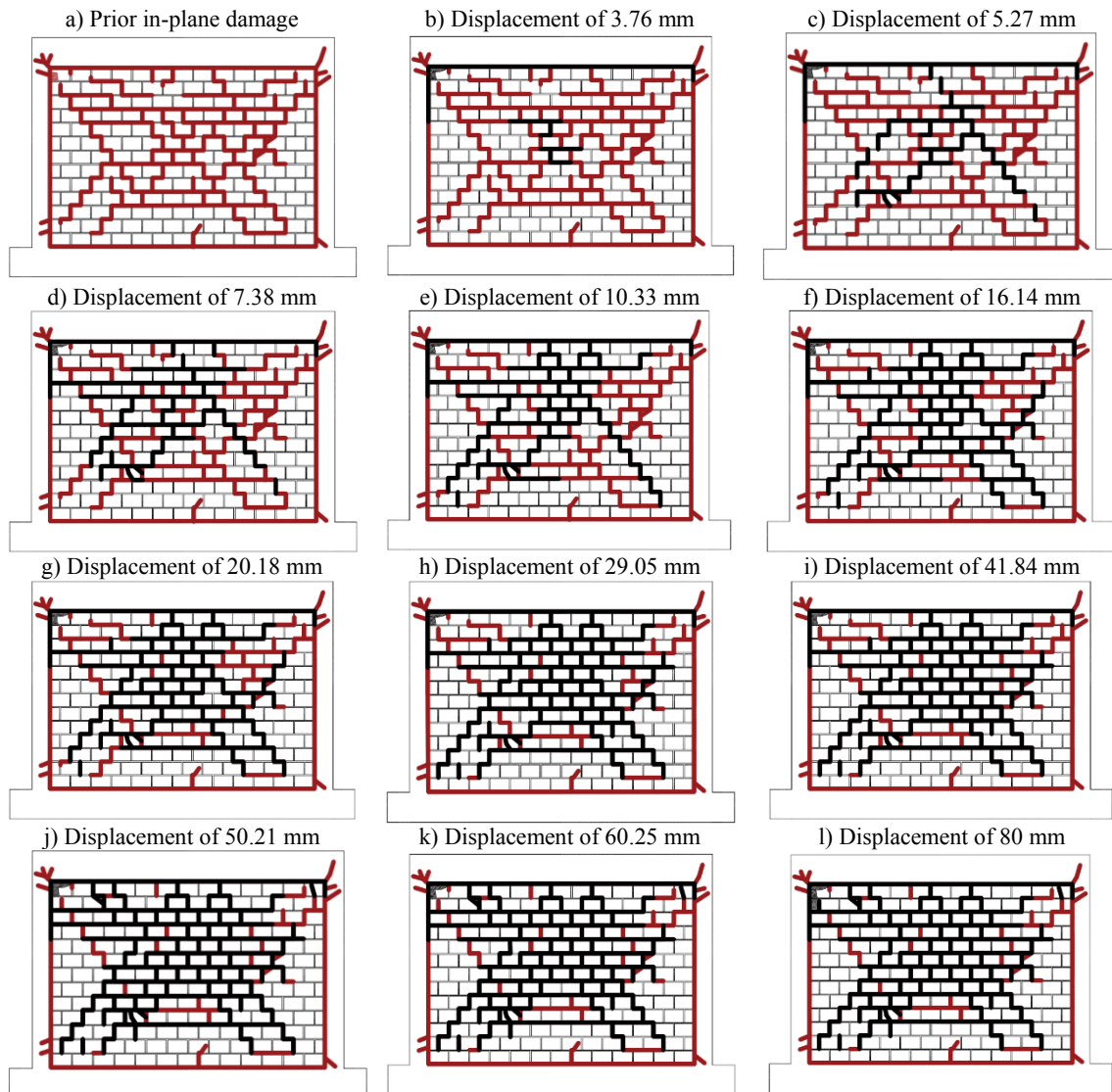


Figure 4.68 Crack propagation of SIF-IO(1%)-2L(NC)-B

This cracking pattern was compatible with the cracking pattern of two-way slabs that have three rigid supports and one almost free edge. The free edge is assumed to be the top interface between infill and rc frame. This boundary can be viewed as a semi-rigid edge as it does not completely restrain the movement of the upper infill-frame interface, neither does it allow to move freely. By applying further displacements to the specimen, more diagonal cracks could be observed in the bottom part of the infill. It should be also mentioned that additional new cracks were developed beyond the pre-existing cracks. Furthermore, it is observed that the pre-existing cracks in the interface between masonry infill and rc frame did not evolve during out-of-plane test, apart from the upper interface.

4.5.6.4 *Deformation of the infill*

The deformation of the masonry infill at different points of the infill is drawn with respect to the deformation measured in the control point. It is clear that all points have lower deformations than the center point, unless LVDT L8, which is located at the top part of the control point, see Figure 4.69.

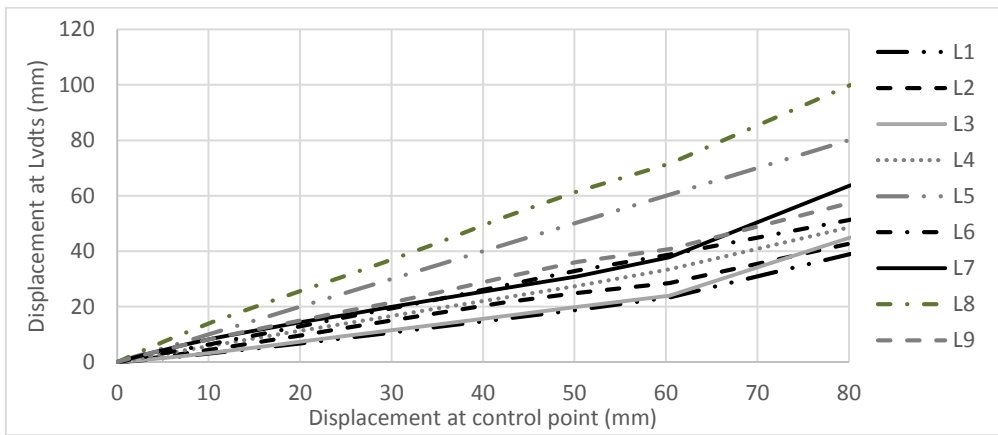


Figure 4.69 Deformation of the infill at different points with respect to the deformation of the control point

The out-of-plane displacement along the central vertical (LVDTs L2, L5 and L8) and central horizontal (LVDTs L4, L5 and L6) profiles are shown in Figure 4.70.

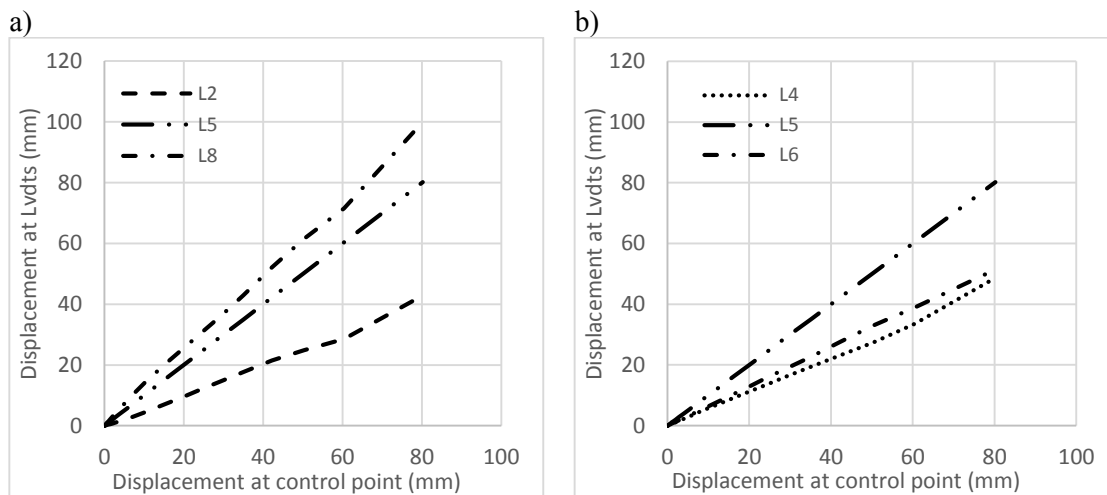


Figure 4.70 Comparison of the deformation of a) central vertical profile b) central horizontal profile

It is evident that along the vertical profile (Figure 4.70a), the displacements are increasing in height, being the maximum displacement of the infill recorded in LVDTs L8 as the result of the sliding of the top interface and behaving like an almost free edge, whereas the bottom interface is totally in contact with the rc frame. The deformation of central horizontal profile is shown in Figure 4.70b. It is observed that similar to the masonry infills discussed previously, the displacements measured in the LVDT L4 and L6 are very close, which demonstrate the symmetric deformation of the specimen in the horizontal direction.

The sliding of the infill from its surrounding frame in the out-of-plane direction at different interfaces is shown in Figure 4.71. As it was discussed previously in Figure 4.68, it is evident that the sliding of the masonry infill in relation to the rc beam initiated from the beginning of the out-of-plane test. On the other hand, the sliding of the bottom and vertical interfaces is negligible. This also confirms the boundary conditions of the masonry infill, namely three fixed and one almost free boundary.

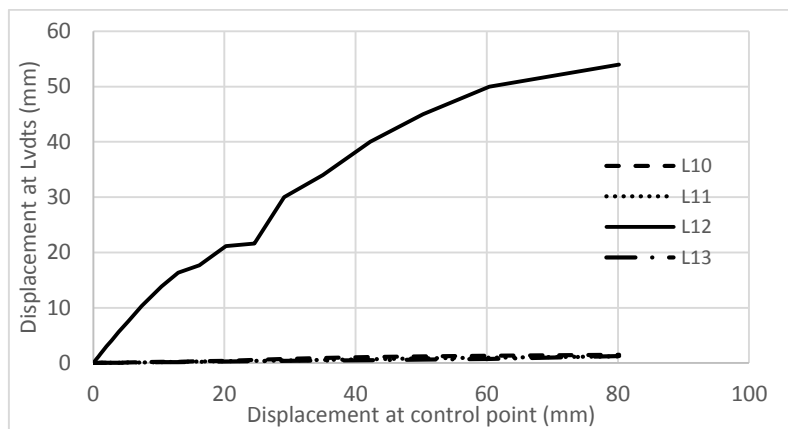


Figure 4.71 Displacement measured in the interface during out-of-plane loading for specimen SIF-IO(1%)-2L(NC)-B

The scheme of the deformation field of the masonry infill at different imposed displacements is shown in Figure 4.72. It is clear that the deformation of the masonry infill is compatible with deformation of a slab with three completely fixed and one almost free boundary at the top since the beginning of the test. It appears that at lower stages of deformation, the major displacement occurred at the top part of the infill. At higher displacements (41.84mm and 80mm), the upper interface deformed less than LVDT L8 along the central vertical profile. This can be associated to some level of friction between the masonry infill and top rc beam.

The plastic deformation of the specimen in the first and second cycles of loading is shown in Figure 4.73. It seems that the plastic deformations of each successive cycles are very similar until the last cycle in which the difference between them increases. From Figure 4.74 it is clear that the plastic deformation of specimen at each cycle could be estimated by polynomial function of second order, similar to the other specimens.



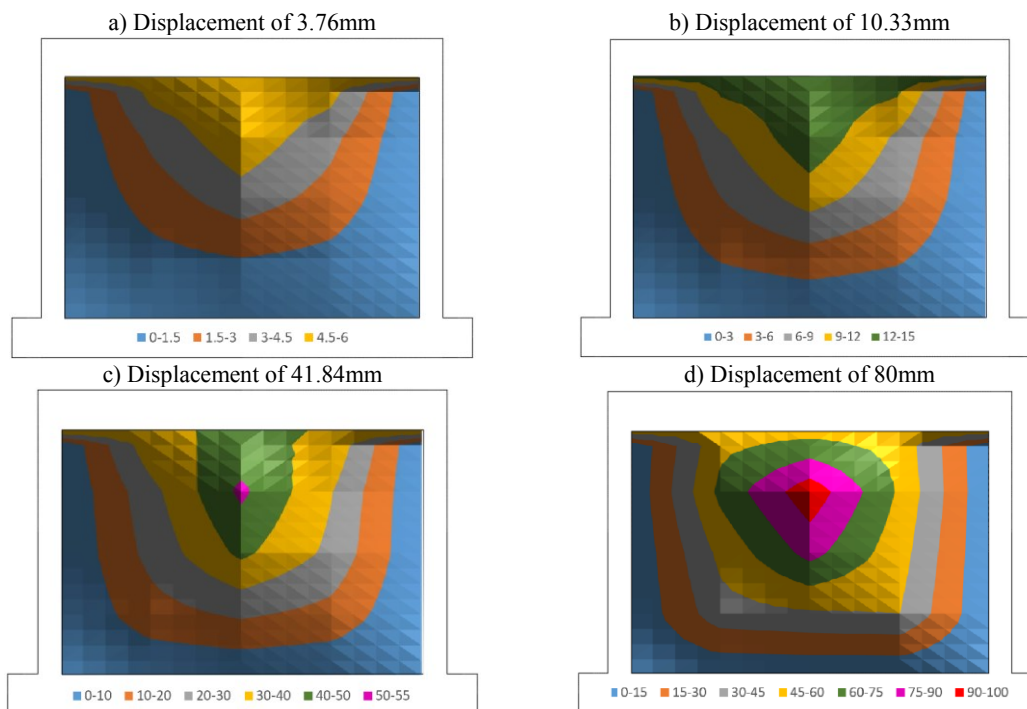


Figure 4.72 Deformation of the infill at different out-of-plane displacements

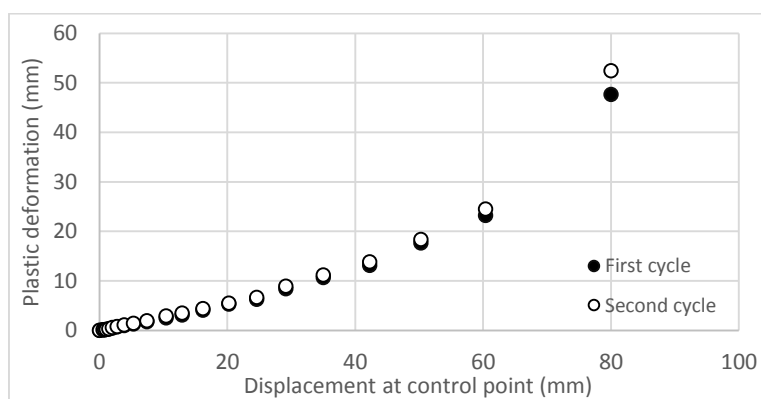


Figure 4.73 Plastic deformation of the specimen at two successive cycles

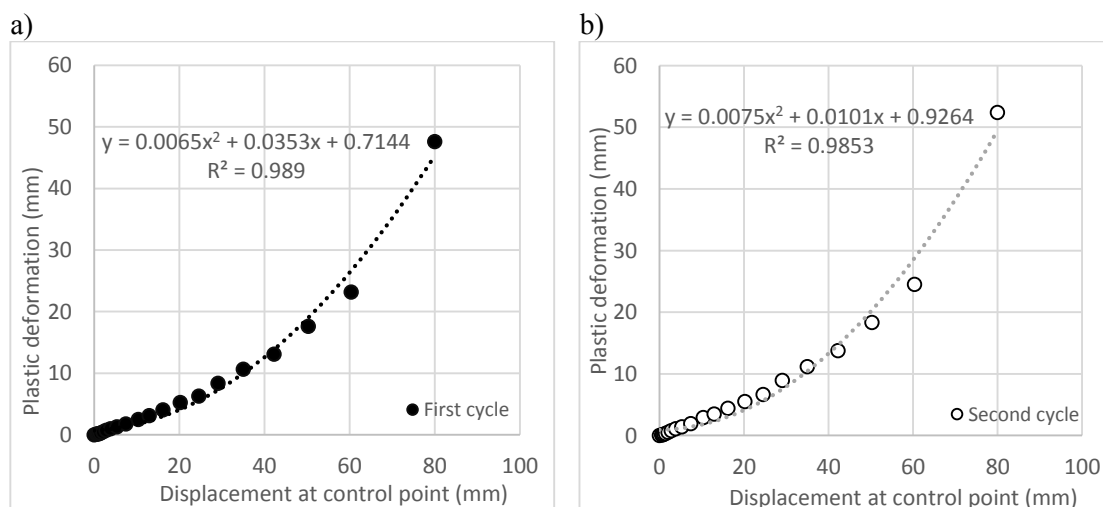


Figure 4.74 Plastic deformation of the specimen at two successive cycles; a) first cycle b) second cycle

#### 4.5.6.5 Energy dissipation capacity

The dissipation of energy until each cycle and the cumulative dissipated energy are shown in Figure 4.75. It is clear that at higher imposed out-of-plane displacements, higher amount of energy dissipation was obtained. This is generally related to the propagation of higher density of cracks at higher displacements. It is clear that the curve of cumulative dissipated energy of this specimen is lower than that of the specimen SIF-IO(0.5%)-2L(NC)-B. At displacement of 80mm, the total amount of dissipated energy by this specimen is 87% of the energy dissipated by the specimen with lower prior in-plane damage (SIF-IO(0.5%)-2L(NC)-B).

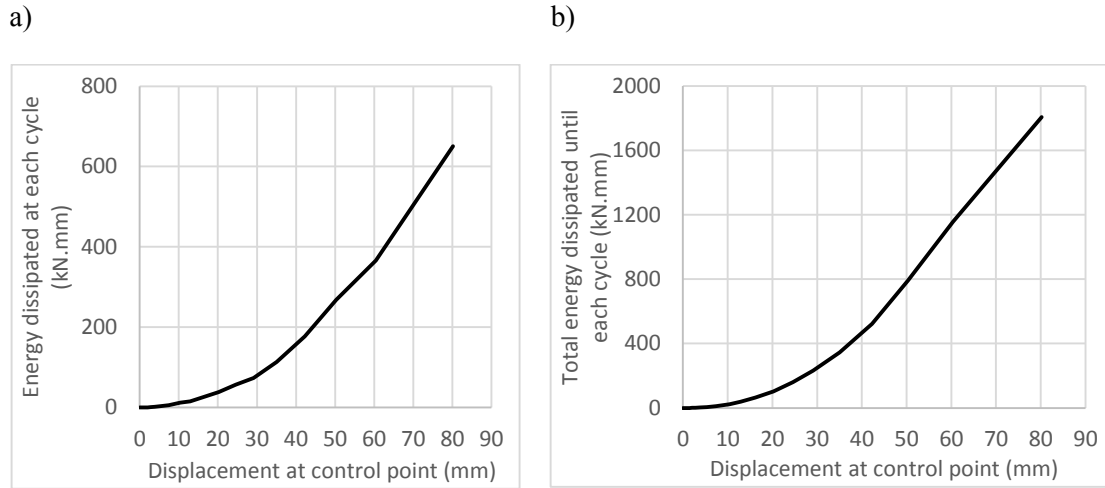


Figure 4.75 a) Energy dissipation in specimen with prior in-plane damage corresponding to 1% lateral drift b) cumulative energy dissipated until each cycle

## 4.6 Comparison of the results

The comparison of results among the specimens was based on different parameters, namely: (1) the influence of prior in-plane damage (2) construction quality (3) presence of openings and (4) energy dissipation capacity

### 4.6.1 Effect of prior in-plane damage on the out-of-plane response

The out-of-plane force-displacement monotonic envelopes of the fully infilled frames constructed with experienced mason (mason type B) are shown in Figure 4.76. The main parameters, namely initial stiffness, secant stiffness at 30% of the maximum out-of-plane force and out-of-plane resistance are presented in Table 4-2.

It is clear that the prior in-plane damage reduces both the stiffness (initial or secant stiffness at 30% of the maximum out-of-plane force) and the lateral strength of the masonry infilled frames and the reduction level depends on the severity of the damage induced by prior in-plane loading. For instance the out-of-plane resistance of the specimen with severe in-plane damage (SIF-IO(1%)-2L(NC)-B) is half of the out-of-plane strength of the specimen without prior in-plane damage. The values for the initial and secant stiffness are 10% and 5% respectively. This emphasizes that the influence of the prior in-plane damage on stiffness is rather high.

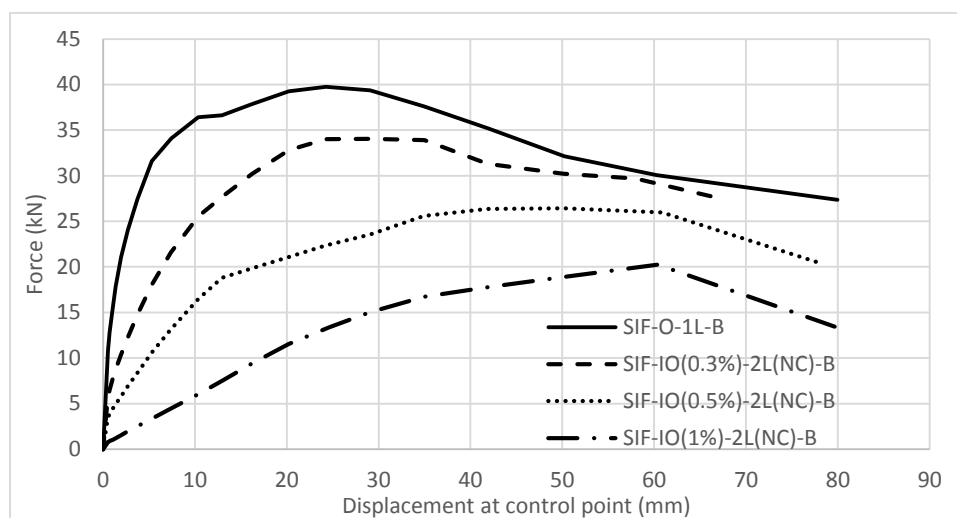


Figure 4.76 Out-of-plane force-displacement monotonic envelopes of specimens constructed with masonry type B

Table 4-2 Secant stiffness and out-of-plane strength of different specimens built with masonry type B

Model	Initial Stiffness (kN/mm)	Secant Initial Stiffness (kN/mm)	Out-of-plane strength (kN)
SIF-O-1L-B	12.5	12.5	39.8
SIF-IO(0.3%)-2L(NC)-B	6.8	4.9	34.0
SIF-IO(0.5%)-2L(NC)-B	3.4	2.0	26.4
SIF-IO(1%)-2L(NC)-B	1.3	0.58	20.3

The variation of the secant stiffness calculated at 30% of the peak force and out-of-plane strength of the specimen with respect to the prior in-plane drift values are shown in Figure 4.77. It is observed that the stiffness of the masonry infills with prior in-plane damage decreases exponentially with the damage corresponding to the distinct imposed lateral drifts of 0.3%, 0.5% and 1%. Thus, the experimental values are well fitted by an exponential function with a coefficient of correlation equal to 0.99. This means that the reduction rate for lower values of prior in-plane drift is higher.

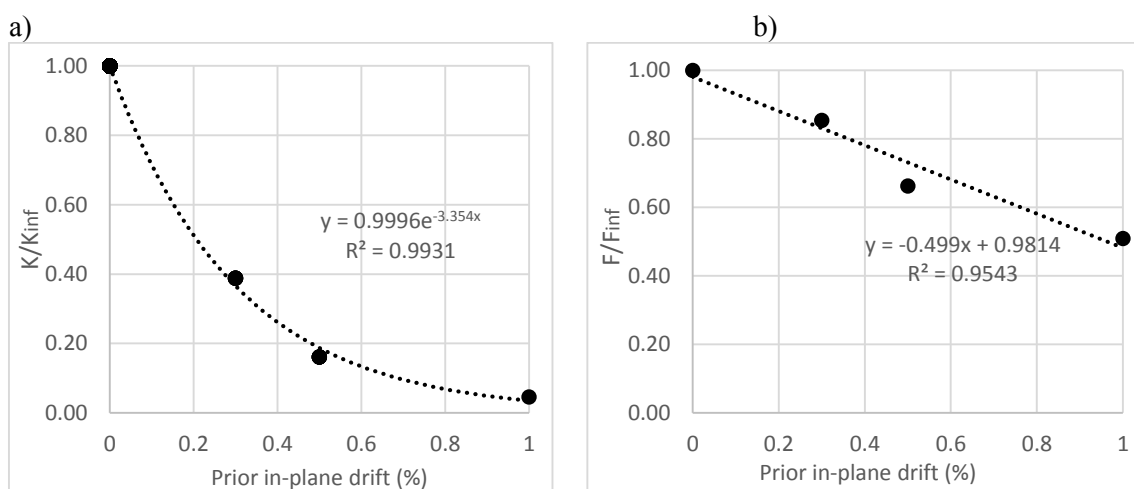


Figure 4.77 Variation of a) initial stiffness and b) out-of-plane strength with respect to prior in-plane drift

On the other hand, the out-of-plane strength decreases slower than the stiffness as the prior in-plane damage increases. This trend of variation is assumed as linear with coefficient of variation of  $R^2=0.95$ , see Figure 4.77b. The masonry infill with prior in-plane damage corresponding to in-plane drift of 1% could withstand 50% of the out-of-plane strength of the specimen with no prior in-plane damage. This could be related to the presence of high axial loads on top of each column which seems to enhance the formation of two-way arching mechanism. With this respect, it would be important to highlight the influence of the axial compression stress in the columns on the out-of-plane resistance after in-plane damage.

The stiffness and out-of-plane resistance of masonry infills with prior in-plane damage can be estimated by taking into consideration the trends displayed in Figure 4.77. The variation of the secant stiffness of damaged specimens can be re-written as:

$$K = K_{inf}(e^{-3.3D}) \quad \text{Eq. 4-1}$$

where  $K$  (kN/mm), is the out-of-plane secant stiffness of the masonry infill subjected to prior in-plane drift of  $D$ (%) and  $K_{inf}$  (kN/mm) is the out-of-plane secant stiffness of the specimen without previous in-plane damage.

Similarly, the out-of-plane strength,  $F$  (kN), of the masonry infills subjected to the prior in-plane drift of  $D$  (%) can be estimated based on the strength of the undamaged infill,  $F_{inf}$  (kN), and taking into account the prior in-plane drift, through the following equation:

$$F = F_{inf} \left( \frac{2-D}{2} \right) \quad \text{Eq. 4-2}$$

The values of the predicted stiffness and out-of-plane strength obtained by the simplified equations are presented in Table 4-3 to be compared with the experimental results. It is concluded that the developed equations could satisfactorily predict the reduction of the secant stiffness and out-of-plane strength of the infilled frames due to presence of prior in-plane damage. The higher value obtained as the error in the prediction of stiffness of the specimen SIF-IO(1%)-2L(NC)-B is not significant since both values are low.

Table 4-3 Comparison between experimental and analytical results

Specimen	K/K <sub>inf</sub>			F/F <sub>inf</sub>		
	Experiment	Simplified equation	Error (%)	Experiment	Simplified equation	Error (%)
SIF-O-1L-B	1.00	1.00	0.0	1.00	1	0.0
SIF-IO(0.3%)-2L(NC)-B	0.39	0.37	-5.1	0.85	0.85	0.0
SIF-IO(0.5%)-2L(NC)-B	0.16	0.19	-18.8	0.66	0.75	13.6
SIF-IO(1%)-2L(NC)-B	0.05	0.04	20.0	0.51	0.5	-2.0

Notice that the values of secant stiffness were always calculated following the same procedure by considering the slope of the line connecting the origin to the point with 30% of the out-of-plane strength. However, it should be mentioned that the specimens were already cracked due to in-plane loading, resulting in an expected reduction on the secant stiffness in the out-of-plane direction. Therefore, if instead of considering the secant stiffness at 30% of the lateral strength the initial stiffness is calculated, the stiffness reduction trend can be represented by an exponential curve as shown in Figure 4.78.

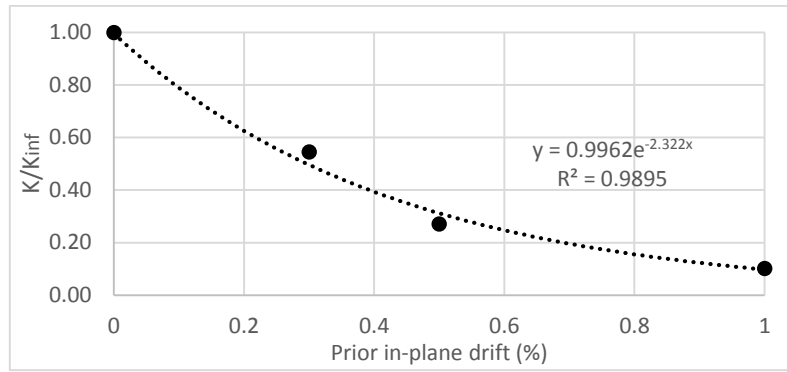


Figure 4.78 Variation of the initial stiffness of the specimens with respect to prior in-plane damage

It is clear that the trend of variation of the initial stiffness is similar to an exponential curve and can be re-written as:

$$K^{in} = K_{inf}^{in} (e^{-2.4D}) \quad \text{Eq. 4-3}$$

Where  $K^{in}$  (kN/mm), is the out-of-plane initial stiffness of the masonry infill subjected to prior in-plane drift of  $D(\%)$  and  $K_{inf}^{in}$  (kN/mm) is the out-of-plane initial stiffness of the specimen without previous in-plane damage. The values of the predicted initial stiffness of the specimens were compared with experimental results and represented in Table 4-4. It is clear that the developed equation could satisfactorily predict the initial stiffness of the damaged specimens.

Table 4-4 Comparison between experimental and analytical results

Specimen	K/K <sub>inf</sub>		
	Experiment	Simplified equation	Error (%)
SIF-O-1L-B	1.00	1.00	0.0
SIF-IO(0.3%)-2L(NC)-B	0.55	0.49	10.9
SIF-IO(0.5%)-2L(NC)-B	0.27	0.30	-11.1
SIF-IO(1%)-2L(NC)-B	0.10	0.09	10.0

The stiffness degradation curves of the specimens constructed by mason B are shown in Figure 4.79. It is clear that the specimens with lower amount of prior in-plane damage exhibited higher initial out-of-plane stiffness. Additionally, it is observed that the initial out-of-plane stiffness of the specimens with less in-plane damage degraded quicker than the specimens with severe in-plane damage.

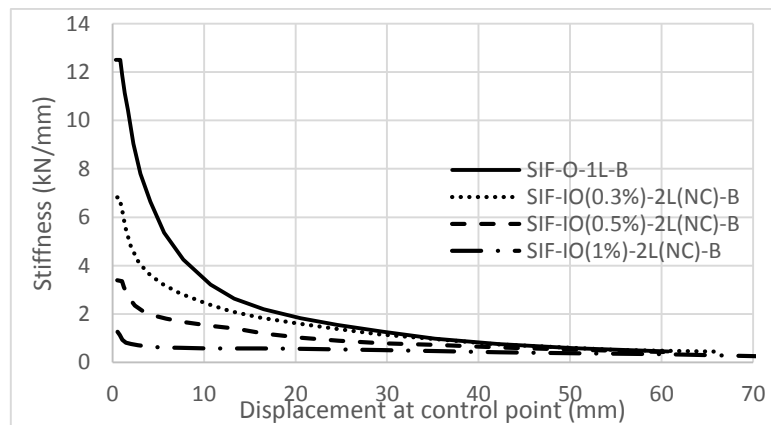


Figure 4.79 Stiffness degradation curve of the specimens constructed by mason B

#### 4.6.2 Effect of workmanship on the out-of-plane response

The out-of-plane response of the specimens constructed by different masons in terms of monotonic envelopes of the force-displacement diagrams are presented in Figure 4.80. The key parameters regarding the in-plane response such as initial stiffness, stiffness at 30% of maximum force and lateral strength are summarized in Table 4-5.

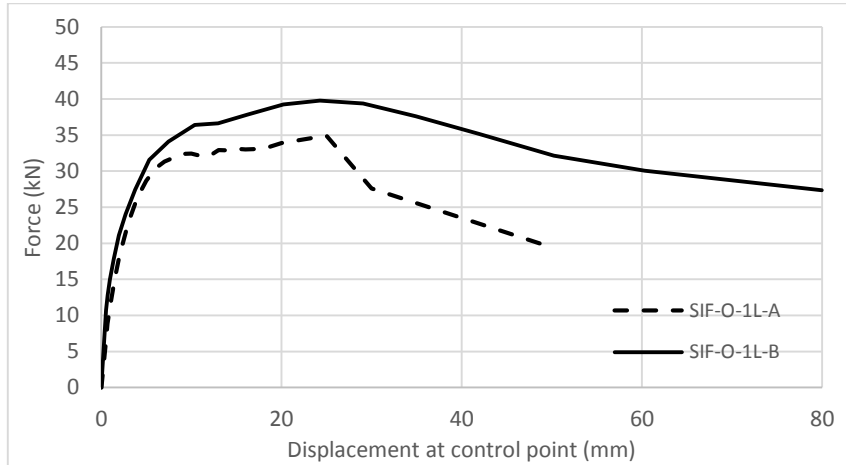


Figure 4.80 Experimental monotonic envelopes for specimens built with different masons

Table 4-5 Comparison between experimental and analytical results

Specimen	Initial Stiffness (kN/mm)	Secant stiffness at 30% of peak force (kN/mm)	Strength (MPa)
SIF-O-1L-A	10.5	10.2	34.9
SIF-O-1L-B	12.5	12.5	39.8

It is clear that both specimens exhibit different out-of-plane responses in terms of initial stiffness and out-of-plane strength. The specimen built by the experienced mason (mason B) presents an initial stiffness of 19% higher than that of specimen built by mason A. In terms of lateral resistance, the specimen built with masonry B presents an out-of-plane resistance of 14% higher than the resistance of specimen built with mason A. These differences may be explained by different workmanship quality of the masonry infill and consequently by different boundary conditions between infill and its surrounding frame. In the specimen constructed by mason A, two-way arching mechanism developed at early out-of-plane displacements and by increasing the imposed displacements, the upper interface slid and became like a semi-free edge, influencing the resisting mechanism. This behavior occurs due to bad filling of the upper row of bricks with mortar, which influences the adequate adherence between the rc frame and the masonry infill. In the specimen constructed by experienced mason B, the two way arching mechanism supported on four sides characterizes the response of the specimen at higher displacements, which contributed to higher out-of-plane strength.

Another aspect to be considered is the ultimate deformation, which in the specimen constructed by mason B is considerably higher than the specimen constructed by mason A. This should be

justified mainly by the different boundary conditions that governed the out-of-plane response of both masonry infills.

Stiffness degradation curves of both specimens are shown in Figure 4.81. It is clear that both specimens represent similar trend of degradations. The only difference relates to the start point of the test in which the specimen constructed with experienced mason represents higher amount of initial stiffness.

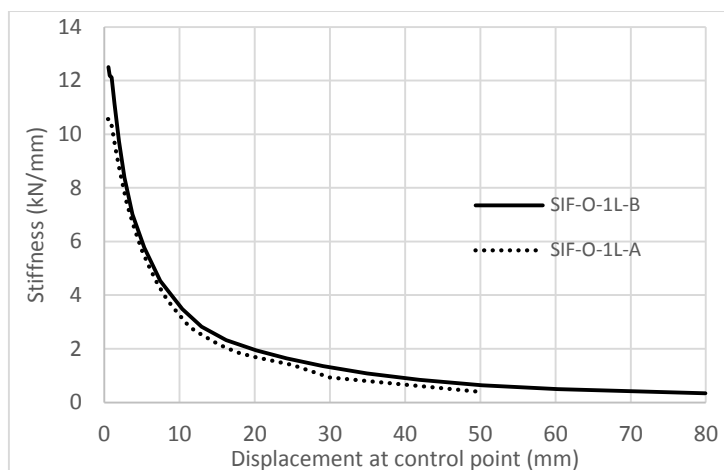


Figure 4.81 Stiffness degradation of masonry infill built by different masons

### 4.6.3 Influence of openings on the out-of-plane response

The force-displacement diagram of specimen with central opening (PIF-O-1L-B) is compared with the reference specimen (SIF-O-1L-B) in their control points, see Figure 4.82. The key parameters of the out-of-plane behavior are also represented in Table 4-6. It is clear that both specimens present practically coincident force-displacement diagrams, being the ascending branch of the diagrams overlapped. The stiffness is practically the same, as well as the out-of-plane strength. The differences relate to: (1) displacement corresponding to the lateral strength, which is lower in case of the specimen with the central opening; (2) ultimate deformation, which considerably lower in case of the specimen with the central opening.

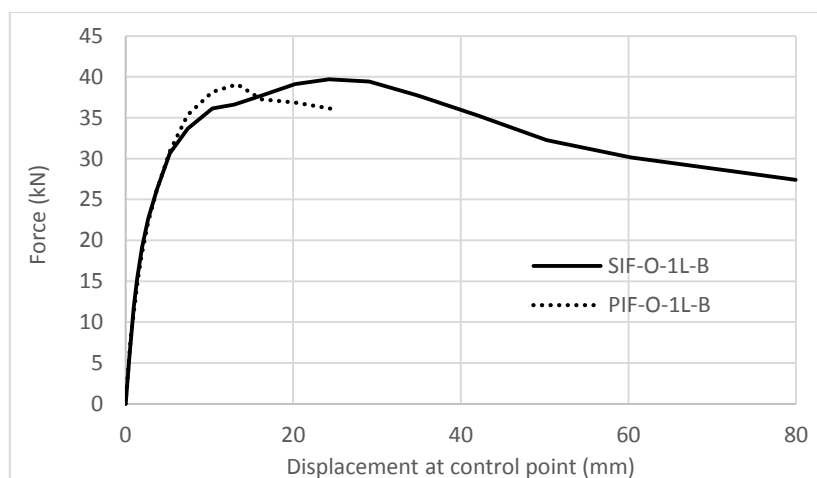


Figure 4.82 Force-displacement diagram of PIF-O-1L-B and SIF-O-1L-B in their control points

Table 4-6 Initial stiffness and out-of-plane resistance of the solid infilled frame and infilled frame with central opening

Specimen	Initial Stiffness (kN/mm)	Strength (MPa)
SIF-O-1L-B	12.5	39.7
PIF-O-1L-B	12.9	39.0

The stiffness degradation of the specimens with respect to their control points are shown in Figure 4.83. It is clear that both specimens represent the same trend of variation.

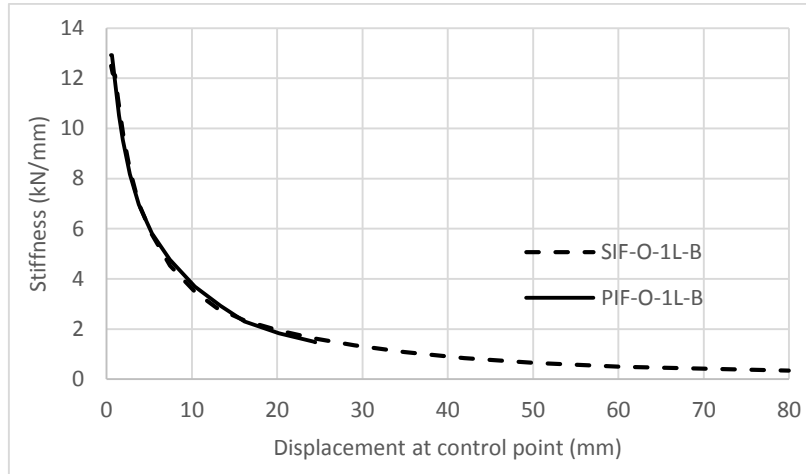


Figure 4.83 Stiffness degradation curve of solid infill and infill with central opening

#### 4.6.4 Plastic or residual deformations in out-of-plane loading

During the out-of-plane unloading process, it is observed that at low levels of displacements when there is no crack formation in the specimen, the deformation in the control point is recovered. This means that at low levels of displacements no residual or plastic deformations were observed. The increase in the imposed out-of-plane displacements led to the initiation of cracks and their propagation, resulting in progressive increase in the plastic (non-recoverable) deformations, see Figure 4.84. As mentioned before, the plastic deformation of the specimens could be approximated by a polynomial function of second order. This means that at the low levels of displacement applied to the specimen, the plastic deformation is low and increases considerably at higher levels of displacements, as a result of the progress of damage. It should be mentioned that the prior in-plane damage appears to be important since the specimens with severe in-plane damage (SIF-IO(0.5%)-2L(NC)-B and SIF-IO(1%)-2L(NC)-B) presented higher amount of plastic deformations than the reference specimen (SIF-O-1L-B). It is also observed that the workmanship can have an important role in the nonlinear behavior of the masonry infill, as it is seen that the plastic deformation is higher, when compared with the specimen constructed by mason B.



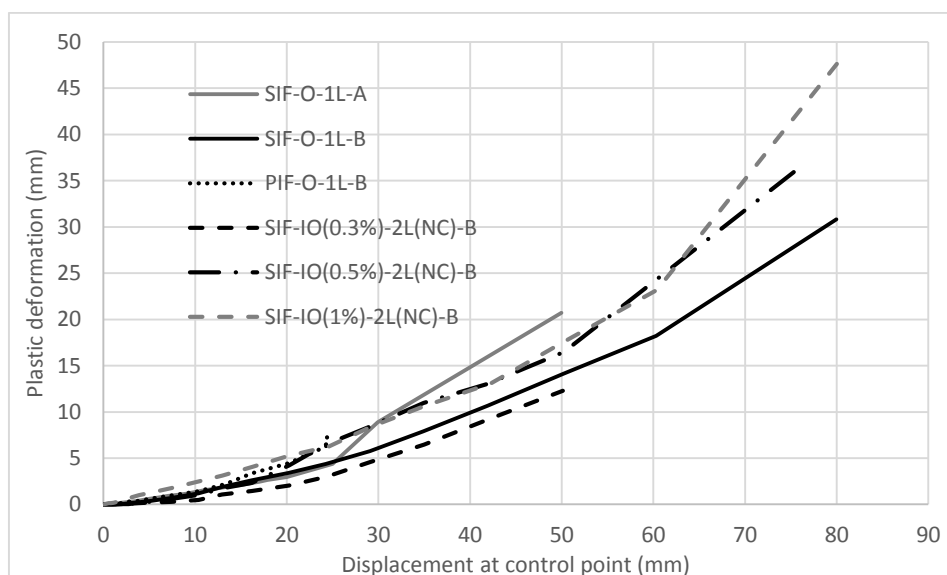


Figure 4.84 Plastic deformations observed in all the specimens

#### 4.6.5 Energy dissipation capacity

The total energy dissipated until each cycle for all specimens tested under out-of-plane loading are shown separately in two graphs, see Figure 4.85 and Figure 4.86. In the first graph, the results of the specimens constructed by the same mason (B) but with different prior in-plane damages are provided, whereas the second graph shows the results of the specimens constructed by different masons and the specimen with central opening.

The influence of prior in-plane damage on the trend of variation of dissipation of energy is evident as shown in Figure 4.85. The dissipation of energy in the damaged brick infills is considerably lower when compared with the reference undamaged masonry infill. This should be justified by the fact that part of the cracks involved in the cracking patterns observed in the out-of-plane loading were formed during in-plane test. This means that a reduced energy is needed to re-open the cracks, in opposite to the energy needed to open new cracks.

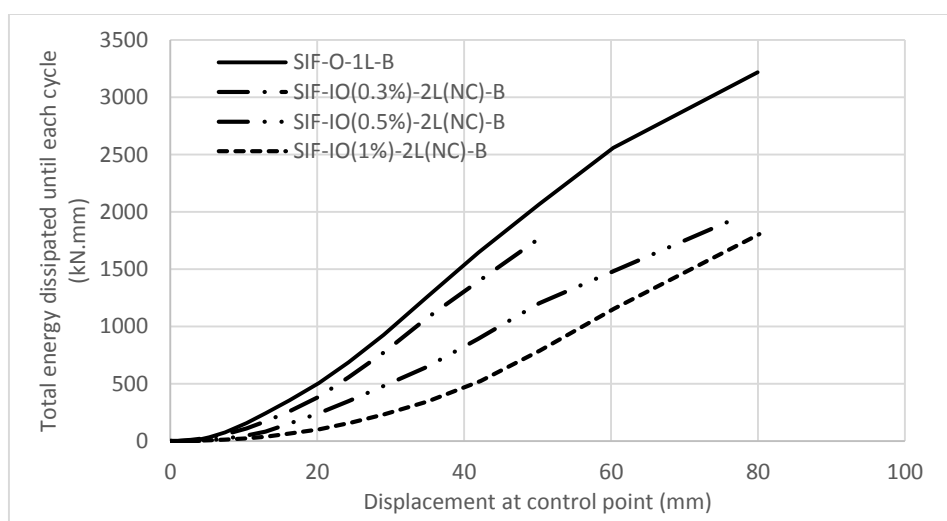


Figure 4.85 Total dissipated energy of specimens with different prior in-plane damage

From Figure 4.86, it is seen that the specimen with solid infill (SIF-O-1L-B) and specimen with central opening (PIF-O-1L-B) exhibit similar response in terms of energy dissipation trend until out-of-plane displacement of 25mm. However, it is also observed that the total amount of dissipated energy in the specimen SIF-O-1L-B is more than three times of the total energy dissipated in specimen with central opening (PIF-O-1L-B). This is attributed to the early collapse of the specimens with central opening.

It is also concluded that the specimen constructed by the experienced mason (SIF-O-1L-B) exhibits considerable higher amount of energy dissipation capacity at the end of the test when compared with specimen constructed by mason A. The total energy dissipation capacity of specimen SIF-O-1L-B is calculated to be more than two times of the dissipated energy obtained in specimen SIF-O-1L-A.

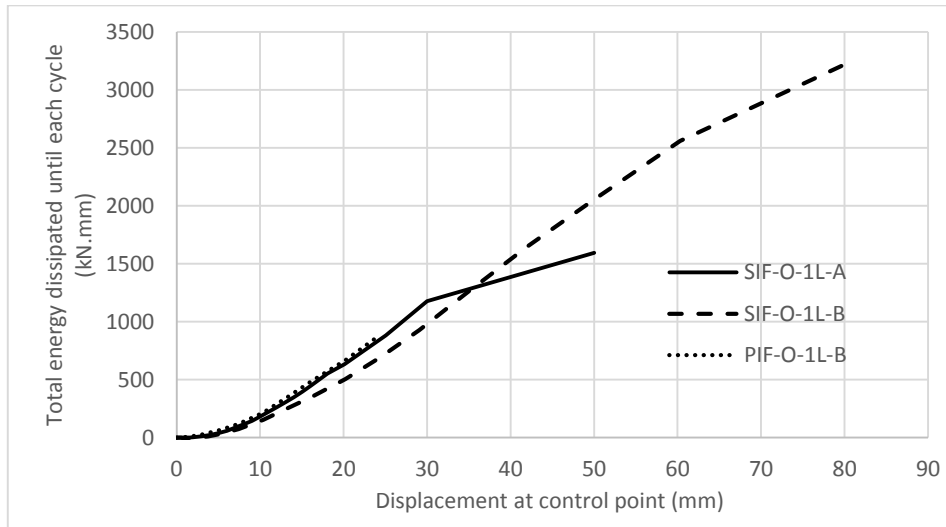


Figure 4.86 Total dissipated energy of specimens constructed by different masons and with central opening

#### 4.7 Conclusions

Based on the analysis of results of the out-of-plane tests, the following conclusions can be drawn:

- 1) Prior in-plane damage results in decreasing of the out-of-plane initial stiffness. It is concluded that the initial stiffness of the specimens varies exponentially with respect to the prior in-plane drift. This means that severe prior in-plane damage leads to lower initial stiffness. Additionally, it is observed that the initial out-of-plane stiffness of the specimens with severe in-plane damage degraded slowly when compared with the specimens having less in-plane damage.
- 2) The masonry infills with prior in-plane damage exhibit lower out-of-plane resistance. A linear variation of the out-of-plane resistance of the specimens with prior in-plane damage was observed.
- 3) The simplified equations derived to predict the initial stiffness and out-of-plane resistance of the specimens with prior in-plane damage, could predict satisfactorily their stiffness and out-of-plane resistance.

- 4) Higher out-of-plane resistance obtained for the specimen with severe prior in-plane damage (1%) can be related to the presence of higher axial forces (40% of axial resistance of each column) on top of columns.
- 5) The workmanship appeared to influence the out-of-plane response of the specimens, leading to the reduction of the initial stiffness and out-of-plane resistance. The bad filling of the gap between the upper rc beam and the masonry infill appears to influence the boundary conditions of the masonry infill and consequently the governing resisting mechanism.
- 6) The presence of small central opening did not change the out-of-plane resistance of the reference specimen but resulted in a significant reduction of the deformation capacity.
- 7) The residual deformation of the specimens, which is more important after the cracking of the specimen, increases with the progress of damage in the masonry infill. The variation of the residual deformation can be approximated by a polynomial function of order 2.
- 8) The energy dissipation capacity of the specimen with solid infill and without any prior in-plane damage is calculated to be significantly higher than the energy dissipation capacity of the specimens that have prior in-plane damage. Also the workmanship affected the energy dissipation capacity of the specimens. The energy dissipation capacity of specimen built with high quality workmanship (SIF-O-1L-B) is calculated to be more than two times of the energy dissipation capacity of the specimen built with poor workmanship (SIF-O-1L-A)

# **CHAPTER 5**

## **STRENGTHENING OF BRICK MASONRY INFILLS**

## **5 Strengthening of brick masonry infills**

### **5.1 Introduction**

The major objective of this Chapter is to assess the effect of strengthening of masonry infills in their in-plane and out-of-plane behavior. First, it was decided to use steel connectors to enable the connection and consequent interaction between the leaves of the masonry infill, and thus, to assess the influence of having both leaves connected on the out-of-plane behavior of the masonry infill. Notice that in the previous chapter regarding the out-of-plane behavior, the experimental tests were only performed in the external walls, taking into consideration that in the great majority of the cavity walls there are not any connections between the leaves in the past traditional construction methodology. Then, it was decided to use textile reinforced mortar (TRM) technique to investigate how this technique could enhance the in-plane and out-of-plane behavior of rc frames with masonry infills. As mentioned in Chapter 2, this technique has been increasingly used in the strengthening of masonry infills and it is revealed to have the potential for seismic strengthening/retrofitting of structures [35].

For the textile reinforced mortar technique two different types of meshes were used, namely a commercial textile mesh and a textile mesh developed at the university in collaboration with the textile department. The developed textile meshes are composed of reinforced braided rods with an external braid of polyester fiber and an internal core which can be composed by glass, carbon or basalt fibers. Based on the results of flexural tests carried out by Martins et al. [35] on masonry wallets reinforced with distinct types of textile meshes embedded in the rendering mortar, it was seen that meshes with glass fibers exhibit a reasonable behavior while are considerably cheaper than meshes with carbon fibers. Taking into account these results, it was decided to strengthen the masonry infill walls with meshes composed of glass fibers, namely the commercial and designed meshes.

This chapter presents the details of the strengthening techniques and the results of in-plane and out-of-plane tests carried out on strengthened specimens. The analysis of results follows the same methodology presented in Chapter 3 and Chapter 4. The main parameters under study consist of force-displacement diagram, stiffness degradation curve, cracking pattern, deformation characteristics and energy dissipation capacity.

### **5.2 Brief overview of the strengthening techniques**

#### **5.2.1 Metal ties connectors**

As mentioned before, a technique that can be easily used in existing rc buildings with masonry infills is the one connecting the internal and external leaves so that they can act together under the out-of-plane loading. In Portugal, the tradition of construction in the past decades was based on using double leaf masonry infills (cavity walls). However, there is no tradition in connecting the leaves and it is believed that the great part of the masonry infills built in the last decades are very vulnerable to out-of-plane action due to the earthquakes. Therefore, it was decided to evaluate the effect of connecting the leaves of the brick infill with metal ties commonly used in the strengthening of existing masonry infills.

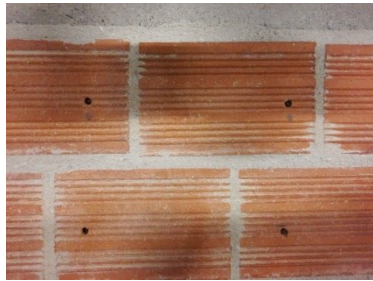
For the connection of internal and external leaves of the masonry infill, metal connectors that can be easily installed were adopted. The connectors are helical metal ties according to what is shown in Figure 5.1. They are simply power-driven into position, via a small pilot hole, using a special installation tool that leaves the end of the helical tie recessed below the outer face of the infill to allow an ‘invisible’ finishing. This is a Dryfix system (provided by Helifix Company), being considered as versatile and rapidly installed mechanical pinning and remedial tying system that requires no resin, grout or mechanical expansion.



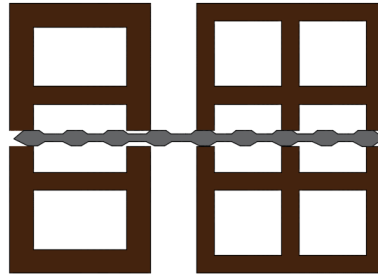
Figure 5.1 Helical ties used for connecting the leaves of brick infills

The installation of this system involves two different steps: (1) drilling some pilot holes by rotary percussion drill (see Figure 5.2a); and (2) driving the ties into the holes by special devices attached to the drilling machine until the outer end is fully recessed below the face of masonry.

a)



b)



c)

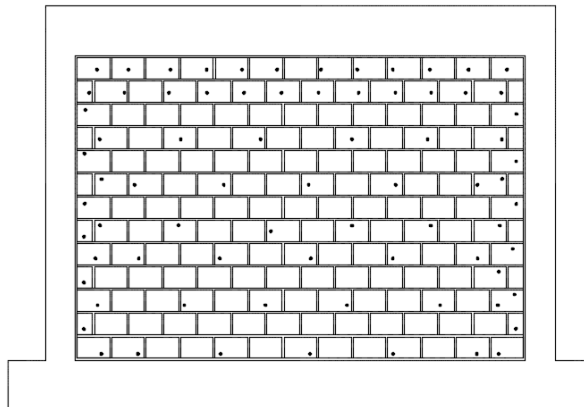


Figure 5.2 Details of the connections of the leaves through metal ties: a) pilot holes in the masonry b) metal tie connecting both leaves together and c) distribution pattern of helical ties

It is clear that no chemical bond was used in this technique to fix the helical pins inside the holes, see Figure 5.2b. The configuration of the helical ties in the masonry infill is shown in Figure 5.2c. Seventy five helical ties were used in the specimen to connect the external and internal leaves together. The number of ties and the distribution pattern for the ties was defined according to the recommendation of the company. To avoid any damage caused by sharp end of the ties to the airbag during out-of-plane loading, thin aluminum plates were attached to the inner end of the holes by means of hot plastic glue.

### 5.2.2 Textile reinforced mortar (TRM)

As mentioned before, a previous work was carried out to design and mechanically validate the textile meshes based on braided composite rods through an enlarged experimental campaign [34, 36, 122]. The braided rods are composite materials composed of an external helicoidally braid in polyester fiber and a nucleus with reinforcing fibers of basalt, glass or carbon fibers. The bond between the external braid and the reinforcing fibers can be ensured in the manufacturing process by adding resin during the braiding process or after the production of the composite braided rods by adding the resin over the external polyester manually (Martins 2013). For the application on the masonry infills, the composite rod was composed of a braided structure with 15 multifilaments of polyester with 11 Tex and one braided element with a simple structure consisting of 8 braided polyester yarns produced at the maximum speed of the production equipment (1.07m/min), see Figure 2.27.

Based on previous experimental campaign, it was decided to use glass fibers in nucleus of the braided rod, as these fibers present a reasonable behavior in terms of additional resistance and deformation capacity of the reinforced masonry, particularly in case of the designed textile mesh.

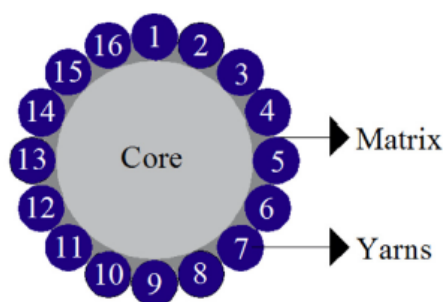


Figure 5.3 Cross section of a braided mesh [35]

To have manufactured meshes that are comparable with commercial meshes, 5 glass multifilaments of the 544 Tex were required, corresponding to density of  $207 \text{ g/m}^2$  (about 92% compared to commercial mesh). Manufacturing of the meshes is carried out by interlacing the composite rods in two directions, assuming that the configuration of the connections of rods in the two directions may promote an additional interlocking and can work as an additional roughness, improving the bond adherence between the meshes and the rendering mortar.

The commercial mesh of glass fibres consists of resistant glass fibres in both directions. Once bidirectional, the mesh density is  $225 \text{ g/m}^2$  with spacing between the fibres of 25 mm. From the technical information, it is seen that the flexural strength is  $45 \text{ kN/m}$  with associated extension at

peak stress less than or equal to 3%. Because the commercial meshes present a spacing of 25 mm, the manufactured meshes were manufactured with the same spacing.

The application of reinforced rendering to the masonry infills follows several steps: (1) definition of the pattern for pilot holes (Figure 5.4a) to place the connectors aiming at improving the adherence of the rendering mortar to the masonry infill; (2) drilling and cleaning the holes and insertion of special plastic row plugs shown in Figure 5.4b in the holes, see Figure 5.5a-b; (3) application of the first thin layer of mortar (Figure 5.5c); (4) positioning of the textile mesh on the first layer of mortar and fixing it by putting the L-shaped glass fiber connectors into the holes (Figure 5.6a); (5) application of the second layer of mortar and rectifying the rendered surface, see (Figure 5.6b,c).

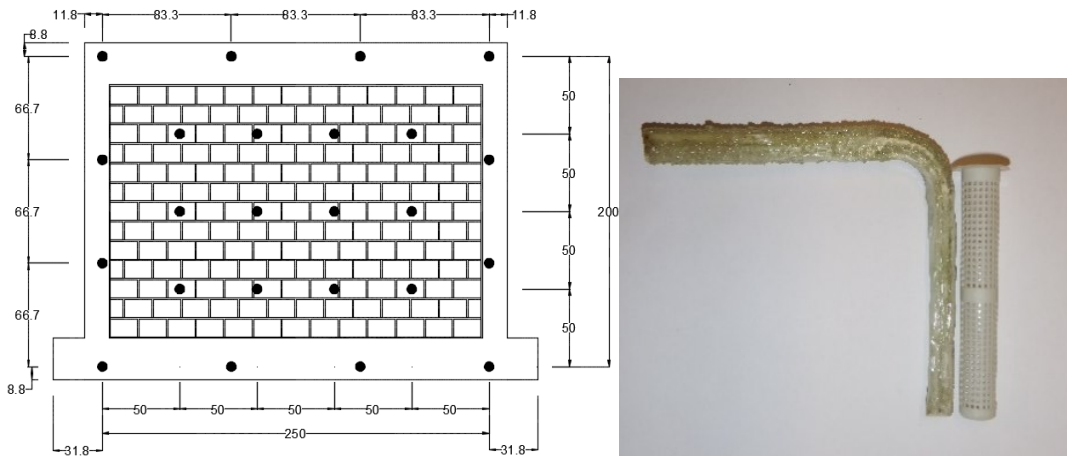


Figure 5.4 Details of the mesh connectors; a) pattern of the connectors b) plastic row plug and glass fiber connector

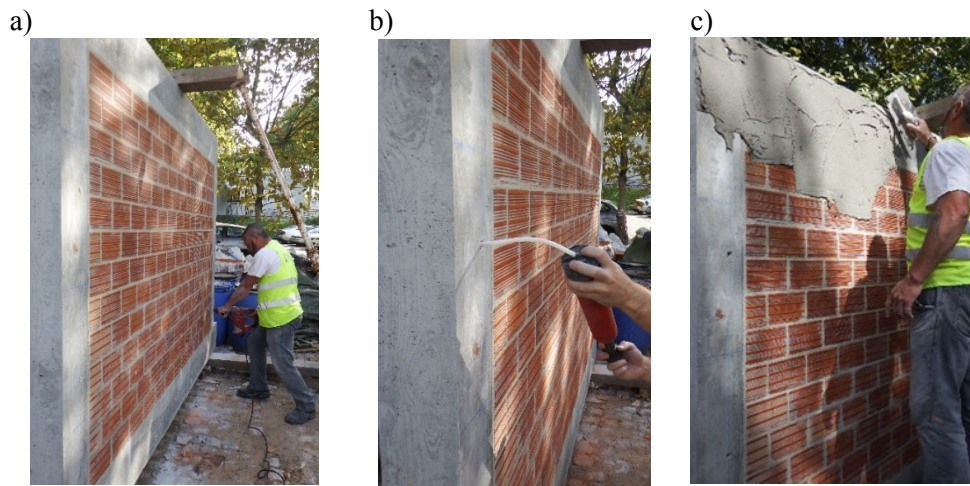


Figure 5.5 Application of the reinforced rendering; a) drilling the pilot holes b) cleaning the holes c) applying the first layer of mortar

Fixing of the textile mesh through L-shaped connectors was made in three steps: (1) first, the textile mesh was placed on the first layer of mortar; (2) then the holes were filled by injecting a special material working as chemical anchor and finally (3) the L-shaped connectors composed of glass fibers were inserted into the holes; see Figure 5.7.



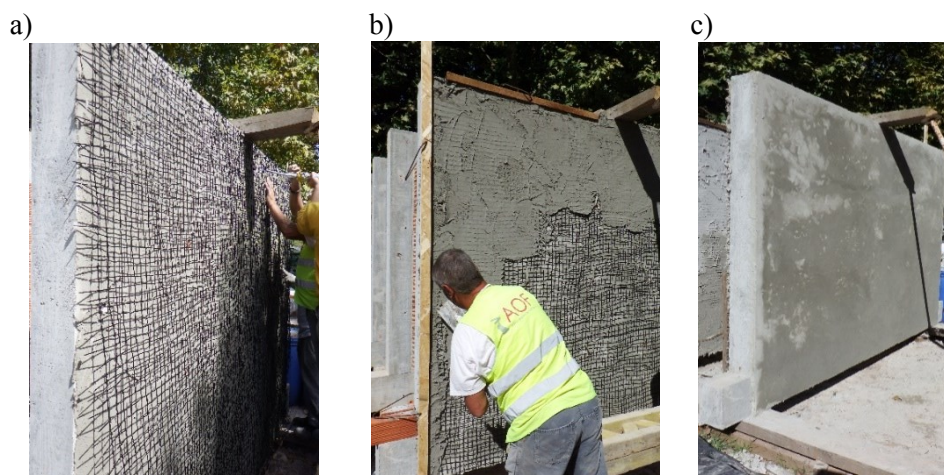


Figure 5.6 Application of the reinforced rendering; a)positioning of the textile mesh b)application of the second layer of mortar c)regularized rendering surface

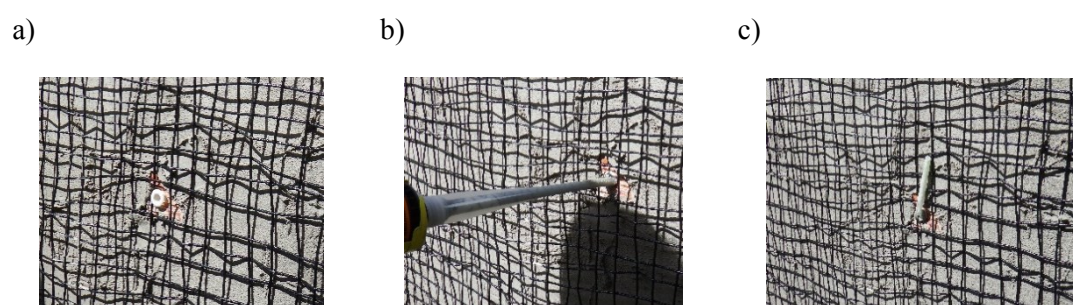


Figure 5.7 Three steps for installing the connectors; a)placing the textile mesh on the first layer of mortar b)filling the hole with chemical anchor c)inserting the connectors into the hole

The total thickness of the rendering was measured as approximately 20mm in all the specimens. The application of the rendering in two successive layers enables the involvement of the textile mesh by the mortar and also adequate development of the adherence between them. The glass fiber connectors were used both in the masonry infill and in the rc frame aiming at avoiding any delamination of the rendering mortar, mainly in case of in-plane loading. The reinforced rendering was applied in the external surfaces of the cavity wall in case of the specimens tested under in-plane loading and in just one external surface of the infill in case of the specimens subjected to the out-of-plane loading. The rendering mortar used in the specimens was a pre-mixed commercial mortar indicated to be applied with the selected commercial textile mesh. An additive was added to the pre-mixed mortar aiming to improve its workability and consequently enhance the mechanical and adhesive characteristics of cement-based rendering mortar.

The quality of the rendering mortar was controlled by testing the consistency of mortar according to EN 1015-3, 1999 [123] in the fresh state and by obtaining the compressive and flexural strength in hardened mortar according to EN 1015-11, 1999 [124]. For the latter case, three samples of mortar were taken for each retrofitting layer to characterize the flexural and compressive strength according to European standard. The results of the experimental characterization of the rendering mortar used for each type of textile mesh in the specimens are summarized in Table 5-1.

Table 5-1 Consistency, compressive and flexural test results of the specimens

Rendering	Flow table (mm)	Compressive Strength (MPa)		Flexural Strength (MPa)	
		Average	C.o.V (%)	Average	C.o.V (%)
Rendering with designed mesh	162	9.11	2.31	3.50	2.59
Rendering with commercial mesh	160	10.44	4.28	3.87	6.62

### 5.3 Description of specimens

A description of the specimens considered in the experimental campaign is summarized in Table 5-2. The labelling of the specimens is done following the same methodology indicated in Chapter 3. The specimen SIF-O-2L(C)-B has double leaf infill connected with metal ties so that the effect of the interaction between the leaves can be assessed in the out-of-plane response. Two specimens to be tested under in-plane loading are strengthened with designed textile mesh developed at university of Minho, SIF(DTRM)-I-2L(NC)-B, and with the commercial textile mesh, SIF(CTRM)-I-2L(NC)-B. Similar reinforcing scheme was adopted in case of the out-of-plane loading, the specimen strengthened with commercial mesh designated by SIF(CTRM)-O-1L-B, and the specimen strengthened with designed mesh designated by SIF(DTRM)-O-1L-B. All specimens were constructed by mason type B.

Table 5-2 Labelling of the retrofitted specimens

Name	Type of Strengthening	Type of loading	Number of leaves
SIF-O-2L(C)-B	Metal ties	out-of-plane	2 leaves
SIF(DTRM)-I-2L(NC)-B	TRM – Designed mesh	In-plane	2 leaves
SIF(CTRM)-I-2L(NC)-B	TRM – Commercial mesh	In-plane	2 leaves
SIF(DTRM)-O-1L-B	TRM – Designed mesh	out-of-plane	One leaf
SIF(CTRM)-O-1L-B	TRM – Commercial mesh	out-of-plane	One leaf

### 5.4 Behavior of the strengthened masonry infills under in-plane loading

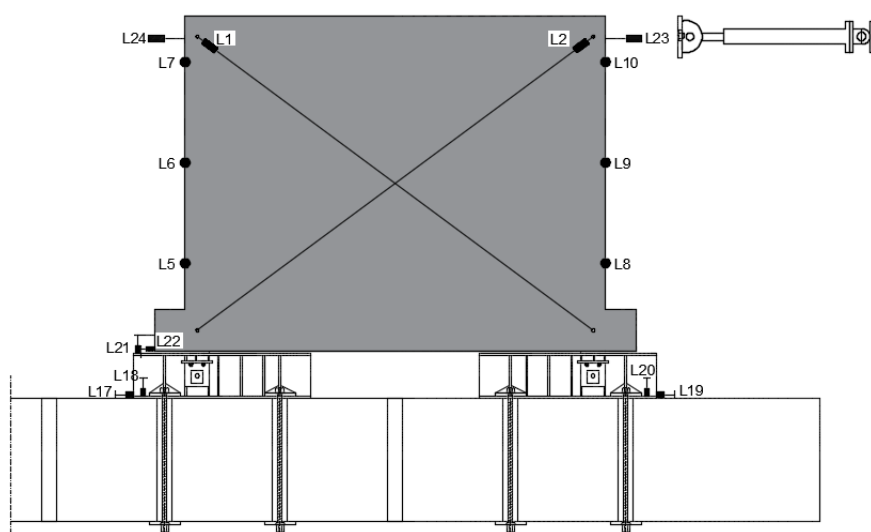
#### 5.4.1 Experimental details

The in-plane testing of the strengthened specimens was carried out similar to the unstrengthened specimens. The test setup and the loading protocol were kept unchanged with respect to those used in the unstrengthened specimens in order to have the same test conditions for comparison of the results.

The instrumentation of the specimen was defined to have the in-plane response of both leaves recorded, see Figure 5.8. Four LVDTs (L1 to L4) were placed along the diagonals to monitor the diagonal deformation of the external and internal leaves. Twelve LVDTs (L5 to L16) were placed on the rendering layer to capture its possible debonding in relation to the rc frame in the out-of-plane direction. Six LVDTs (L17 to L22) were positioned to monitor the possible uplifting and sliding of the specimen from ground and steel profiles and thus control the reliability of the test

setup. Finally two LVDTs, L23 and L24, were placed on the top beam to investigate the horizontal displacement at the top rc beam in the direction of the applied load.

a)



b)

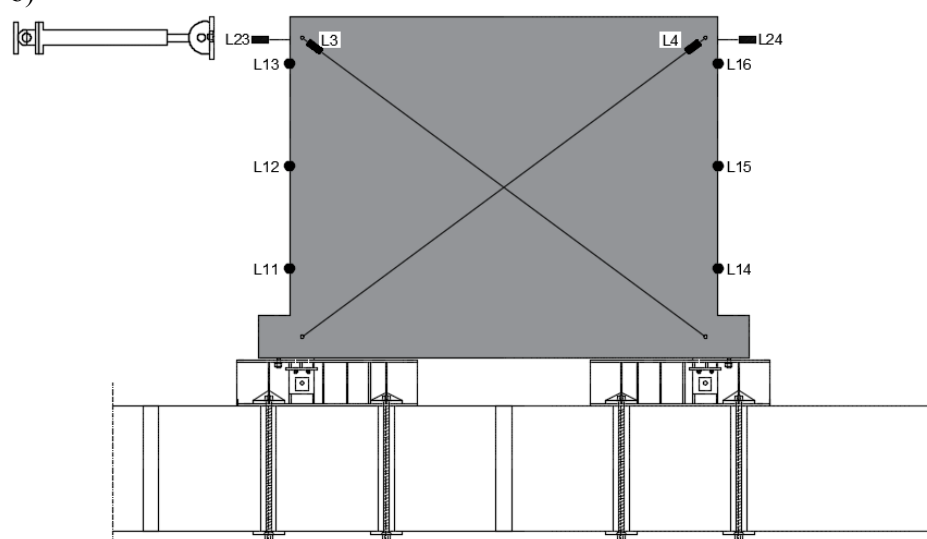


Figure 5.8 Instrumentation of the specimen for in-plane loading a)external leaf b)internal leaf

## 5.4.2 Results - specimen SIF(CTRM)-I-2L(NC)-B

### 5.4.2.1 Lateral load-displacement response

The force-displacement diagram obtained for the specimen strengthened with commercial textile mesh under cyclic in-plane loading is shown in Figure 5.9. It is clear that this specimen presents higher initial stiffness when compared with the reference unstrengthened specimen. The cracking initiation occurred at the lateral drift of 0.1% both in the positive and negative directions. The first cracks were horizontal and adjacent to the top interface between upper rc beam and the brick infill in the negative direction. The maximum lateral force of the specimen in the negative direction (201kN) was observed at this lateral drift.

When the force was applied in the positive direction, the first diagonal crack developed at the central region of the brick wall at the lateral drift of 0.1% corresponding to the lateral force of 185kN.

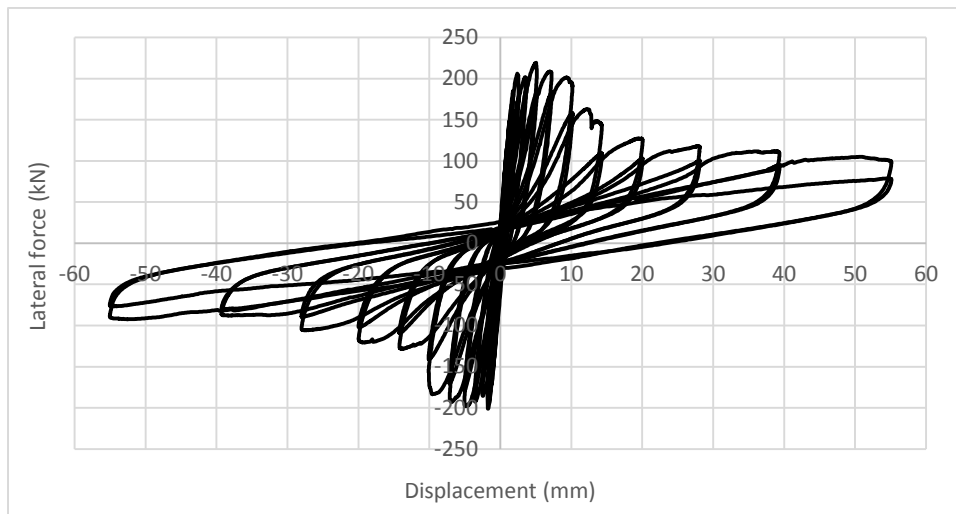


Figure 5.9 Force-displacement diagram of specimen SIF(CTRM)-I-2L(NC)-B

After crack initiation, the application of further displacements in the positive direction led to the increase of the lateral force until it reached the maximum value of 219kN at the lateral drift of 0.27%. In the negative direction at this stage the lateral resistance has already started to decrease.

After the peak in-plane lateral resistance, a progressive decrease of the resistance was observed, being more significant at the lateral drift of 0.75%, both in positive and negative directions. The reduction in the lateral resistance is calculated as 30%. This should be related to the fast progression of cracks. After this lateral drift, the increase of the imposed displacement resulted in a very smooth decrease of the lateral resistance, as observed in Figure 5.9. It is noticed that almost a plateau is achieved for higher displacements, appearing like a residual lateral resistance approximately equal to 92kN in the negative direction and 105kN in the positive direction. The residual strength observed in this specimen is about two times of the lateral strength of the bare frame.

The monotonic force-displacement envelope recorded at each displacement cycle is shown in Figure 5.10. It is clear that there is no degradation in the lateral force until the initiation of cracks both in the positive and negative directions. The strength degradation started at lateral drift of 0.1% where the cracking initiated in both directions. After this, the lateral strength degradation remains practically constant until the end of the test.

Based on the monotonic force-displacement diagram of the specimen, it is possible to derive the key parameters characterizing the in-plane behavior, namely the initial stiffness, the lateral strength and the displacement corresponding to the lateral strength, see Table 5-3. The initial stiffness is defined as the secant stiffness of the specimen at the first cracking point, according to Eq. 5-1.

$$K_e = \frac{H_{cr}}{d_{cr}} \quad \text{Eq. 5-1}$$

In which  $H_{cr}$  and  $d_{cr}$  are the lateral force and displacement of the specimen at first cracking point respectively.

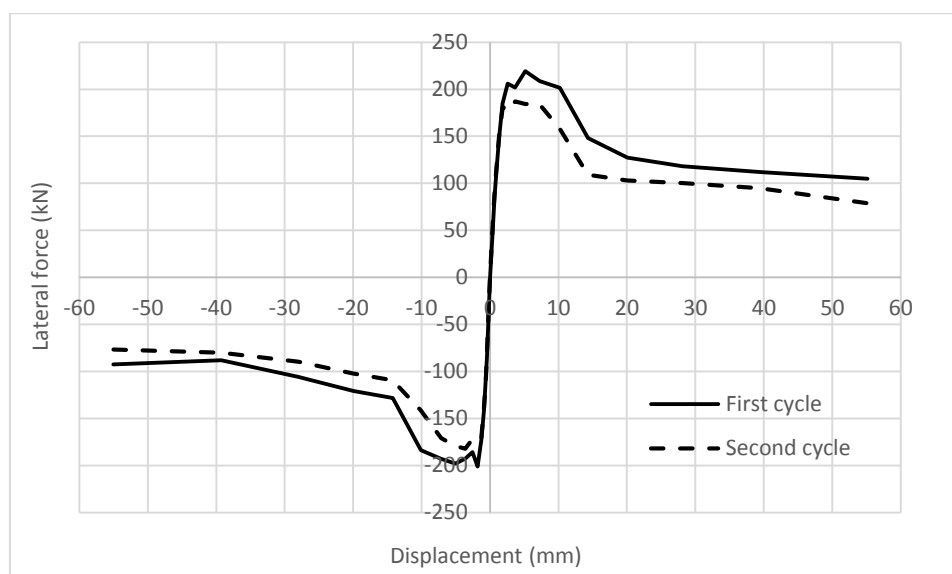


Figure 5.10 Monotonic force-displacement envelopes of SIF(CTRM)-I-2L(NC)-B at each successive cycles

The lateral strength of the specimen ( $H_{max}$ ) is defined as the maximum force obtained in the force-displacement diagram and  $d_{H_{max}}$  represents the displacement related to the maximum force attained during the cyclic test. It is clear that the strengthened specimen represented higher initial stiffness and lateral strength with respect to the unstrengthened specimens.

Table 5-3 Key parameters describing the in-plane behavior of bare frame

Positive direction					Negative direction				
$H_{cr}$ (kN)	$d_{cr}$ (mm)	$K_e$ (kN/mm)	$H_{max}$ (kN)	$d_{H_{max}}$ (mm)	$H_{cr}$ (kN)	$d_{cr}$ (mm)	$K_e$ (kN/mm)	$H_{max}$ (kN)	$d_{H_{max}}$ (mm)
185.0	1.84	100.8	219.2	5.15	-201.1	-1.82	110.5	-201.1	-1.82

#### 5.4.2.2 Stiffness degradation curve

The stiffness of the specimen at each imposed lateral displacement during in-plane loading is shown in Figure 5.11. It is calculated as the slope of the line connecting the point in the monotonic force-displacement diagram corresponding to a certain displacement and the origin. It is clear that the trend of variation of the stiffness at positive and negative directions is similar. With this respect, at the first levels of loading after initiation of crack, significant decrease in the stiffness of the specimen could be observed. The reduction of the stiffness at lateral drift of 1% in the positive and negative directions was about 95% in relation to the initial stiffness, meaning that a huge reduction of stiffness was recorded. .

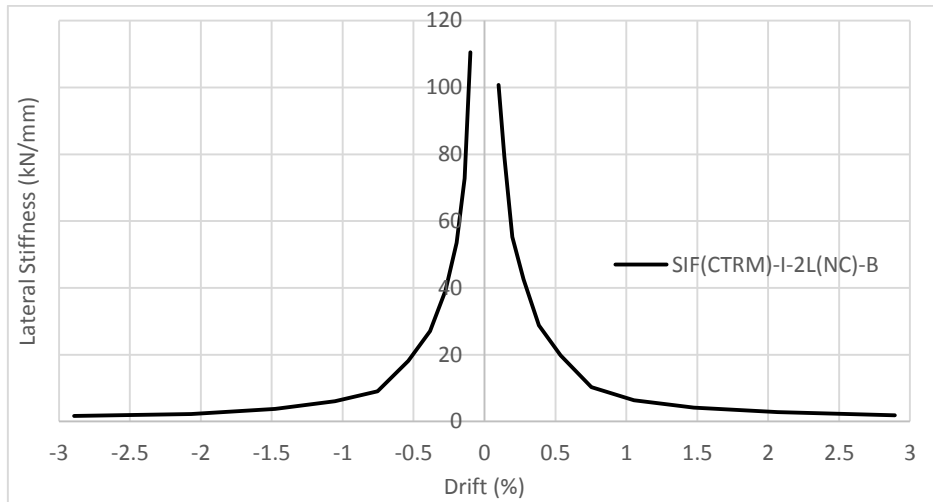


Figure 5.11 Stiffness degradation curve of specimen SIF(CTRM)-I-2L(NC)-B

#### 5.4.2.3 Cracking patterns

The cracking progress during in-plane loading is shown in Figure 5.12. As described before, the first cracking initiated at the lateral drift of 0.1% corresponding to lateral force of 201kN in the negative direction through the opening of some horizontal cracks adjacent to the upper interface between top rc beam and the brick infill. At the same lateral drift some diagonal cracks opened at central region of the brick infill when the lateral force is applied in positive direction, see Figure 5.12a.

After this stage, the application of increasing lateral displacements resulted in the progress of cracking in the brick infill, being visible in the rendering mortar. At the displacement of 5.23mm corresponding to the lateral drift of 0.27% in the positive direction, some horizontal cracks opened near to the interface between bottom rc beam and the infill, see Figure 5.12c. Additionally, it was observed that diagonal cracks extended until the corners of the wall.

The crack density observed in the rendering mortar is more significant from the lateral displacement of 14.35mm, corresponding to the lateral drift of 0.75%. No major additional visible cracks can be seen until the end of the test for a lateral drift of 2.89%. It seems that the increasing of the imposed lateral drift beyond 0.75% resulted in the increasing of the width of the cracks.

By analyzing the results of the LVDTs placed in the added retrofitting layer to record the possible debonding of that layer from the rc frame which are presented in Figure 5.13 (external leaf) and Figure 5.14 (internal leaf), it is seen that the detachment of the reinforced rendering layer initiated at very low imposed displacements and it was totally separated from rc frame until end of the test. In more detail, it should be mentioned that the detachment in the upper left part of the infill initiated both in the internal and external leaves locally at the lateral drift of 0.07%. It is stressed that the detachment measured by the LVDTs is related to the detachment of the added layer from the rc frame due to the shear failure of the connectors. No significant detachment was observed in the brick infill, even after the test.

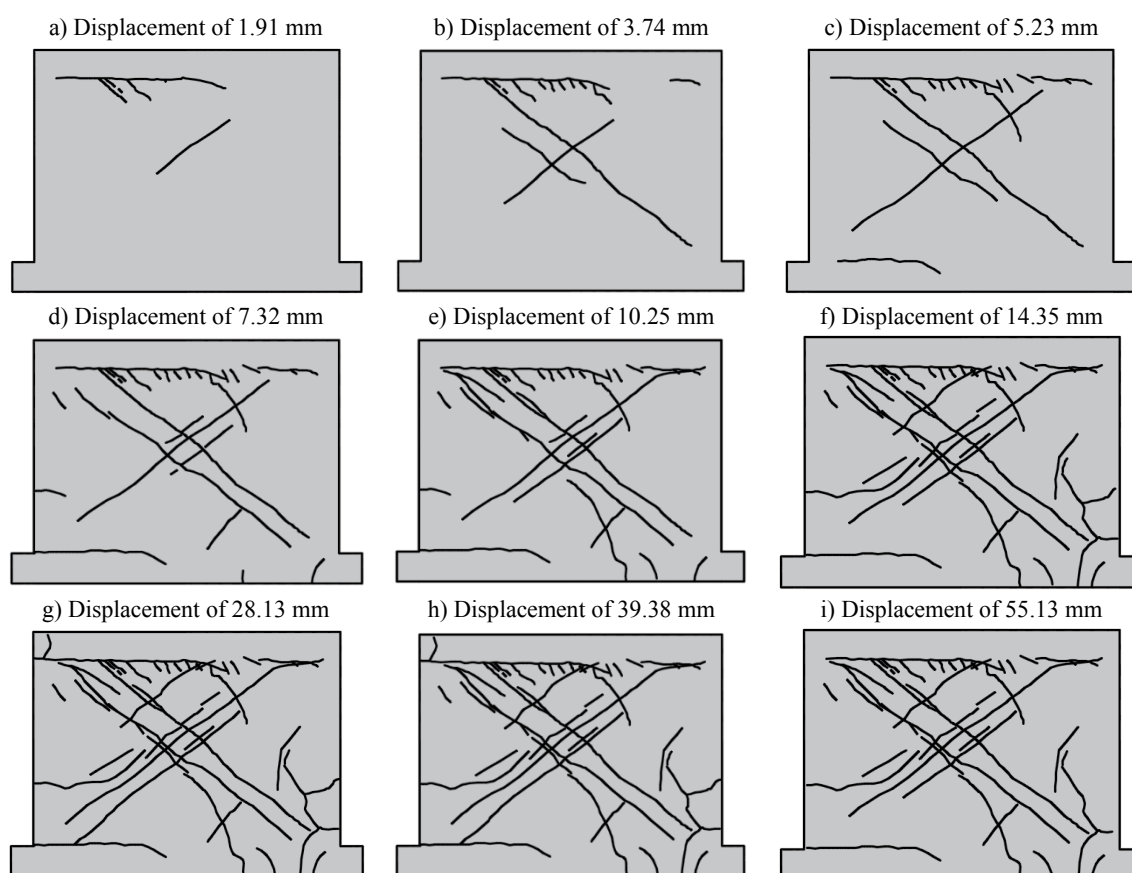


Figure 5.12 Crack propagation of SIF(CTRM)-I-2L(NC)-B

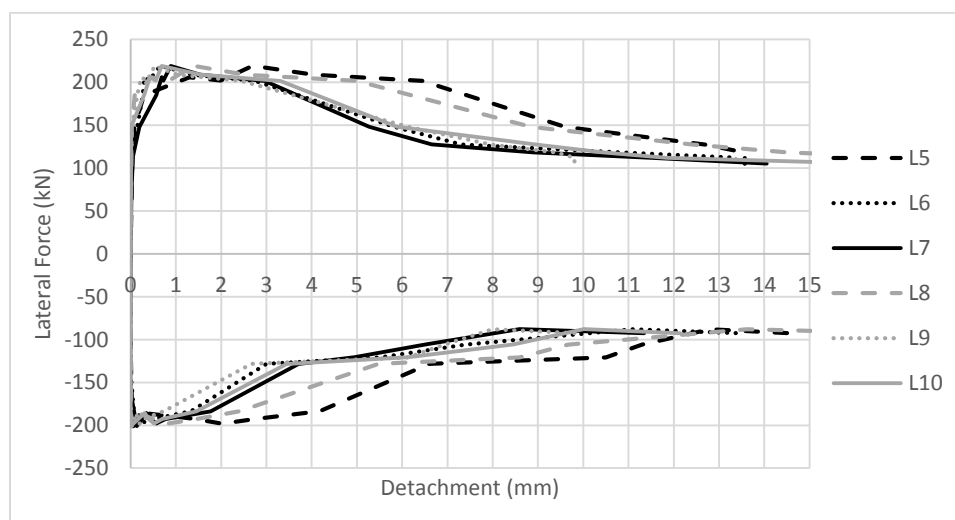


Figure 5.13 Detachment of the reinforced mortar layer applied on external leaf from rc frame at different points

The detachment of the reinforcing layer from the rc frame increases as the lateral displacement increases being practically the same along internal and external leaves. The strengthening layer of the external leaf was completely detached from the rc frame at lateral drift of 0.27%, corresponding to a lateral force of 219kN. The total detachment of the internal leaf was practically observed at lateral drift of 0.2% corresponding to the lateral force of 201kN. A view of the

detachment of the reinforced mortar layer from the rc frame at the beginning and at the end of the test along with the shear failure of the connectors at the rc columns are shown in Figure 5.15.

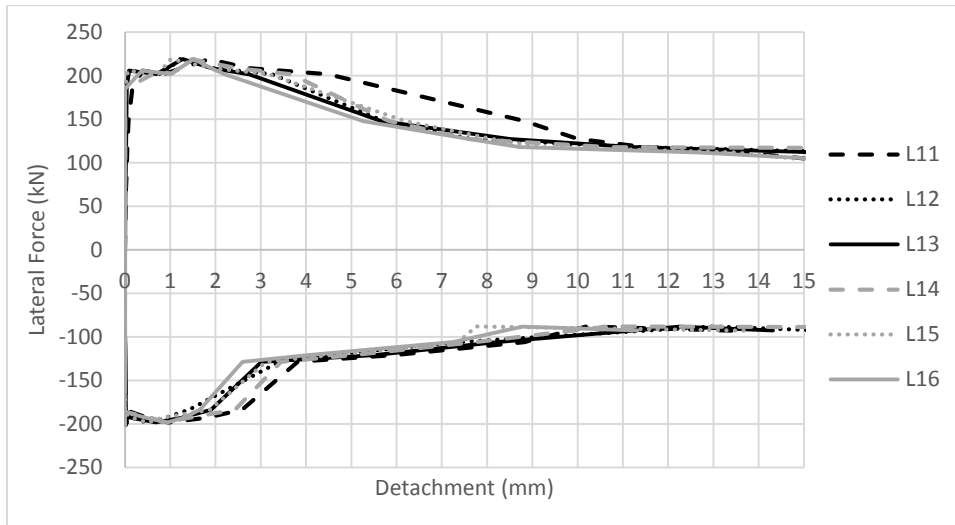


Figure 5.14 Detachment of the reinforced mortar layer applied on internal leaf from rc frame at different points

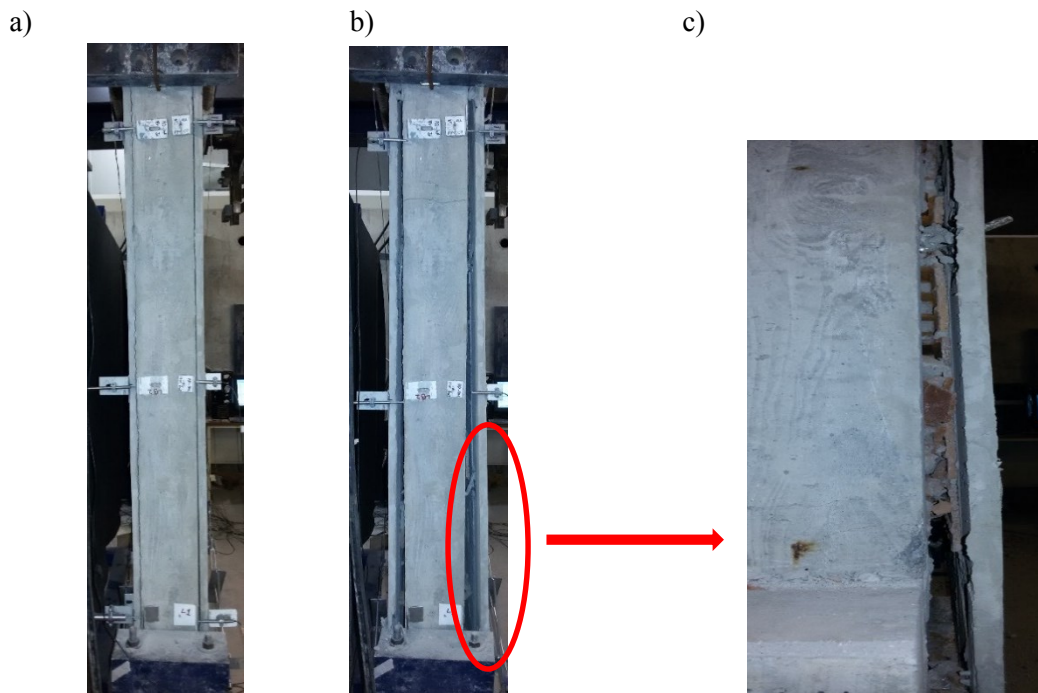


Figure 5.15 Detachment of the reinforced mortar layer at lateral drift of a) 0.27% b) 2.89% c) shear failure of the connectors between retrofitting layer and rc frame

From the results obtained, it seems that other type of connectors should be used in the rc frame. Besides, it should be mentioned that the failure of the connectors is brittle and thus more ductile material should be selected. On the other hand, it appears that the connectors behaved in appropriate way in case of brick infill, as no detachment of the reinforced mortar layer from the masonry infill was detected. After the test, the reinforced mortar layer was removed mechanically to obtain information about the damage of the brick infill. It was seen that the masonry units crushed along the rc frame-brick interfaces, see Figure 5.16. This could be related to the higher concentration of compressive stresses along the edge of the brick infill. It also appears that no



additional cracks were formed in the brick infill apart from the crushing in the bricks adjacent to the rc frame. This appears to indicate that the reinforced mortar layer acts as a damage controller by limiting the development of cracks in the brick infill.



Figure 5.16 View of the crushing of bricks of the infill after removing some parts of the retrofitting layer in specimen SIF(CTRM)-I-2L(NC)-B

Due to the detachment of the reinforced mortar layer from the rc frame at the early stages of the loading, it was not possible to record the average shear distortion of specimen by means of diagonal LVDTs placed on the region where detachment took place.

#### 5.4.2.4 *Energy dissipation capacity*

The dissipation of energy in the specimen is calculated as the area of the loop corresponding to a certain displacement level in the force-displacement diagram. The dissipation of energy at each cycle is shown in Figure 5.17. It is observed that the energy dissipation started after cracking of the specimen at lateral drift of 0.1% and higher amplitudes of displacements imply higher energy dissipation capacities. This is generally related to higher density of cracks developed at the higher displacement amplitudes.

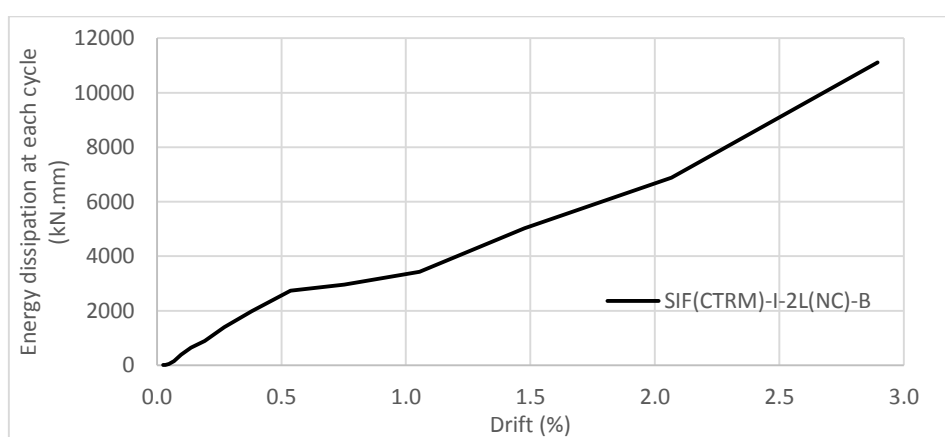


Figure 5.17 Energy dissipation of the strengthened specimen at each cycle

The total energy dissipated until each cycle is calculated by cumulating the energies dissipated until that cycle, see Figure 5.18. It is observed that the total amount of dissipated energy is increasing at higher amplitudes. The specimen presents 32% higher energy dissipation capacity

at lateral drift of 1% when compared with reference unstrengthened specimen of SIF-IO(1%)-2L(NC)-B.

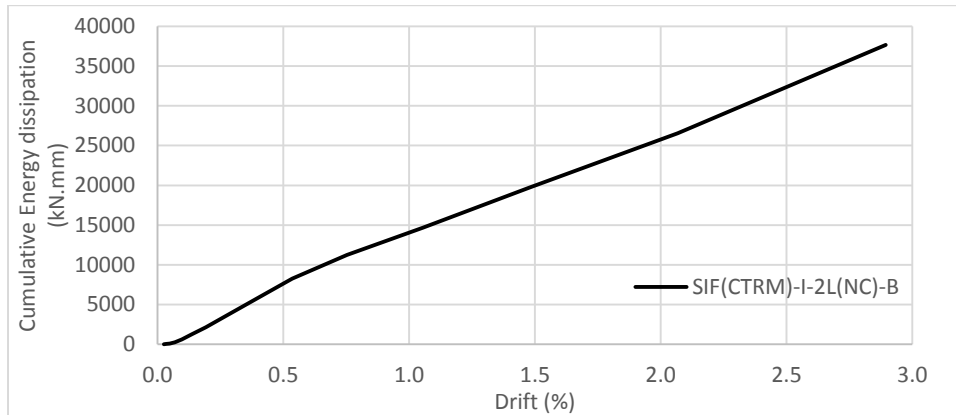


Figure 5.18 Total dissipation of energy until each cycle

### 5.4.3 Results - specimen SIF(DTRM)-I-2L(NC)-B

#### 5.4.3.1 Lateral load-displacement response

The in-plane response of the rc frame with brick infill strengthened with the novel textile mesh in terms of force-displacement diagram is shown in Figure 5.19. The specimen exhibited almost a symmetric response towards positive and negative directions. In the positive direction, the stiffness of the specimen started to decrease after initiation of the cracks at the lateral drift of 0.1% corresponding to the lateral force of 195.9kN. The specimen attained a maximum lateral resistance of 227.1kN at the lateral displacement of 3.6mm corresponding to the lateral drift of 0.2%. After this point, the slope of the force-displacement diagram reduced significantly and the increase on the imposed lateral displacement led to the progressive reduction of the lateral resistance, particularly after the lateral displacement of 7.2mm corresponding to the lateral drift of 0.38%.

In the negative direction, the specimen presented linear response diagram until crack initiation at lateral drift of 0.1% corresponding to the lateral force of 185.1kN. Applying further displacements led to gradual increase of the lateral force until it reached the maximum value of 205.3kN at the lateral drift of 0.2%. By applying further displacements, the lateral force remained almost unchanged until the lateral drift of 0.27%, from which a progressive reduction in the lateral force was recorded. The force corresponding to the maximum lateral displacement was 80kN, which is significantly higher than the resistance of the bare frame (60%).

The monotonic envelope corresponding to the hysteretic force-displacement diagram at each successive cycles is shown in Figure 5.20. As expected, there is no strength degradation in the specimen until the lateral drift of 0.1%, corresponding to the crack initiation point. The strength degradation in the specimen starts after its cracking similar to what was observed in the previous specimens. Besides, similar to the specimen strengthened by commercial textile mesh, the strength degradation remains almost constant after the peak load.

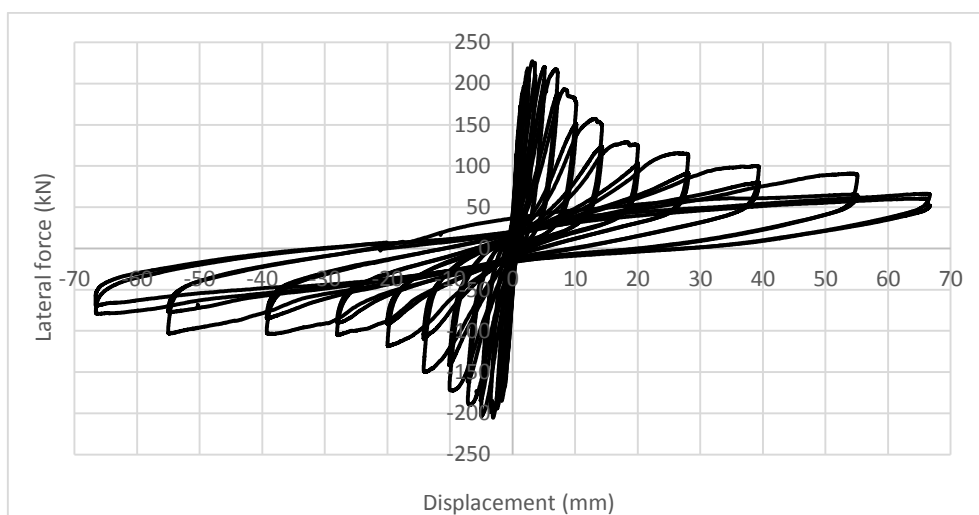


Figure 5.19 Force-displacement diagram of specimen SIF(DTRM)-I-2L(NC)-B

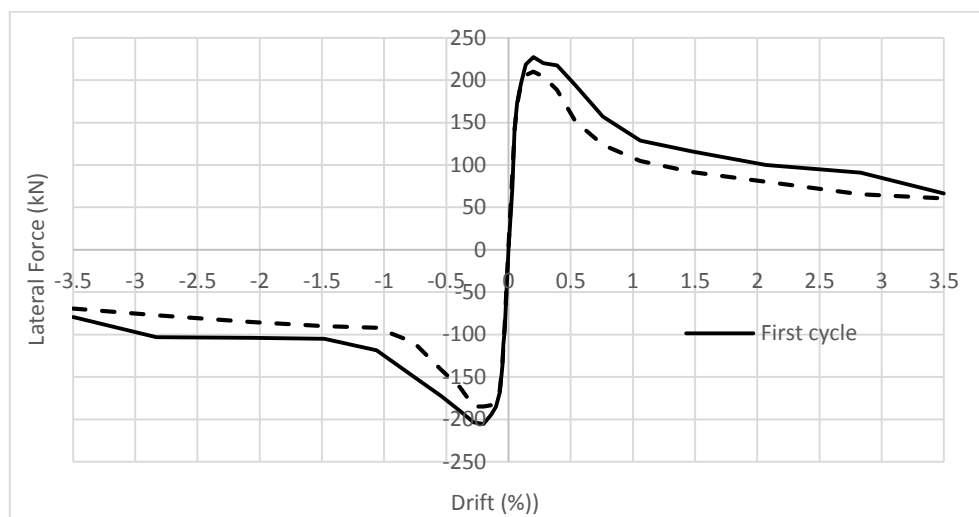


Figure 5.20 Monotonic envelope obtained in specimen SIF(DTRM)-I-2L(NC)-B at each successive cycles

The key parameters regarding the in-plane behavior of the specimen are derived from its monotonic force-displacement diagram, namely the force and displacement related to the first cracking of the specimen ( $H_{cr}$ ,  $d_{cr}$ ), secant stiffness regarding the first cracking point ( $K_e$ ), maximum force attained during in-plane loading ( $H_{max}$ ) and the displacement related to the maximum force ( $d_{Hmax}$ ), see Table 5-4. It is clear that both strengthening techniques represent similar response in terms of initial stiffness and lateral strength.

Table 5-4 Key parameters related to the in-plane behavior of bare frame

Positive direction					Negative direction				
$H_{cr}$ (kN)	$d_{cr}$ (mm)	$K_e$ (kN/mm)	$H_{max}$ (kN)	$d_{Hmax}$ (mm)	$H_{cr}$ (kN)	$d_{cr}$ (mm)	$K_e$ (kN/mm)	$H_{max}$ (kN)	$d_{Hmax}$ (mm)
195.9	1.85	106.1	227.1	3.60	-185.1	-1.79	103.5	-205.3	-3.62

### 5.4.3.2 *Stiffness degradation curve*

The stiffness degradation curve of the specimen is shown in Figure 5.21. It is clear that the specimen exhibits symmetric response in positive and negative directions and the degradation rate in the low levels of lateral drifts is very significant. The initial stiffness of the specimen degraded about 95% until lateral drift of 1% in the positive and negative directions. It is also observed that the trend of variation of the stiffness for both strengthening techniques is relatively similar.

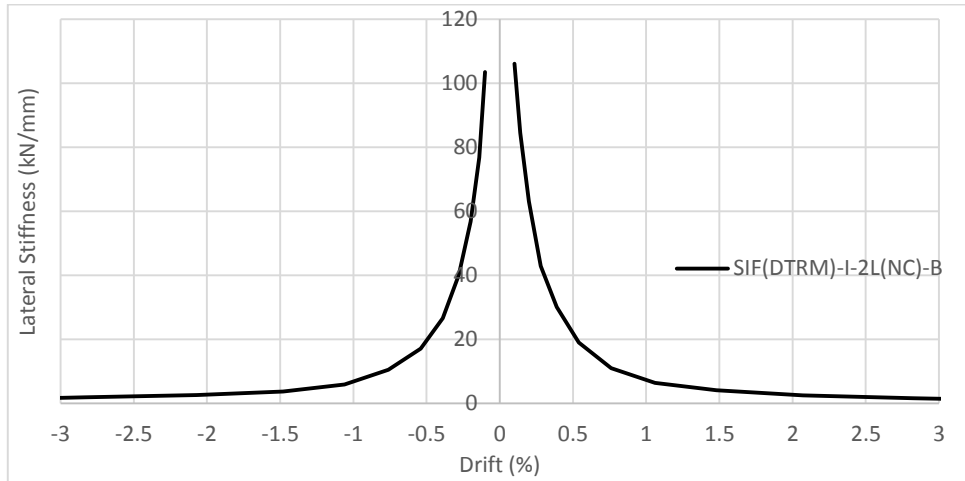


Figure 5.21 Stiffness degradation curve of specimen SIF(DTRM)-I-2L(NC)-B

### 5.4.3.3 *Crack patterns*

The crack patterns obtained in specimen SIF(DTRM)-I-2L(NC)-B for different values of lateral displacement are shown in Figure 5.22. The cracks that formed at early stages of loading at lateral displacement of 0.69 and 0.97 mm corresponding to the lateral drifts of 0.04% and 0.05% are assumed as local cracks, which developed due to the non-smooth finishing of the strengthening layer adjacent to the steel plates placed at the top beam of the rc frame.

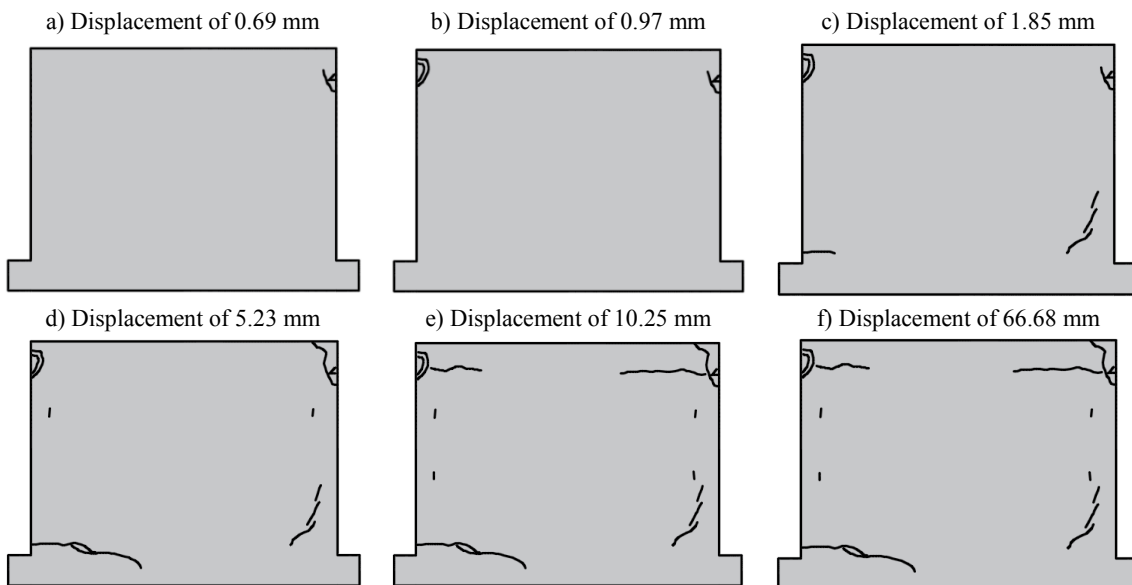


Figure 5.22 Crack propagation of SIF(DTRM)-I-2L(NC)-B

The first significant cracking in the specimen which resulted in the reduction of the secant stiffness was initiated at the lateral drift of 0.1% in both positive and negative directions corresponding to lateral forces of 195.9kN and -185.1kN respectively. After this point, the increase on the imposed lateral displacements resulted in the development of some minor cracking in the strengthening mortar layer, mainly at the level of horizontal and vertical interfaces between the rc frame and brick infill, see Figure 5.22c.

At the lateral displacement of 5.23mm (lateral drift of 0.27%), some cracking was also observed at the neighborhood of the points where shear connectors were positioned on the rc frame. It seems that at this stage the connectors were totally failed due to the shear forces induced by in-plane loading. The cracking pattern did not change significantly after this lateral drift until the end of the test for a lateral drift of 3.5%. Due to the formation of small number of cracks in the retrofitting layer, it appears that few cracks were reflected in the retrofitting layer in the specimen and it seems that the damage progress appears to be better controlled when the designed textile mesh is used.

The strengthening mortar layers started to detach from the rc frame at early stages of loading (lateral drift of 0.07% in both directions) as can be observed from the evolution of the displacement measured at the LVDTs placed to measure eventual debonding of the mortar layer, see Figure 5.23 and Figure 5.24.

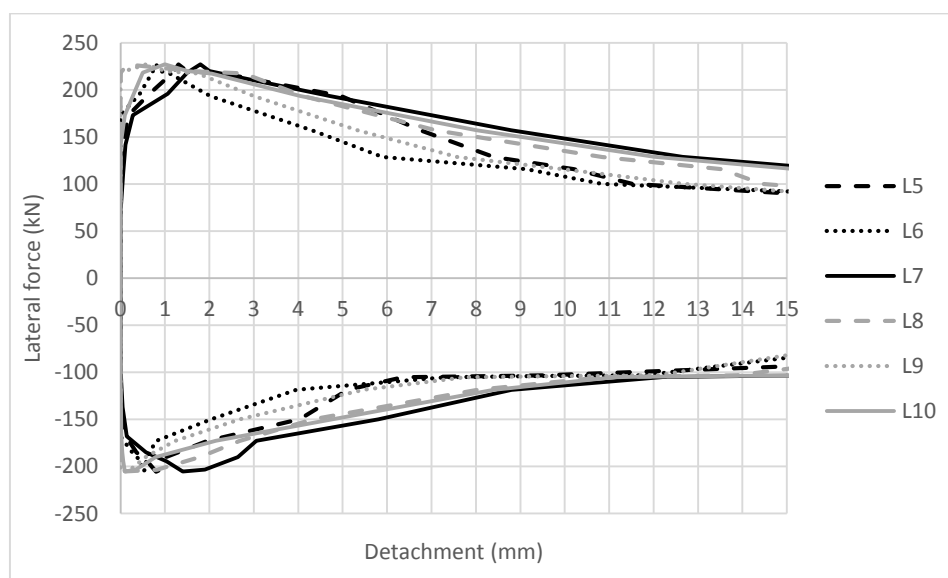


Figure 5.23 Detachment of the strengthening mortar layer from the specimen SIF(DTRM)-I-2L(NC)-B at its external side

At the lateral drift of 0.2%, corresponding to the lateral force of 227.1kN, the strengthening mortar layer was fully detached from the rc frame both at the internal and external leaves. This detachment can be visualized from Figure 5.25a. It is observed that the displacements measured by different LVDTs are very similar, which indicates that the separation of the mortar layer from the rc frame was practically uniform along the height of the specimen. Due to the increase in the detachment of the strengthening mortar layer applied on the internal leaf at higher lateral drifts it bulged in the out-of-plane direction.

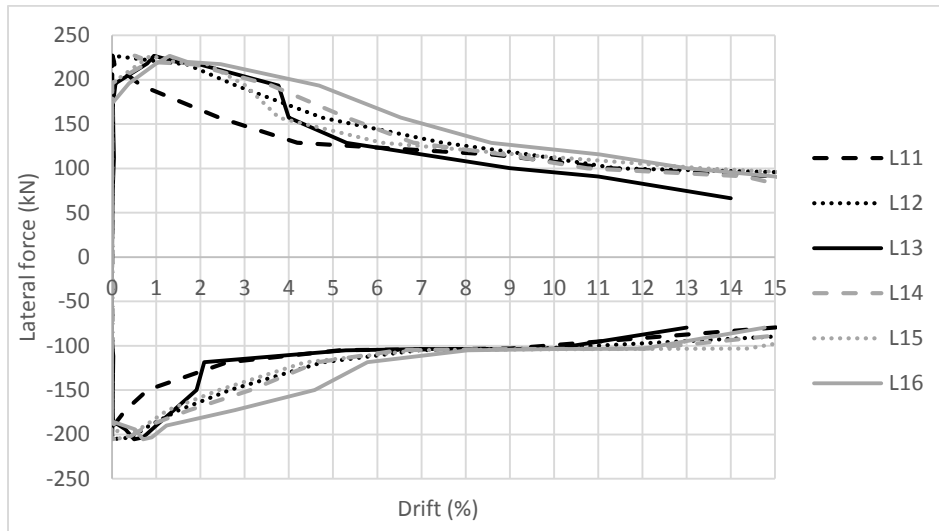


Figure 5.24 Detachment of the strengthening mortar layer from the specimen SIF(DTRM)-I-2L(NC)-B at its internal side

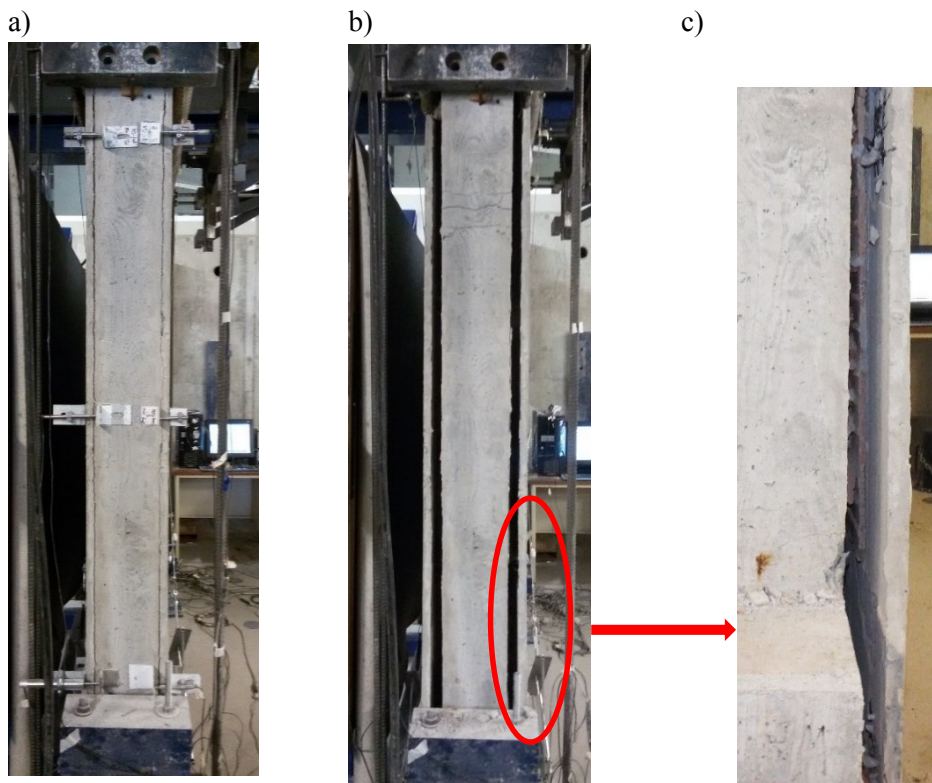


Figure 5.25 Detachment of the strengthening mortar layer at lateral drift of a) 0.2% b) 3.5% c) shear failure of the connectors between retrofitting layer and rc frame

After finishing the test, the external leaf was removed from the specimen and rotated by crane in order to investigate the cracking developed in its inner side after the in-plane test, see Figure 5.26. Similarly to the specimen strengthened with commercial textile mesh, the brick units adjacent to the infill-rc frame interface were completely crushed. Additionally, no visible cracks were observed in the brick infill.



Figure 5.26 External leaf of the brick infill wall crane after the test

The detachment of the strengthening mortar layer from the rc frame disabled the record of reliable displacement in the diagonals to calculate the average shear distortion of both internal and external leaves.

#### 5.4.3.4 *Energy dissipation capacity*

The energy dissipation capacity of the specimen until each cycle is compared with the specimen with commercial textile mesh and shown in Figure 5.27. It is clear that both specimens present similar energy dissipation until lateral the drift of 1%. After this stage, the dissipation of energy at each cycle for specimen strengthened with commercial textile mesh is slightly higher. At lateral drift of 2.89% the difference between the energy dissipation curves increased to 15%.

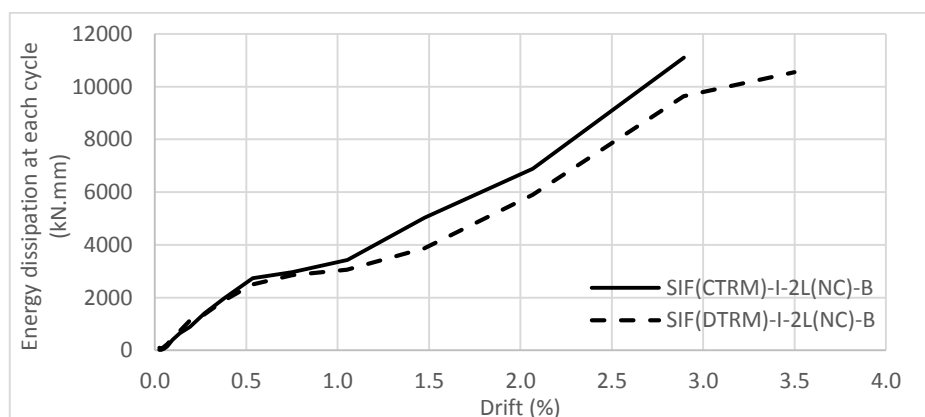


Figure 5.27 Energy dissipation capacity of the strengthened specimens at each cycle

The total energy dissipation capacity of the strengthened specimens is shown in Figure 5.28. It is clear that total energy dissipation capacity of the specimens increased by imposing further displacements to the specimen. This is generally related to the propagation of more cracks at higher displacements, which is the main cause of dissipation of energy. By comparing the results of both strengthened specimens it is observed that they present similar trend for the variation of energy dissipated with the lateral drift.

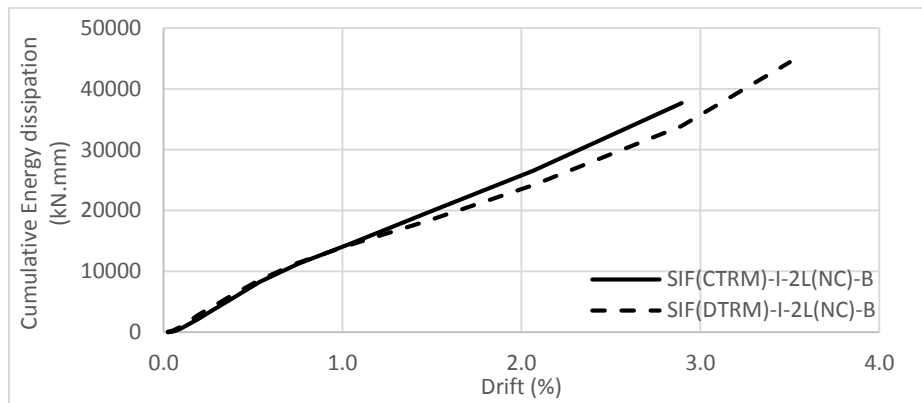


Figure 5.28 Total energy dissipation capacity of the strengthened specimen until each cycle

### 5.5 Behavior of strengthened masonry infills under out-of-plane loading

As mentioned before, two different techniques were employed to enhance the out-of-plane behavior of traditional masonry infills. First, the external and internal leaves of the masonry infill were connected by means of special steel ties to promote the behavior of the brick masonry infill under out-of-plane loading and therefore evaluate its performance in terms of stiffness, resistance and crack distribution. In a second phase, the brick infills were strengthened with textile reinforced mortar (TRM) technique by using the designed and commercial textile meshes, as described in detail previously, and by using the same strengthening application procedure. The test setup and the loading protocols used to test the strengthened specimens under out-of-plane loading were similar to the test setup used for the reference specimens in order to have a logical basis for comparison of the results.

The instrumentation adopted for the specimens is shown in Figure 5.29. The instrumentation of the specimen with the leaves connected with steel ties (SIF-O-2L(C)-B) is similar to the one adopted in the reference specimen (unstrengthened brick infills). In case of the rc frame with brick infill strengthened with TRM technique, additional LVDTs were used to record the possible detachment of the retrofitting layer from the rc frame. For this, three LVDTs were placed on the right side (L13 to L15) of the strengthened mortar layer, three on the left side (L10 to L12), one LVDT at the base of the added layer (L16) and one LVDT at the top part (L17).

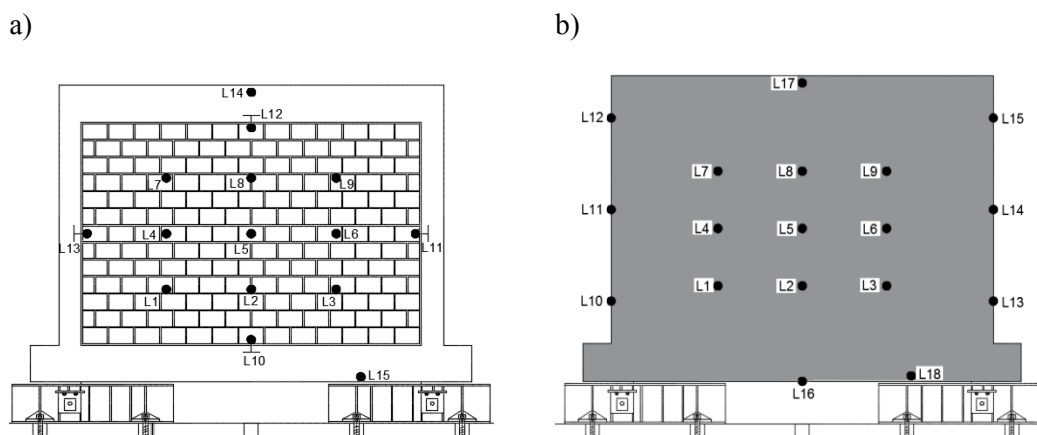


Figure 5.29 Instrumentation adopted in the out-of-plane testing a) SIF-O-2L(C)-B b) specimens strengthened with TRM technique



## 5.5.1 Results - specimen SIF-O-2L(C)-B

### 5.5.1.1 Load-displacement response

The force-displacement diagram obtained in the specimen SIF-O-2L(C)-B subjected to out-of-plane loading is shown in Figure 5.30. A long horizontal crack developed at one third of the height in relation to the upper rc frame-infill interface at the lateral displacement of 2.69mm corresponding to the out-of-plane load of 24.8kN. The pre-peak regime is very considerable, being the peak resistance of 47.3kN attained at the lateral out-of-plane displacement of 29.1mm. The post-peak branch is long and is characterized by the progressive reduction of the strength and stiffness. The lateral resistance at ultimate displacement of 80mm is about 31.5kN, representing a decrease of 33.4% regarding the peak resistance. The infill did not totally collapse at displacement of 80mm but to protect the instrumentation, the test was stopped.

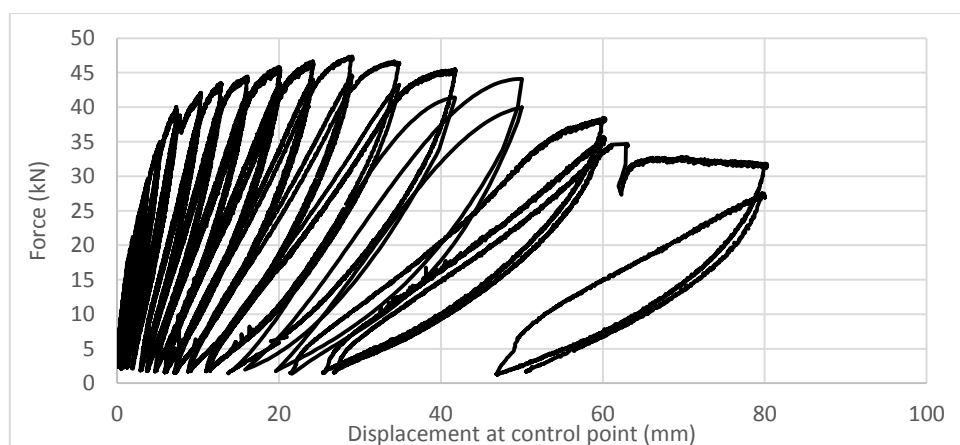


Figure 5.30 Force-displacement diagram of the specimen SIF-O-2L(C)-B under out-of-plane loading

The monotonic force-displacement diagram defined at each successive cycles is shown in Figure 5.31. Until the crack initiation, no strength degradation in the second cycles was observed. The strength degradation initiated after cracking and increased until maximum lateral resistance was attained, keeping practically constant values during the out-of-plane loading. The strength degradation is calculated as 12% at the ultimate displacement.

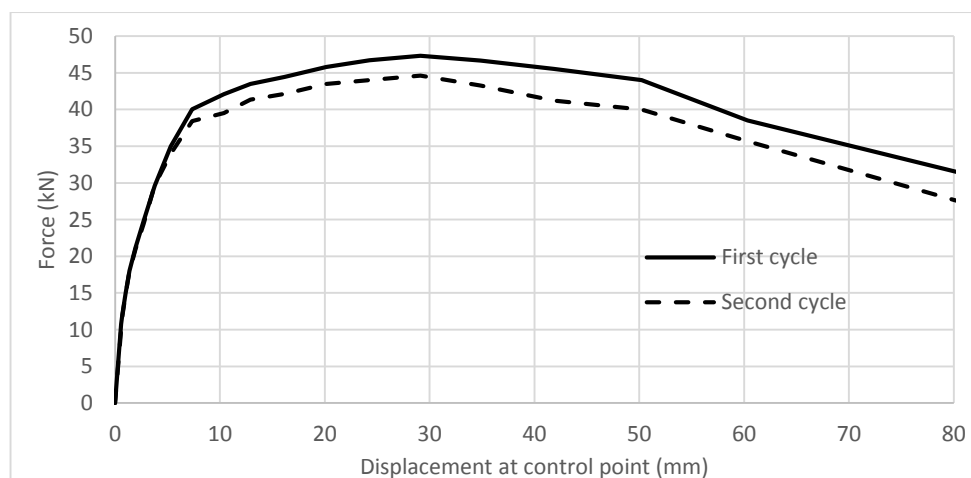


Figure 5.31 Monotonic force-displacement envelope of the specimen SIF-O-2L(C)-B at each successive cycles

### 5.5.1.2 *Stiffness degradation curve*

The stiffness of the specimen during out-of-plane loading is shown in Figure 5.32. It is calculated as the slope of the line connecting the maximum force in the monotonic force-displacement diagram to the origin. It is clear that the trend of variation of the stiffness is logarithmic meaning that degradation rate is considerably higher at low levels of imposed displacements. A degradation of 75% in the initial stiffness was recorded until out-of-plane displacement of 10mm. It is also observed that this specimen presented higher initial stiffness than the reference specimen SIF-O-1L-B. This confirms the effectiveness of connecting both leaves on enhancing the stiffness of the structure.

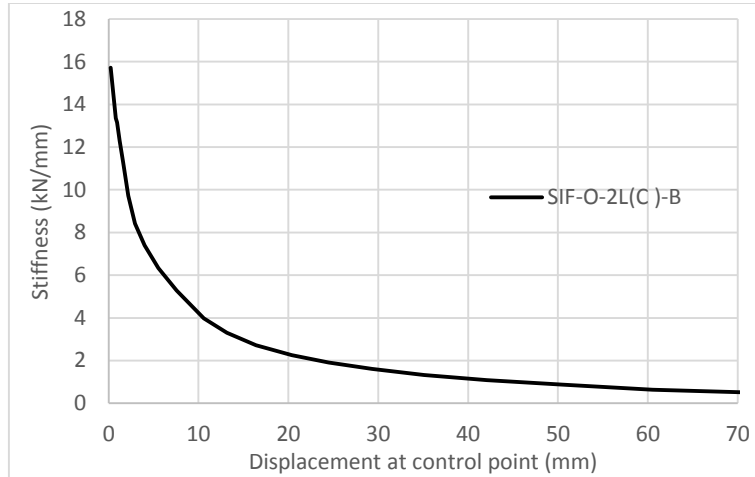


Figure 5.32 Stiffness degradation curve of specimen SIF-O-2L(C)-B

### 5.5.1.3 *Crack patterns*

The crack propagation observed in the double leaf wall under out-of-plane loading is shown in Figure 5.33. The first cracking initiated approximately at one third of the height of the wall from the top interface along the horizontal unit-mortar joints at displacement of 2.69mm corresponding to the out-of-plane force of 24.8kN (Figure 5.33a). This crack extended in length at out-of-plane displacement of 3.76mm (Figure 5.33b). At the displacement of 5.27mm, another horizontal crack initiated at fourth row of the infill from its bottom part, corresponding to approximately one third of the height of the infill from its bottom part, see Figure 5.33c. The diagonal cracking along unit-mortar interfaces initiated at the out-of-plane displacement of 7.38mm corresponding to the out-of-plane force of 40kN. Additional diagonal cracks developed from the upper horizontal crack towards the upper and bottom corners (Figure 5.33e). The first cracking in the rc frame developed at the upper left corner at the displacement of 12.91mm corresponding to the force of 43.5kN, see Figure 5.33f. Also at this displacement level, the upper interface between the brick infill and the rc frame started to crack, which should be related to the out-of-plane sliding of the top interface. The increase on the imposed lateral displacement resulted in the extension of previous cracks and at the displacement of 20.18mm an additional crack at mid span of upper rc beam developed (Figure 5.33h). It should be stressed that the cracking progresses until the out-of-plane resistance is attained and at this stage the major cracking was already developed. This appears to justify the long pre-peak observed in the force-displacement diagram. The opening of horizontal cracks and formation of diagonal cracking from the central part of the walls towards the upper and bottom corners are associated to the development of the two-way resisting arching mechanism. At higher imposed lateral displacements, additional cracks developed in the brick infill (Figure 5.33m-o),

the upper and lateral interfaces cracked and, consequently, some level of sliding occurred in the interfaces. The specimen presented a considerable cracking at displacement of 80mm and it was decided to stop the test to avoid any damage on the LVDTs, see Figure 5.34.

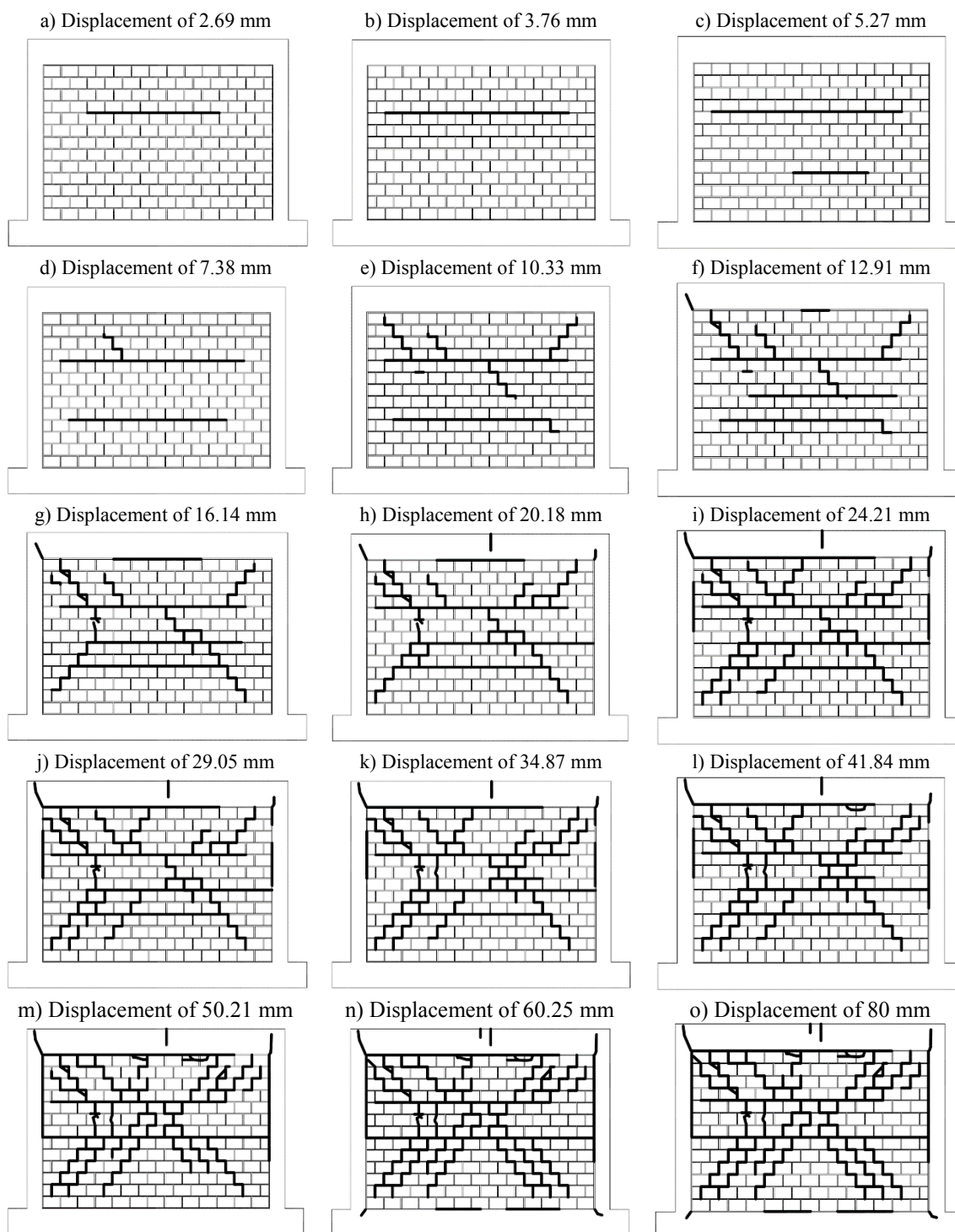


Figure 5.33 Crack propagation of SIF-O-2L(C)-B – external leaf

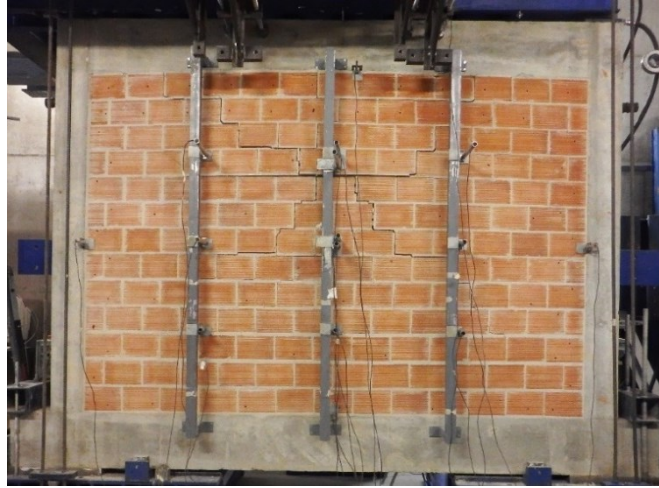


Figure 5.34 Cracking of the specimen at the end of the test

5.5.1.4 **Deformation of the infill**

The deformation of the brick infill at different points during out-of-plane loading is shown in Figure 5.35. It is clear that the control point, which is assumed as mid-point of the brick infill, records the highest displacement during the test. It is also seen that the displacement measured in LVDT L8 approximates the displacement of control point, being a consequence of the sliding of the upper interface. This evolution of displacements indicates that the deformation is approximately symmetric in the horizontal direction, which can be also assessed by direct comparing of the displacements measured in the central horizontal profile (LVDT L4, L5 and L6) presented in Figure 5.36.

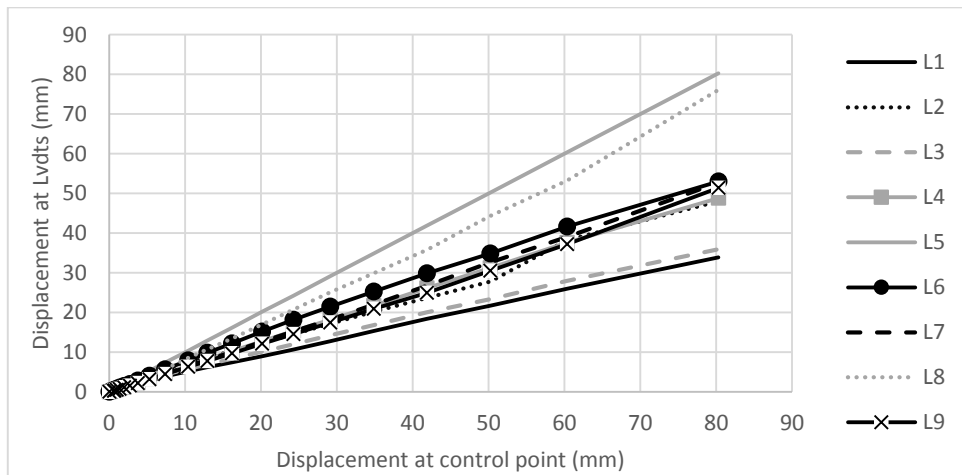


Figure 5.35 Deformation of the infill at measured points

The displacements measured along the central vertical profile (LVDT L2, L5 and L8) shown in Figure 5.37 indicate that similar displacements are measured in LVDT L2 and L8 until the lateral displacements of 12.91mm. After this lateral displacement, it is evident that the upper part of the infill deforms more than the bottom part. As already discussed, this behavior is related to the sliding of the upper interface. This is also confirmed through the analysis of the displacements measured by LVDT L12 (Figure 5.38), placed in the specimen to measure the possible sliding of the upper interface between the top rc beam and the brick infill. It is clear that after crack initiation

of the upper interface at displacement of 12.91mm, it exhibits higher displacements associated to the sliding, when compared to the other interfaces. The sliding of this interface increases as the imposed lateral displacement in the control point increases. The cracking of the left and right interfaces during out-of-plane loading can be also explained by the sliding value represented in Figure 5.38. However, it should be noticed that these values are very low. As expected, the displacement measured by the LVDT L10 is zero, being compatible with the absence of cracks in the bottom interface between the bottom rc beam and the brick infill.

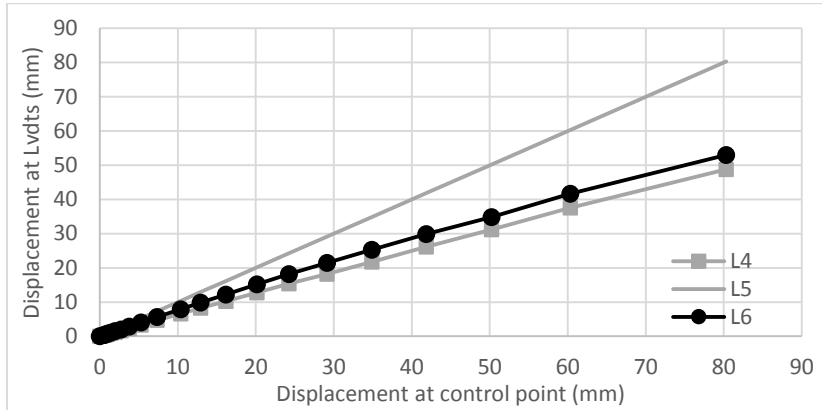


Figure 5.36 Displacement of the LVDTs along the central horizontal profile of the brick infill

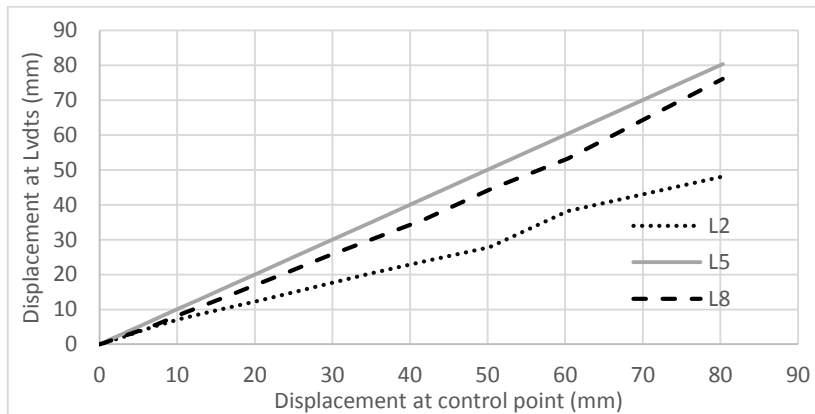


Figure 5.37 Displacement of the LVDTs along the central vertical profile of the brick infill

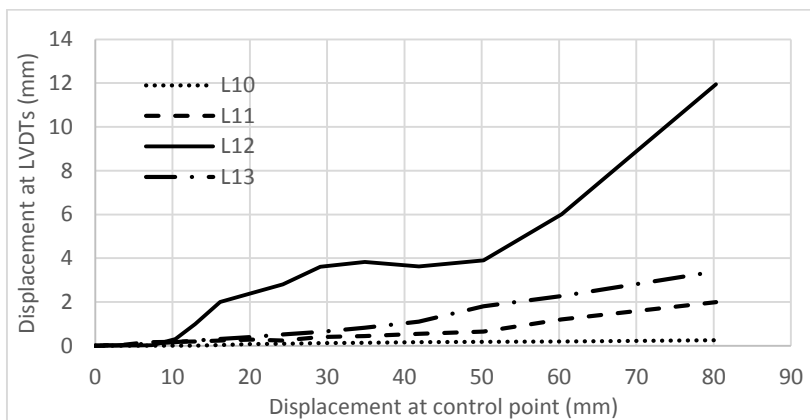


Figure 5.38 Displacements measured on the interfaces between brick infill and rc frame

The deformation map of the brick infill due to the out-of-plane loading, obtained based on the displacements measured in the brick infill and interfaces, is shown graphically in Figure 5.39. By analyzing the deformation patterns of the infill at different stages, it is concluded that two-way resisting arching mechanism was formed from beginning of the test. By increasing the lateral displacement applied on the control point, the upper interface slid, leading to asymmetric deformation pattern along the height of the brick infill. On the other hand, the symmetry on the horizontal deformation remains until the end of the out-of-plane test, being associated to similar behavior of the vertical interfaces.

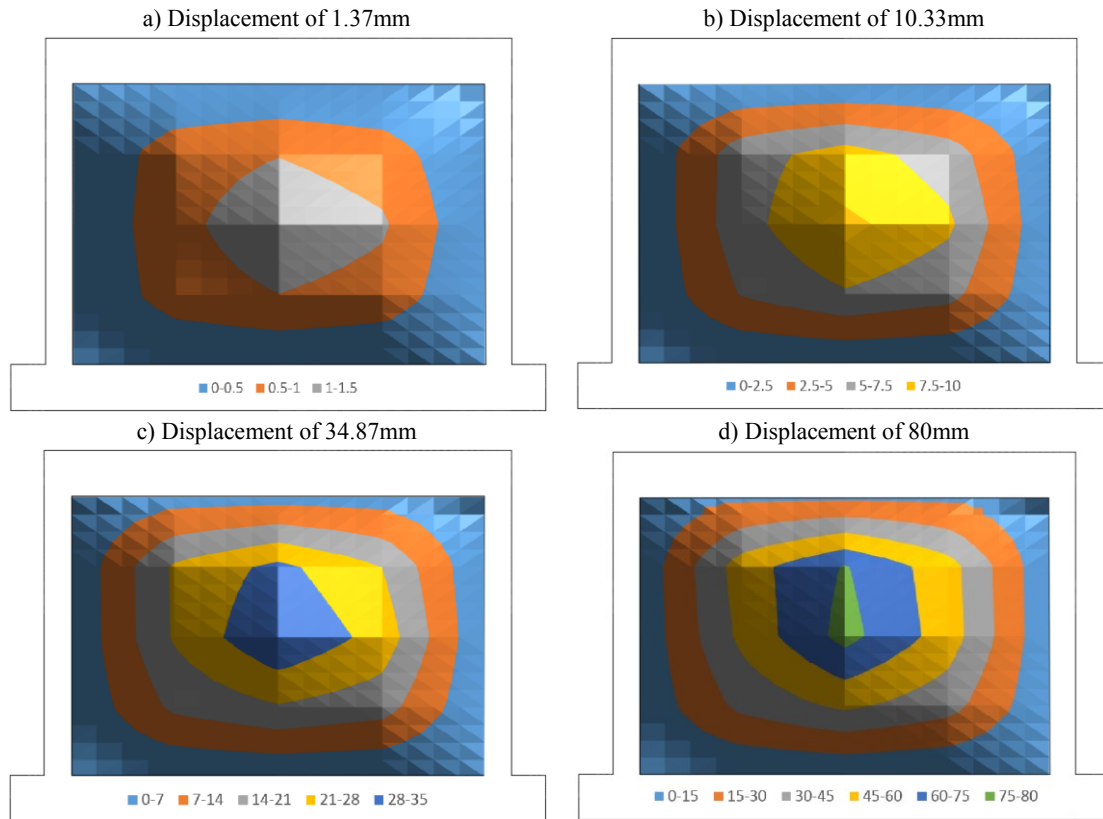


Figure 5.39 Deformation of the infill at different out-of-plane displacements

The plastic deformations of the specimen at two successive cycles are shown in Figure 5.40 and Figure 5.41. It is clear that similarly to the previously tested specimens, the increasing rate of the plastic deformation at higher displacements is considerably higher. It is also observed that the plastic deformation of the specimen at two successive cycles is similar. As presented in Figure 5.41, the plastic deformations of the specimen could be represented by a polynomial function of order 2 meaning that higher amplitudes of displacements lead to higher plastic deformations.

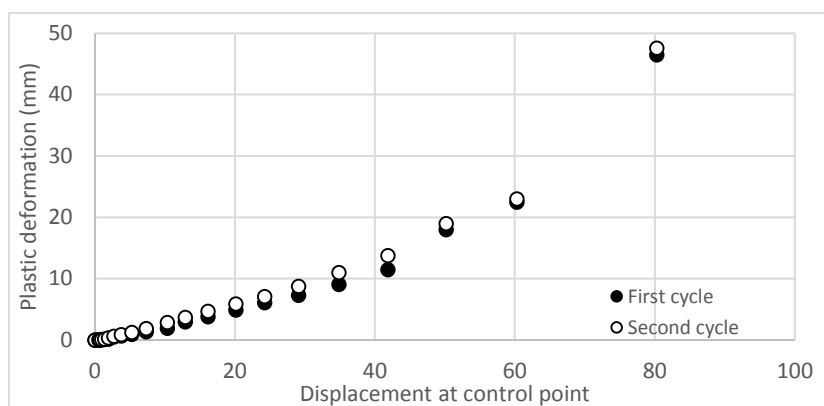


Figure 5.40 Plastic deformation of the specimen at two successive cycles

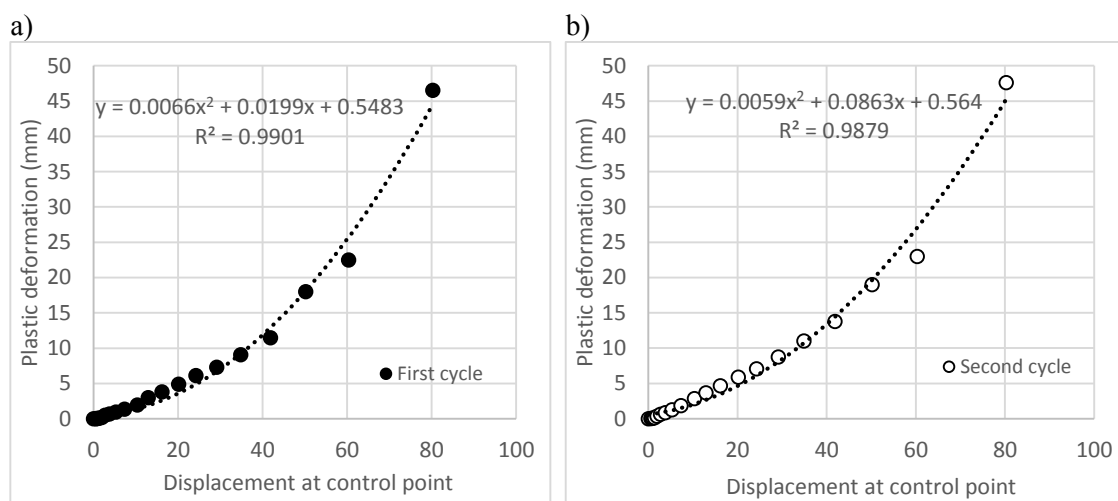


Figure 5.41 Plastic deformation of SIF-O-2L(C)-B at two successive cycles; a) first cycle b) second cycle

### 5.5.1.5 Energy dissipation capacity

The energy dissipation capacity of the specimen at each cycle is calculated as the area enclosed in the loops of each cycle in the force-displacement diagram and is shown in Figure 5.42. It is clear that the dissipation of energy increases by applying further displacements to the control point. The main reason for this behavior is related to the propagation of cracks at higher imposed displacements which dissipates energy.

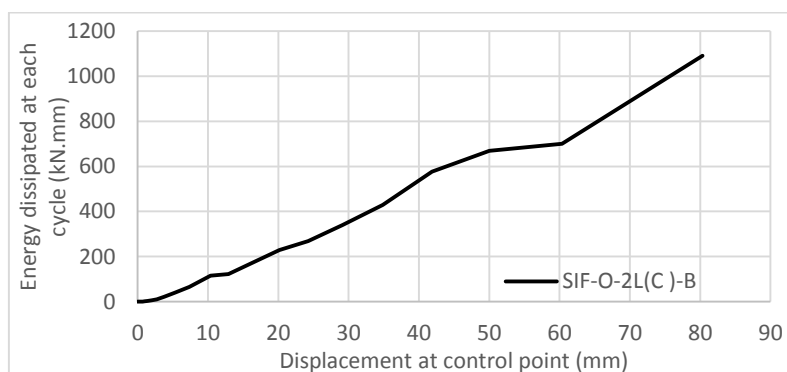


Figure 5.42 Energy dissipation capacity of the specimen at each cycle

The total energy dissipation of the strengthened specimen until each cycle is shown in Figure 5.43 and compared with the energy dissipation capacity of the reference specimen SIF-O-1L-B (Chapter 4). It is clear that the strengthened specimen presents higher total energy dissipation capacity than the reference specimen. The increase of the total dissipation of the energy at the end of the test for strengthened specimen is calculated as approximately 50%.

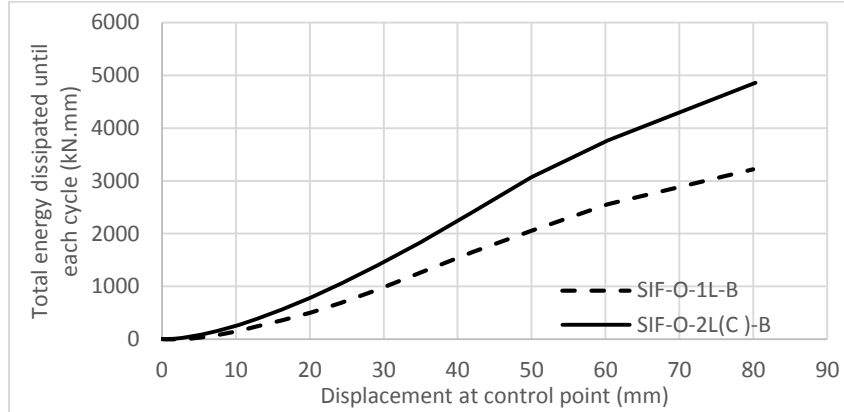


Figure 5.43 Total energy dissipated until each cycle compared with SIF-O-1L-B

### 5.5.2 Results - specimen SIF(CTRM)-O-1L-B

As previously mentioned, the specimens strengthened with textile reinforced mortar were tested under out-of-plane loading by considering the same test setup and the loading protocol used in the reference specimen. In the specimen where the commercial textile mesh was applied, the fixation of the steel tubes that support the LVDTs measuring the deformation of the brick infill was done directly to the added mortar layer. This resulted in erroneous measuring of the displacements of the brick infill by detaching the added layer from rc frame, even if the masonry infill deformed considerably as seen in Figure 5.44.

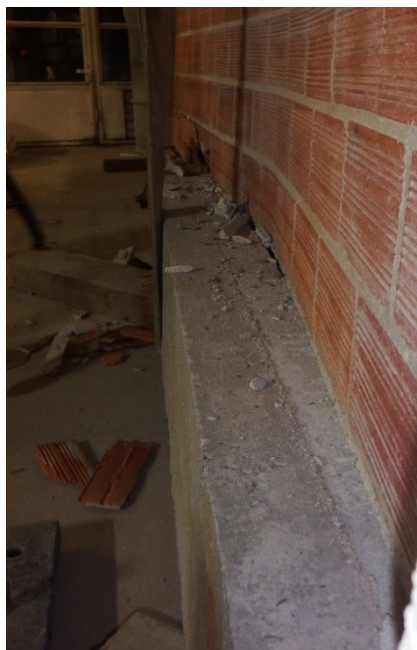
After finishing the test, the final deformation of the infill was checked and it was observed that the brick infill was detached from the upper and bottom rc beams. This indicates that the deformation of the masonry was predominantly along the horizontal direction, which should be associated to the one way horizontal bending of the masonry infill. The deformation of the wall in relation to its initial configuration was measured, and displacements of about 80mm and 102mm were obtained at the bottom and top rc beams. The erroneous deformation measured by the LVDTs resulted from the detachment of the retrofitting layer at the early stages of loading. Thus the displacements measured by LVDTs are displacements measured in relation to a movable reference with unknown real displacements. In any case, it should be underlined that the deformation pattern of this specimen should be clearly distinct from the one recorded in the specimens without reinforced mortar layer, as sliding of the brick infill from the bottom rc beam was considerable, contrarily to the reference specimen, where no sliding occurred at the bottom interface. This is also associated to the predominant bending developed in the horizontal direction.



a)



b)



c)



Figure 5.44 Final deformation of the infill; a)total deformation, b)detachment of the wall from bottom rc beam c)detachment of the wall from upper rc beam

The force-displacement diagram displayed in Figure 5.45 relates to the real force measured by the load cells and the “relative” displacement measured in the control point (LVDT L5) in relation to the points where the steel tubes were fixed.

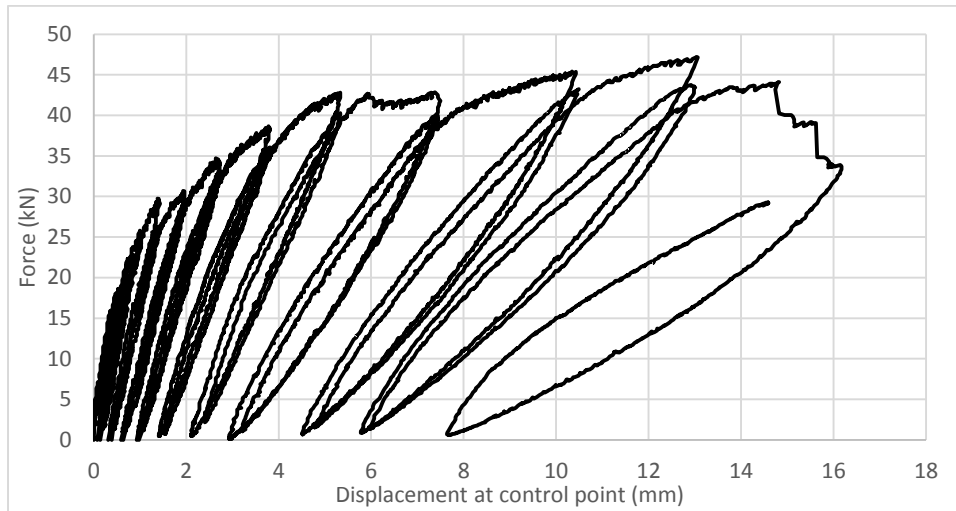


Figure 5.45 Force-relative displacement measured in the control point for specimen SIF(CTRM)-O-1L-B

The propagation of cracks in the reinforced mortar layer is shown in Figure 5.46. Due to the erroneous displacements measured in the LVDTs, no displacement values were associated to the cracking patterns. It is clear that the first cracking relates to a horizontal crack initiating from mid-height of the infill. By increasing the out-of-plane displacement in the control point, the horizontal crack extends and reaches the right side of the specimen. This appears to indicate that at early stages of deformation the brick infill bends in both vertical and horizontal directions. Horizontal cracking of the specimen along with considerable sliding of the brick infill through top and bottom rc beams make the predominant flexural bending happens along horizontal direction. Also it could be concluded that the vertical cracks observed in the specimen are results of horizontal bending of the infill.

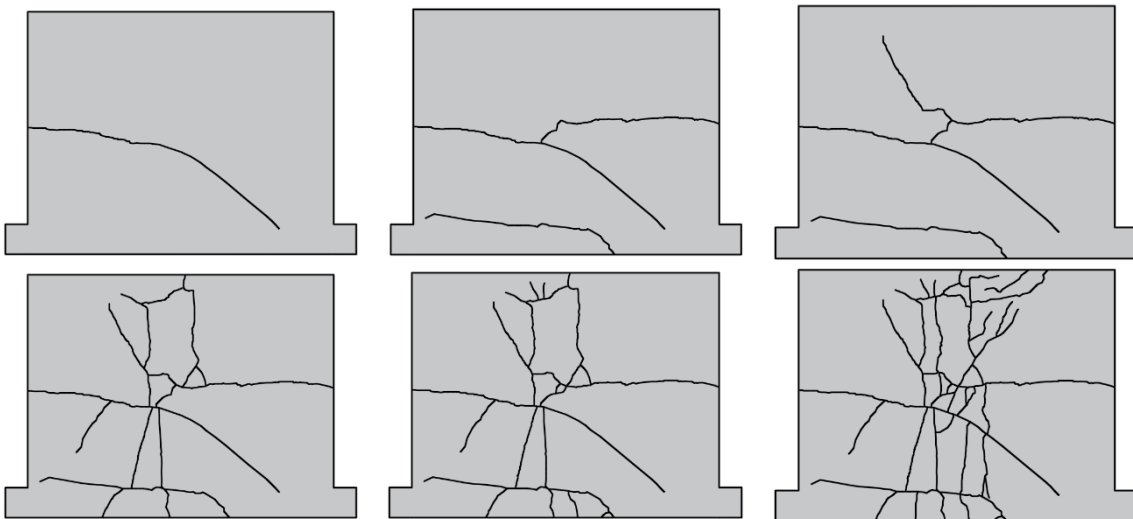


Figure 5.46 Crack propagation recorded in the reinforced mortar layer in specimen SIF(CTRM)-O-1L-B

After the test, the specimen was lifted by a crane to investigate the damage progress in its internal part, see Figure 5.47. It is observed that the damage pattern included only the crushing of the bricks adjacent to the top and bottom interfaces. This indicates a good adhesion of the rendering mortar to the brick infill, enabling a composite behavior and an effective stress redistribution from the brick infill to the reinforced rendering mortar.



Figure 5.47 Out-of-plane damage in the interior part of the infill

### 5.5.3 Results - specimen SIF(DTRM)-O-1L-B

To overcome the problems encountered in the previous specimen for measuring the exact deformation of the infill, some modifications were made in this specimen for placement of the supports of LVDTs. The supports of the LVDTs measuring the deformation of the infill were directly mounted on the RC beams by cutting the retrofitting layer and fixing to the RC beams as shown in Figure 5.48. It seems that in this case, the detachment of the retrofitting layer will not cause any problems in the testing program.

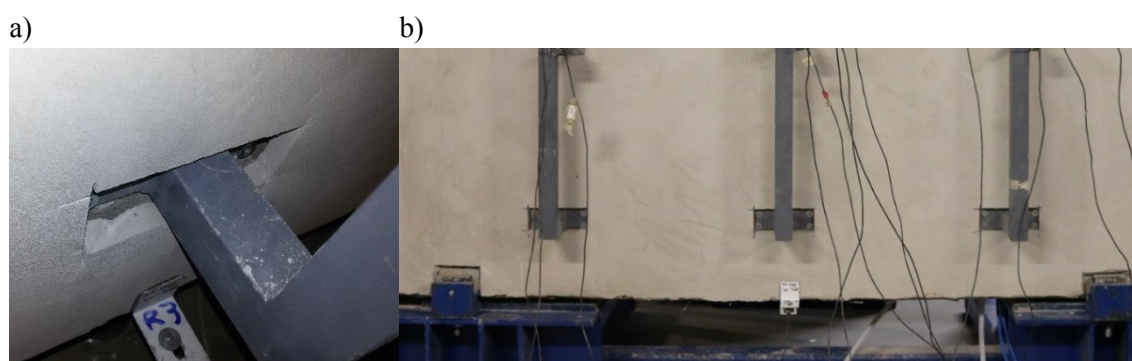


Figure 5.48 Alternative connection of the LVDTs supports to the rc beams of the frame

#### 5.5.3.1 Load-displacement response

The force-displacement diagram recorded in the specimen reinforced with the textile mesh composed of the composite braided rods is shown in Figure 5.49. At very early stages of loading, at displacement of 0.5mm, the reduction in the slope of force-displacement diagram was observed, which probably can be related to the local detachment of the reinforced mortar layer from rc frame or minor cracking of the infill that was not reflected to the reinforced mortar layer. This local detachment was not captured by the LVDTs placed on the specimen, which indicates that it could happen in areas near to the interfaces between infill and RC frame.

The first visible crack on the reinforced mortar layer was detected at the displacement of 1.92mm, corresponding to the force of 33.4kN by formation of central horizontal crack along the length of the wall. This crack resulted in the significant reduction in the slope of the force-displacement

diagram. It is evident that after the displacement of 2.70mm corresponding to the out-of-plane resistance of 39.3kN, the increase on the out-of-plane resistance was very slight until the peak. The maximum resistance was about 44.5kN and was achieved at the displacement of 35.13mm. It is important to notice that there is almost a plateau until the attainment of the out-of-plane resistance, which appears to indicate that an important redistribution of forces is achieved, which can be associated to a distributed damage. Based on the force-displacement diagram it is seen that the plastic deformations attained very important values, which differentiate its response with the one exhibited by the specimen without reinforced mortar layer. This appears to indicate that the damage is developed in cumulative deformational state of the infill, contrary to what happened in the reference specimens where considerable percentage of the deformation was recovered.

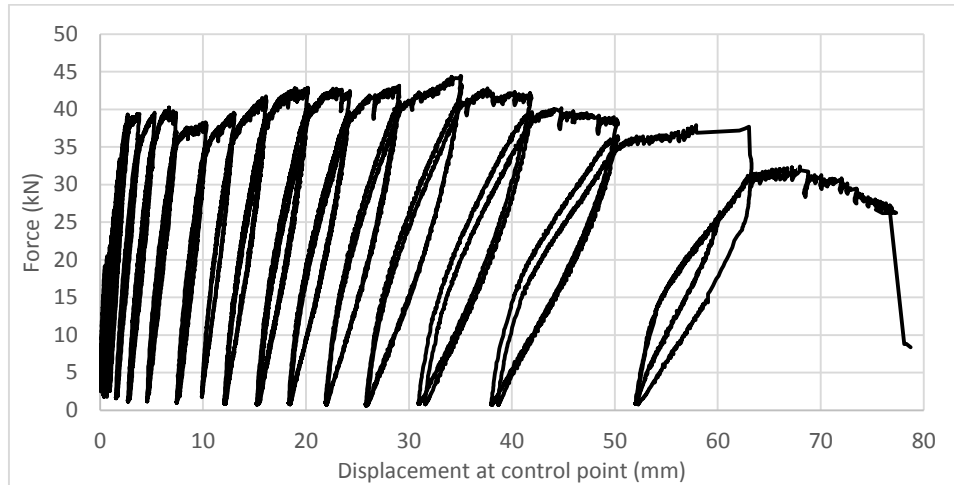


Figure 5.49 Force-displacement diagram of the specimen SIF(DTRM)-O-1L-B

The post peak regime is characterized by the slow decrease on the lateral resistance until the last cycle. The maximum displacement recorded was about 77.3mm, after which the resistance immediately dropped to 8.4kN. This sudden drop is associated to the collapse of the interface between the bottom rc beams and the brick infill, see Figure 5.50.

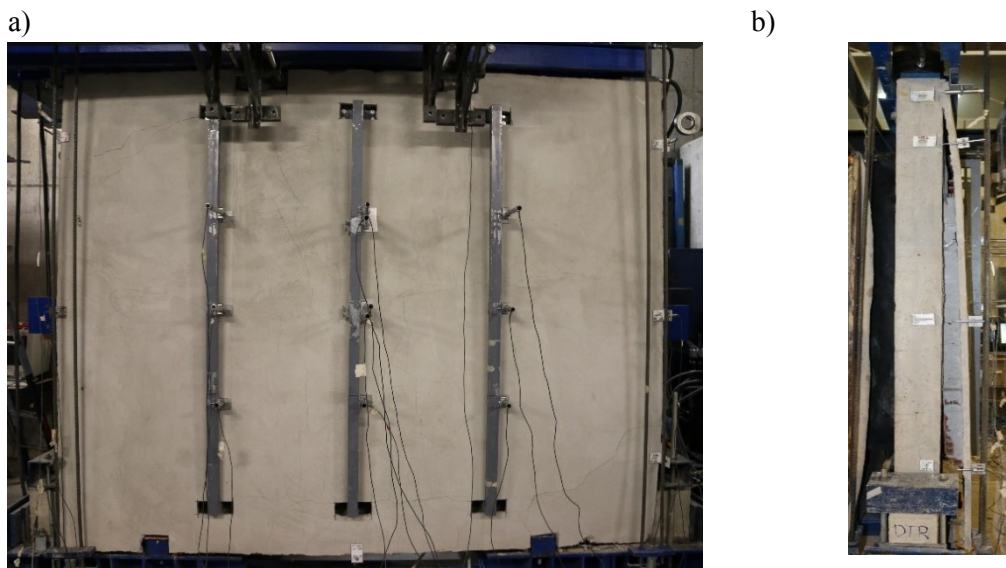


Figure 5.50 Final state of the specimen SIF(DTRM)-O-1L-B a)front view b)lateral view

From Figure 5.51, where the monotonic force-displacement envelopes at each successive cycles are shown, it is clear that until the cracking initiation, no strength degradation was observed. After initiation of the cracks in the specimen, the out-of-plane resistance reduces in the second cycles for the same imposed displacement level. It seems that the strength degradation is practically constant until the displacement of 60mm, in which higher reduction of 30% on the resistance of the first cycle was recorded.

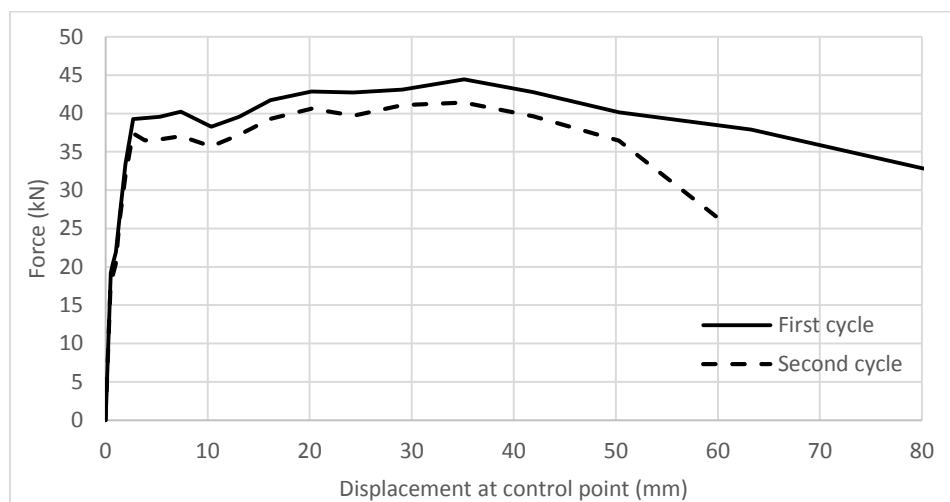


Figure 5.51 Monotonic force-displacement envelope of the specimen SIF(DTRM)-O-1L-B for successive cycles

### 5.5.3.2 *Stiffness degradation curve*

The stiffness of the specimen calculated as the secant stiffness at each point in the monotonic force-displacement diagram and shown in Figure 5.52. The specimen has higher initial stiffness with respect to the unstrengthened specimens. The trend of variation of the curve is also logarithmic, meaning that its degradation rate at lower imposed displacements is considerable. The initial stiffness of the specimen in the out-of-plane direction degraded about 88% until out-of-plane displacement of 10mm.

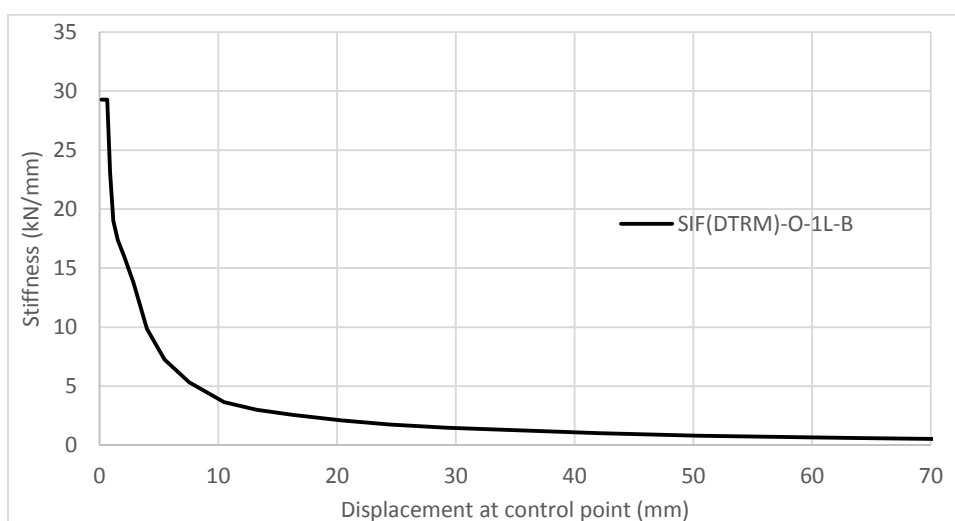


Figure 5.52 Stiffness degradation curve of specimen SIF(DTRM)-O-1L-B

### 5.5.3.3 Crack patterns

The cracking pattern recorded during the out-of-plane test for distinct levels of out-of-plane displacements is shown in Figure 5.53. As mentioned before, the first cracking that was observed at displacement of 1.92mm was composed of a horizontal crack at mid height of the brick infill, see Figure 5.53a.

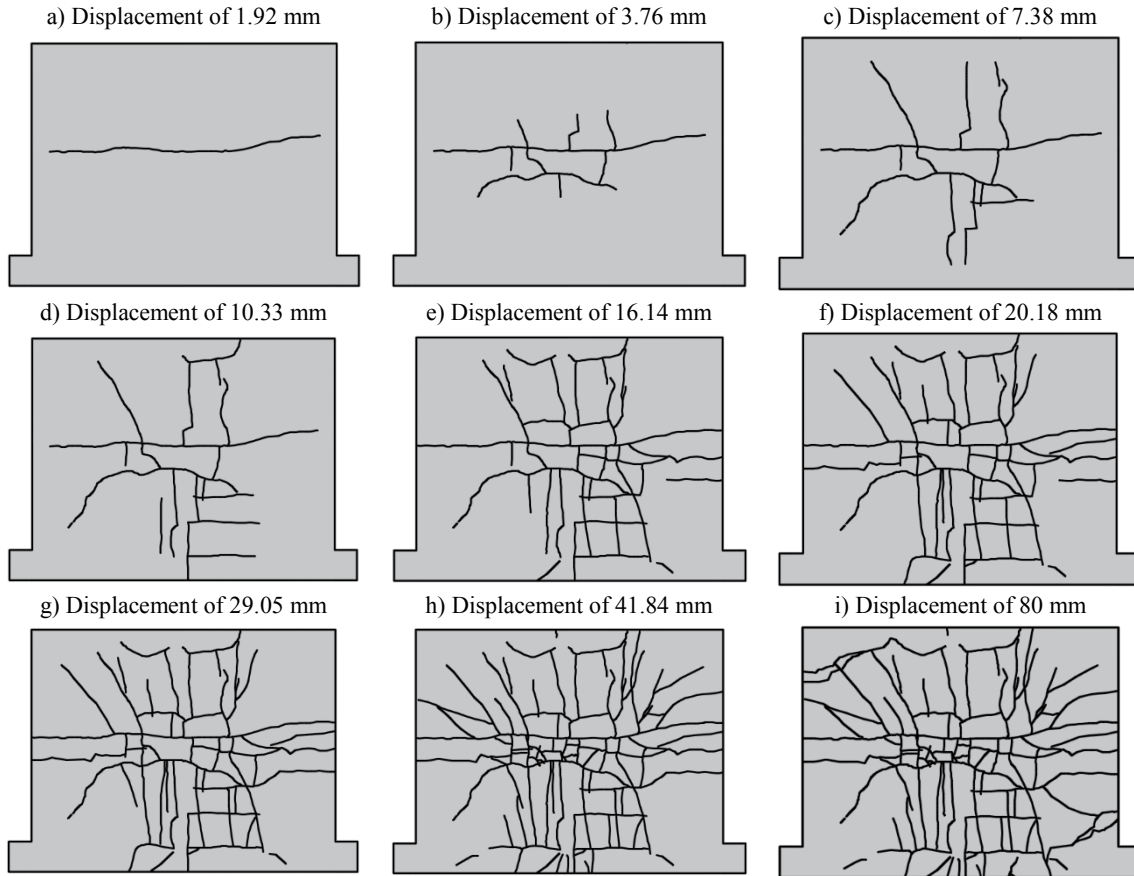


Figure 5.53 Crack propagation in specimen SIF(DTRM)-O-1L-B

For higher imposed out-of-plane displacements, crack propagation was observed in the vertical direction at the central part of the infill initiated from the central horizontal crack (Figure 5.53b-c). These cracks extended and reached the top and bottom part of the specimen at displacement of 10.33mm, see Figure 5.53d. At the out-of-plane displacement of 16.14mm the horizontal crack extended to reach the right and left side of the specimen and at displacement of 20.18mm other horizontal cracks formed extending along the length of the specimen, see Figure 5.53e-f. The reinforced mortar layer was fully cracked when the maximum out-of-plane force was reached (imposed displacement of 35.13mm). By applying higher displacements, the crack density continued to enlarge and the crack opening increased.

The detachment of the reinforced mortar layer from the rc frame was captured at out-of-plane displacement of 3.76mm at mid height of the right rc column (L14), see Figure 5.54. At the displacement of 7.38mm, the displacement measured in LVDT L16 increased sharply, indicating the detachment of the reinforced mortar layer from the bottom rc beam. The displacement measured by this LVDT continued to increase significantly for subsequent increasing imposed displacements, achieving the value of 10mm for the lateral displacement of 30mm. The

displacement measured by LVDT L11 was increased for almost 1mm after the lateral displacement of 7.38mm. The values of displacement measured by LVDT L11 and L14 are practically the same during the out-of-plane test, indicating the symmetric deformation until the last displacement level. It is clear that the values of displacements are very low, indicating that the detachment of the reinforced mortar layer is very limited, apart from the one observed at the bottom rc beam. Notice that the generalized increasing of displacements measured by the LVDTs placed along the perimeter of the rc frame was only significant at the last out-of-plane displacement levels, corresponding to the collapse of the infill. This appears to indicate the adequate stress transfer from the brick infill to the reinforced mortar layer, resulting in the smeared cracking of the reinforced mortar layer, as previously mentioned.

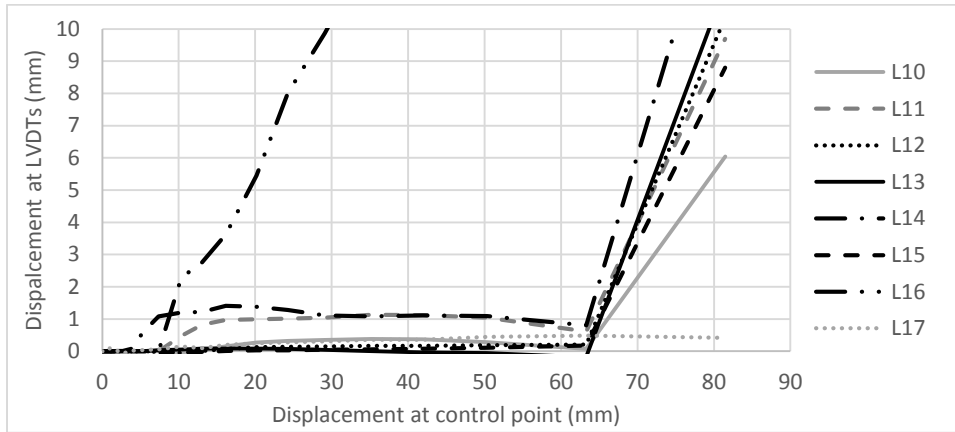


Figure 5.54 Deformation in LVDTs capturing the detachment between reinforced mortar layer and the rc frame with brick infill

5.5.3.4 *Deformation of the infill*

The analysis of the displacement of the brick infill along different alignments can be carried out from Figure 5.55. It is clear that the LVDTs along the central vertical profile (L2, L5 and L8) present the highest displacements, being in this case particularly close, contrarily to the reference specimen in which there was a clear difference between LVDT L5 and the other two LVDTs (L2 and L8), at least for early stages of deformation, see Figure 5.56. By analyzing the results of the horizontal central profile (L4, L5 and L6) it is seen that the displacements recorded in L4 and L6 are very close and clearly lower than the maximum displacements at mid span, see Figure 5.57.

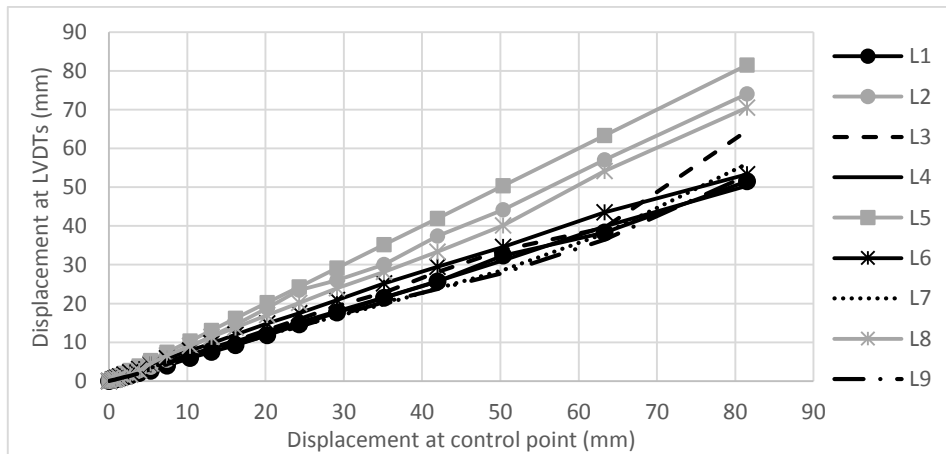


Figure 5.55 Deformation of the infill at different positions

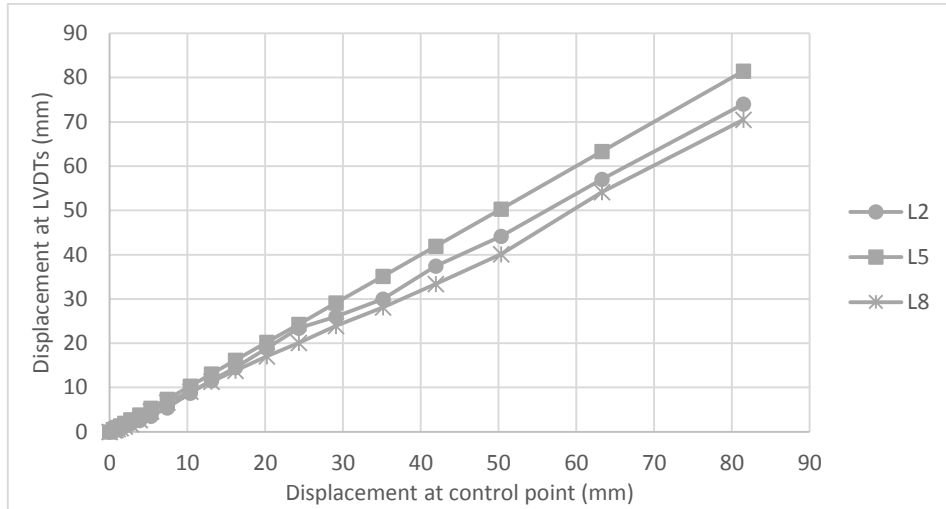


Figure 5.56 Displacements along the central vertical profile

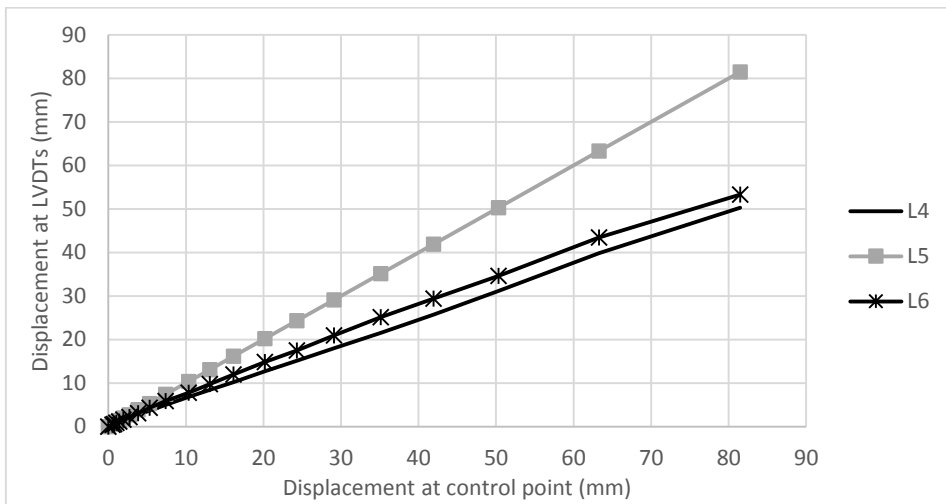


Figure 5.57 Displacements along the central horizontal profile

By combining the information of the horizontal and vertical profiles (Figure 5.56 and Figure 5.57), it is concluded that the final deformation appears to be as a result of one way predominant flexure.

The deformation of the infill at different levels of imposed out-of-plane displacements is shown in Figure 5.58 via contour lines. It is evident that the control point of the specimen always has the maximum deformation among the other points. It is also observed that at the first levels of loading the specimen deforms symmetrically in the horizontal and vertical directions, see Figure 5.58a-b. At higher imposed displacements, by considerable sliding of infill through the bottom rc beam the predominant flexural bending could be confirmed as horizontal.

As shown in Figure 5.50b, at final stages of loading, the lower interface between the rc beam and the brick infill collapsed and it bulged outside. This is also reflected in the deformation shape given in Figure 5.58c-d.



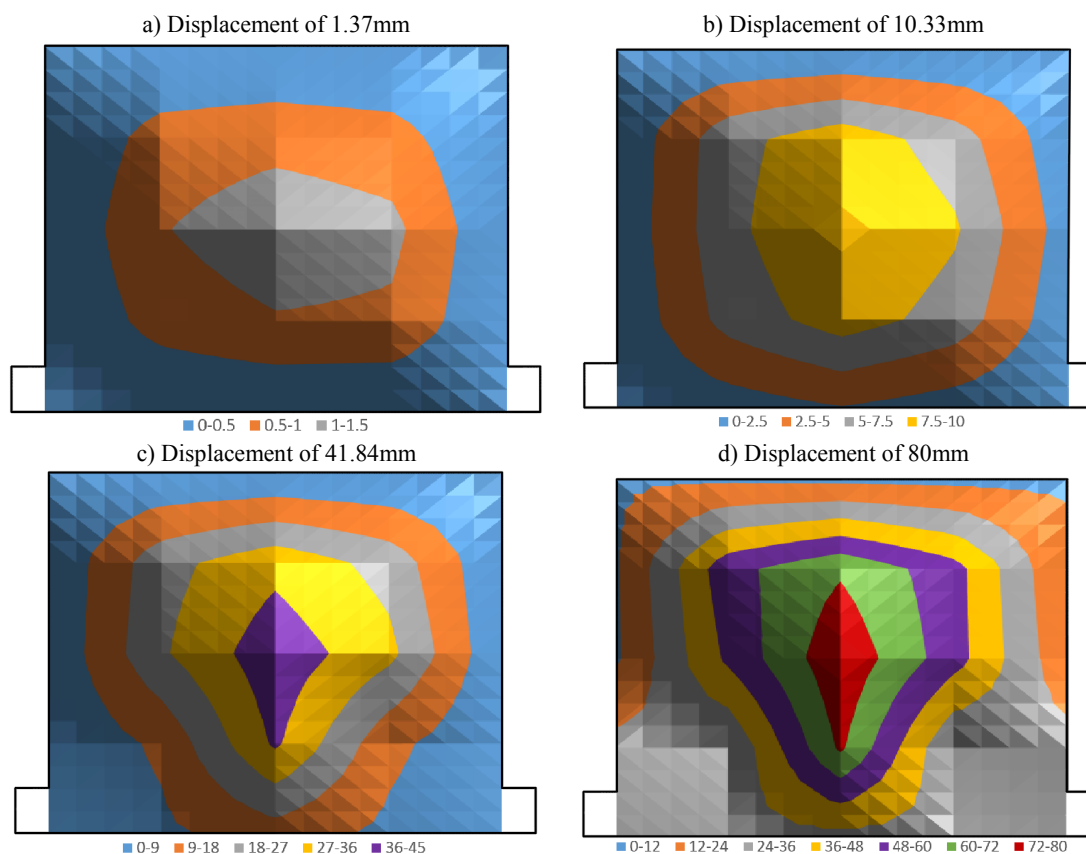


Figure 5.58 Deformation of the infill at different out-of-plane displacements

One of the reasons of detachment of the retrofitting layer from rc frame is inefficiency of the connectors applied in the rc frame. The connectors were made of glass fibers and were placed on the specimen by means of special resin. It seems the resins malfunctioned during out-of-plane loading and the connectors slid and finally detached from the rc frame, see Figure 5.59.

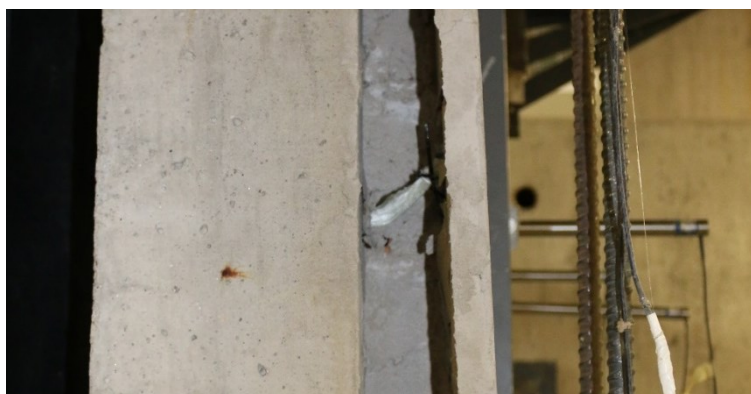


Figure 5.59 Detachment of the connectors from rc frame

The progression of plastic deformation at two successive cycles during out-of-plane loading is shown in Figure 5.60. It is clear that this specimen has represented higher amounts of plastic deformations in the first and second cycles which contrarily to the previously tested specimens its trend of variation can be approximated by a line with  $R^2$  of almost 1. The plastic deformations of this specimen at the first and second cycles of distinct out-of-plane displacements seems to be similar.

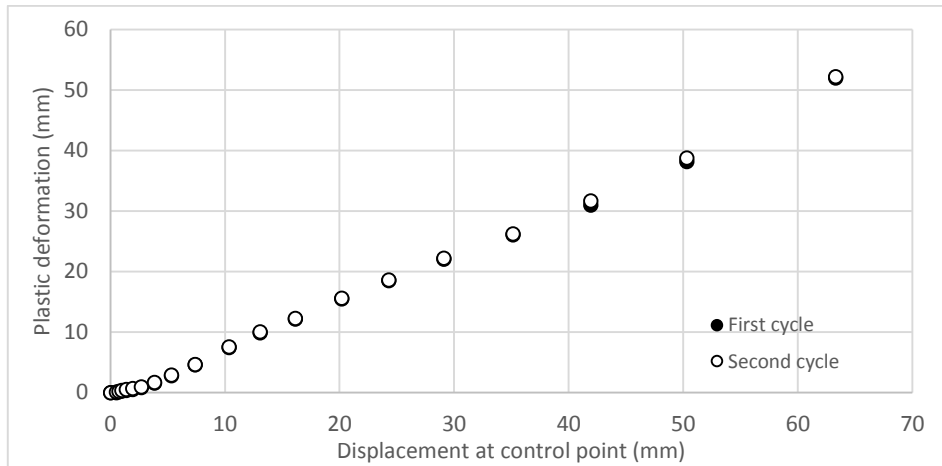


Figure 5.60 Plastic deformations in the strengthened specimen at each successive cycles

During the out-of-plane test, it was also noticed that in the unloading process, small amount of imposed displacement was recovered, which is reflected by the cumulative plastic deformation following a linear trend as the lateral drift increases, see Figure 5.61.

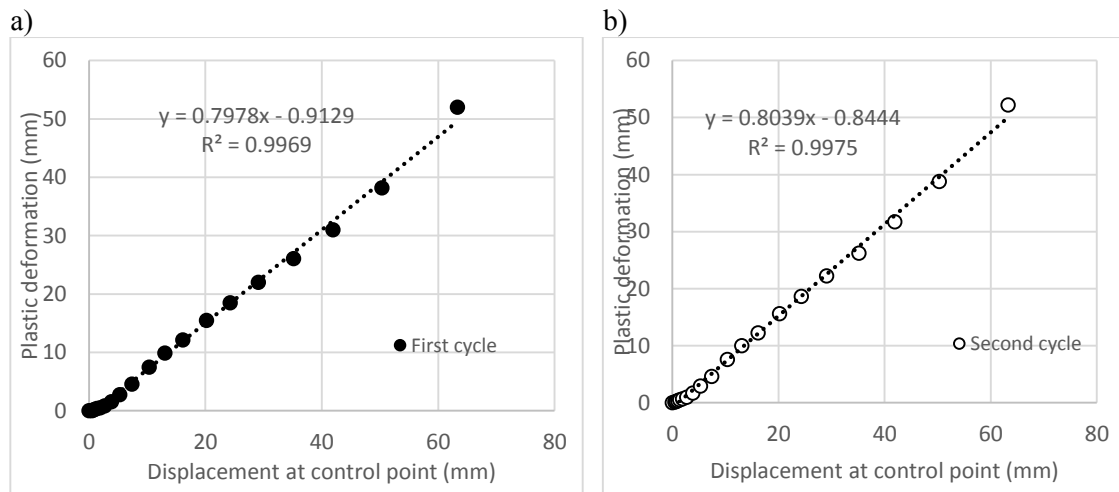


Figure 5.61 Plastic deformation at two successive cycles; a) first cycle b) second cycle

### 5.5.3.5 Energy dissipation capacity

The energy dissipation capacity of the specimen at each cycle is shown in Figure 5.62. The increasing trend of variation at larger displacements is related to the propagation of more cracks in the specimen.

The total energy dissipation capacity of the strengthened specimen until each cycle is calculated and compared with reference specimen, see Figure 5.63. It is clear that both specimens represented higher dissipation of energy at higher imposed displacements. It is also observed that the strengthened specimen dissipated more energy than the reference specimen during the out-of-plane loading. The increase in the total energy dissipation capacity of strengthened specimen is calculated as 20%.

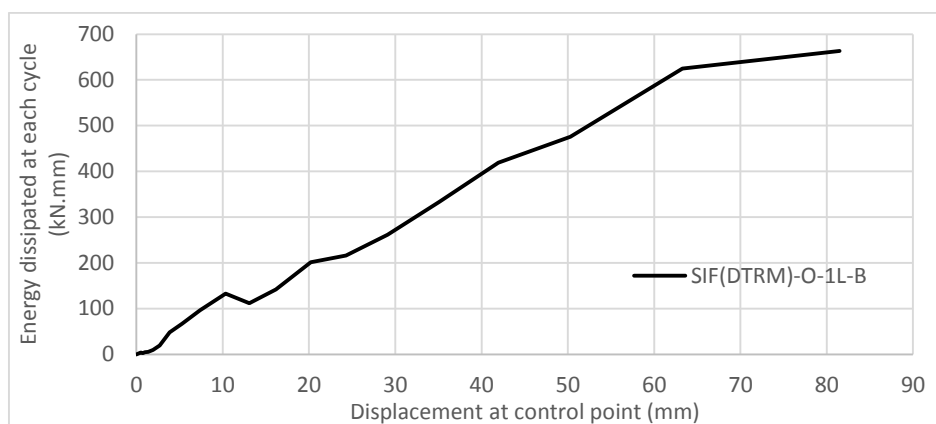


Figure 5.62 Energy dissipation capacity of the strengthened specimen at each cycle

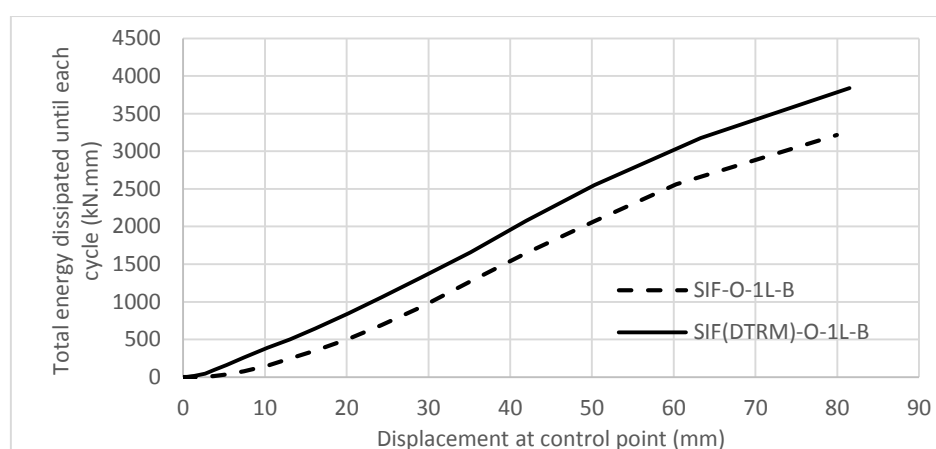


Figure 5.63 Total energy dissipation capacity of the strengthened specimen until each cycle compared with reference specimen

## 5.6 Comparison of the results

### 5.6.1 In-plane behavior

The monotonic envelopes of the force-displacement diagrams of the strengthened and unstrengthened specimens are shown in Figure 5.64 and the key parameters characterizing their in-plane behavior in terms of lateral stiffness and resistance are presented in Table 5-5. The rc frames with brick infills tested until distinct in-plane lateral drifts of 0.3%, 0.5% and 1% are also included in the comparison. It is clear that the addition of textile reinforced mortar improved the in-plane behavior of rc frames with brick infills. In average, the increase of the in-plane lateral stiffness and resistance was 43% and 41% respectively, when the designed textile meshes were applied. When the commercial textile meshes were used, the lateral stiffness and lateral resistance increase by 44% and 38% respectively. These results appear to indicate that the performance of the textile meshes is very similar.

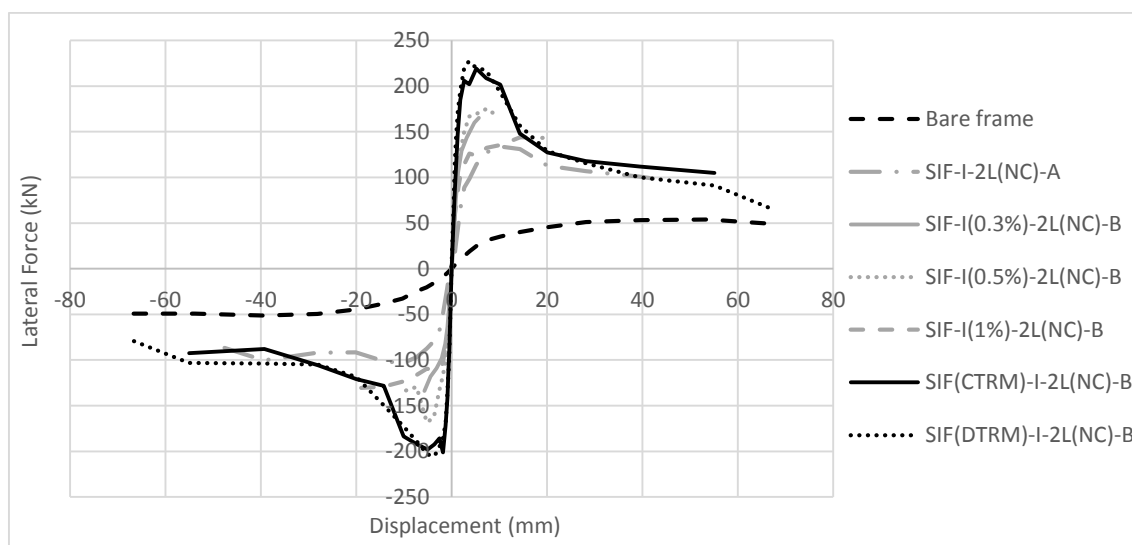


Figure 5.64 Force-displacement envelopes for unstrengthened and strengthened specimens

Table 5-5 Lateral stiffness and strength of strengthened and unstrengthened specimens

Model	Positive Direction		Negative Direction		Average	
	Stiffness (kN/mm)	Strength (kN)	Stiffness (kN/mm)	Strength (kN)	Stiffness (kN/mm)	Strength (kN)
Bare Frame	5.1	53.9	4.6	51.4	4.9	52.7
SIF-I-2L(NC)-A	33.4	133.9	27.4	103.6	30.4	118.8
SIF-IO(0.3%)-2L(NC)-B	78.0	165.4	70.7	133.8	73.3	152.9
SIF-IO(0.5%)-2L(NC)-B	84.1	175.2	77.3	168.4		
SIF-IO(1%)-2L(NC)-B	65.1	143.9	64.7	130.6		
SIF(CTRM)-I-2L(NC)-B	100.8	219.2	110.5	201.1	105.7	210.2
SIF(DTRM)-I-2L(NC)-B	106.1	227.1	103.5	205.3	104.8	216.2

The trend of variation of the lateral stiffness of unstrengthened and strengthened specimens is shown in Figure 5.65. It is clear that at early stages of loading, strengthened specimens have higher initial stiffness than unstrengthened specimen. By increasing the imposed displacements, the difference between the stiffness of unstrengthened and strengthened specimens is decreased and at lateral drift of 0.75% in the positive and negative directions, they have exhibited similar results.

An important aspect to be considered in strengthened specimens is related to the damage developed in the brick infills. According to the damage accumulated in the brick infill after the in-plane testing shown in Figure 5.66, it is seen that the application of the reinforced mortar layer on the specimens decreases significantly the damage of brick infill. At the end of the test at lateral drift of 2.5% in the unstrengthened specimen, the brick infill presents an almost smeared crack

patterns composed of cracks along the unit-mortar interfaces with different widths. On the contrary, in the case of the brick infills reinforced with textile meshes, the damage of the brick infill is associated to the crushing of units along the interface between the rc frame and the brick infill. Similar results were also found by Lourenço et al. [34] in static cyclic and dynamic tests of brick infill where a reinforced mortar layer (steel mesh) was added to brick infills. The reinforced mortar layer appears to work as damage concentrator, as the major cracking developed in the rendering. This possibly enables a more simplified and economic retrofitting intervention after the occurrence of a seismic event.

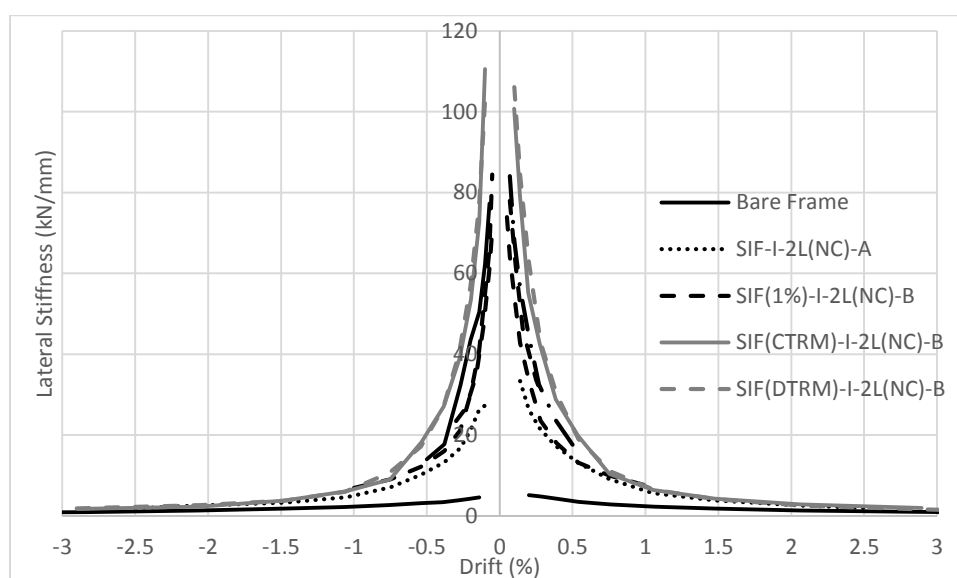


Figure 5.65 Stiffness degradation curves of unstrengthened and strengthened specimens

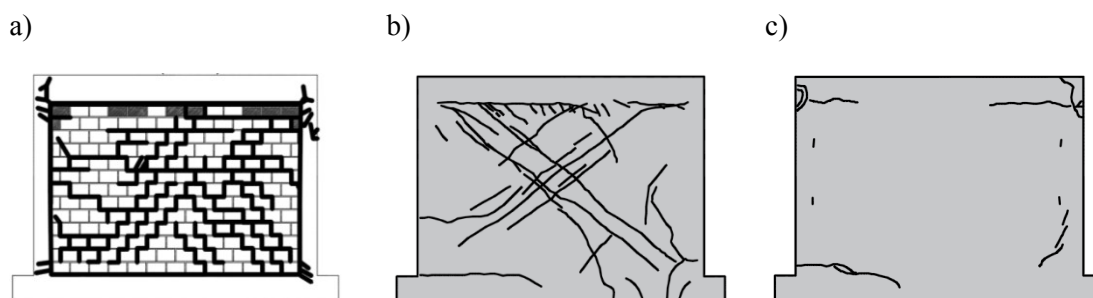


Figure 5.66 Comparison of the damage of the brick infill after the test a) unstrengthened brick infill b) strengthening with commercial textile mesh c) strengthening with designed textile mesh

One of the problems observed in the in-plane behavior of the retrofitted specimens is detachment of the retrofitting layer from rc frame at early stages of loading. It is clear that during earthquakes, in-plane and out-of-plane loads will interact and it is important to avoid the shear failure of the connectors. However, it should be noticed that no debonding of the reinforced mortar layer from the brick infill was observed, which means that the glass fibers connectors can be a possibility to improve the adherence of the textile meshes to the brick infills. In this case, it would be important to study an alternative connector for the rc frame.

The energy dissipation capacity of unstrengthened and strengthened specimens are shown in Figure 5.67. It is clear that both strengthened specimens have similar energy dissipation capacity which are considerably higher than the energy dissipation capacity of unstrengthened specimens.

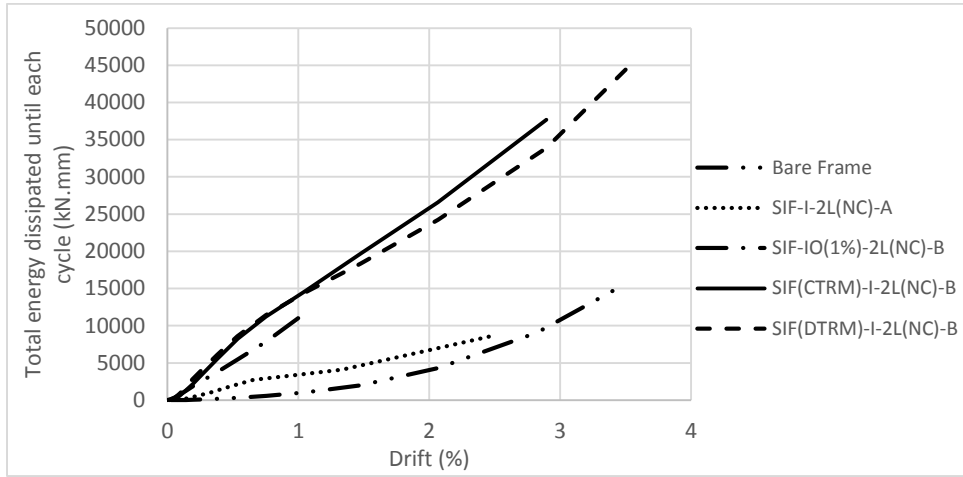


Figure 5.67 Energy dissipation capacity of strengthened and unstrengthened specimens

### 5.6.2 Out-of-plane testing

The out-of-plane force-displacement envelopes obtained for the unstrengthened and strengthened brick infills are shown in Figure 5.68. The parameters related to the initial stiffness, secant stiffness at 30% of the maximum force and out-of-plane resistance of the distinct specimens are represented in Table 5-6.

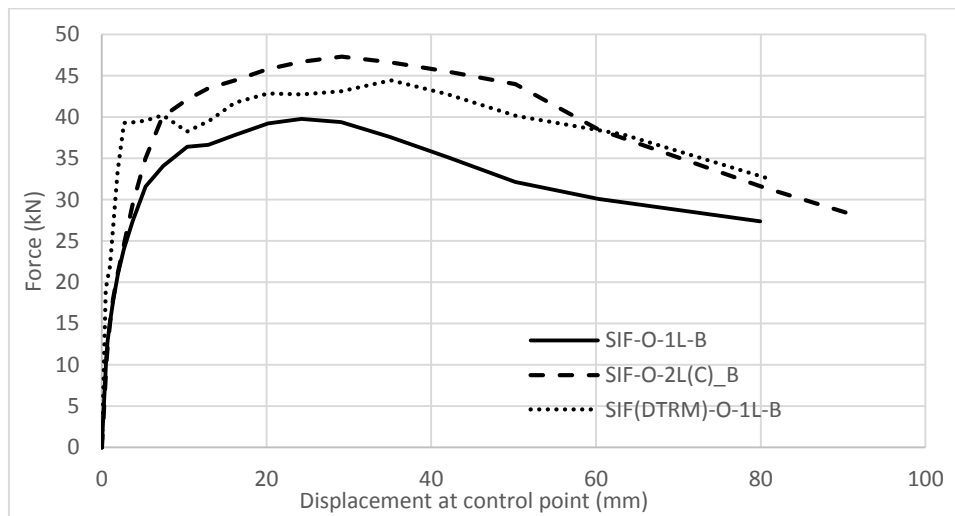


Figure 5.68 Monotonic envelop obtained in out-of-plane tests

It is clear that the consideration of the steel ties to link the internal and external leaves resulted in the increase of the lateral resistance and ultimate deformation capacity. The out-of-plane resistance increased by 18.8% and the initial stiffness increased by 25.6% in relation to the reference specimen of SIF-O-1L-B.

The addition of a reinforced mortar layer based on textile meshes resulted in the moderate increase of the out-of-plane resistance and significant increase of the initial and secant stiffness. It should be mentioned that it was expected that the out-of-plane strength obtained in the strengthened brick infill could be higher. This could be related to the pre-mature detachment of the retrofitting layer from rc frame which limited the efficiency of this technique for out-of-plane loading.

Table 5-6 Comparison of the secant stiffness and out-of-plane resistance

Specimen	Initial stiffness (kN/mm)	Secant Stiffness at 30% of peak force (kN/mm)	Strength (kN)	Increase in initial stiffness (%)*	Increase in secant stiffness (%)*	Increase in strength (%)*
SIF-O-1L-B (Reference)	12.5	12.5	39.8	-	-	-
SIF-O-2L(C)-B	15.7	13.2	47.3	25.6	5.6	18.8
SIF(CTRM)-O-1L-B	-	-	47.2	-	-	18.6
SIF(DTRM)-O-1L-B	29.3	29.3	44.5	1.3 times	1.3 times	11.8

\*Increase with respect to reference specimen

The comparison of the force-displacement hysteresis curves of the strengthened and unstrengthened specimens are shown in Figure 5.69. It is observed that in the specimen strengthened with TRM technique, higher plastic deformations could be obtained at the end of each cycle with respect to the reference specimen. This should be associated to the change of the deformation characteristics. In the reference specimen and even in the double leaf brick infill, the resisting mechanism was associated to the two-way arching mechanism. In this mechanism it was possible to observe that part of the deformations were recovered during the unloading process as the majority of the cracks were partially closed. It is believed that the resisting mechanism observed in the strengthened specimens was predominantly horizontal bending of the composite material composed of the brick infill and the reinforced mortar layer where important permanent deformation was developed.

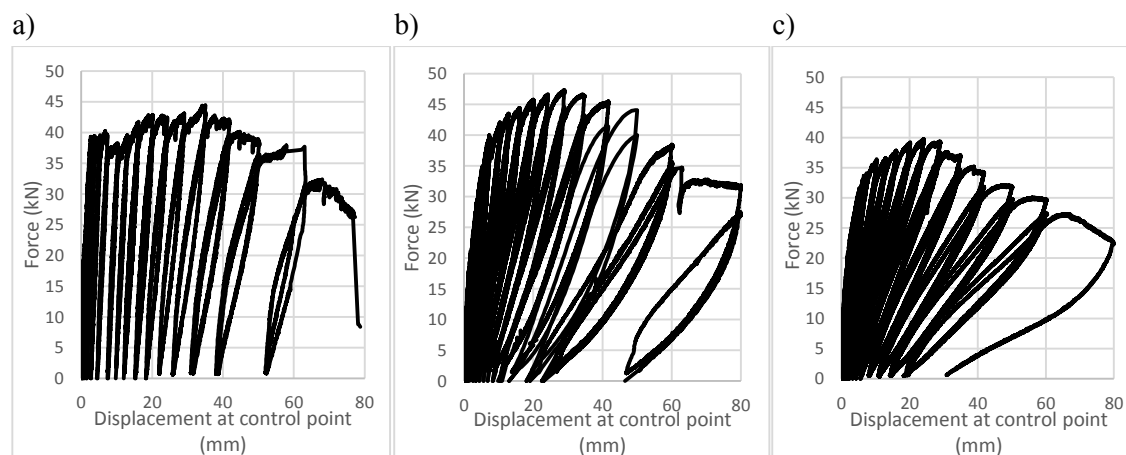


Figure 5.69 Force-displacement hysteresis for a) SIF(DTRM)-O-1L-B b) SIF-O-2L(C)-B c) SIF-O-1L-B

The stiffness degradation curves of the strengthened and reference specimen during out-of-plane loading are shown in Figure 5.70. It is clear that the strengthened specimens have exhibited higher initial stiffness than the reference specimen. Generally all the specimens have degraded their initial stiffness at lower displacements but it seems that the degradation rate for specimens with higher initial stiffness is higher. For instance, the strengthened specimen of SIF(DTRM)-O-1L-B degraded 88% of its initial stiffness at imposed displacement of 10mm, while the reference specimen (SIF-O-1L-B) degraded 72% of the initial stiffness until displacement of 10mm. The value for specimen SIF-O-2L(C)-B is calculated as 75%.

The total energy dissipation capacity of the strengthened and reference specimens until each cycle is shown in Figure 5.71. It is observed that the strengthened specimens present higher ability to dissipate energy when compared to the reference specimen. The increase for specimen strengthened with textile reinforced mortar at the end of the test with respect to the reference specimen is calculated as 19%. This value for specimen with double leaves connected by steel ties was calculated as 51%.

The cracking patterns of the strengthened and reference specimens at the end of the test are shown in Figure 5.72. It is observed that in the specimens strengthened with TRM technique, most of the cracks are concentrated in the added mortar layer and the damage of the brick infill is only associated to the crushing of the bricks adjacent to the upper and bottom interfaces. In this case it seems that the added mortar layer works as damage concentrator and enables us to use this technique as retrofitting technique for damaged infills.

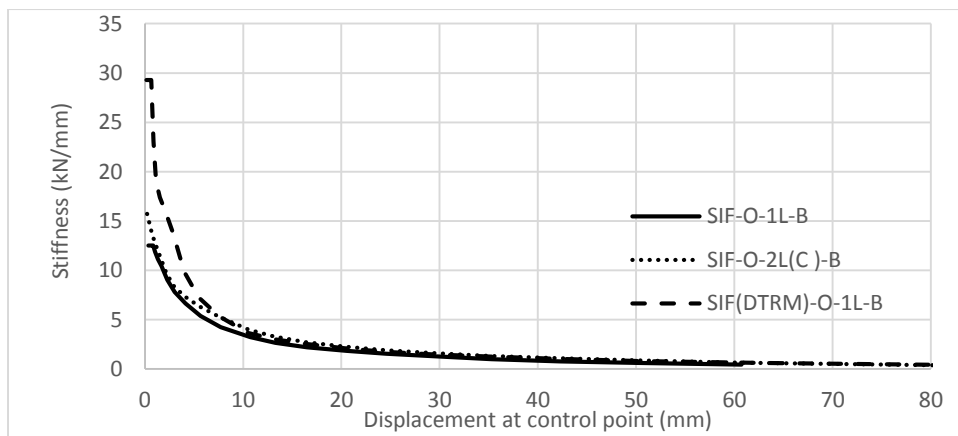


Figure 5.70 Stiffness degradation curves of strengthened versus reference specimen

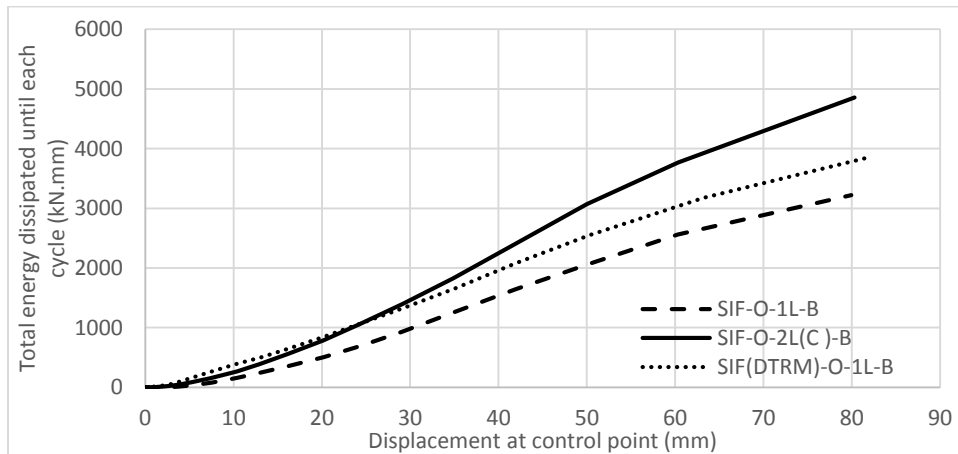


Figure 5.71 Energy dissipation capacity of strengthened specimens versus reference specimen



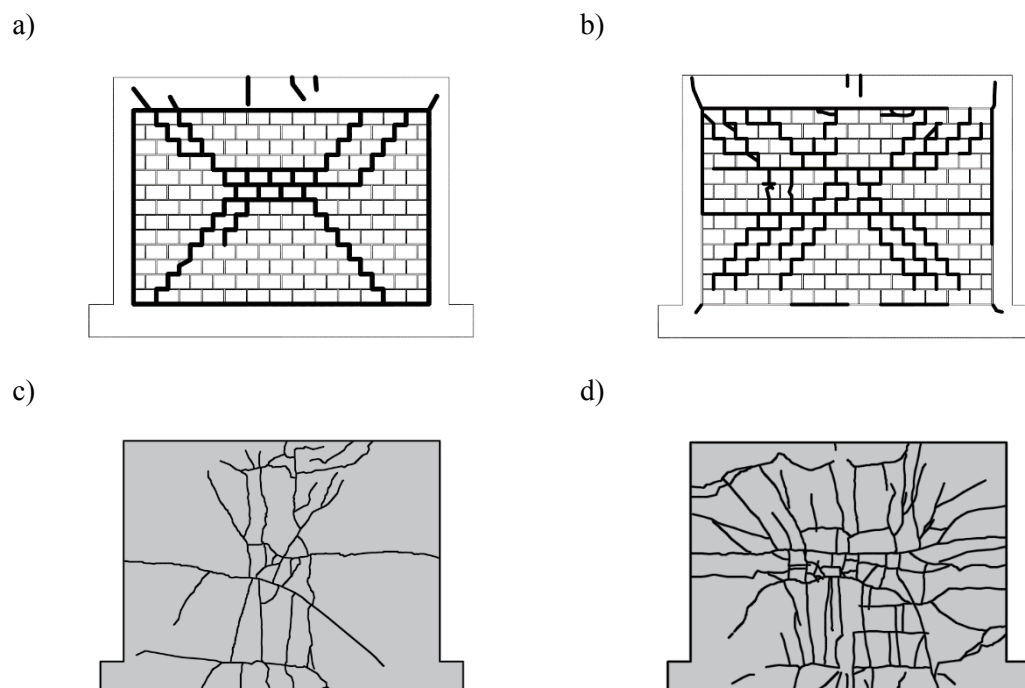


Figure 5.72 cracking pattern at the end of the test for specimens a)SIF-O-1L-B b)SIF-O-2L(C)-B  
 c)SIF(CTRM)-O-1L-B d)SIF(DTRM)-O-1L-B

## 5.7 Conclusions

Based on the test results of the specimens it could be concluded that;

- 1) The textile reinforced mortar (TRM) technique enhances the in-plane behavior of infilled frame, namely the initial stiffness and lateral strength. The effectiveness of this technique relies also on effectiveness of shear connectors fixing the retrofitting layer to the brick infill, as no detachment of the rendering from the brick infill occurred.
- 2) It seems that glass fiber shear connectors provided by the commercial company are not effective solutions to prevent the detachment between retrofitting layer and RC frame.
- 3) It is clear that the effectiveness of the retrofitting technique in the in-plane direction by using developed textile meshes is similar to commercial meshes which makes the retrofitting process economically custom-designed.
- 4) The TRM technique applied on the brick infill under out-of-plane loading significantly enhances the initial stiffness of the infilled frame, but the increase in the out-of-plane resistance is moderate.
- 5) It is clear that TRM technique could significantly increase the residual deformation of the infilled frame, without significant cracking of the brick infill.

- 6) The reinforced mortar layer appears to work as damage concentrator when the specimen is subjected to the in-plane or out-of-plane loading, as the major cracking developed in the rendering mortar.
- 7) By connecting the exterior and interior leaves of the infill with steel ties, an increase of 25.6% and 18.8% was observed in the initial stiffness and out-of-plane resistance of reference specimen respectively.
- 8) Specimens strengthened with textile reinforced mortar represented similar energy dissipation capacities in the in-plane or out-of-plane directions. Besides these specimens have represented higher energy dissipation capacity than the reference specimen.



# **CHAPTER 6**

## **CHARACTERIZATION OF THE MECHANICAL PROPERTIES**

## **6 Characterization of the mechanical properties**

This chapter aims to characterize the mechanical properties of the components of the brick masonry used in infill walls tested under in-plane and out-of-plane loading. The information about the mechanical properties of masonry components and assemblages helps in the analysis of the experimental results that were carried out on rc frames with masonry infills and also are important for further numerical analysis of the masonry infills.

In a first phase, the mechanical properties of masonry materials, such as the brick and mortar are presented and discussed. The mechanical properties include the compressive and flexural strength of mortar and compressive strength of units to distinct direction of loading. All mechanical properties are obtained based on standard procedures following European standards.

In a second stage, the mechanical properties of the brick masonry as a composite material were also obtained, including: (1) compressive strength in the direction normal to the bed joints based on uniaxial compression tests; (2) tensile and shear strength based on diagonal compression test; (3) flexural strength in the direction parallel and perpendicular to the bed joints based on flexural tests; (4) shear properties of unit-mortar interfaces through initial shear tests. All the mechanical properties were obtained based on standard tests.

### **6.1 Characterization of masonry components**

#### **6.1.1 Fresh and hardened properties of mortar**

The characterization of the mechanical properties of mortar was carried out on specimens casted with the mortar used in the construction of the brick masonry infill walls. This procedure was followed aiming at evaluating the construction quality. The mortar specimens were prepared by considering the same procedure for all constructed infill walls. The construction of the masonry infills was carried out by using a premixed mortar of class M5, taking into account that it would be a mortar with a resistance close to the one used in the past decades in the construction of infills in rc buildings. In addition, in order to avoid problems with the quality of mortar, it was decided to use a premixed mortar. In general, a bag of premixed mortar with 25kg was mixed with 3.5kg of water by an electrical mixer, following the recommendation of the mortar producer. The sampling of the mortar was carried out during the construction of the masonry infill walls both for the analysis of the consistency [123] and determination of compressive and flexural strength [124].

The consistency is a measure of plasticity and it is an indicator of workability of mortar. The consistency of the mortar was characterized through flow table tests carried out according to European standard [123]. The mortar was placed in an adequate mold at the center of the disc of the flow table, by introducing it in two layers. Each layer was compacted by at least 10 short strokes to ensure uniform filling of the mold. After approximately 15 seconds, the mold was raised vertically and the mortar was spread out by jolting the flow table 15 times at constant frequency of approximately one per second, see Figure 6.1.

One mold was prepared for each brick infill wall to obtain the flexural and compressive strength of the mortar, see Figure 6.2. Each mold contains three prisms of 160mmx40mmx40mm. The

flexural tests were carried out in the prismatic specimens and the uniaxial compression tests were carried out in the broken halves resulting from the flexural test.



Figure 6.1 Test procedure for evaluation of mortar consistency; a)preparation of the mold b)placing the mortar in the mold and compacting c)removing the mold and jolting the flow table d)measure two vertical diameters of the mortar



Figure 6.2 Mold used for determining the flexural and compressive strength of mortar

The preparation of the mortar specimens was made according to European standard EN1015-11:1999 [124] by placing the mortar into the mold in approximately two equal layers, being each layer compacted by 25 strokes. Then the molds were placed in a chamber with controlled environment (temperature of 20°C and RH of approximately 95%) and after two days the specimens were removed from the molds. Finally, the flexural and uniaxial compression tests were carried out at the age of 28 days, see Figure 6.3. The weight of the mortar samples was measured before performing the flexural tests.

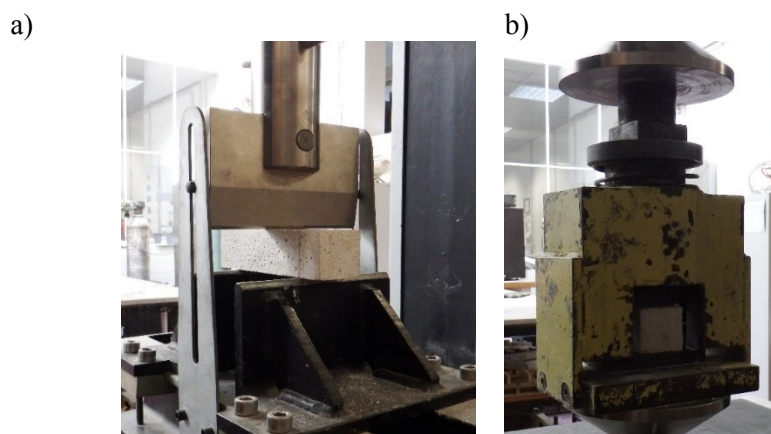


Figure 6.3 a)Flexural and b)compressive testing of the mortar

The results of the consistency, flexural and uniaxial compression tests, namely the flow table, compressive strength,  $f_m$ , and flexural strength of mortar,  $f_f$ , are presented in Table 6-1. The information about the coefficient of variation is indicated inside brackets. The detailed results are presented in Appendix I. It seems that even if mixing process of the mortar was controlled during the construction of masonry infills, some scatter was found both in fresh and hardened properties.

Table 6-1 Consistency, compressive and flexural strength of mortar

Specimen	Leaf	Flow table (mm)	$f_m$ (MPa)	$f_f$ (MPa)
SIF-I-2L(NC)-A	external	180	3.84 (9.63)	1.48 (8.21)
	internal	181	3.41 (7.02)	1.46 (6.50)
SIF-O-1L-A	external	177	4.25 (7.14)	1.75 (1.87)
PIF-O-1L-B	external	172	3.74 (3.18)	1.46 (3.45)
	Lintel	181	28.04 (5.03)	5.85 (4.88)
SIF-IO(0.3%)-2L(NC)-B	external	172	3.79 (5.44)	1.47 (7.75)
	internal	173	4.55 (3.64)	1.97 (3.62)
SIF-IO(0.5%)-2L(NC)-B	external	171	5.34 (2.66)	2.32 (2.60)
	internal	162	5.46 (4.35)	2.19 (7.58)
SIF-O-1L-B	external	179	3.79 (6.02)	1.64 (4.85)
SIF-O-2L(C)-B	external	171	4.30 (2.90)	1.43 (5.72)
	internal	165	3.69 (4.98)	1.25 (5.22)
SIF-IO(1%)-2L(NC)-B	external	161	5.49 (5.75)	2.20 (11.55)
	internal	181	2.76 (4.99)	1.26 (7.60)
SIF(DTRM)-I-2L(NC)-B	external	170	3.05 (6.66)	1.32 (1.96)
	internal	171	2.87 (7.38)	1.20 (9.04)
SIF(DTRM)-O-1L-B	external	167	3.27 (6.05)	1.24 (7.85)
SIF(CTRM)-I-2L(NC)-B	external	165	3.98 (4.15)	1.82 (7.30)
	internal	157	6.18 (5.81)	2.51 (6.02)
SIF(CTRM)-O-1L-B	external	162	4.29 (5.04)	1.44 (5.89)

By organizing the results obtained for the mortar used in the construction of each leaf of the brick infills, the average values of the compressive and flexural strength of mortar were obtained (the coefficient of variation is indicated inside brackets), see Table 6-2. Based on the results, it is clear that the coefficient of variation of the flexural and compressive tests for the mortar used in the internal leaf is relatively high. In spite of similar mixing procedure used in all specimens, it is possible that some non-measurable variations could occur during the mixing of the mortars. However, it appears that the average values obtained for compressive and flexural strength of each leaf are very close, which can be an indicative that a reasonable workmanship was applied in the construction of the brick infills.

Table 6-2 Summary of the mechanical properties of mortar for each leaf of the brick infill

Leaf	$f_m$ (MPa)	$f_f$ (MPa)
External	4.09 (17.7)	1.63 (20.7)
Internal	4.13 (31.7)	1.69 (31.2)

## 6.1.2 Mechanical properties of bricks

### 6.1.2.1 Dimension of the bricks

As mentioned before, the units used in the construction of the brick infills were considered with reduced dimensions to comply with the requirements of the reduction of the geometry of the brick infills (half scale infills). In the absence of the possibility to produce reduced scale units in the Portuguese market, it was decided to investigate alternative solutions in Spain. Taking into account that the typical thickness of double leaf brick infills are 15cm for the external leaf and 11 cm for the internal leaf, it was decided to use brick units produced in Spain with theoretical dimensions of 24.5cmx11.5cmx8cm and 24.5cmx11.5cmx6cm (length x height x thickness) for the external and internal leaves respectively. To have the similar height to length ratio of the units of the prototype in the reduced scale units, the length of the bricks was cut to have the length of 17.5mm. The dimensions of the bricks were measured based on EN772-16:2000 [125] by taking two measurements near the edges of each specimen (length,  $l_u$ , height,  $h_u$ , thickness,  $t_u$ ), see Figure 6.4 and Figure 6.5. The information about the measurements of the dimensions of the bricks is summarized in Table 6-3 and Table 6-4.

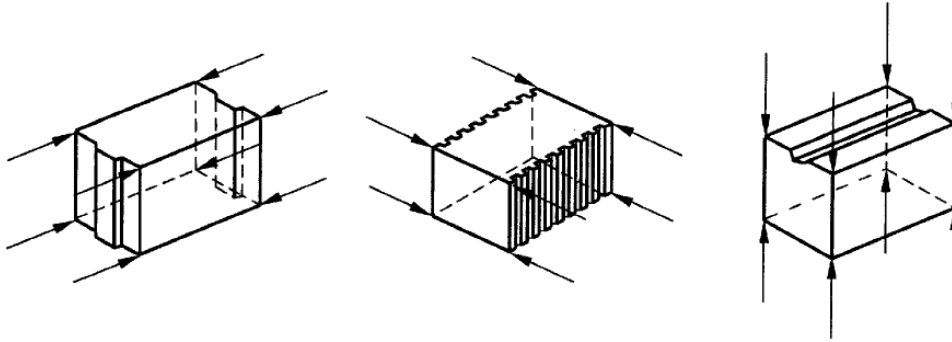


Figure 6.4 Measurement positions taken for the bricks



Figure 6.5 Measurement of the dimensions of the bricks



Table 6-3 Measurement of the thick bricks used in exterior leaf

	Length, $l_u$				Height, $h_u$				Thickness, $t_u$			
	$l_1$	$l_2$	$l_3$	$l_4$	$h_1$	$h_2$	$h_3$	$h_4$	$t_1$	$t_2$	$t_3$	$t_4$
<b>S1</b>	177.24	178.16	176.43	177.12	115.14	115.10	114.54	115.05	72.12	76.34	72.29	76.83
<b>S2</b>	177.36	177.65	178.20	177.54	114.86	114.43	113.7	115.47	76.03	72.33	75.52	77.28
<b>S3</b>	177.82	178.93	174.24	175.31	114.14	114.89	115.09	114.67	76.52	72.41	75.88	76.92
<b>Av.</b>	177.17				114.76				75.04			

Table 6-4 Measurement of the thin bricks used in interior leaf

	Length, $l_u$				Height, $h_u$				Thickness, $t_u$			
	$l_1$	$l_2$	$l_3$	$l_4$	$h_1$	$h_2$	$h_3$	$h_4$	$t_1$	$t_2$	$t_3$	$t_4$
<b>S1</b>	176.72	177.13	175.14	175.52	113.34	113.21	113.15	113.36	58.84	56.61	55.02	58.77
<b>S2</b>	176.18	176.76	176.15	175.52	113.49	112.85	112.47	112.42	58.51	59.07	59.19	56.49
<b>S3</b>	175.14	175.31	177.57	177.41	113.20	114.15	113.07	114.02	55.56	58.77	55.24	59.26
<b>Av.</b>	176.21				113.23				57.61			

### 6.1.2.2 Compressive strength of bricks

The compressive strength of the bricks was obtained according to the European Standard EN-772-1:2000 [126]. For this, nine specimens were prepared in three directions of loading, namely in the direction parallel to the height, parallel to the horizontal perforation and parallel to the thickness. Three bricks of thickness 58mm (theoretical thickness of 60mm) and six bricks of thickness 75mm (theoretical thickness of 80mm) were considered in the experimental testing program. The preparation of the specimens was carried out by capping their surfaces with mortar M10 or polyester, which satisfies the requirements of the standard, see Figure 6.6. The specimens were kept at laboratory environment with almost constant relative air humidity (RH) and temperature (temperature of 20°C and RH close to 65%).



Figure 6.6 Surface preparation of the brick specimens with a) mortar b) polyester

### 6.1.2.3 Compressive strength – direction parallel to the perforations

The bricks were subjected to the uniaxial compressive load parallel to the perforations, see Figure 6.7a, to obtain the strength and elastic modulus of the brick in this direction. A thick plate was placed in the top of the units to apply the uniform uniaxial load. The vertical displacements were measured based on two displacement transducers placed in both sides of the unit surface,

see Figure 6.7a. As it is shown in Figure 6.7b, specimens were crushed by the formation of the vertical cracks along the length.

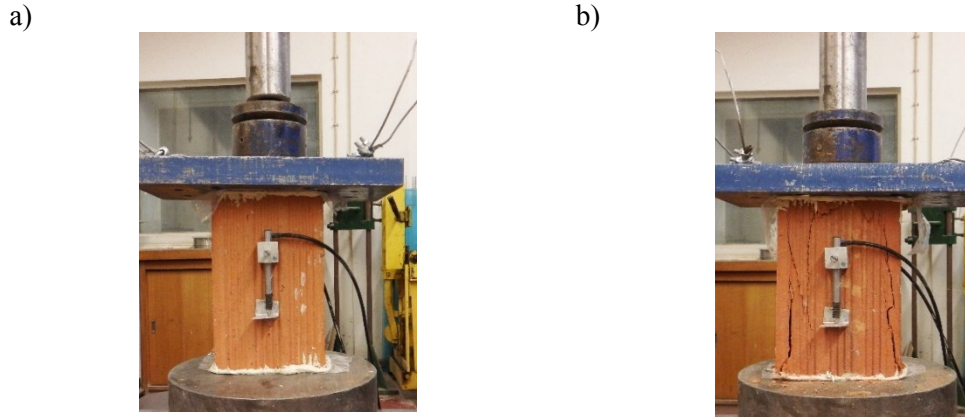


Figure 6.7 Uniaxial compression tests of brick parallel to perforation a) before test b) after test

The compressive strength of each specimen,  $f_b$ , was calculated by dividing the maximum force,  $F_{i,max}$ , by the loaded area,  $A_i$ , which is considered to be the gross area of the units, see Eq. 6-1

$$f_b = \frac{F_{i,max}}{A_i} \quad \text{Eq. 6-1}$$

The elastic modulus of the bricks in direction parallel to the perforation,  $E_i$ , was calculated as the secant modulus at 1/3 of the uniaxial compression strength, see Eq. 6-2.

$$E = \frac{F_{i,max}}{3 \times \varepsilon_i \times A_i} \quad \text{Eq. 6-2}$$

Where  $\varepsilon_i$  is the strain corresponding to one third of the compressive strength. The results in terms of compressive strength and elastic modulus of the tested bricks of thickness of 75mm and 58 mm are presented in Table 6-5 and Table 6-6 respectively. By comparing the results, it is observed that both compressive strength and elastic modulus of the bricks with thickness of 58mm along the perforations is considerably higher than the values obtained for the bricks with thickness of 75mm. This result should be associated to the number of perforated rows, given that the units with 75mm thickness have 2 rows of holes, whereas the other bricks have only one row.

Table 6-5 Compressive strength and elastic modulus of bricks with thickness of 75mm

Specimen	$F_{max}$ (KN)	A (mm <sup>2</sup> )	$f_b$ (MPa)	$0.33 F_{max}$ (KN)	$\varepsilon_i$ (mm/mm)	E (MPa)
1	25.18	8625.28	2.92	7.55	2.11E-04	4603.74
2	14.77	8530.76	1.73	4.43	2.08E-04	2773.94
3	26.35	8656.53	3.04	7.90	2.58E-04	3929.28
4	16.81	8551.23	1.97	5.04	1.36E-04	4810.61
5	21.15	8590.19	2.46	6.35	2.79E-04	2944.49
6	26.43	8609.81	3.07	7.93	2.18E-04	4690.79
<b>Average</b>			2.53			3958.81
<b>C. o. V. (%)</b>			22.8			22.9

Table 6-6 Compressive strength and elastic modulus of bricks with thickness of 58m

Specimen	$F_{max}$ (KN)	A (mm <sup>2</sup> )	$f_b$ (MPa)	$0.33 F_{max}$ (KN)	$\epsilon_i$ (mm/mm)	E (MPa)
1	55.58	6581.51	8.44	18.53	3.70E-04	7598.40
2	51.60	6545.73	7.88	17.20	2.54E-04	10351.56
3	54.00	6608.46	8.17	18.00	2.38E-04	11467.94
<b>Average</b>			8.17			9805.97
<b>C. o. V. (%)</b>			3.4			20.3

#### 6.1.2.4 Compressive strength – direction parallel to the height

The uniaxial compression tests in the direction parallel to the height or perpendicular to the bed joints was carried out by taking into account the same test setup and procedure previously described. Six bricks with thickness of 75mm and three bricks with thickness of 58mm were prepared and tested, see Figure 6.8. Due to the lower height of the bricks it was not possible to put LVDTs on both sides to measure the vertical displacements, meaning that the modulus of elasticity was not measured. The results in terms of compressive strength of the bricks are presented in Table 6-7 and Table 6-8. The comparison of results of both types of bricks reveals that the bricks with thickness 58mm present higher compressive resistance, being close to the value provided by the manufacturer. On the other hand, it is considered that the average compressive strength obtained for brick units with thickness of 75mm is lower than the value specified by the manufacturer.

a)



b)



Figure 6.8 Compressive testing of the brick parallel to height a) before test b) after test

Table 6-7 Compressive strength and elastic modulus of bricks with thickness of 75m

Specimen	$F_{max}$ (KN)	A (mm <sup>2</sup> )	$f_b$ (MPa)
1	20.84	13349.92	1.56
2	21.38	13240.93	1.61
3	20.75	13309.13	1.56
4	25.34	13313.85	1.90
5	21.28	13358.11	1.59
6	15.31	13174.95	1.16
<b>Average</b>			1.57
<b>C. o. V. (%)</b>			15.1

Table 6-8 Compressive strength and elastic modulus of bricks with thickness of 58m

Specimen	$F_{max}$ (KN)	$A$ (mm <sup>2</sup> )	$f_b$ (MPa)
1	26.57	10348.81	2.57
2	21.61	10309.48	2.10
3	37.12	10341.16	3.59
<b>Average</b>			2.75
<b>C. o. V. (%)</b>			27.7

#### 6.1.2.5 Compressive strength – direction parallel to the thickness

The compressive strength of the bricks parallel to their thickness was determined by testing six bricks with thickness of 75mm and three bricks with thickness of 58mm, see Figure 6.9. Because it was not possible to place LVDTs on the both side of the bricks to measure the vertical displacements, the elastic modulus of the bricks was not calculated. The strength of the bricks in direction parallel to the thickness is listed in Table 6-9 and Table 6-10. It is clear that the strength of the bricks of thickness 58mm is considerably higher than the strength obtained for the bricks with the thickness of 75mm, which should be associated to the geometry and percentage of perforations. The comparison of the compressive strength obtained for the bricks in the three directions of loading confirmed the anisotropic nature of the bricks, as it was expected. The highest strength was obtained in direction parallel to the perforations when compared to the strength obtained in directions parallel to the thickness and parallel to the height.

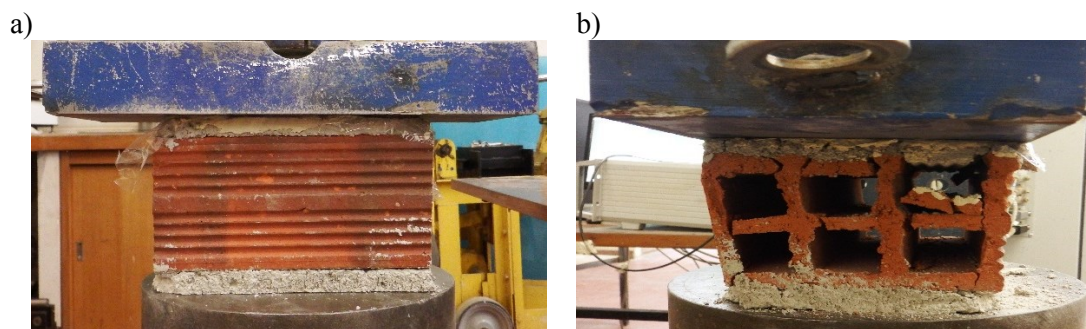


Figure 6.9 Compressive testing of the bricks in direction parallel to thickness a) before test b) after test

Table 6-9 Compressive test results of all specimens with thickness of 75mm in direction parallel to their thickness

Specimen	$F_{max}$ (KN)	$A$ (mm <sup>2</sup> )	$f_b$ (MPa)
1	24.19	20255.65	1.19
2	23.26	20288.95	1.15
3	40.38	20223.82	2.00
4	42.80	20388.69	2.10
5	44.2726	20340.59	2.18
6	47.97074	20392.65	2.35
<b>Average</b>			1.83
<b>C. o. V. (%)</b>			28.6

Table 6-10 Compressive test results of all specimens with thickness of 58mm in direction parallel to their thickness

Specimen	$F_{max}$ (KN)	$A$ (mm <sup>2</sup> )	$f_b$ (MPa)
1	110.23	20038.77	5.50
2	100.33	19990.87	5.02
3	80.45	19881.46	4.05
<b>Average</b>			4.86
<b>C. o. V. (%)</b>			15.3

## 6.2 Characterization of masonry assemblages

Due to the differences found in the compressive resistance of the bricks with different thicknesses, it was decided to characterize the masonry assemblages built with the brick units with thickness of 75mm and 58mm. This is justified by the fact that even if the difference found in the strength of the masonry assemblages is mitigated when the different units are used, it is important to have the mechanical characteristics of both brick infill masonry. However, due to the limited number of unit with thickness of 58mm it was decided to consider reduced number of specimens. Besides, the out-of-plane tests on brick infills was only carried out on the external leaf with the highest thickness.

### 6.2.1 Compressive strength of masonry

The main scope of this section is to obtain the compressive strength, as well as the elastic modulus, of the masonry used in the construction of the infill walls, under compressive loading. The compressive strength of the masonry was determined by testing three wallets of masonry with thickness of 75mm and one wallet of thickness 58mm. The lower number of specimens of masonry with thickness of 58mm is related to the smaller number of available units. The dimensions of the specimens along with their instrumentation to measure the vertical displacements within the specimen are shown in Figure 6.10.

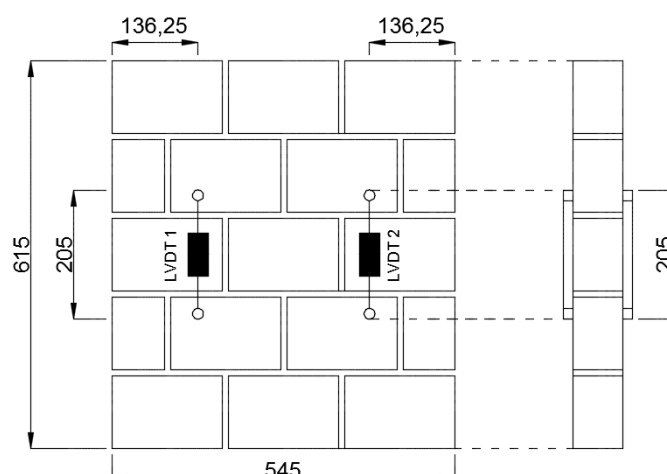


Figure 6.10 Masonry specimen configuration for compression tests

Two displacement transducers (LVDTs) were placed in each side of the specimen, see Figure 6.10. The specimens were built on a flat surface and the top surface of the specimens was

rectified by chemical plaster so that uniform uniaxial compressive load could be applied to the specimen. The specimens were kept in the laboratory environment during 28 days before the testing. The loading of the specimens was applied on the top of the specimens following the recommendation of European standard EN1052-1:1999 [127]. The thick steel profile mounted at the top of the specimen aimed at obtaining uniform vertical load, see Figure 6.11a.

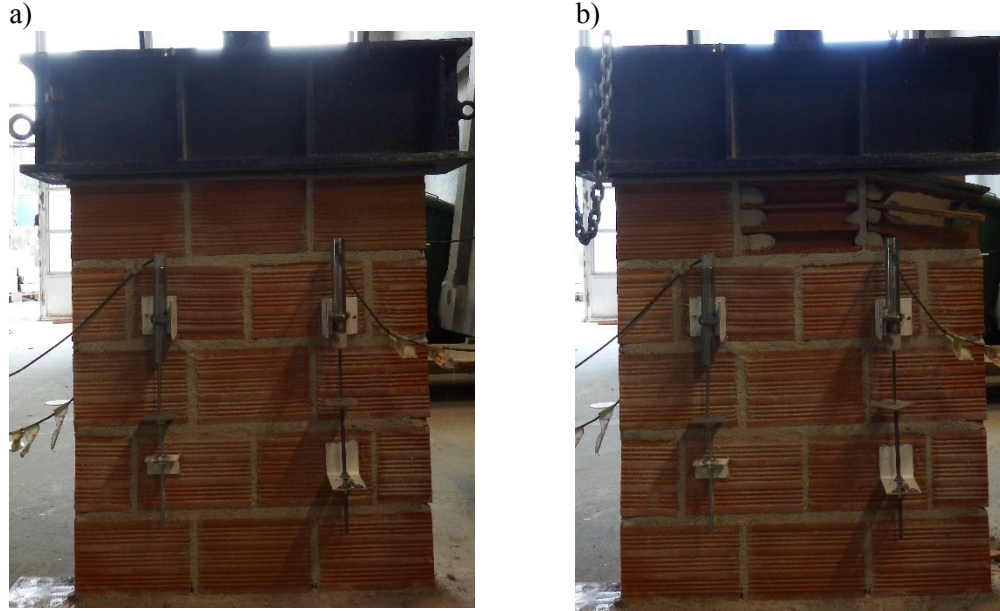


Figure 6.11 Details of compressive testing a)before test b)after test

The cracking pattern is composed of some vertical cracks developed at the top row of the masonry specimen, which resulted in the crushing of the upper row of the bricks, see Figure 6.11b.

The compressive strength of each specimen was calculated by dividing the maximum force,  $F_{max}$ , by the cross section of the specimen in the direction perpendicular to the uniaxial loading,  $A$ , according to equation Eq. 6-3:

$$f_c = \frac{F_{max}}{A} \quad \text{Eq. 6-3}$$

The vertical deformations measured by the displacement transducers (LVDTs) placed on the specimen were used to calculate the elastic modulus of masonry,  $E$ . It was calculated as a secant modulus for 33% of the maximum force, according to equation Eq. 6-4.

$$E = \frac{F_{max}}{3 \times \varepsilon \times A} \quad \text{Eq. 6-4}$$

In which  $\varepsilon$  is the strain calculated by dividing the vertical deformation measured by each LVDTs by the distance.

The stress-strain diagrams obtained for all specimens are shown in Figure 6.12 and the values of elastic modulus and compressive strength are presented in Table 6-11. The force-displacement diagrams obtained for all specimens are very similar. After the linear pre-peak regime, there is a

short nonlinear pre-peak until the maximum strength is attained. After this, a relatively short descending branch was obtained in all specimens. It is seen that the difference between the compressive strength of masonry with thickness of 75mm and 58mm is lower than the difference found for the compressive strength of the units. In addition, it is observed that the elastic modulus obtained in the masonry specimens with the thickness of 58mm is close to the average value found in masonry with thickness of 75mm.

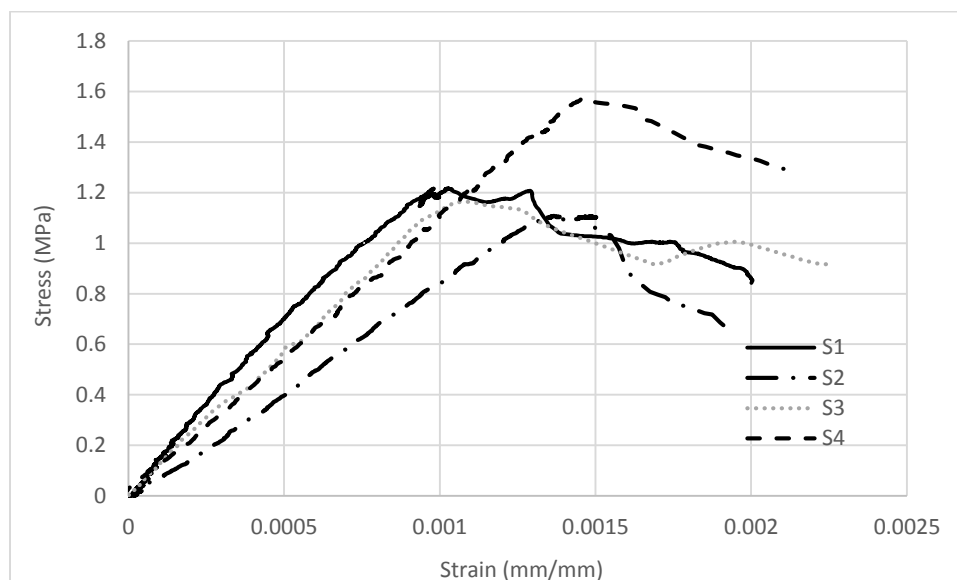


Figure 6.12 Stress-strain diagrams under uniaxial compressive loading

Table 6-11 Summary of the results of the specimens under uniaxial compressive loading

Specimen	$A$ (mm <sup>2</sup> )	$F_{max}$ (KN)	$f_c$ (MPa)	$\epsilon$ (mm/mm)	$E$ (MPa)
S1	42598.84	50.40	1.23	2.63E-04	1556.96
S2	42358.20	45.78	1.12	4.46E-04	837.30
S3	42446.12	47.20	1.16	2.79E-04	1381.59
S4	31697.57	50.35	1.59	4.59E-04	1154.72

A statistical study was performed on the test results of the specimens with thickness of 75mm to calculate the standard deviation and coefficient of the variation of the compressive strength and elastic modulus, see Table 6-12. It seems that the variation of the elastic modulus of the specimens is relatively high. Although extreme care was performed on transportation of the specimens from storage area to the testing area in the laboratory but this could be related to the formation of thin cracks inside specimens due to the transportation.

Table 6-12 Statistical information for specimen of thickness 75mm

	Standard Deviation	Average	Coefficient of Variation (%)
Compressive Strength (MPa)	0.056	1.17	4.8
Elastic Modulus (MPa)	375.26	1258.6	29.8

Characteristic compressive strength of the masonry could be calculated as the minimum value of the following equations;

$$f_k = \frac{f}{1.2} \text{ or } f_k = f_{i,\min} \quad \text{Eq. 6-5}$$

Based on the equation Eq. 6-5, the characteristic compressive strength of the masonry for each leaf is represented in Table 6-13.

Table 6-13 Characteristic compressive strength of masonry infill

Infill with nominal thickness of	Characteristic compressive strength for infill $f_k$ (Mpa)
75mm	1.0
58mm	1.3

### 6.2.2 Tensile and shear strength of masonry

Aiming at obtaining the tensile and shear resistance of masonry assemblages, it was decided to carry out diagonal compression tests, see Figure 6.13, following the recommendations of ASTM standard [128]. Diagonal compression tests were performed on three masonry specimens with thickness of 75mm and on one specimen with thickness of 58mm. Two displacement transducers (LVDTs) were placed on each side of the masonry specimens to monitor the extension and shortening of the diagonals, see Figure 6.13a. The typical cracking patterns obtained in the specimens are shown in Figure 6.14.

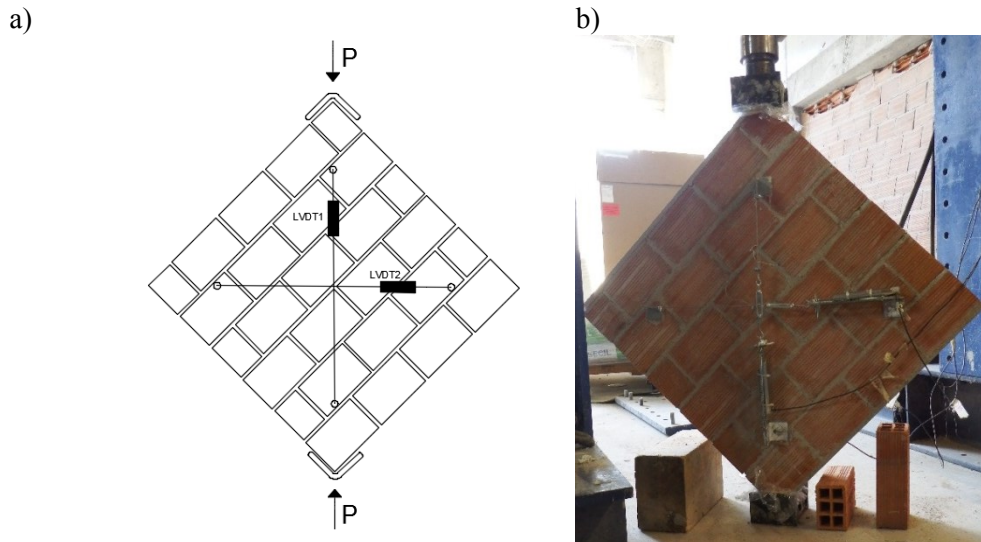


Figure 6.13 Diagonal shear test of masonry specimens a) scheme b) view of the specimen before testing

In general, the cracking of the specimens initiated at upper corner, passing through the unit-mortar interfaces, reaching the lower corner of the specimen and dividing the specimen approximately in two halves. No cracking of the units was recorded in the specimens.



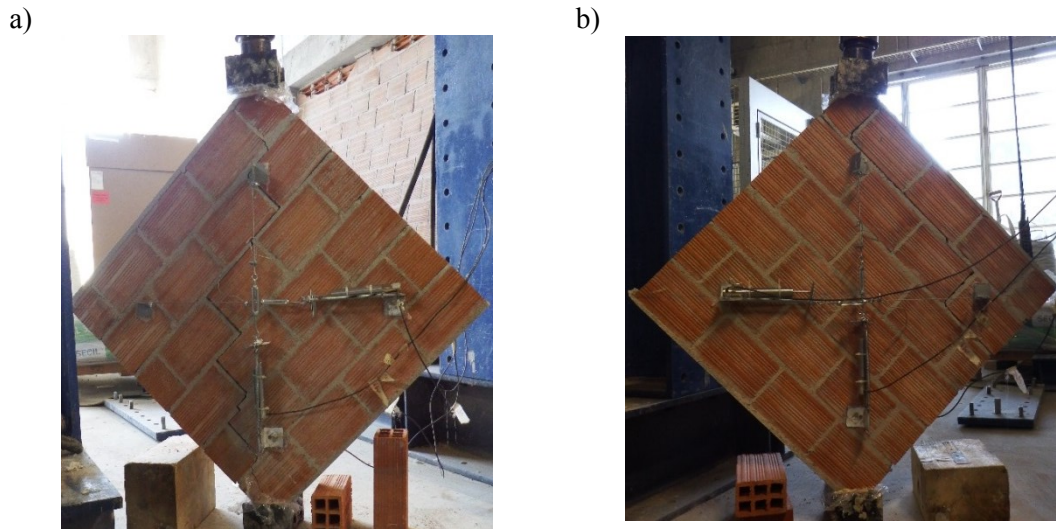


Figure 6.14 Cracking patterns a) specimen S2 b) specimen S1

The shear stress during loading was calculated as:

$$\tau = \frac{0.707P}{A_n} \quad \text{Eq. 6-6}$$

Where  $\tau$  is the shear stress,  $P$  is the applied load (N) and  $A_n$  is the net area of the specimen ( $\text{mm}^2$ ) which is calculated as:

$$A_n = \frac{(W + h)}{2} tn \quad \text{Eq. 6-7}$$

In which  $W$  is the width of the specimen (mm),  $h$  is the height of the specimen (mm),  $t$  is the thickness of the specimen (mm) and  $n$  is the percentage of the gross area of the unit that is solid expressed as decimal. The percentage of the gross area was calculated as 60% for both type of the bricks.

The shear strain of the specimen during loading was also calculated based on the results of the LVDTs that were placed on the specimens, according to the following expression:

$$\gamma = \frac{\Delta V + \Delta H}{L} \quad \text{Eq. 6-8}$$

Where  $\gamma$  is the shear strain of the specimen (mm/mm),  $\Delta V$  is the vertical shortening (mm),  $\Delta H$  is the horizontal extension of the specimen (mm) and  $L$  is the vertical gage length (mm).

Shear modulus of masonry,  $G$ , was calculated by dividing the shear stress by the shear strain:

$$G = \frac{\tau}{\gamma} \quad \text{Eq. 6-9}$$

The shear stress-strain diagrams for all specimens are shown in Figure 6.15 and its key parameters such as shear strength,  $\tau$ , and shear modulus,  $G$  are listed in Table 6-14.

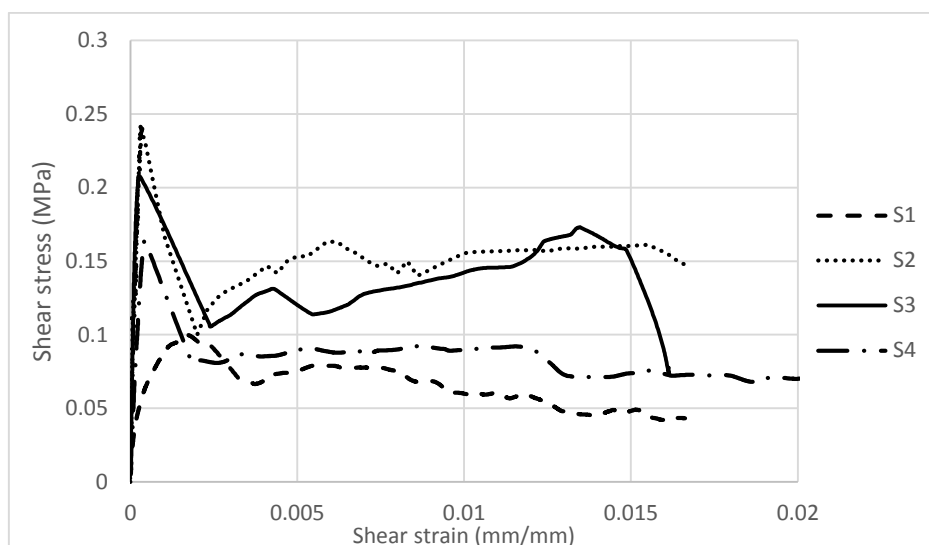


Figure 6.15 Stress-strain diagrams obtained for diagonal testing

Table 6-14 Shear strength and shear modulus obtained for the wallets tested under diagonal compression

Specimens	Thickness (mm)	$\tau$ (MPa)	$G$ (MPa)
S1	75	0.1	717.7
S2	75	0.25	1262.8
S3	75	0.22	1242.9
S4	58	0.17	1017.1

It is clear that the specimen S1 exhibits very low shear strength and shear modulus when compared to the other specimens. Also as described before, its cracking pattern is different from the other specimens, see Figure 6.14b. This could be related to the invisible cracking of the specimen during transportation or installation in the test setup. Using the results of this specimen in the statistical study will lead to high coefficient of variation. To avoid this, it was not considered in the calculation of the average shear strength, see Table 6-15.

Table 6-15 Statistical information for specimen of thickness 75mm

	Average	Coefficient of Variation (%)
Shear Strength (MPa)	0.24	9.0
Rigidity Modulus (MPa)	1252.8	1.1

### 6.2.3 Flexural behavior of masonry

The flexural resistance of the brick masonry was obtained in two different directions, namely in directions parallel and perpendicular to the bed joints.

The dimensions of the specimens adopted for flexural testing in the parallel and perpendicular direction to the bed joints are shown in Figure 6.16. These dimensions were defined according to European standard EN 1052-2 (1999) [129].

The test setup defined for the flexural tests is presented in Figure 6.16 and Figure 6.17 and it was defined according to the recommendation of European standard [129]. In the test setup, the specimen was placed vertically and the flexural load was applied in the horizontal direction. This was decided based on the test setup facilities and on the fragility of the specimens, due to their reduced thickness. The outer bearings were placed at a distance of 50mm from the end of the specimens. The distance between the points where the load was applied was about 0.58 and 0.56 times of the distance between outer bearings in specimens tested in direction parallel and perpendicular to the bed joints respectively. Four LVDTs were placed on the specimens to capture the deformation during loading. Three of the LVDTs were placed on the left side of the specimen, measuring the deformation of the specimen at mid span and at the points where their distance from the central point is 25% of the span. Another LVDT was placed in the right side of the wallet to measure its displacement at mid span.

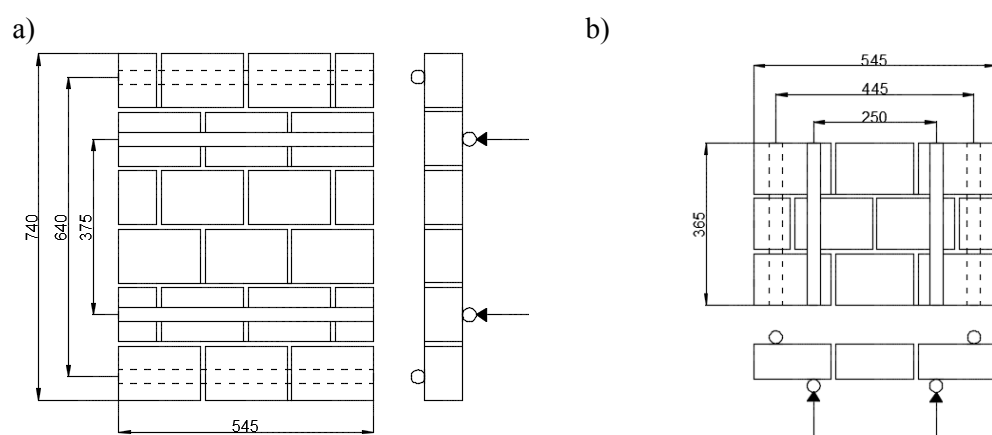


Figure 6.16 Dimension of brick masonry under flexure a) parallel to bed joints b) perpendicular to bed joints

The specimens were constructed and cured in laboratory environment and transported very carefully to the location where the test setup was mounted. For this a pre-compression was applied to confine the specimen and to avoid any disturbance of the specimens during transportation, see Figure 6.17b.



Figure 6.17 Details of experimental testing a) test setup for flexural testing b) transportation of the specimens

### 6.2.3.1 Flexural testing parallel to the bed joints

Four specimens were tested in the direction parallel to the bed joints, namely three specimens with thickness of 75mm and one with thickness of 58mm. The flexural tests were carried out under displacement control by monotonically increasing the displacement by 0.1mm/sec.

The typical cracking pattern observed in the specimens is composed of only horizontal cracks in the mortar joints located between the loading points, see Figure 6.18. The force-displacement diagrams of all specimens are shown in Figure 6.19.



Figure 6.18 Horizontal cracking of the mortar joints due to flexural testing parallel to the bed joints

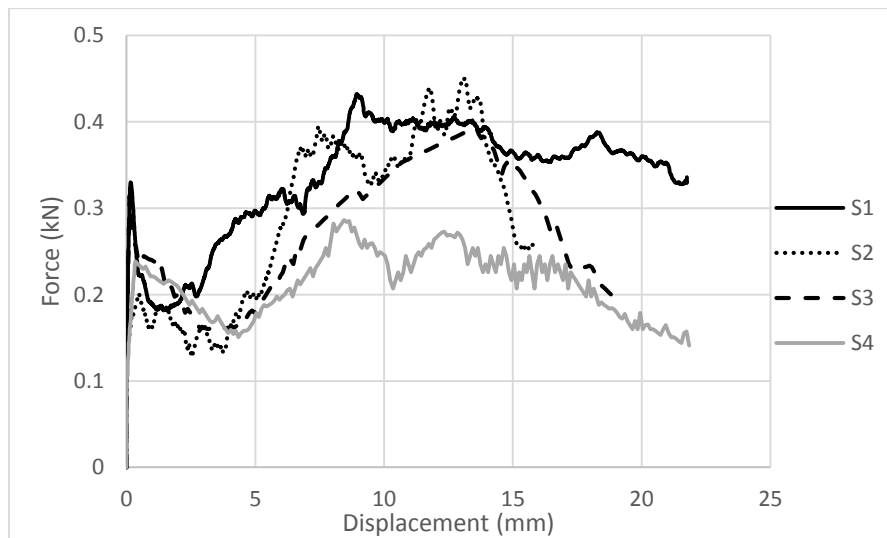


Figure 6.19 Force-displacement diagram of all specimen in flexural test parallel to bed joint

It is observed that similar response was observed for all of the specimens. For the first levels of loading, the displacement increased linearly. The initial cracking resulted in the sudden drop of flexural capacity. After this point, the load was recovered and reached its maximum resistance and then the specimen was collapsed.

The flexural strength of the specimens was calculated by the following equation;

$$f_x = \frac{3F_{max}(l_1 - l_2)}{2bt_u^2} \quad \text{Eq. 6-10}$$

In which  $f_x$  is the flexural strength of each specimen (MPa),  $F_{max}$  is the maximum force observed during loading (N),  $l_1$  is the distance between outer bearings (640 mm),  $l_2$  is the distance between load points (375 mm),  $b$  is the width of the specimen perpendicular to the direction of span (mm) and  $t_u$  is the thickness of the specimen (mm).

The flexural strength obtained for each specimen in direction of parallel to the bed joint is indicated in Table 6-16. It is observed that the flexural strength of all specimens is very low and the flexural strength of thicker specimens (75mm) is similar to the value obtained for the specimen with thickness of 58mm, as expected.

Table 6-16 Flexural strength of each specimen parallel to bed joint

Specimen	$F_{max}$ (N)	$l_1$ (mm)	$l_2$ (mm)	$b$ (mm)	$t_u$ (mm)	$f_x$ (MPa)
S1	432.1	640	385	545.6	75.12	0.054
S2	450.1	640	385	545.2	75.26	0.056
S3	393.9	640	385	545.8	74.96	0.049
S4	286.1	640	385	545.1	58.24	0.059

The statistical study for the flexural strength of the specimen with thickness of 75 mm was performed and represented in Table 6-17. It is observed that the coefficient of variation between the specimens is relatively low.

Table 6-17 Statistical study for the flexural strength in specimen with thickness of 75mm

	Standard Deviation	Average	Coefficient of Variation (%)
Flexural strength parallel to bed joint (MPa)	0.0034	0.053	6.4

The characteristic flexural strength of the specimens parallel to the bed joints could be calculated by dividing the average compressive strength of the specimens by a factor of 1.5 as:

$$f_{xk} = \frac{f_{mean}}{1.5} \quad \text{Eq. 6-11}$$

Following this procedure, a characteristic value for the flexural strength in direction parallel to the bed joints is calculated as 0.035MPa.

### 6.2.3.2 Flexural testing perpendicular to the bed joints

The flexural tests on the brick masonry in direction perpendicular to the bed joints were performed in the same test setup presented previously. In this case, the specimens had to be transported to the testing area, rotated and placed into testing machine very carefully to avoid any cracking of the specimens, see Figure 6.20.



Figure 6.20 Flexural testing of the specimen perpendicular to the bed joints

During the positioning of the masonry specimen with thickness of 58mm (S4) in the test setup, it cracked horizontally through the first bed joint. Due to this problem, the first row was removed and the test was performed on the rest of the specimen with a lower width.

The typical cracking pattern of the specimens is shown in Figure 6.21a. The cracking of the specimens consisted of the horizontal and vertical cracks passing through all bed joint and head joints between the loading points.

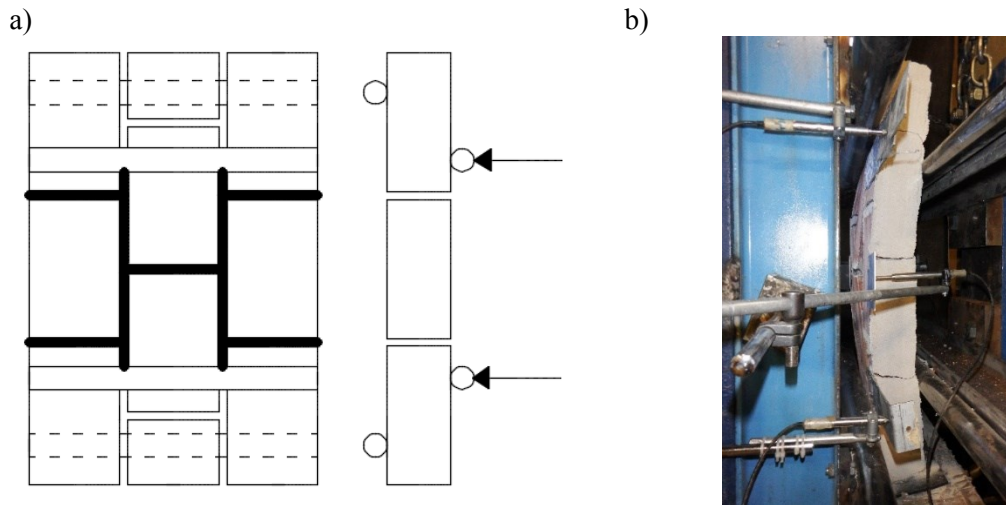


Figure 6.21 a)Cracking pattern of the specimens and b)its deformation in flexural test perpendicular to the bed joints

The force-displacement diagrams obtained in the flexural testing perpendicular to the bed joints are shown in Figure 6.22. It is observed that the specimens of S1, S2 and S3, which have the same thicknesses, exhibits similar behavior. Very low flexural force was obtained for the specimen S4, which should be associated mainly to its lower thickness, lower width resulted by its previous cracking during transportation. The irregular shape of the pre-peak branch is attributed to the progressive cracking of the specimen, leading to progressive redistribution of stresses.

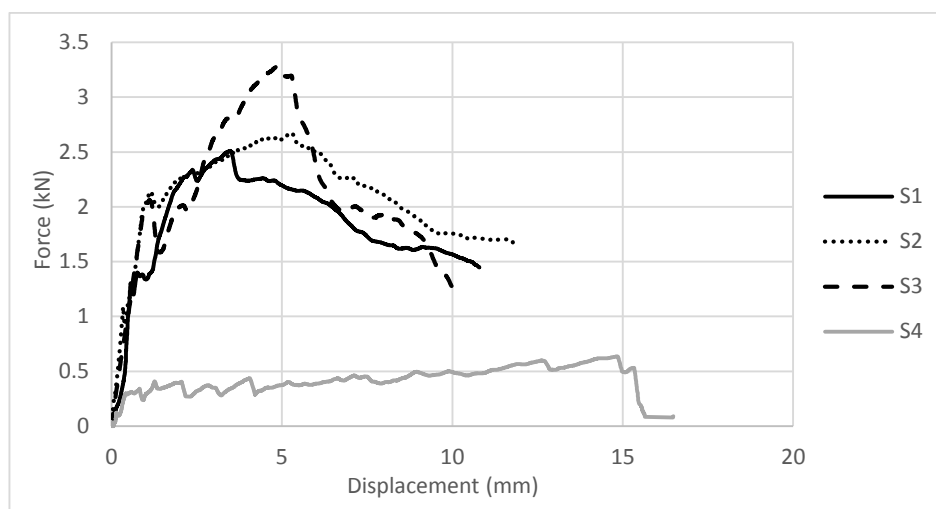


Figure 6.22 Force-displacement diagram of the specimens in flexural test perpendicular to the bed joints

The flexural strength of the specimens was calculated based on the equation Eq. 6-10 and it is presented in Table 6-18. It is clear that, as expected, the flexural strength of the specimens in direction of perpendicular to the bed joints is higher than the flexural strength in direction of parallel to the bed joints.

Table 6-18 Flexural strength of the specimens perpendicular to the bed joints

Specimen	$F_{max}$ (N)	$l_1$ (mm)	$l_2$ (mm)	$b$ (mm)	$t_u$ (mm)	$f_x$ (MPa)
S1	1821.436	445	250	365.5	75.26	0.26
S2	1944.923	445	250	365.8	75.18	0.28
S3	2372.103	445	250	365.4	75.32	0.34
S4	636.8205	445	250	243.2	58.16	0.23

The statistical study for the test results of the specimen with thickness of 75mm was performed and the results are given in Table 6-19. It is observed that the coefficient of variation of the flexural strength perpendicular to the bed joints among the specimens of thickness 75mm is reasonable. It is also evident that the flexural strength of the specimen constructed with bricks of thickness 58mm is close to that of the specimen with thickness of 75mm.

Table 6-19 Statistical study for the flexural strength parallel to bed joint in specimen with thickness of 75mm

	Standard Deviation	Average	Coefficient of Variation (%)
Flexural strength perpendicular to bed joint (MPa)	0.04	0.29	14.0

Characteristic value for the flexural strength in direction perpendicular to the bed joints is calculated as 0.19MPa by using Eq. 6-11.

### 6.2.4 Shear properties of the unit-mortar interfaces

The in-plane initial shear strength of horizontal bed joints in the masonry was determined by testing nine specimens with the configuration shown in Figure 6.23.



Figure 6.23 Specimens for initial shear test

The specimens were constructed with three bricks on top of each other with two mortar bed joints. The construction of the specimens and the curing process were performed according to the European standard EN1052-3:2003[130].

The specimens were tested in shear under four-point load with pre-compression perpendicular to the bed joints. Because the compressive strength of the units is less than 10MPa, the pre-compression loads were defined so that they represent reasonable values without any type of compression failure. Therefore, confining compressive stresses of 0.1MPa, 0.3MPa and 0.5MPa were adopted, see Table 6-20. Three specimens were tested for each confining stress level, equalizing a total of 9 specimens. The confining stress was kept constant during the tests with a maximum variation of 3% in specimen S7.

The specimens were placed on the testing machine and when it was necessary, polyester was used to level the surfaces of the specimens which are in contact with the steel plates. This is made to have a uniform shear stresses on the specimen. Four LVDTs were placed on the specimen (three in one side and one in the opposite side) to capture the sliding and also possible uplifting between the bricks, see Figure 6.24a.

Typically, the cracking was initiated at the bed joint mortars by sliding of the central brick in the loading direction, see Figure 6.24b. As it is shown in Figure 6.24b, the shear failure of the specimens occurred by shear failure at the unit-mortar interface, being an acceptable failure mode defined in the European standard [130].

The values of the confining stress applied in the specimens and the corresponding shear forces obtained in the shear tests are presented in Table 6-20.

The shear stress was calculated by dividing the maximum shear force by the gross area of the brick units. Based on the results, it is clear that by increasing the pre-compression level, the shear strength of the specimens increased.

For better understanding the shear behavior of the specimens, the force-sliding diagrams are shown in Figure 6.25. Three different behaviors can be identified with respect to the pre-



compression level. For the confining stress level of 0.1MPa, the center brick practically did not slide until the maximum shear strength is reached. At this stage, the central brick started to slide suddenly which resulted in the sudden drop in the shear force. For the confining stress level of 0.3MPa, the sliding of the center brick was initiated gradually after the shear strength of the specimen was achieved, and practically almost no strength degradation was occurred. Contrary to the specimens with confining stress levels of 0.1MPa and 0.3MPa, for the confining stress of 0.5Mpa, the sliding of the specimen started before the shear strength of the specimen was reached. It is observed that the sliding of the specimen was initiated at lower shear stress and it increased progressively until it reached the shear strength of the specimen. After this point, the sliding of the specimen increased rapidly which resulted in very smooth decrease of the shear stress in the post-peak regime.

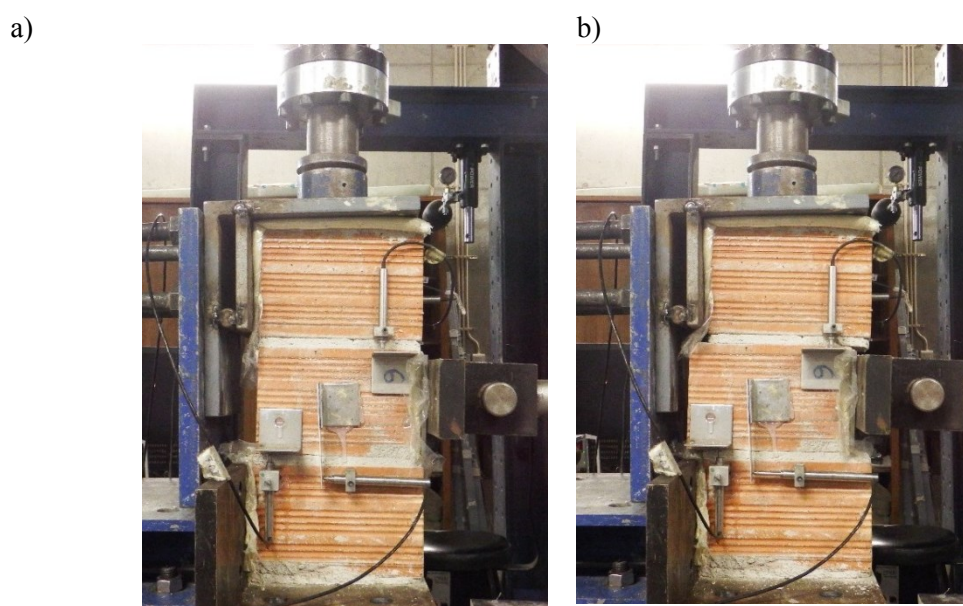


Figure 6.24 Initial shear test; a)general configuration b)typical failure pattern

Table 6-20 Shear strength of the specimens due to pre-compression level

Specimens	S1	S2	S3	S4	S5	S6	S7	S8	S9
<b>Pre-compression (MPa)</b>	0.1	0.1	0.1	0.3	0.3	0.3	0.5	0.5	0.5
<b>Maximum shear force (kN)</b>	6.2	7.3	6.8	7.6	8.6	8.0	12.4	13.6	12.5
<b>Shear strength (MPa)</b>	0.24	0.28	0.26	0.29	0.33	0.31	0.47	0.52	0.48

The variation of shear strength against the normal confining stress is shown in Figure 6.26 for all specimens. Linear fitting of the experimental results was carried out, resulting in statistical correlation with a coefficient of correlation  $r^2$  equal to 0.87, which appears to be reasonable. Based on this linear fitting, it was possible to obtain the key parameters defined in the Coulomb's friction criterion. An average values of about 0.18 and 0.58 were calculated for the cohesion and friction coefficient. The cohesion is obtained by intersecting the fitting line in Figure 6.26 with the vertical axis. The angle of internal friction is also considered as the slope of the fitting line in Figure 6.26.

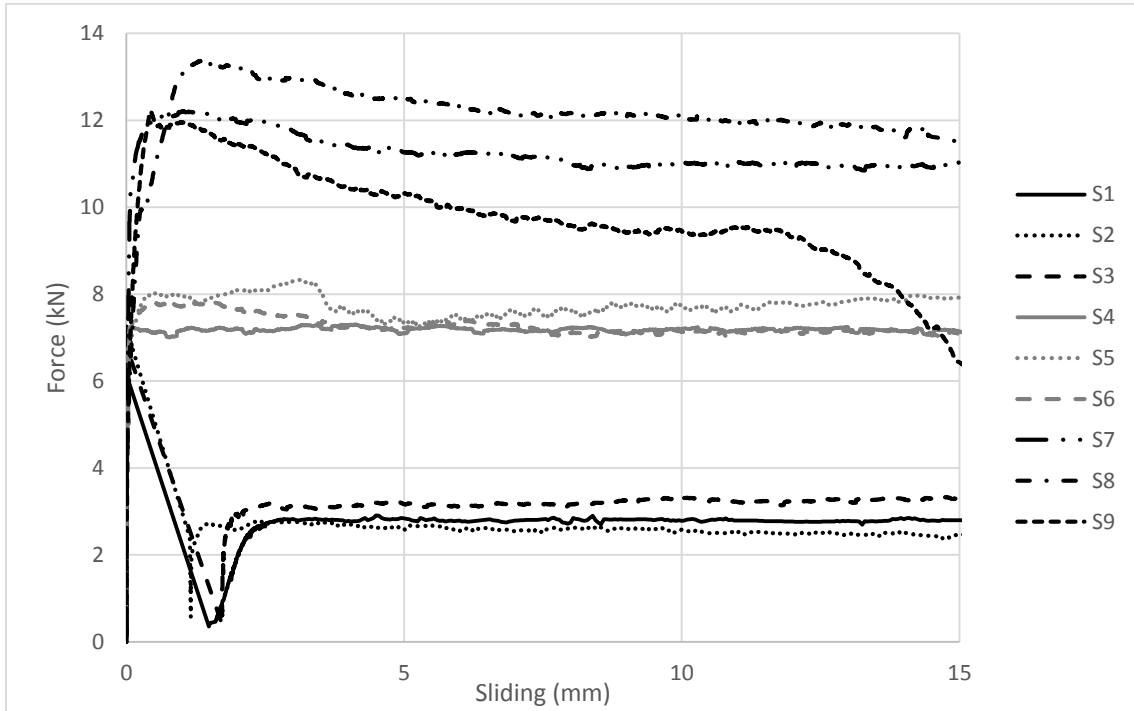


Figure 6.25 Force-displacement diagram of the specimens due to shear forces

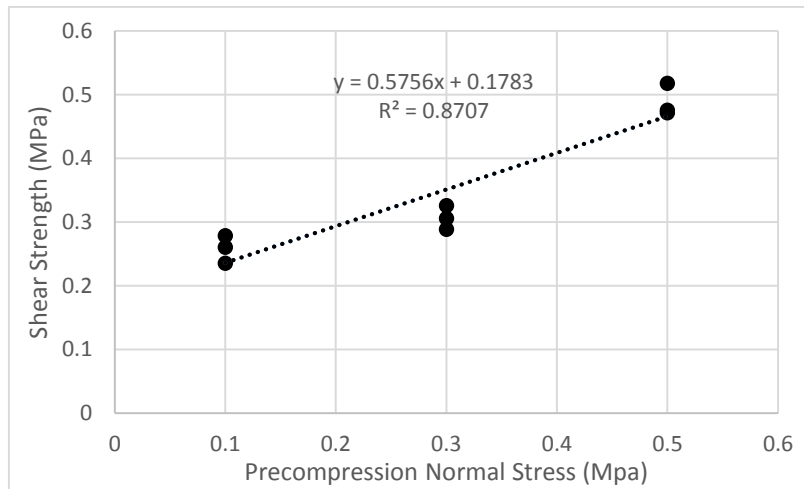


Figure 6.26 Correlation between shear strength and normal stress

The characteristic shear strength and characteristic angle of internal friction of the masonry could be calculated as:

$$f_{v0k} = 0.8f_{v0} \tag{Eq. 6-12}$$

$$\tan \alpha_k = 0.8 \tan \alpha \tag{Eq. 6-13}$$

Based on these equations, Table 6-21 represents the characteristic values for the shear strength and internal friction of the specimen.

Table 6-21 Characteristic value for initial shear strength of masonry

Infill with nominal thickness of	$f_{v0k}$ (MPa)	$\alpha_k$
75mm	0.14	0.46

### 6.3 Conclusions

Mechanical characterization of the masonry used in the infills was carried out in this chapter and based on the analysis of their results the following conclusions were made:

- 1) The real thickness of the bricks is different with their nominal thickness reported by the manufacturer.
- 2) The bricks represented anisotropic behavior in terms of their compressive strength and elastic modulus at different directions.
- 3) Higher amount of compressive strength and elastic modulus were obtained for bricks with thickness of 58mm. Their compressive strength and elastic modulus is calculated as about three times of the compressive strength and elastic modulus of the bricks with thickness of 75mm.
- 4) It is seen that the difference between the compressive strength of masonry with thickness of 75mm and 58mm is significantly lower than the difference found in the compressive strength of the units. The same behavior was also observed for the elastic modulus. The compressive strength and elastic modulus of the masonry wallets with thickness of 58mm are 1.36 and 0.92 times of the compressive strength and elastic modulus of the masonry wallets with thickness of 75mm.
- 5) The diagonal shear test performed on wallets with different thicknesses revealed that the shear strength and shear modulus of the masonry wallets with thickness of 75mm are 1.4 and 1.2 times of the shear strength and shear modulus of wallets with thickness of 58mm.
- 6) Flexural tests were performed on wallets and it was concluded that the specimens with different thicknesses represented similar flexural strengths. It is also concluded that the flexural strength of the specimens in direction of perpendicular to the bed joints are significantly higher than their flexural strength in direction of parallel to the bed joints.
- 7) Higher amount of confining stress in the specimens tested under initial shear test increased the initial shear strength of the specimens. Based on different levels of confining stresses different behaviors in terms of force-sliding curves were obtained.

# **CHAPTER 7**

## **NUMERICAL ANALYSIS OF RC FRAMES WITH BRICK INFILLS**

## 7 Numerical Analysis of rc Frames with Brick Infills

### 7.1 Introduction

Numerical modelling is usually seen as a powerful tool, complementary to the experimental analysis to analyze problems related to structural engineering. In spite of an extensive experimental program presented before on rc frames with brick infills under in-plane and out-of-plane loading (Chapter 3 and 4), it was not possible to assess the influence of several parameters in the in-plane and out-of-plane response of infilled frames. For example, parameters like the presence of openings, its distribution on the infill and also material properties of the infill are not taken into account. Therefore, it was decided to analyze the influence of different parameters in the mechanical behavior of infilled frames under in-plane loading through numerical modelling. This work enables a better understanding of detailed behavior of rc frames with brick infills subjected to different conditions beyond the experimental testing.

Generally, as described in Chapter 2, there are two approaches for numerical modelling of infilled frames, namely macro-modelling approach by replacing the masonry infill with diagonal struts and micro-modelling approach. In the micro-modelling approach, finite element method is usually used to model both the rc frame and brick infill by considering different levels of detail, see Figure 7.1. The macro-modelling approach mentioned in Figure 7.1d relates the representation of the masonry with finite elements and considering it as homogenous and isotropic material, being different from the macro-model approach based on diagonal struts [94]. In the detailed micro-modelling approach, the infill panel is modelled as a set of three different components: brick, mortar and interface between mortar and brick. In the simplified micro model, infill is modelled as a set of two different elements: expanded brick and interface elements. Interface elements represent the behavior of the mortar and also the interface between mortar and brick.

This Chapter is composed of two parts, namely: (1) calibration of a numerical model to analyze the in-plane behavior of rc frame with brick infills based on available experimental results and performing parametric study considering different parameters and focusing on a more detailed analysis on the influence and configuration of the openings, and (2) calibration of a finite element model to analyze the out-of-plane behavior of brick infills based on the experimental results obtained in Chapter 4.

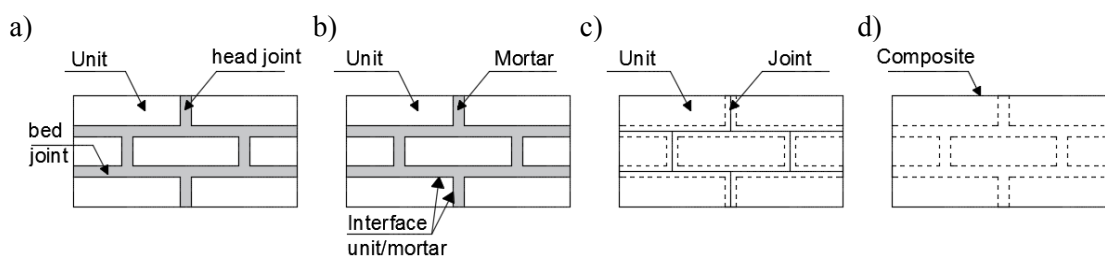


Figure 7.1 Different details that can be adopted micro-modelling approach: (a) masonry wall; (b) detailed micro-model; (c) simplified micro-model; (d) finite element macro-model

## 7.2 In-plane numerical modelling of rc frames with brick infills

### 7.2.1 Numerical model

The numerical model used to analyze the in-plane cyclic behavior of rc frame with brick masonry infill walls was defined based on the experimental results obtained by Paulo-Pereira [3]. The details of the reinforced concrete frame are shown in Figure 7.2. The rc frame was designed according to EC8 [131] considering an average span often found in representative Portuguese RC buildings. The masonry infill was built with traditional bricks with horizontal perforation commonly used in the construction of brick infills in Portugal.

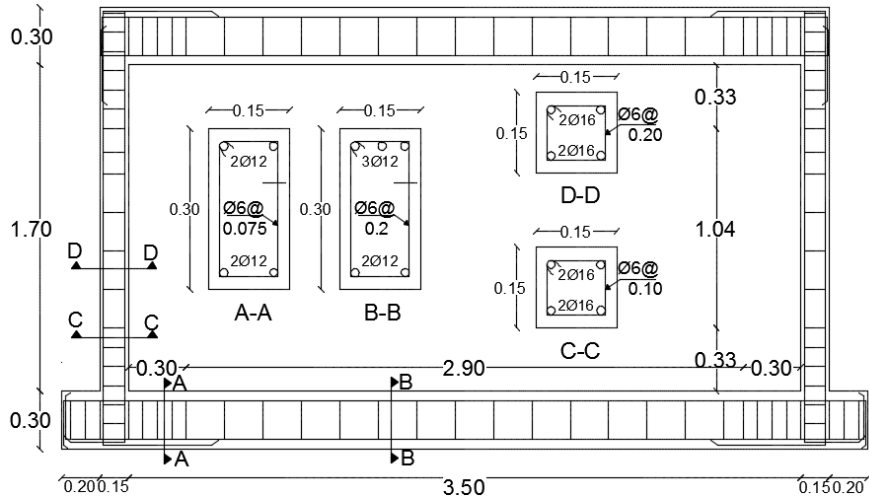


Figure 7.2 Geometry and reinforcement scheme of the rc frame (dimensions in m) [3]

The numerical analysis of the in-plane behavior of reinforced concrete frames with brick masonry infill walls was based on finite element modelling carried out in the commercial software DIANA [132]. For this purpose, a bi-dimensional model of the reinforced concrete frame with brick masonry infill was adopted. The masonry infill and its surrounding frame was represented by four-node plane-stress elements. Reinforcement was also added to the concrete frame by using embedded bars (perfectly bonded). The connection between the masonry infill wall and the reinforced concrete frame was simulated through four-node interface elements. The lower beam of the frame was fixed by preventing any translation in x and y directions in the numerical analysis. This boundary condition is the same as the one used in the testing campaign. A vertical load of 50kN was put on the top of each column because it is expected that the vertical load is not transmitted by the top beam to the masonry infill. In fact, it is considered that the brick infill is a non-structural element, unless the top slab or beam deforms due to creep or additional loading, and some vertical loading is transferred to the masonry infill, which is not the scope of this research. The schematic finite element modelling of the rc frame with brick infill is shown in Figure 7.3.

The non-linear behavior of the concrete and masonry was represented by a Total Strain Crack Model based on a fixed stress-strain law concept available in the commercial Diana [132]. The model describes the tensile and compressive behavior of the material with one stress-strain relationship in the local coordinate system that is fixed upon crack initiation. Exponential and parabolic constitutive laws were used to describe the tensile and compressive behavior of concrete and masonry infill respectively, as shown in Figure 7.4.

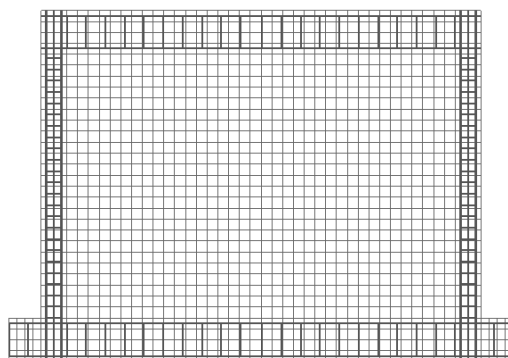


Figure 7.3 Finite element model of the rc frame with brick infill

An interface cap model with modern plasticity concepts proposed by Lourenço and Rots (1997) [133] was used for interface elements describing the connection between the brick masonry infill and the enclosure rc frame. The interface material model is appropriate to simulate fracture, frictional slip as well as crushing along the interface [133]. As it is shown in Figure 7.5, fracture of the interface is controlled by its tension mode, shear behavior is controlled by Coulomb friction behavior and finally crushing is controlled by the cap in compression mode.

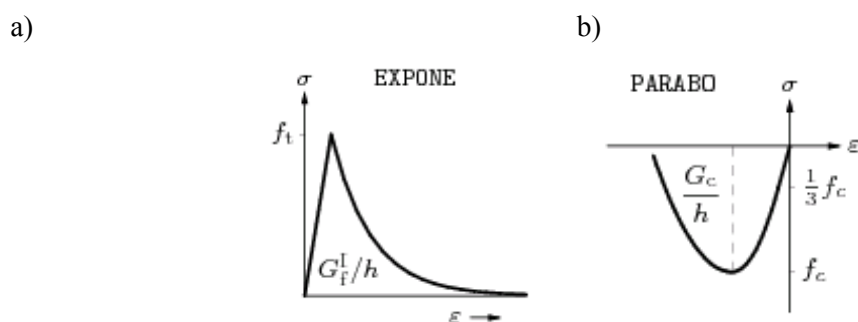


Figure 7.4 Stress-strain relationship adopted for Total Strain Crack model: a) exponential softening curve to describe tension and b) parabolic constitutive laws to describe compression

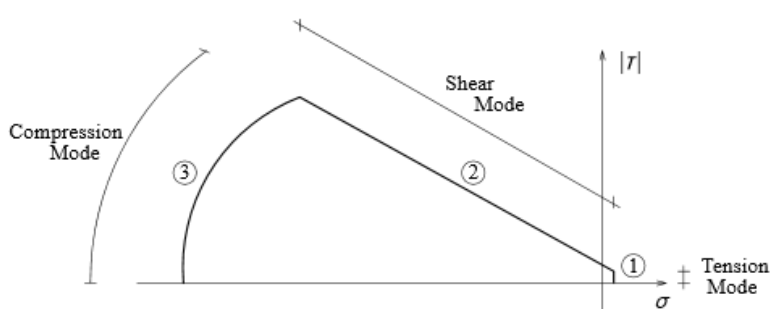


Figure 7.5 Two-dimensional interface yield function [134]

## 7.2.2 Validation of the numerical model based on experimental results

The numerical model was validated based on the experimental results obtained by Paulo-Pereira [3] in three rc frames with distinct types of brick infills tested under in-plane cyclic loading. The cyclic loading was applied in the plane of the panels in both positive and negative orientations by increasing the levels of the imposed horizontal displacement up to a pre-defined value of lateral

drift. For each lateral drift, three cycles of loading and unloading were performed. This methodology of applying quasi-static load has been used by many researchers to simulate the response of the structure to the action of earthquakes [135].

Table 7-1 provides information about the materials and geometrical configurations adopted for the masonry infill walls. Two single leaf masonry infills were tested: (1) one without rendering (Wall-Ref-01) and (2) and the other rendered with mortar (class M5) in both sides with 10mm thickness (Wall-Ref-02). The third masonry wall (Wall-JAR) was reinforced at the bed joints, at each two courses, with prefabricated trussed reinforcement composed of two longitudinal bars connected by diagonal bars (Murfor RND 4/100 with 2 $\phi$ 4 longitudinal bars). The bricks which are representative of the materials used for masonry infills in Portugal in the last decades are horizontally perforated. The monotonic envelopes of the cyclic hysteresis diagrams of force-displacement diagrams are presented in Figure 7.6. The displacement was measured at the center of top beam-column node in the opposite corner to the one where the horizontal actuator is connected. The results in terms of secant stiffness, lateral resistance and failure modes are summarized in Table 7-2.

Table 7-1 Information about the components of each brick masonry infill masonry wall

Specimen	Type of Panel	Components	Characteristics of materials
Wall-Ref-01	Simple (without rendering)	Brick Mortar	With dimensions of 0.30x0.20x0.15 m Mortar M5 with 10 mm thickness
Wall-Ref-02	Simple (with rendering in both sides)	Brick Mortar Rendering	With dimensions of 0.30x0.20x0.15 m Mortar M5 with 10 mm thickness Mortar M5 with 10 cm thickness in each side
Wall-JAR	Reinforced panel	Brick Mortar Exterior rendering Interior rendering Reinforcement	With dimensions of 0.30x0.20x0.15 m Mortar M5 with 10 mm thickness Mortar M5 with 10 mm thickness Projected gypsum BEKAERT- Murfor RND 4/100 with 2 $\phi$ 4 longitudinal bars

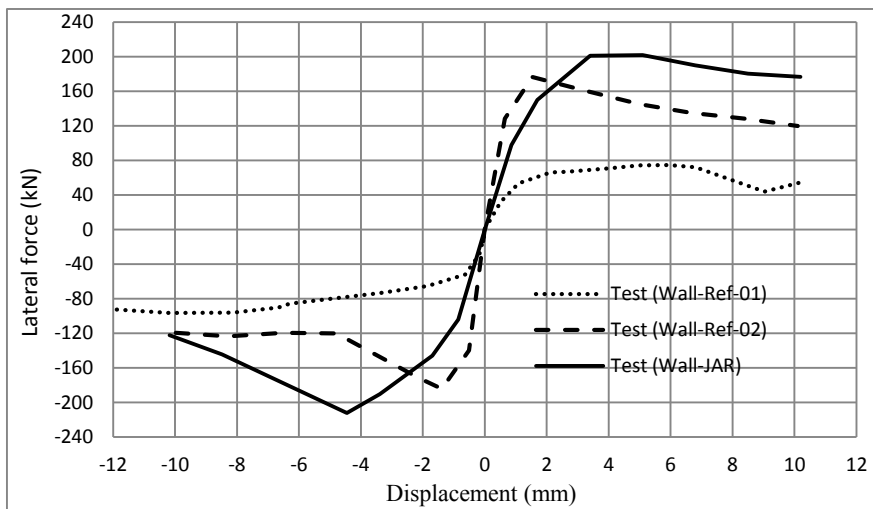


Figure 7.6 Pushover diagrams of the test specimens

Based on the results it is possible to observe that the rendering, applied in the interior and exterior surfaces, increases the initial stiffness and load carrying capacity of the infilled frame, while the use of bed joint reinforcement mostly increases load carrying capacity of the infilled frame.



Table 7-2 Secant stiffness and lateral strength of test specimens

Test Specimen	Average stiffness at 30% of maximum force (N/mm)	Average maximum force (N)	Failure mode
Wall-Ref-01	111800	85400	Infill Crushing
Wall-Ref-02	235600	181400	Infill Crushing
Wall-JAR	128400	207100	Infill Crushing

The mechanical properties of the masonry and the concrete used in the experimental campaign are indicated in Table 7-3. These were obtained based on a set of experimental tests carried out by Paulo-Pereira (2013) [3], namely compressive and flexural tests on brick masonry wallets.

Table 7-3 Mechanical properties of the components for walls specimens [3]

Mechanical Properties	Concrete	Wall-Ref-01	Wall-Ref-02	Wall-JAR
Young Modulus (GPa)	31.5	1.67	3.83	4.43
Poisson's ratio	0.15	0.13	0.237	0.175
Tensile Strength (MPa)	2.35	0.25	0.4	0.5
Mode-I fracture Energy (N/mm)	0.10	0.02	0.03	0.03
Compressive Strength (MPa)	31.5	1.00	1.26	1.97
Compressive Fracture Energy (N/mm)	8.0	1.0	1.0	1.0
Yield Stress of Reinforcements(MPa)	-	500	500	500

A brief scheme of the crack patterns of the test specimens are presented in Figure 7.7. It is seen that the crack pattern is composed of cracks in the perimeter of the infill due to the separation of the infill from its enclosing frame and crushing of the infill in the vicinity of the horizontal load applied to the specimen. Crushing of the upper corners of the masonry infill walls occurred in all walls and can be considered as the main feature of the failure mode, see Figure 7.8.

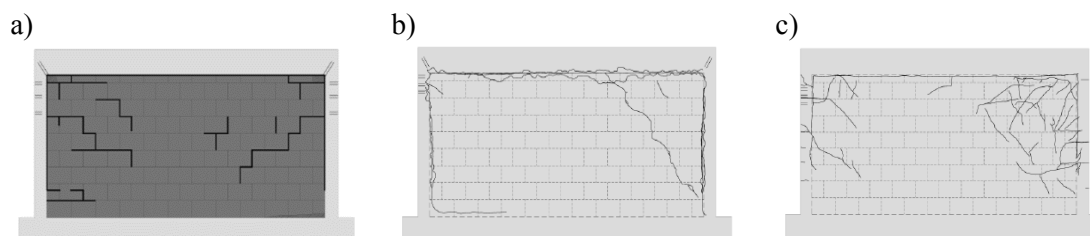


Figure 7.7 Crack patterns of test specimens a) Wall-Ref-01 b) Wall-Ref-02 c) Wall-JAR



Figure 7.8 Crushing of loaded corner in the test specimen

It is intended to validate the numerical model with the test results of Wall-Ref-01 and then check how the validated model could predict the test results of Wall-Ref-02 and Wall-JAR.

The validation of the numerical model with Wall-Ref-01 was made by defining the material properties of the interface cap model so that both numerical pushover diagrams and failure modes are comparable with the data provided in the experimental campaign. The summary of the mechanical properties adopted for the interface is presented in Table 7-4, namely the material parameters describing the tensile fracture behavior (tensile strength,  $f_t$ , and mode I fracture energy,  $G_f^I$ ), the shear fracture process (cohesion,  $c$ , friction angle,  $\phi$ , dilatancy angle,  $\psi$ , and mode II fracture energy,  $G_f^{II}$ ) and the compression behavior (compressive strength,  $f_c$ , and compressive fracture energy,  $G_c$ ).

Table 7-4 Mechanical properties adopted for the interface elements

Elastic Properties		$K_n$ (N/mm <sup>3</sup> )		$K_s$ (N/mm <sup>3</sup> )	
		9.3		5.4	
Nonlinear Properties	Tension	$f_t$ (N/mm <sup>2</sup> )		$G_f^I$ (N/mm)	
		0.05		0.05	
	Shear	$c$ (N/mm <sup>2</sup> )	$\phi$	$\psi$	$G_f^{II}$ (N/mm)
		0.07	0.5	0.0001	0.3
	Compression	$f_c$ (N/mm <sup>2</sup> )		$G_c$ (N/mm)	
		30		8	

The comparison between the force-displacement diagrams obtained in the experimental and numerical analysis for the wall “Wall-Ref-01” is carried out in Figure 7.9. It is observed that there is a good agreement of the numeric monotonic curve and the monotonic experimental envelopes for positive and negative directions (for convenience the results of “test-” is shown in positive directions), either in terms of lateral resistance and ultimate deformation.

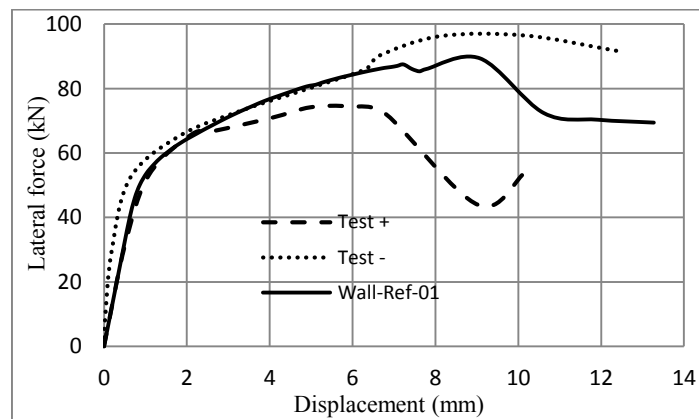


Figure 7.9 Lateral force-displacement obtained in numerical analysis and experimental test (Wall-Ref-01)

It is seen that there is also a good agreement in the pre-peak regime, where the linear stiffness and the pre-peak nonlinear regime are well described by the numerical model. As a result of numerical analysis, when in-plane lateral load is applied, the infilled frame acts as a monolithic resisting system at low lateral load level. As the load increases, the infill tends to partially separate from the enclosure frame and stress concentration along a strut develops. This behavior is schematically shown in Figure 7.10a. The left upper and bottom right corners of infill detached from the RC

frame for lateral loads of 55kN and of 65kN respectively, which agrees with the test results. It should be also noticed that the failure mode of the numerical model is compatible with one recorded in the test results. As shown in Figure 7.10b, the deformed mesh found in the numerical model of the infill panel at failure demonstrates the crushing of the infill in the extremities of the diagonal compression strut. This result matches with the failure mode of the test results shown in Figure 7.8.

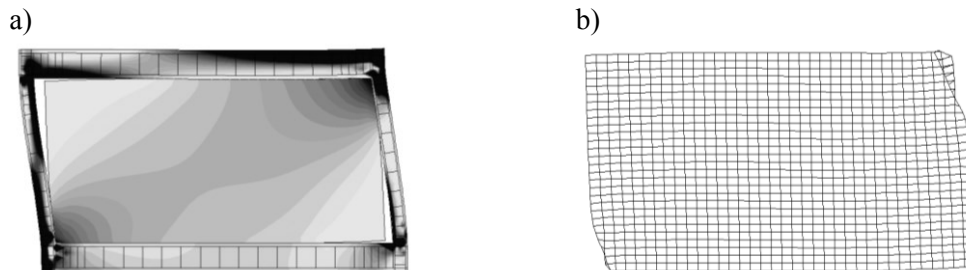


Figure 7.10 a) Schematic distribution of minimum principal stresses in numerical model (Wall-Ref-01)  
b) Deformed mesh of the infill panel at failure

For the Wall-Ref-02 and Wall-JAR, there was the need to update the mechanical properties of interface elements to take into account the rendering at both sides of the wall and the reinforcement at the bed joints. It is evident that the presence of rendering and also bed joint reinforcement change the mechanical properties of the interface elements representing the connection between infill and the surrounding frame.

The mechanical properties of the interface elements of Wall-Ref-02 and Wall-JAR were calculated by modifying the mechanical properties of interface considered in Wall-Ref-01. The update of the mechanical properties of the masonry infill with rendering at both sides was made by considering the geometrical association of the masonry infill with the thickness  $t_w$ , and the new mortar layers with thickness  $t_r$ , as is seen in Figure 7.11. Thus, the equivalent value of the interface's tensile strength in specimen Wall\_Ref\_02 is obtained through Eq. 7-1:

$$f_{tin} = \frac{(f_{ti} \times t_w) + (f_{tr} \times t_r)}{t_{all}} \quad \text{Eq. 7-1}$$

Where  $f_{tin}$  is the equivalent tensile bond strength of the interface in new condition (with rendering),  $f_{ti}$  is the tensile bond strength of the interface without rendering,  $f_{tr}$  is the tensile bond strength of the rendering material,  $t_w$  is the thickness of the infill wall without rendering (15 cm),  $t_r$  is the thickness of the mortar rendering layers (1 cm) and  $t_{all}$  is the entire thickness of the wall after rendering. The mechanical properties of the interface after adding the rendering such as elastic properties (shear and normal stiffness), cohesion and also Mode II fracture energy are also calculated according to the same averaging procedure. The summary of the mechanical properties of the interface updated after rendering for the specimens Wall-Ref-02 and Wall-JAR is presented in Table 7-5. It was considered that the friction and the dilatancy angles can be considered roughly the same for the rendering walls.

The static nonlinear analysis performed on the walls Wall-Ref-02 and Wall-JAR to evaluate their in-plane cyclic behavior is summarized in Figure 7.12, where the numerical nonlinear monotonic and experimental monotonic envelopes of force-displacement diagrams can be compared. Also here, for convenience, the results obtained in both directions are represented in positive directions.

It is seen that the numerical model can predict very satisfactorily the results of the experimental tests. The numerical results confirm again that rendering of the infilled masonry walls results in a considerable increase on the in-plane lateral resistance.

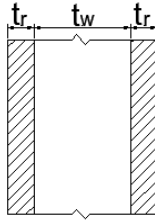


Figure 7.11 Thickness of the brick infill masonry walls after rendering in contact with the concrete enclosure

Table 7-5 Mechanical Properties of the interface after rendering

Interface mechanical Properties	Wall-Ref-02	Wall-JAR
Normal stiffness, $K_n$ (N/mm <sup>3</sup> )	24.18	33.48
Shear Stiffness, $K_s$ (N/mm <sup>3</sup> )	14.04	19.44
Tensile strength, $f_t$ (N/mm <sup>2</sup> )	0.13	0.18
Mode I fracture energy, $G_f^I$ (N/mm)	0.13	0.18
Cohesion, $c$ (N/mm <sup>2</sup> )	0.2	0.263
Mode II fracture energy, $G_f^{II}$ (N/mm)	0.9	1.1

The numerical results in terms of secant stiffness, calculated as a slope of force-displacement diagram at 30% of the maximum lateral resistance, and lateral strength are given in Table 7-6. Rendering has increased the lateral strength of the wall about 100% and putting bed joint reinforcement along with both side rendering has increased about 130%. Both specimens fail due to infill crushing in the numerical model, which is compatible with experimental results.

It should be also stressed that the numerical model is also able to catch the effect of the addition of horizontal reinforcement at the bed joints on the lateral resistance. An increase of 12% on the lateral resistance was recorded in case of specimen Wall-JAR in relation to wall Wall-Ref-02. It is therefore concluded that the proposed numerical model adequately replicates the experimental tests.

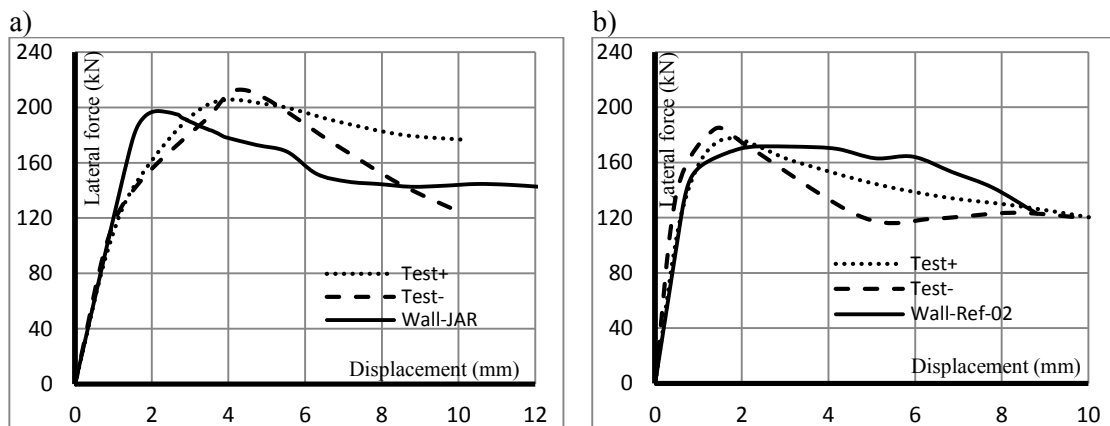


Figure 7.12 Comparison of the force-displacement diagrams obtained in experimental program with numerical analysis: a) Wall-JAR b) Wall-Ref-02

Table 7-6 Results of numerical analysis in terms of initial stiffness, lateral resistance and failure mode

Numerical Model	Secant stiffness at 30% of $F_{max}$ (N/mm)	Lateral Resistance, $F_{max}$ (N)	Failure Mode
Wall-Ref-02	201000	171500	Infill Crushing
Wall-JAR	120000	197500	Infill Crushing

### 7.2.3 Analysis of the material properties

#### 7.2.3.1 Parameters under study

The parametric analysis aims to evaluate the effect of different parameters on the in-plane response of masonry infilled frames. In detail, the work presented in this section can be divided in four parts: (1) analysis of the effect of mechanical properties of the infill on the in-plane response of infilled frame (2) assessment of the influence of the size of central window openings on the lateral stiffness and resistance; (3) evaluation of the influence of the type and location of the openings in the lateral stiffness and resistance; (4) assessment of the influence of the openings in the width of the diagonal compression strut that represents the masonry infill.

#### 7.2.3.2 Analysis of the effect of the compressive strength of infill

In a first numerical analysis, the compressive strength of brick masonry was taken as 2MPa and 5MPa to investigate the effect of its variation on the in-plane behavior of infilled frames. As it is shown in Figure 7.13, increasing the infill's compressive strength leads to the increase in the lateral strength of the rc frame with masonry infill. By increasing infill's compressive strength from 1MPa (used in the calibration of the numerical model) to 2MPa, infilled frame's lateral strength increased about 15%, whereas by increasing its compressive strength from 2MPa to 5MPa, the increase in its lateral strength is about 64%. The improvement of the lateral strength of the masonry infilled rc frame by increasing the compressive strength of masonry is much associated to the crack patterns and damage developed in the composite structure. In fact, the damage pattern is much related to the crushing of masonry at the ends of the compression strut at the contact between the masonry infill and the frame. This means that by increasing the compressive strength of masonry, the damage due to masonry crushing is delayed and occurs for higher values of stresses developed in the walls, corresponding to higher values of the lateral load applied.

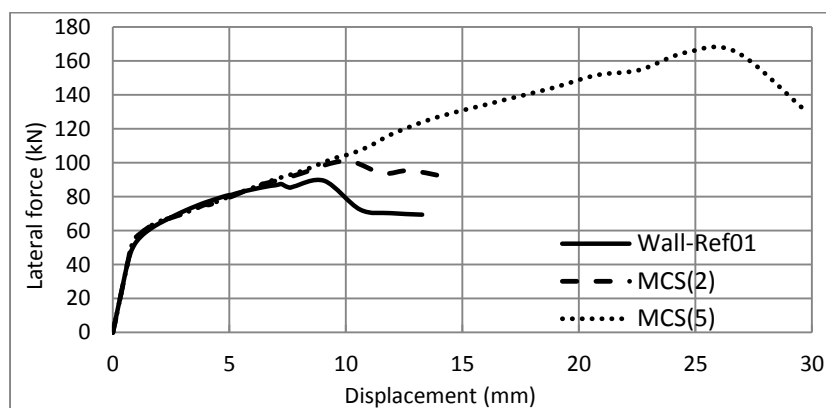


Figure 7.13 Pushover diagrams of the numerical models

Usually the masonry materials with higher compressive strengths have higher fracture energies. To simulate this condition, the infill's compressive strength and the compressive fracture energy were increased by two times to have the compressive strength of 2MPa and compressive fracture energy of 2N/mm. The results of the static nonlinear analysis in terms of force-displacement diagrams are shown in Figure 7.14.

It can be concluded that the simultaneous increasing of the compressive strength of the brick infill from 1MPa to 2MPa and the compressive fracture energy from 1N/mm to 2N/mm, leads to the increase of the maximum lateral strength of about 23%.

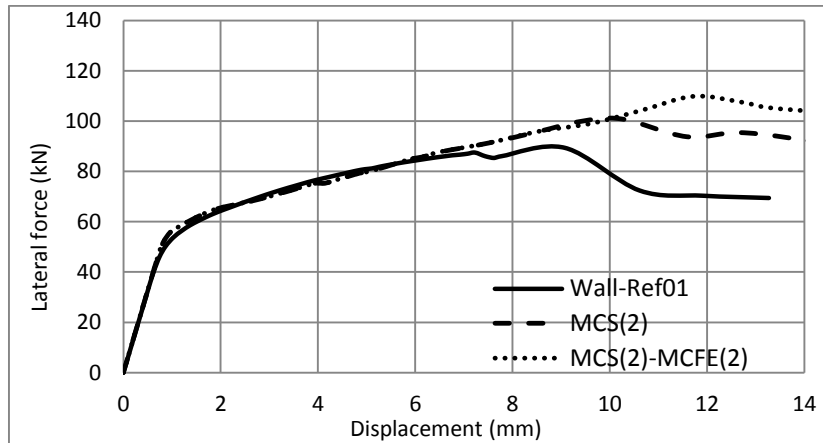


Figure 7.14 Pushover force-displacement diagrams obtained in the numerical model

### 7.2.3.3 Analysis of the influence of the tensile strength of brick infill

The effect of the tensile strength of brick masonry infill on the in-plane behavior is evaluated by varying the tensile strength of masonry from 0.25MPa to 0.5MPa. The tensile fracture energies are kept constant to investigate only the effect of tensile strength. From the results obtained, it is observed that the force-displacement diagram of the model with increased tensile strength do not show any change in terms of maximum lateral strength, see Figure 7.15. The force-displacement diagrams of both models are the same until the peak load, which means that infill's tensile strength does not have significant effect on the load-displacement diagram of this type of rc frames with brick infills until the peak loads. Beyond the peak load, no significant changes were also recorded.

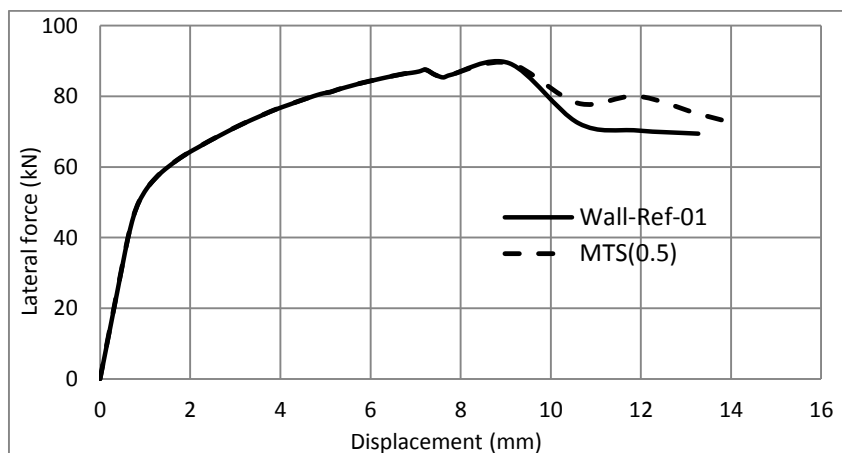


Figure 7.15 Comparison of the force-displacement diagrams for models with varying tensile strength of masonry

### 7.2.3.4 Analysis of the influence elastic modulus of brick masonry

The influence of the elastic stiffness of the masonry infill on the in-plane behavior of the rc frame with brick infill is analyzed by increasing the elastic modulus by 100%. As it is shown in Figure 7.16, an increase of 100% in the elastic modulus of the infill lead to the increase in the initial stiffness of about 80% and to the increase in the lateral strength of about 5%. In the latter case, the increase appears to be negligible. The elastic modulus has also an important influence on the displacement at which the maximum lateral resistance is attained. The crushing of the infill panel initiates at a displacement of 9.6mm in the specimen with the reference elastic modulus, whereas in the wall with the higher elastic modulus, the lateral resistance is attained at lateral displacement of 4.8mm. This means that in the panel with higher elastic modulus the cracking in the compressive zones develops earlier with respect to reference wall.

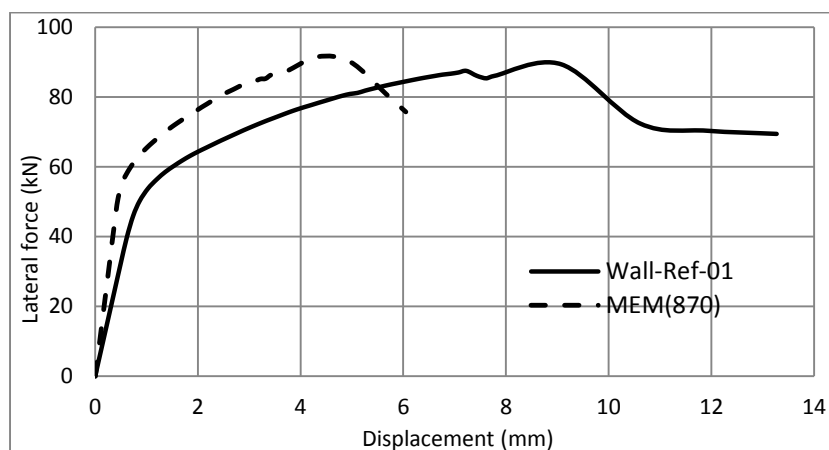


Figure 7.16 Force-displacement diagrams for RC frame models with distinct stiffness of the brick masonry infill

## 7.2.4 Influence of openings in the in-plane response

### 7.2.4.1 Analysis of central openings

In the first step, the influence of the presence and size of a central opening in the in-plane behavior of the rc frame with brick infill is investigated by considering different openings in the numerical model calibrated based on the experimental results. The variation of the area of the central opening is defined by multiplying the original dimensions of the infill by a factor ( $a$ ), see Figure 7.17 and Table 7-7. Here, the model name is defined by  $O(x\%)$ , where  $x$  is the ratio of opening area with respect to the total infill area. The boundary conditions were the same as the ones considered in the calibrated model. Static nonlinear analysis was performed by applying increasing lateral load at the upper beam.

The crack propagation of the specimen with the central opening having an area of 30% of the area of the brick infill is presented in Figure 7.18. The lateral load is applied from right to left. At early stages of loading, cracks appeared at upper right and bottom left corners of the openings as a result of the stress concentration along the compression strut. By increasing the lateral load, the cracking path extends to the other corners of the opening and appears also in the surrounding rc elements. This occurs in all numerical models with any percentage of openings. As the lateral load increases, the cracking density increases considerably resulting in the failure of the composite structure.

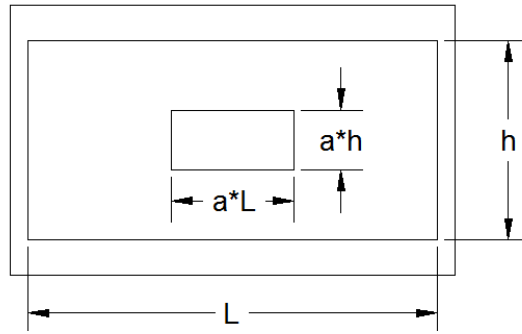


Figure 7.17 Geometry of the central openings

Table 7-7 Geometrical characterization of the openings (dimensions in mm)

Model Name	a (constant)	Length of Opening	Height of Opening	Length of Infill	Height of Infill
O(0%)	0	0	0	3500	1700
O(9%)	0.3	1050	510	3500	1700
O(12%)	0.35	1225	595	3500	1700
O(15%)	0.39	1365	663	3500	1700
O(20%)	0.45	1575	765	3500	1700
O(25%)	0.5	1750	850	3500	1700
O(30%)	0.55	1925	935	3500	1700
O(36%)	0.6	2100	1020	3500	1700
O(39%)	0.625	2187.5	1062.5	3500	1700
O(42%)	0.65	2275	1105	3500	1700
O(45%)	0.675	2362.5	1147.5	3500	1700
O(49%)	0.7	2450	1190	3500	1700
Bare Frame	1	3500	1700	0	0

The distribution of minimum principal stresses (compressive stresses) over the infilled frame show that for low levels of loading, two diagonal struts form within the infill passing through the upper left and lower right corners of the openings, see Figure 7.19. This means that, for low levels of loading, the formation of crack in lower left and upper right corners is due to tensile stresses and then, by increasing the lateral load, the cracks form in the areas where strut has formed around the lower right and upper left corners of opening, due to compressive stresses.

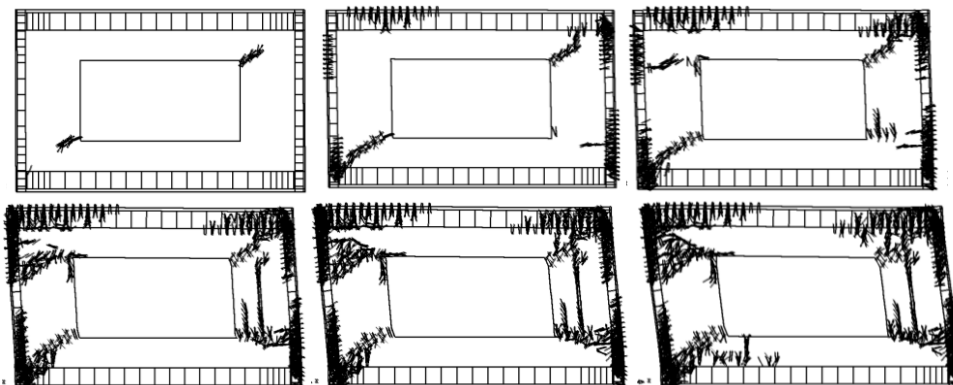


Figure 7.18 Schematic representation of crack propagation in the numerical models by increasing the lateral load



Pushover force-displacement diagrams of the numerical models are represented in Figure 7.20 for better understanding the influence of opening area on the in-plane behavior. All the numerical analysis were continued until the lateral drift of 2% to obtain the relevant parameters such as initial stiffness, lateral strength and the displacement corresponding to the lateral strength. By analyzing the force-displacement diagrams, it is clear that the variation of the percentage of the central opening influences the lateral behavior of the infilled frames, particularly lateral stiffness, calculated as the secant stiffness at 30% of the lateral resistance, lateral strength and displacement at which the lateral strength is achieved.

It is observed that the displacement corresponding to the peak lateral load increases as the opening area increases, see Figure 7.20. This is related to the reduction of the contribution of the masonry infill for the lateral strength as the area of the central opening of the masonry infill increases. At the limit, when the percentage of the central opening is very high, the behavior of the infilled frame approaches the behavior of the bare frame. It is also observed that by increasing the area of the central opening, the lateral strength and stiffness decreases. It should be noticed that at small opening areas the decrease rate of the lateral stiffness is higher than the lateral strength, as can be seen in Figure 7.21.

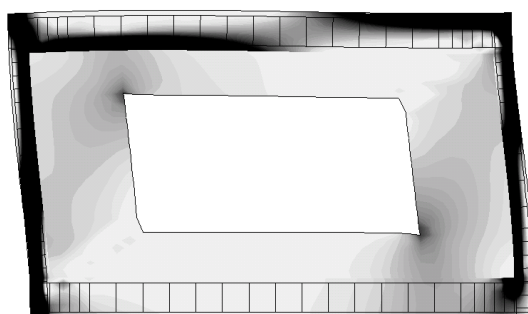


Figure 7.19 Schematic distribution of minimum principal stresses

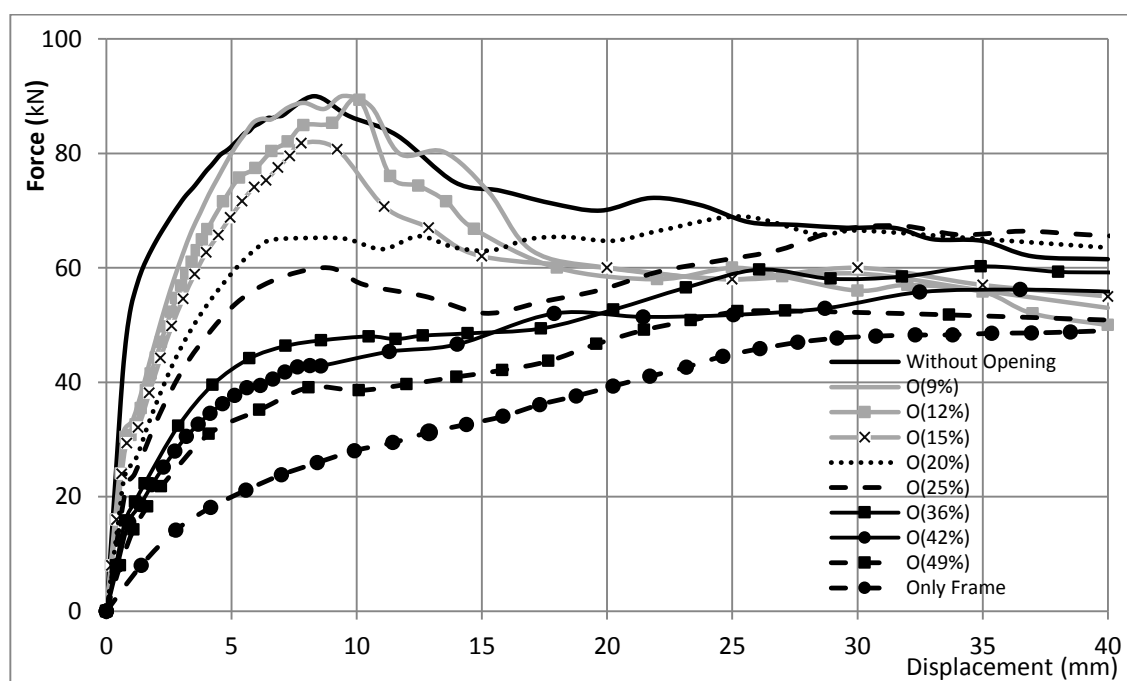


Figure 7.20 Pushover diagrams of the numerical models with increasing opening ratio

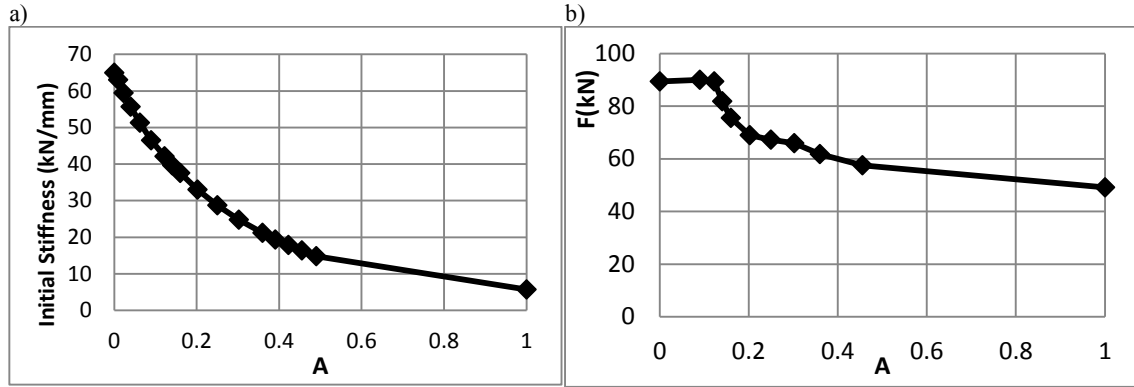


Figure 7.21 Influence of the opening area  $A$  on the mechanical properties of the rc masonry infill: a) variation of initial stiffness; b) variation of lateral strength

The trend of variation of the initial stiffness of infilled frames is compared with the one obtained by Asteris [54] and by Giannakas 's [55], see Figure 7.22.

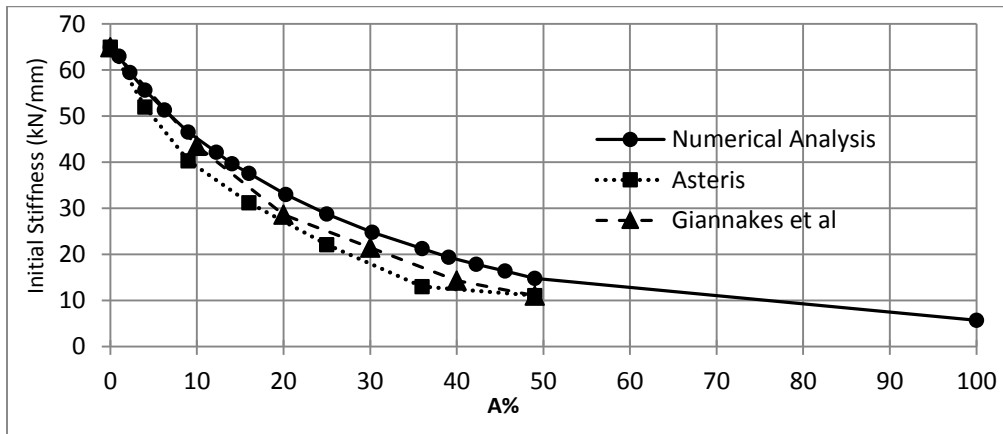


Figure 7.22 Trend of variation of initial stiffness in relation to opening area for different authors

It is observed that the variation of the initial stiffness obtained in this numerical analysis is similar to the analytical work of Giannakas et al [55] until 49% of opening area to infill area.

Aiming to mathematically define the variation of the lateral resistance and stiffness over varying opening area, a simplified approach was considered to predict the initial stiffness of the masonry infilled rc frame with central opening, see Eq. 7-2:

$$K_{co} = [(K_{fill} - K_{bare}) \times (1 - A)^n] + K_{bare} \quad \text{Eq. 7-2}$$

Where  $K_{co}$  is the initial stiffness of the infilled frame with central opening,  $K_{fill}$  is the initial stiffness of the solid infilled frame,  $K_{bare}$  is the initial stiffness of the frame and  $A$  is the ratio between opening area and the area of the infill. A best fit provides a value for “ $n$ ” equal to 3, with a coefficient of determination  $r^2$  of 0.988. Thus, Eq. 7-2 can be rewritten as (Figure 7.23a):

$$K_{co} = [(K_{fill} - K_{bare}) \times (1 - A)^3] + K_{bare} \quad \text{Eq. 7-3}$$

A simplified approach is also used to determine the mathematical equations for the lateral strength of the masonry infilled rc frames for any area of central opening as shown in Figure 7.23b. In this approach, the lateral strength is assumed to be expressed as:

$$F_{co} = [(F_{fill} - F_{bare}) \times (1.1396 \times (1 - A))^n] + F_{bare} \quad \text{Eq.7-4}$$

Where  $F_{co}$  is the lateral strength of the infilled rc frame with central opening,  $F_{fill}$  is the lateral strength of the solid infilled frame and  $F_{bare}$  is the lateral strength of the reinforced concrete frame. The best fit is obtained for a value of  $n$  equal to 4.3 with an  $r^2$  equal to 0.975. Based on this, the Eq.7-4 can be rewritten as:

$$F_{co} = [(F_{fill} - F_{bare}) \times (1.1396 \times (1 - A))^{4.3}] + F_{bare} \quad \text{Eq.7-5}$$

Although the calibration of the numerical model was based on the solid infill, the global results of the numerical model with the central opening is satisfactorily compatible with the test results of other researchers [7, 51]. For instance, the movement of the opening towards the center of the span results in further decrease of the lateral strength and stiffness as it is clear in other numerical study [51].

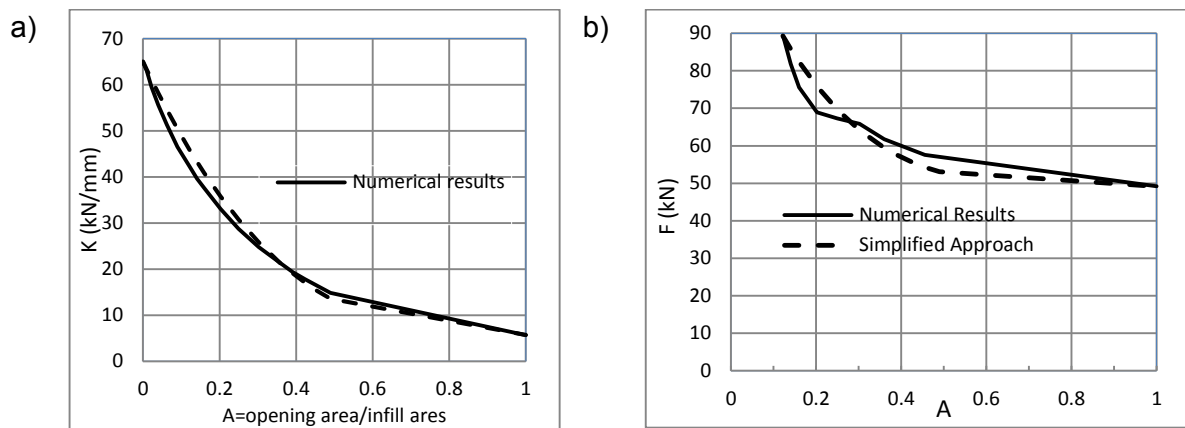


Figure 7.23 Simplified and detailed approaches for: a) initial stiffness; b) lateral strength

7.2.4.2 Analysis of different types of openings

The central opening can be representative of some geometrical configurations of masonry infill walls, but other types of openings can be found within masonry infills, typically associated with double windows and combinations of windows and doors. The most common openings of South European countries were categorized by [120] and are shown in Figure 7.24.

As the position of the opening is known to affect the lateral behavior of rc frames with masonry infills [7, 54], it was decided to carry out a detailed study about the influence of the distinct types of openings that are considered as typical openings in masonry infill walls in south European countries.

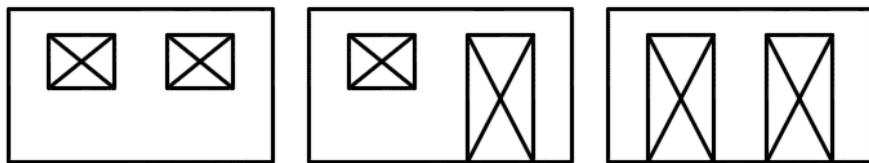


Figure 7.24 Typical openings in masonry infill walls in southern European countries

The distribution of the minimum principal stresses corresponding to the first steps of loading in the  $-x$  direction for the three openings typologies is presented in Figure 7.25. It is seen that three diagonal struts develop in the piers, namely the central pier between openings and the lateral piers

between the openings and the rc frame. The inclination of the struts and the stresses developed depend on the height to length ratio of the piers. This stress distribution shows that the diagonal struts provide the stiffness of the infilled frame and also withstand the lateral load that is applied to the structure, meaning that the cross section or the width of the piers in which the diagonal struts develops is of utmost importance. By comparing the diagonal struts within the infills of walls O(2W)1, O(2D)1 and O(DW)1, see Figure 7.25 for wall labels, it can be easily predicted that the stiffness and lateral strength of wall O(2W)1 is considerably larger than walls O(2D)1 and O(DW)1, which is attributed to higher width of the three struts formed in the wall O(2W)1. This is the base for developing analytical work on predicting the lateral stiffness and strength of masonry infills with openings, which is made later in this section. The initial cracks develop in the corners due to the tensile stresses and then by increasing the lateral load, cracks appear in the corners where compressive struts were formed, due to the large compressive stresses, see Figure 7.26. This crack propagation pattern occurs similarly in the distinct models with typical openings. Taking into account the three opening typologies for the masonry infill walls, it was decided to study the influence of the different positions of openings in its in-plane behavior, as shown from Figure 7.27 to Figure 7.29.

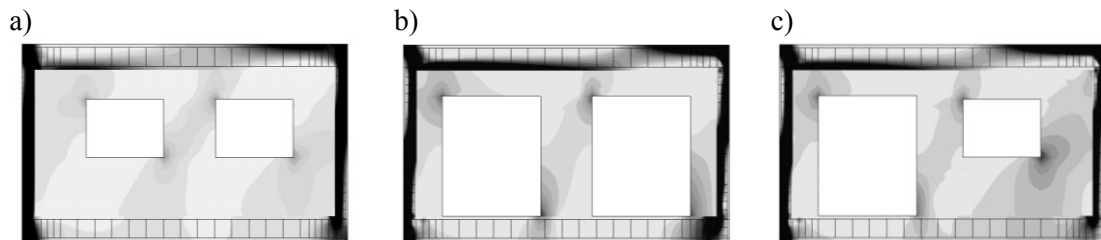


Figure 7.25 Schematic distribution of minimum principle stresses; a) in wall O(2W)1; b) wall O(2D)1 (left); c) wall O(DW)1 (right)

All walls were numerically simulated in DIANA software considering the material properties used in the calibrated model of Wall-Ref-01 and analyzed by performing static nonlinear analysis. The results in terms of initial stiffness and lateral strength are given in Table 7-8. In the cases where the openings are not symmetric within each typology, the minimum value of initial stiffness and lateral strength are represented because of the cyclic nature of the earthquakes. For instance from walls O(2W)2 and O(2W)3, the one which had the minimum value for initial stiffness and lateral strength, namely O(2W)3, is selected to be investigated in Table 7-8.

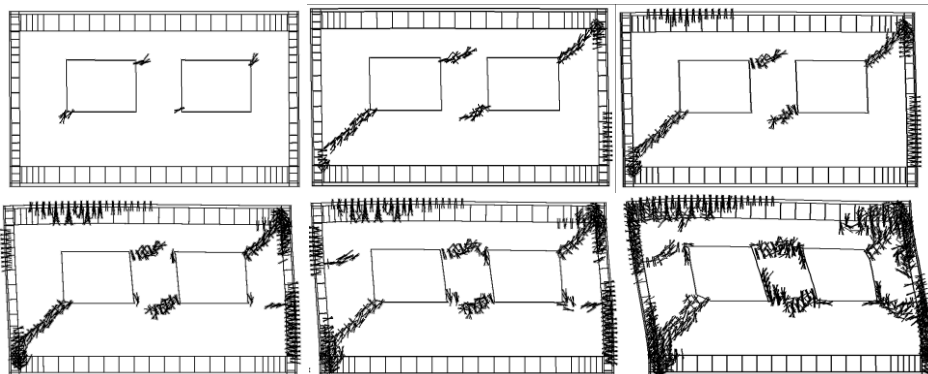


Figure 7.26 Crack propagation in wall O(2W)1

Considering the results listed in Table 7-8, it can be easily concluded that in all opening configurations, moving the openings toward the boundaries increases the initial stiffness and

lateral strength of the infilled frames. Similar trend has been pointed out by Asteris [54] in masonry infill walls with the variation of the geometry and location of a window. For instance, by moving the two window openings to the nearest point with enclosure frame (walls O(2W)1 and O(2W)4), the initial stiffness and lateral strength increase about 24% and 19% respectively.

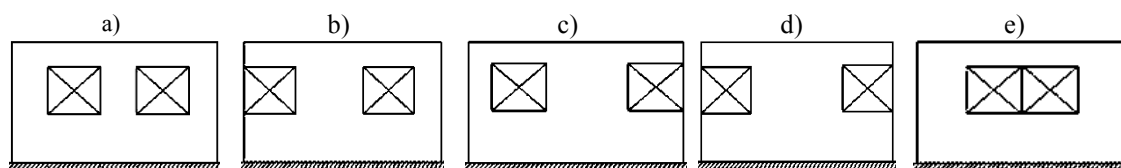


Figure 7.27 Possible positions of window openings: a)O(2W)1, b)O(2W)2, c)O(2W)3, d)O(2W)4, e)O(2W)5

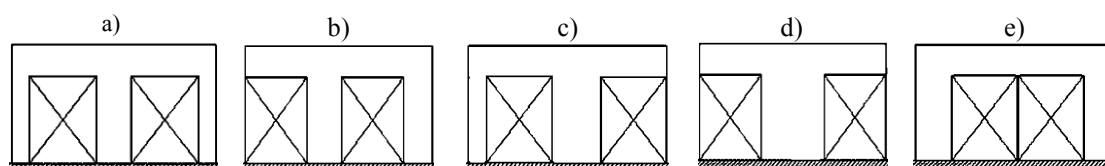


Figure 7.28 Possible positions of door openings: a)O(2D)1, b)O(2D)2, c)O(2D)3, d)O(2D)4, e)O(2D)5

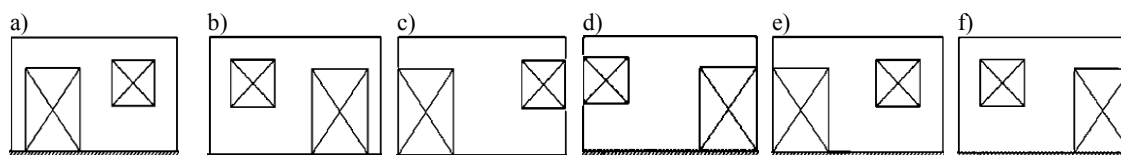


Figure 7.29 Possible positions of door and window openings: a)O(DW)1, b)O(DW)2, c)O(DW)3, d)O(DW)4, e)O(DW)5, f)O(DW)6

In case of the walls with two similar door openings adjacent to the borders, the maximum increase of initial stiffness and lateral strength is 41% and 3% respectively. For the case of one window and one door opening the increase in stiffness and strength is about 30% and 7% respectively, when the openings are moved to the borders. Moving of the openings towards boundaries is more effective in terms of initial stiffness in the walls that have larger opening areas.

Table 7-8 Initial stiffness and lateral strength of the different models

Wall Name	A	Initial Stiffness (N/mm)			Lateral Strength (N)		
		Numerical Results (N/mm)	Simplified approach (N/mm)	Error (%)	Numerical Results (N)	Simplified approach (N)	Error (%)
O(2W)1	0.20	28490	35150	23.4	65100	75010	15.2
O(2W)3		32260	35150	9.0	68510	75010	9.5
O(2W)4		35410	35150	0.7	77710	75010	3.5
O(2W)5		30240	35150	16.2	66050	75010	13.6
O(2D)1	0.54	12250	11410	-6.9	54840	51640	-5.8
O(2D)3		14440	11410	-21.0	57060	51640	-9.5
O(2D)4		17250	11410	-33.8	56370	51640	-8.4
O(2D)5		15970	11410	-28.5	55030	51640	-6.2
O(DW)2	0.37	19900	20360	2.3	58240	58680	0.8
O(DW)4		25870	20360	-21.3	62240	58680	-5.7
O(DW)6		22770	20360	-10.6	59970	58680	-2.1
			<b>Average</b>	15.8			7.3

On the other hand, as it is shown in Figure 7.30, the increase in the lateral strength by moving the openings toward boundaries in the walls with lower opening areas is higher than in the case of walls with higher openings area. In practical terms, this means that in the walls with high percentage of openings (more than 50%), moving them towards the boundaries does not increase the lateral strength.

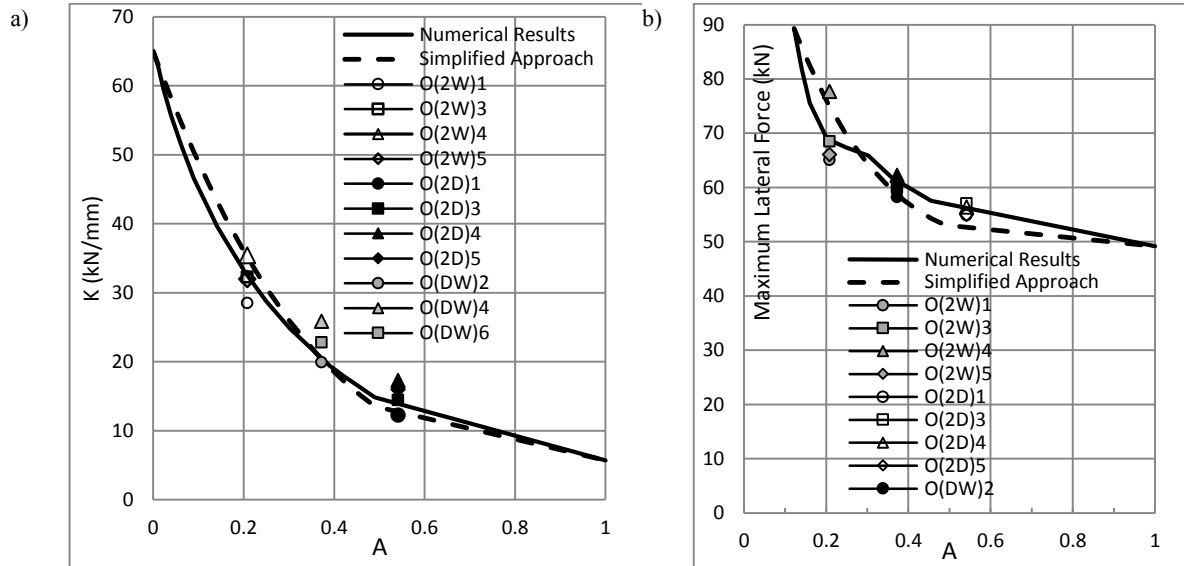


Figure 7.30 Prediction of key parameters of the in-plane behavior of the walls; a) initial stiffness and b) lateral strength of the walls with different opening types

The simplified approach that was developed in the previous section for infills with central openings was used to predict the initial stiffness and lateral strength of the masonry infills with distinct typical openings, see Table 7-8. It is observed that this simplified approach can predict the initial stiffness of the masonry infilled rc frames with distinct openings with an average error of 16% (with a maximum of 34%). For the lateral strength, the average error and the maximum error is much more reasonable (typically, below 10%). Although the simplified approach is considered to be a good solution for predicting the initial stiffness of the walls with central openings, it cannot consistently capture the stiffness of the models with other types of openings. For instance, the error in predicting the initial stiffness of the wall O(2D)4 by the simplified approach is high (about 34%).

Given the considerable error obtained for the stiffness, it was decided to develop an empirical equation to predict the in-plane stiffness of masonry infilled rc frames with distinct types of openings at any position, based on the equation developed for masonry infills with a central opening. To do this, the initial stiffness calculated through Eq.7-3 for masonry infill with central openings is multiplied by a correction parameter, denoted as a position factor,  $\alpha$ , which takes into account the geometrical relations of the individual piers of the infill:

$$K = K_{CO} \times \alpha \quad \text{Eq.7-6}$$

The position factor,  $\alpha$ , takes into consideration the relation of stiffness of the different piers and is defined by the following equation, by considering an inverse fitting procedure:

$$\alpha = \frac{\sum \left( \frac{b_i}{h_i} \right)^{1.035}}{\sum \left( \frac{b_i}{h_i} \right)} + A^3 \sum \left( \frac{b_i}{h_i} \right)^{2.5} \quad \text{Eq.7-7}$$

Where,  $b_i$  is the width of the piers and  $h_i$  is height of the openings and  $A$  is the total area of the openings, see Figure 7.31. Table 7-9 shows that the equation satisfactorily takes into account the changes in position of the openings, given that an average error of approximately 7% was obtained in relation to the stiffness obtained in the numerical analysis.

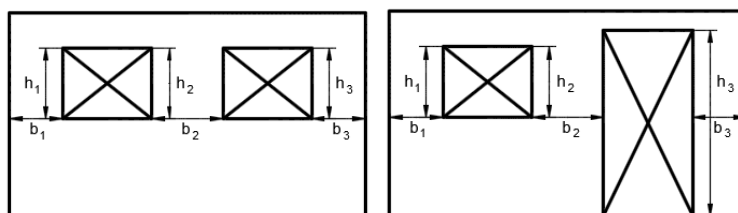


Figure 7.31 Width and height of the piers to be used for calculation of Eq.7-7

Table 7-9 Results of empirical equation compared with numerical results

Wall Name	A	$b_i$ (m)	$h_i$ (m)	K (Eq. 7-6) (N/mm)	Numerical (N/mm)	Error (%)	
O(2W)1	0.2	0.6	0.68	32260	28490	13.2	
		0.6	0.68				
		0.48	0.68				
O(2W)3		0.48	0.68	33580	32260	4.1	
		1.2	0.68				
O(2W)4		1.68	0.68	35710	35410	0.8	
O(2W)5		0.84	0.68	33140	30240	9.6	
		0.84	0.68				
O(2D)1		0.54	0.3	1.4	13960	12250	13.9
			0.6	1.4			
	0.3		1.4				
O(2D)3	0.3		1.4	14620	14440	1.2	
	0.9		1.4				
O(2D)4	1.2		1.4	15630	17250	-9.4	
O(2D)5	0.6		1.4	14300	15970	-10.5	
	0.6		1.4				
O(DW)2	0.37		0.6	0.68	21310	19900	7.1
			0.54	0.68			
		0.3	1.4				
O(DW)4		1.44	0.68	27490	25870	6.3	
O(DW)6		0.6	0.68	22740	22770	-0.1	
		0.84	0.68				
					<b>Average</b>	6.9	

#### 7.2.4.3 Equivalent width of the diagonal strut for infills with openings

In this section it is intended to replace the infill with any typical opening by an equivalent diagonal strut with width  $w$  to have the same initial stiffness. Notice that as already mentioned, it is common that the masonry infills are replaced by diagonal struts in the macro-modelling approach,

mainly when the numerical modeling of rc buildings with masonry infills is needed. There are several empirical formulas for solid masonry infills, but information is lacking in case of masonry infills with openings. Therefore, a new numerical model was constructed using four-noded plane stress elements for the rc frame and truss elements for struts equivalent to the masonry infills, see Figure 7.32.

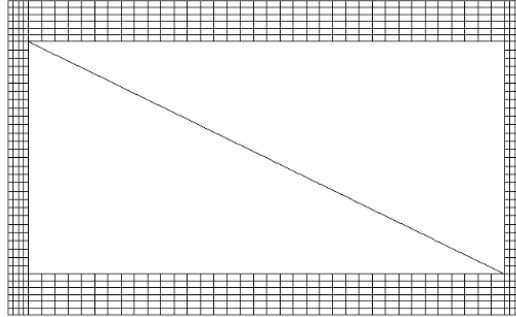


Figure 7.32 Replacement of masonry infill with a diagonal strut

As the initial stiffness is the parameter under evaluation, linear elastic analysis of the model was carried out. Different values for the width of the equivalent diagonal strut were considered in the linear elastic analysis to investigate how it affects the lateral stiffness of the rc frame with masonry infills under in-plane loading. In Figure 7.33, the relation between the stiffness and the ratio of the width ( $w$ ) to length ( $d$ ) of strut ( $w/d$ ) is shown. The linear fitting to the numerical stiffness obtained for different values of the strut width (coefficient of correlation  $r^2$  equal to 0.9998) reveals that the stiffness increases linearly with the width of the strut.

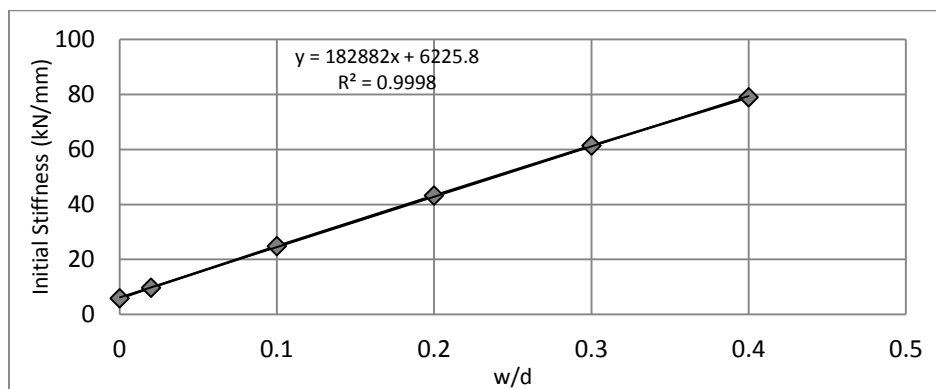


Figure 7.33 Variation of initial stiffness with the width of diagonal strut

From these results, it is concluded that the ratio of the width of the diagonal strut,  $w$ , to the diagonal length of the masonry infill wall,  $d$ , ratio ( $w/d$ ) equal to 0.32 corresponds to the initial stiffness of the frame with solid masonry infill. This means that the solid masonry infill within the frame which is modelled herein can be replaced by a diagonal strut with a width,  $w$ , of 1.25m.

In this scope, several equations have been proposed in the past to calculate the width of the diagonal strut to replace the solid infill panel without openings [71, 72, 77]. Thus, the equivalent width of diagonal strut obtained with numerical analysis carried out in this work was compared with the width of the diagonal strut given by different equations found in literature, see Figure 7.34. From the results, it is observed that generally the proposed equations provide lower values for the width of the equivalent strut in relation to the value found from the numerical



analysis. The width of the equivalent diagonal strut calculated from FEMA 356 [1] is the most conservative.

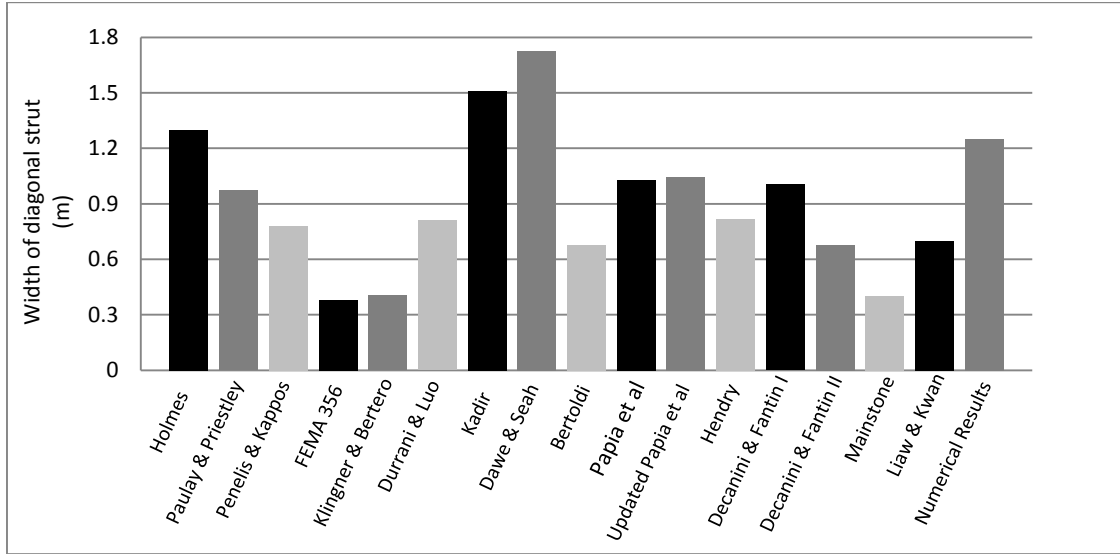


Figure 7.34 Equivalent width of strut for different proposed equations

It seems that the updated Papia et al. equation [69] provides the closest value to the numerical result. According to that equation, which is adopted here, the equivalent width of the diagonal strut is given by:

$$w_{fill} = \frac{k \cdot c}{d \cdot z} \frac{1}{(\lambda^*)^2} \beta \quad \text{Eq.7-8}$$

$$k = 1 + (18\lambda^* + 200)\varepsilon_v \quad \text{Eq.7-9}$$

$$\varepsilon_v = \frac{F_y}{2A_{col}E_{fr}} \quad \text{Eq.7-10}$$

$$\lambda^* = \frac{E_{inf}}{E_{fr}} \frac{t \cdot h'}{A_{col}} \left( \frac{h'^2}{l'^2} + \frac{1}{4} \frac{A_{col}}{A_{beam}} \frac{l'}{h'} \right) \quad \text{Eq.7-11}$$

$$c = 0.249 - 0.0116\nu + 0.567\nu^2 \quad \text{Eq.7-12}$$

$$\beta = 0.146 + 0.0073\nu + 0.126\nu^2 \quad \text{Eq.7-13}$$

$$\begin{cases} z = 1 + 0.25 \left( \frac{l}{h} - 1 \right) & 1 \leq \frac{l}{h} \leq 1.5 \\ z = 1.125 & 1.5 < \frac{l}{h} \end{cases} \quad \text{Eq.7-14}$$

Where,  $w_{fill}$  is width of the strut for solid infilled frame,  $l$  is the length of infill,  $h$  is height of infill,  $l'$  is the length of frame between two centerline of columns,  $h'$  is the height of frame between two centerlines of beams,  $t$  is the thickness of infill,  $E_{inf}$  and  $E_{fr}$  are the modulus of elasticity of infill and frame respectively,  $A_{col}$  is the cross-section of column,  $A_{beam}$  is the cross-section of beam and  $\nu$  is the Poisson's ratio of infill. This formula will be used next for predicting the equivalent width of the strut.

Aiming at obtaining an updated expression for the width of the diagonal strut to simulate the presence of openings in the masonry infills, the linear variation of initial stiffness with respect to the width of diagonal strut (Figure 7.33) results in:

$$K = \frac{w}{w_{fill}} \left( K_{fill} - K_{bare} \right) + K_{bare} \quad \text{Eq.7-15}$$

Here,  $w$  corresponds to the width of equivalent strut for an infilled frame with stiffness  $K$ ,  $K_{fill}$  is the stiffness of the rc frame with solid masonry infill and  $w_{fill}$  is the width of equivalent strut for solid infilled frame derived from Eq.7-8. Replacing  $K$  in Eq.7-15, incorporating Eq.7-6 and Eq.7-3 will lead to:

$$w = w_{fill} \cdot \alpha \cdot f(A) + \frac{(\alpha - 1)w_{fill}K_{bare}}{K_{fill} - K_{bare}} \quad \text{Eq.7-16}$$

This means that a system of infilled frame with any percentage of openings can be replaced by a frame with equivalent diagonal strut of width  $w$  given by Eq.7-16.

#### 7.2.4.4 *Practical guideline for using equivalent diagonal strut method*

The proposed equation for calculating the width of an equivalent diagonal strut (Eq.7-16), can be used for practical purposes in multi-story structures. To do this, it is necessary to calculate  $K_{fill}$  and  $K_{bare}$  for each one-bay one-story frame inside the structure. Obtaining the width of the strut equivalent to the masonry infill without openings,  $w_{fill}$ , from Eq.7-8, which is only related to the geometry of the infilled frame, will lead to calculation of  $K_{fill}$  for each one-bay one-story frame, using the following equation that was proposed by Mainstone [61]:

$$K_{fill} = \frac{E_{inf} w_{fill} t}{\sqrt{l'^2 + h'^2}} \cos^2(\theta) \quad \text{Eq.7-17}$$

Here,  $\theta$  is the angle of the diagonal strut to horizontal direction (degrees). Bazan and Meli [62] proposed a dimensionless parameter,  $\beta$ , which evaluates the relative stiffness of the rc frame ( $K_{bare}$ ) to the infilled panel ( $K_{fill}$ ), given by:

$$\beta = \frac{E_c A_c}{G_i A_i} \quad \text{Eq.7-18}$$

Here,  $E_c$  is the modulus of elasticity of the rc column,  $A_c$  is the gross area of the column,  $G_i$  is the shear modulus of the infill and  $A_i$  is the area of the masonry panel in the horizontal plane. Once the stiffness of the solid infill and bare frame are calculated,  $K_{fill}$  and  $K_{bare}$ , these parameters can be replaced in Eq.7-16 for calculation of the width of the equivalent diagonal strut representing the masonry infill of each one-bay one-story frame inside the multi-story structure. To calculate the lateral strength of the one-bay, one-story infilled frame with any type of openings it is also needed to calculate the strength of the infill,  $F_{fill}$ , and the strength of the bare frame,  $F_{bare}$ , separately. The lateral resistance of the bare frame,  $F_{bare}$ , can be calculated as:

$$F_{bare} = \frac{4M_p}{h'} \quad \text{Eq.7-19}$$

Here,  $M_p$ , is the plastic moment of the column cross-section [136]. The lateral strength of the infilled frame is calculated based on the equation proposed by Stafford Smith and Coull [65]

$$F_{fill} = f'_m t \frac{\pi}{2} \sqrt{\frac{4E_c I_c h_i}{E_i t}} \quad \text{Eq.7-20}$$

Here,  $f'_m$  is the compressive strength of masonry of the infill wall,  $E_c$  and  $I_c$  are the modulus of elasticity and moment of inertia of the rc column,  $t$  is the thickness of the infill and  $E_i$  is the modulus of elasticity of the infill panel. Based on the results of Eq.7-19 and Eq.7-20, the lateral strength of the infilled panel with any type of opening,  $F_{co}$ , can be calculated from Eq.7-5. The strength of the equivalent strut for brick infills with any type of opening is calculated as:

$$\sigma_s = \frac{F_{co}}{tw \cos \theta} \quad \text{Eq.7-21}$$

Aiming at validating the equations proposed herein to calculate the width of the diagonal strut that describe the behavior of a masonry infilled rc frame with any distribution of openings, three different finite element numerical models were built, as shown in Figure 7.35, corresponding to different number of floors and a random distribution of openings in the infills. The nonlinear material models and mechanical properties were the same as the ones used for the model calibration. The same frames were also modelled by considering the masonry infills replaced by diagonal struts whose width,  $w$ , is calculated through Eq.7-16. A comparison was made in terms of initial stiffness and lateral strength between both models, see Table 7-10. By analyzing the results, it is observed that the numerical model with the equivalent diagonal strut, adopted the proposed formulation, can satisfactorily predict the initial stiffness and lateral strength of multi-storey infilled frames with an error lower than 14%. It is considered that these results validate the ability of Eq.7-16 and Eq.7-5 for predicting the initial stiffness and lateral strength of multi-storey infilled frames with any distribution of openings in the infills.

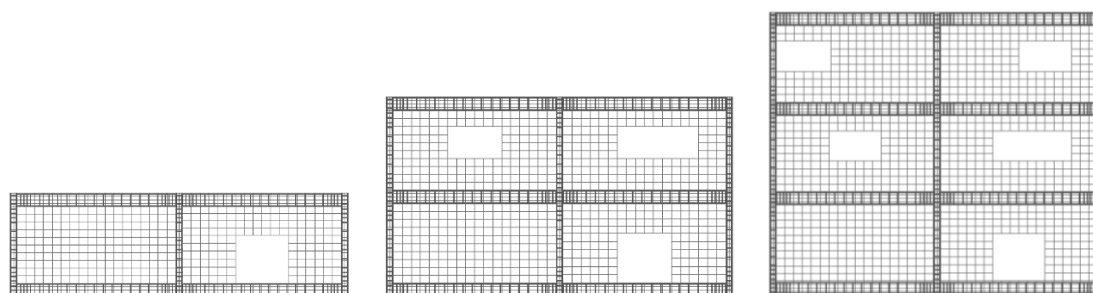


Figure 7.35 Numerical modelling of three multi-story structures in DIANA

Table 7-10 Comparison of the analysis of results between the finite element modelling and equivalent diagonal strut model

Model	Finite element modelling		Equivalent diagonal strut model		Error in Stiffness (%)	Error in Strength (%)
	Initial Stiffness (KN/mm)	Lateral Strength (KN)	Initial Stiffness (KN/mm)	Lateral Strength (KN)		
One-story	119.5	170.4	107	177.9	10.5	-4.4
Two-story	54.5	177.1	47.8	201.8	12.3	-13.9
Three-story	35.8	181.9	31.2	189.7	12.8	-4.3

### 7.3 Out-of-plane behavior of masonry infilled reinforced concrete frames

This section aims at modelling and validating a numerical model to analyze the out-of-plane behavior of rc frames with brick infills. For this, the numerical modelling of the rc frame with masonry infill wall tested under out-of-plane loading (SIF-O-1L-B) was carried out in the commercial finite element software DIANA [132]. The numerical model was validated based on the force-displacement diagram and also on the cracking patterns and failure mode.

#### 7.3.1 Numerical model for out-of-plane behavior

The numerical model for analyzing the out-of-plane response of rc frames with brick infills was based on the geometry and reinforcement scheme of the reduced scale specimen of SIF-O-1L-B, see Figure 7.36 and Figure 7.37.

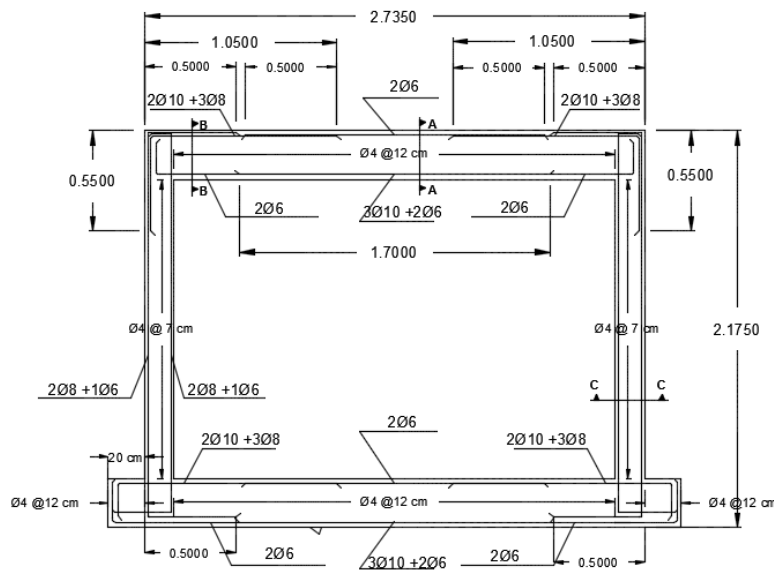


Figure 7.36 Geometry and reinforcement scheme of the reduced scale specimens

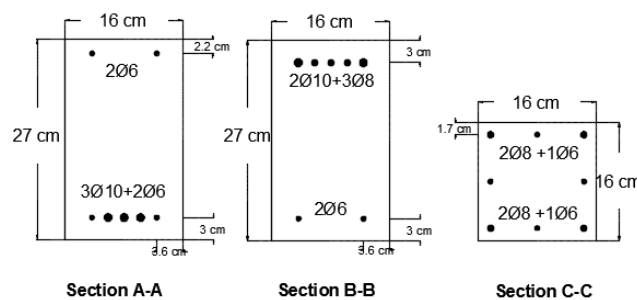


Figure 7.37 Cross-sections of columns and beams in reduced scale specimens

Three dimensional finite element modelling of the specimens was carried out in DIANA software by assuming the masonry infill and concrete as homogeneous materials. Masonry infill and concrete were modelled with four-noded shell elements, whereas the interface between infill and its surrounding frame was modelled by 2+2 noded interface elements. The reinforcement was added to the concrete elements by using embedded bars, perfectly bonded, see Figure 7.38. The lower concrete beam was fixed totally to prevent any movement in x, y and z directions, whereas

the upper beam was fixed just in the out-of-plane (z) direction. These boundary conditions are representative of the ones used in the experimental testing. The vertical load of 160 KN, corresponding to 40% of column's axial load capacity was applied at the top of each column because it is expected that the vertical load is not transmitted by the top beam to the masonry infill, as it is considered a non-structural element, unless the top slab or beam deforms due to creep or additional loading.

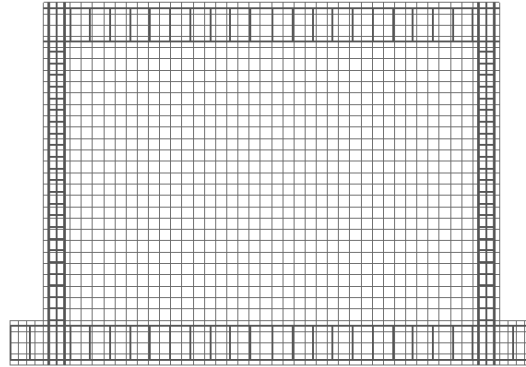


Figure 7.38 Finite element modelling of the rc frame with brick infill in DIANA software

The non-linear behavior of the concrete and masonry was described by a Total Strain Crack Model based on a fixed stress-strain law concept available in the commercial software Diana [132]. The model describes the tensile and compressive behavior of the material with one stress-strain relationship in the local coordinate system that is fixed upon crack initiation. Exponential and parabolic constitutive laws were used to describe the tensile and compressive behavior of concrete and masonry infill respectively, see Figure 7.39. The nonlinear behavior of the interface between infill and concrete frame was modelled by three dimensional coulomb friction interface model which enables the description of delamination (tension cut-off) and relative shear-slipping of two planes (Coulomb friction), see Figure 7.40. For three-dimensional analysis the compression cap is not implemented in DIANA.

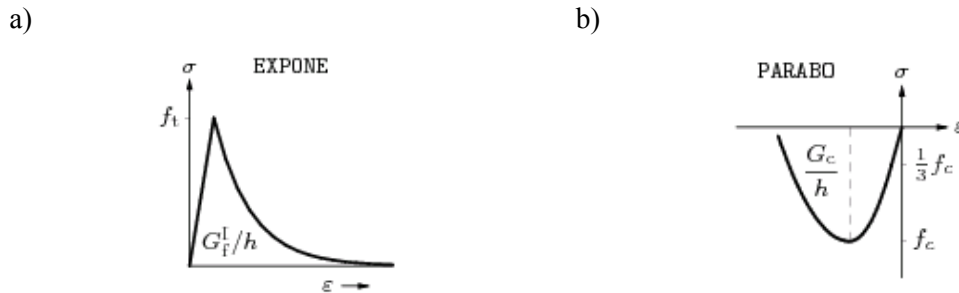


Figure 7.39 Stress-strain relationship adopted for Total Strain Crack model: a)exponential softening curve to describe tension and b)parabolic constitutive laws to describe compression

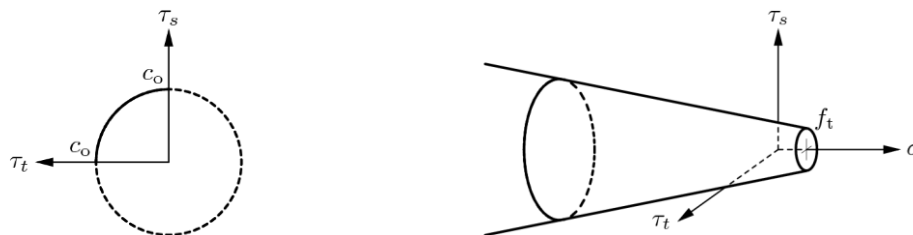


Figure 7.40 Three dimensional interface material law

### 7.3.2 Validation of the numerical model based on experimental results

The major drawback regarding the use of coulomb friction interface model is the lack of material properties as no data is available for the behavior of the interface between the masonry infill and the frame. Therefore, the calibration of the numerical model was made based on the mechanical properties of the masonry infill and rc frame, obtained in chapter 6, and by defining the mechanical properties of the interface elements to fit the force-displacement diagrams and cracking patterns obtained in numerical and experimental models.

The summary of the mechanical properties adopted for the interface elements is presented in Table 7-11, namely the material parameters describing the tensile behavior (tensile strength,  $f_t$ ) and the shear behavior (cohesion,  $c$ , friction angle,  $\phi$ , dilatancy angle,  $\psi$ ).

Table 7-11 Mechanical properties adopted for the interface elements

Elastic Properties		$K_n$ (N/mm <sup>3</sup> )		$K_s$ (N/mm <sup>3</sup> )
		9.3		5.7
Nonlinear Properties	Tension	$f_t$ (N/mm <sup>2</sup> )		
		0.05		
	Shear	$c$ (N/mm <sup>2</sup> )	$\tan\phi$	$\psi$
		0.3	0.5	0.0001

The numerical and experimental force-displacement diagrams obtained by the nonlinear numerical analysis and by the out-of-plane test are shown in Figure 7.41. It is seen that a very good agreement between numerical and experimental results was obtained. The numerical initial stiffness, lateral strength and ultimate deformation capacity are very close to the values obtained in the experimental test.

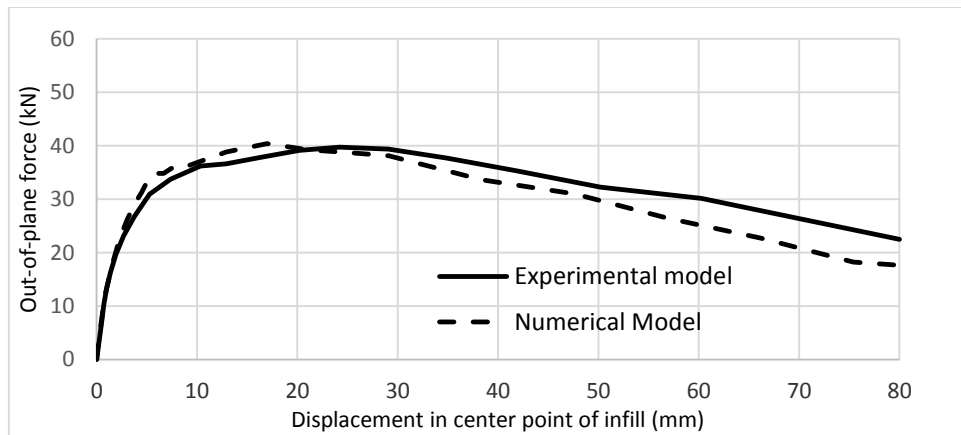


Figure 7.41 Force-displacement diagrams of the numerical and experimental model

The major difference is related to the displacement corresponding to the maximum out-of-plane resistance, which is first attained in the numerical model. Besides the strength degradation after peak load is slightly higher in the numerical model.

The cracking patterns obtained for different out-of-plane displacements in the numerical model are shown in Figure 7.42. It is observed that the cracking of the specimen was initiated through the development of horizontal cracks in the central region of the masonry infill, similar to what happened in the experimental test. By increasing the out-of-plane displacement, diagonal cracks

developed from the horizontal cracks that previously formed extending towards the upper corners of the masonry infill. Further loading of the specimen resulted in the development of diagonal cracking from the horizontal cracks towards the bottom corners of the masonry infill. It should be mentioned that the cracking pattern is fully in agreement with the experimental cracking patterns obtained for the reference specimen.

The cracking of the surrounding frame was initiated by the formation of some cracks in connection point of upper rc beam and rc columns. Additionally, some vertical cracks at the mid span of the upper rc beams developed. This cracking pattern in the upper beam also matches the cracking pattern observed in the experimental test.

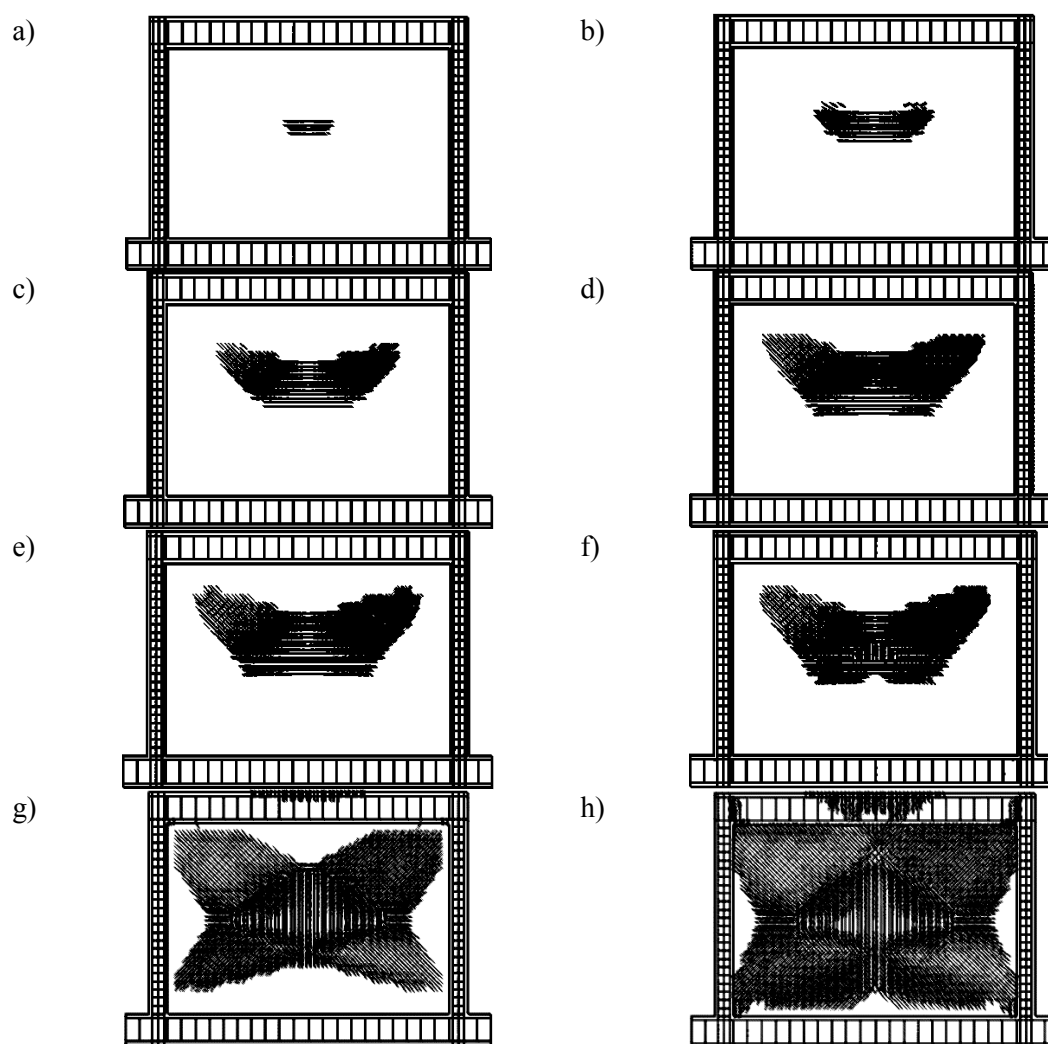


Figure 7.42 Propagation of cracks in the numerical model

## 7.4 Conclusions

In this work a numerical model of a one-bay and one-storey masonry-infilled reinforced concrete frame was modelled using the DIANA software and calibrated based on the results obtained from experimental in-plane cyclic tests. Subsequently, an extensive parametric numerical analysis was carried out to investigate the influence of different parameters on the in-plane behaviour of the infilled frames. It should be noted that the results presented here relate only to strong RC frames with weak masonry infills, from which the following conclusions can be drawn:

1. The presence of openings decreases the initial stiffness of the infilled frames. An increase of the opening area decreases the initial stiffness of the infilled frame, with the rate of this decrease being greater for a lower opening percentage and vice versa.
2. Increasing the opening area reduces the lateral strength of infilled frames, with the rate of this decrease being greater for smaller opening areas than for larger opening areas.
3. Increasing the opening area in the infill results in the maximum lateral resistance of the infilled frame being obtained at larger displacements.
4. Equations derived from parametric numerical simulation can satisfactorily predict the initial stiffness and lateral strength of the masonry-infilled reinforced concrete frames with central openings.
5. For infilled frames with typical openings (window and door openings with different locations in the walls), an empirical formula was developed taking into account the position of the openings. This formula can satisfactorily predict the initial stiffness of the infilled frames.
6. It was observed that an increase of the width of the diagonal strut increases the initial stiffness of the infilled frames linearly. It was concluded that infill panels with any type of opening can be replaced by an equivalent strut, whose width can be calculated according to the proposed formula, taking into account different types of openings and relative positioning within the masonry infill.

Additionally, a numerical model was built in the commercial software Diana for the analysis of the out-of-plane behaviour of rc frames with brick infills taking into account the experimental results of specimen SIF-O-1L-B. Based on the results, it is considered that very good agreement between numerical and experimental results was achieved, meaning that further parametric study can be developed based on the numerical model.





# **CHAPTER 8**

## **CONCLUSION**

## 8 Conclusion

The main objectives of this thesis were the experimental characterization of the in-plane and out-of-plane behavior of rc frames with brick infills (double leaf walls), which are characteristic of construction in Portugal in the last decades. Complementary, it was aimed at providing strengthening technique that can improve the seismic behavior of brick infills, such as textile reinforced mortar technique and application of steel ties connecting both leaves of the infill together. Finally, it was intended to provide a proposal for calculating the stiffness and strength of brick infills with a random distribution of openings subjected to in-plane loading.

To accomplish the thesis objectives, an extensive study was carried out to investigate the in-plane and out-of-plane response of the masonry infilled rc frames by conducting experimental tests and numerical analysis. The masonry infilled rc frames assumed in this research are considered as typical construction of South European countries in 1980s. The experimental program consisted of three different parts, namely: (1) in-plane static cyclic testing of infilled rc frames; (2) out-of-plane testing of infilled frames; (3) strengthening of infilled rc frames and their cyclic testing under the in-plane and out-of-plane loading. The numerical work was also composed of three steps, namely: (1) calibration of a finite element model based on experimental results available in literature; (2) parametric analysis and proposal of expressions for the calculation of the in-plane stiffness and strength of brick infills with a random distribution of openings; (3) calibration of a numerical model to describe the out-of-plane behavior of unstrengthened solid brick infills based on the experimental results obtained in this thesis.

In the first part of the experimental program, in-plane static cyclic testing of rc frames with brick infills (double leaf walls) was carried out on five half-scale specimens: one specimen of bare frame tested until failure; (2) one rc frame with brick infill tested until failure; (3) three rc frames with solid brick infills constructed with different mason and tested until three different lateral drifts, namely 0.3%, 0.5% and 1%. As mentioned before, reduced scale specimens were adopted to comply with some limitations at the laboratory of Civil Engineering department. The reduced scale specimens were designed according to the representative prototype of brick infilled frame. Based on the results obtained in the in-plane cyclic tests, it is concluded that: (1) double leaf infills presented very similar shear distortions along the cyclic in-plane testing, which reveals that the load is adequately transferred to the both leaves of the brick infill; (2) in spite of using low-strength masonry infills, their presence within the bare frame significantly increased the initial stiffness, lateral strength and energy dissipation capacity. Besides, it is important to stress that the presence of brick infills limited the amount of damage on rc frame for the present testing conditions; (3) depending on the type of workmanship, the increase in the initial stiffness was calculated as 5.2-14 times and the lateral strength was calculated as 1.3-1.9 times in comparison with the bare frame; (4) the stiffness of the rc frame with brick infills decreased significantly as a result of the cumulative damage. In the other words, the stiffness degradation was particularly evident at early stages of loading; (5) the workmanship affected the lateral strength and stiffness of the brick infilled frames, as the lateral strength and stiffness of the rc frames with brick infills tested until the lateral drift 05% and 1%, in which it is assumed that their lateral strength was achieved until imposed lateral drifts, are clearly higher than the lateral strength and stiffness obtained in the brick infill tested until collapse.

In the second part of the experimental program, six half-scale specimens were subjected to the out-of-plane loading: (1) two solid brick infills; (2) one specimen with a central opening; (3) three specimens with previous in-plane damage. The out-of-plane loading was applied by means of an airbag so that uniform loading on the infill could be assured. The out-of-plane tests were carried out in displacement control method. From the experimental results obtained in the distinct specimens it was concluded that: (1) in-plane damage has an important influence on the out-of-plane behavior of brick infills. All specimens with prior in-plane damage exhibited lower stiffness and strength when compared to the undamaged brick infills, but the reduction was higher for specimens with higher levels of in-plane damage. The crack pattern was mainly affected when the separation of the upper interface between the brick infill and rc frame occurred, which was valid particularly to higher levels of in-plane damage (in-plane lateral drift of 1%). The experimental results allowed also to derive simplified equations to predict the out-of-plane stiffness and resistance of specimens with prior in-plane damage; (2) the out-of-plane behavior was greatly affected by the workmanship used in the construction of the brick infills. One of the consequences of poor workmanship was the change of the boundary conditions of the infill, as the upper interface was poorly filled with mortar, affected the connection between the brick infill and the rc frame. The different boundary conditions resulted in the change of the cracking pattern and failure mechanism along with the out-of-plane stiffness, strength and energy dissipation capacity; (3) the presence of a central opening in the brick infill did not appear to change considerably the response of the brick infill under out-of-plane loading. However, significant reduction in the ultimate deformation capacity of the brick infill under out-of-plane loading was observed. The results obtained can be related to the low opening area (about 12%).

In the last part of the experimental program, different strengthening techniques were applied to investigate their performance on the improvement of the in-plane and out-of-plane behavior of brick infills. Two strengthening techniques were considered, namely: (1) textile reinforced mortar (TRM) applied in specimens tested under in-plane and out-of-plane behavior. Two textile meshes were used, namely commercial textile meshes of glass fibers and textile meshes that developed at the department of Civil Engineering of University of Minho. The latter mesh was also a glass fiber mesh so that it was directly comparable with the commercial one; (2) steel ties for the connection of the leaves of the double brick infills subjected to out-of-plane loading. From the experimental results, the main conclusions were drawn as: (1) the brick infills strengthened with commercial and designed textile meshes presented very similar in-plane response, resulting in very close values of initial stiffness, lateral strength and energy dissipation capacity. The textile reinforced mortar was applied to enhance the initial stiffness, lateral strength and energy dissipation capacity of the reference specimen. The unique problem observed during the in-plane testing was related to the early detachment of the strengthening layer from the rc frame that limited the effectiveness of this technique; (2) the level of performance of the textile reinforced mortar on the out-of-plane response of brick infills was not so high, namely at the level of the stiffness, strength and energy dissipation capacity. This was related to the early failure of the glass fiber shear connectors around rc frame that is believed to limit the effectiveness of this technique. After detachment of the added layer, the retrofitting layer could not perform completely its role on preventing falling of debris to reduce injuries during earthquakes. However, an important contribution of the added layer was that it controlled the damage of the brick infills. In effect, the reinforced mortar layer appeared to work as damage concentrator when the specimen was subjected to the in-plane or out-of-plane loading, as the major cracking developed in the rendering mortar, leaving the brick infill almost without damage. Under out-of-plane loading, the damage

of the infills was mainly concentrated at the boundaries in connection between rc frame and brick infill; (3) the connection of the leaves of the brick infills through steel ties under out-of-plane loading revealed the effectiveness of this technique, even if the increase in the out-of-plane resistance was moderate (close to 20%). However, it should be stressed that the connected brick infill presented higher dissipation of energy and higher deformation capacity when compared with the reference specimen. Based on these results, it was considered that the connection of the leaves with steel ties will improve definitely the out-of-plane response of the traditional brick infills and thus will reduce their seismic vulnerability.

Finally, in relation to the experimental characterization of masonry materials and masonry assemblages, it should be stressed that it was possible to obtain the mechanical properties of brick infills that will be used in the future for the detailed numerical analysis of the brick infills tested in the experimental campaign.

In the numerical analysis of rc frames with brick infills, two numerical models of one-bay and one-storey masonry-infilled reinforced concrete frame were built using the DIANA software: (1) one numerical model to analyse the in-plane behaviour; (2) one numerical model to analyse the out-of-plane behaviour. The numerical model to analyse the in-plane behaviour was calibrated based on experimental results available in literature. Subsequently, an extensive parametric study was carried out to investigate the influence of different parameters on the in-plane behaviour of the infilled frames, namely the material properties of brick infills, geometry and presence of random distribution of openings. It was concluded that the presence of openings in the infill reduces the initial stiffness and lateral strength of infilled frames. However, it should be mentioned that the clear reduction on the in-plane lateral resistance is only evident after the area of the openings is higher than 15% of the total area of the brick infills. Important output of this thesis and a contribution for the state of the art, are the empirical equations developed to predict the initial stiffness and lateral strength of infilled frames with any type of openings. In addition, the width of the equivalent diagonal strut that replaces the brick infills when a macro-modelling approach is followed, was also updated taking into consideration the random distribution of openings, which is considered to be an important contribution for the state of the art. It was also concluded that the proposed approach to calculate the width of the equivalent strut is rather accurate for multi-bay multi-storey infilled rc frames. Additionally, a numerical model was built in the commercial software of Diana for the analysis of the out-of-plane behaviour of rc frames with brick infills. Based on the results achieved, it is considered that very good agreement between numerical and experimental results was achieved, meaning that further parametric study can be developed.

## **8.1 Future works**

Based on the work carried out in this thesis, it is considered that in spite of important outcomes achieved in this thesis, additional research is needed to advance the state of the art. For this, some recommendation are provided for future work:

1. Considering the important role of the in-plane damage on the out-of-plane response of the brick infills, it is important to consider other in-plane damage levels to build a more accurate interaction curve relating the in-plane damage with the out-of-plane strength and stiffness.

2. Analyse the influence of the out-of-plane damage on the in-plane resistance of the brick infills. The methodology should be similar to the one followed for the analysis of the influence of the in-plane damage on the out-of-plane response. Notice that when earthquakes occur, simultaneous in-plane and out-of-plane loadings are induced. It is considered that there is no information available in the literature, which justifies the relevance of this work.
3. Consider different percentages of opening areas and evaluate in a more accurate way the influence of the openings on the out-of-plane response of brick infills.
4. Analyse the monolithic behaviour of specimens with connected leaves in the traditional double leaf walls by using different configurations of steel ties. In spite of loading transfer was ensured in the studied configuration it would be important to apply strain gauges in the steel ties to analyse the stress levels during the cyclic out-of-plane testing.
5. It is considered that it will be important to derive expressions for the prediction of the out-of-plane resistance of brick infills, taking into account different parameters that influence the out-of-plane resistance, namely the previous in-plane damage level.
6. Observing the deficient behaviour found in the experimental results of the in-plane cyclic tests and particularly out-of-plane tests, it is recommended to use more adequate connectors to link the reinforced rendering mortar to the rc frame.
7. Use the textile reinforced mortar as a retrofitting technique after inducing some level of damage under in-plane or out-of-plane loading, aiming at analysing the possibility of using this technique as a retrofitting technique after occurrence of low to moderate earthquakes.
8. In terms of numerical analysis, it will be important to provide further advances in the out-of-plane numerical modelling based on finite element analysis, by analysing the influence of the different parameters through a detailed parametric analysis.

## References

- [1] Kyriakides MA. Seismic Retrofit of Unreinforced Masonry Infills in Non-ductile Reinforced Concrete Frames Using Engineered Cementitious Composites Stanford University; 2011.
- [2] Mehrabi AB, Shing PB. Performance of Masonry-Infilled R/C Frames under In-Plane Lateral Loads: Analytical Modelling. Proceedings from the NCEER Workshop on Seismic Response of Masonry. San Francisco, California, 1994. p. 45-50.
- [3] Pereira MFP. Avaliação do desempenho das envolventes dos edifícios face à acção dos sismos: Universidade do Minho; 2013.
- [4] Asteris PG, Giannopoulos IP, Chrysostomou CZ. Modeling of Infilled Frames With Openings. The Open Construction and Building Technology Journal. 2012;6, (Suppl 1-M6):81-91.
- [5] Chrysostomou CZ, Asteris PG. On the in-plane properties and capacities of infilled frames. Engineering Structures. 2012;41:385-402.
- [6] Crisafulli F. Seismic Behavior of Reinforced Concrete Structures with Masonry Infills. New Zealand: University of Canterbury; 1997.
- [7] Kakaletsis DJ, Karayannis CG. Influence of Masonry Strength and Openings on Infilled R/C Frames Under Cycling Loading. Journal of Earthquake Engineering. 2008;12:197-221.
- [8] Saari WK, Hajjar JF, Schultz AE, Shield CK. Behavior of shear studs in steel frames with reinforced concrete infill walls. Journal of Constructional Steel Research. 2004;60:1453-80.
- [9] Mallick DV, Garg RP. Effect of openings on the lateral stiffness of infilled frames. Proceedings-Institution of Civil Engineers. UK, 1971. p. 193-209.
- [10] Mosalam K, White R, Gergely P. Static Response of Infilled Frames Using Quasi-Static Experimentation. Journal of Structural Engineering. 1997;123:1462-4169.
- [11] Mosalam KM, Gergely P, White RN, Ayala AG. Effect of Geometrical Configuration on the Seismic Response of Infilled Frames. Proceeding of the Eleventh World Conference on Earthquake Engineering. 1996.
- [12] Tasnimi AA, Mohebkah A. Investigation on the behavior of brick-infilled steel frames with openings, experimental and analytical approaches. Engineering Structures. 2011;33:968-80.
- [13] Dawe JL, Seah CK. Behaviour of masonry infilled steel frames. Canadian Journal of Civil Engineering. 1989;16:865-76.
- [14] Pook LL, Dawe JL. Effect of Interface Conditions Between a Masonry Shear Panel and Surrounding Steel Frame. Proceedings of the Fourth Canadian Masonry Symposium. 1986;2:910-21.
- [15] Tong X, Hajjar JF, Schultz AE, Shield CK. Cyclic behavior of steel frame structures with composite reinforced concrete infill walls and partially-restrained connections. Journal of Constructional Steel Research. 2005;61:531-52.
- [16] Miranda E, Bertero VV. The Mexico Earthquake of September 19, 1985-Performance of Low-Rise Buildings in Mexico City. Earthquake Spectra. 1989;5:121-43.
- [17] Elnashai AS. Analysis of the damage potential of the Kocaeli (Turkey) earthquake of 17 August 1999. Engineering Structures. 2000;22:746-54.
- [18] Jain SK, Lettis WR, Murty CVR, Bardet JP. Bhuj, India Earthquake of January 26, 2001 Reconnaissance Report. Earthquake Spectra. 2002;Supplement A to Vol 18.

- [19] Braga F, Manfredi V, Masi A, Salvatori A, Vona M. Performance of non-structural elements in RC buildings during the L'Aquila, 2009 earthquake. *Bull Earthquake Eng.* 2011;9:307-24.
- [20] ElGawady M, Lestuzzi P, Badoux M. A Review of Conventional Seismic Retrofitting Techniques for URM. 13th International Brick and Block Masonry Conference. Amsterdam,2004.
- [21] Oliveto G, Marletta M. Seismic Retrofitting of Reinforced Concrete Buildings Using Traditional and Innovative Techniques. *ISET Journal of Earthquake Technology.* June-September 2005;42:21-46.
- [22] Altin S, Anil Ö, Kara ME, Kaya M. An experimental study on strengthening of masonry infilled RC frames using diagonal CFRP strips. *Composites Part B: Engineering.* 2008;39:680-93.
- [23] Binici B, Ozcebe G, Ozcelik R. Analysis and design of FRP composites for seismic retrofit of infill walls in reinforced concrete frames. *Composites Part B: Engineering.* 2007;38:575-83.
- [24] ElGawady MA, Lestuzzi P, Badoux M. Aseismic retrofitting of unreinforced masonry walls using FRP. *Composites Part B: Engineering.* 2005;37:148-62.
- [25] Erdem I, Akyuz U, Ersoy U, Ozcebe G. An experimental study on two different strengthening techniques for RC frames. *Engineering Structures.* 2006;28:1843-51.
- [26] Ozkaynak H, Yuksel E, Buyukozturk O, Yalcin C, Dindar AA. Quasi-static and pseudo-dynamic testing of infilled RC frames retrofitted with CFRP material. *Composites Part B: Engineering.* 2011;42:238-63.
- [27] Valluzzi MR, Tinazzi D, Modena C. Shear behavior of masonry panels strengthened by FRP laminates. *Construction and Building Materials.* 2002;16:409-16.
- [28] Yuksel E, Ozkaynak H, Buyukozturk O, Yalcin C, Dindar AA, Surmeli M et al. Performance of alternative CFRP retrofitting schemes used in infilled RC frames. *Construction and Building Materials.* 2010;24:596-609.
- [29] Chen W-W, Yeh Y-K, Hwang S-J, Lu C-H, Chen C-C. Out-of-plane seismic behavior and CFRP retrofitting of RC frames infilled with brick walls. *Engineering Structures.* 2012;34:213-24.
- [30] Tu Y-H, Chuang T-H, Liu P-M, Yang Y-S. Out-of-plane shaking table tests on unreinforced masonry panels in RC frames. *Engineering Structures.* 2010;32:3925-35.
- [31] Willis CR, Seracino R, Griffith MC. Out-of-plane strength of brick masonry retrofitted with horizontal NSM CFRP strips. *Engineering Structures.* 2010;32:547-55.
- [32] Papanicolaou C, Triantafillou T, Papathanasiou M, Karlos K. Textile reinforced mortar (TRM) versus FRP as strengthening material of URM walls: out-of-plane cyclic loading. *Mater Struct.* 2008;41:143-57.
- [33] da Porto F, Guidi G, Verlato N, Modena C. Effectiveness of plasters and textile reinforced mortars for strengthening clay masonry infill walls subjected to combined in-plane/out-of-plane actions / Wirksamkeit von Putz und textilbewehrtem Mörtel bei der Verstärkung von Ausfachungswänden aus Ziegelmauerwerk, die kombinierter Scheiben- und Plattenbeanspruchung ausgesetzt sind. *Mauerwerk.* 2015;19:334-54.
- [34] Lourenço PB, Vasconcelos G, Leite J, Pereira P. Lessons learned from the testing of RC frames with masonry infills and proposals for new solutions / Untersuchungen an mit Mauerwerk ausgefachten Stahlbetonrahmen und neue Lösungsvorschläge. *Mauerwerk.* 2016;20:99-123.
- [35] Martins A, Vasconcelos G, Figueiro R, Cunha F. Experimental assessment of an innovative strengthening material for brick masonry infills. *Composites Part B: Engineering.* 2015;80:328-42.



- [36] Mora J. Innovative retrofitting materials for brick masonry infill walls University of Minho; 2012.
- [37] Kusumastuti D. Report on the West Sumatra Earthquake of September 30, 2009. MCEER Bulletin2010.
- [38] Guevara LT, García LE. International network for the design of earthquake resilient cities (INDEREC).
- [39] Bertero V, Brokken S. Infills in seismic resistant building. *Journal of Structural Engineering (ASCE)*. 1983;109:1337–61.
- [40] Buonopane S, White R. Pseudodynamic Testing of Masonry Infilled Reinforced Concrete Frame. *Journal of Structural Engineering*. 1999;125:578-89.
- [41] Mehrabi A, Benson Shing P, Schuller M, Noland J. Experimental Evaluation of Masonry-Infilled RC Frames. *Journal of Structural Engineering*. 1996;122:228-37.
- [42] Pujol S, Fick D. The test of a full-scale three-story RC structure with masonry infill walls. *Engineering Structures*. 2010;32:3112-21.
- [43] Altin S, Anil Ö, Kara ME. Strengthening of RC nonductile frames with RC infills: An experimental study. *Cement and Concrete Composites*. 2008;30:612-21.
- [44] Flanagan R, Bennett R. In-Plane Behavior of Structural Clay Tile Infilled Frames. *Journal of Structural Engineering*. 1999;125:590-9.
- [45] Klingner RE, Bertero V. Infilled frames in earthquake-resistant construction. Earthquake Engineering Research Center: University of California, Berkeley, CA, USA. ; 1976.
- [46] Mallick DV, Severn RT. The Behaviour of Infilled Frames under Static Loading. *Proceedings of the Institution of Civil Engineering*,. 1967;38:639-56.
- [47] Hashemi A, Mosalam KM. Shake-table experiment on reinforced concrete structure containing masonry infill wall. *Earthquake Engineering & Structural Dynamics*. 2006;35:1827-52.
- [48] Gergely P, White RN, Mosalam KM. Evaluation and Modelling of Infilled Frames. *Proceeding from NCEER Workshop on Seismic Response of Masonry, San Francisco, California*. February 1994:51-6.
- [49] Liauw TC, Kwan KH. Static and cyclic behaviours of multistorey infilled frames with different interface conditions. *Journal of Sound and Vibration*. 1985;99:275-83.
- [50] Mallick DV, Severn RT. Dynamic Characteristics of Infilled Frames. *Proceedings of the Institution of Civil Engineers*. 1968;39:261-88.
- [51] Kakaletsis DJ. Masonry infills with window openings and influence on reinforced concrete frame constructions. *Seventh International Conference on Earthquake Resistant Engineering Structures*. Cyprus, 2009.
- [52] Surendran S, Kaushik HB. Masonry infill RC frames with openings: review of in-plane lateral load behaviour and modeling approaches. *The Open Construction and Building Technology Journal*. 2012;6:126-54.
- [53] Fiorato AE, Sozen MA, Gamble WL. An investigation of the interaction of reinforced concrete frames with masonry filler walls. *Department of Civil Engineering, University of Illinois, Urbana-Champaign IL, USA*1970.
- [54] Asteris P. Lateral Stiffness of Brick Masonry Infilled Plane Frames. *Journal of Structural Engineering*. 2003;129:1071-9.
- [55] Giannakas A, Patronis D, Fardis M. The influence of the position and the size of openings to the elastic rigidity of infill walls. *8th Hellenic Concrete Conf. Xanthi, Kavala, Greece*1987. p. 49-56.
- [56] Holmes M. Steel Frames with Brickwork and Concrete Infilling. *Proceeding of the Institution of Civil Engineers*. 1961;19( 6501):473-5.

- [57] Holmes M. Combined Loading on Infilled Frames. *Proceeding of the Institution of Civil Engineers*. 1963;25:31-8.
- [58] Stafford SB. Lateral Stiffness of Infilled Frames. *Proceeding of the American Society of Civil Engineering, Journal of Structural Division*. 1962;88(ST6):183-99.
- [59] Stafford SB. Behavior of Square Infilled Frames. *Proceeding of the American Society of Civil Engineering, Journal of Structural Division*. 1966;92( ST1):381-403.
- [60] Stafford SB, Carter C. A Method of Analysis for Infilled Frames. *Proceeding of the Institution of Civil Engineers*. 1969;44:31-48.
- [61] Mainstone RJ. On the stiffness and strength of infilled frames. *Proceeding of Institution of Civil Engineers (ICE)*. 1971;Supplement (IV):57-90.
- [62] Bazan E, Meli R. Seismic Analysis of Structures with Masonry Walls. *Proceeding of the Seventh World Conference on Earthquake Engineering*. Istanbul, Turkey, 1980. p. 633-40.
- [63] Bashandy T, Rubiano N, Klingner R. Evaluation and Analytical Verification of Infilled Frames Test Data. Champaign, IL: U.S. Army Construction Engineering Research Laboratories 1995.
- [64] Mainstone RJ, Weeks GA. The influence of bounding frame on the racking stiffness and strength of brick walls *Second International Brick Masonry Conference*. Stoke-on-Trent, England 1970.
- [65] Stafford S, Coull A. *Tall building structures: Analysis and design*. New York: Wiley; 1991.
- [66] Flanagan RD, Bennett RM. In-plane analysis of masonry infill materials. *Practice Periodical on Structural Design and Construction*. 2001;6(4):176-82.
- [67] Zarnic R, Gostic S. Masonry infilled frames as an effective structural sub-assembly. *Seismic Design Methodologies for the Next Generation of Codes*, Fajfar P, Krawinkler H (eds). Balkema, Rotterdam, 1997. p. 335–46.
- [68] Lourenço PB, Alvarenga RC, Silva RM. Validation of a simplified model for the design of masonry infilled frames. *Masonry International, British Masonry Society*. 2006;19(1):15-26.
- [69] Amato G, Fossetti M, Cavaleri L, Papia M. An Updated Model of Equivalent Diagonal Strut for Infill Panels Eurocode 8 Perspectives from the Italian Standpoint Workshop. *Doppiavoce, Napoli, Italy*, 2009. p. 119-28.
- [70] Bertoldi SH, Decanini LD, Gavarini C. Telai tamponati soggetti ad azioni sismiche, un modello semplificato: confronto sperimentale e numeric. *Atti del 6 Convegno Nazionale ANIDIS*, 1993. p. 815-24.
- [71] Cavaleri L, Papia M. A new dynamic identification technique: application to the evaluation of the equivalent strut for infilled frames. *Engineering Structures*. 2003;25:889-901.
- [72] Dawe JL, Seah CK. Analysis of concrete masonry infilled steel frames subjected to in-plane loads. *Proceeding of the 5th Canadian Masonry Symposium*. Vancouver 1989. p. 329–40.
- [73] Decanini LD, Fantin GE. Modelos simplificados de la mamposteria incluida en porticos. Caracteristicas de rigidez y resistencia lateral en estado limite. *Jornadas Argentinas de Ingenieria Estructural*. Buenos Aires, Argentina, 1986. p. 817-36.
- [74] Durrani AJ, Luo YH. Seismic retrofit of flat-slab buildings with masonry infills. *NCEER workshop on seismic response in Masonry Infills* 1994.
- [75] Hendry AW. *Structural masonry*. London: MacMillan Education Ltd. ; 1990.

- [76] Kadir MRA. The structural behaviour of masonry infill panels in framed Structures: University of Edinburgh; 1974.
- [77] Mainstone RJ. Summary of paper 7360. On the stiffness and strength of infilled frames. ICE Proceedings 1971.
- [78] Smith BS. Behaviour of square infilled frames. Proceedings of the American Society of Civil Engineers, Journal of Structural Division. 1966;92:381-403.
- [79] Smith BS, Carter C. A method of analysis for infilled frames. ICE Proceedings 1969. p. 31-48.
- [80] Te-Chang L, Kwok-Hung K. Nonlinear behaviour of non-integral infilled frames. Computers & Structures. 1984;18:551-60.
- [81] Flanagan R, Tenbus M, Bennett R. Numerical modelling of clay tile infills. Proceedings from NCEER workshop on seismic response of Masonry. San Francisco, California, February, 1994. p. 63-8.
- [82] Zarnic R. Modelling of response of masonry infilled frames. Proceedings of tenth European conference on earthquake engineering. Vienna, Austria 1994. p. 1481-6.
- [83] Chrysostomou CZ. Effects of Degrading Infill Walls on the Nonlinear Seismic Response of Two-Dimensional Steel Frames: Cornell University; 1991.
- [84] König G. The state of the art in earthquake engineering research. Experimental and numerical methods in earthquake engineering. 1991;2:1-22.
- [85] Symakezis CA, Vratsanou VY. Influence of infill walls on RC frames response. Proceedings of eighth European conference on earthquake engineering. Lisbon, Portugal, 1986. p. 6.5/47-53.
- [86] Thiruvengadam V. On the natural frequencies of infilled frames. Earthquake Engineering & Structural Dynamics. 1985;13:401-19.
- [87] Leuchars JM, Scrivener JC. Masonry Infill Panels subjected to cyclic in-plane loading. Bulletin of the New Zealand national society for earthquake engineering 1976;9:122-31.
- [88] Doudoumis IN, Mitsopoulou EN. Nonlinear Analysis of Multistorey Infilled Frames for Unilateral Contact Conditions. Proceedings of the Eighth European Conference on Earthquake Engineering. Lisbon, Portugal 1986. p. 63-70.
- [89] Andreus U, Cerone MD, Asdia P, Iannozzi F. A Finite Element Model for the Analysis of Masonry Structures under Cyclic Actions. Proceedings of the Seventh International Brick and Masonry Conference. Melbourne, Australia 1985. p. 479-88.
- [90] Rodrigues H, Varum H, Costa A. A non-linear masonry infill macro-model to represent the global behaviour of buildings under cyclic loading. Int J Mech Mater Des. 2008;4:123-35.
- [91] Puglisi M, Uzcategui M, Flórez-López J. Modeling of masonry of infilled frames, Part I: The plastic concentrator. Engineering Structures. 2009;31:113-8.
- [92] Puglisi M, Uzcategui M, Flórez-López J. Modeling of masonry of infilled frames, Part II: Cracking and damage. Engineering Structures. 2009;31:119-24.
- [93] Hashemi A, Mosalam K. Seismic Evaluation of Reinforced Concrete Buildings Including Effects of Masonry Infill Walls. College of Engineering, University of California, Berkeley: Pacific Earthquake Engineering Research Center; 2007.
- [94] Lourenço PB. Computational strategies for masonry structures [Diss, Technische Universiteit Delft, 1996]. Delft: Delft University Press; 1996.
- [95] Ali S, Page A. Finite Element Model for Masonry Subjected to Concentrated Loads. Journal of Structural Engineering. 1988;114:1761-84.
- [96] Lotfi H, Shing P. Interface Model Applied to Fracture of Masonry Structures. Journal of Structural Engineering. 1994;120:63-80.

- [97] Mehrabi AB, Shing PB, Schuller MP, Noland JL. Performance of masonry-infilled R/C frames under in-plane lateral loads. University of Colorado, Boulder CO, USA1994.
- [98] Page AW. Modelling the In-Plane Behaviour of Solid Masonry under Static Loading. Proceedings of the International Workshop on Unreinforced Hollow Clay Tile1992. p. 2-5.
- [99] King G, Pandey P. The Analysis of Infilled Frames Using Finite Elements. Proceedings of the Institution of Civil Engineers 1978. p. 749-60.
- [100] Mosalam KM, Gergely P, White RN, Zawilinski D. The Behaviour of Frames with Concrete Block Infill Walls. Proceedings of the First Egyptian Conference on Earthquake Engineering 1993. p. 283-92.
- [101] Dawe JL, Yong TC. An Investigation of Factors Influencing the Behavior of Masonry Infill in Steel Frames Subjected to In-Plane Shear. Proceedings of the Seventh International Brick Masonry Conference. Melbourne, Australia, 1985. p. 803-14.
- [102] Franklin HA. Nonlinear Analysis of Reinforced Concrete Frames and Panels. Department of Civil Engineering, University of California, Berkeley; 1970.
- [103] Dafnis A, Kolsch H, Reimerdes H. Arching in Masonry Walls Subjected to Earthquake Motions. Journal of Structural Engineering. 2002;128:153-9.
- [104] Dawe JL, Seah CK. Out-of-plane resistance of concrete masonry infilled panels. Canadian Journal of Civil Engineering. 1989;16:854-64.
- [105] Drysdale R, Essawy A. Out-of-Plane Bending of Concrete Block Walls. Journal of Structural Engineering. 1988;114:121-33.
- [106] Flanagan R, Bennett R. Bidirectional Behavior of Structural Clay Tile Infilled Frames. Journal of Structural Engineering. 1999;125:236-44.
- [107] FEMA356. Prestandard and Commentary for the Seismic Rehabilitation of Buildings. November 2000.
- [108] Dazio A. Effect of boundary conditions on the out-of-plane behavior of unreinforced masonry walls. 14th World Conference on Earthquake Engineering. Beijing, China2008.
- [109] Angel R, Abrams D, Shapiro D, Uzarski J, Webster M. Behaviour of reinforced concrete frames with masonry infills. Urbana-Champaign, IL, USA, 1994.
- [110] Henderson RC, Fricke KE, Jones WD, E. BJ, Bennett RM. Summary of a Large- and Small-Scale Unreinforced Masonry Infill Test Program. Journal of Structural Engineering. 2003;129:1667-75.
- [111] Calvi GM, Bolognini D. Seismic response of reinforced concrete frames infilled with weakly reinforced masonry panels. Journal of Earthquake Engineering. 2001;5:153-85.
- [112] Kadysiewski S, Mosalam KM. Modeling of Unreinforced Masonry Infill Walls Considering In-Plane and Out-of-Plane Interaction. College of Engineering, University of California, Berkeley: Pacific Earthquake Engineering Research Center; 2009.
- [113] Mohyeddin A, Goldsworthy HM, Gad EF. FE modelling of RC frames with masonry infill panels under in-plane and out-of-plane loading. Engineering Structures. 2013;51:73-87.
- [114] Shrive NG. The use of fibre reinforced polymers to improve seismic resistance of masonry. Construction and Building Materials. 2006;20:269-77.
- [115] Sevil T, Baran M, Bilir T, Canbay E. Use of steel fiber reinforced mortar for seismic strengthening. Construction and Building Materials. 2011;25:892-9.
- [116] Bernat-Maso E, Escrig C, Aranha CA, Gil L. Experimental assessment of Textile Reinforced Sprayed Mortar strengthening system for brickwork wallettes. Construction and Building Materials. 2014;50:226-36.

- [117] Elsanadedy HM, Almusallam TH, Alsayed SH, Al-Salloum YA. Flexural strengthening of RC beams using textile reinforced mortar – Experimental and numerical study. *Composite Structures*. 2013;97:40-55.
- [118] Papanicolaou C, Triantafillou T, Lekka M. Externally bonded grids as strengthening and seismic retrofitting materials of masonry panels. *Construction and Building Materials*. 2011;25:504-14.
- [119] FEMA461. Interim Testing Protocols for Determining the Seismic Performance Characteristics of Structural and Nonstructural Components. 2007.
- [120] Furtado A, Costa C, Rodrigues H, Arêde A. Characterization of structural characteristics of Portuguese buildings with masonry infill walls stock. 9th International Masonry Conference. University of Minho, Guimarães, Portugal 2014.
- [121] 318-08 A. Building Code Requirements for Structural Concrete (ACI 318-08) and Commentary. American Concrete Institute; 2008.
- [122] Martins A. Solution of seismic strengthening for masonry infills: University of Minho; 2013 (in Portuguese).
- [123] EN1015-3. Methods of test for mortar for masonry- Part3: Determination of consistence of fresh mortar (by flow table).
- [124] EN1015-11:1999. Methods of Test for Mortar for Masonry. Part11: Determination of Flexural and Compressive Strength of Hardened Mortar.
- [125] EN772-16:2000. Methods of test for masonry units- Part16: Determination of dimensions.
- [126] EN772-1:2000. Methods of Tests for Masonry Units. Part1: Determination of Compressive Strength.
- [127] EN1052-1:1999. Methods of test for masonry- Part1: Determination of compressive strength.
- [128] E519-02 A. Standard Test Method for Diagonal Tension (Shear) in Masonry Assemblages.
- [129] EN1052-2:1999. Methods of test for masonry- Part2: Determination of flexural strength.
- [130] EN1052-3:2003. Methods of test for masonry- Part3: Determination of initial shear strength.
- [131] Eurocode8. Design of Structures for Earthquake Resistance. December 2003.
- [132] CEST. DIANA User's Manual, Release 9.3
- [133] Lourenço PB, Rots JG. Multisurface Interface Model for Analysis of Masonry Structures. *Journal of Engineering Mechanics*. 1997;123:660-8.
- [134] Lourenço PB. Analysis of Masonry Structures with Interface elements; Theory and Applications. In: TNO Building and Construction Research CM, editor. 1994.
- [135] Vasconcelos G, Lourenço P. In-Plane Experimental Behavior of Stone Masonry Walls under Cyclic Loading. *Journal of Structural Engineering*. 2009;135:1269-77.
- [136] Dubey SKD, Kute SY. Experimental investigation on the ultimate strength of partially infilled and steel-braced reinforced concrete frames. *International Journal of Advanced Structural Engineering*. 2013;5.

## Appendix I

### Compressive and Flexural Tests of Mortar Samples

Table I- 1 Test results of mortar used in the specimen SIF-I-2L(NC)-A

		S1		S2		S3		S.D	Average	C. o. V (%)
<b>SIF-I-2L(NC)-A</b> <b>external leaf</b>	Slump	180								
	$W$ (gr)	510.0		498.5		511.1				
	$f_t$ (MPa)	1.55		1.34		1.55		0.12	1.48	8.21
	$f_c$ (MPa)	4.33	3.56	3.34	3.71	4.13	3.97	0.37	3.84	9.63
		S1		S2		S3		S.D	Average	C. o. V (%)
<b>SIF-I-2L(NC)-A</b> <b>internal leaf</b>	Slump	181								
	$W$ (gr)	488.3		487.3		484.2				
	$f_t$ (MPa)	1.57		1.39		1.44		0.10	1.46	6.50
	$f_c$ (MPa)	3.80	3.44	3.08	3.25	3.45	3.44	0.24	3.41	7.02

Table I- 2 Test results of mortar used in the specimen SIF-O-1L-A

		S1		S2		S3		S.D	Average	C. o. V (%)
<b>SIF-O-1L-A</b>	Slump	177								
	$W$ (gr)	497.8		503.1		504.9				
	$f_t$ (MPa)	1.78		1.72		1.77		0.03	1.75	1.87
	$f_c$ (MPa)	4.70	4.39	4.00	3.83	4.30	4.28	0.30	4.25	7.14

Table I- 3 Test results of mortar used in the specimen PIF-O-1L-B

		S1		S2		S3		S.D	Average	C. o. V (%)
<b>PIF-O-1L-B</b> <b>external leaf</b>	Slump	172								
	$W$ (gr)	486.2		493.3		489.4				
	$f_t$ (MPa)	1.46		1.51		1.41		0.05	1.46	3.45
	$f_c$ (MPa)	3.75	3.56	3.87	3.77	3.84	3.65	0.12	3.74	3.18
		S1		S2		S3		S.D	Average	C. o. V (%)
<b>Lintel</b>	Slump	181								
	$W$ (gr)	573.2		571.5		566.6				
	$f_t$ (MPa)	6.18		5.74		5.65		0.29	5.85	4.88
	$f_c$ (MPa)	28.5	29.9	28.9	27.8	27.2	25.9	1.41	28.04	5.03

Table I- 4 Test results of mortar used in the specimen SIF-IO(0.3%)-2L(NC)-B

SIF-IO(0.3%)-2L(NC)-B external leaf		S1		S2		S3		S.D	Average	C. o. V (%)
	Slump	172								
	$W$ (gr)	510.0		498.5		511.1				
	$f_t$ (MPa)	1.45		1.59		1.37		0.11	1.47	7.75
	$f_c$ (MPa)	3.97	3.85	3.48	3.88	3.98	3.59	0.21	3.79	5.44
SIF-IO(0.3%)-2L(NC)-B internal leaf		S1		S2		S3		S.D	Average	C. o. V (%)
	Slump	173								
	$W$ (gr)	488.3		487.3		484.2				
	$f_t$ (MPa)	2.02				1.92		0.07	1.97	3.62
	$f_c$ (MPa)	4.73	4.72	4.46	4.31	4.63	4.45	0.17	4.55	3.64

Table I- 5 Test results of mortar used in the specimen SIF-IO(0.5%)-2L(NC)-B

SIF-IO(0.5%)-2L(NC)-B external leaf		S1		S2		S3		S.D	Average	C. o. V (%)
	Slump	171								
	$W$ (gr)	486.2		493.3		489.4				
	$f_t$ (MPa)	2.34		2.36		2.25		0.06	2.32	2.60
	$f_c$ (MPa)	5.54	5.43	5.16	5.35	5.20	5.37	0.14	5.34	2.66
SIF-IO(0.5%)-2L(NC)-B internal leaf		S1		S2		S3		S.D	Average	C. o. V (%)
	Slump	162								
	$W$ (gr)	573.2		571.5		566.6				
	$f_t$ (MPa)	2.35		2.02		2.21		0.17	2.19	7.58
	$f_c$ (MPa)	5.47	5.70	5.44	5.05	5.69	5.41	0.24	5.46	4.35

Table I- 6 Test results of mortar used in the specimen SIF-O-1L-B

SIF-O-1L-B		S1		S2		S3		S.D	Average	C. o. V (%)
	Slump	179								
	$W$ (gr)	510.0		498.5		511.1				
	$f_t$ (MPa)			1.70		1.58		0.08	1.64	4.85
	$f_c$ (MPa)	4.08	3.97	3.47	3.64	3.69	3.87	0.23	3.79	6.02

Table I- 7 Test results of mortar used in the specimen SIF-O-2L(C)-B

		S1		S2		S3		S.D	Average	C. o. V (%)
<b>SIF-O-2L(C)-B</b>  <b>external leaf</b>	Slump	171								
	$W$ (gr)	485.1		476.2		478.6				
	$f_t$ (MPa)	1.52		1.36		1.41		0.08	1.43	5.72
	$f_c$ (MPa)	4.32	4.53	4.21	4.32	4.18	4.26	0.12	4.30	2.90
		S1		S2		S3		S.D	Average	C. o. V (%)
<b>SIF-O-2L(C)-B</b>  <b>internal leaf</b>	Slump	165								
	$W$ (gr)	485.1		476.2		478.6				
	$f_t$ (MPa)	1.31		1.18		1.25		0.07	1.25	5.22
	$f_c$ (MPa)	3.85	3.62	3.44	3.56	3.77	3.92	0.18	3.69	4.98

Table I- 8 Test results of mortar used in the specimen SIF-IO(1%)-2L(NC)-B

		S1		S2		S3		S.D	Average	C. o. V (%)
<b>SIF-IO(1%)-2L(NC)-B</b>  <b>internal leaf</b>	Slump	181								
	$W$ (gr)	467.7		482.9		484.8				
	$f_t$ (MPa)	1.23		1.18		1.36		0.10	1.26	7.60
	$f_c$ (MPa)	2.49	2.74	2.83	2.85	2.80	2.83	0.14	2.76	4.99
		S1		S2		S3		S.D	Average	C. o. V (%)
<b>SIF-IO(1%)-2L(NC)-B</b>  <b>external leaf</b>	Slump	161								
	$W$ (gr)	500.2		503.6		495.8				
	$f_t$ (MPa)	1.92		2.41		2.29		0.25	2.20	11.55
	$f_c$ (MPa)	5.06	5.52	5.85	5.82	5.22	5.46	0.32	5.49	5.75

Table I- 9 Test results of mortar used in the specimen SIF(DTRM)-O-1L-B

		S1		S2		S3		S.D	Average	C. o. V (%)
<b>SIF(DTRM)-O-1L-B</b>	Slump	167								
	$W$ (gr)	456.2		453.4		454.6				
	$f_t$ (MPa)	1.26		1.13		1.32		0.10	1.24	7.85
	$f_c$ (MPa)	3.54	3.23	3.01	3.14	3.46	3.24	0.20	3.27	6.05

Table I- 10 Test results of mortar used in the specimen SIF(DTRM)-I-2L(NC)-B



		S1		S2		S3		S.D	Average	C. o. V (%)
<b>SIF(DTRM) -I-2L(NC)-B</b>	Slump	170								
	$W$ (gr)	463.6		465.2		455.8				
	<b>external leaf</b> $f_t$ (MPa)	1.32		1.29		1.35		0.03	1.32	1.96
	$f_c$ (MPa)	3.01	2.74	3.02	3.36	3.13	3.00	0.20	3.05	6.66
		S1		S2		S3		S.D	Average	C. o. V (%)
<b>SIF(DTRM) -I-2L(NC)-B</b>	Slump	171								
	$W$ (gr)	455.8		459.6		456.8				
	<b>internal leaf</b> $f_t$ (MPa)	1.32		1.18		1.10		0.11	1.20	9.04
	$f_c$ (MPa)	2.85	2.76	3.01	3.03	3.07	2.52	0.21	2.87	7.38

Table I- 11 Test results of mortar used in the specimen SIF(CTRM)-I-2L(NC)-B

		S1		S2		S3		S.D	Average	C. o. V (%)
<b>SIF(CTRM) -I-2L(NC)-B</b>	Slump	165								
	$W$ (gr)	454.0		445.1		438.3				
	<b>external leaf</b> $f_t$ (MPa)	1.96		1.80		1.70		0.13	1.82	7.30
	$f_c$ (MPa)	3.97	3.71	4.11	3.95	3.93	4.19	0.16	3.98	4.15
		S1		S2		S3		S.D	Average	C. o. V (%)
<b>SIF(CTRM) -I-2L(NC)-B</b>	Slump	157								
	$W$ (gr)	471.0		477.1		461.1				
	<b>internal leaf</b> $f_t$ (MPa)	2.35		2.53		2.65		0.15	2.51	6.02
	$f_c$ (MPa)	6.35	6.03	5.59	6.12	6.64	6.35	0.36	6.18	5.81

Table I- 12 Test results of mortar used in the specimen SIF(CTRM)-O-1L-B

		S1		S2		S3		S.D	Average	C. o. V (%)
<b>SIF(CTRM) -O-1L-B</b>	Slump	162								
	$W$ (gr)	465.1		462.4		464.5				
	$f_t$ (MPa)	1.41		1.54		1.38		0.09	1.44	5.89
	$f_c$ (MPa)	4.14	3.95	4.42	4.36	4.28	4.56	0.22	4.29	5.04